Cranfield
UNIVERSITY


**ADEL GHENAIET**

# TURBOMACHINERY PERFORMANCE DEGRADATION DUE TO EROSION EFFECT

SCHOOL OF ENGINEERING

Department of Power, Propulsion
& Aerospace Engineering

**PhD THESIS**

Cranfield
UNIVERSITY

SCHOOL OF ENGINEERING

Department of Power, Propulsion
& Aerospace Engineering

**PhD THESIS**

Academic Year 2000-2001

**ADEL GHENAIET**

# TURBOMACHINERY PERFORMANCE DEGRADATION DUE TO EROSION EFFECT

Supervisors: Prof. R.L. Elder
Dr. S.C. Tan

September 2001

This thesis is submitted in fulfilment of the requirements
for the degree of Doctor of Philosophy

# ABSTRACT

Erosion of gas turbines operating in sandy or dusty environments can result in serious damage to the engine components, particularly the compressor unit. This phenomenon is a result of the ingestion of the sand particles into the engine and their consequent abrasive impacts on the blade surfaces. In order to understand the mechanism of sand ingestion and the resulting performance degradation, a general methodology has been developed for predicting the trajectories of particles, the erosion rates and blade profile changes, with predictive capabilities for performance degradations within more general configurations of turbomachines. This methodology was applied to an axial fan with upstream guide vanes (contra whirl) and was supported by experimental results.

The numerical models for calculating the particle trajectory are based on the Lagrangian tracking technique and the eddy lifetime concept. The turbulence effect is assumed to prevail as long as the particle eddy interaction time is less than the eddy lifetime, and the displacement of a particle relative to the eddy is less than the eddy length. The flow field was solved separately using the Navier-Stokes finite volume flow solver " *TASCflow* " commercially available from *ASC*. The governing equations of the particle motion are solved using the Runge-Kutta Fehlberg technique. The tracking of particles and their locations is based on a finite element interpolation method. The developed Fortran code for predicting particle trajectory and erosion due to particle impact accounts for different types of boundary conditions and handles different frames of reference. The fragmentation of particles after rebound was also implemented.

The number of particles seeded upstream of the IGV blades can be determined either by a user defined concentration profile or by a measured concentration profile. Also, particles can be seeded separately in a group at a release position. In the present study, the concentration profile and the initial particle velocity and angle of particle spread were determined from a laser transit anemometer. Two types of particles were used, a narrow size bandwidth (150-300micron) quartz particle and MIL-E5007E quartz particle, both of which have a normal distribution. The global rate of erosion, the reduced mass of blades and the changes of the blade geometry were predicted and compared with experimental results at different concentration levels.

The baseline axial fan characteristics were measured at different mass flow conditions at a constant speed of rotation. To assess the effects of erosion, the characteristic measurement was repeated after each step of sand ingestion. The predicted aerodynamic performance; adiabatic efficiency, pressure rise coefficient and stall margin before and after erosion degradation were also determined from a developed Fortran program, which is basically a mean line method that uses advanced correlations for aerodynamic losses.

Prediction of the particle trajectories show that high numbers of impacts (and maximum erosion) occurred near leading edge and tip region, which were also borne out by locally injected sand tests. The global rate of erosion and the consequent changes

of the blade geometry were also predicted and compared with experimental results. The erosion pattern at high concentration of MIL-E5007E sand particles depicts net loss of material over the leading edge and the tip corner. The tip clearance increased markedly with a rounding of blade leading edge, which is the main cause of the decrease in efficiency, pressure rise, and surge margin. A parametric study with turbulence and fragmentation effects show that both parameters can influence the erosion rate and blade geometry deterioration. The results of the aerodynamic performance simulation using mean line method, which includes an erosion fault model, show good agreement with experimental results.

# ACKNOWLEDGEMENTS

I would like to thank Professor Robin Elder and Dr Jason Tan for their supervision and invaluable encouragement and support over the four years.

Also I would like to thank Dr Antonios Tourlidakis and Dr Aly El-Zaafrani for their help.

I am indebted to Mr Bernard Charnley, Mr Peter Timmis, Mr Dick Luterly and Mr Len Struthers for their technical supports in doing my experimental work.

My deep gratitude to Professor Farhang Bakhtar and Dr Paul Ivey for reviewing my Thesis

# CONTENTS

## FIGURES



## TABLES



## FLOWCHARTS

# LIST OF ILLUSTRATIONS

## FIGURES 2

## FIGURES 3

## FIGURES 4

## FIGURES 5

## FIGURES 6

## TABLES

## FLOWCHARTS

# NOTATIONS

| | |
|---|---|
| A | area |
| AR | aspect ratio |
| ASC | Advanced Scientific Computing Ltd |
| C | concentration |
| $C_h$ | effective static pressure rise |
| $C_p$ | static pressure rise coefficient, specific heat constant |
| c | chord |
| $C_D$ | drag coefficient |
| $C_L$ | lift coefficient |
| $D_{eq}$ | equivalent diffusion factor |
| d | diameter |
| el | element |
| f | frequency |
| F | force |
| h | height, depth of penetration, manometer level |
| H | enthalpy, shape factor |
| i | incidence angle |
| I | current |
| Ifind | programmed function for element direction searching |
| Ifix | Fortran intrinsic function |
| Inter | outlet plane from the blade passage at the interface plane |
| J | Jacobian |
| J1 | Hub to shroud vertex line at mid blade pitch J=1 (figure 2-5) |
| J10 | Hub to shroud vertex line passing by node J=10 in the wake (figure 2-5) |
| J30 | Hub to shroud vertex line passing by node J=30 in the wake (figure 2-5) |
| K | profile correction factor |
| $K_b$ | blockage factor |
| k | turbulent kinetic energy |
| ks | sand roughness |
| L | characteristic length |
| l | length, length scale |
| m | mass flow rate, deviation angle parameter |
| $M_{ts}$ | total mass of sand per second and per centimetre square |
| N | number, normal vector, shape function, rotation per minutes |
| P | pressure |
| Q | total amount of sand per second |

| | |
|---|---|
| q | dynamic pressure head |
| R | electrical resistance |
| Ra | centre line averaged roughness |
| Re | Reynolds number |
| r | radius |
| o | throat spacing |
| t | time, thickness |
| T | temperature |
| Ti | turbulence intensity |
| Trail | outlet plane passing at blade trailing edge |
| s | slip factor, pitch |
| $S_M$ | surge margin |
| u' | turbulent velocity |
| U | peripheral velocity |
| V | absolute velocity, voltage |
| W | relative velocity, electrical power |
| z | axial direction |

***Greek letters***

| | |
|---|---|
| $\alpha$ | absolute flow angle |
| $\beta$ | relative flow angle, particle impacting angle |
| $\delta$ | deviation flow angle |
| $\delta^*$ | boundary layer displacement thickness |
| $\varepsilon$ | erosion parameter (mg/g), rate of dissipation of turbulence |
| $\varepsilon_0$ | overall erosion parameter (mg/g) |
| $\phi$ | flux, flow coefficient |
| $\eta$ | efficiency, first local co-ordinate |
| $\gamma$ | gas constant |
| $\Gamma$ | flux function in the finite volume descritisation, circulation |
| $\omega$ | loss coefficient, speed of rotation (rd/s) |
| $\Omega$ | work done factor |
| $\Pi$ | pressure ratio |
| $\rho$ | density |
| $\nu$ | kinematic viscosity, endwall boundary layer tangential force thickness |
| $\mu$ | dynamic viscosity |
| $\theta$ | tangential co-ordinates |
| $\theta^*$ | momentum thickness |
| $\psi$ | pressure rise coefficient, stage load coefficient |
| $\sigma$ | variance, solidity |
| $\xi$ | stagger angle, random number, second local co-ordinate |
| $\zeta$ | loss coefficient , third local co-ordinate |
| $\tau$ | relaxation time, tip clearance |

*Subscripts*

| | |
|---|---|
| a | ambient, absolute, axial |
| aer | aerodynamic |
| al | aluminium |
| b | blade |
| c | corrected , choke |
| D | drag |
| e | eddy, eroded |
| eff | effective |
| el | element |
| F | fan |
| f | fluid |
| G | geometrical |
| h | hub |
| i | impact , initial, inlet |
| imp | impact |
| L | local |
| L.E | leading edge |
| IN | input |
| int | interaction |
| m | minimum, mean |
| max | maximum |
| n | nominal, normal |
| p | particle, profile |
| o | outlet, optimum, throat spacing, origin |
| r | radial, relative, rotor, rotation |
| ref | reference |
| R | transit |
| T | tip |
| t | tangential, total, throat |
| T.E | trailing edge |
| te | trailing edge |
| s | stator, stage, shaft, secondary, shroud, stall |
| st | Standard, stainless steel |
| z | axial |
| w | working, wall |
| 1,2 | at impact, at rebound |
| 0,1,2 | inlet IGV, inlet rotor, outlet rotor |
| ' | nominal condition |
| + | relative to the pressure side of the blade |
| - | relative to the suction side of the blade |
| ∞ | upstream condition |

# CHAPTER 1

# INTRODUCTION

## 1.1 AN OVERVIEW ON TURBOMACHINERY EROSION

Gas turbine engines operating in a hostile environment that is polluted with small particles are susceptible to erosion damage. Most of the ingested dust particles are found to have diameter between 0 - 1000μ. Examination of a number of natural dust samples indicates that quartz is usually the most abundant erosive constituent, rarely falling below 70 % by weight (Harris, 1996). Small dust particles less than 5 micron do not erode but tend to deposit on engine components. Dusty environments may be encountered by aircraft at very low flight altitude, or at several thousands feet altitude due to sandstorm in areas like Middle East and North Africa.

Several serious aircraft accidents have been related to jet engines failures, due to operation in particulate environment (Tabakoff, 1987), (Dunn et al, 1996). The danger posed by volcanic clouds to commercial aircraft has been dramatically illustrated during the past ten years, (Hamed and Tabakoff, 1990). Tests performed at the University of Cincinnati by Hamed and Tabakoff (1990) showed that volcanic ash is four times more erosive than quartz particles.

The tendency of an aircraft engine to ingest ground particles during ground operation is a well-known phenomenon. During high power setting at take off, the ground vortex has the capability of picking up particles from the ground, which are then ingested into the engine (Peterson, 1986). Thrust reverser can also blow solid particles into the engine intake.

During take-off or landing, helicopters need to use the effect of the down-wash to create additional lift. The down-wash associated with hover manoeuvre and multiple pick-ups with rotor turning may generate a severe dust cloud around the aircraft (Mann et al, 1994), which circulate up and over the rotor blades to re-enter the circling air from above, inevitably a great deal of dust enters the engine.

Recent experience has emerged from the Gulf conflict. Edwards and Rouse (1994), reported that significant number of helicopter engines suffered severe performance losses during the Desert Storm operation. The RN Sea-king squadron reported a net reduction in service of its helicopters to only 100 hours (Hammick, 1991). In some cases the mean time between engine overhauls was reduced to less than 50 hours (Johannes et al, 1995). Paramour and Jennings (1993) highlighted the need for

fully integrated particle separators on military helicopters. Sirs (1993) pointed out that all UK helicopters were fitted with some types of particle separator during Desert Storm operations, but they were inefficient for smaller particles. Four main types of dust were responsible for the engine degradation; relatively coarse and abrasive sand from inner desert; finer sand found near the coast, coarse red sand found in northern Kuwait, and the pervasive fine dust suspended in the air. The Kuwaiti flown areas were catastrophic for helicopter engines with unexpected effect on helicopters life cycle, curtailing the operational availability and significantly increasing the cost of operation (Paramour and Jennings, 1993).

The intensity and pattern of compressor and turbine erosion are dependent on the physical properties of the impacting particles, concentration, size, velocity and the direction of particle at collision, as well as the blade geometry and its material. If particles are of erosive nature, their impacts can produce severe erosion damage leading to structural failure. The surface quality and the optimised blade profile deteriorates with time when exposed to particulate flow. The profile changes and the increase of surface roughness lead to a decrease in engine performances. In general erosion of blades is classified into primarily and secondary erosion, according to the dynamics of the particles and the flow interaction. The damage of the blades is caused mainly by direct material impingement of large particles, and even by re-circulation of fine particles (1-2μm) through the blade passage in the secondary flow (Neilson and Gilchrist, 1968).

Inspections of several engines in service exhibited deterioration due to ground particles and the major contribution of losses is due to the compressor. As they are located at the front section of gas turbine engines, they naturally suffer more erosion. As particles collide with blades, they break up into smaller ones thereby causing further erosion. The aerodynamic losses due to particle ingestion in the compressor are mostly through an increase in the tip clearance and a degradation of an optimised rotor profile by a reduction in chord length and leading edge tip corner rounding and thinning. The loss in performance is usually a gradual process, but sometimes, drastic loss can be experienced when the structural integrity of the rotor is affected and parts break away (Harris, 1996). Statistical evaluation of flight engines gave the following broad pictures of damage of compressor components due to erosion (Schmucker and Schaffler, 1994): The damage was spread over all stages. Two third of rotor blades suffered erosion at the leading and one third at trailing edge. The change in the tip clearance by 1% was found to reduce the mass-flow and the efficiency by 2%, and the surge margin by 7.5%.

Richardson and Smakula (1979) examined a JT9D turbofan with an extended service usage and investigated the three damage mechanisms that lead to the high-pressure compressor performance deterioration; rotor tip clearance wear, airfoil surface roughness build up and rotor blade contour change. Wulf (1980) related the rate of wear to the time of usage. He claimed that, within 6000 - 8000 hours of engine operation, compressor blades had blunt leading edges with an increased surface roughness. The inspection of a fairly new CFM56 turbofan after particle ingestion showed similar effects on its HP compressor (Peterson, 1986).

In high-pressure turbine blades the erosion damage due to sand ingestion was mainly due to tip clearance and airfoil roughness increases. There were also blade leading edge and tip distress due to internal cooling cavity caused by deposition and blockage (Hamed and Tabakoff, 1990), thus reducing the coolant flow rates (Kuk, 1994), and also glazing of the blades (Kerr, 1989).

In 1998 Pratt & Whitney (Quinn, 1999) investigated a number of JT8D-15 engines in service with the Algerian Airlines and made the following assessments: A total number of 13 engines were found with HP turbine erosion with cooling hole penetration on newly replaced blades (2911 hours with 2447 cycles). The HP compressor blades of these engines were found to have severe erosion (appendix A). Stages 7 through 10 of the HP compressor were scrapped due to severe erosion and missing of material and the rate of erosion reached was 0.003 inch per 1000 hours.

There is an increasing trend toward designing modern engines which are inherently more resistant to the effect of sand ingestion because of the increasing tip speed, reduced blade thickness and tight running clearance making them more prone to erosion damage. The question raised is how to minimise erosion damage of these aero-engines. One solution is to reduce the amount of dust ingested and the other is to coat the blades prone to erosion damage. For helicopters, the integral particle separator was a major innovation in the design. Early systems have barrier filters installed on several engines that remove most of the larger diameter fractions of the dust from the air. However, those filters have not proved to be a success in increasing the engine lifetime. Thus, an inertial particle separator was developed, which works by imparting a pronounced swirl to the entering airflow, centrifuging up to 95 % of the ingested foreign objects in the air stream to the outside (Elsayed and Hegazy, 1995).

For the transport aircraft, the advent of high bypass turbofan engines having larger intakes and long fan blades, increased the frequency of ingested particle (Alge and Moehring, 1994). As it is not possible to install any separator, the only option is either blade coating or optimising the curvature of the annular spacing between the fan exit and the core inlet (Hamed and Tabakoff, 1990). The centrifugal effect of the fan tends to deflect heavy particles through the bypass duct, thus erosion of the core compressor is reduced.

The detection and the evaluation of an engine deterioration rate have always been a big challenge to the gas turbines industry. Methods of deterioration detection fall into two categories, which consist in quantifying the overall engine aircraft performance loss usually in terms of increased fuel consumption or a reduced take off thrust on hot days, then identifying the components responsible for this deterioration. The amount of engine performance loss is a function of the operating load, operating environment and time. The rate of this degradation is expected to correlate with the number of engine throttle movements at high power rather than the hours of running (Crosby, 1986). The degradation in performance is primarily due to increased loss in the rotating components, which results in defects of adiabatic efficiency, flow capacity and pressure rise (Zaita et al, 1997).

The particle dynamics within the blades of a turbomachine depend on the wide variety of flow components. First of all large axial, radial and centrifugal pressure gradients exist within the flow passages due to the turning of the fluid within the blades row. Secondly, this turning redistributes the incoming vorticity field and generates cross flows (Japikse, 1976). There are also a wide variety of viscous flow phenomena existing in the blade passages. Primarily there are the boundary layers, which exist on all blade and endwall surfaces. When pressure gradients are strong, separations can occur. Also, there are regions of wakes developing downstream the blades trailing edges. All these complex flow features do affect the trajectories of particles, their impact locations and the whole operation of the turbomachine.

Particles ingestion not only degrade the aerodynamic performance of optimised compressor blades but also aggravate the tendency of the boundary layer to separate thus affecting the stability and the operating range of compressors. The manifestations in sand ingestion, which can reduce engine stability (Edwards and Rouse, 1994) are as following: By compressor efficiency reduction due to eroded profiles the turbine temperature should increase to produce a constant power, as a consequence the line of operation is higher and closer to the surge line. Similarly if the efficiency of a turbine is decreased, or its nozzle throat is reduced due to glazing the operating temperature increases though, the operating line rises and may reach the surge limit.

## 1.2 REVIEW ON INVESTIGATION OF TURBOMACHINERY PERFORMANCE DEGRADATION

The following sections give a review of the past and current methodologies on the flowfield computation, particle trajectory, turbulent effects, erosion and particle rebound modelling. It also includes a review of the experimental and numerical techniques on the aerodynamic performance degradation due to sand ingestion into a turbomachine.

The use of traditional procedures based on experiments to assess engine life and performance degradation is usually very expensive and reveals limited information of individual components. It is therefore vitally important to be able to predict areas prone to erosion so that lifetime can be extended through the application of special coatings depending on the application of the turbomachine.

The use of simulation to study erosion phenomena is sometimes used in the design of new engines. Most of the simulation programs to compute particle trajectory are based on Lagrangian tracking models. These models, when combined with CFD tools and erosion models will give locations of impacts and the amount of erosion.

The prediction of blade erosion in multistage turbomachines presents a very difficult task, because it involves many factors such as; the flow conditions, stator and rotor relative position, blade geometry, particles and blade materials and particle rebound characteristics (Hamed and Fowler, 1983), (Grant and Tabakoff, 1975).

### 1.2.1 Flowfield Solving Techniques

Historically a number of approaches have been used to solve flow field through a turbomachine. Singularity methods were often used to compute two-dimensional incompressible potential flow (Gostelow, 1973), (Perkins and Horlock, 1975). The secondary flow theory was developed to predict three-dimensional rotational flow in blade cascade (Horlock and Lakshminarayan, 1976). During the sixties finite difference approaches were used to calculate two dimensions compressible inviscid flow. Both streamline curvature and stream function approaches were applied on the meridional and blade to blade flow surfaces by Katsanis and McNally (1969) to obtain a quasi three-dimensional solution. Later Katsanis (1970) developed a method for calculating transonic velocities on a blade-to-blade stream surface of a turbomachine applicable for axial, radial or mixed flow turbomachine. This program has been used extensively by Tabakoff and Hamed when predicting particle trajectory within turbomachinery blades (Tabakoff, 1984).

A great deal of progress has been made for the development of the solution of potential equation (Habashi, 1980), (Hafez et al, 1979), where the finite difference (Dodge, 1976), (Ives and Liutermoza, 1976) and the finite volume or the finite element method were applied to discretise the potential equation to obtain a set of algebraic equations (Caughey and Jameson, 1979), (Dulikravich and Caughey, 1980).

The time-marching methods are well-established for solving Euler equations which constitutes the highest level of approximation of non viscous flows, and they were used to solve both two-dimensional and three-dimensional transonic flows, (Denton, 1975), (Denton and Singh, 1979), (Ucer et al 1989). An alternative approach to the time marching procedure for the solution of the steady state time averaged Navier-Stokes equations is the, so called, 'pressure correction' approach. Several pressure correction strategies have emerged, which vary in the way of deriving the process for the pressure field computation. One the most extensively used pressure correction techniques is the SIMPLE algorithm of Patankar and Spalding (1972). The SIMPLE algorithm was later improved by new version of SIMPLER Patankar (1980), and PISO (Issa, 1986).

Recently, a commercial code TASCflow developed by the Advanced Scientific Computing Ltd (1995) has extensive capabilities to deal with different turbomachinery applications. This code solves for real flows through blade passages by including a variety of boundary conditions, tip clearance and stage interfaces. TASCflow is a finite element based finite volume method, such a combined technique retains much of the geometric flexibility of finite element method as well as the important conservation properties of the finite volume method, and models the equations for the conservation of mass, momentum and energy in terms of the dependent variables; velocity, pressure and enthalpy.

### 1.2.2 Simulation of particle trajectory

The prediction of particle trajectories and blade erosion in turbomachinery depends on many factors such as; the rotational speed, blades row location, blade geometry and its material, particle characteristics and flow conditions (Hamed, 1988a). Three dimensional particle trajectory calculations through axial flow turbomachines were first reported by Hussein and Tabakoff (1973). Later, Hussein and Tabakoff (1974) developed a code for predicting three dimensional particle trajectories through rotating and stationary turbomachinery blade rows. The particle trajectory calculation consisted of the numerical integration of three equations of motion by the numerical technique known as ' Hamming predictor corrector '. The results show many particles impacting the blade leading edges, pressure sides and the trailing edges. Another integration technique consisted of the piece-wise exact solution PES method, with a set of linearised and uncoupled equations and was used by Menguturk et al (1986) to solve particle trajectory in a multistage turbine. The erosion pattern in twisted guide vanes was first studied by Hamed and Fowler (1983) and Hamed (1984). In such a configuration, the maximum erosion by larger particles was located at the hub near the trailing edge. The hub and tip contouring combined with the twisted vanes produced large radial and axial acceleration for the large particles, with a centrifugation effect. The impact locations and the erosion pattern were found to be dependent on the location of the concerned stage, but the impacts on the blade suction surfaces were found to be insignificant (Tabakoff, 1987). Tabakoff and Hamed (1986) working on a two-stage gas turbine demonstrated that the magnitude and the direction of the particle velocities as they enter subsequent blade rows are strongly affected by their size. The results show that erosion damage generally increases with increasing particle diameter and density, flow turning, flow velocity, and with decreasing blade size.

The equations of motion of a solid particle were solved iteratively using Runge Kutta Felhberg method in a predefined flowfield of a three dimensional gas turbine intake by Tan (1984). The particle tracking in the computational grid was based on the values of local co-ordinates for each particle crossing from one element to another.

Particle trajectories in radial compressors are consistently different from those in axial flow machines due to the nature of the flow and the direction of centrifugal forces. Larger particle sizes have almost a straight path after collision, while the smaller ones after collision, they follow the main gas flow. On the blade pressure side the collisions are distributed over the entire surface with largest impacts in the middle area. But on the suction side the collisions are mainly closer to the blade leading edge and impeller hub is subjected to fewer collisions than the impeller casing (Elfeki and Tabakoff, 1987). Much higher erosion rates are observed in radial inflow turbine due to higher particle concentrations consistently impacting smaller metal area due to the very high centrifugal forces and the direction of the flow (Eroglu and Tabakoff, 1990). Even particles smaller than 5μm cause serious loss over the engine life as claimed by Montgomery and Clark (1962).

For the predictions of particle laden turbulent flow, two common approaches are usually employed; Eulerian and Lagrangain approaches, which differ from each other in handling the dispersed phase. The Eulerian approach treats both the continuous and dispersed phase as two interpenetrating continua where the conventional time averaged

transport equations for the additional phase are solved to predict the field distributions of momentum and volume fraction of each phase (Lixing, 1993). On the other hand the Lagrangian approach handles discrete particle dispersion using a stochastic method by tracking a large number of individual particle trajectories to achieve a stochastically significant solution (Chen and Pereira, 1995). A simple comparison between these two approaches indicates that the Lagrangian method is somewhat more economical (Abbas et al, 1981), and is able to handle more detailed physical description of the particle phase, such as interaction of particles with the walls. Furthermore, the Lagrangian model is more stable and easier to apply than the Eulerian model especially to erosion prediction. On the other hand, the Eulerian description is favoured by high concentrations of particle phase (Humphrey, 1990).

The behaviour of dispersed particles laden turbulent flow depends largely on the concentration and size of particles with respect to the scale of turbulence of the fluid. At high concentrations, particle interactions are not only limited to direct physical contact but they also have collective influence on the fluid flow. Non interacting particles are assumed when the ratio of the solid particles volume to the total volume is less than the value 0.001 (Humphrey, 1990). According to Upton (1974) the concentration of particulate found in most countries ranges from 0.01-0.1 ppm. In desert areas, however, the concentration increases from 0.1 to 700 ppm.

The interaction between turbulent eddies and immersed small particles is referred to as turbulent particle dispersion. The current modelling methods for turbulent particle dispersion are based on several assumptions with regards to the nature of turbulence (Hinze, 1959). The lifetime of an eddy is the time interval for which the eddy maintains its original size before it completely dissipates due to the convection of the vorticity and the mechanism of vortex stretching. Taylor was one of the early researchers who attempted to mathematically describe particle dispersions in turbulent homogenous flows (Shirolkar and Mcquay, 1998). Methods based on his approach have been successfully used to model dispersions of particles. The inertial force of a particle tends to dampen the fluctuations in the velocity within an eddy, depending on the characteristic relaxation time according to Shirolkar et al (1996). Gosman and Ioannides (1981) defined the minimum time taken by a particle to cross an eddy, which is dependent on the relative velocity between the particle and the fluid flow.

The Lagrangian models are classified into two categories; models based on the eddy lifetime concept, Gosman et al (1980), Chen and Crowe (1984), and the time correlated dispersion models, Zhuang et al (1989), Chen and Pereira (1995). One of the early stochastic models of turbulent dispersion is due to Duckowicz (1980). Gosman et Ioannides (1983) developed a stochastic method in the spirit of Dukowicz's. However, it differs in the details of the gas-phase turbulence treatment and the manner in which it is thought to interact with the droplet motion. This interaction is held to occur over a time interval that is the minimum of the turbulent eddy lifetime and the residence time of particle (droplet) in the eddy. The turbulence is assumed to be isotropic and have a Gaussian probability distribution function PDF. The fluctuating fluid velocity along the particle trajectory is randomly sampled from a Gaussian PDF and the particle is allowed to interact with an eddy over a time of interaction. A particle will remain trapped within

an eddy until the turbulent structure around the fluid particle vanishes by exceeding the random lifetime of the fluid domain.

In the original deterministic dispersion model no particle turbulent diffusion was assumed, but some authors included recently the particle diffusion effect by introducing the concept of particle drift force (Abbas et al, 1981). A complete review of the stochastic trajectory model is given by Crowe et al (1991) and Elghobashi et al (1994).

### 1.2.3 Particle rebound after impact

The restitution factors are defined as the ratio of the particle velocities and angles before and after impact. Hussein and Tabakoff (1973) were the first to investigate the restitution characteristics of non-erosive solid particles using high-speed photography. Grant et al (1974) determined the rebound characteristics of high-speed solid particles using erosion wind tunnel. Later, Tabakoff et al (1996) gave rebound factors for 150 μm sand particles impacting typical turbomachinery target materials namely; 2024 Aluminium, TiAl-4 Titanium, AM355 stainless steel and Rene41. Similar experiments were carried out by Tan et al (1994) at Cranfield University using a transit laser anemometer to test the rebound factors of different materials. In these experiments the particles at impacts were separated from air by a combination of the Coanda effect and the particle inertia.

The impact at a given velocity and angle of impingement is in practice randomised by several factors such as; the non-homogeneous hardness, irregularity in shape and the target roughness (Wakeman and Tabakoff, 1983). In general the local angle of impact between the small particles and the eroded surface may deviate considerably from the approach angle before impact (angle of velocity close to wall) (Finnie, 1958), (Rao and Buckley, 1985). For reliable numerical predictions, an appropriate modelling of the collision process of spherical or non-spherical particles with smooth or rough walls based on a purely empirical approach should be extended in some way to account for stochastic effects. Among them are; wall roughness and non-sphericity of particle, Sommerfield and Huber (1999). The rebound characteristics are distributed around their average by approximated normal distributions. The width of these distributions can be described by their standard deviations. Recent works by Tabakoff and Hamed (1996) and Tan et al (1994) gave estimates of mean and standard deviations for the restitution factors for different materials used in turbomachinery. Details of these published restitution factors are available in appendix C.

### 1.2.4 Erosion mechanism and prediction

The studies concerning erosion are predominately experimental. In more recent investigations, insight into actual mechanism of erosion has been obtained by examining the target surface using metallographic techniques and electron microscopy (Tabakoff and Balan, 1983a), (Rao and Buckley, 1985). Finnie (1960) carried out tests on a range of materials under controlled conditions, and concluded that the amount of surface material

removed by solid particles in a fluid stream is dependent on the conditions of the fluid flow and on the mechanism of material removal. The ductile materials undergo weight loss by a process of plastic deformation in which material is removed by displacing or cutting action of the eroding particles. While in brittle materials, material is removed by intersection of cracks, which radiate out from the point of impact of the eroding particle. Tilly (1974) and Bitter (1963) showed that erosion of ductile materials might occur in two stages, where an indentation is firstly produced. Then, the plastic deformations at the exit side of the impact craters form lips followed by a break up of fragments from the hardened lips due to tangential component of impinging velocity.

Tabakoff and Balan (1981) and Tabakoff et al (1979) revealed that the increase in surface roughness is associated with ripple formation due to eroding particles. At very low quantities of impacting particles the surface is roughened due to the cutting and the plowing tracks. As the amount of particle increases craters join together to form a well-defined ripple pattern. The value of the surface roughness for various angles of attack reaches a steady state at high and low angle of attack, with a maximum between 20 to 45 degree (Tabakoff and Balan, 1983a).

Erosion phenomenon is strongly dependent on particle size. The larger the particle diameter, the smaller is the degree of cutting wear, and greater the degree of deformation wear becomes, (Zhong and Kiyoshi, 1996) referred to Hashimoto (1974). The erosion rate increases with an increase of diameter, but there is a limiting value depending on the elastic and plastic characteristics of the material and wearing environment (Zhong and Kiyoshi, 1996).

The erosion rate was correlated against the hardness of the erodent by Goodwin et al (1984). Rao and Buckley (1985) meanwhile, provided a useful correlation between erosion rate and material properties such as; hardness, strain energy, melting point and the exposure time. The erosion rate defined as volume or mass of material removed per unit mass of impacting particles is a function of the particle velocity, angle of impingement and target material. The erosion of ductile materials increases with the angle of attack with maximum erosion occurs around 20 to 25 degrees. Finnie et al (1967) firstly reported basic data on erosion obtained from sand blasting erosion test rig.

The development of erosion prediction models in gas turbines began with several experiments to obtain the basic erosion data. Sage and Tilly (1969) and Tilly (1969) were among the early researchers who attempted to quantify the erosion effects in turbomachinery. Two test facilities were built at Cincinnati University: The first one was designed to obtain the basic erosion data such as particle impact and rebound characteristics over a stationary specimen. The second test facility was designed to simulate and to measure the erosion of stationary and rotating blades (Grant and Tabakoff, 1975), (Tabakoff and Hamed, 1977).

The quantifying erosion data was not directly applied to real turbomachines until Grant and Tabakoff (1974) generated an erosion model and verified it on an axial compressor stage. The erosion model developed by Grant and Tabakoff (1975) used 2024-aluminium alloy with silica sand as the abrasive particle. The rate of erosion is expressed as milligrams of removed material divided by grams of impacting particles.

The erosion process was shown to depend on two mechanisms; one predominant at low impact angle and the other at high impact angle. Tabakoff et al (1974) produced a correlation for a variety of metals used in turbomachinery design, given in details in appendix D.

Many aspects of the erosion process require deep investigation, they concern particle - surface interaction, particle fragmentation, secondary flow and boundary layer effects. The strong viscous effect in boundary layers alters the relative velocities of particles, and hence the erosion. Under some conditions related to boundary layer thickness, normal velocity component and particle diameter, some particles will not penetrate deeply to strike the surface (Humphrey, 1990). Wenglarz (1982), showed a significant boundary layer reduction of erosion for particles less than 4μm. Secondary motion arising from lateral curvature of the main flow can significantly affect the velocity and erosion potential of small particles. Masson and Smith (1972) demonstrated this effect in various curved flow configurations. Also, Hamed (1989) and Ling and Huang (1986) show that secondary flow significantly influences the dynamics of fine particles and tends to transport them in the end wall region towards the trailing edge suction side. Consequently, the predicted erosion including secondary flow showed maximum erosion at the trailing edge. Detailed discussions of the effect of secondary flow on particle paths in curved channels and blade cascades are related to Ulke and Rouleau (1976).

On the effect of temperature on erosion behaviour, several investigators have argued that localised high temperature conditions created by high-speed impacts can soften and even melt surfaces at the impact locations. Humphrey (1990) showed that, increasing the carrier gas temperature tends to reduce the particle velocity and angle of impact. Erosion at smaller impact angle but at high flow temperature is similar when particle has larger impact angle but at low temperature. Tabakoff and Hamed (1988) performed a series of experiments in a high temperature erosion wind tunnel. They found that under hot flow conditions, surfaces were subjected to more than twice the erosion encountered under cold flow conditions. The influence of temperature should be accounted for through a correction parameter when calculating the erosion rate, (Tabakoff, 1988).

Particle fragmentation is a known phenomenon, however, only a few authors have published results due to the difficulties in sampling particles in multiple conditions of testing. Particle fragmentation and secondary erosion have been discussed in various works (Neilson and Gilchrist, 1968a), (Neilson and Gilchrist, 1968b), (Tilly, 1973) and (Goodwin et al, 1984). Tests show that under certain conditions a particle shatters into smaller fragments upon striking the surface and fragments move radially outward, causing what has been called by Tilly and Sage (1970) "secondary erosion". The smaller fragments may well be the cause of additional and often critical erosion at previously unknown locations through repeated or multiple impacts. The size of a particle, its impact velocity and angle are the major contributors for the fragmentation. For each material there is a threshold size below which fragmentation does not occur. Tan and Elder (1992) tested the fragmentation of three quartz particle sizes at three velocities and angles of impingement against several target materials.

### 1.2.5 Performance degradation testing and prediction

Motivated by the disastrous nature on engine performance degradation due to dust ingestion, a programme designed to ascertain the vulnerability and survivability of airborne gas turbine engines was initiated at Calspan Advanced Technology Center (Dunn et al, 1987). Where a unique test facility for a full-scale engine research technology was built to test aero-engines according to the procedure of military specification MIL-E5007D (Dunn et al, 1983).

In standard erosion tests of gas turbines, the dust concentration is usually about $0.2g/m^3$, but higher concentrations of $0.7g/m^3$ have been used to simulate severe conditions, eg a dust cloud (Tan, 1988). In some simulation models where axial fans are involved, the particle concentration distribution used tends to follow the approach adopted by Rolls-Royce for its helicopter engine environmental protection programme (Kerr, 1989), where the peak of concentration is at 75% of the vane height, appendix B.

Usually the erosion of the engine components is associated with deterioration of the blade profiles such as; blunting of leading edge, increasing tip clearance, thinning of the trailing edge and an increase in the overall surface roughness. Balan and Tabakoff (1984) have reported detailed investigation of the effects of erosion on the blade shape, the surface roughness and their consequence on the aerodynamic performance of an axial compressor. The losses are either permanent or temporary or both, depending on the nature of particles (Tabakoff and Balan, 1981). The temporary loss of performance was measured experimentally and was shown to be dependent on the rate of particles to the mass flow (Tabakoff et al, 1976). If particles are erosive they cause a permanent loss of performance due to the change in the aerodynamic characteristics of the blade (Hamed and Fowler, 1983). The change in the airfoil and its surface roughness due to dust ingestion were found to vary with the blade loading (Tabakoff et al, 1980). In order to estimate the effect of erosion on blade geometry, Schmucker and Schaffler (1984) defined a geometry loss parameter and related the drop of axial compressor performances to it.

Tabakoff and Balan (1983b) carried out several experiments on an NACA axial flow compressor to study the erosion effect on the aerodynamic performance. The blades made from aluminium were tested first in a low speed cascade tunnel. The erosion damage by air laden solid particles resulted in a change in the airfoil geometry and the quality of the surface. The blade leading edge and the pressure side were severely eroded with an increase in surface roughness, as a consequence the pressure distribution around the blade profile changed, which caused an early transition to the boundary layer. The blade suction surface remained unaffected for most of the experiments. Three distinctive regions of loss in efficiency against sand mass flow parameter were revealed by Tabakoff and Hamed (1983). At first there is a steep increase in loss followed by a plateau, then increasing again. The erosion of turbomachine blades differs significantly from the cascade erosion (Hamed and Fowler, 1983) due to several factors such as; the particle blade impact locations as well as their impacting velocities and impingement angles relative to the blade surfaces. The tests of an axial compressor carried out by Tabakoff and Balan (1983c) showed that loss in efficiency was related to blade leading edge and increased tip leakage due to severe erosion. They also noticed that there is no change in the slope of the stage performance,

but rather, there is an overall shift of the pressure coefficient and efficiency versus flow coefficient. When this compressor was subjected to an ingestion of 25 kg of sand, a noticeable deterioration of 3.5% in stage loading coefficient and 4% in efficiency over 605 seconds was measured (Tabakoff, 1986).

Elfeki and Tabakoff (1987) produced the first erosion tests and predictions for centrifugal compressors. Palmer and Waterman (1995) performed erosion tests on backswept splitter-bladed impellers, and concluded that the leading edges of the first stage impeller blades were eroded on the pressure side with the highest erosion near the hub. But the erosion of the second stage impeller was negligible due to particle fragmentation in the first stage. Mann and Warnes (1994) described the mechanical failure of a number of impeller vanes of the GEM turboshaft engines, where some impeller blades had simply sheared away from the tip to about two thirds of vanes heights.

Schwind and Mc Millan (1982) have given the details necessary for the simulation of the effects of erosion on multistage compressors by providing both new and eroded blade profile measurements after an extensive wear in airline service. In such simulations both stage characteristics and compressor map were calculated by the stacking technique. To quantify the loss of aerodynamic performance, the compressor stage performance map is extrapolated into a complete compressor map in this manner: The deteriorated stage performance is determined from loss correlation and the measured blade erosion. Then, the deteriorated stage performance maps are stacked to arrive at an overall deteriorated compressor map (Tabakoff et al, 1990).

The overall performances of a gas turbine engine are governed by the performance of its individual components. If a fault occurs in an individual component, then it affects the overall engine performance, which can be evaluated by a matching calculation procedure (Zaita et al, 1997). Earlier workers used the scaling of the individual component characteristics to represent the performance degradation of the whole machine. The current trend (Lakshminarasimha and Saravanmuttoo, 1986), (Aker and Sararanamutto, 1989), (Muir et al, 1988) is to develop procedures to scale the sub-components such as compressor and turbine stages and to combine them together to develop a deteriorated component performance map.

## 1.3 THESIS LAYOUT

The objective of this study is to develop and validate a numerical model for predicting aerodynamic performance degradation in an axial fan. The methodology adopted is based on an experimental and numerical prediction of particle trajectories (through an axial fan stage), erosion, blade geometry deterioration (due to particle impacts) and the resulting aerodynamic performance degradation.

A complete solution for the flowfield within axial fan blading is presented first, then, followed by the prediction of particle trajectories, location of impacts and erosion, which are validated by the local injection of sand particle tests. Also, the prediction of

blade geometry deterioration and the aerodynamic performance degradation are validated against the global injection tests results.

Following the introductory Chapter 1, Chapter 2 describes the full gas flow solution using the code TASCflow, with a detailed description of the flowfield features within the axial fan blades. The choice of this code was made as it is a representative of all commercial codes that are finding increasing favour in the field of turbomachinery.

A detailed modelling of particle dynamics in axial turbomachinery airflow is presented in Chapter 3. The Lagrangian model was used to solve separately the path of solid particles, taking into account all the flow components and their effects on a particle trajectory. Also, the detailed description of the developed code to solve particle trajectory using a Lagrangian model based on the eddy lifetime concept in multiple frames of reference is thoroughly discussed in this chapter. The erosion prediction and the resulting blade geometry deterioration are presented in Chapter 4.

The theoretical study was complemented by experimental work to validate the numerical simulation results. A transit laser anemometer was used to measure the different distributions of particle concentrations and also for particle tracking. A full test schedule was traced to assess the performance and the geometry degradation due to dust ingestion using the narrow bandwidth size (150-300micron) and (0-1000micron) MIL-E 5007E sand particles at different concentration levels. Details of the experimental procedure and the results found are presented in Chapter 5.

A full description of a mean line procedure and its implementation to predict aerodynamic performance degradation is discussed throughout Chapter 6. The results of this method are also supported by CFD computations for the eroded rotor blade. Finally, a methodology for the prediction of the axial fan component life is also presented.

# CHAPTER 2

# COMPUTATIONAL FLUID DYNAMICS FOR THE AXIAL FAN

## 2.1 INTRODUCTION

The flowfield within the blading of the axial fan is solved by the code TASCflow, which uses a full discretisation for the averaged conservation equations of Navier Stokes within finite volumes. This code, commonly used for turbomachiney applications, is capable of predicting the flow phenomena (e.g. secondary flow, and tip clearance flow), which are known to affect erosion in the tip and near the trailing edge of the rotor blades. The complete flowfield solution as obtained by TASCflow contributed in improving the particle trajectory computation results.

The aerodynamic parameters related to IGVs and rotor blades are derived from mass averaging of the flow properties upstream and downstream the fan stage. The flow information and the computational geometry data required by the particle trajectory code are taken from the CFD results and arranged in separate data files.

Presented in the following sections are; the flow solving technique, computational grid, boundary conditions, flowfield results and their post-processing in order to determine the aerodynamic parameters and the axial fan stage performance, then followed by a discussion.

## 2.2 SOLVING TECHNIQUE

The time averaging turbulent flow Navier Stokes equation is solved using CFD code TASCflow, which solves for real flows through turbomachinery blading including a variety of boundary conditions and tip clearance flow. TASCflow models the equations for the conservation of mass, momentum and energy in terms of the dependent variables such as; velocity, pressure and enthalpy. The fluctuating components are not solved directly but they are expressed in terms of mean fluctuating values. TASCflow is a finite element based finite volume method, such a combined technique retains much of the geometric flexibility of finite element method as well as the important conservation properties of the finite volume method (TASCflow, 1995). The finite volume method proceeds by integrating the Navier Stokes averaged values using the Gauss theorem as follows.

$$\frac{\partial}{\partial t}\left(\int_{v}\rho\phi dv\right)+\int_{s}\rho u_j\phi dn_j=\int_{s}\Gamma_{eff}\left(\frac{\partial\phi}{\partial x_j}\right)dn_j+\int_{v}S_\phi dv \qquad 2\text{-}1$$

The flowfield within the blades of the studied axial fan stage shown in figure 2-1 and figure 2-2, is solved in a relative frame of reference, where it is assumed to be steady. All the diffusion terms are evaluated by summation of the derivatives of the shape function. The advection terms are computed by using a linear profile scheme (LPS) and a mass weighted skew upstream differencing scheme, which incorporate the physical advection correction (MWS - PAC).

The computational domain consists of an extended inlet nose sector, an inlet guide vane, a rotor blade and a step-discharging duct sector. Four attached sub-grids and three interfaces constitute the global three-dimensional H type structured grid. Figure 2-3, figure 2-4 show respectively mid span and meridional grid surfaces. The dimensions of the sub-grids according to the numbering order I J K, are; 35x29x24 for the extended inlet sector, 60x39x24 for the IGV, 60x39x30 for the rotor, and 40x29x50 for the discharging duct. A total number of 208720 mesh points are involved in generating the global computational grid. Dense clustering around the IGV and rotor blades and near the hub and shroud is used for a better resolution of the boundary layers and the wakes from the blades trailing edges as shown in figure 2-5 and figure 2-6. Six grid lines are distributed in the tip clearance to capture the leakage and the vortex formation from the blade tip, figure 2-7. The figure 2-6 shows an average stage interface grid where the flow parameters are passed from stator to rotor as averaged values, and the relative initial rotor blade position is at mid of IGV pitch. Another type of interface known by frozen stage interface where the flow parameters are passed instantaneously from stator to rotator is also used, and the rotor blade leading edge is in the wake of the IGV blade, figure 2-3.

The following boundary conditions are used (figure 2-8):

- The inlet and outlet surfaces are boundaries through which mass flow, momentum and energy are transferred. The code allows several combinations of boundary conditions for the inlet and outlet of the computational domain. In case this study, the following physical boundary conditions; constant total pressure and mass flow boundary conditions are applied at the inlet and at outlet of the computational domain respectively.
- The rotor blade and hub constitute the rotating surface.
- The IGV blade, shrouds and extended computational domains are stationary.
- The meridional hub to shroud planes (one pitch apart) are periodic boundaries.
- The bottoms of the extended inlet and the outlet diffuser sectors are assumed symmetrical planes.
- All the walls are considered adiabatic

The rotor and IGV blades as they are solid objects in the computational domain are removed from the grid by specifying block-off from the grid.

The grid is checked for the minimum skew angle, which should be greater than 20deg. Also, the grid aspect ratio should be lower than value of 100. These are necessary criteria for a good convergence of the solution. To satisfy such criteria, the sub-domains of the rotor and the IGV are subdivided into 8 sub-regions and the vertices are distributed in such a manner to avoid the minimum skew angle, which frequently appears near the leading and trailing edge of the blades. The IGV grid and the rotor grid are linked by specifying attaching grids, where the mass, energy and momentum fluxes are transferred either in a frozen interface where the flow parameters are transmitted locally, or in an averaged stage interface, where the flow information is passed averaged.

For the ease of obtaining a converged solution, first, the mass flow boundary condition is specified at inlet and the static pressure at outlet. These boundary conditions are more robust and facilitate the convergence of the solution. The static pressure at outlet is approximated from the expected fan pressure ratio. After convergence, the results are used as an initial guess. Then, the TASCflow code is run with the physical boundary conditions; total pressure at inlet and mass flow at outlet. Initially, the robust upwind scheme with physical advection correction was used. Then, it was changed to a linear profile scheme, which gave better results. The computing time reached 52000 seconds to achieve 250 steps in the preliminary scheme. However, 700 steps were used in the linear profile scheme. A maximum residual of $5 \times 10^{-6}$ was reached in a global computing time equal to 134800 seconds.

## 2.3 TURBULENCE MODEL

The most widely used and validated turbulence model from engineering experience is the k-ε model with wall functions. Basically, this turbulence model uses gradient diffusion to relate the Reynolds stress to the mean velocity gradient and the turbulent viscosity. The turbulent length scale is estimated from the kinetic energy k and its dissipation rate ε. The boundary conditions for k and ε at the wall are based on the wall functions as suggested by Launder and Spalding with the normalised distance calculated at the node closest to the wall. The turbulent kinetic energy is determined from the solution of a semi empirical transport equation. A crude approximation for the inlet uniform distribution for k and ε derived in literature (Versteeg and Malalasekera, 1995) is as follows.

$$k = \frac{3}{2}\left(V_{ref} T_i\right)^2 \qquad 2\text{-}2$$

$$\varepsilon = C_\mu^{3/4} \frac{k^{3/2}}{l} \qquad l = 0.07\,L \qquad 2\text{-}3$$

$T_i$ : turbulence intensity,
L : characteristic length,
$C_\mu = 0.09$

### 2.3.1 Roughness inclusion

The roughness as equivalent to a diameter of sand grain might interfere with the first grid line in the clustering region (White, 1991). Consequently, the first line of the clustering must not intersect with roughness crests. It is more convenient to use an estimate for the friction factor derived from the profile loss coefficient function of Reynolds number to correct the effective thickness in the logarithmic region (Schlichting, 1979). Then, it is possible to tune the blending parameters set for the wall functions in the code TASCflow.

### 2.3.2 RNG turbulence model

The standard k–ε model is very limited in fluid dynamic problems with swirling flows and large rapid strains encountered in curved boundary layers and diverging passages, such as in turbomachinery. It is well known that a centrifugal force suppresses the turbulence on the convex side and amplifies it on the concave side. For turbomachine blades, turbulence is amplified and destabilised on the pressure side, contrary to the suction side (Lakshminarayana, 1996). The RNG group at Princeton University modified the standard k–ε model using a statistical mechanics approach with new mathematical formulations, providing a rigorous basis for the extension of eddy viscosity models in k-ε. The new modified model is known as RNG k–ε (Yakhot et al, 1992 ), which contains a strain dependant correction for the rate of production, which is the source of inaccuracy in the standard model. The notable thing about this RNG model is that all the constants are calculated explicitly.

The generalised RNG model is presented as follows.

$$\frac{\partial \overline{K}}{\partial t} + U\nabla \overline{K} = 2\upsilon_T S_{ij}^2 - \overline{\varepsilon} + \frac{\partial}{\partial x_i}\left(\alpha_K \upsilon \frac{\partial \overline{K}}{\partial x_i}\right) \qquad 2\text{-}4$$

$$\frac{\partial \overline{\varepsilon}}{\partial t} + U\nabla \overline{\varepsilon} = 2C_{\varepsilon 1}\frac{\overline{\varepsilon}}{\overline{K}}\upsilon_T S_{ij}^2 - C_{\varepsilon 2}\frac{\overline{\varepsilon}^2}{\overline{K}} - \mathrm{R} + \frac{\partial}{\partial x_i}\left(\alpha_\varepsilon \upsilon \frac{\partial \overline{\varepsilon}}{\partial x_i}\right) \qquad 2\text{-}5$$

$$\mathrm{R} = 2\nu_0 S_{ij}\overline{\frac{\partial u_i}{\partial x_i}\frac{\partial u_i}{\partial x_j}}$$

$\nu_t\ \nu_0\ \nu$ , are turbulent, mean and total viscosity
$C_{\varepsilon 1}$ =1.42
$C_{\varepsilon 2}$ =1.68
$\alpha_k = \alpha_\varepsilon$ =1.39
The Van Karman constant k = 0.4 , then β = 0.012

The mean strain is defined by

$$S_{ij} = \frac{1}{2}\left(\frac{\partial U_i}{\partial x_j} + \frac{\partial U_j}{\partial x_i}\right)$$

## 2.4 GEOMETRICAL DATA

The studied axial fan designed by AK-Fans Company is made from cast aluminium. The geometry parameters for the IGV and rotor blades are obtained using a CAD package. From measurements of rotor blade profile at the root and the tip as illustrated by the drawings of figures 2-9, 2-10, the mean section profile is deduced as shown by figure 2-11. The roughness was measured using a profilemeter `Tallysurf` within Cranfield precision laboratory. The overall stage geometry parameters for IGV and rotor are given by the following data:

| | | |
|---|---|---|
| Shroud diameter | | 170.02 mm |
| Tip rotor diameter | | 169.37 mm |
| Hub rotor diameter | | 110 mm |
| Tip clearance | | 0.326 mm |
| Hub tip ratio | | 0.647 |
| Roughness of cast blades (rough) | Ra | 2.746μm |
| Roughness of coated blades (smooth) | Ra | 0.196μm |
| Axial spacing IGV- rotor | | 15 mm |

*Rotor C4 blade profiles parameters*

| | |
|---|---|
| Chord of the root section | 43.08 mm |
| Chord of the tip section | 45.57 mm |
| Camber line radius at the root | 63.80 mm |
| Camber line radius at the tip | 76 mm |
| Tip blade section axial lean | 1.89 mm |
| Tip blade section tangential lean | 1.17mm |
| Maximum thickness of the blade | 10% |
| Stagger angle at the root | 48 deg |
| Stagger angle at the tip | 55.25 deg |
| Inlet angle at the root $\beta_{1Gr}$ | 67.72 deg |
| Outlet angle at the root $\beta_{2Gr}$ | 28.25 deg |
| Inlet angle at the tip $\beta_{1Gt}$ | 72.69 deg |
| Outlet angle at the tip $\beta_{2Gt}$ | 37.79 deg |

*Rotor mid section profile parameters*

| | |
|---|---|
| The mean chord | 44.24 mm |
| The mean camber line radius | 69.5 mm |
| The mean stagger angle | 51.71 deg |
| Mean rotor inlet angle $\beta_{1Gm}$ | 70.27 deg |
| Mean rotor outlet angle $\beta_{2Gm}$ | 33.15 deg |

*IGV C4 blade profile parameters*

| | |
|---|---|
| Chord of the blade | 57.14 mm |
| Stagger angle | 27.36 deg |
| Inlet blade angle $\alpha_0$ | 0 deg |
| Outlet blade angle $\alpha_1$ | 54.76deg |

## 2.5 MEAN LINE PRELIMINARY FLOW CALCULATION

To solve the flow field through the axial fan stage over its range of operation, some parameters at design point are required in order to set the inlet and outlet boundary conditions and also the initial guess values to run TASCflow code. The concerned parameters are; the mass flow, the pressure ratio and flow angles. Preliminary one dimensional calculations are done for them at mid span, which are presented in the following subsection.

### 2.5.1 Axial fan flow angles

The nominal incidence angle is calculated from the nominal condition for high stagger axial fan blades according to McKenzie (1980). The rotor flow deviation from the rotor is based on an NGTE correlation, where the parameter 'm' is obtained from the Wallis's extrapolated curve. Further details are given in Chapter 6.

$$\delta = m\theta\sqrt{\frac{s}{l}} \qquad 2\text{-}6$$

The nominal condition yields the following flow angles for the rotor blade at the mean profile section.

| | |
|---|---|
| The mean inlet incidence angle | $i_n = -7.89$ deg |
| The mean flow deviation angle | $\delta_m = 13.19$ deg |
| The nominal inlet flow angle | $\beta_{1m} = 62.38$ deg |
| The nominal outlet flow angle | $\beta_{2m} = 45.35$ deg |

The design parameter at the maximum efficiency yields the following flow angles for the rotor blade as computed in chapter 6.

| | |
|---|---|
| The design mean incidence flow angle | $i^* = -3.19$ deg |
| The design mean deviation flow angle | $\delta_r^* = 15.46$ deg |
| The inlet mean design flow angle | $\beta^*_{1m} = 67.08$ deg |
| The outlet mean design flow angle | $\beta^*_{2m} = 48.61$ deg |

The deviation angle of the IGV blade is obtained from a graphical correlation developed by Ainely and Mathieson for NGV turbine blades, (Japiske and Baines, 1994).

$$\delta_{IGV} = 17.65 \text{ deg}$$

From the velocity triangles at the mean section, figure 2-13 and considering the speed of rotation 11300 rpm. The velocity components are calculated as follows.

$$W_\theta = U + V_\theta$$

$$V_{\theta 1m} = V_{z1m} \tan \alpha_{1m}$$
$$W_{\theta 1m} = V_{z1m} \tan \beta_{1m}$$
$$V_{z1m} \tan \beta_{1m} = \omega r_m + V_{z1m} \tan \alpha_{1m}$$

Which yields the following velocity values:

$U_m = 79.69 m/s \qquad V_{Z1m} = 49.46 m/s$
$V_{\theta 1m} = 37.48 m/s \qquad W_{\theta 1m} = 117.17 m/s$
$V_{1m} = 62.12 m/s \qquad W_{1m} = 127.21 m/s$

### 2.5.2 Distribution of flow angles

By considering the equilibrium equation for the compressible flow, and assuming no radial profile of the enthalpy or entropy (Lewis, 1996), the axial velocity distribution can be easily computed by the following equation.

$$\frac{dH_t}{dr} - T\frac{dS}{dr} = V_z \frac{dV_z}{dr} + \frac{V_\theta}{r}\frac{d(rV_\theta)}{dr} \qquad 2\text{-}7$$

$$\tan \alpha_1 = \frac{V_{\theta 1}}{V_{z1}} = f(r) \qquad 2\text{-}8$$

Replacing in equation 2-7.

$$V_{z1}\frac{dV_{z1}}{dr} + \frac{V_{z1}\tan\alpha_1}{r}\frac{d(rV_{z1}\tan\alpha_1)}{dr} = 0$$
$$\left(1+\tan^2\alpha_1\right)\frac{dV_{z1}}{dr} + \frac{\tan\alpha_1}{r}\frac{d(r\tan\alpha_1)}{dr}V_{z1} = 0 \qquad 2\text{-}9$$

As the outlet IGV angle is constant, the integration of the radial equilibrium equation yields the following absolute velocity distribution.

$$V_1 = V_{t1}\exp\left(-\int_{rt}^{r}\frac{\sin^2\alpha_1}{r}dr\right)$$

Which is equivalent to the non-dimensional axial velocity distribution.

$$\frac{V_{z1}}{V_{z1t}} = \left(\frac{r_t}{r}\right)^{\sin^2\alpha_1}$$

From the definition of the mean axial velocity and the mass flow rate downstream of IGVs, the value of axial velocity at different radial positions is related to the mean axial velocity by the following expression.

$$\frac{V_{z1}}{V_z}=\left[\frac{1-\left(r_h/r_t\right)^2}{1-\left(r_h/r_t\right)^{2-\sin^2\alpha_1}}\right]\left(1-\frac{\sin^2\alpha_1}{2}\right)\left(\frac{r}{r_t}\right)^{-\sin^2\alpha_1} \qquad 2\text{-}10$$

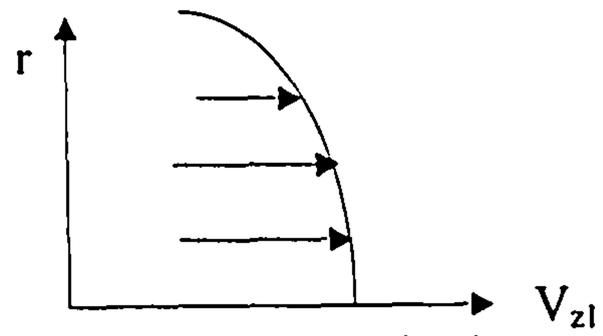

Axial velocity distribution

At standard conditions $T_{t0}=288k$, $P_{t0}=1atm$,

$$\frac{T}{T_t}=1-V_z^2/2T_tcp \qquad \frac{p}{P_t}=\left(\frac{T}{T_t}\right)^{\gamma/\gamma-1} \qquad \rho=1.2$$

The design mass flow rate

$$m=\rho V_z\pi\left(r_t^2-r_h^2\right)=0.785\,kg/s$$

By applying the radial equilibrium equation at the rotor outlet, which includes the compression work variation, yields an expression for the outlet velocity variation.

$$\frac{dH_{t2}}{dr}=\frac{dH_{t1}}{dr}-\frac{d\Delta W_C}{dr}=-\frac{d}{dr}UV_{0lt}\left(\frac{r_t}{r}\right)^{\sin\alpha_1} \qquad 2\text{-}11$$

The distribution of axial velocity at outlet from the rotor is dependent on the unknown tip axial velocity

$$V_{z2}=\sqrt{V_{z2t}^2+2U_tV_{0lt}\left[1-\left(\frac{r}{r_t}\right)^{\cos^2\alpha_1}\right]} \qquad 2\text{-}12$$

From the conservation of the mass flow a supplement equation for the distribution of the axial velocity arises, which allows an iterative solving for the outlet axial velocity assuming initial values.

$$m=2\pi\int_{r_h}^{r_t}\rho r\sqrt{V_{z2t}^2+2U_tV_{0lt}\left[1-\left(\frac{r}{r_t}\right)^{\cos^2\alpha_1}\right]}dr \qquad 2\text{-}13$$

## 2.6 AXIAL FAN PERFORMANCE

The CFD codes available nowadays especially TASCflow are powerful and allow good predictions of the turbomachinery flowfields. The computation of the aerodynamic performance needs either a kind of available post-processing interface or an auxiliary program to process the obtained results. The values obtained for the efficiency or the pressure rise coefficient depend on the way that they are defined for the given turbomachine, and the way the loss expressions are derived in the energy balance. The next subsections explain the procedure used to process CFD results implemented in a Fortran program

### 2.6.1 Profile losses

The profile losses include the losses due to blade boundary layers and wakes through viscous and turbulent dissipation. Furthermore, the trailing vortex systems in the blade wake and its eventual mixing and dissipation give rise to an additional loss. The high losses are concentrated near the annulus wall and in the tip clearance region toward the trailing edge, but they decrease as the flow proceeds downstream, because of the flow redistribution toward the inner radius and by flow mixing.

### 2.6.2 Secondary flow and endwall losses

These losses include some of the kinetic energy in the secondary flow as well as losses associated with the formation, development, diffusion, and dissipation of the vortices generated. The indirect effect of the secondary flow is to transport the wall boundary layer toward the corner formed by the blade suction surface and the wall, and initiate wall stall which interacts with the blade stall region in the corner. The losses due to secondary flow are usually lumped together with the annulus and hub wall boundary layer losses and are called endwall losses. The flows at the exit from the IGV and from the rotor in the endwall region have high turning angles, which tend to increase the secondary losses.

### 2.6.3 Tip leakage flow losses

These losses arise from flow leakage in the tip clearance region of the rotor blade. The leakage flow interaction with the main flow generates flow perturbation with a vortex formation, resulting in mixing losses. Additional losses arise due to mixing between the blade boundary layers transported toward the tip region due to a low pressure caused by the tip vortex and the endwall flow. End wall losses including tip clearance loss may account for approximately 50-70% of total losses (Lakshminarayana, 1996).

The aerodynamic parameters are derived from CFD results using mass flow averaged with respect to a defined surface.

$$\bar{f}_k = \sum_i \sum_j f_{ijk} m_{ijk} \Big/ \sum_i \sum_j m_{ijk}$$

The global mass averaged rotor loss coefficient.

$$\varpi_R = \frac{(\Delta P_{tr})_R}{1/2 \rho W_1^2} \qquad 2\text{-}14a$$

The global mass averaged IGV loss coefficient.

$$\varpi_{IGV} = \frac{(\Delta P_t)_{IGV}}{1/2 \rho V_1^2} \qquad 2\text{-}14b$$

The total pressure head is defined relatively to the tip of the rotor blade.

$$\psi = \Delta P_{t\_stage} \Big/ \bar{\rho} U_t^2 \qquad 2\text{-}15$$

The total to total adiabatic efficiency referring to the mid section flow properties is calculated as follows.

$$\eta_{tt} = 1 - \left[ \frac{\varpi_R \left( \frac{W_1}{U_m} \right)^2 + \varpi_{IGV} \left( \frac{V_1}{U_m} \right)^2}{2 \left( \frac{\Delta H_t}{U_m^2} \right)} \right] \qquad 2\text{-}16$$

The theoretical enthalpy increase at design point is normalised by the mean peripheral speed as follows.

$$\left( \frac{\Delta H_t}{U_m^2} \right)_* = \left( \frac{\overline{V}_{\theta 2}}{U_m} \right)_* - \left( \frac{\overline{V}_{\theta 1}}{U_m} \right)_* = \left[ \frac{\tan \beta_1 - \tan \beta_2}{\tan \beta_1 - \tan \alpha_1} \right]_* \qquad 2\text{-}17$$

To include all types of losses in the definition of total-total isentropic efficiency, the inlet total absolute pressure was integrated using the mass flow as a weighing function at the inlet of one IGV blade passage, and similarly for the rotor outlet. The power input to the rotor is directly computed from the integration of the static pressure distribution over the rotor blade wet surfaces.

The integration of the static pressure on the rotor blade surface yields the following performance parameters for the smooth blades given in table 2-1.

Table 2-1 Axial fan stage aerodynamic performance

| | |
|---|---|
| Torque (one blade) | -0.3498 mN |
| Torque (all blades) | -3.4980 mN |
| Power (all blades) | -4138.93 W |
| Thrust (one blade) | 7.7330 N |
| Thrust (all blades) | 77.335 N |
| Flow coefficient $\Phi_t$ | 0.488 |
| Flow coefficient $\psi_t$ | 0.4221 |
| Absolute-total-pressure inlet IGV | 101190.5 |
| Density at inlet IGV | 1.216 |
| Rotor total pressure loss coefficient | 0.135 |
| IGV total pressure loss coefficient | 0.037 |
| Total-to-total isentropic efficiency | 0.8125 |
| Total-to-static isentropic efficiency | 0.4758 |

The averaged flow quantities related to the rotor inlet and outlet are given in the following table 2-2.

Table 2-2 Axial fan stage flow parameters

| *Quantity* | *Inlet* | *Outlet* |
|---|---|---|
| Mass-flow | 0.785 | 0.785 |
| Density | 1.207 | 1.251 |
| Static-pressure | 98570 | 104100 |
| Absolute-total-pressure | 101100 | 106400 |
| Static-enthalpy | 285900 | 291300 |
| Total-enthalpy | 288000 | 293100 |
| Absolute Velocities: | | |
| Speed | 63.65 | 58.08 |
| Radial-velocity | -0.155 | -0.494 |
| Tangential-velocity | -40.29 | 24.63 |
| Axial-velocity | -48.98 | -49.52 |
| Circumferential-velocity | 40.31 | 24.94 |
| Meridional-velocity | 49.0 | 49.74 |
| Absolute-flow-angle | 39.43 | 26.35 |
| Relative Velocities: | | |
| Speed | 133.8 | 78.08 |
| Tangential-velocity | -124.4 | -59.49 |
| Circumferential-velocity | 124.4 | 59.66 |
| Relative-flow-angle | 68.50 | 50.1 |

The following table 2-3 gives details of the processed CFD results using the post-processing Fortran program *CFD_PERF.*

Table 2-3 Mass averaged axial fan performance

| m kg/s | Φ | Ψ | η | Power w | $i_h$ ° | $i_m$ ° | $i_s$ ° | $\delta_h$ ° | $\delta_m$ ° | $\delta_t$ ° | $\alpha_1$ ° |
|---|---|---|---|---|---|---|---|---|---|---|---|
| 0.55 | 0.337 | 0.283 | 0.657 | 2362.86 | 3.309 | 3.050 | 2.92. | 14.747 | 23.95 | 33.41 | 30.708 |
| 0.60 | 0.367 | 0.318 | 0.708 | 2687.84 | 2.647 | 2.166 | 1.815 | 14.929 | 22.467 | 30.265 | 31.187 |
| 0.65 | 0.396 | 0.406 | 0.794 | 3323,86 | 2.291 | 1.159 | 0,157 | 15.52 | 19.017 | 22.77 | 32.035 |
| 0.70 | 0.426 | 0.417 | 0.807 | 3616.36 | 1,37 | 0.086 | -1.067 | 15.733 | 18.067 | 20.66 | 32.231 |
| 0.75 | 0.457 | 0.421 | 0.812 | 3881.17 | 0,434 | -0.923 | -2.180 | 16.057 | 17.425 | 19.05 | 32.348 |
| 0.80 | 0.488 | 0.422 | 0.812 | 4138.93 | -0.5 | -1.925 | -3.23 | 16.262 | 16.937 | 17.87 | 32.435 |
| 0.85 | 0.52 | 0.419 | 0.808 | 4388.28 | -1.399 | -2.864 | -4.2 | 16.423 | 16.547 | 16.931 | 32.503 |
| 0.90 | 0.551 | 0.414 | 0.802 | 4622.3 | -2.241 | -3.740 | -5.108 | 16.583 | 16.26 | 16.197 | 32.569 |
| 0.95 | 0.583 | 0.407 | 0.792 | 4838.94 | -3.037 | -4.564 | -5.960 | 16.74 | 16.068 | 15.647 | 32.615 |
| 1.00 | 0.615 | 0.396 | 0.780 | 5034.36 | -3.772 | -5.333 | -6.657 | 16.957 | 15.955 | 15.212 | 32.666 |

For the position of the rotor blade in the wake of IGV blades with respect to the frozen interface configuration, higher losses result from the interaction of the IGV wake with the leading edge of the rotor blade. As a consequence, the adiabatic efficiency and pressure rise coefficient reduce to 0.811 and 0.4214 respectively.

The CFD results for rough axial fan stage gave the following values for the pressure rise coefficient, efficiency and aerodynamic loss factors.

- Rotor total pressure loss coefficient = 0.1494
- IGV total pressure loss coefficient = 0.0767
- Total-to-total isentropic efficiency = 0.80171
- Total-to-static isentropic efficiency = 0.465

There is a net difference in performance between the rough and the smooth blading of 1.35% in efficiency and 2.37% in pressure rise coefficient.

## 2.7 DISCUSSION

Viscosity and the turbulence are among the major contributors for the aerodynamic losses. The viscous effect clearly reduces the efficiency by a loss in stagnation pressure both in the IGV and in the rotor. Figures 2-14 and 2-15 show the mean and tip section total pressure loss near the design point. At high mass flow rate a separation was evident on the pressure side of the rotor blade at mid span (figure not shown). Near surge the separation occupies a larger area on the suction side. Figures 2-16 and 2-17 show flow velocity at mid span and in tip clearance at design point, similarly at low mass flow rate, figures 2-18 and 2-19. When rotor blades traverse the IGV wakes during one revolution, parts of wakes are ingested by the rotor row and are convected downstream, figures 2-20 and 2-21. Thus, causes further increase of pressure and density inside the passage and disturbance to the relative velocity distribution around the leading edge, figures 2-22 and 2-23.

The pressure distribution on the rotor blade at mid span, figure 2-24 shows an upper loading of the leading edge with a region of high Mach numbers on the suction

side, see figure 2-26. Figure 2-25 and figure 2-27 show static pressure and relative Mach number in the tip clearance of the rotor blade, showing high leakage over the tip. The change of incidence due to the IGV wake increase this loading near leading edge, but the trailing edge is downloaded due to local separation and variation of flow direction. The thickness of IGV trailing edge leads to high separation locally with an over turning of the flow, source of high loss, figure 2-14. The static pressure distributions around hub, mid and tip sections of the rotor blade show noticeable variations with mass flow rates, figures from 2-28 to 2-33. The tip section blade pressure distribution at low mass flow rate is a good indicator for blade stalling, in such a situation it is practically unloaded, figure 2-32.

The rotation, curvature, and radial pressure gradients introduce a three-dimensional character for the flow boundary layer. This boundary layer is thin at the hub and thick at the endwall near the tip. The wakes give rise to an appreciable radial mixing flow as the flow proceeds downstream. The total pressure distribution and velocity plot near the trailing edge depicts a three dimensional structure of the wake. Due to high mixing the wake decays faster, but less close to the hub. The thick endwall compared to the aspect ratio especially towards suction side introduces flow separations, which are caused by an increase in the pressure gradient along the streamwise direction. The hub corner is more likely to stall at design point, and there is migration of flow particles up from hub to shroud, with a region of circulation, figure 2-34. The strong interaction between the inviscid core flow and the viscous layers both in boundary layer and in the end wall regions results in a wake and jet flow structure, which is clearer at low mass flow rate figure 2-35.

The most complex flow features occur in the tip clearance region. The leakage around the tip of the rotor blade develops into a vortex, figure 2-36, and mixes out with the annulus wall boundary layer figure 2-37. The vector plot on the outlet area near the trailing edge reveals the formation of vortex tube near the hub, figure 2-37. In the core of the vortices the flow is transported outward normal to the surface. The leaning of the rotor blades and the high rotation seem to reduce flow separation near the hub for this blade design. The tip clearance seems to increase the flow balance in the blade corner, which induces more re-circulation of the flow and a strong vortex followed by a wake diffusing in large area, figure 2-15. Close to the tip there are three regions of clearance flow with different behaviours near the tip and shroud as shown by figure 2-38 to 2-41 corresponding to two rotor positions. A small highly loaded region near the leading edge of the blade rotor produces a strong clearance vortex. The wall jet in the middle tends to deflect down and mixes out. At the trailing edge the high vortex formation deflects the flow and meets the uprising radial flow on the suction side, figure 2-37. Figure 2-42 shows the effects of IGV wakes on the relative velocity vectors in the tip clearance.

By solving IGV and rotor flowfield using a frozen stage interface where the physical quantities are passed integrally from stator to rotor, several initial rotor positions should produce better results. In fact, the blade and annulus wall boundary layer developments and mixing across blade row interface introduce large viscous losses and flow deviation different from an average stage interface. The spanwise mixing is related to the flowfield in inter rows regions caused by secondary flow, including wakes and tip leakage flow and unsteadiness. The radial transport of mass,

momentum, energy and turbulence causes considerable dissymmetry in the flow as well as large gradients in the flow field, this is dependent on stator rotor interaction.

The plots of the flow angle at outlet from IGV against the blade height at three cross pitch positions, figure 2-44 and the averaged outlet flow angle downstream IGV, figure 2-46 exhibit abrupt change near the trailing edge and across the IGV wake. Similar trends for the rotor relative flow angle at three pitch positions, which are illustrated, by an abrupt turning around the trailing edge, figure 2-48 and 2-51. There is a clear evidence of opposite intense trailing edge vortices due to low aspect ratio, but the flow angle is smeared out far downstream with larger flow diffusion near the tip of blade, as plotted in figure 2-53 for several blade heights. The total relative pressure exhibits similar trends near the trailing edge similar to the relative meridional flow velocity as shown by figures 2-54 to 2-56. As the flow proceeds downstream the total relative pressure tends to mix out as shown by figures 2-57 to 2-59.

The rotor outlet axial velocity depicts higher velocity close to the shroud and a lower axial velocity near the hub, figure 2-47. The lower axial velocity near the hub is due to blade leaning, which tends to increase the static pressure. Also, there is evidence of blockage near the shroud from the slope of axial velocity, figure 2-47 plotted at several pitch positions, (where J10 is a position in the trailing edge wake). The figure 2-49 shows the average velocities near the trailing edge and at the interface plane.

The flow field downstream of the rotor and along the diffusing pipe does show a large eddy extending from the back of the rotor, which is characterised by high re-circulation and a strong interaction with high velocity jet from the rotor, figure 2-60, 2-61. This is accompanied by high losses of total pressure, figure 2-63. The recovery static pressure point is reached as far as the rotational flow momentum is converted into pressure and the jet annular flow is completely mixed out with the central separation. Figure 2-62.

The roughness has small effect on the static pressure distribution, but its effect appears almost entirely on the suction surface, where it tends to thicken the boundary layer and to cause higher velocity in the core flow. Even at design point, the effect of the roughness produces a decambering effect on the blade profile, which tends to decrease slightly the loading over the trailing edge of the blade, resulting in an increased outlet flow angle, figure 2-66.

The computed pressure rise coefficient and the total-total adiabatic efficiency are shown in figure 2-67. The design mass flow is around 0.785 kg/s, which corresponds to an efficiency of 0.8125, and a maximum of pressure rise coefficient of 0.422 for the smooth blades. The limit of the stability is characterised by an abrupt decline in pressure rise coefficient and in efficiency. The predicted stalling point is around 0.65kg/s, at which the convergence rate exhibited strong oscillations with the number of computation steps. The results obtained after including the surface roughness show a loss of 1.35% in efficiency and 2.37% loss in pressure rise coefficient due to increased friction.

A comparison between CFD and measured performance characteristics in figure 2-68, shows slight differences, which are attributed to several causes such as: The

variation of the speed of rotation of the fan with throttling during tests. Also, the flow pattern behind the rotor is very complex, which could affect the pressure distribution around the trailing edge. Additionally, the location of the averaging plane was very close to the rotor blade trailing edge because of the design constraints. Normally it should be at least one chord after the trailing edge.

## 2.8 CONCLUSIONS

Viscosity and turbulence are among the major contributors to the axial fan stage losses. The viscous effect clearly reduces the efficiency by a loss in stagnation pressure. When the rotor blade cuts the IGVs wakes during one revolution, parts of wakes are ingested by the rotor row and convected downstream, thereby causing further increase of pressure and density inside the passage and disturbance to the relative velocity distribution around the leading edge of the rotor blade. The pressure distribution on the rotor blade shows an upper loading of the leading edge with a region of high Mach numbers on the suction side. The change of the incidence due to the IGV wake tends to increase this loading. The total pressure distribution and the velocities near the trailing edge depict the three dimensionality of the wake structure. The thick endwall compared to the aspect ratio especially towards suction side induces flow separations caused by pressure gradient along the streamwise direction. The hub corner is more likely to stall at design point, and there is pronounced migration of flow upward from hub to shroud. The most complex flow features occur in tip clearance region, where the leakage around the tip of the blade develops into a vortex and mixes out with the annulus wall boundary layer.

A large eddy extending from the back of the rotor characterised by high re-circulations interacts with the high velocity jet from the rotor outlet and produces supplement of total pressure losses as shown in figure 2-60 and 2-61. The recovery point of static pressure is reached as far as the rotational flow momentum is converted into a static pressure and the jet annular flow pattern is completely mixed out.

The frozen stage interface was shown to produce a better description of the flow features especially near the leading edge of the rotor blades as compared to the average stage interface.

The predicted flowfield was used as one of the main inputs to the trajectory code, the others being the particle properties such as particle diameters, densities concentration etc.

The flow patterns near the leading edge and tip clearance, in addition to the secondary flow near trailing edge are expected to influence the trajectories of particles and their impact locations. The complete solution of the flowfield, with the description of all flow components, is needed in order to accurately resolving the particle trajectories near the blade leading edge and tip region. Also, the vortex formation, flow circulation areas and the strong viscous effects are expected to have an effect on erosion.

The flow solution is also used to interpret the results of aerodynamic performance degradation and to assess the effect of blade erosion on the static pressure distribution, and the flow pattern through this axial fan rotor blading

# CHAPTER 3

# PARTICLE TRAJECTORY COMPUTATION

## 3.1 INTRODUCTION

The three dimensional particle trajectories with the spatial distribution of impacts are computed through an axial fan stage with a set of inlet guide vanes (contra-whirl). The numerical model implemented in the developed Fortran trajectory code uses a Lagrangian tracking technique based on the eddy lifetime concept. The governing equations of the particle motion are solved using the seventh order Runge-Kutta Fehlberg method. The tracking of particles and their locations are based on the finite element interpolation method. The trajectory modelling and the assumptions made with a description of the computation tasks are presented throughout the following sections, followed by a discussion of the results and a comparison with experimental results to validate the trajectory code.

## 3.2 DYNAMIC MODELLING

The motion of solid particles is described in a Lagrangian way by solving a set of differential equations along the trajectory in order to calculate the change of particle location when moving in a compressible gas stream through an axial turbomachine. The dynamic equation of particle motion is derived similarly to Tchen approach (Lixing, 1993), which considered a generalised equation of particle motion with Stokesian drag. By using the method of intuitive superposition of various possible forces involved, four categories of forces are identified and classified as follows.

- Forces that act on a particle due to its motion
- Forces that act due to the motion of the surrounding fluid
- Body forces
- Buoyancy forces

The summation of all these components equals the inertia force.

$$m_p \frac{d\vec{V}_p}{dt} = \vec{F}_D + \vec{F}_{vm} + \vec{F}_p + \vec{F}_b + \vec{F}_B + \vec{F}_g + \vec{F}_{TD} + \vec{F}_S + \vec{F}_M \qquad 3\text{-}1$$

$F_D$ Drag force
$F_{vm}$ Virtual mass force
$F_P$ Pressure gradient force
$F_b$ Buoyancy force
$F_B$ Basset force
$F_g$ Gravity force
$F_{TD}$ Drift force due to the turbulence diffusion
$F_S$ Saffman force
$F_M$ Magnus force

- In most fluid particle systems the drag force is dominating the particle motion and consists of a friction and form drag. For small Reynolds Numbers ($Re_p$<0.5) viscous effects are dominating and no separation is observed, this is referred as the Stokes regime (Sommerfeld, 2000).

$$C_D = 24/\mathrm{Re}_p \qquad 3\text{-}2$$

The aerodynamic drag force due to the flow around the particle encompassing skin and form drag is calculated according to Morsi and Alexander (1972), who gave the following drag coefficients for spherical particles.

$$\begin{aligned}
C_D &= 24\,Re_d^{-1} && 0 < Re \le 0.1 \\
C_D &= 22.73\,Re_d^{-1} + 0.903\,Re_d^{-2} + 3.69 && 0.1 < Re \le 1 \\
C_D &= 38.8\,Re_d^{-1} - 12.65\,Re_d^{-2} + 0.36 && 1 < Re \le 10 \\
C_D &= 46.5\,Re_d^{-1} - 116.667\,Re_d^{-2} + 0.61667 && 10 < Re \le 100 \\
C_D &= 98.33\,Re_d^{-1} - 2778\,Re_d^{-2} + 0.3644 && 100 < Re \le 1000 \\
C_D &= 148.67\,Re_d^{-1} - 47500\,Re_d^{-2} + 0.35713 && 1000 < Re \le 5000
\end{aligned} \qquad 3\text{-}3$$

The turbulence level of the upstream airflow essentially causes a reduction of the critical Reynolds number as shown by Torobin and Gauvin (1961), and does affect the drag coefficient.

For irregularly shaped particles, a shape factor is applied to the drag force. This one is expressed as the ratio of the volume of a particle to the diameter of an equivalent spherical particle having the same projected area. The shape factor for a spherical particle is $\pi/6$, which gives a correction factor of 1.0. The correction factor for quartz particle was found to be 0.4, and the resulting shape factor for AC coarse sand is 0.2618, Breitman et al (1985). Also, a simplified approach to consider the non-sphericity of particle uses modified drag coefficients, which are provided for different non-spherical particles by Haider and Levenspiel (1989).

The drag force including the shape factor is calculated as follows.

$$\vec{F}_D = \frac{\pi}{8} d_p^2 \rho_f \frac{C_D}{S_F} \left(\vec{V}_f - \vec{V}_p\right) \left|\vec{V}_f - \vec{V}_p\right| \qquad 3\text{-}4$$

$S_F$ : shape factor

• The motion of a particle in the vicinity of a rigid wall results in an increase of the drag coefficient and is additionally associated with a transverse lift force. The motion of a particle normal to a wall was considered by Brenner (1961). On the other hand, a particle motion parallel to a wall was analysed by Goldman et al (1967). Although, analytical solutions for both cases are available only for very small Reynolds numbers.

• The local pressure gradient in the flow gives rise to an additional force in the direction of the pressure gradient. Combining the pressure gradient with the shear stress produces an expression function of the ratio of the flow density to the particle density. It is obvious, that in gas solid flows the pressure force may be neglected since the ratio of densities is very small (Sommerfeld, 2000).

• The acceleration or deceleration of a particle in the fluid flow also requires to accelerate or to decelerate a certain fraction of the surrounding fluid, this is the so-called added mass, or virtual mass force. The basset force is caused by the lagging of the boundary layer development on the particle with the changing relative velocity and need to be integrated all over the trajectory path, and is referred as history force (Rudinger, 1976). Analytic solutions for both forces are only possible for small particle Reynolds numbers (Sommerfeld, 2000). Usually these forces are neglected.

• If a particle is sufficiently large and there is large velocity gradient, for example near the walls, there will be a particle lifting force called Saffman force. In another definition related to Humphrey (1990), the Saffman force is due to fluid shearing forces. The magnitude of Saffman force depends on the lift coefficient which is function of the velocity gradient as formulated by Hamed (1988b).

$$\vec{F}_S = \frac{3}{4} \frac{\rho_{air}}{\rho_p} \frac{C_L}{d_p} \left\|\vec{V}\right| - \left|\vec{V}_p\right\| \left[\vec{V} - \vec{V}_p\right] \qquad 3\text{-}5$$

$$C_L = \frac{62.4}{\pi} \left[\frac{d_p}{\left\|\vec{V}\right| - \left|\vec{V}_p\right\|}\right]^{1/2} \left|\frac{\partial \vec{V}_p}{\partial y}\right|^{1/2} \mathrm{Re}_d^{-1/2}$$

• Another expression for Saffman force as derived by Sommerfeld (2000) introduces a correction function for higher Reynolds numbers as follows.

$$\overrightarrow{F_{LS}} = 1.615 d_p^2 \left(\rho_f \mu_f\right)^{0.5} \left(\frac{1}{|\vec{\omega}_f|}\right)^{0.5} \left[\left(\overrightarrow{V_f} - \overrightarrow{V_p}\right) \times \overrightarrow{\omega_f}\right] f\left(\mathrm{Re}_p, \mathrm{Re}_S\right) \qquad 3\text{-}6$$

Fluid rotation: $\vec{\omega}_f = \nabla \times \vec{V}_f$

The respective shearing stress and particle Reynolds numbers are:

$$\mathrm{Re}_S = \frac{\rho_f d_p^2 |\vec{\omega}_f|}{\mu_f}, \qquad \mathrm{Re}_p = \frac{\rho_f d_p |\vec{V}_f - \vec{V}_p|}{\mu_f} \tag{3-7}$$

The correction function $f(Re_p, Re_s)$ is proposed by Mei (1992) as follows.

$$\mathrm{Re}_p \le 40 \qquad f(\mathrm{Re}_p, \mathrm{Re}_s) = [1 - 0.3314\beta^{0.5}]\exp\left(-\frac{\mathrm{Re}_p}{10}\right) + 0.3314\beta^{0.5}$$

$$\mathrm{Re}_p > 40 \qquad f(\mathrm{Re}_p, \mathrm{Re}_s) = 0.0524(\beta\,\mathrm{Re}_p)^{0.5} \qquad \beta = \frac{\mathrm{Re}_s}{2\,\mathrm{Re}_p}$$

Particles rotating in fluid flow may also experience a lift force called Magnus force. High particle rotations may be for example induced by particle wall collision. For particle Reynolds number less than one, Rubinow and Keller (1961) derived an analytical expression for this force.

.

$$\overrightarrow{F_{LR}} = \pi r_p^3 \rho_f \vec{\Omega} \times \left(\overrightarrow{V_f} - \overrightarrow{V_p}\right) \tag{3-8}$$

$$\vec{\Omega} = \frac{1}{2}\nabla \times \vec{V}_f - \vec{\omega}_p$$

This expression is extended for higher particle Reynolds Number by introducing a lift coefficient as developed by Crowe et al (1998).

$$\overrightarrow{F_{LR}} = \pi \frac{\rho_f d_p^2}{8} C_{LR} \left|\overrightarrow{V_f} - \overrightarrow{V_p}\right| \frac{\vec{\Omega} \times \left(\overrightarrow{V_f} - \overrightarrow{V_p}\right)}{|\vec{\Omega}|} \tag{3-9}$$

For small particle Reynolds number, the lift coefficient becomes.

$$C_{LR} = \frac{\mathrm{Re}_R}{\mathrm{Re}_p}$$

The rotation Reynolds number: $\mathrm{Re}_R = \dfrac{\rho_f d_p^2 |\vec{\Omega}|}{\mu_f}$

For high Reynolds number, Rubinow and Keller (1961) proposed a graphical relation to compute the lift coefficient.

The inclusion of this force in equation 3-1 needs a supplementary equation for the torque to solve for the particle velocity of rotation.

### 3.2.1 Derivation of particle trajectory equation

The particle position is referred to the reference axes by a simple transformation matrix. The fixed frame is designated by $(O,X,Y,Z)_A$ , and the rotating frame is $(O,X, Y,Z)_R$ . The cylindrical co-ordinates $(r,\theta,z)$ are suitable for flowfield and particle dynamics computations in turbomachinery.

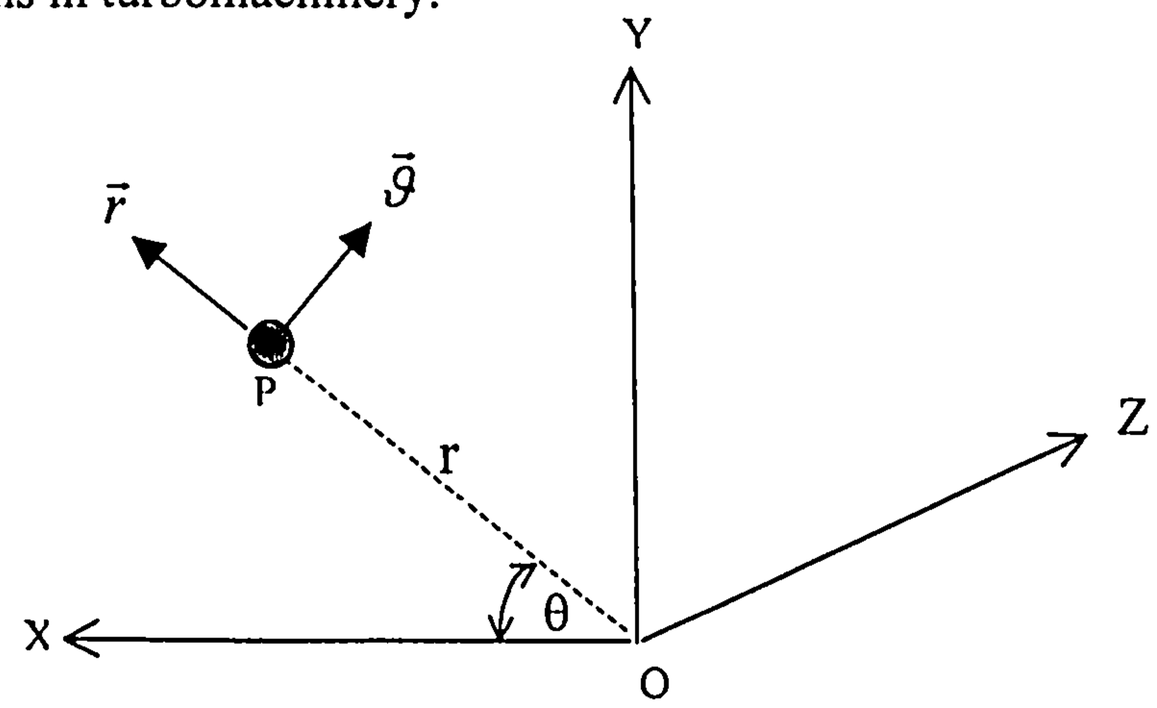


Figure 3-1 Reference frame

The equations of motion of solid particles throughout rotor blades are derived in the relative rotating frame, by considering polar co-ordinates.
If 'r' is a radial position of the particle in the flow path, the particle vector position is the summation of radial and axial velocity components.

$$\overrightarrow{OP} = r_p\vec{r} + z_p\vec{z}$$

The first derivative with respect to time is given by the following expression.

$$\frac{\overrightarrow{dOP}}{dt} = \frac{d(r_p\vec{r})}{dt} + \frac{d(z_p\vec{z})}{dt}$$

$$= \dot{r}_p\vec{r} + r_p\frac{d\vec{r}}{dt} + \dot{z}_p\vec{z} + z_p\frac{d\vec{z}}{dt}$$

$$= \dot{r}_p\vec{r} + r_p\left|\vec{\Omega}\right|\vec{\vartheta} + \dot{z}_p\vec{z}$$

The second derivative yields.

$$\frac{d^2\overrightarrow{OP}}{dt^2} = \frac{d}{dt}\left(\dot{r}_p\vec{r} + r_p\left|\vec{\Omega}\right|\vec{\vartheta} + \dot{z}_p\vec{z}\right)$$

$$= \ddot{r}_p\vec{r} + \dot{r}_p\vec{\Omega}\times\vec{r} + \dot{r}_p\left|\vec{\Omega}\right|\vec{\vartheta} + r_p\left|\dot{\vec{\Omega}}\right|\vec{\vartheta} + r_p\left|\vec{\Omega}\right|\vec{\Omega}\times\vec{\vartheta} + \ddot{z}_p\vec{z} + \dot{z}_p\vec{\Omega}\times\vec{z}$$

$$= \ddot{r}_p\vec{r} - r_p\left(\dot{\theta}_p \pm \omega\right)^2\vec{r} + 2\dot{r}_p\left(\dot{\theta}_p \pm \omega\right)\vec{\vartheta} + r_p\ddot{\theta}\vec{\vartheta} + \ddot{z}_p\vec{z}$$

$$m\frac{d^2\overrightarrow{OP}}{dt^2} = m\left[\ddot{r}_p - r_p\left(\dot{\theta}_p + \omega\right)^2\right]\vec{r} + 2m\left[\dot{r}_p\left(\dot{\theta}_p + \omega\right) + r_p\ddot{\theta}\right]\vec{\vartheta} + m\ddot{z}_p\vec{z} \qquad 3\text{-}10$$

The inertia forces are equal to the sum of the external forces and the body forces. By neglecting other components of the external forces, the equations of motion of a solid particle, including inertia, aerodynamics and gravity forces are formulated with respect to a system of axes attached to the entrance of the blade row of the corresponding turbomachine.

$$m\frac{d^2\overrightarrow{OP}}{dt^2}=\vec{F}_D+\vec{F}_g+\vec{F}_b+\vec{F}_s \qquad 3\text{-}11$$

The equation 3-10 yields the following system of differential equations.

$$\begin{cases}\dfrac{\partial^2 r_p}{\partial t^2}=G\left(V_{rf}-V_{rp}\right)+r_p\left(\omega+\dfrac{V_{0p}}{r_p}\right)^2-g\left(1-\dfrac{\rho_f}{\rho_p}\right)\sin\theta_p+\dfrac{F_{Sr}}{m_p}\\ r_p\dfrac{\partial^2\theta_p}{\partial t^2}=G\left(V_{0f}-V_{0p}\right)-2V_{rp}\left(\omega+\dfrac{V_{0p}}{r_p}\right)-g\left(1-\dfrac{\rho_f}{\rho_p}\right)\cos\theta_p+\dfrac{F_{S0}}{m_p}\\ \dfrac{\partial^2 z_p}{\partial t^2}=G\left(V_{zf}-V_{zp}\right)+\dfrac{F_{Sz}}{m_p}\end{cases} \qquad 3\text{-}12$$

Which can be reduced to a first order system of six equations.

$$\begin{cases}F_1=V_{rp}=\dfrac{\partial r_p}{\partial t}\\ F_2=\dfrac{V_{\theta p}}{r_p}=\dfrac{\partial\theta_p}{\partial t}\\ F_3=V_{zp}=\dfrac{\partial Z_p}{\partial t}\\ F_4=\dfrac{\partial V_{rp}}{\partial t}=G\left(V_{rf}-V_{rp}\right)+r_p\left(\omega+\dfrac{V_{0p}}{r_p}\right)^2-g\left(1-\dfrac{\rho_f}{\rho_p}\right)\sin\theta_p+\dfrac{F_{Sr}}{m_p}\\ F_5=\dfrac{\partial V_{\theta p}}{\partial t}=G\left(V_{0f}-V_{0p}\right)-2V_{rp}\left(\omega+\dfrac{V_{0p}}{r_p}\right)-g\left(1-\dfrac{\rho_f}{\rho_p}\right)\cos\theta_p+\dfrac{F_{S\theta}}{m_p}\\ F_6=\dfrac{\partial V_{zp}}{\partial t}=G\left(V_{zf}-V_{zp}\right)+\dfrac{F_{SZ}}{m_p}\end{cases} \qquad 3\text{-}13$$

The aerodynamic factor is function of fluid and particle velocity as follows.

$$G=\frac{3}{4d_p}\frac{\rho_f}{\rho_p}\frac{C_D}{S_F}\sqrt{\left|V_{fr}-V_{pr}\right|^2+\left|V_{f0}-V_{pr}\right|^2+\left|V_{fz}-V_{pz}\right|^2}$$

The particle velocity is decomposed into peripheral and relative velocities, depending whether a particle is travelling from stator to rotor or vice versa.

$$\vec{V}_P = \vec{W}_P + \vec{U}_P \qquad 3\text{-}14$$

$$\vec{W}_P = \vec{V}_P - \vec{U}_P$$


Figure 3-2 Velocity triangle across an interface plane

The components of particle relative velocity with respect to cylindrical co-ordinates are given as follows.

$$\vec{W}_p = V_r\vec{r} + V_\theta\vec{\theta} + V_z\vec{z} - U_p\vec{\theta}$$

$$W_{p_r}\vec{r} + W_{p\theta}\vec{\theta} + W_{p_z}\vec{z} = V_{p_r}\vec{r} + V_{p\theta}\vec{\theta} - r\omega\vec{\theta} + V_{p_z}\vec{z}$$

## 3.3 TURBULENCE EFFECT MODELLING

In turbulent flows, the particle trajectories are not deterministic and two identical particles injected from a single point at different times may follow separate trajectories due to randomness of the instantaneous flow velocity. The prediction of particle motion in turbulent flows requires an accurate estimation of the main and turbulent flow components. A vast majority of particulate flows use the Lagrangian model. In such a model, it is assumed that the particle phase is a discrete system with a velocity slip between gas and particle phases. One of the early stochastic models of turbulent dispersion is due to Dukowicz (1980). In this model, the turbulence is assumed to be isotropic and have a Gaussian probability distribution function (PDF).

The model adopted in the current study is based on the eddy lifetime concept, as presented by Gosman and Ioannides (1983), because of its ease in implementation. It is assumed that the fluid velocity and the relaxation time are constant over small time steps. The fluctuating fluid velocity that corresponds to a particular eddy is randomly sampled by using a normal probability distribution function that is obtained from local turbulence properties. When a particle enters an eddy, the fluctuating velocity is added to the local mean fluid velocity. The turbulent flow velocity is assumed to prevail as long as the particle eddy interaction time is less than the eddy lifetime and the displacement of particle relative to the eddy is less than the eddy length.

A particle will remain trapped within an eddy until the turbulent structure around the fluid particle vanishes by exceeding the random lifetime of the fluid domain. The

turbulent velocity, eddy lifetime and length are calculated based on the local turbulence properties of the flow and a random number (Fluent_5, 1998).

$$u' = \Gamma\sqrt{2/3\,k} \qquad 3\text{-}15$$

$\Gamma$ : random number

The second important element in this approach is the manner of determining the time of interaction over which the particle interacts with a randomly sampled velocity field. Two possible events might occur; if the particle moves sufficiently slowly relative to the gas it remains within the eddy during the whole of its lifetime. Otherwise, if the relative velocity between the particle and the gas flow is sufficiently high, the particle traverses this eddy. The interaction time scale is defined as the minimum of the eddy lifetime and the transit time by Brown and Hutchinson (1979).

$$t_{\text{int}} = \min(t_R, t_e) \qquad 3\text{-}16$$

The dissipation length scale of an eddy is given by.

$$l_e = \frac{C_\mu^{3/4} k^{3/2}}{\varepsilon}$$

The eddy lifetime is estimated according to Gosman and Ioannides (1983).

$$t_e = \frac{l_e}{|V_f|}$$

The model used is based on the expressions for the length scale and lifetime published in reference (Shirolkar et al, 1996).

$$t_e = A\frac{k}{\varepsilon}, \qquad l_e = \frac{Bk^{3/2}}{\varepsilon} \qquad A/B = \sqrt{1.5} \qquad 3\text{-}17$$

With the relaxation time defined as follows.

$$\tau_p = \frac{24\rho_p d_p^2}{18\mu_f C_D \,\mathrm{Re}_p} \qquad 3\text{-}18$$

The transit time scale can be estimated for the simplified and linearised form of the equation of motion within an eddy as follows.

$$t_R = -\tau_p Ln\left[1 - \frac{l_e}{\tau_p |V_f - V_p|}\right] \qquad 3\text{-}19$$

If $\frac{l_e}{\tau_p|V_f - V_p|} > 1$ this implies that the particle is inside the eddy.

For turbulent tracking the time step used to compute the particle trajectory is limited by the lifetime of the eddy, and the time required for the particle to traverse this eddy.

## 3.4 BOUNDARY CONDITIONS

The inlet boundary conditions are; particle initial location, particle size distribution and particle concentration in addition to the initial ratio of particle velocity to air velocity. These two last parameters are obtained by laser anemometer measurements. The treatment of the particle trajectories in the CFD boundaries such as; the periodic surfaces, tip region, etc.. are described in details in chapter 2 according to figure 2-8.

- The periodic boundary conditions are commonly used when a better modelling for both the flow and the particle trajectory is needed near the leading edge of blades, in tip clearance and in trailing edge wake. The computation of a particle trajectory continues across the pitch-wise direction from the north to the south of the periodic surfaces and vice versa.

- The magnitude of the impact velocity and its direction relative to a target surface constitute the essential data needed to evaluate the erosion rate. When there is an impact with the blade surface, the impact velocities and angles are used for erosion calculation. The trajectory computation beyond the impacted point is continued using the rebound or restitution ratios obtained experimentally, which define the rebound velocity (and angle) of the particle. The particle is considered to be in collision with a wall, when it is within half-particle diameter tolerance from the wall.

- As the particle approaches a solid wall, the no–slip condition as imposed in this modelling imposes a surface normal gradient in the fluid velocity component tangential to the surface, which in turn can affect the drag exchange between fluid and particles traversing the boundary layer. The consideration of Saffman force component may compensate for this effect near the walls as explained by Humphrey (1990).

- When a particle crosses a point on a plane of symmetry, the reflection angle is equal to the incident angle and the computation continues beyond this point of symmetry.

- The particle trajectory parameters from a row are passed through a successive row or domain in a real time.

- In the tip clearance region the particle movement is considered in the absolute frame of reference, as a consequence, the initial particle velocity must be transformed to

absolute velocity when entering the tip clearance region and to a relative velocity when leaving this region.

From the rotor to the tip region the tangential velocity $V_\theta = V_\theta - \omega r$
From the tip region to the rotor the tangential velocity $V_\theta = V_\theta + \omega r$

### 3.4.1 Normal vector to a symmetrical plane

The normal vector to a plane of symmetry is used when computing the velocity components of the incident and the reflected particle velocity. The normal vector to a plane '$\Pi_T$' figure 3-3, containing the particle velocity $V_{P1}$ and the axis of rotation z, is calculated from the vector product relations.

$$\vec{N} = \frac{\vec{Z} \times \overrightarrow{V_{p1}}}{\left\| V_{p1} \right\|} \qquad 3\text{-}20$$

The normal vector perpendicular to z axis lying on the plane $\Pi_T$

$$\overrightarrow{N_T} = \vec{Z} \times \vec{N} \qquad 3\text{-}21$$

The leaving symmetrical vector is deduced by symmetry.

$$\overrightarrow{V_{p2}} = V_{p1Z}\vec{Z} - V_{p1NT}\overrightarrow{N_T}$$

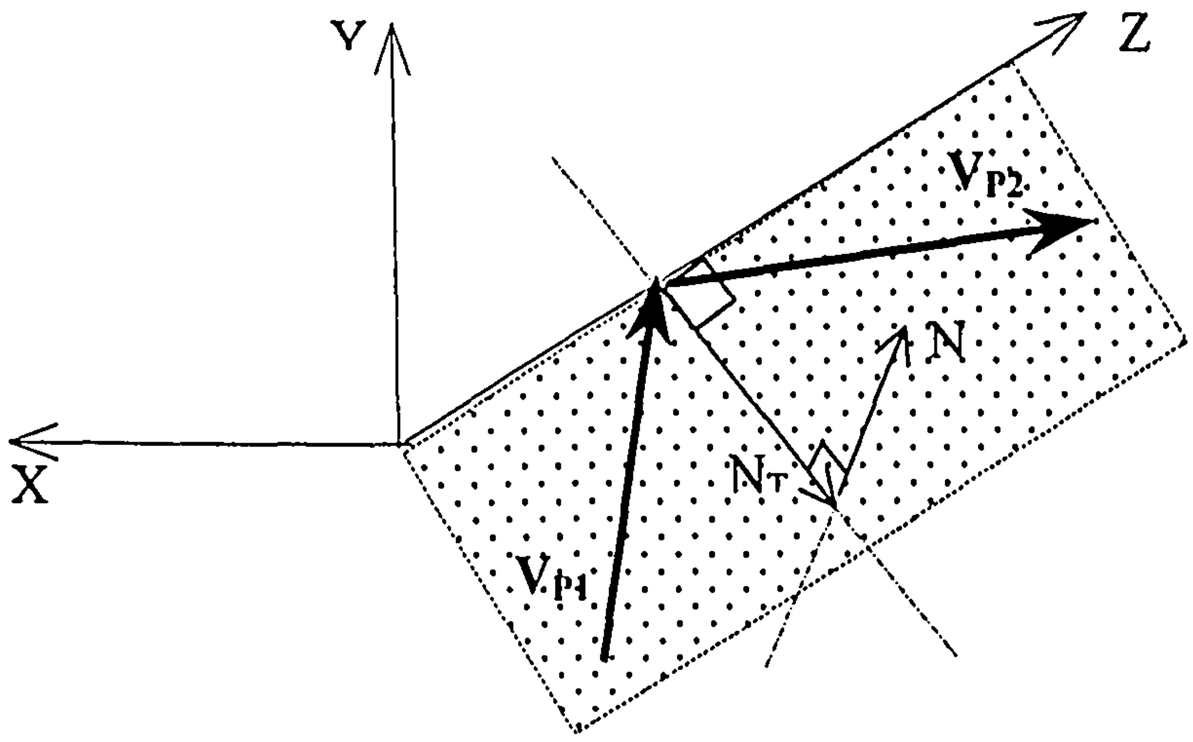


Figure 3-3 Unit vectors on the plane of symmetry

### 3.4.2 Normal and tangential vectors to a surface

The unit vectors at an impact point on a solid surface are used to compute the components of impact and rebound particle velocities. In general, the normal vector to a point on a curvilinear surface defined by the function $s = f(x, y, x)$ is derived from the expression of the gradient on a surface.

$$\vec{N} = \nabla s = \begin{pmatrix} \frac{\partial s}{\partial x} \\ \frac{\partial s}{\partial y} \\ \frac{\partial s}{\partial z} \end{pmatrix}$$

The explicit expression for the curvilinear surface is not available, but its physical co-ordinates are related to the local co-ordinates. The physical derivatives are obtained using the Jacobian matrix transformation, which transforms regular hexahedron with straight edges to irregular hexahedron with curved edges.

$$\begin{cases} \frac{\partial s}{\partial \xi} = \frac{\partial s}{\partial x}\frac{\partial x}{\partial \xi} + \frac{\partial s}{\partial y}\frac{\partial y}{\partial \xi} + \frac{\partial s}{\partial z}\frac{\partial z}{\partial \xi} \\ \frac{\partial s}{\partial \eta} = \frac{\partial s}{\partial x}\frac{\partial x}{\partial \eta} + \frac{\partial s}{\partial y}\frac{\partial y}{\partial \eta} + \frac{\partial s}{\partial z}\frac{\partial z}{\partial \eta} \\ \frac{\partial s}{\partial \zeta} = \frac{\partial s}{\partial x}\frac{\partial x}{\partial \zeta} + \frac{\partial s}{\partial y}\frac{\partial y}{\partial \zeta} + \frac{\partial s}{\partial z}\frac{\partial z}{\partial \zeta} \end{cases}$$

$$[J] = \begin{bmatrix} \frac{\partial x}{\partial \xi} & \frac{\partial y}{\partial \xi} & \frac{\partial z}{\partial \xi} \\ \frac{\partial x}{\partial \eta} & \frac{\partial y}{\partial \eta} & \frac{\partial z}{\partial \eta} \\ \frac{\partial x}{\partial \zeta} & \frac{\partial y}{\partial \zeta} & \frac{\partial z}{\partial \zeta} \end{bmatrix} \qquad 3\text{-}22$$

In matrix form, this involves the inverse of the Jacobian [J]. The outward normal vector with respect to the surface in the direction Xi …(X,Y or Z) is given by.

$$\vec{N} = \pm \begin{bmatrix} \frac{\partial X_i}{\partial X} \\ \frac{\partial X_i}{\partial Y} \\ \frac{\partial X_i}{\partial Z} \end{bmatrix} = \pm [J]^{-1} \begin{bmatrix} \frac{\partial X_i}{\partial \xi} \\ \frac{\partial X_i}{\partial \eta} \\ \frac{\partial X_i}{\partial \zeta} \end{bmatrix} \qquad 3\text{-}23$$

The tangential direction of this vector on a curved surface figure 3-4 may be derived from the vector product as follows.

$$\vec{T} = \frac{\vec{N} \times \vec{V}_{pl} \times \vec{N}}{\left\| \vec{N} \times \vec{V}_{pl} \times \vec{N} \right\|} \qquad 3\text{-}24$$

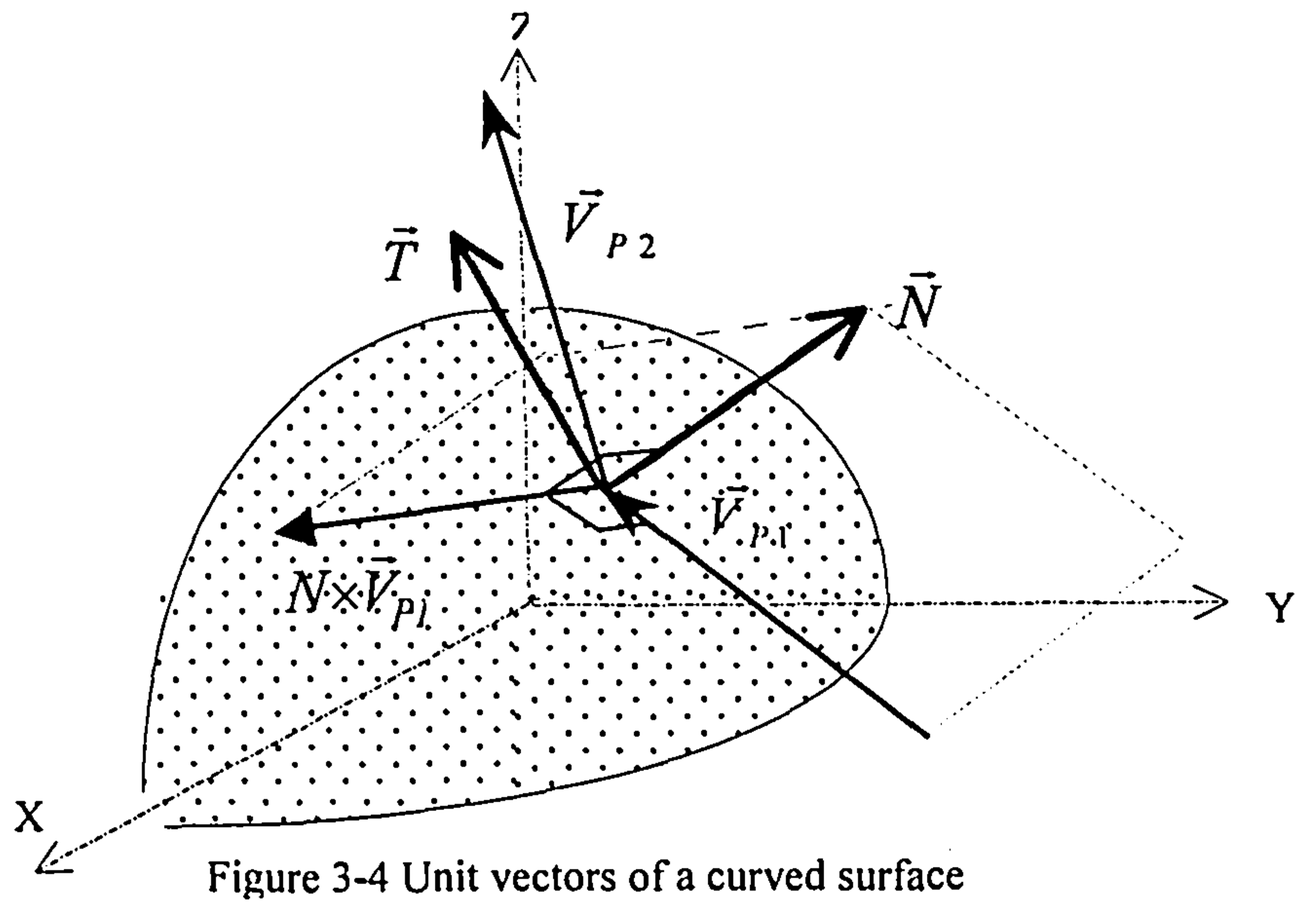


Figure 3-4 Unit vectors of a curved surface

The impact angle is calculated simply from the normal and tangential velocity components.

$$\beta_1 = tan^{-1}\left[\frac{V_{PN1}}{V_{PT1}}\right] \qquad 3\text{-}25$$

The rebound particle velocity and angle are computed from the rebound factors, which are determined experimentally. The fitting polynomials for the restitution ratios are detailed in appendix C.

$$V_{P2}/V_{P1} = a_0 + a_1\beta_1 + a_2\beta_1^2 + a_3\beta_1^3 + a_4\beta_1^4 \qquad 3\text{-}26$$

$$\beta_{P2}/\beta_{P1} = b_0 + b_1\beta_1 + b_2\beta_1^2 + b_3\beta_1^3$$

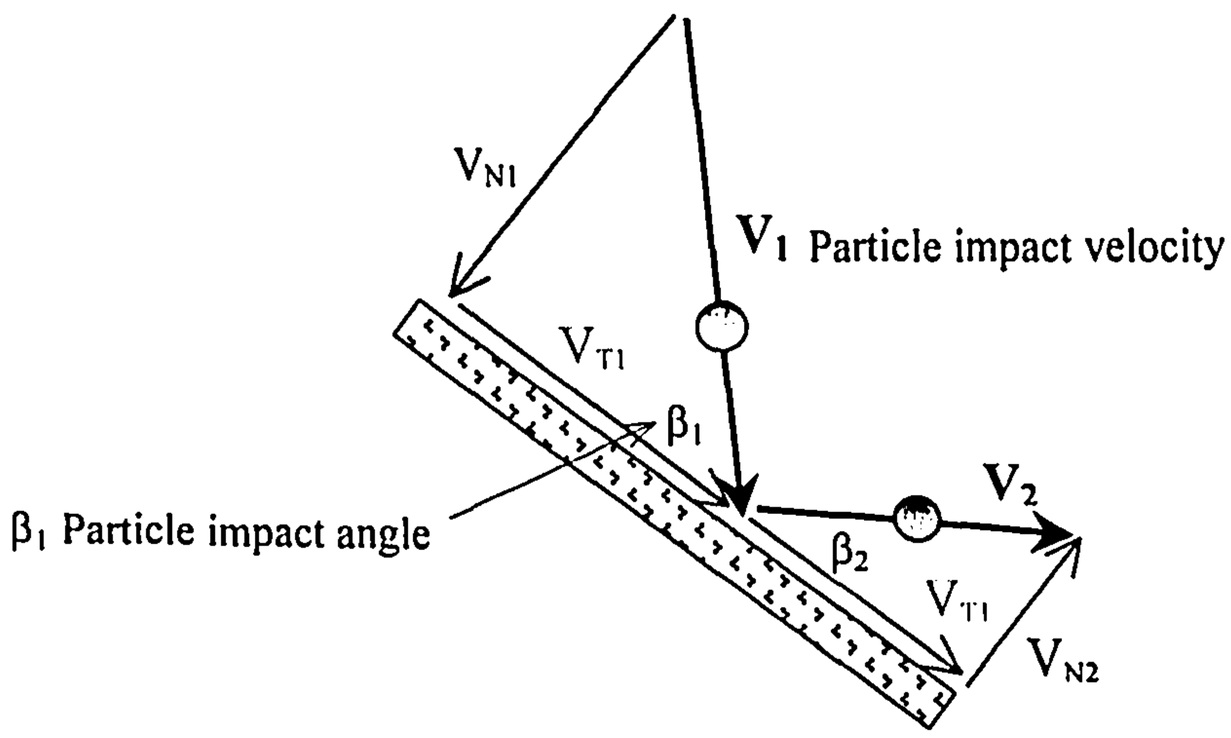


Figure 3-5 Particle velocities and angles before and after impact

## 3.5 ROTOR-STATOR INTERFACE

For each released particle, the new rotor position is determined as function of the time taken by a particle to cross the inlet and the IGV domains. As the rotor stator interface is of sliding mesh, the angular shift of the rotor is computed by applying the periodicity of the rotor blades. The new angular position of the rotor is written as follows:

$$\Delta\theta = \omega \Delta t$$

$$if\ \Delta\theta \geq 2\pi \ \Rightarrow\ \Delta\theta = Mod\left[\Delta\theta\ ,\ 2\pi\right] \qquad 3\text{-}27$$

The new rotor position relative to the initial position at the moment of particle release is computed by.

$$\Theta_R = \Theta_{Ri} + \Delta\theta \qquad 3\text{-}28$$

An implemented searching technique (subroutine *LOCATION* ) is used to find the new element in the adjacent domain sharing the same interface plane, which is supposed to capture the particle. The procedure is based on the vector product around the particle. For a finite surface of an element attached to the interface plane, if the direction of the vector product around this particle doesn't change, then the particle lies on the interface surface. The six faces of the concerned element are visited one by one.

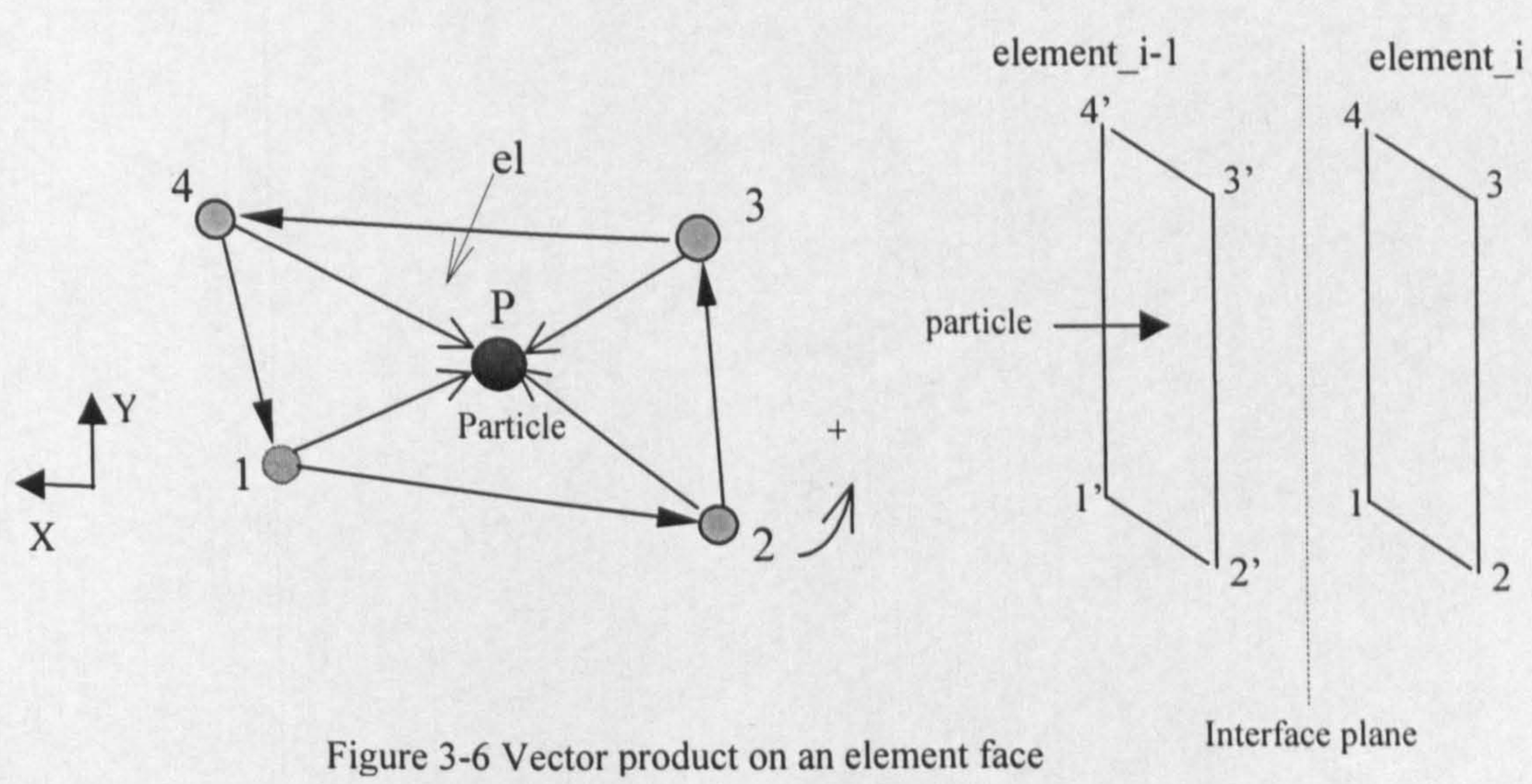


Figure 3-6 Vector product on an element face

For a given element *el* the vector product around the particle P is as follows.

$$\forall i,k\ \ 1...4 \qquad \overrightarrow{V_{ik}} = \left(X_k - X_i\right)\vec{x} + \left(Y_k - Y_i\right)\vec{y}$$

$$\overrightarrow{V_{iP}} = \left(X_P - X_i\right)\vec{x} + \left(Y_P - Y_i\right)\vec{y}$$

$$\forall i,k \quad \frac{\overrightarrow{V_{ik}} \times \overrightarrow{V_{iP}}}{\left|\overrightarrow{V_{ik}} \times \overrightarrow{V_{iP}}\right|} = \pm 1 \quad is\ constant \quad \Rightarrow \quad P \in el$$

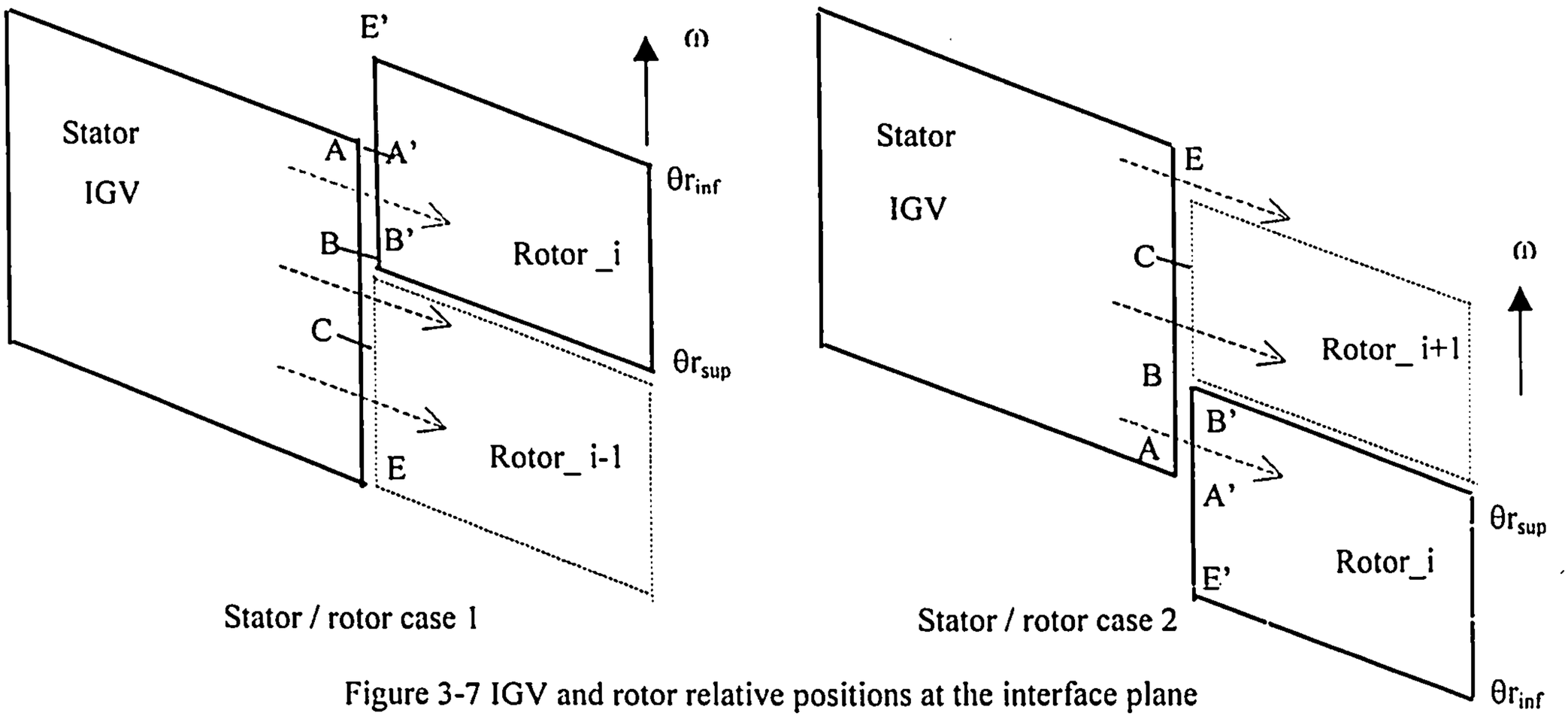


Figure 3-7 IGV and rotor relative positions at the interface plane

The particle exiting the boundary AB, continues its path straight through interface A'B'. By applying the searching technique, the element intercepting the particle is easily found. When a particle is exiting boundary CE, the stator is rotated backward in case 1, and forward in case 2 according to the following relations.

$$\theta_p \rangle \theta_{r\,sup} \quad \Rightarrow \quad \theta_p = \theta_p - \frac{2\pi}{N_{bIGV}} \qquad 3\text{-}29$$

$$\theta_p \langle \theta_{r\,inf} \quad \Rightarrow \quad \theta_p = \theta_p + \frac{2\pi}{N_{bIGV}}$$

Then the searching technique is applied to locate the particle in the interface face A'E' based on the actual particle position.

For particles exiting boundary BC, the rotor is rotated backward to the position $rotor_{i-1}$. In this instance the particle is located respectively to the face B'C', then the particle trajectory is continued relative to this domain until it reaches another periodic surface. The search procedure is started to find the element in the rotor initial position, which contains the particle, based on the local co-ordinates values (subroutine *TRANS* ). The different situations are illustrated by figure 3-13. The tolerance requirement is that the maximum local co-ordinate of a particle inside the anticipated element shouldn't exceed the value 1.05.

$$MAX|\xi i| \leq 1.05 \quad \Rightarrow \quad p \in el$$

When crossing an interface plane from the stator to the rotor, the tangential velocity is modified as following considering a negative rotational speed, $\omega < 0$

$$V_\theta = V_\theta - \omega r$$

From the rotor to the stator the tangential velocity becomes.

$$V_\theta = V_\theta + \omega r$$

Since the blade rotational speed is much higher than the particle velocity at the entrance to the rotor, the position of the rotor blades relatively to the stator may be assumed arbitrarily (Hussein and Tabakoff, 1973). Two positions of the rotor were considered in this study: One corresponds to the rotor leading edge in the wake of the IGV blades and the second corresponds to a position between the IGV blades.

## 3.6 FINITE ELEMENT INTERPOLATION

For a hexahedron element, it is possible to have a linear variation of a field variable if one degree of freedom is chosen at each of the eight corner nodes. The first order linear interpolation model may be expressed in local co-ordinates. The origin of the natural system co-ordinates lies in the intersection of lines joining mid points of the opposite faces of the hexahedron with sides defined by $\xi = \pm 1$, $\eta = \pm 1$, $\zeta = \pm 1$, figure 3-14c. The interpolation polynomial inside an isoparametric first order continuity function using local co-ordinates, according to Connor and Brebbia (1976) is as following.

$$\Phi = \alpha_1 + \alpha_2\xi + \alpha_3\eta + \alpha_4\zeta + \alpha_5\xi\eta + \alpha_6\xi\zeta + \alpha_7\eta\zeta + \alpha_8\xi\eta\zeta \qquad 3\text{-}30$$

The interpolation polynomial can be also written as function of the nodal values. Where N is the shape function given for a three-dimension isoparametric element.



$$\Phi = \sum_{i=1} N_i \Phi_i$$

For a rectangular element with eight nodes, the first order interpolation shape function is given by.

$$N_i = \frac{1}{8}(1+\xi_i\xi)(1+\eta_i\eta)(1+\zeta_i\zeta) \qquad i = 1,8 \qquad 3\text{-}31$$

The integration of the set of differential equations based on the seventh order Runge Kutta Fehlberg routine gives the particle position in the physical co-ordinates r,θ,z, which are converted into Cartesian co-ordinates. For the purpose of the tracking of particles in different cells using directrix values as indicated by figure 3-14b, the local co-ordinates are calculated. The computation of the local co-ordinates involves solving three non-linear interpolation equations.

$$X = \sum_{i=1}^{8} N_i X_i \qquad Y = \sum_{i=1}^{8} N_i Y_i \qquad Z = \sum_{i=1}^{8} N_i Z_i \qquad 3\text{-}32$$

Since this set of equations is non-linear, the Newton-Raphson iterative method (Ledermann, 1981) is applied. A converged solution is reached when the value of 'f' is negligible.

$$f_j = \sum_{i=1}^{8} N_i X_{ij} - X_j \quad = 0 \qquad j = 1,3$$

By expanding this function close to the converged solution and retaining the first order terms yields.

$$-f_{nj} = \sum_{i=1}^{3} \frac{\partial f_{nj}}{\partial \xi_i} \Delta \xi_i \qquad 3\text{-}33$$

To solve the system of equations the method of Cramer is used to calculate the increment $\Delta\xi_i$ . The local co-cordinates values are updated until the convergence is reached.

$$\xi_{n+1,j} = \xi_{nj} + \Delta \xi_j$$

- **Gradient components calculation**

The gradient of a nodal value, for example the flow velocity relatively to a computation cell is dependent on the Jacobian matrix [J].

$$\frac{\partial U}{\partial X} = [J]^{-1} \begin{bmatrix} \partial U/\partial \xi \\ \partial U/\partial \eta \\ \partial U/\partial \varsigma \end{bmatrix} \qquad 1 \quad line \quad matrix$$

$$\frac{\partial V}{\partial Y} = [J]^{-1} \begin{bmatrix} \partial V/\partial \xi \\ \partial V/\partial \eta \\ \partial V/\partial \varsigma \end{bmatrix} \qquad 2 \quad line \quad matrix \qquad 3\text{-}34$$

$$\frac{\partial W}{\partial Z} = [J]^{-1} \begin{bmatrix} \partial W/\partial \xi \\ \partial W/\partial \eta \\ \partial W/\partial \varsigma \end{bmatrix} \qquad 3 \quad line \quad matrix$$

The derivative with respect to local co-ordinates becomes respectively.

$$\frac{\partial U}{\partial \xi} = \sum_{i=1}^{8} \frac{\partial N_i}{\partial \xi} U_i \quad , \quad \frac{\partial U}{\partial \eta} = \sum_{i=1}^{8} \frac{\partial N_i}{\partial \eta} U_i \quad , \quad \frac{\partial U}{\partial \zeta} = \sum_{i=1}^{8} \frac{\partial N_i}{\partial \zeta} U_i$$

$$\frac{\partial U}{\partial \xi} = \sum_{i=1}^{8} 1/8\, \xi_i (1+\eta\eta_i)(1+\varsigma\varsigma_i) U_i$$

$$\frac{\partial U}{\partial \eta} = \sum_{i=1}^{8} 1/8\, \eta_i (1+\xi\xi_i)(1+\varsigma\varsigma_i) U_i \qquad 3\text{-}35$$

$$\frac{\partial U}{\partial \zeta} = \sum_{i=1}^{8} 1/8\, \zeta_i (1+\xi\xi_i)(1+\eta\eta_i) U_i$$

## 3.7 SEVENTH ORDER RUNGE-KUTTA FEHLBERG

The difficulties of providing a satisfactory step width control to Range-Kutta methods have been largely overcome by recent development due to Fehlberg (1968). The Runge-Kutta Fehlberg formulas contain a step size control, which is based on a complete coverage of the leading local truncation error term, Fehlberg (1969). Naturally these formulas require more evaluations steps of differential equations than the known classical R-K without step size control procedure. However, they require fewer evaluations per step than the known classical formulas. The permissible increase in time step together with the reduced number of evaluations per step accounts for its superiority compared to other R-K methods. The leading truncation error term at each step is determined by computing two approximations for the solution.

For a set of differential equation $y' = f(x, y)$,
With initial values $f(x_0, y_0)$.

In the customary way of the classical R-K methods we set.

$$\begin{cases} f_0 = f(x_0, y_0) \\ f_k = f\left(x_0 + \alpha_k h, \quad y_0 + h\sum_{\lambda=0}^{k-1} \beta_{k\lambda} f_\lambda\right) \end{cases} \qquad k = 1,2,3.....,12 \qquad 3\text{-}36$$

And we require the seventh order R-K Felhberg in the form of.

$$\begin{cases} Y_1 = Y_0 + h\sum_{k=0}^{10} C_k f_k + O(h^8) \\ \hat{Y}_1 = Y_0 + h\sum_{k=0}^{12} \hat{C}_k f_k + O(h^9) \end{cases} \qquad 3\text{-}37$$

Where $h$ is the step size used in the numerical method and the coefficient $C_k, \hat{C}_k \beta_{k\lambda}$ are the weighting coefficients, which are given by Fehlberg (1968).
The estimation of the leading truncation error term at every step in the R-K Felhberg technique involves the calculation of two approximations of the solution. The difference between them gives the leading term in the local truncation error as follows.

$$err = h\sum_{k=0}^{10}(\hat{C}_k - C_k) f_k + h[\hat{C}_{11} f_{11} + \hat{C}_{12} f_{12}]$$

The resulting maximum error is in the order of $O(10^{-6})$. The truncation error takes the form of.

$$err = \frac{41h}{840}(f_0 + f_{10} - f_{11} - f_{12}) \qquad 3\text{-}38$$

The system of differential equations (3-13) can be rewritten as follows:

$$F_j = F_j(r_p, V_{rp}, V_{\theta p}, V_{zp}) \qquad j = 1,6$$

The two approximations of solution at step (n+1), according to 3-36 and 3-37.

$$\begin{cases} Y_{n+1i} = Y_{ni} + h\sum_{k=0}^{10} C_k T_{jk} + \mathrm{O}(h^8) \\ \hat{Y}_{n+1i} = Y_{ni} + h\sum_{k=0}^{12} \hat{C}_k T_{jk} + \mathrm{O}(h^9) \\ T_{jk} = F_j\left(Y_i + h\sum_{\lambda=0}^{k-1} \beta_{k\lambda} T_{j\lambda}\right) \qquad k = 1,2,3,\ldots\ldots\ldots\ldots,12 \end{cases} \tag{3-40}$$

Where.

$$\begin{cases} i = 1,4 \\ T_{jk} = F_j(Y_i) \\ Y_1 = r_p, \quad Y_2 = V_{rp}, \quad Y_3 = V_{\theta p}, \quad Y_4 = V_{zp} \end{cases}$$

And the resulting error for the set of equations is given by.

$$err_j = \frac{41h}{840}\left(T_{j0} + T_{j10} - T_{j11} - T_{j12}\right)$$

### 3.7.1 Stability of the method

In general, the Runge-Kutta methods are one step convergent methods. In order to choose a reasonable time step, one needs some estimate of the error during integrating across one step. The time step should be small enough to achieve the required accuracy. On the other hand, it should be as large as possible to keep rounding errors under control and to avoid an excessive number of derivatives evaluations (Carnahan et al, 1969). R-K methods are quite stable with reasonable time-step but instability can arise if a too large time step is used. It may be possible to keep the propagation error under control, especially during the early course of the integration by choosing sufficiently small steps.

### 3.7.2 Treatment of particle trajectory near a boundary

In order to reach a convergent solution rapidly near a boundary, the time step was chosen to be fairly large around the first 20 steps of integration. Then, an accelerated reduction of time step is maintained in order to bring particle near a boundary condition within the prescribed tolerance. Figure 3-8 shows the time step evolution function of number of steps near a specified boundary.

- Treatment for a wall boundary condition when local co-ordinates are less than unity.
  - Find the direction of the walls if more than one:

$$\forall\, i = 1,3 \quad |\eta_i| \le 1 \qquad\qquad if\ wall[elm, \mathrm{Ifind}(\eta_i, \mathrm{i})]\ \ true \ \Rightarrow\ \ I_w$$

- Identify the nearest wall.

$$\forall\ j = 1, I_w \qquad , \max_{j=1,I_w}(\eta_j) \ \Rightarrow \quad J_{imp} = j$$

The necessary condition of particle impact is given by the product of the velocity by the normal vector on the surface.

$$\left(\vec{n} \bullet \overrightarrow{V_p}\right) < 0$$

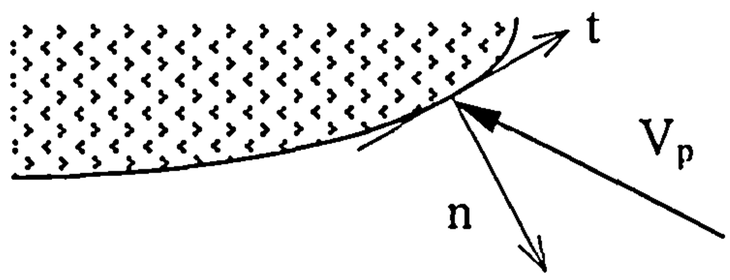


- The full impact condition including the tolerance ε of the proximity of the particle from the wall is governed by.

$$\begin{cases} If \quad \left|\eta_{imp}\right| > (1-\varepsilon) \quad and \quad \left(\vec{n} \bullet \overrightarrow{V_p}\right) < 0 \quad \Rightarrow \quad imapct \\ otherwise \qquad \Delta t \downarrow \end{cases} \qquad 3\text{-}41$$

- If this condition is not satisfied, then the time step is reduced and the last step is repeated.

- For the case of one or more local co-ordinates being greater than unity the following procedure is applied.

$If \quad \left|\eta_{imp}\right| > 1 \quad \Rightarrow$ Search for the new element using the directrix increment.

As the new element is found the local co-ordinate is recalculated as follows.

$$\eta_i^{'} = Ifix\left(\frac{\eta_i}{|\eta_i|}\right).\left|\eta_i\right| - 1\left|\right.$$

The necessary condition of impact yields:

$$\left(\vec{n} \bullet \overrightarrow{V_p}\right) \geq 0$$

Within the specified tolerance, the impacting condition is constrained by.

$$\begin{cases} If \quad \left|\eta_{imp}\right| \leq (1+\varepsilon) \qquad and \qquad \left(\vec{n} \bullet \overrightarrow{V_p}\right) \geq 0 \quad \Rightarrow \ impact \\ otherwise \qquad \Delta t \downarrow \end{cases} \qquad 3\text{-}42$$

Similar treatments are also carried out for the symmetrical boundaries.

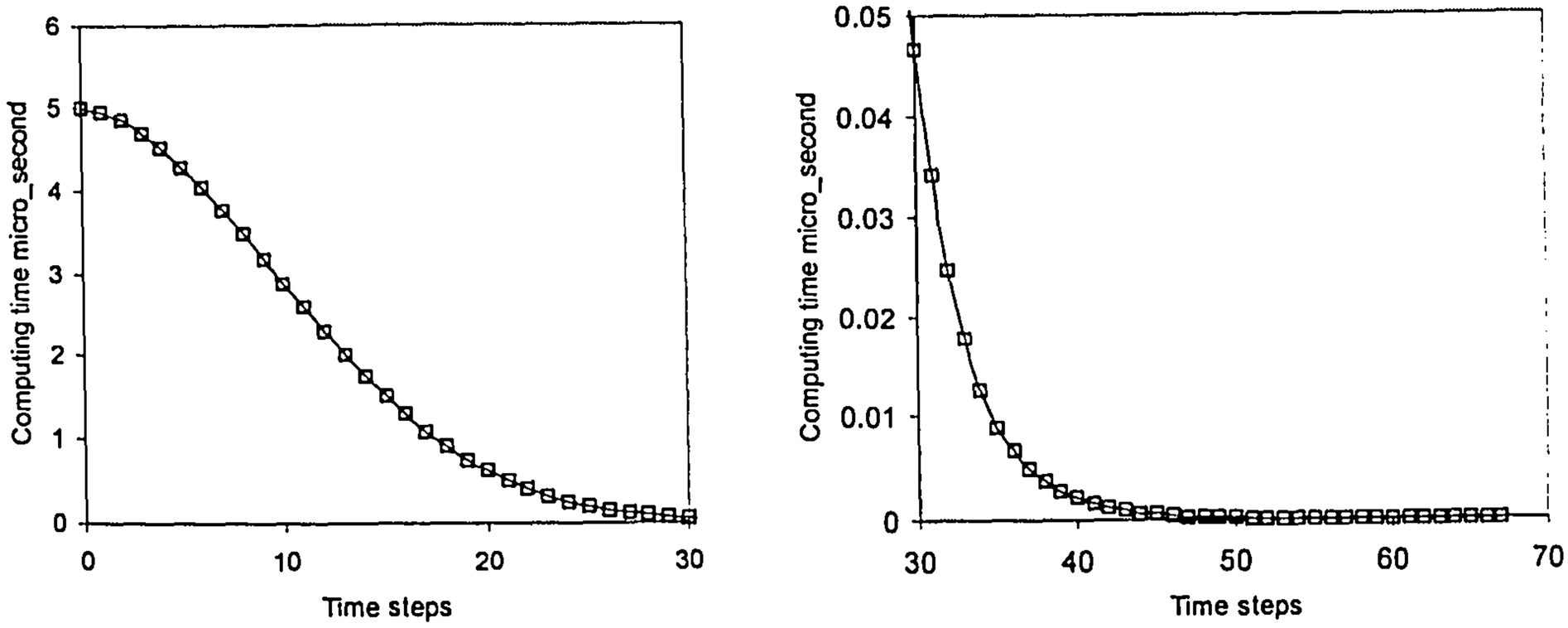


Figure 3-8 Computing time step function of step number

## 3.8 THE SOLUTION PROCEDURE

The Lagrangian based integration procedure considering the turbulent flow effect is presented in the flow-chart F3-1. The time step for integration is obviously the eddy particle interaction time. The computation of the particle trajectory consists of the numerical integration of the set of differential equations using the seventh order R-K Fehlberg method. The flow properties are interpolated for the given particle position using finite element method. The position of the particle is found in cylindrical co-ordinates and transformed into Cartesian co-ordinates. To search for particle position, the physical co-ordinates have to be transformed to the local co-ordinates. If the local co-ordinates are less than or equal to unity, the particle is considered to be within the initial element. If not, this element is incremented using directrix values as shown by figure 3-14b, and the search procedure is continued. Similar technique was used by Tan, (1984). As the new element is found, the flow parameters are interpolated and the new Jacobian matrix coefficients are updated. The interpolated flow properties are used to compute the particle trajectory step by step.

A logical test is done at each step to check for a possible boundary condition. If any, the time step is reduced to bring the particle within a certain tolerance close to this boundary. Each type of boundary condition (wall, periodicity, symmetry, tip clearance, stage interface) has got an assigned logical parameter, which serves to identify the type of boundary. If a particle reaches a wall for example, then the unit normal and tangential vectors are computed, and the rebound velocity and angle are calculated, and are used to compute the erosion rate. If there is a periodic boundary condition, the particle position is moved to the opposite boundary surface, but the velocity and its direction are conserved. If the particle reaches a stage interface, then a search procedure is started to determine precisely the location of the particle in the adjacent domain.

## 3.9 INITIAL LOCATIONS OF PARTICLES

In the present study, particles can be released as a group with similar physical characteristics distributed as prescribed or measured concentration profile, or simply as a random distribution. When particles are defined (and injected) as a group, a single particle is needed to be injected at one node or several particles representing several groups with different particle sizes are injected over a range of nodes. The particle group can also be subdivided into classes, each class representing a subset of the group with a given particle size and fraction of the total mass flow. The following initial locations can be used in the present modelling of particle trajectories

- Point a discrete nodal co-ordinates
- Line group of continuous flux element edges defined by a variation in a single co-ordinate direction.
- Surface group of continuous flux element faces defined by a variation in two co-ordinates directions

### 3.9.1 Global injection initial particle locations

The initial locations of sand particles are dependent on the specified concentration profile along the radial co-ordinate of the annular inlet sector. The sand particle concentration distribution along the blade height was measured by a laser transit anemometer. The concentration profile was deduced from the ratio of the count number $N/N_{max}$ obtained from the time of flight curve, see Chapter 5.

The measured concentration profile expressed as milligrams of particles per meter cube of air is given as follows.

$$C(r) = \frac{\rho_a C_m}{\frac{2m_a}{(r_t^2 - r_h^2)}\int_{r_h}^{r_t} \frac{N(r)}{N_{\max}} r dr}\left[\frac{N(r)}{N_{\max}}\right] \qquad mg/m^3 \qquad 3\text{-}43$$

The equivalent mean concentration $C_m$ based on the integration area:

$$C_m = \frac{2}{r_t^2 - r_h^2}\int_{r_h}^{r_t} C(r) r\, dr$$

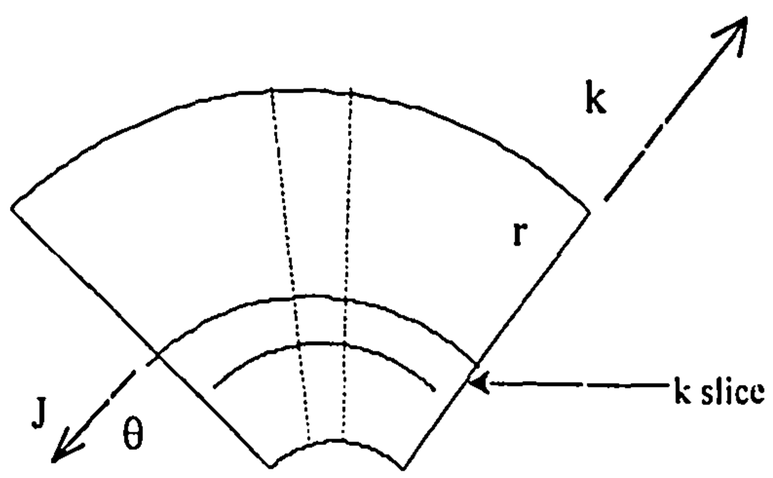


Figure 3-9 Inlet sector of the computational domain

The approximated total particle number is obtained from the mean concentration across the inlet passage.

$$N_p = \frac{0.6\dot{m}_a C_m}{N_{bIGV}\,\rho_a \rho_p \overline{d}_p^3 \left(r_t^2 - r_h^2\right)} \qquad 3\text{-}44$$

The actual number of particles $C_i$ and $C_{jk}$, are the local values of concentration relative to an annular strip and a discrete element belonging to the inlet sector.

$$N_p = \frac{0.6\dot{m}_a \sum_{i=1} C_i A_i}{N_{bIGV}\,\rho_a \rho_p \overline{d}_p^3 \left(r_t^2 - r_h^2\right)}$$

The distribution of particles as dictated by the concentration profile relatively to discrete elements of the inlet sector is carried out by the subroutine *IN_PART*.

$$N_p = \frac{0.6\dot{m}_a \sum_{j=1}^{J} C_{jk} A_{jk}}{N_{bIGV}\,\rho_a \rho_p \overline{d}_p^3 \left(r_t^2 - r_h^2\right)} \qquad 3\text{-}45$$

The equivalent radial discrete distance between successive particles is calculated by.

$$\Delta r_{k-1,k} = \sqrt{\frac{A_k}{N_{pk}}}$$

The number of particles along a radius and a circumferential direction of one slice are as follows.

$$N_r = \frac{r_{k-1,k}}{\Delta r_{k-1,k}}, \qquad M_0 = \frac{N_P}{N_r} \qquad 3\text{-}46$$

For a given sector of an annulus limited between two radius and two angles, a polar mapping ( Knupp and Steinberg, 1994) is used to refine the grid in each slice in order to set accurately the particle positions within the inlet sector. Then, the initial positions of particles according to the initial grid are found by using a searching technique based on the vector product as described in section 3-5. The finer grid is generated according to the following algorithm based on polar co-ordinates.

$$0 \le r_0 < r_1 \qquad 0 \le \theta_0 < \theta_1 \le 2\pi$$

$$\begin{aligned} X(\xi,\eta) &= r\cos\theta \quad , \quad Y(\xi,\eta) = r\sin\theta \\ \theta &= \theta_1 + (\theta_0 - \theta_1)\xi \quad , \quad r = r_0 + (r_1 - r_0)\eta \end{aligned} \qquad 3\text{-}47$$

The particle diameters are randomly distributed around a mean value by using the subroutine statistics.

$$d_p = \overline{d}_p + \Gamma\sigma \qquad 3\text{-}48$$

Iterations are repeated until a convergence of particle mass rate is reached.

$$Q_P = \sum_{n}^{K} \sum_{m}^{M_0} \sum_{k}^{N_R} \rho_P \frac{\pi}{6} d^3_{P(nmk)}$$

### 3.9.2 Local injection initial particle locations

From the mass rate of particles released from an injector pipe, the total number of particles $N_p$ is calculated from the following numerical series.

$$4\pi r_p / 2r_p + 8\pi r_p / 2r_p + \cdots\cdots\cdots\cdots + (M-1)^{4\pi r_p}/_{2r_p} + 1 = N_p$$

Which can be simplified to the following expression after summation.

$$\pi M(M-1) = N_p - 1$$

Where M is the number of particles along a normal axis of the pipe injector, which can be computed by the following relation

$$M = \frac{-\pi + \sqrt{\pi^2 - 4(1 - N_p)}}{2\pi} \qquad 3\text{-}49$$

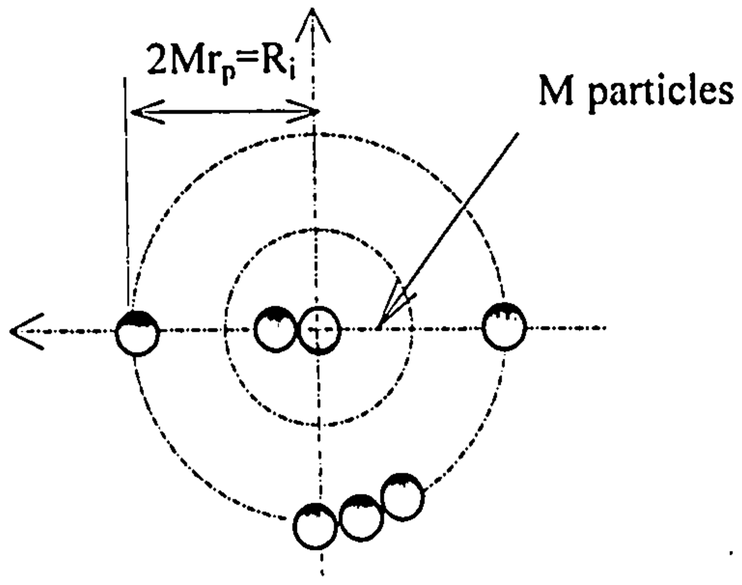


Figure 3-10 Pipe injector particles distribution

The initial particle velocity and its radial component are determined from experimental measurements by using laser anemometer. The angle of spread is computed from the concentration profile at a given distance from the pipe injector. This angle of spread is divided by the number of layers, according to the relation 3-49.

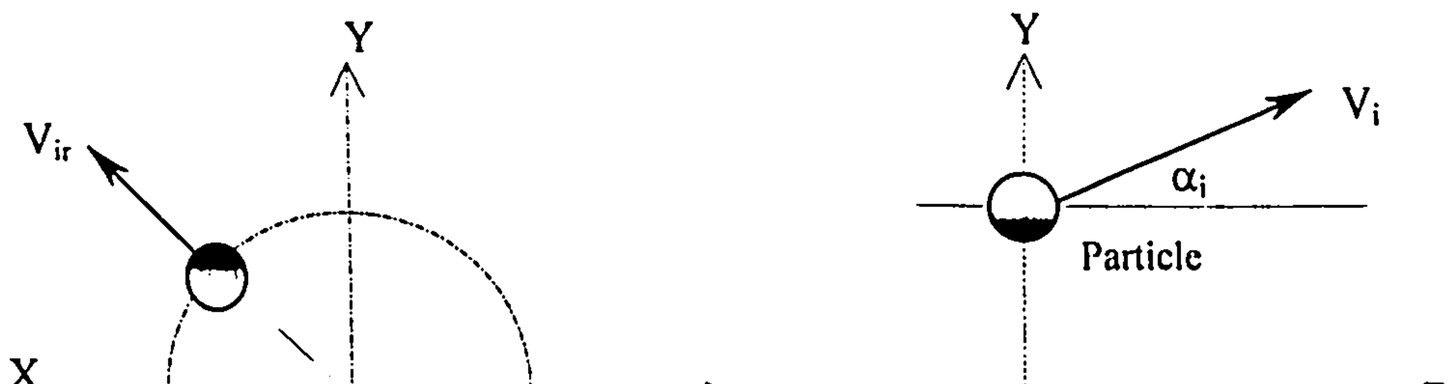


Figure 3-11 Initial velocity from a pipe injector

## 3.10 PROBABILISTIC SIMULATION

The physical problem of natural dust ingestion into a turbomachine is heterogeneous. The particles which are entrained in the air intake come in various sizes, shapes and compositions. The initial locations of particles in the inlet vary radially and circumferentially. In addition, the initial position of the rotor relatively to IGVs is unknown. Also, particles do not rebound in the same manner near a wall, thus, the restitution ratios are defined within standard deviation values. Variation in these factors will affect the particle trajectory and the locations of impacts as well as the quantity of material removed.

The simulation of particle dynamics and erosion involves randomly distributed particles size and rebound factors. These parameters have inherent variance, which can be characterised by probability density distribution functions. The cumulative continuous frequency for a given random phenomenon between 0 and infinity is obtained by integration of its distribution function.

$$F(X) = P(X \leq \infty) = \int_0^{\infty} f(x)dx$$

The most frequently occurring value of x is the average

$$\mu = average\ (x) = \int_0^{\infty} xf(x)dx$$

The standard deviation is defined by.

$$\sigma^2 = average\left[(x-\mu)^2\right] = \int_0^{\infty} x^2 f(x)dx - \mu^2$$

The most frequently encountered statistical problems are those involving the Gaussian distribution.

$$f(x) = \frac{1}{\sigma\sqrt{2\pi}} \exp - \left[ {(x-\mu)^2}/{2\sigma^2} \right]$$

For a given random number between –1 and +1, the more probable variable lies in the following interval.

$$\mu - \xi\sigma \leq x \leq \mu + \xi\sigma \qquad 3\text{-}50$$

As an example, the following sampling curve 3-12 gives the particle size distribution in a cumulative form. The second curve represents the derived frequency of occurrence using a splint fitting. A statistical treatment leads to the determination of the mean and the variance used for generating a random distribution function.

Two types of sand particles are used; a narrow bandwidth sand particle (150-300 micron) and a broader size distribution according to MIL-E 5007E (0-1000 micron), figure 3-15 and figure 3-16. A number of methods are detailed in the literature to define the characteristic size of solid particles. A useful discussion is given in reference (Faddick, 1980), (Wiedenroth, 1978). The sizes of a particle, their impact velocities and angles of impingement are major contributors for the fragmentation. A correlation for

particle fragmentation involving both velocity of impact and angle of impact was included in the trajectory code. The step particle size after fragmentation is stored for later calculations.

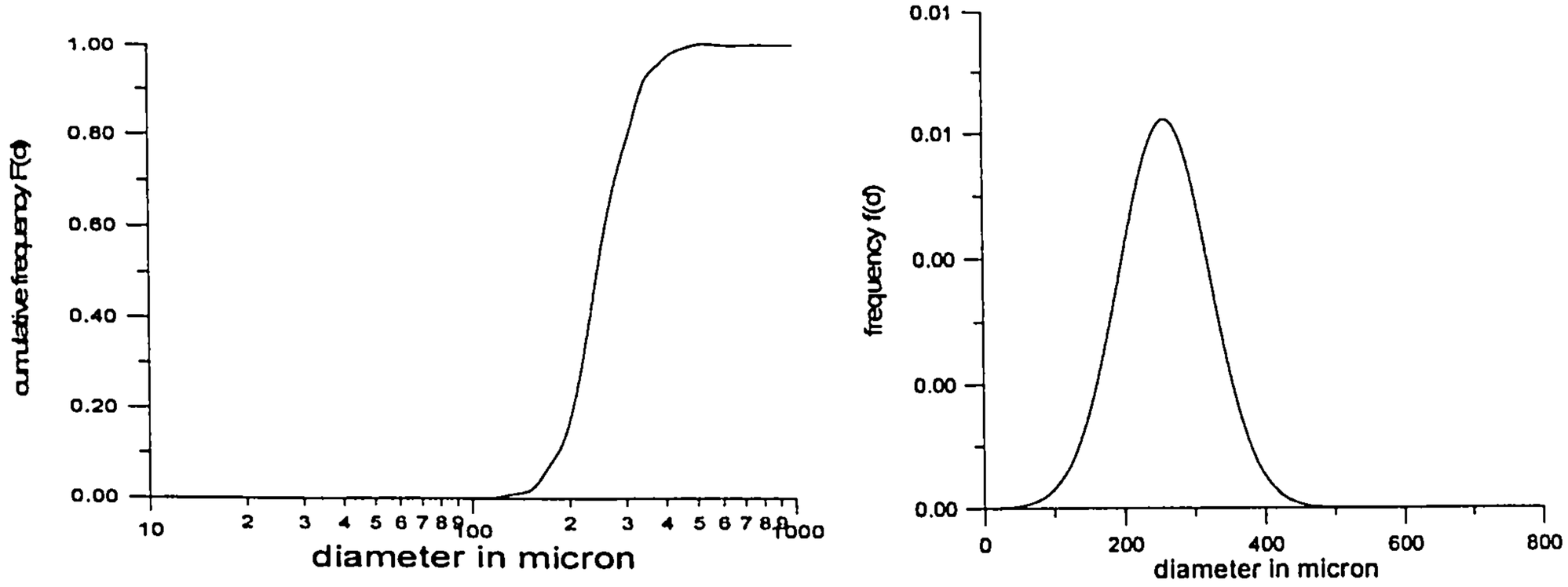


Figure 3-12 Cumulative distribution of particle size and the derived frequency

## 3.11 PROGRAM STRUCTURE

*PARTRAJ* is a developed Fortran program for predicting particle trajectory and erosion of turbomachinery blades, which includes different types of boundary conditions and handles multiple frames of reference. This program consists of several subroutines as shown in flow-diagram F3-2. The core of this program is the subroutine *TRAJ*, which solves particle trajectory including different types of boundary conditions and frames of reference. This subroutine calls principally *RKUTTA*, *INTVEL* and *TRANSF* subroutines, see the flowchart F3-3.

The subroutine *RKUTTA* uses the seventh order R-K Fehlberg to solve the second order differential equations of solid particle motion. The particle position is available in the physical r,θ,z co-ordinates, but particle tracking in computational cells is based on the local co-ordinates. The physical co-ordinates are converted to the local co-ordinates by using the subroutine *TRANSF*, which is based on the Newton method to solve a non-linear system of equations. If the values of local co-ordinates are less or equal one, the particle is within the initial element if not, more iterations are required to refine the particle position within an accurate element.

The principal subroutines are listed below with a description of their functions:

| *Subroutine* | *Function* |
|---|---|
| **PARTRAJ** | Main program to control the different print files, call for subroutines to read the specific data files and initiate the computations. |
| **TRAJ** | Computes the particle trajectories, tracks particle inside finite element cells and checks for boundary conditions. |

| | |
|---|---|
| **IN_PART** | Reads the control and the initialising data |
| **REDATA** | Reads the geometry of each domain, defines the domain topology with the numbering and the orientation of the surfaces of elements and determines their directrix. Each boundary condition for a given node is read and stored for the subroutine TRAJ |
| **DISTRIB** | Distributes particles in the specified inlet area according to the concentration profile of the released particles. A switch control parameter allows either a local or global injection |
| **INTVEL** | Interpolates for the flowfield components |
| **LOCATION** | Searches for the actual element, which contains the particle |
| **RKUTTA** | Integrates the equations of motion of a particle numerically using Runge Kutta - Fehlberg seventh order method |
| **JACOBI** | Computes the Jacobi matrix of transformation in local co-ordinates |
| **TRANSF** | Transforms global co-ordinates to local co-ordinates. |
| **REFL** | Computes the particle rebound properties, using the tangential and normal restitution expressions |
| **VECN** | Computes the unit normal vector at a point of impact using the Jacobian matrix coefficients |
| **ACOEFF** | Computes the matrix of interpolation function |
| **SPLINT** | Interpolates for a given data array using splint interpolation method |
| **STATISTIC** | Calculates the mean and variance of a given distribution variable |
| **RANDOM** | Generates random numbers |
| **EROSION** | Computes the rebound velocity, and the rate of erosion |
| **OUTPUT** | Computes the mass of material removed and the depth of impact, and distributes erosion rate on the nodes of the impacted element. Also, calculates the profile geometry deterioration, and store data for post-processing |

All the matrices and arrays memory allocations and common variables are passed throughout subroutines by using the '*include*' statement for the common block *COMMB*, shown in table 3-1.

The subroutine *IN_PART* reads the following initialising variables;

| *Designation* | *Variable* |
|---|---|
| Fragmentation parameter | IFRAG |
| Turbulence switch | ITURB |
| Local injection switch | INJECT |
| Annular or parallelepiped intake switch | ISECTOR |
| Hub radius | RADH |
| Tip radius | RADT |
| Number of stator blades | NBIGV |
| Number of rotor blades | NBROT |
| Total mass flow | XMTOT |
| Inlet total pressure | HEAD |
| Aerodynamic shape factor | SFACTR |
| Particle density | RHO |
| Initial velocity ratios in axial, radial and tangential direction | VRATIO (k), k=1,3 |
| Time step | DT |
| total time | TDT |
| Axial termination limit | ZLIMIT |
| Radial termination limit | RLIMIT |
| Diameter limit | DIALIMIT |
| Rotational speed | OMEGA |
| Number of groups of material used | NGRP |
| First element | MS1 |
| Last element | MS2 |
| Material type | ITYPE |
| Injector mass rate | CONCINJ |
| Spread angle | ALFDIF |
| Radial position fraction | RRINJ |
| Angular position | TETAINJ |
| Axial position | ZINJ |
| First element for particles distribution | ISM1 |
| Parameter used in Random function generator | IRAND |

All these parameters are read in this order from the input file '*dinput.dat* ' see table 3-2

The particle concentration profile '*conc.dat*' is read by *DISTRIB* and the size distribution 'dia.dat' is read by ' *IN_PART* ', both are shown in table 3-5 and table 3-6 respectively.

To specify the type of boundary condition as read by *REDATA* a parameter **LT** was assigned to each node constituting the global computational domain.

**LT = 1** node in the flow field
**LT = 2** node on the periodic surface
**LT = 3** node in the tip leakage zone
**LT = 5** node on the wall
**LT = 6** node on the symmetrical plane

Samples of the geometry and flowfield data read by subroutine *REDATA* are shown in table 3-3 and table 3-4.

The preparation of the geometry with the specified boundary conditions and the flow field data is achieved by an interface FORTRAN program ' *Spliturbful.for* '. The data read by this interface are taken from the CFD results, file '*RSF*' obtained from *TASCFlow* code.

The tracking of a particle through the computational domain elements requires searching for different elements traversed by this particle. This is achieved by calculating the local particle co-ordinates, figure 3-14c and ensuring that they are within the prescribed tolerance. There are 6 directrix (Tan, 1984), for the six faces of an element. Each directrix, which depends on the local co-ordinates values is used to increment the element number when searching the next element. Also, it gives an indication when a particle is crossing an interface. The nodes and the faces of an element with their directrix are shown in figure 3-14b and 3-14c. The subroutine *REDATA* is used to define the sub-domains and the global domain topology and to order the numbering and the orientation of the surfaces of each element and its directrix.

## 3.12 CAPABILITIES OF THE TRAJECTORY CODE

The trajectory code *TRAJPART* was run for different test cases consisting of simple bluff bodies represented by half-tandem cylinders and full tandem cylinders placed in a rectangular section of a wind tunnel. These tests served to ascertain the turbulence modelling as discussed in section 3.3. Also, these examples served to demonstrate the trajectory modelling capabilities in dealing with turbulence effect, handling of the particle impacts and rebounds and symmetry.

The first two test cases consisted of half tandem cylinders with a linear wall on the top and a plane of symmetry passing through the bottom. These cases were run at Reynolds numbers ($9x10^4$, $3x10^4$). A second test case consisting of full cylinders was performed to demonstrate the effects of the turbulence dissymmetry on particle trajectories at a given Reynolds number.

As conclusions; large sand particles (150-300microns) seeded locally with an initial velocity and angle of spread and those seeded globally with a uniform concentration deviate considerably from the streamlines. After rebound on a wall they tend to follow ballistic trajectories, figures 3-17 and 3-18. On the symmetrical boundary the reflection angle is equal to the incident angle, this boundary condition allows trajectory computation to be continued beyond this limit, figure 3-19.

The small particles of 10 micron tend to follow streamlines, figure 3-20a. In the wake regions fine particles within eddies follow the whole flow patterns till they completely dissipate their energy, but some particles may acquire kinetic energy and escape from eddies. The effect of turbulence on particles was obvious through a comparison of the fine particles dynamic behaviour with and without turbulence, figures (3-20a, 3-20b). Also, the location of impacts may change and their number may increase due to circulation. The intensity of turbulence is very high between the two cylinders, with an evidence of a dissymmetry as shown by figure 3-21a. The trajectories of fine

particles and the fluid streak-lines are similar after including the turbulence effect, figure 3-21b compared with figure 3-21c.

## 3.13 TRAJECTORY COMPUTATION THROUGH THE AXIAL FAN

The domain used for the particle trajectory computation is the CFD computational domain, which was discussed earlier in chapter 2 (figure 2-8). The number of released particles depends on the concentration of sand particles, the fan operating condition and particles sizes. The time step used for trajectory integration lies between 0.5μs to 1μs. The initial conditions are; particle initial locations, which depend on concentration in addition to the initial ratio of particle velocity to air velocity measured by laser anemometer (chapter 5).

The main outputs of this code are; the file '*Ipvdat.dat*' table 3-7, containing the particle co-ordinates, the traversed elements, the velocities and the particle diameter. The file " *Impdat.dat* " gives the co-ordinates of impacts, velocities and rebound of impacts and the rates of erosion table 3-8. A Fortran program '*fv_traj.for*' is used to make the necessary transformations for the particle trajectory and impact locations for the purpose of the visualisation and plotting by the software *FIELDVIEW*.
The *Output* subroutine stores the erosion contours and the eroded blade geometry.

### 3.13.1 Local injection particle trajectory simulation

For the simulations of local injection particle trajectory, the initial release velocity and the angle of spread were determined by the laser transit anemometer measurements across plane ' I ' at 50mm upstream the IGVs, (Chapter 5). The initial release positions were concentrated within 3mm diameter around the pipe injector in radial and tangential direction.

The predicted trajectories from the three initial release positions show a noticeable deviation from the mean flow path due to the radial particle spread figures 3-22, 3-23, 3-24 and 3-25, which was also evident from the measured concentration profiles figure 5-35. Larger particles tend to follow ballistic trajectories after hitting solid walls, but smaller particles tend to follow streamlines. It may be seen that many particles impact the blade leading edges, the pressure side and the trailing edge. Other particles cross the stage without any collision.

A high number of impacts are found near the leading edge because of the high relative velocity and angle, figure 3-33. Also, they are found near the tip region due to the high centrifugation force, figure 3-34. Some particles are entering the rotor blades with a high negative incidence angle, as a result a region of multiple impacts is clear around the leading edge on the suction side, in figure 3-22 and figure 3-23. Some impacts on the trailing edge of IGV are due to the rebounding particles from rotor leading edge and due to spread of particles, figure 3-22.

When seeding near the tip, an area of impacts is evident towards the tip trailing edge corner, figure 3-34. When the injector is moved near the hub an area of impacts

appears near the hub figure 3-35. Obviously, because of lower impinging velocities in this region the erosion rate is lower.

The predicted trajectories show tip particles migrating from the pressure to suction side of the blade via the tip clearance, and in the process causes tip erosion, figure 3-22 and 3-23. In the tip clearance the particles entrained by the flow lose their initial centrifugation force, and after repeated impacts on the shroud their sizes reduced.

The predicted particle velocities and their directions are in good agreement with the laser measurements. In the case of local injection, the figures 3-38a 3-38b give approached results with the experiments shown by figure 5-36. The predicted local concentrations upstream IGVs at the three release positions as illustrated by figure 3-40 agree well with the measured concentrations in figure 5-35.

### 3.13.2 Global injection particle trajectory simulation

For the global particle injection trajectory simulations, the initial locations of particles are distributed in radial and tangential directions according to the measured concentration profile. The initial particle release velocities were determined by the laser transit anemometer measurements across plane ' II ' at 35mm upstream the fan nose, where the trajectory computation is started. This simulation is based on randomly distributed particle size and rebound factors.

A high number of impacts are found near the leading edge because of the high inlet relative velocity, and near the tip region due to high centrifugation, figure 3-26. Some impacts on the pressure side of IGV blades are due to the spread of particles and rebounding from rotor leading edge, figure 3-27. The particles migrate from the pressure to the suction side of the rotor blade via the tip clearance, and in the process, cause tip erosion.

Particles that impinge on the nose when seeding globally are deflected towards the hub and the shroud after impacts, figure 3-28, thus increasing the sand concentration toward the centre of the annular passage, which is similar with the measured concentration profile.

There is also a large change in the trajectory path from the stationary frame to the rotating frame due to the change in absolute velocity, figure 3-29.

The predicted concentrations upstream of IGV, figure 3-41 show similar trend as the measured concentration profiles, figure 5-39. On the other hand, the predicted concentration downstream the rotor blade shows a large number of particles highly centrifuged towards the tip, but a good quantity of them is still contained in the core of the flow. The number of particle diverted toward the shroud tends to increase after a distance from the trailing edge because of shroud impacts as depicted by figure 3-30 and by the predicted concentration profile 3-42. The measured concentration profile at 16 mm from the trailing edge, figure 5-45 shows roughly similar trend. Because of the difficulties in using laser anemometer near the shroud and due to particle deposition on the glass window no data was taken in this area.

In the case of global injections, the results of particle velocity and directions figures 3-39a and 3-39b agree well with the experimental results, figures 5-40 and 5-41.

The trajectories of fine particles (10μm) are strongly influenced by the flowfield and tend to follow streamlines, figure 3-31. In the zones of high turbulent kinetic energy such as; near the wall, in the tip leakage and in the trailing edge wakes, the dynamic of particle is different after including turbulence, figure 3-32. When particles are crossing eddies many of them may even reenergize, but others dissipate their energy. As consequence, the number of impacts may increase in some areas and reduce in others due to turbulence effect.

Figure 3-36 and figure 3-37 provide a qualitative description of the particle impact locations due to global injection of particles. Some areas are impacted with low velocities, which appear as low rate of erosion contours as shown by the figures relative to erosion contours of the chapter 4.

## 3.14 CONCLUSIONS

The particle trajectories through the axial fan stage were based on modeled physical descriptions of particle dynamics using a Lagrangian tracking model including turbulence effect and fragmentation. The simulations were carried out for a narrow size bandwidth (150-300microns) and MIL-E5007E (0-1000microns) sand particles. The results of particle trajectories due to local injection obtained for the narrow size bandwidth (150-300microns) sand particles were validated against the results of local injection tests.

The predicted trajectories show tip particles migrating from pressure to the suction side and in the process causes tip erosion. A high number of impacts were found near the leading edge and toward the tip region. The impacts on rotor blade suction surface were restricted to the leading edge only, because of the negative incidence angle of the particles at the rotor inlet due to high circumferential velocity. Smaller particle impacts are restricted to the corner of the blade tip towards trailing edge. In general, good agreements with the experimental results were found in terms of the impacts at the leading edge and along the tip region of the rotor blade. The effect of particle concentration, turbulence, fragmentation and size of particles were demonstrated for different case studies. A significant variation in the computed three dimensional trajectories when considering turbulence effect for the small size particles was revealed.

The developed code *PARTRAJ* was very useful in visualising the three dimensions particle trajectories, the area of impacts in addition to the determination of the parameters necessary for erosion calculation. However, there is a need to improve the used fragmentation correlation and to track separately the fragments from the main particle paths. Also, it is necessary to use a moving grid for the rotor domain in order to improve the results for the particle impact locations.

# CHAPTER 4

# EROSION PREDICTION

## 4.1 INTRODUCTION

This chapter presents the prediction of the axial fan blades erosion and the blades geometry deterioration. The blade material erosion was based on the three dimensional particle trajectory simulations, which provided the spatial distribution of particle impacts, velocities and angles at impacts over the blade surfaces. An existing semi empirical erosion model corrected for the case of the cast aluminium was used to compute erosion rates based on the impact data. The following sections present the prediction of erosion rates and the changes of the rotor blade geometry, including the effects of fragmentation and turbulence. A comparison with experimental results together with a discussion is also provided.

## 4.2 EROSION TESTING OF CAST ALUMINIUM

This testing was carried out in order to assess the erosion rate of the cast aluminum and to make the necessary modification to the constants involved in the correlation developed by Grant and Tabakoff (1974), for the 2024-aluminium alloy.

A sand blasting test rig was assembled to measure the rate of erosion for the aluminum casting, figure 4-3. The main features in such a testing procedure are to control airflow velocity, particle flow-rate and the angle of attack between the abrasive (sand particles) and the surface roughness of a circular specimen shown by figure 4-5. The sand particle size range was between 100-350micron (mean diameter 220 micron), figure 4-6.

The operation of the test apparatus is described as follows: The particles were feed by gravity into the mixing section of the injector, figure 4-4, where the air and particle mixture was accelerated through a smaller orifice. The sand is fed under gravity to the particle injector. The flow of particles is controlled via a restriction orifice in the bottom of the hopper. Sand particles are collected in a conical container underneath the blasting test chamber. The finer particles due to fragmentation are taken out by a vacuum cleaner from the top of the test chamber.

The air is supplied from a tank having a capacity of 1000 litre at a pressure of 10 bars. The jet velocity from the injector was calibrated using the static pressure difference measured from two pressure tapings and a pitot tube. The velocity of

particles is then related to the indicated pressure difference, and corrected with a correction factor deduced from previous laser measurements (chapter 5).
The angle of impingement is maintained by holding the tested specimen in a fixed direction. The simple design as shown in figure 4-5 allows quick replacement and weighing of the test specimen. Tests were carried out at different angles of attack (from 15 to 80 degree) and at three velocities. Impact velocities up to 60 m/s were achieved. The higher velocity was limited by the pressure supply.

The test results for the aluminum casting show maximum erosion rates occurring at higher angles of impact compared with Grant's model. This is probably due to the difference in the material structure of the specimen used. The cast aluminum is more ductile and tends to erode faster than the 2024-aluminium alloy. The peak of maximum erosion has shifted toward angle 35° degree instead of 25° degree referring to Grant's model (1974), figure 4-7.

The surface quality of the tested specimen when exposed to particulate flow deteriorates with time under the flux of sand particles, and the surface roughness increases. The rate of erosion is a strong function of the angle of attack, velocity and particle size. At selective angles of attack the craters join together to form ripple pattern, which defines the surface roughness. From the observed micrographs of figures 4-8 obtained by using a scanning electronic microscope (obtained at a particle impact velocity of 55 m/s) ripple patterns were evident up to 60° angle of attack. At higher impact angle there is formation of craters, which join together. The wavelength of ripple increases with time of exposure and the angle of attack, but it reaches a steady state with time. The maximum peaks of erosion are found between 30 to 45 degrees.

## 4.3 PARTICLE FRAGMENTATION

The size of a particle, its impact velocity and angle of impact are the major contributors for particle fragmentation, but for the specified material there is a threshold size below which fragmentation does not occur. Tan and Elder (1992) tested the fragmentation of three quartz particle sizes at three velocities (50, 80, 150m/s) and angles (15, 30, 75, 45 degree) for several target materials. By sampling the erodent after tests the new size distribution curves were plotted. In figure 4-9 the particle size (180-210) and the curves obtained after fragmentation is presented. The fragmentation factor is defined as the ratio of the particle break-up diameter by the initial particle diameter. To implement the fragmentation effect in the developed trajectory code, a statistical analysis was applied to derive the density function from the particle size distribution, then the values of mean and standard deviation were deduced. As a result a graphical correlation for the fragmentation is presented in figures 4-10 to 4-11.

*Fragmentation factor = particle break-up diameter / particle initial diameter*

## 4.4 PREDICTION OF BLADE EROSION

The erosion rate defined as mass of material removed per unit mass of impacting particles is a function of the particle velocity, angle of impingement and the target material:

$$\varepsilon = \frac{m\_erosion}{m_p} \qquad 4\text{-}1$$

Where $m_p$ is the cumulative mass of dust ingested by the turbomachine, and 'erosion' refers to the removed mass from the blade surfaces. The cumulative mass of particles is calculated as follows.

$$m_p = particle\ concentration \times velocity \times inlet\ area \times exposure\ time$$

The erosion rate is calculated by the semi-empirical correlation developed by Grant and Tabakoff (1974), which was derived from testing 2024-aluminium alloy using silica sand as the abrasive particle see appendix D.

$$\varepsilon = K_1 f(\beta_1)(V_{1T}^2 - V_{2T}^2) + f(V_{1N}) \qquad 4\text{-}2$$

The maximum erosion for this material occurs at an angle of attack around 20 to 25 degrees. However, according to the tests carried out for cast aluminium (section 4-2) this angle was found between 30-40 degree. This is because of the different physical structures of the two types of aluminium material.

In the erosion studies, the basic parameters involved are the particle concentration, the time of exposure, the particle to air velocity ratio and the dimensions of the blade cascade. The material removed is a strong function of the mass of particles impacting the blade surfaces. A parameter designated by $M_{ts}$ is used to quantify the total amount of particles passed through a cascade inlet area in a time interval 't '.

$$M_{ts} = C_m t \rho V_z \qquad kg/cm^2 \qquad 4\text{-}3$$

$C_m$ : mean concentration
t : time unity second
ρ : fluid flow density
$V_z$ : axial velocity

The total amount of sand particle per second passed through a single cascade passage is written as follows.

$$Q = M_{ts} hs \qquad kg \qquad 4\text{-}4$$

The weight loss from the blade is essentially a linear relation with the cumulative particles mass rate. The overall average erosion rate per blade is expressed by the ratio of mass loss to the total ingested mass of particles.

$$\varepsilon_0 = \Delta m / Q \qquad mg/g \qquad 4\text{-}5$$

The local value of erosion on a given solid face of a discretised element is distributed among the four nodes of this face using the distance of impact point from the neighbouring nodes as a weighing criterion.
The nodal value of erosion at the node ($i$) for the element ($el$), and for the impact index ($step$) is calculated by the following expression.

$$EROSN(step, node_i) = EROS(step).\frac{1/d_i}{\sum_{i=1}^{4} 1/d_i} \qquad 4\text{-}6$$

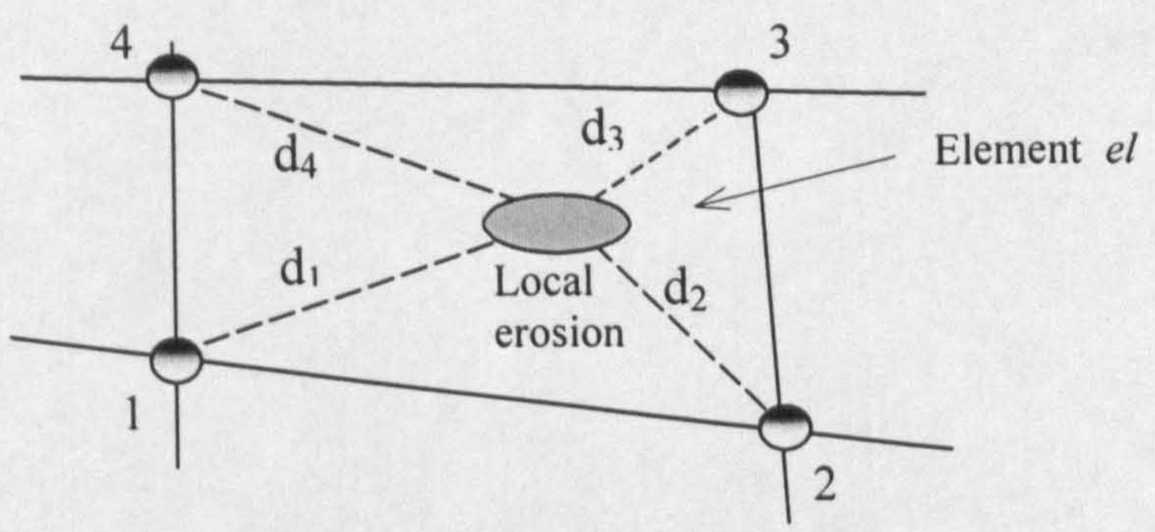


Figure 4-1 Erosion distribution among the nodes of an impacted face

For multiple impacts on the same surface, it is necessary to calculate the cumulative values of erosion on the nodes constituting this surface. Another summation is applied for faces sharing the same nodes.

$$EROSM(node_i) = \sum_{step=1}^{N_{imp}} EROS(step, node_i) \qquad 4\text{-}7$$

Since the particle can be assumed to be spherical and rigid. The contact area and the depth of penetration is calculated from the removed volume assuming a hemispheric penetration.

$$Vol = \frac{\pi}{3} h^2 (3R - h) \qquad 4\text{-}8$$

The volume of the spherical sector is equivalent to the volume of indentation when the particle has reached full penetration (Rao and Buckley, 1985). The removed volume may be related to the material characteristics by the following formula.

$$\frac{\pi}{3} h^2 (3R - h) = \frac{m_1 V_{N1}^2}{2\sigma_{MAX}} \qquad 4\text{-}9$$

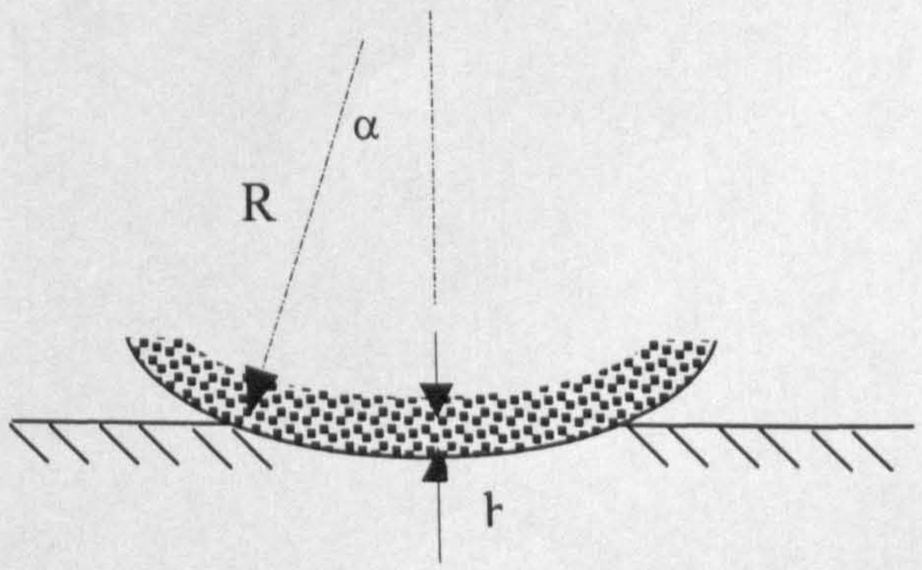


Figure 4-2 depth of impact

*Distribution of penetration depth on the impacted face of an element*

The area of impact by one particle is calculated as follows.

$$\alpha = \cos^{-1}\left(1 - \frac{h}{R}\right)$$

$$area_{\_imp} = 2\pi R^2 (1 - \cos\alpha) \qquad 4\text{-}10$$

The distribution of depth of impact on the face of an element among the neighbouring nodes, taking into account multiple impacts is calculated by the following expression.

$$depth_{(node)} = \sum_{i=1}^{istep} \frac{area_{\_imp\,(node,\ i)}}{area_{\_el}} depth_{(i)} \qquad 4\text{-}11$$

The eroded blade geometry is deduced from the predicted erosion values on the nodes by adding the algebraic normal depth to the initial geometry of the blade. The tip clearance and the chord changes after particle impacts are computed by the subroutine *OUTPUT* in the trajectory code *PARTRAJ*.
The following points give the percentage of blade geometry deterioration:

- The tip chord.

$$C_t = \left\{ \begin{array}{l} [coord\,(I_s, J_l, K_f, 1) - coord\,(I_f, J_l, K_f, 1)]^2 + [coord\,(I_s, J_l, K_f, 2) - coord\,(I_f, J_l, K_f, 2)]^2 \\ + [coord\,(I_s, J_l, K_f, 3) - coord\,(I_f, J_l, K_f, 3)]^2 \end{array} \right\}^{1/2} \qquad 4\text{-}12$$

- The variation in the tip chord.

$$\Delta c_t\% = 100\left[1 - \frac{C_t}{C_{tin}}\right] \qquad 4\text{-}13$$

- The equivalent mean variation of the blade chord.

$$\Delta c_m\% = 100\left[1 - \frac{\frac{1}{r_t - r_h}\int_0^{r_t - r_h} c\,dr}{C_m}\right] \qquad 4\text{-}14$$

- The variation in the tip clearance is given by.

$$\Delta\tau\% = 100\left[\frac{\frac{1}{C_t}\int_0^{c_t}(r_s - r_t)\,dc}{\tau_{in}} - 1\right] \qquad 4\text{-}15$$

## 4.5 COMPARISON BETWEEN TESTS AND PREDICTIONS

The following tables give a comparison of the predicted and the measured erosion rates, mass erosion per blade and the geometry deterioration of the tested rotor blade. The predictions supported by experimental results were done for the global sand particle injection at low and mean concentrations using narrow bandwidth sand (150-300micron), and at high concentration using MIL-E 5007E (0-1000micron) sand particles. The tests involving global injection of sand particle will be introduced later in section 5.6 of Chapter 5.

Table 4-1 Comparison between measured and predicted erosion and geometry deterioration using low concentration (127mg/m$^3$) of narrow bandwidth (150-300micron) sand particle

| | Mean tested value | Predicted value |
|---|---|---|
| Erosion rate mg/g | 0.607 | 0.2957 |
| Eroded mass after 3 hours mg | 42.03 | 27.652 |
| Tip clearance increase % | 2.15 | 2.5107 |
| Tip chord decrease % | 0.56 | 0.3426 |
| Mean equiv chord decrease % | 0.1213 | 0.1452 |

Table 4-2 Comparison between measured and predicted erosion and geometry deterioration using mean concentration (420mg/m$^3$) of narrow bandwidth (150-300micron) sand particle

| | Mean tested value | Predicted value |
|---|---|---|
| Erosion rate mg/g | 0.504 | 0.2854 |
| Eroded mass after 2.5 hours mg | 129 | 78.233 |
| Tip clearance increase % | 4.32 | 6.7676 |
| Tip chord decrease % | 1.152 | 0.7338 |
| Mean equiv chord decrease % | 0.234 | 0.3686 |

Table 4-3 Comparison between measured and predicted erosion and geometry deterioration using high concentration (775mg/m$^3$) of MIL-E 5007E (0-1000micron) sand particle

| | Mean tested value | Predicted value |
|---|---|---|
| Erosion rate mg/g | 0.653 | 0.4098 |
| Eroded mass after 2.25hours mg | 242 | 180.358 |
| Tip clearance increase % | 15.01 | 16.4149 |
| Tip chord decrease % | 2.59 | 1.7379 |
| Mean chord decrease % | 0.517 | 0.9339 |

## 4.6 EFFECTS OF TURBULENCE FRAGMENTATION AND SIZE

The following tables summarises the effects of turbulence, particle fragmentation and particle size on the predicted rate of erosion, and the subsequent changes of tip clearance and the chord of the rotor blade by simulating global seeding of sand particle at different concentrations.

Table 4-4 Effects of turbulence and fragmentation on predicted erosion and geometry deterioration using low concentration (127mg/m$^3$) of narrow bandwidth (150-300micron) sand

| | Without turbulence | With turbulence | Without fragmentation |
|---|---|---|---|
| Erosion rate mg/g | 0.3036 | 0.2957 | 0.4519 |
| Eroded mass after 3 hours | 28.39 | 27.652 | 42.254 |
| Tip clearance increase % | 2.4679 | 2.5107 | 3.7841 |
| Tip chord decrease % | 0.3930 | 0.3426 | 0.6197 |
| Mean equiv chord decrease % | 0.1629 | 0.1452 | 0.2504 |

Table 4-5 Effects of turbulence and fragmentation on predicted erosion and geometry deterioration using mean concentration (420mg/m$^3$) of narrow bandwidth (150-300micron) sand

| | Without turbulence | With turbulence | Without fragmentation |
|---|---|---|---|
| Erosion rate mg/g | 0.2917 | 0.2854 | 0.443 |
| Eroded mass after 2.5hours mg | 79.965 | 78.2335 | 121.428 |
| Tip clearance increase % | 6.9468 | 6.7676 | 11.5213 |
| Tip chord decrease % | 0.8402 | 0.7338 | 1.4544 |
| Mean equiv chord decrease % | 0.3943 | 0.3686 | 0.6428 |

Table 4-6 Effects of turbulence and fragmentation on predicted erosion and geometry deterioration using high concentration (775mg/m$^3$) of MIL-E 5007E (0-1000micron) sand

| | Without turbulence | With turbulence | Without fragmentation | Bandwidth (150-300) |
|---|---|---|---|---|
| Erosion rate mg/g | 0.418 | 0.4098 | 0.6787 | 0.2919 |
| Eroded mass - 2.25 hours mg | 183.9 | 180.358 | 298.74 | 128.48 |
| Tip clearance increase % | 18.2373 | 16.4149 | 31.7016 | 10.6516 |
| Tip chord decrease % | 1.8261 | 1.7379 | 3.2347 | 1.3758 |
| Mean equiv chord decrease % | 0.9564 | 0.9339 | 1.5137 | 0.7560 |

## 4.7 DISCUSSION

Figure 4-12a shows the predicted erosion pattern due to local injection of (150-300micron) sand particles at mid height of IGVs. The predicted erosion near the leading edge on the pressure side shows good agreement with experimental erosion pattern, but less well near the mid-chord tip region where the greater erosion area was further away from the tip as shown in figures 5-52 and 5-53. On the suction side, however, better agreement was found near the blade leading edge as shown in figure 4-12b and figure 5-54. The erosion here is mainly due to particles entering the rotor blades with a high negative incidence angle. There was no noticeable erosion on the remainder of the suction side. The rotor tip, however, shows signs of erosion that has been caused by particles migrating from pressure to the suction side of the blade via the tip clearance (see figure 4-13). The erosion predictions for local injection near the tip, figure 4-13,

show a good agreement with test results as shown by figure 5-56. Erosion of the tip region extends to (nearly) the whole length of the chord, and the distinctive eroded pattern near the leading edge was also predicted. Figure 4-14 shows the erosion patterns due to local seeding near the hub. They show generally good agreement near the leading edge, but over–predict the erosion pattern near the trailing edge. A possible explanation for this is that the particles that 'misses' the trailing edge are smaller than predicted due to fragmentation.

The prediction of erosion pattern obtained with global injection of (150-300micron) sand particles is shown in figures 4-15a,b, this corresponds to a concentration of 127 mg/m$^3$. For mid concentration (420mg/m$^3$) the erosion pattern is shown in figure 4-16a,b. The prediction was carried out with the conditions obtained from the experimental measurements. A high number of impacts are found near the leading edge and tip region, figure 5-57. In general, good agreement with experimental was found in terms of the erosion at the leading edge and along the pressure side tip region. When the sand concentration was increased to a higher concentration (775 mg/m$^3$) using MIL-E 5007E sand particles, the erosion pattern shown in figure 4-17 has similar trend compared with the experimental pattern, figure 5-58. The figure 4-20 shows erosion rates due mainly to impacts by particles crossing the tip clearance. To assess the effect of turbulence, fragmentation and particle size, erosion simulations were done at different concentrations. As a result, the erosion rates and geometry degradation of rotor blade are compared in table 4-1 to 4-3. The first remark, there is a net increase in erosion rate without fragmentation, figure 4-19. In fact, as a particle fragments into smaller debris, the new particle diameter is obtained by multiplying it by the rate of fragmentation. On the other hand, the separate trajectories of fragments and their subsequent secondary erosion were not considered in this code, this is why the predicted erosion with fragmentation is lower. Also, it is demonstrated that the turbulence tends to affect the erosion rate for smaller particles in the regions of high turbulence especially in the tip clearance region, figures 4-23a, 4-23b. For example, the simulations for fine particles 30 ± 10 microns figures 4-23a, 4-23b, show that particles are impacting mostly on the trailing edge, and the turbulence effect was very clear by comparison of figure 4-22a with figure 4-22b.

Figures 4-24 and 4-25 show typical predicted profiles at mid span and tip due to the erosion by a high concentration of MIL-E 5007E sand particles after 2.25 hours. They also revealed the effect of turbulence on erosion. The computation of blade deterioration is based on the procedure outlined in section 4.4. The tip chord reduced by 1.73 % and the tip clearance increased by 16.41%, compared to the measured average of 2.59% and 15% respectively over the four steps of sand ingestion. The eroded leading edge hub - tip line is depicted by figure 4-26, which shows a rounding of the blade near the tip (curve highlighted by triangles).

## 4.8 CONCLUSIONS

The maximum values of the rotor blade erosion are generally larger than the maximum values for IGV blade erosion, which was also confirmed by tests. The

maximum rotor blade erosion is concentrated along the leading edge and toward the blade tip corner. The predicted erosion near the leading edge on the pressure side shows good agreement with experimental results but less well near the mid-chord tip region, where the greater erosion area was further away from the tip. On the suction side, better agreement was found near the leading edge. The rotor tip shows signs of erosion that have been caused by particles migrating from the blade pressure side to suction side through the tip clearance.

Distinctive erosion patterns were evident for the different heights of local seeding, which are in good agreement with experiments.

For global ingestion of sand particles (MIL-E 5007E) at high concentration, high number of impacts were found near the leading edge and in the tip region, which is validated by experimental results.

From the parametric study for turbulence and fragmentation effects, it was demonstrated that the turbulence affects the erosion rates and patterns for smaller particles, especially in the region of high turbulence such as in the tip clearance and wakes. The fragmentation is another important parameter, which was shown to influence the erosion rate. As a particle fragments into smaller debris, they can produce secondary erosion areas, consequently, the paths of these fragments should be traced independently from the main particle paths.

The application of particle trajectory, rebound characteristics and erosion model to predict blade material loss indicate that they can also be successfully utilised in identifying the erosion prone areas and also in predicting geometry deterioration percentages, which can be used as erosion fault model in the performance degradation simulation program.

# CHAPTER 5

# EXPERIMENTAL INVESTIGATION OF EROSION AND PERFORMANCE DEGRADATION

## 5.1 INTRODUCTION

An experimental investigation was conducted to assess the trajectory code capabilities and to study the effects of sand ingestion on the aerodynamic performance of an axial fan. To achieve this goal a test facility was built according to the British standard requirements. The experimental work was divided into two types of testing: Firstly, local injection tests, which were intended to generate qualitative erosion patterns in order to validate the trajectory code results. Secondly, the global sand injection tests were carried out near the design point in order to assess the degradation of the aerodynamic performance. The laser transit anemometer was an essential instrument for particle concentration and velocity measurements during these experiments.

## 5.2 TEST RIG LAYOUT

The tested turbomachine is a single stage axial fan consisting of ten twisted C4 rotor blades with a mean chord length 45mm, and a set of inlet guide vanes consisting of seven C4 blades, as illustrated by figure 2-1 and figure 2-2. The full diameter of the rotor is 169.32mm with a hub-tip ratio 0.652. A hemispheric shape is added to the front area of the hub to improve the air distribution upstream the IGVs. The outlet flow is discharging through a step duct without a de-swirl device. The rotor is driven by a three phase 400Hz electric motor, which operates at a nominal speed of 11300 rpm.
The test rig was built according to the "D3" design as prescribed by BS848 standardisation (1997). The major features of this test-rig shown in figure 5-6 are the following:

- A conical intake having an angle of 30 degree is used to measure the mass flow rate. It was machined from aluminium and attached to the upstream ducting by a mean of a simple stepped joint.
- The upstream ducting has a length of 600mm from the first static pressure taping ST1, and holds several static tapings. The static pressure taping ST1 is used to determine the mass flow rate through the fan. The static pressure tapping ST2 is

used with the static pressure tapping ST3 to calculate the inlet suction losses in order to have the total inlet pressure to the fan stage. The total temperatures are measured by using half shielded stem-mounted thermocouples positioned at the centre of the duct in the plane ST1 at a distance of 1.25 times the pipe diameter from the inlet, which allows the measurement of the air flow density. Another thermocouple is located near ST3 taping to measure the inlet total temperature of the fan.

- For a circumferential velocity profile measurements across one pitch of the IGV blades and for fine adjustments of the reference line for injection, the casing is movable.
- The flow from the back of the rotor discharges directly through a duct. Due to the geometry change behind the rotor there is a big wake region extending along the centre of the duct. Several static pressure tapings from ST4 to ST5_7 were used to determine the static pressure recovery point. This discharging duct is connected to an extra pipe to allow for a diffusion of the rotational component of flow velocity. A half shielded thermocouple located downstream of the rotor is used to measure the outlet airflow total temperature.
- The throttling butterfly valve is located sufficiently far downstream of the fan to avoid any flow distortion.
- The test Reynolds number based on the rotor blade chord is around $4x10^5$.

A long flexible pipe discharging outside the test house was connected to the rig to prevent sand particles from escaping into the test house. Also, the flanges between adjacent pieces of ducting are airtight.

Two settings for particle injection were used, figure 5-7 and figure 5-8. The local injector was located inside the duct at 135mm upstream of the IGV, and aligned with the main direction of the flow. The global sand particle injector consisting of a venturi tube, which is connected to a pressurised air supply is located outside the ducting, figure 5-9.

## 5.3 INSTRUMENTATION

The aim of these subsections is to give detailed descriptions of the instrumentation used in the experimental work, for local and global sand injection tests and for the aerodynamic performance degradation assessment tests. To fully define the aerodynamic characteristics, measurements of rotational speed, input power, current and temperature are required in addition to pressure difference measurement. Figure 5-6 shows the locations of different instrumentation used.

### 5.3.1 Rotational speed

A magnetic pick-up is used to measure the rotational speed of the axial fan rotor. This instrument is preferred because of its robustness. However, the output signal

depends on the blade material and on the magnetic field interference. The optical system was used as redundant speed checks when measuring the base line characteristics. But, later it was removed from the rig due to risk of damaging the optical cell by sand particles and was replaced by the magnetic pickup. The uncertainty for the magnetic pick up should not exceed 0.25% of the shaft speed (Japikse, 1986), otherwise the speed measurement errors will affect drastically the tangential velocity components, and consequently the relative flow angles, efficiency and pressure rise.

### 5.3.2 Temperature

Five temperatures were measured; the ambient temperature, intake temperature, fan inlet and outlet total temperatures, and also the electric motor temperature. This latter was used to estimate the electrical losses. The heat loss from the motor is considered as a heat rejection to the airflow. In the actual test rig, the temperature probes were placed in the centre of the flow passage as recommended by BS848 (1997), because the annular section is small and air velocity is low.

Half-shielded J thermocouples made from chromel-constantan, chromel-alumel were used for all the temperature measurements. The radiation heat transfer is minimised by placing a shield over the thermocouple. In addition, a small vent at the rear of the probe is used to balance the heat loss with the thermal energy from the fluid by convective heat transfer. The shielded probes can also reduce the free stream velocity, resulting in a higher recovery factor that gives a measured temperature very close to the flow total temperature. The accuracy of the thermocouple depends on the flow velocity and its fluctuation. This type of thermocouple is inherently quite stable with an accuracy of 0.5°C, and generally does not need frequent re-calibration. Care must be exercised when using the temperature measurement to calculate the adiabatic stage efficiency of this low-pressure ratio axial fan. Small temperature measuring errors can impact the accuracy of the temperature difference. Some of the errors are due to flow fluctuations behind the rotor and also due to the thermal energy transferred from the measured point by heat conduction down to the probe stem and by radiation to surrounding surfaces. In the actual performance measurement the adiabatic efficiency was related to the power measurement because of the temperature difference inaccuracy.

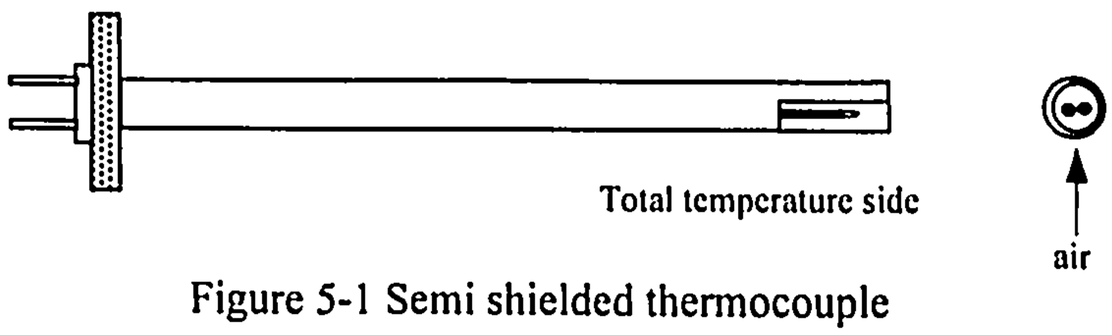


Figure 5-1 Semi shielded thermocouple

### 5.3.3 Static pressure

The static pressure in this standardised testing airway is an average of four wall tapings readings. The static pressure taps are installed in constant area ducts away from abrupt bends and area changes, with a great care to assure that the taping is burr free and flush with a surface. The bore diameter of the taping is 1.5mm. The change of area was made progressive to the capillary tubes to avoid rapid fluctuations of the manometer

reading, so that the average reading is within 1%. The pressure was observed over a period of not less than one minute for each point on the fan aerodynamic characteristic (Wallis, 1961). Before the starting of any measurement, inspection and cleaning of static pressure taps were made after a prolonged test rig operation.

### 5.3.4 Total pressure

The total pressure at the rotor outlet is measured indirectly by using the average of static pressure readings, then from mass flow rate and flow area the value of the total pressure is deduced (HMSO, 1961). This is quite reasonable because the air velocity is low (less than 60 m/s). The rotor outlet total pressure is measured far downstream from the rotor to allow for diffusion of the circumferential momentum and to reach the static pressure recovery. By a correction for the losses due to the step diffusion, the total pressure from the rotor outlet is determined. Several static pressures were measured through the discharge duct to assess the flow downstream of the rotor. The necessary mixing length downstream of the fan rotor corresponds to the maximum of the curve relating static pressure to the length of discharging duct. The fan total inlet pressure is considered to be equal to the atmospheric pressure associated with the suction losses (Logan, 1995). The inlet losses are measured by means of different static tapings from the reference plane.

### 5.3.5 Mass flow rate

Accurate test rig flow measurements are required in the generation of the aerodynamic performance. Pressure measurement coupled with the known geometry and calibration flow coefficients are used to calculate resultant flow rates. In this test set-up the mass flow rate is measured by means of a conical intake, where the basic dimensions are referred to BS848 (1997) as shown below. This short flowmeter has no limitations to carry out full tests due to its small pressure drop.

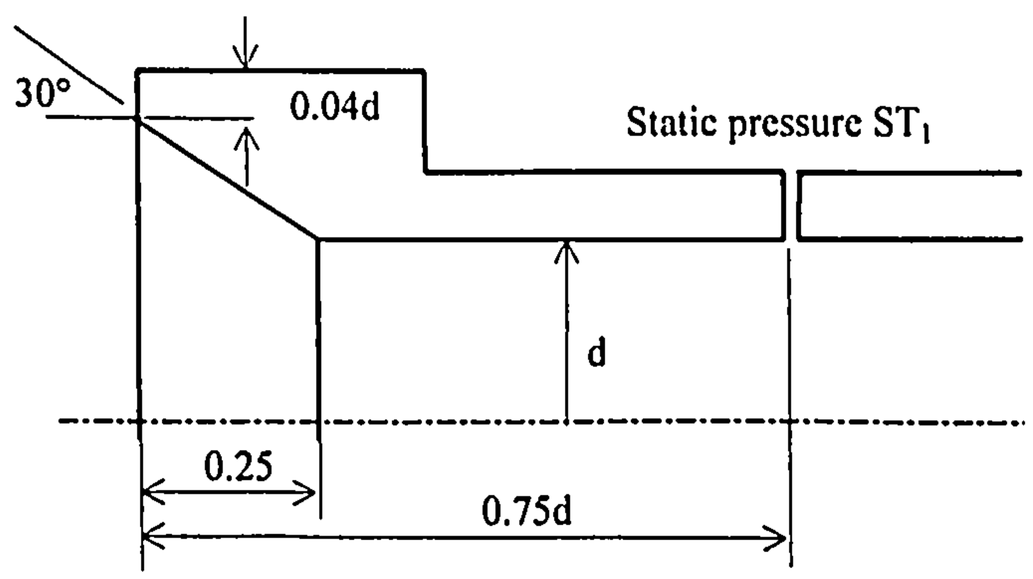


Figure 5-2 Dimensions of the conical intake

This conical intake as designed offers the possibility to be used uncalibrated for a wide range of Reynolds number and throat static pressure difference:

$$\frac{P_a - \Delta P}{P_a} \geq 0.96 \qquad \Delta P \langle 4000\ P_a \qquad Re_d \langle 20000$$

The mass flow-rate, which is a function of pressure difference, air density and throat diameter, is expressed by.

$$\dot{m} = \alpha\varepsilon\pi \frac{d^2}{4}\sqrt{2\rho\Delta P} \qquad 5\text{-}1$$

The compound flow coefficient '**αε**' is determined from a calibration curve, and is approximated in the following form.

$$\alpha\varepsilon = m \log_{10} \mathrm{Re}_d + c \qquad 5\text{-}2$$

If $d \leq 0.5m$ $m = 0.01107$ $c = 0.8824$

If $\mathrm{Re_d} = 210^5$ $(\alpha\varepsilon)_{max} = 0.94$

BS1042 (1997) gives other forms of the compound coefficients depending on the Reynolds number.

$$\alpha\varepsilon = 1 - 0.5 Re_d^{-0.2} \quad 210^4 < Re_d < 310^5$$

$$\alpha\varepsilon = 0.960\, Re_d > 310^5$$

The uncertainty in the compound coefficient for $\mathrm{Re_d} \geq 210^5$ is about 1.5%. An additional uncertainty due to low Reynolds number is added.

$$\pm\left(\frac{210^4}{\mathrm{Re}_d} - \frac{1}{15}\right)$$

Calibration of the conical intake

For calibrating the conical intake used in this test rig a conventional cylindrical 4mm probe with three drilled tapings at 5mm from the tip was used. The probe is introduced through a small hole drilled through the pipe ducting and controlled by a micrometer traverse mechanism. The 40 degree two static drills are used to align the probe with the flow. The size of the probe relatively to the duct diameter was checked for the nearest approach to the wall, which is required by the numerical integration method for the flow velocity (Ower and Pankhurst, 1966). The wall proximity effects on both components of the Pitot static combination and the possible errors due to the displacement of the effective centre of a Pitot tube in a transverse total pressure gradient will disable the probe to read accurately in nearby wall. A correction factor for this type of probe was measured by Filbee (1990).

With this type of conical intake having an angle of 30 degree, the pressure loss is minimised. The flow at three-quarter diameter from the intake is uniform as explained by Pearsall (1963). To calibrate this conical intake, the total pressure, differential pressure head and total temperature were recorded. BS1042 (1997) recommends that,

the traversed section should be subdivided into a set of annular concentric passageways and a number of diametrical traverses.
The ideal mass flow rate as indicated by the conical inlet is determined from the differential pressure in mm of water column.

$$m = \alpha\varepsilon \frac{\pi d^2}{4} \sqrt{2\rho_a g \rho_w \Delta h_{wi}} \qquad 5\text{-}3$$

The mass flow rate is integrated from the local velocity measured by total pressure probe, figure 5-14.

$$V_i = \sqrt{2 \frac{g\rho_W \Delta h_{wi}}{\rho_a}} \qquad 5\text{-}4$$

The mean axial velocity deduced from the integration of the velocity profile is calculated by Simpson integration method.

$$\overline{V} = \frac{2}{r_t^2} \sum_{1}^{N} V_i r_i \Delta r_i \qquad 5\text{-}5$$

The mass flow is computed from the area average velocity, measured density and the intake throat area.

$$m = \frac{\pi}{4} d^2 \rho \overline{V} \qquad 5\text{-}6$$

A Fortran program called *CALIB* detailed in the flowchart of appendix H was used for the data reduction and for computing the mass flow rate and the calibration coefficients. The calibration curve, figure 5-15 shows good agreement with the curve calculated by BS standard coefficients, figure 5-17. A least square interpolation based on a root square power law allowed for the computation of the compound coefficient. The test coefficient (0.912) is very close to the value given by standardisation (0.945) (4.5%). Also, a graphical relation for the total pressure loss through this intake is determined, which is used in the calculation of the fan aerodynamic performance, figure 5-16.

### 5.3.6 Power measurement

The power input to the axial fan over the specified performance range was determined by a classical method based on an averaging of a sufficient number of readings. The net power from an electrical motor for a direct drive is deduced from its electrical power input reduced by the summation of electrical losses. For the complete evaluation of the electrical losses, the measurements of voltage, current, frequency, speed of rotation and the slip of induction were made at each operation point. For measuring the power consumed by the fan an integrating auto-ranging wattmeter " HEME DIGITAL ANALYST " was utilised.

The rotor is mounted directly on the motor shaft. The losses between shaft and rotor are due only to disc windage. The losses involved in the calculation of the net shaft power, (Fitzgerald et al, 1981) are mainly.

- Losses in the rotor and stator windings of the electrical motor
- Core losses consisting of eddy-current and hysterisis. These losses are constant regardless of load
- Friction and windage, which are constant unless the speed is changing.

In order to evaluate the wiring loss, the temperature of the motor was measured by an embedded thermocouple into the hub where the motor is housed. The thermocouple installation should satisfy a good thermal contact. The resistance of the electrical windings $R_H$ is function of the hub temperature $T_H$, and the reference electrical motor resistance $R_i$ measured at 15°c.

$$R_H = R_i \frac{234.5 + T_H}{234.5 + T_i}$$

The method of calculating the electric motor efficiency is taken from the reference BS4999 (1997) PART3. This reference describes the methods of testing of electric motors, where the computation procedure is presented as follows.

- The shaft power is deduced from losses induced.

$$W_S = W_{IN} - 3I^2 R_{S2} - Fixed\ loss - Rotor\ copper\ loss \qquad 5\text{-}7$$

- The fixed loss is determined when the electrical motor is unloaded.

$$Fixed\ loss = Motor\ \ unloaded - 3I^2 R_{S1} \qquad 5\text{-}8$$

- The motor slip factor 's'

$$s = \frac{N_S - N}{N_S} \qquad 5\text{-}9$$

- The rotor copper loss is calculated via slip factor from the following relation

$$Rotor\ copper\ loss = (Rotor\ input\ \ power).s \qquad 5\text{-}10$$

The synchronous speed is evaluated according to the reference (Fitzgerald et al, 1981). Where $N_p$ designates the number of poles and f the frequency of the AC three-phase power generator. The measured electrical frequency was varying (370-390Hz) with the power consumed and throttling. The electrical motor nominal frequency is 400Hz.

$$N_S = \frac{120\,f}{N_p}$$

The power supply in the three-phase circuit is given by.

$$W_{IN} = V_P I_P COS\theta_P \qquad 5\text{-}11$$

Subscripts L, P means line and phase current or voltage.
For Y circuit, $I_L=\sqrt{3}\, I_P$ , and $V_L=V_P$
$\cos\theta_p$ is the power factor.

- The net power to the fan rotor is the shaft power reduced by windage loss.

$$W_r = W_S - windage \qquad 5\text{-}12$$

### 5.3.7 Sand Injection

Two types of sand injector were used in the experimental work. The first injector was used for local injection of sand particles, in order to validate the developed trajectory code. This injector was constructed by simply connecting a 3mm T tube to unpressurised dust hopper, thus seeding is purely due to gravity. The hopper in figures 5-10 has a variable stroke plunger operated by a DC current motor to control the flow of sand particles. The figure 5-12 shows the arrangements for this type of injector. The global injector was used for global injection tests to generate the blade profile loss in order to assess the performance degradation. It consists in a venturi tube that works at a pressure 65PSI, and located upstream of the inlet duct, figures 5-9, 5-13. The injector was designed to deliver air particles mixture at a release velocity, which is expected to match the conical intake velocity. The particles were taken from the bottom of the hopper by depression. A detailed design drawing for this injector is available in figure 5-18. The static pressure at the inlet of the venturi is measured, as well as the particle mass concentration. The pressure valve and the speed of the plunger served to adjust the concentration of particles.

### 5.3.8 Concentration measurement

The laser transit anemometer was used to measure the concentration distribution upstream of the fan nose and IGV, figure 5-13 and figure 5-8. Since the basic principle of the laser anemometry is the detection of scattered light from the particles, the strength of the reflected signal, which is proportional to the number of particles passing through the two beams would provide the information on the dust concentration at the measuring volume. The measurement of the concentration profile needs the laser beam to be traversed across a series of points equally spaced.
The concentration profile along a radial distance is deduced from the measured non-dimensional particle count number $N/N_{max}$ . Each count number corresponds to the maximum number of events taken from the curve of time of flight distribution. By measuring the mean concentration $C_m$ ($mg/m^3$), which is the ratio of the mass of sand particles seeded in milligrams per second by the volume flow rate of air through the ducting in meter cube per second. The concentration distribution along a blade height takes the form of the equations 5-13 and 5-14 for global and local sand particle

injections respectively. By using subroutines; *spline, integration* and *statistics* for the concentration distribution, the mean value and the standard deviation were obtained.

- For global injection

The mean value of the measured concentration distribution based on the area integration corresponds to the amount of sand consumed divided by the volume of air per second:

$$C_m = \frac{2}{r_t^2 - r_h^2} \int_{r_h}^{r_t} C(r) r \, dr$$

The averaged measured concentration profile is equivalent to the average of count number ratio obtained from laser measurement across the blade height or the radius of the duct.

$$\overline{\left[\frac{N(r)}{N_{\max}}\right]} = \frac{2}{\left(r_t^2 - r_h^2\right)} \int_{r_h}^{r_t} \left[\frac{N(r)}{N_{\max}}\right] r dr$$

The actual measured concentration distribution (milligrams of sand particles by meter cube of air) is derived from particle count number and the integration of the normalised particle count. $C_m$ is the mean value of the concentration used at the time of experiment.

$$C(r) = \frac{\rho_a C_m}{\frac{2m_a}{\left(r_t^2 - r_h^2\right)} \int_{r_h}^{r_t} \frac{N(r)}{N_{\max}} r dr} \left[\frac{N(r)}{N_{\max}}\right] \qquad mg/m^3 \qquad 5\text{-}13$$

- For local injection

The concentration profile initially follows a Gaussian shape from the release injector pipe and tends to spread upstream the IGV blade. The concentration profile is derived from the number of counts as follows.

$$C(r) = \frac{\rho_a C_m}{\frac{m_a}{\left(r_t - r_h\right)} \int_{r_h}^{r_t} \frac{N(r)}{N_{\max}} dr} \left[\frac{N(r)}{N_{\max}}\right] \qquad mg/m^3 \qquad 5\text{-}14$$

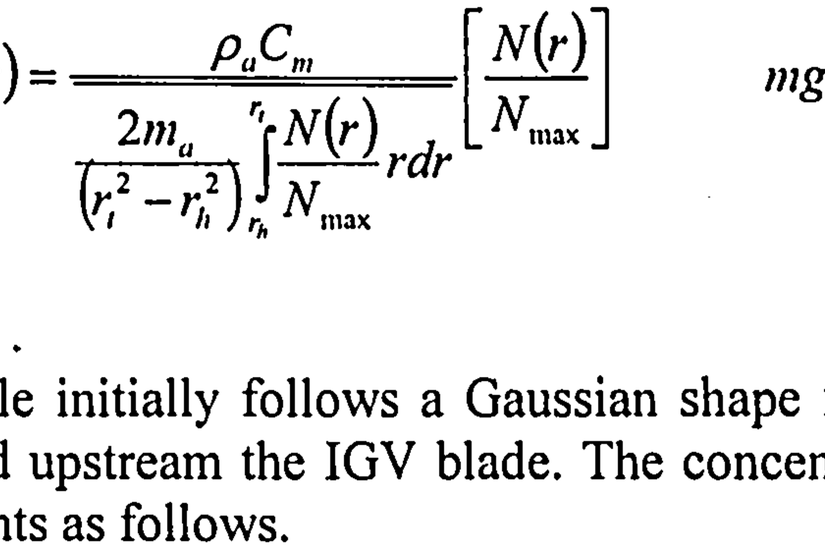


Figure 5-3 Typical Gaussian concentration profile

The particle size distribution is obtained by using conventional sieves. Two types of sand were used in the tests; a narrow size bandwidth (150-300microns) and MIL-E5007E (0-1000 micron) with their distributions depicted in figure 3-14 and figure 3-15. The chemical analysis gave 98.5% $SiO_2$ and 1% $Al_2O_3$, which are the principal erodent components. The specific gravity of sand lies between 2600 and 2700 $kg/m^3$.

### 5.3.9 The Transit Laser Anemometer

A fibre L2F-300mw laser 'POLYTEC' anemometer within Power Engineering and Propulsion Department at Cranfield University, figure 5-19, was used to measure the sand particle concentrations and velocities. The laser beam, coupled into the optical head is split into two beams of equal power by means of a relatively large Wollaston beam-splitter prism. This prism produces collimated slightly diverging beams of orthogonal polarisation from the input beam (Schodl, 1974). Two lights focussed spots are formed by the front lens of the probe, figure 5-20. The scattered light from each spot is directed to photo-multiplier tubes PMT. The diameter of the focussed beam (spot) is about 10 micron. The separation of the two beams axis is about 0.2 mm (Schodl, 1988), which makes a light gate in which a particle passing through, produces two successive pulses, which are stored in memory. As a result a spectrum of a number of measured time intervals versus time of flight is obtained from one focused beam to another (Schodl, 1980), (Eckardt, 1986). By setting the plane containing the beams to slightly different flow angles and by accumulating the same number of particles entering the probe volume, more velocity histograms are obtained as long as the chosen setting angles of the plane are within the range of the velocity angle fluctuations. A probability distribution of beam transit time is established to compute components of the flow (Schodl, 1991). The incontestable advantage over the Doppler system is the shorter probe length (Gill, 1981), allowing measurement to be taken closer to solid surfaces. When utilising this system, it is always preferable to try to limit the size of the flat windows without compromising the aerodynamic surface beyond acceptable limits (Ahmed et al, 1991). Details for this measuring technique are given in appendix F. The most important restriction on the application of laser anemometers is the background radiation generated by laser light reflections at the hub and at the casing window. To reduce the noise and to prevent surges of light, which may damage the PMT, the hub and shroud were painted black. For the accessibility of the laser beam to the respective measuring points, figure 5-21, glass windows were fitted at 35mm upstream the inlet nose, at 50mm upstream IGVs and at 16mm downstream the rotor, figures 5-22 to 5-24. The allowed blockage in the flow was 0.5mm for the upstream windows and 1mm downstream of the rotor.

### 5.3.10 Preliminary laser testing

**Laser calibration**

The laser calibration doesn't need to be done very often, since the optical arrangements are very stable. Because this system was moved from its original place, calibration tests were necessary to check the setting parameters and the optics. The calibration tests were carried out using ' Disa 55 D90 ' standard convergent nozzles,

60mm$^2$ and 120mm$^2$, at different air supply pressures. The arrangement for such experiment is depicted by figure 5-25. As a result, the spot separation was set at the value 180. The measurements across different planes from the nozzle exit needed the laser measuring volume to be traversed. For each position the laser head was rotated by means of stepper motor. The measurements through the defined points are carried out by specifying incremental intervals for the traverse table and by selecting sequential measurements mode.

Figure 5-30a and 5-30b depict air velocities and directions at different axial positions from the nozzle exit (5mm, 20mm, 50mm), which is nearly constant and very close to the mean throat velocity calculated from the dynamic pressure measured by a digital micro-manometer ' Druck '. Beyond the nozzle exit section the flow starts to diffuse both along streamwise and cross direction, with an important radial velocity component. The axial intensity of turbulence is higher near the orifice edge and in the mixing area along the free jet, figure 5-30c.

**Free jet droplets concentration measurement**

The principle of the concentration profile measurement is based on the counting of particles crossing the laser beam at a fixed angular position. The number of particles corresponds to the number of events, where the maximum count number is read from the time of flight against the number of events curve. If the seeded particle number used is very low, the sampling number in the initialisation data file of the operating software must be increased to 50000 particles.

The concentration profile of water-propanol droplets seeded through a nozzle pipe of 12mm diameter, figure 5-26 shows nearly constant concentration at exit, figure 5-31a. But it tends to spread due to diffusion in the streamwise direction more than in the shear region. The spreading in the streamwise and transverse directions differs at the centreline, while being similar in the shear region. The spreading in cross sections takes place in a similar way along radial and tangential directions, figure 5-31a. The velocity and direction of particle droplets are illustrated by figures 5-31b and 5-31c.

**Confined flow concentration measurement**

Smoke particles (oil vapour) were injected in the flow upstream the intake, figure 5-27. The objective of the test is to demonstrate the ability to measure particles through the fitted glass window and near the walls, and to assess the level of signal to noise ratio. The window had to be cleaned several times due to condensation and coalescence of fine vapour droplets. The smoke particles tends to follow the main streamlines, therefore, they mainly concentrate in the core flow upstream of the IGVs. This was evident from the smoke concentration distribution at 50mm upstream of the IGVs, figure 5-32.

**Free jet and Concentration measurement from a venturi**

This test was intended to measure the velocity of air and particles and the angle of spread from a venturi injector. The arrangement for this test is shown in figure 5-28.

The measuring volume of the laser beam was moved across two planes, the first at 5mm and the second at 15mm from the exit. The air was supplied at a pressure of 65 PSI. The flow velocity at the exit was disturbed by early flow separations emerging from the divergent part of the venturi, and by the effect of the wall thickness of the outer diameter, figures 5-33a, 5-33b. Two shedding vortices emerging from the inside of the divergent mix out with the surrounding stagnant flow. Beyond the exit plane, the flow tends to recover its axial velocity, afterwards it starts to diffuse with a big variation in the axial velocity profile. Due to the high turbulence, the measurements were very difficult across the mixing layers. The concentration peaks in the centre, because the jet of particles did not mix uniformly with the air in the divergent part of the venturi as shown by figure 5-33c.

**Concentration measurement from the pipe injector**

The local sand injector consisting of a 3mm tube was tested separately to investigate the shape of sand particles spread from the pipe. The injector pipe was mounted inside a larger pipe of 16mm diameter pressurised at 70 PSI, which was used to boost sand particles out from the injector, figure 5-29.
The concentration profiles at three planes, at exit, 10mm and 60mm respectively exhibit an important spread both in the streamwise and the transversal direction, figure 5-34. The angle of spread is related to the radial diffusion of particles and is computed from an equivalent standard deviation value.

## 5.4 VALIDATION OF THE TRAJECTORY CODE USING LOCAL INJECTION TESTS

The local injection tests were carried out to assess the capabilities of the developed code to predict particle trajectories within an axial fan stage. The assessment of the area of impacts would be qualitative rather than quantitative. A low concentration (95mg/s) of sand particles (narrow bandwidth 150-300 micron) were seeded locally by using a 3mm T injector placed at the mid blade pitch at a distance of 135 mm upstream IGVs. This position was constrained by the design of the rig and the dimension of the glass window, which made practically impossible to bring the pipe injector closer to the IGV leading edge as shown by figure 5-21. The fan was run at a speed 11300 rpm near the design mass flow rate 0.785 kg/s and pressure rise coefficient 0.4.

In order to generate qualitative erosion patterns both the rotor and IGV blades were sprayed with four layers of different colour spray paint. Three spare rotors were painted for this purpose. The colours were arranged in the following order: white, blue, red and yellow. A constant layer by pass was roughly obtained by maintaining a constant level during spraying with two passes each layer.

It must be noted that these types of test do not show rates of erosion but only indicate areas of erosion. Three injection heights were chosen; mid blade height, 1/4 blade height and 3/4 blade height. The concentration profile was measured by using

the transit laser anemometer at a plane located at 85mm from the sand injector, figure 5-12 and 5-21. The threshold controls were increased, and the laser power was reduced to a minimum when sand particles were seeded in the airflow. Such precaution was necessary to reduce the surge of light coming from solid particles. The last 2mm from the hub and shroud were the most difficult measurement areas, due to the large number of particles impacting the shroud and hub at different angles of impact and reflected off with different rebound angles. These effects made the signal quality very poor and no data was obtained. The procedure for measurements of particle concentration and particle velocity with direction is summarised in the following points:

- The laser anemometer was aligned with the datum point on a flat surface machined flush with the shroud. The reflected light at low laser power was contrasted back onto a piece of paper placed on the laser head. The focal distance corresponded to a best contrast of the spots.
- The fan was started to run at the operating point (design) corrected for the atmospheric conditions.
- The air velocity and the flow angle were measured in the centre of the duct (for plane II) and at mid IGV span (for plane I).
- The speed of the control motor and the injector plunger stroke were adjusted by moving the sliding connector rode to achieve the needed particle rate. As the rate may increase due to the suction of air the exact value of the mean concentration was deduced from weighing the quantity of sand seeded and the time last to run the rig.
- Before the particle concentration measurement started, the noise from the background flare was determined. This step was repeated when releasing sand particles for a short time to check the noise level from the particles and the background flare when the laser beam is near the shroud. Then, the power was reduced and the thresholds and attenuator levels were set for the two-discriminator channels. All the settings were kept unchanged during concentration measurement.
- One angular position for the laser beam was selected, which corresponds to the guessed particle directions. Number of readings was taken according to the number of particle sample of the initialisation data file. In the sequential measurements mode, the number of particle sampling was chosen as a compromise in order to minimise the time of wear of the glass window without affecting the results of the measurements.
- When the sequential measurement mode was selected in the operating software, the measuring volume was traversed automatically by 2 mm for each step.
- The count number corresponding to peek values of the time of flight, was plotted against the traverse distance, and was normalised by the maximum count number.
- For the measurement of the particle velocity and its direction, the angular position of the laser beam was incremented by means of a stepper motor to generate several probability distribution curves for particle velocity and direction. The processed data gives automatically the mean velocity and its direction. But, if the range of the step angles is narrow, an error message is printed out.

The measurement of particle velocities and directions required a higher number of sampling particles, which needed longer time than for the concentration measurement. The bad transparency of the glass window due to particle deposition and wear made this measurement very hard. Several cleaning were necessary to improve the quality of the

signal due to particle deposition. A polishing was needed after a long time of usage, then the window was replaced.

### 5.4.1 Injection at mid height

The particle injector was located at mid blade height. A mass of 408g of sand was injected during a period of 1.3 hours, which is equivalent to a rate of 87.5mg/s. The test was halted to take pictures of erosion patterns, then was continued during an extra period of 1.7hours. The measured concentration figure 5-35, follows a bell shape profile. At mid blade height injection, the peak of concentration profile was aligned with the direction of injection. An approximation by a Gaussian distribution gives a standard deviation 3.25. At a distance 85 mm from the injector, the jet of particles spreads nearly 4.3 times of its original size.

### 5.4.2 Injection near the hub

The pipe injector was moved 1/4 blade height above the hub. The mass of particles seeded was 430g during 1.3 hour, which is equivalent to a rate of 92 mg/s . There is an expected bias in the peak of the concentration distribution towards the hub figure 5-35 resulting from an increased number of impacts and rebounds that deflected the particle stream toward the core flow. The equivalent standard deviation is 3.35.

### 5.4.3 Injection near the tip

The last position of the injector corresponded to a 3/4 blade height above the hub. The mass of the sand particles was 445g in 1.3 hours, which is equivalent to a mass rate of 95 mg/s. Similar trend was observed, but the 'spread' in the concentration was less pronounced, figure 5-35. A net area of impacts was evident on the shroud. Local examination of the erosion pattern of the IGV's shroud showed an impacted area extending circumferentially nearly three (IGV) blades. Upstream of the IGV, however, the region of impacts was restricted along the seeding line, with a clear layer due to fine particle deposition on the window. The peak of concentration profile was aligned with the main direction of seeding with an equivalent standard deviation 2.4.

### 5.4.4 Particles velocities

In order to measure the velocities of particles along the line of injection, the laser measuring volume was traversed across many axial positions for the three heights of injections. Particles reached the flow velocity at 80mm distance from the pipe injector. From an extrapolation of the curve relating velocity with distance from the injector, the release velocity was determined. The local flow velocity was also measured and the ratio of particle release velocity to air velocity was finally determined.
Figure 5-36 shows the variation of particle velocities along the particle trajectory path for the different release heights, and they all reached the measured local flow velocity nearly at 80mm distance from the pipe injector.

### 5.4.5 Discussion

The sand particles are shown to spread along their seeding lines from the three heights of injection. The results for the concentration profiles and velocity along the seeding lines are in good agreement with the prediction achieved by the trajectory code (figure 5-35 with figure 3-40) and (figure 5-36 with figure 3-38). The erosion patterns are depicted by figures 5-52 to 5-56 for the three heights of injection. Figure 5-53 to 5-54 show the erosion patterns due to local injection of sand particles (150-300micron) at mid-blade height. They are depicting noticeable erosion around the leading edge. On the suction side, however, the erosion is concentrated along the leading edge due to particles entering the rotor with a negative incidence angle, but there is no noticeable erosion on the remaining of the suction side. Some impacts on trailing edge of IGV blades are due to the particle spread and particles rebounding from rotor leading edge, which is confirmed from particle trajectory prediction. The rotor tip, however, shows signs of erosion were caused by particles migrating from the pressure to the suction side of the blade via the tip clearance as agreed by the particles trajectories. The erosion pattern on the pressure side shows a broader eroded area, which is extending towards the root figure 5-53. This slight difference from prediction is attributed to the particle that rebounded from leading edge suction side and from the shroud and travelled towards the pressure side, and to the variation in the rotor position (which was fixed in the computations). For the local seeding near the hub, the impacts on the pressure side spread from the root of blades to the tip because of particle bouncing near the hub, figure 5-55. When seeding near the tip, the impacts occupy the full tip region of blades and erosion of the tip region extends to (nearly) the whole length of the chord, figure 5-56.

The results for local impacts and erosion prediction by the trajectory code are in good conformity with test results, (figures 3-33 to 3-35) and (figures 4-12 to 4-14) in comparison with (figures 5-52 to 5-56). Globally, the areas of impacts, velocities of particles and concentrations were successfully predicted. However, the lower pressure surface of the blade was underestimated due to many reasons: The computation of a particle trajectory within rotor blading needed to freeze the rotor, as consequence some particles may impact the blade pressure side at a higher radius. Also the erosion pattern in this critical area was sensitive to the initial relative position between IGV blades and the rotor blades as revealed by erosion pattern. The other reason is due to the variation of rebound properties after painting the blades, in addition to blade roughness, which made harder the wear-off of paint. A method of calibrating the painted surface to assess the real rebound characteristic prior doing tests and particle trajectories simulations should be carried out in the future.

## 5.5 THE FAN AERODYNAMIC PERFORMANCE

To assess the aerodynamic performance degradation of the axial fan due to ingestion of sand particles, the baseline performance of the rough rotor blades was measured initially at different mass flows. The stage performance is defined from the total pressure, total temperature, mass flow-rate, shaft power and the speed of rotation. The following parameters were measured:

- Atmospheric pressure, dry and wet atmospheric temperatures
- Rotational speed
- Electrical power, voltage, current and motor temperature
- Static pressures at upstream and downstream of the axial fan
- Upstream and downstream total temperatures

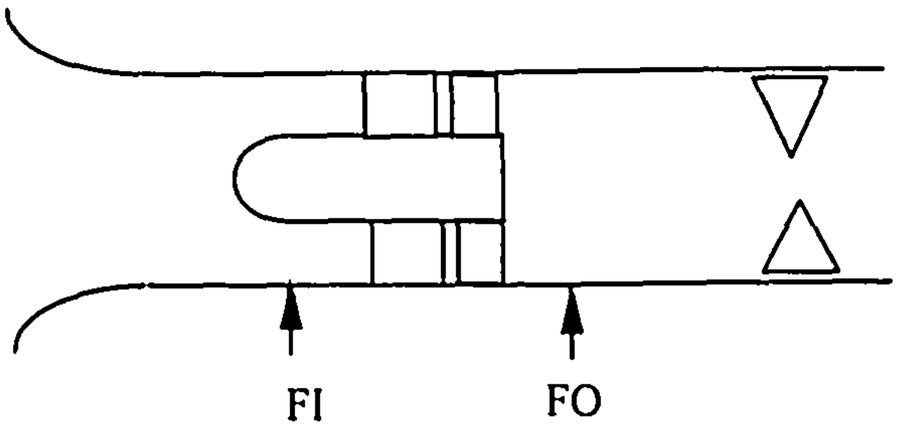


Figure 5-4 Axial fan testing airway

There are several simple things that can be done throughout the tests to minimise measurement errors. Before testing starts, it is recommended that the test rig be leak checked. Record temperatures and pressures at all measuring points prior to the start of testing. The testing was accomplished at different times and ambient air temperature, the operating point was corrected for the testing atmospheric conditions. Also, time was allowed for the test rig to achieve equilibrium before data were acquired. To stabilise the intake operating temperature, the test house was fully opened.

In the absence of flow resistance such as wire screens at inlet, the inlet total head is equal to atmospheric pressure less the losses due to pipe friction. For this axial fan designed without stator blading, the static pressure measured at the wall downstream of the rotor is varying along the diffusing duct. The rate of variation depends on the amount of swirl and the separated flow after the rotor step, which extends along the centre of the duct. The total head of the pressure rise, including the swirl momentum, is greater than the difference of static pressure. Several static pressure measurements were taken along the discharging duct in order to determine the recovery point for the static pressure, figure 5-6. The total pressure was calculated from the mass flow and the local static pressure. The loss due to sudden enlargement was considered according to (ESDU 72011, 1981) as detailed in appendix I.

Closely spaced throttling points were necessary for an evidence of sharp changes in the performance characteristic curves. Finer adjustments were necessary when approaching the surge line. The mass flow was adjusted by means of a throttling butterfly valve. When stalling of the rotor blading occurred an audible note was given out, which is an indication of the onset of stall. Afterwards, an abrupt change in pressure rise was noticed from the change of the noise tone and the decrease of the mass flow and fan pressure head. The fan was continued to operate in the unstable branch of characteristics, figure 5-46. The pressure distribution recorded along the discharging pipe exhibits unsteadiness of pressure near the stall point and along the unsteady branch of the aerodynamic characteristic. During surge the air outlet temperature rises up, as well as the temperature of the motor. The unsteady branch of characteristics was run at once to avoid damaging rotor blades.

Because of the noticeable drifting in the temperature measured by the semi-shielded thermocouple, due to unsteady flow behind the rotor, the adiabatic efficiency was derived from the measurements of electrical power, figure 5-47. The motor efficiency was derived after calculating electrical losses, figure 5-48. During experiments it was noticed that the speed of the motor was not constant, but it increased with throttling, figure 5-49.

The axial fan aerodynamic performances were determined and corrected to the standard atmospheric condition, figures 5-50 and 5-51. A mean corrected rotational speed was assigned to the characteristic curves. The calculation procedure used for data reduction is as follows.

- As the shaft power is known, the adiabatic efficiency takes generally this form:

$$\eta_{tis} = \frac{\Delta H_{tis}}{W_r} \qquad 5\text{-}15$$

- Where the isentropic enthalpy increase is given by:

$$\Delta H_{tis} = \frac{\gamma}{\gamma - 1} R T_{tFi} \left[ \left( \frac{P_{tFo}}{P_{tFi}} \right)^{\frac{\gamma - 1}{\gamma}} - 1 \right] \qquad 5\text{-}16$$

- The pressure rise factor is equivalent to the total pressure head normalised by the square of tip peripheral speed.

$$\psi_t = {\Delta P_{t\_stage}} \Big/ {\rho U_t^2} \qquad 5\text{-}17$$

- The fan corrected mass-flow rate.

$$\dot{m}_c = \dot{m} \frac{Pa_{st}}{P_{tFi}} \sqrt{\frac{T_{tFi}}{Ta_{st}}} \qquad 5\text{-}18$$

- The fan corrected speed of rotation

$$N_c = N \sqrt{\frac{Ta_{st}}{T_{tFi}}} \qquad 5\text{-}19$$

The details of the axial fan stage performance computations are explained in appendix G. Also, the Fortran program *CHARA* used for the data reduction and the calculation of the fan aerodynamic performance is presented in the flowchart of appendix H.

### 5.5.1 Discussion

The maximum diffusion downstream of the fan rotor and the static pressure recovery occurs at a station about two and half diameters from the rotor outlet. This was determined by exploring the static pressure along the discharging duct, as illustrated by the curve of pressure against the duct length, figure 5-46. The axial fan reaches its maximum efficiency 0.805 at a corrected mass flow 0.785 kg/s, the maximum pressure rise coefficient is 0.4. These two measured values are close to the prediction obtained by CFD computations, that give a maximum efficiency 0.812 and a maximum pressure rise coefficient 0.422

The axial fan unit suffered from an abrupt stall at a corrected mass flow rate 0.615. After stall inception the mass flow decreases suddenly from 0.615 kg/s to 0.38kg/s. The static pressure along the discharging duct shows a non regular trend, because of the intensity of unsteadiness, figure 5-46. The pressure head reaches a minimum, as far as the throttling was continued in the unstable branch, but later, it started to increase due to trapped flow between the rotor outlet and the throttling.

## 5.6 GLOBAL SAND INJECTION EROSION TESTING

The global injection tests were carried out for the following purposes: firstly, to reveal the erosion patterns resulting from a global ingestion of sand particles and to make comparisons with predictions. Secondly, this type of tests simulates the behaviour of an axial fan operating in a sandy atmosphere, and it is possible to assess the deterioration of blade geometry and the aerodynamic performance reduction.
Two rotor blades were painted and tested at a low concentration, 127mg/m$^3$ and another at a severe concentration, 775mg/m$^3$.
Figures 5-9 and 5-11 show the general set-up of the pressurised venturi injector working at 65 PSI figure 5-18. The position of the injector was set after matching the conical jet of particles with the frontal intake area. The distance between the injector and the intake depends on air pressure and sand concentration.

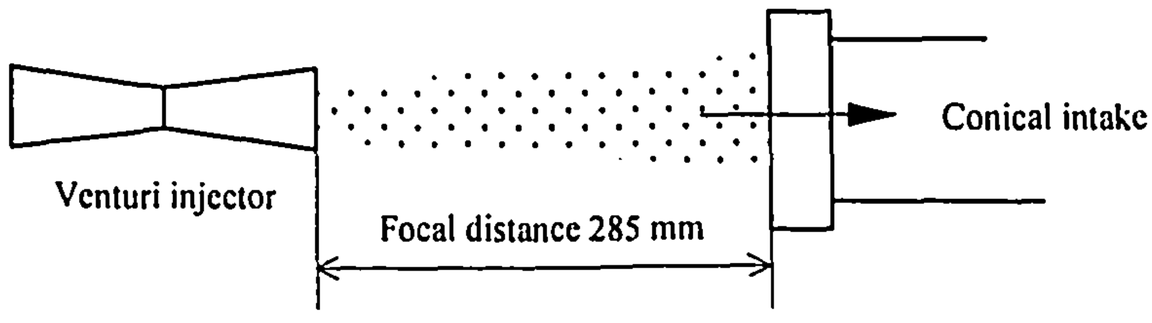


Figure 5-5 Position of the venturi from the intake

The testing conditions corresponded to atmospheric pressure 1002.5 mbar, temperature 19c and humidity 61%. The measurement by transit laser anemometer in the centre of the plane ' II ', figure 5-13 gave the values of air velocity, flow direction, normal and transversal turbulence intensity as following; 29.9m/s 92.3degree, 3.7, 10.7, respectively. Similar measurements at plane ' I ' upstream IGVs gave air velocity, flow direction, normal and transversal turbulence intensity as following; 54.4m/s, 91.2degree, 4.2, 5.5 respectively.

A global mass of sand (934g) was consumed in 3hours, which corresponds to a concentration of 127mg/m$^3$. The rate of paint and aluminium wear off was 1.49mg/g.

Another test carried out at a severe concentration 775mg/m$^3$, using MIL-E5007E sand particles during 45 minutes only gave similar erosion pattern, but with high rates of erosion.

The concentration profiles of sand particles with the corresponding velocities were measured across two planes. The first one at 35 mm upstream the fan nose, and the second at 50mm upstream the IGVs. The concentration profiles exhibit a peak towards the transition from the free stream to the annular passage, figure 5-37. This is probably due to impacts with the inlet nose and deflection towards the annular flow section. Figure 5-38 shows the corresponding particle velocity peaks. As the particles progress toward the IGVs, they tend to spread, as shown in figure 5-39.

Figures 5-40 and 5-41 depict the variation of the particle velocities and their directions from hub to shroud as measured by laser anemometer across plane ' I '. The flow velocity and its direction were also measured and compared to particle velocities and angles, figure 5-42. The particle and flow velocities are closer towards the core flow and near the hub, but there is a noticeable difference near the tip. Due to the initial particle bouncing on the inlet nose and on the shroud, the particle angle is different from flow angle. The measurement of particle velocity and its direction usually needs several sampling particles, as consequence the rate of window wear becomes higher due to longer exposure time, which made particle velocity at rotor outlet difficult to measure due to strong impacts. Measurement at rotor outlet was limited to the particle concentration and the air velocity and its direction, which show good agreement with CFD, but there are some discrepancies towards the walls, figure 5-44. The measured concentration downstream of the rotor shows large number of particles highly centrifuged towards the shroud, although, a good quantity is still contained in the core of flow, figure 5-45. The laser signal was very poor near the shroud due to particle impacts and rebounds.

The erosion pattern obtained after global sand injection at low concentration 127mg/m$^3$, during 3 hours shows net leading edge erosion extending to the entire tip corner. Many particles impacted the pressure side along a strip near to the tip of blades, figure 5-57. Due to the high relative velocity at rotor inlet, many particles hit the suction side around the leading edge and rebound to hit the next pressure side closer to the tip. The roughness increased from 0.196 micron (painted blade) to 2.74 micron (cast aluminium roughness). This local change in roughness was responsible for aerodynamic performance losses of the smooth painted blades, figure 5-62. The adiabatic efficiency and the pressure rise reduced by 1.8% and 2.5% respectively. The erosion pattern, figure 5-58 is similar to the previous at low concentration, but it took only 45 minutes when the high concentration 775g/m$^3$ of MIL-E5007E sand was applied.

## 5.7 AERODYNAMIC PERFORMANCE DEGRADATION TESTING

To assess the effect of sand ingestion on the aerodynamic performance of the axial fan stage, series of tests were carried out. The baseline aerodynamic performances of the rough rotor were measured initially at its operating speed at different mass flows.

Then, sand particles were seeded near design point for low, medium and high sand concentration; 127mg/m$^3$, 420mg/m$^3$ and 775mg/m$^3$ respectively. The narrow size bandwidth (150–300micron) sand particles were used at low and medium concentration, while MIL-E-5007E (0-1000 micron) particles were used at a high concentration.
The tests were halted occasionally so that the mass of eroded blade could be weighed, and the tip chord and tip clearance could be recorded. Then, the eroded fan aerodynamic characteristics were measured.

The initial fan geometry at 15°c

- Tip diameter 169.37 mm
- Shroud diameter 170.02 mm
- Tip chord 45.285 mm
- Hub chord 43.08 mm
- Roughness Ra 2.95 micron

Tests at low concentration using the narrow size bandwidth sand (150-300micron) revealed no significant changes in the aerodynamic performance even for a long time of running 17.55 hours, due to the initial polishing of the sand casting blades surfaces. Table 5-1a and 5-1b show the erosion and geometry changes throughout the test steps.

Table 5-1a

| step | P atm Pa | T amb °C | Hum % | Time hours | Mass Sand g | Mass removed g | Diameter Tip mm | Diameter shroud mm | Chord mm |
|---|---|---|---|---|---|---|---|---|---|
| 1 | 101128 | 23 | 55 | 2.55 | 586 | 0.525 | 169.34 | 170.053 | 44.71 |
| 2 | 101362 | 18.75 | 55 | 3 | 688 | 0.453 | 169.25 | 170.06 | 44.5389 |
| 3 | 101570 | 19.5 | 72 | 3 | 661 | 0.408 | 169.367 | 170.064 | 44.272 |
| 4 | 100113 | 22 | 58 | 3 | 675 | 0.415 | 169.3418 | 170.066 | 43.942 |
| 5 | 100297 | 17 | 68 | 3 | 695 | 0.410 | 169.3037 | 170.067 | 43.8912 |
| 6 | 100859 | 20 | 68 | 3 | 710 | 0.414 | 169.164 | 170.007 | 43.688 |

Table 5-1b geometry deterioration due to low concentration of narrow size bandwidth (150-300micron) sand particles

| step | Time hours | Mass Sand g | Mass erosion Per blade g | Erosion rate mg/g | Tip clearance mm | % Tip clear increase | Reduction Chord mm | % chord reduction |
|---|---|---|---|---|---|---|---|---|
| 1 | 2.55 | 586 | 0.0525 | 0.895 | 0.349 | -0.2857 | 0.582 | 1.2852 |
| 2 | 5.55 | 1276 | 0.0453 | 0.65843 | 0.365 | 4.2857 | 0.751 | 1.6584 |
| 3 | 8.55 | 1935 | 0.04087 | 0.61724 | 0.371 | 6 | 1.025 | 2.263 |
| 4 | 11.55 | 2610 | 0.0415 | 0.61 | 0.373 | 6.571 | 1.347 | 2.974 |
| 5 | 14.55 | 3319 | 0.0412 | 0.5782 | 0.376 | 7.428 | 1.396 | 3.0826 |
| 6 | 17.55 | 4029 | 0.0412 | 0.583 | 0.3825 | 9.285 | 1.601 | 3.535 |

The tests at mid concentration, using narrow size bandwidth (150-300micron) sand, revealed a higher rate of wear, but the aerodynamic characteristics dropped slightly

Table 5-2a

| step | P atm Pa | T amb °C | Hum % | Time hours | Mass Sand g | Mass removed g | Diameter Tip mm | Diameter shroud | Chord mm |
|---|---|---|---|---|---|---|---|---|---|
| 1 | 100681 | 24 | 74 | 2.55 | 2493 | 1.323 | 169.3062 | 170.1038 | 43.180 |
| 2 | 100674 | 17.5 | 66 | 2.973 | 2717 | 1.318 | 169.2783 | 170.1165 | 42.672 |
| 3 | 97919 | 15 | 78 | 2.5 | 2250 | 1.12 | 169.2656 | 170.1292 | 42.164 |

Table 5.2b geometry deterioration due to low concentration of narrow size bandwidth (150-300micron) sand particles

| step | Time hours | Mass Sand g | Mass erosion Per blade g | Erosion rate mg/g | Tip Clearance mm | % Tip clear increase | Reduction Chord mm | % chord reduction |
|---|---|---|---|---|---|---|---|---|
| 1 | 2.55 | 2493 | 0.1323 | 0.53068 | 0.399 | 4.3137 | 0.514 | 1.176 |
| 2 | 5.523 | 5210 | 0.1318 | 0.4851 | 0.4165 | 8.88 | 1.014 | 2.321 |
| 3 | 8.023 | 7460 | 0.112 | 0.488 | 0.4287 | 12.078 | 1.522 | 3.484 |

Tests at high concentration using MIL_E 5007E sand particles revealed a large drop in the aerodynamic performance and steep changes in blade geometry due to the concentration level and the nature of sand particles used.

Table 5-3a

| step | P atm Pa | T amb °C | Hum % | Time hours | Mass Sand g | Mass removed g | Diameter Tip mm | Diameter shroud mm | Chord mm |
|---|---|---|---|---|---|---|---|---|---|
| 1 | 100286 | 16.5 | 66 | 2.20 | 3880 | 2.306 | 169.2275 | 170.1546 | 41.275 |
| 2 | 100783 | 23 | 60 | 2.40 | 3518 | 2.124 | 169.164 | 170.2054 | 40.513 |
| 3 | 100874 | 21.5 | 60 | 2.33 | 3783 | 2.57 | 169.0624 | 170.230 | 39.014 |
| 4 | 101297 | 26 | 56 | 2.10 | 3547 | 2.99 | 168.859 | 170.281 | 37.769 |

Table 5-3b geometry deterioration due to high concentration of MIL-E5007E (0-1000 micron) sand particles

| step | Time hours | Mass Sand g | Mass erosion Per blade g | Erosion rate mg/g | Tip Clearance mm | % Tip clear increase | Reduction Chord mm | % chord reduction |
|---|---|---|---|---|---|---|---|---|
| 1 | 2.2 | 3880 | 0.2306 | 0.594 | 0.4535 | 5.734 | 0.889 | 2.1085 |
| 2 | 4.6 | 7398 | 0.2124 | 0.6037 | 0.475 | 10.735 | 1.652 | 3.918 |
| 3 | 6.9 | 11181 | 0.257 | 0.6793 | 0.584 | 36.146 | 3.153 | 7.478 |
| 4 | 9 | 14728 | 0.299 | 0.843 | 0.711 | 65.753 | 4.394 | 10.421 |

## 5.8 DISCUSSION

In order to study the degradation in performance of the studied axial fan, series of global sand ingestion tests were carried near the design point. The erosion pattern obtained with a global injection of narrow size bandwidth (150–300micron) sand particle for duration of 3 hours is shown in figure 5-57. There is a net leading edge erosion extending to the entire tip corner. Many particles impacted the pressure side along a strip close to the tip of blades. To accelerate the degradation of the fan

aerodynamic performance, it was decided to use MIL-E 5007E sand (0-1000 micron). The sand concentration was also increased to 775mg/m$^3$. At this high concentration the erosion pattern that took 45 minutes only, figure 5-58 is similar to that obtained at lower concentration, for a longer time of running, figure 5-57.

The local change in the blade roughness accounts for some of the performance degradation, but most of losses are due to major changes of the tip region of the blade. The erosion of the blade after 9 hours of running under the severe MIL-E5007E sand particle concentration is shown in figure 5-59, where a large part of the blade leading edge tip corner was removed to give a rounded leading edge profile. The tip clearance has also increased markedly, with a developed burr on the tip towards the suction side. Whilst there was small drop in the performance when the narrow size bandwidth (150-300microns) sand was used at a relatively low concentration, Table 5-1, table 5-2. There was a marked decrease in adiabatic efficiency and pressure rise coefficient for 6.7% and 3.44% respectively with MIL-E5007E sand at high concentration for duration of 9 hours of sand ingestion, figure 5-63. The Table 5.3a, and 5.3b show detailed measurements of the erosion rate and blade geometry changes. The surge point moved from a mass flow of 0.615 kg/s to 0.71 kg/s, representing a decrease of 51.8 % in surge margin. The loss in the axial fan performances (pressure rise, efficiency and stall margin) with respect to time and the quantity of sand ingested are clearly illustrated by figures 5-64a and 5-64b. At the end of these tests, the tip clearance increased by 65.7% and the tip chord reduced by 10.4 %. The changes in tip clearance and tip chord are depicted by figures 5-65 to 5-70. The anticipated changes in the aerodynamic performance are due to the resulting increase in the angle of attack, which tends to shift the stall point to higher mass flow-rates. The roughness was reduced not too much (2.95 micron to 2.27 micron), because of the initial polishing of the rough surfaces. An examination of the blade surface after tests showed a ripple formation that appeared on the pressure side similar to the tested cast aluminium specimen in figure 4-8.

The measured mass removed and the rate of erosion figures 5-71 to 5-73, show an initial phase of incubation due to removing of crests from the blade surfaces. But, later variation in erosion rate with time of sand particle ingestion at low and mid concentrations reached a plateau, because the process of erosion becomes harder after the initial polishing. At high concentration of MIL-E5007E sand particle, the mass eroded and the rate of erosion continued to rise due the nature of the sand particle used.

## 5.9 MEASUREMENT ERRORS

The parameters used to assess axial fan stage aerodynamic performance are calculated using measured values of basic quantities such as; pressure, temperature geometry etc.. Measurement errors occur in the process of acquiring data, and those errors are propagated through the calculations yielding uncertainty in the results. The uncertainty is the maximum error, which might reasonably be expected and is a measure of accuracy. Measurement error has two components: a fixed error, called bias, and a random error. The random error or precision is seen in repeated measurements. At the same conditions, each measurement has the same bias. The standard deviation is used as a measure of the precision error (Poti and Rabe, 1988). A combination of bias and

precision is presented to express a reasonable limit for the error called the measurement uncertainty, Abernethy (1985).

$$U = \left| B + t_{95} S \right| \qquad 5\text{-}20$$

Where B is the bias limit, S is the precision index, and t95 is the 95$^{th}$ percentile point for Student's distribution with values lying between (1.96 - 2.04) according to Abernethy and Thompson (1973).

The performance parameter calculated from measurement values has an associated uncertainty due to errors. The sensitivity of the performance parameters (eg efficiency) to individual errors is determined by propagating the bias and precision errors through the relation defining this performance parameter. For example, the measured temperature, pressure etc are propagated to the value of mass flow rate. The effect of the propagation of errors may be approximated with Taylor's series, where the partial derivatives are multiplied by the corresponding measurement errors and combined into the calculation bias and precision terms. The general form for a parameter depending on several measurements is as follows.

$$f(x_1, x_2, x_3, \ldots, x_n)$$

$$S_f = \left[ \left( \frac{\partial f}{\partial x_1} S_{x1} \right)^2 + \left( \frac{\partial f}{\partial x_2} S_{x2} \right)^2 + \ldots\ldots\ldots\ldots + \left( \frac{\partial f}{\partial x_n} S_{xn} \right)^2 \right]^{1/2}$$

$$B_f = \left[ \left( \frac{\partial f}{\partial x_1} B_{x1} \right)^2 + \left( \frac{\partial f}{\partial x_2} B_{x2} \right)^2 + \ldots\ldots\ldots\ldots + \left( \frac{\partial f}{\partial x_n} B_{xn} \right)^2 \right]^{1/2}$$

The uncertainty in the measured value is given by.

$$U_f = B_f + 2S_f \qquad 5\text{-}21$$

The details for the computation of the effect of measurements errors in temperature, pressure, velocity of rotation and geometrical dimensions on the measured mass flow rate, pressure rise coefficient and adiabatic efficiency are explained in appendix J.

### 5.9.1 Basic precision and bias errors incurred during measurements

The following table 5-4 summarises the basic measurement errors encountered during the tests

Table 5-4 basic errors during measurements

| Basic parameter | | Bias | Precision index |
|---|---|---|---|
| Pressure | Pa | 4 | 4 (0.4-0.5 mm$H_2O$) |
| Temperature | °C | 0.5 | 0.5 |
| Diameter and length | mm | 0.1 | 0.1 |
| Displacement | mm | 0.01 | 0.01 |
| Current | A | 0.1 | 0.1 |
| Power consumed | kW | 0.01 | 0.01 |
| Resistance | Ω | 0.01 | 0.01 |
| Frequency | Hz | 1 | 1 |
| Frequency of rotation | Hz | 1 | 1 |

### 5.9.2 Estimated uncertainty of the fan performance parameters

The following table 5-5 gives the propagation of the basic errors incurred during measurements on the fan operating parameters such as mass flow, air power, pressure rise coefficient and adiabatic efficiency.

Table 5-5 uncertainty of measured parameters

| Parameter | | Bias error | Precision error | Uncertainty | Relative error % |
|---|---|---|---|---|---|
| Low flow rate | kg/s | $4.27\ 10^{-3}$ | $5.16\ 10^{-3}$ | $1.46\ 10^{-2}$ | 1.5 |
| High flow rate | kg/s | $8.1\ 10^{-3}$ | $1.6\ 10^{-3}$ | $4.0\ 10^{-2}$ | 2.0 |
| Low mass flow shaft power | w | 27.36 | 27.36 | 82.1 | 2.9 |
| High mass flow shaft power | w | 51.5 | 51.5 | 103 | 2.76 |
| Minimum mass flow air power | w | 28.72 | 56.82 | 142.38 | 2.39 |
| Maximum mass flow air power | w | 26.41 | 51.5 | 129.4 | 1.70 |
| Minimum mass flow loading factor | | 0.0019 | 0.0035 | 0.0089 | 2.8 |
| Maximum mass flow loading factor | | 0.0021 | 0.00389 | 0.0089 | 2.82 |
| Minimum mass flow efficiency | | 0.0126 | 0.0214 | 0.0556 | 7 |
| Maximum mass flow efficiency | | 0.0083 | 0.0087 | 0.0257 | 3.25 |

## 5.10 CONCLUSIONS

Attempts were made to validate the results of the particle trajectory code upon local sand particle injection experimental tests. The results for the particle concentration profiles and particle velocities along the seeding lines agree well with the prediction achieved by the trajectory code. Globally, the areas of impacts, velocities of particle and concentrations are successfully predicted. Noticeable erosion was found around the leading edge. The rotor tip shows signs of erosion that were caused by particles migrating from the pressure side to the suction side. On the suction side, however, the erosion was concentrated along the leading edge, but there is no erosion on the remaining of the suction side.

The aerodynamic performance degradation due global ingestion of sand particles was recorded at each step of ingestion by measuring the total pressure difference, the power consumed and the mass flow rate. Also, the particle concentrations and velocities were measured at upstream fan nose and upstream IGVs. The tests of global seeding of sand particle using the MIL_E5007E depicted noticeable leading edge erosion, with an extended erosion along the tip of the pressure side. The tip clearance also increased markedly with a developed burr on the tip towards the suction side, in addition to a rounding of the blade leading edge. As consequence, the adiabatic efficiency, pressure rise coefficient and surge margin dropped drastically.

The eroded mass and the rate of erosion of the rotor exhibit an initial phase of incubation due to polishing effect, followed by a plateau function of the time of running. However, at high concentration, the mass eroded and the rate of erosion tend to increase, because of the nature of sand particles used.

# CHAPTER 6

# PREDICTION OF THE AXIAL FAN PERFORMANCE DEGRADATION

## 6.1 INTRODUCTION

This chapter presents a developed Fortran program for predicting the aerodynamic performance of the axial fan stage based on mean line method that uses advanced correlations for aerodynamic losses. This was subsequently extended to predict the degradation in performance due to the effects of erosion by sand ingestion, which are mainly attributed to the blade chord reduction, tip clearance and surface roughness increase. The erosion fault model used is based on percentages of the blade geometry deterioration for the blade chord, tip clearance and roughness, which were obtained by direct measurements and also predicted by the trajectory code. The results obtained indicate that erosion caused a decrease in the pressure rise coefficient, adiabatic efficiency and surge margin. The erosion damage has also a significant effect on the aerodynamic lift coefficient, which is related to the static pressure redistribution. Comparison between experimental results obtained from the testing of the axial fan stage and those predicted show good agreement. CFD computations were also carried out to analyse the flow pattern through the eroded rotor blades. A method for predicting life expectancy for this type of turbomachinery is also presented in this chapter.

## 6.2 PREDICTION OF THE BASE LINE AERODYNAMIC PERFORMANCE

The velocity triangles for this contra-whirl IGV axial fan stage at design point are illustrated by figure 2-13. This design configuration permits significantly higher level of work coefficient than other configurations (McKenzie, 1997), due to the high relative velocity at rotor inlet produced by the high deflection of inlet guide vanes contra-whirl. In general there are many methods for predicting axial compressor performance on the mean line basis. They all depend on the variation of the air outlet angle as function of the inlet angle, and the variation of losses or efficiency as function of inlet angle. By introducing the secondary losses and the work factor, the data are corrected to give an approximation to the three-dimensional stage performance based on mid span geometry.

The aerodynamic characteristics of the studied axial fan consisting of C4 profiles are calculated using semi-empirical correlations of total pressure losses. These are dependent upon a number of parameters; including blade profile, blade aspect ratio, space chord ratio, thickness to chord ratio, tip clearance, aerodynamic loading, Mach number and Reynolds number. Before the derivation of loss expressions and the work equation, the flow design conditions are calculated and the variation of the deviation flow angle is also derived.

### 6.2.1 Prediction of incidence and deviation angles

Axial flow compressors developments have particularly benefited from an isolation of specific geometrical parameters and the generation of appropriate data both experimentally and theoretically. The setting of optimum incidence condition for a cascade and the prediction of the resulting deviation angle are dependent upon both camber and stagger angles. The work of Carter has provided correlations for both incidence and deviation angles as function of camber and stagger angles, which were referred to an optimum incidence.

**a) <u>Incidence angles</u>**

- The optimum incidence angle is defined for a maximum lift to drag ratio, and it is function of optimum camber, space chord ratio and deflection. According to Carter's data (Horlock, 1973b), a correlation for the optimum incidence function of space chord ratio, camber and stagger angles is presented by Miller and Wasdell (1987) as follows.

$$I_o = X + \frac{Y}{s/l} - Z\theta \qquad 6\text{-}1$$

- By iterations for the maximum lift drag ratio using the off-design loss variation, which is related to the minimum loss, a value for the minimum incidence is determined. The minimum loss flow angles can also be obtained from a graphical data plotted for inlet and outlet flow angles at the optimum camber and stagger angles, (Lewis, 1996), which gives the following flow angles.

$$\beta_1 = 63.75\,\text{deg} \qquad \beta_2 = 43.69\,\text{deg}$$

- The reference incidence defined by Lieblein (1965) in the middle of loss range is given as follows.

$$i_{ref} = (K_i)_{sh}(K_i)_{th}(i_0)_{10} + n\theta \qquad 6\text{-}2$$

A correction value '–1' was suggested by Casey (1987), because blade cascade operates at constant stagger angle whereas Lieblein's measurements were carried out at constant air angles.

• The nominal incidence as defined by Howell at 80% of stalling deflection is expressed by the following relation due to Wallis (1968).

$$C_L^{\cdot}\left(\frac{\cos\beta_1}{\cos\beta_2}\right)^{2.75} = 2 \qquad 6\text{-}3$$

Replacing in the lift coefficient by the drag coefficient and the blade cascade geometry parameters yields the following equation.

$$\left[2\left(\frac{s}{l}\right)\cos\beta_m(\tan\beta_1-\tan\beta_2)-C_D\tan\beta_m\right]\left(\frac{\cos\beta_2}{\cos\beta_1}\right)^{2.75} = 2 \qquad 6\text{-}4$$

The nominal inlet flow angle is located by using an iterative Newton technique. The derivative of expression 6-4 with respect to inlet flow angle '$\beta_1$' yields the following expression.

$$\left[\frac{2\left(\frac{s}{l}\right)\left(1+\tan^2\beta_1\right)}{\sqrt{1+\tan^2\beta_m}}-\frac{\left(\frac{s}{l}\right)(\tan\beta_1-\tan\beta_2)\tan\beta_m\left(1+\tan^2\beta_1\right)}{\left(1+\tan^2\beta_m\right)^{3/2}}-1/2C_D\left(1+\tan^2\beta_1\right)\right]\left(\frac{\cos\beta_2}{\cos\beta_1}\right)^{2.75}$$

$$+2.75\left[\frac{2\left(\frac{s}{l}\right)(\tan\beta_1-\tan\beta_2)}{\sqrt{1+\tan^2\beta_m}}-C_D\tan\beta_m\right]\left(\frac{\cos\beta_2}{\cos\beta_1}\right)^{1.75}\frac{\cos\beta_2\sin\beta_1}{\cos^2\beta_1} \qquad 6\text{-}5$$

An initial guess for the nominal inlet flow angle used McKenzie's (1980) correlation derived at maximum efficiency condition.

$$\tan\beta_m = \tan\xi + 0.213 \qquad 6\text{-}6$$

• The stalling incidence function of camber and stagger angle was derived by Raley as reported in reference (Wright and Miller, 1991), where the involved constants are given in a graphical form.

$$I_s = A+\frac{B}{s/l}-C\theta \qquad 6\text{-}7$$

• The choking incidence corresponds to a flow condition for which the mass flow parameter ($MFP^*$) reaches a critical value evaluated at the cascade throat area, (Mattingly et al, 1987).

$$\frac{m_t\sqrt{T_{t1}}}{A_t P_{t1}} = MFP^* \qquad 6\text{-}8$$

Where the critical mass flow parameter is given by.

$$MFP^* = \frac{\sqrt{\gamma / R}}{\left\{\frac{\gamma+1}{2}\right\}^{\frac{\gamma+1}{2(\gamma-1)}}} \qquad 6\text{-}9$$

The mass flow rate through the axial fan cascade is calculated using the blade spacing, blade height and inlet conditions.

$$m_t = m_1 = \rho_1 V_{z1} sh \qquad 6\text{-}10$$

**b) <u>Deviation angle</u>**

The basic correlation for the blade deviation angle at a nominal condition is due to Howell (Horlock, 1973b), which later was presented by Carter in this form.

$$\delta = m\theta\left(s/l\right)^n \qquad 6\text{-}11$$

The parameter ' m ' is a function of blade staggering, camber line and blade pitch.
The parameter 'n' takes value 0.5 for compressor cascades. For inlet guide vanes, Carter suggested an exponent value '1', (Gostelow, 1984).

At higher stagger and deviation angles estimates based on the NTGE correlation have been seen to under-predict the deviation angle. Its extrapolation to high stagger angles and space chord ratios, more pertinent to the axial fan design was highlighted by Wallis (1972). For a high solidity balding a blend between cascade and isolated aerofoil design method was required (Wallis, 1968). The modified parameter 'm' derived from a blend of isolated profile and cascade data at high stagger angles is presented graphically in figure M-1 (appendix M), which can be fitted by the following polynomial depending on stagger angle.

$$m = 10^{-8}\xi^4 - 10^{-6}\xi^3 + 0.0001\xi^2 - 0.001\xi + 0.2307 \qquad 6\text{-}12$$

Similarly to NGTE, the NACA provided an experimental correlation for the deviation angle for NACA and C4 airfoil series, which was evaluated at reference incidence angle by Lieblein (1965).

$$\delta_{ref} = \delta_0 + \frac{m_{\sigma=1}}{\sigma^b}\theta \qquad 6\text{-}13$$

$$\delta_0 = (K_\delta)_{sh} \cdot (K_\delta)_{th} (\delta_0)_{10} \qquad 6\text{-}14$$

The IGV blades are geometrically similar to turbine NGV, thus the outlet flow angle are related to the throat area and to the blade spacing as mentioned by Gordon and Korakianitis (1998).

$$\alpha_1 = -11.15 + 1.154 \cos^{-1}\left(\frac{o}{s}\right) + 4\left(\frac{s}{e}\right) \qquad 6\text{-}15$$

A graphical relation for the outlet flow angle due to Ainley and Mathieson (Japiske and Baines, 1994) can also be used. A significant under-turning of the core flow for this IGV blades was confirmed from the previous CFD results and from experiments carried out by Filbee (1990).

### 6.2.2 Off-design deviation angle

To predict the off design characteristics knowledge of the variation of flow deviation angle is required. At high stagger angles and space chord ratios, the assumption of a constant outlet angle becomes non-valid. Lieblein (1960) evaluated the variation of the deviation with incidence, and evaluated the derivative expressing the rate of change of the deviation angle with incidence at a reference incidence.

The deviation angle is dependent on incidence and inlet flow angle. For a fixed stagger angle the variation in flow angle is equal to the variation in incidence. Consequently, the derivative of the deviation with incidence at a constant stagger is a summation of two derivatives.

$$\left.\frac{d\delta}{di}\right|_{\xi} = \left(\left.\frac{\partial\delta}{\partial i}\right|_{\beta_1} + \left.\frac{\partial\delta}{\partial\beta_1}\right|_{i}\right) \qquad 6\text{-}16$$

If the stagger and flow angle vary simultaneously for a constant incidence, the second term of the derivative yields.

$$\left.\frac{\partial\delta}{\partial\beta_1}\right|_{i} = \left.\frac{\partial\delta}{\partial\beta_1}\right|_{i=iref} - \left(\left.\frac{\partial\delta}{\partial i}\right|_{\beta_1}\right)\left(\frac{\partial i}{\partial\beta_1}\right)_{i=iref} \qquad 6\text{-}17$$

By differentiating deviation angle at the reference incidence yields the derivative at reference flow angle.

$$\left.\frac{\partial\delta}{\partial\beta_1}\right|_{i=iref} = (K_\delta)_{sh}(K_\delta)_t \left.\frac{\partial(\delta_0)_{10}}{\partial\beta_1}\right|_{i=iref} + \frac{\theta}{\sigma^b}\left.\frac{\partial m_{\sigma=1}}{\partial\beta_1}\right|_{i=iref} - \theta\frac{m_{\sigma=1}}{\sigma^b} ln\sigma \left.\frac{\partial b}{\partial\beta_1}\right|_{i=iref} \qquad 6\text{-}18$$

By differentiating the incidence with respect to the flow inlet angle, yields the derivative at the reference incidence.

$$\left.\frac{\partial i}{\partial\beta_1}\right|_{i=iref} = (K_i)_{sh}(K_i)_{th} \left.\frac{\partial(i_0)_{10}}{\partial\beta_1}\right|_{i=iref} + \theta\left.\frac{\partial n}{\partial\beta_1}\right|_{i=iref} \qquad 6\text{-}19$$

The derivative of the deviation with incidence at reference inlet flow angle is given graphically by Lieblein (1965), figure M-2 (appendix M). The NASA data throughout figures M-2 to M-4 allows computing all components of equation 6-18. The used interpolation polynomials constants are presented in appendix K.

By knowing the slope of the deviation angle, the variation of the flow deviation is approximated by a linear relation, with respect to incidence angle as follows.

$$\delta = \delta_{ref} + \left(d\delta/di\right)_{ref}\left(i - i_{ref}\right) \qquad 6\text{-}20$$

### 6.2.3 Aerodynamic performance prediction

The prediction of the aerodynamic performance of an axial flow compressor at off-design point has been a problem ever since their appearance. Three techniques were commonly used, they are: The blade element theory assuming radial equilibrium, stage stacking and a simplified method involving scaling of overall characteristics, which is an extension of that used by Howell and Bonham (Robbins and Dugan, 1965). In this section, at first is presented the Howell-Bonham method, then a method based on Lieblein and Koch-Smith correlations.

**a) <u>Howell - Bonham method</u>**

In Howell and Bonham modelling for the axial flow compressors characteristics, the reference stage efficiency is calculated excluding the tip clearance loss and the Reynolds number effect.

$$\eta_{ref} = 1 - \left[\frac{\varpi_r\left(\frac{W_1}{U}\right)^2 + \varpi_{IGV}\left(\frac{V_1}{U}\right)^2}{2\left(\frac{\Delta H_t}{U^2}\right)}\right] \qquad 6\text{-}21$$

***<u>IGV losses</u>*:** From direct analogy between the IGV and the turbine NGV, the profile loss of IGV blades is based on the outlet velocity from the cascade. This loss is evaluated from Ainley's correlation, which is presented as total pressure loss factor function of air outlet angle and space chord ratio as given by figure M-5 of appendix M, adapted from reference (Horlock, 1973a)

$$\varpi_{IGV} = \frac{\Delta P_t}{1/2\rho V_1^2} \qquad 6\text{-}22$$

The secondary loss due to Ainely and Mathieson (Horlock, 1973a) is defined by the following expression.

$$\varpi_s = \lambda\left[\frac{C_L}{s/l}\right]^2 \frac{cos^2 \alpha_1}{cos^3 \alpha_m} \qquad 6\text{-}23$$

Dunham and Came (1970) suggested that Ainely's secondary loss parameter could be rewritten as in order to become more applicable to lower aspect ratio machines by introducing the correction factor.

$$\lambda = 0.0334\left(\frac{l}{h}\right)cos\,\alpha_1 \qquad 6\text{-}24$$

Then, the total pressure loss is a summation of the profile and the secondary losses including the trailing edge thickness loss (Japiske and Baines, 1994).

$$\varpi_{IGV} = \varpi_s + \varpi_p \qquad 6\text{-}25$$

***Rotor losses*** : The rotor profile loss is estimated from Howell's correlation presented in appendix M-6, adapted from (Horlock, 1973b). To interpolate between different space-chord ratios a Lagrange interpolation technique is used. The Howell drag coefficient and the total pressure loss coefficient are related by the following expression.

$$C_D = {}^{s}\!/_{l}\,\varpi_p \frac{\cos^3 \beta_m}{\cos^2 \beta_1} \qquad 6\text{-}26$$

The flow patterns near the endwalls are determined by the secondary flow, whose strength depends mainly on the thickness of the upstream boundary layer and on the amount of the blade turning (Denton and Cumpsty, 1987). The losses due to secondary flows are strongly dependent on lift coefficient. Stewart et al (1960) based on comparison of the better known correlations and backed by experiments suggested the following secondary flow loss coefficient.

$$\varpi_s = \frac{\varpi_p\, cos\,\xi}{\sigma.AR} \qquad 6\text{-}27$$

The reference rotor loss is calculated by the summation of profile loss and secondary loss.

$$\varpi_r = \varpi_p + \varpi_s \qquad 6\text{-}28$$

***Tip clearance loss:*** More recent studies have concentrated on measuring the tip leakage flow in great detail, Bindon (1989) for turbines and Storer for compressors (Denton, 1993). Lakshminarayana (1996) based on an inviscid analysis and backed by experimental data obtained the following semi-empirical relation for the tip clearance loss.

$$\Delta\eta_{tip}=\frac{0.7\left(\tau/h\right)\psi}{\cos\beta_m}\left[1+10\sqrt{\frac{\phi\ t/h\ AR}{\psi\cos\beta_m}}\right] \qquad 6\text{-}29$$

Robinson (1982) suggested a simple relationship, which doesn't include the stage loading for unloaded fans.

$$\Delta\eta=\frac{2.74}{1-r_h/r_t}\left(\frac{\tau}{h}\right) \qquad 6\text{-}30$$

**Reynolds number:** The effect of Reynolds number as discussed in the literature includes reduction in efficiency, change in deflection and effects on stall pressure rise capability. A general relationship presented by Schaffler (1979) relates the effect of Reynolds when using relations 6-26 and 6-27.

$$(1-\eta)\propto Re^{-n} \qquad 6\text{-}31$$

**b) Lieblein's profile loss**

Many correlations have been developed since Howell's data for profile loss estimation was available. Lieblein (1959) developed a profile minimum loss parameter based on the defect in the momentum at blade trailing edge. The trailing edge momentum thickness was correlated against the equivalent diffusion factor, for which a more general expression was developed by Koch and Smith (1976), see appendix L, presented as follows.

$$D_{eq}=\frac{W_{max}}{W_{0TE}}=\frac{W_m}{W_1}\frac{W_{max}}{W_m}\frac{W_1}{W_{OTE}} \qquad 6\text{-}32$$

Once the momentum thickness and the shape factor are obtained, the profile loss coefficient is calculated by the following expression (Gordon and Korakianitis, 1998).

$$\varpi_p=2\left(\frac{\theta^*}{l}\right)\frac{\sigma}{\cos\beta_2}\left(\frac{\cos\beta_1}{\cos\beta_2}\right)^2\left[\frac{2}{3-1/H_2}\right]\left[1-\left(\frac{\theta^*}{l}\right)\frac{\sigma H_2}{\cos\beta_2}\right]^{-3} \qquad 6\text{-}33$$

The ratio of the trailing edge momentum thickness to the chord length and the ratio of the form factor to the chord length are function of diffusion factor as illustrated by figure M-7 (appendix M). Corrections are made for Reynolds number, surface roughness and Mach number.

***Effect of roughness:*** In fluid mechanics, roughness is usually specified in terms of an equivalent sand grain roughness. It is therefore, necessary to relate sand roughness to the surface finish as specified by the surface centre line averaged roughness (Schaffler, 1979)

$$k_s=8.9R_a$$

The critical roughness Reynolds number is set at 90. Above this value, the boundary layer characteristics depend only on the ratio of the blade surface roughness to the chord length. The criterion for hydraulic smoothness according to Koch and Smith (1976) is given by.

$$\frac{Wk_s}{\nu} \leq 90 \qquad 6\text{-}35$$

**c) <u>Endwall losses</u>**

These losses include both secondary flow losses and losses due to the wall boundary layer. It is difficult to separate these two sources of losses, as consequence they are lumped together and called endwall losses (Lakshminarayana, 1996). The effects of tip clearance, aspect ratio and blade loading on the endwall losses were demonstrated as following: As tip clearance increases the total loss is observed to increase and the maximum achievable loading decreases. As aspect ratio increases, the total loss is observed to decrease at low levels of loading, but increases at high loading (Wright and Miller, 1991). A powerful method developed by Smith and subsequently simplified by Koch and Smith (1976) related the efficiency loss due to the presence of endwall effects to the two properties of an endwall boundary layer; the displacement thickness and the tangential force thickness. As the tip clearance is increased, an increase in the blockage due to end wall boundary layer is noticed. The boundary layer thickness is normalised by the average stagger spacing and is correlated against the reduced stage pressure rise coefficient for a given normalised tip clearance. The displacement and tangential thickness graphical correlations are illustrated by figures M-9. The correction to the efficiency including the end wall losses yields.

$$\eta = \eta_{ref} \frac{1 - \left(2\overline{\delta^*}/\overline{s\cos\xi}\right)\left(\overline{s\cos\xi/h}\right)}{1 - \left(2\overline{\nu}/2\overline{\delta^*}\right)\left(2\overline{\delta^*}/\overline{s\cos\xi}\right)\left(\overline{s\cos\xi/h}\right)} \qquad 6\text{-}36$$

The reduced stage pressure rise coefficient used in the graphical correlation is the ratio of the effective stage static pressure rise coefficient to the maximum pressure rise coefficient according to the definition given by Koch (1981).

$$\Omega = {Cp}/{Cp_{\max}} \qquad 6\text{-}37$$

Gordon and Korakianitis (1998) suggested that it is probably sufficiently accurate to estimate the reduced stage pressure rise coefficient simply by the following ratio, involving flow angles.

$$\frac{\left(\Delta p/q\right)_{il}}{\left(\Delta p/q\right)_{il,\max}} = \frac{1 - \dfrac{\cos^2\beta_1}{\cos^2\beta_2}}{1 - \dfrac{\cos^2\beta_{1mx}}{\cos^2\beta_{2mx}}} \qquad 6\text{-}38$$

**d) Blockage factor**

The value of the blockage factor used to correct the axial velocity is based on the boundary layer displacement thickness at each end wall. Howell and Calvert (1981) developed the following expression for the blockage factor depending on tip clearance and hub tip ratio.

$$K_b = 1 - \left(0.002 + \frac{3\varepsilon}{d_t}\right)\frac{1 + \left(d_h/d_t\right)^2}{1 - \left(d_h/d_t\right)^2} \qquad 6\text{-}39$$

### 6.2.4 Off-design axial fan characteristics prediction

Howell and Bonham (1950) introduced an approximate method for assessing the axial compressor temperature rise characteristic at off-design. The results of the correlation were generated from several low speed experimental axial flow compressors. The temperature rise characteristics has been non-dimensionalised with respect to the maximum efficiency, figure M-10. For a given value of flow coefficient and by knowing values $(\Delta H_t/U^2)_{\eta max}$ and $(V_a/U)_{\eta max}$, the off-design values are easily deduced from the graphical relation. In such a procedure, the maximum efficiency of the stage is firstly located, afterwards the tip leakage and Reynolds corrections are introduced to recalculate the maximum efficiency.

$$\eta/\eta_{MAX} = \frac{\left(\Delta H_t/UV_a\right)}{\left(\Delta H_t/UV_a\right)_{MAX}} \qquad 6\text{-}40$$

The maximum loading factor is determined from Euler pump equation according to the velocity triangles shown in figure 6-1. The Euler work is given by the following expression, including the blockage factor and the work done factor.

$$\Delta H_t = \Omega U\left(V_{\theta 2} - V_{\theta 1}\right)$$

if $W_{\theta 2} \geq U$ $\quad \Delta H_t = \Omega U\left[\left(-\left(V_{a2}\tan\beta_2 - U\right)\right) - \left(-\left(V_{a1}\tan\beta_1 - U\right)\right)\right]$

if $W_{\theta 2} < U$ $\quad \Delta H_t = \Omega U\left[\left(U - V_{a2}\tan\beta_2\right) - \left(-\left(V_{a1}\tan\beta_1 - U\right)\right)\right]$

The stage loading coefficient is calculated by the flowing expression.

$$\frac{\Delta H_t}{U^2} = \frac{\Omega\left(\tan\beta_1 - \frac{V_{a2}}{V_{a1}}\tan\beta_2\right)}{\tan\beta_1 - \tan\alpha_1} \qquad 6\text{-}41$$

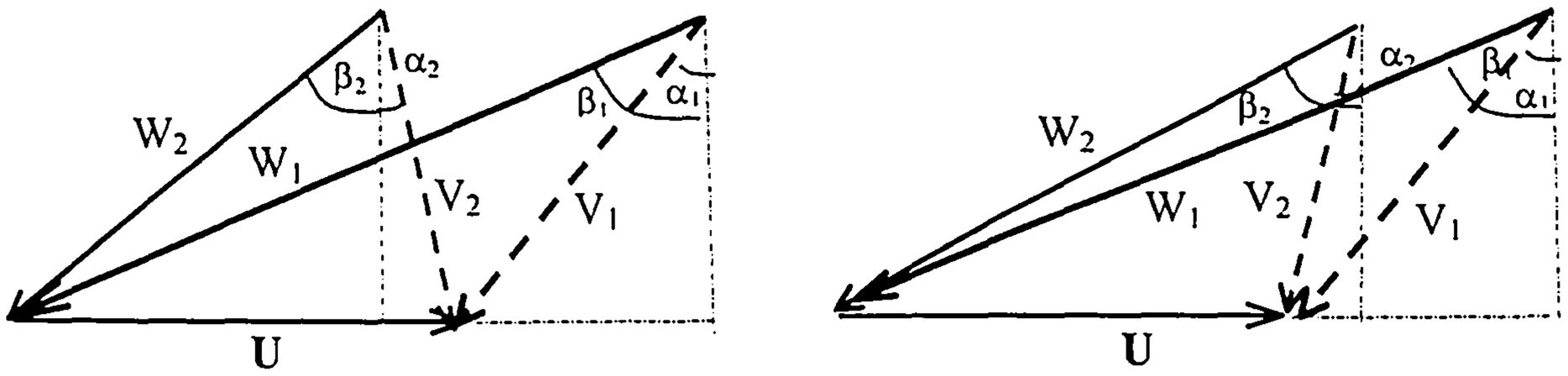


Figure 6-1 Off-design velocity triangles

In the two dimensional analytical methods (subsections b,c of sections 6.2.3). The operating range is defined as the range of inlet flow angle within which the profile loss coefficient is less than twice the minimum loss value. The Lieblein's classical two-dimensional correlation has been used as the basis for predicting the minimum profile losses with a correction for Reynolds number and roughness. The off-design profile loss coefficient is corrected for incidence angle using Jansen and Mofatt factor (1967).

$$\left(\omega/\omega_m\right)_{inc} = 1. + 0.1667\chi + 0.8333\chi^2 \qquad 6\text{-}42$$

$$\chi = 2\frac{|i - i_{ref}|}{\Delta\beta}$$

$\Delta\beta$ : operating range of flow angle

Also, Miller and Wasdell (1987) provided a graphical relation for the off-design blade profile loss between choking incidence and stalling incidence.

$$\left(\omega/\omega_m\right)_{inc} = f\left(\frac{i-i_m}{i_s-i_m}\right) \qquad \left(\omega/\omega_m\right)_{inc} = f\left(\frac{i-i_m}{i_m-i_c}\right) \qquad 6\text{-}43$$

The endwall losses are evaluated for each operating point based on Koch-Smith correlations

The relationship of stage temperature rise and total pressure rise of the unit is simply derived from stage loading factor and adiabatic efficiency definitions.

$$\frac{\Delta P_t}{\overline{\rho}U^2} = \eta_s \frac{\Delta H_t}{U^2} \qquad 6\text{-}44$$

Where the pressure rise coefficient relatively to rotor tip radius is defined by.

$$\psi = \frac{\Delta P_t}{\rho U_T^2} \qquad 6\text{-}45$$

### 6.2.5 Stalling point

With the nominal value of deflection defined at 80% of the stalling deflection (Lewis, 1996), the uncorrected stalling deflection can be simply related to flow incidence by a spline fitting curve.

$$\varepsilon^* = \quad 1.25\varepsilon' \qquad \text{6-46}$$

The increase in stalling incidence and flow range obtained with reducing aspect ratio, was accounted for by modifying the stalling tangent air deflection using an empirical correction factor derived from the work of Howell and Calvert (1981)

Early investigations attempted to define a quantitative measure of the aerodynamic loading and to determine the loading at stall. Leiblein (1959) defined the well-known diffusion factor concentrating on the suction surface diffusion process. The variation in the limiting stalling diffusion has been related to the high staggering, and to the endwall effects; such as tip clearance and blading aspect ratio. It is very often that the flow in the annulus endwall region, which is the central cause of the rotating stall onset, Smith (1970). In order to approach this it has been found useful to view blade passages in another way namely as a diffuser (Greitzer, 1988). On this principle, Koch (1981) examined the stalling pressure rise capability of different axial compressors on a mean line basis. He presented a procedure for estimating the maximum pressure rise potential of axial flow compressor stages, and correlated the stall pressure rise coefficient against the two dimensional diffuser performance. The available data were corrected against more pertinent factors, which include Reynolds number, normalised tip clearance and axial spacing, figures M-11.
The re-energising process as commented by Koch (1981) that occurs at high stagger angles and affects the stall pressure rise does not occur in the case of this contra-whirl IGV axial fan due to high reaction as seen from the velocity triangles. The effective static pressure rise is given by.

$$C_{h\,eff} = \frac{C_p T_1 \left[ \left( P_2 / P_1 \right)^{\gamma - 1/\gamma} - 1 \right]_{stage}}{1/2 \left( W_{1r}^2 + V_s^2 \right)} \qquad \text{6-47}$$

The surge margin is calculated according to the definition given by Cumpsty (1989).

$$S_M = 100 \left[ 1 - \frac{\Pi_w m_s}{\Pi_s m_w} \right] \% \qquad \text{6-48}$$

### 6.2.6 The mean line computer program

A Fortran program called *FANCHAR* was developed based on the mean line method, which consisted in a one dimensional calculation procedure by using empirical correlations for losses referring to the mean radius of the machine. The different

subroutines and their relationships are presented in the flowchart F6-1. The input data are read in a free format, Table 6-1. The data consist in the number of blades, speed of rotation, geometry of the annulus, stagger angles tip clearance, surface roughness and some parameters related to the blades profiles.

**Main subroutines**

| | |
|---|---|
| DSLOPEN | calculates the variation of the deviation angle with respect to incidence |
| HOWELL | calculates drag coefficient on blade profile |
| IGVLOSS | calculates the total IGV pressure losses |
| XLEBLEIN | calculates the profile loss at minimum incidence using momentum thickness |
| RECORR | correct for the effect of viscosity and roughness |
| ENDWALL | calculates the endwall loss |
| OFFLOSS | calculates the off-design profile losses |
| IGVLOSS | calculates the IGV total loss |
| STALL | searches for the stall point based on Koch criteria |
| SPLINT | searches abscissa for a given ordinate |
| FLAGR | interpolates between two sets of data |
| SIMPSON | integrates along given values |

### 6.2.7 Discussion

The prediction method for the axial fan aerodynamic performance was based on a mean line approach and depended on some empirical correlations more appropriate to compressor cascades. The first procedure used basic correlations for the profile and secondary-flow losses, and the off-design points used Bonham-Howell graphical relation. However, this method shows its inability to give good predictions when compared to experimental results, figure 6-3. The noticeable difference is related to the inadequacies of the empirical correlations to estimate the end wall losses, especially for this high staggering rotor design operating at high reaction.

In the second procedure, which used Lieblein and Koch-Smith correlations, the profile loss was based on the rate of diffusion, which is recognised as the essential factor to control boundary layer growth and separation. The endwall boundary layer losses were calculated from Smith and Koch correlations. The figure 6-3 shows that after introducing such correlations, the method provided a good prediction. Although, there is a difference between measurement and prediction results near the stalling point, which influenced the value of end wall losses, in addition to the maximum reaction used in designing the axial fan stage. Koch suggested that a constant 0.95-0.98 should be used to correct the maximum stalling pressure rise coefficient for high reaction cascades, but his data is very scattered.

The application of the mean line method to the studied axial fan has highlighted some difficulties in finding the minimum loss incidence for this high staggering blade design. Furthermore, the variation of profile losses with incidence was introduced in the

simple form as presented by Jansen and Mofatt (1967). In general the second procedure shows a satisfactory agreement with the experimental results.

## 6.3 AERODYNAMIC LOSSES DUE TO EROSION

The aerodynamic losses in an axial machine due to erosion by particle ingestion are mainly attributed to the blade chord reduction, tip clearance increase and surface roughness. This section explains the inclusion of losses due to blade geometry deterioration. The previous program *FANCHAR* is extended here to include erosion fault model based on geometry deterioration by erosion and the subsequent extra aerodynamic losses. Details of this program are depicted in flow-diagram F6-2. The last line in the input data, Table 6-1 represents the percentage of changes in the blade chord, tip clearance and roughness.

### 6.3.1 Loss due to leading edge erosion

This loss is based mainly on blade chord reduction, which affects the stagger, inlet blade angles and aerodynamic lift coefficient.

**a) <u>Modelling of blade chord reduction</u>**

For a given C4 blade profile, the camber line equation relative to an attached reference frame is as follows.

$$(y-y_0)^2+(x-x_0)^2=R^2$$

$$y=\sqrt{R^2-\left(x-c/2\right)^2}-\sqrt{R^2-\left(c/2\right)^2} \qquad 6\text{-}49$$

The slope of the camber line is given by

$$\frac{dy}{dx}=\frac{\frac{1}{2}-\frac{x}{c}}{\sqrt{\left(\frac{R}{c}\right)^2-\left(\frac{x}{c}-\frac{1}{2}\right)^2}} \qquad 6\text{-}50$$

The tangent of the new camber line at the origin gives the blade inlet geometry angle.

$$\beta_{G1}=\tan^{-1}\left(\frac{dy}{dx}\right)=\tan^{-1}\left[\frac{\frac{1}{2}}{\sqrt{\left(\frac{R}{c}\right)^2-\frac{1}{4}}}\right] \qquad 6\text{-}51$$

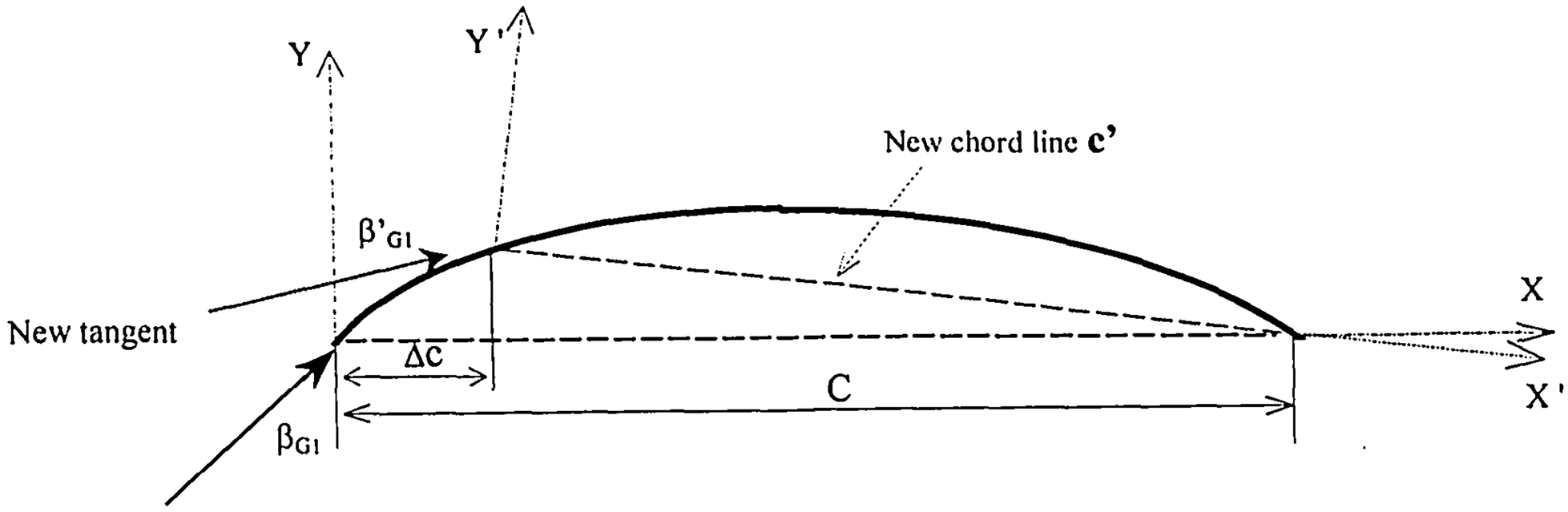


Figure 6-2 the variation in the camber line

The reduction in the chord after erosion is computed by.

$$c' = c\left[\left(\sqrt{\left(\frac{R}{c}\right)^2 - \left(\frac{\Delta c}{c} - \frac{1}{2}\right)^2} - \sqrt{\left(\frac{R}{c}\right)^2 - \frac{1}{4}}\right)^2 + \left(1 - \frac{\Delta c}{c}\right)^2\right]^{1/2} \qquad 6\text{-}52$$

The new blade angle at the blade leading edge is as follows.

$$\beta'_{G1} = \tan^{-1}\left(\frac{dy'}{dx'}\right) = \tan^{-1}\left[\frac{\frac{1}{2}}{\sqrt{\left(\frac{R}{c'}\right)^2 - \frac{1}{4}}}\right] \qquad 6\text{-}53$$

The relative change in the blade staggering after chord reduction is computed from the new chord slope.

$$\Delta\xi = \tan^{-1}\left[\frac{y_{(\Delta c)}}{c - \Delta c}\right] = \tan^{-1}\frac{\sqrt{\left(\frac{R}{c}\right)^2 - \left(\frac{\Delta c}{c} - \frac{1}{2}\right)^2} - \sqrt{\left(\frac{R}{c}\right)^2 - \frac{1}{4}}}{1 - \frac{\Delta c}{c}} \qquad 6\text{-}54$$

The variation in the blade inlet geometry angle with respect to the initial frame of reference is the sum of the relative variations of the camber line tangent and the stagger angle.

$$\Delta\beta_{G1} = \left(\beta_{G1} - \beta'_{G1}\right) + \Delta\xi \qquad 6\text{-}55$$

The new camber angle 'θ' is computed from the difference of the blade tangents at new leading edge and at trailing edge.

$$\theta' = \left|\left|\frac{dy'}{dx'}\right|_{c-\Delta c} - \left|\frac{dy'}{dx'}\right|_{c}\right| = 2\tan^{-1}\left[\frac{1/2}{\sqrt{\left(\frac{R}{c'}\right)^2 - \frac{1}{4}}}\right] \qquad 6\text{-}56$$

**b) <u>Aerodynamic effect of blade chord reduction</u>**

It will thus be reasonable to assure that cutting at the leading edge dominates any change in lift coefficient from the blade shape deformations. Due to the high loading at the leading edge of an airfoil, it is expected that any change in this region will increase the angle of zero lift and will decrease the blade lift coefficient (Batcho et al, 1986), (Batcho, 1987). Since erosion is accompanied by a blunting of leading edge, an expression based on classical thin airfoil theory may be developed to relate the change in lift coefficient due to blade chord reduction. Based on the thin airfoil theory, the lift coefficient may be derived from the total circulation around a cambered airfoil (Anderson, 1984) as follows.

$$\Gamma = \int_0^c \gamma(\xi)d\xi = \frac{c}{2}\int_0^\pi \gamma(\theta)\sin\theta d\theta$$

$$\Gamma = cV_\infty\left[A_0\int_0^\pi(1+\cos\theta)d\theta + \sum_{n=1}^{\infty}A_n\int_0^\pi \sin n\theta\sin\theta d\theta\right] \qquad 6\text{-}57$$

From the standard integration tables, the first and second integral values yields.

$$\int_0^\pi(1+\cos\theta)d\theta = \pi$$

$$\int_0^\pi \sin n\theta\sin\theta d\theta = \pi/2. \qquad 0 \qquad n>1$$

The circulation depends only on the first terms of the series.

$$\Gamma = cV_\infty\left[\pi A_0 + \pi/2\, A_1\right] \qquad 6\text{-}58$$

The lift coefficient is related to circulation around the profile by the following expression.

$$C_L = 2\pi\left[\beta + \frac{1}{\pi}\int_0^\pi \frac{dy}{dx}(\cos\theta - 1)d\theta\right]$$

By transforming x into θ the lift coefficient is finally calculated as follows.

$$C_L = 2\pi\left[\beta + \frac{1}{\pi}\int_0^\pi \frac{\frac{\cos\theta}{2}(\cos\theta-1)}{\sqrt{\left(\frac{R}{c}\right)^2 - \frac{\cos\theta^2}{4}}}d\theta\right] \qquad 6\text{-}59$$

The loss in lift coefficient due to the reduction of blade chord is equivalent to the difference of the lift coefficients before and after erosion.

$$\Delta C_{L} = 2\pi \left[ \Delta\beta + \frac{1}{\pi} \int_{0}^{\pi} \frac{\frac{\cos\theta}{2}(\cos\theta - 1)}{\sqrt{\left(\frac{R}{c}\right)^{2} - \frac{\cos\theta^{2}}{4}}} d\theta - \frac{1}{\pi} \int_{0}^{\pi} \frac{\frac{\cos\theta}{2}(\cos\theta - 1)}{\sqrt{\left(\frac{R}{c'}\right)^{2} - \frac{\cos\theta^{2}}{4}}} d\theta \right] \qquad 6\text{-}60$$

In order to estimate the difference in lift coefficient of a blade cascade a modifying constant 0.5 is introduced by Shepherd (1959).

**c) <u>Blade profile loss</u>**

The effect of chord reduction and blade blunting of a blade appear in a supplement of the drag loss coefficient calculated by the new expression for the drag coefficient. The blade surface boundary layer loss varies significantly with Reynolds number and surface roughness, thus, a correction was done using curves relating the profile pressure loss to Reynolds number and roughness (Koch and Smith, 1976).

The new drag loss coefficient as derived includes a term of lift coefficient loss and the effect of the variation of blade geometry parameters.

$$C_{De} = \frac{1}{\tan\beta_{me}} \left\{ C_{D} \tan\beta_{m} + \Delta C_{L} - 2\left[ \left(\frac{s}{l}\right) \cos\beta_{m} (\tan\beta_{1} - \tan\beta_{2}) - \left(\frac{s}{l}\right)_{e} \cos\beta_{me} (\tan\beta_{1e} - \tan\beta_{2e}) \right] \right\} \qquad 6\text{-}61$$

The drag coefficient is related to the total pressure loss by:

$$\omega = C_{De} \frac{\cos\beta_{1e}^{2}}{\cos\beta_{me}^{3}} \left(\frac{l}{s}\right)_{e} \qquad 6\text{-}62$$

The supplement of the profile drag coefficient.

$$\Delta C_{D} = C_{De} - C_{D} \qquad 6\text{-}63$$

The decrease in efficiency due to drag increase is computed by the following expression.

$$\Delta\eta_{e} = \Delta C_{D} \frac{\cos\beta_{1e}^{2}}{\cos\beta_{me}^{3}} \left(\frac{l}{s}\right)_{e} \left[ \frac{\left(\frac{W_{1}}{U_{m}}\right)^{2}}{2\left(\frac{\Delta H_{te}}{U_{m}^{2}}\right)} \right] \qquad 6\text{-}64$$

To account for the uneroded portion of the blade near the hub, the developed method used a mean blade chord variation rather than a tip chord variation. The mean chord is equivalent to the blade area change and is calculated as follows.

$$C_{me} = \frac{C_{T0}(R_{T0} - R_H) + (C_{T0} - C_H)(R_{T0} - R_H) - \int_{rh}^{rt} l(h)dh}{(R_{T0} - R_H)} \qquad 6\text{-}65$$

Which results in the percentage of mean chord reduction.

$$\Delta C\% = \frac{C_m - C_{me}}{C_m}\% \qquad$$

### 6.3.2 Secondary flow and tip clearance losses

The loss due to secondary flow is strongly dependent on the lift coefficient and on the blade chord length (Hill and Peterson, 1965).

$$\xi_{sec} = 0.018\phi^2 C_L^2 \left(c/s\right)\cos\beta_m \qquad 6\text{-}66$$

An expression for the change in adiabatic efficiency for an axial flow compressor due to tip clearance combined with the definition of cascade lift coefficient is derived by Schwind and McMillan, (1983). The tip clearance loss increases with the increase of the tip clearance after erosion.

$$\xi_{tip} = \left[\frac{0.759}{\frac{\bar{r}}{r_t}}\sqrt{\frac{\phi^2 \sigma C_L}{\sin^3\beta_m \cos(\beta_m)}} + \frac{1.17\phi}{\sigma^2 \frac{\bar{r}}{r_t}\tan(\beta_m)}\right]\Psi_{is}\,\lambda \qquad 6\text{-}67$$

Therefore, as the tip clearance and the secondary flow losses are lumped together, the effects of blade geometry degradation on the endwall losses are evaluated similarly to procedure of section 6.2.3

## 6.4 COMPARISON BETWEEN MEASURED AND PREDICTED PERFORMANCE DEGRADATION

The program *FANCHAR* was run for the measured and the predicted eroded geometry as computed by the trajectory code. The results of these simulations are compared with measured results in the following tables.

Table 6-2 Measured performance degradation

| Time | Efficiency | Pressure rise coefficient | Degradation efficiency % | Degradation Pressure rise coefficient % | Mass flow at stall kg/s | Degradation of stall mass flow % | Pressure rise coefficient at stall | Stall Margin % | Degradation of stall margin % |
|---|---|---|---|---|---|---|---|---|---|
| 0 | 0.8025 | 0.3952 | 0 | 0 | 0.616 | 0 | 0.371 | 20.94 | 0 |
| 2.2 | 0.7815 | 0.393 | 2.61 | 0.556 | 0.634 | 2.92 | 0.377 | 20.37 | 2.71 |
| 4.6 | 0.7687 | 0.3878 | 4.21 | 1.872 | 0.648 | 5.19 | 0.373 | 18.83 | 10.08 |
| 6.9 | 0.7492 | 0.3813 | 6.64 | 3.517 | 0.68 | 10.38 | 0.37 | 15.57 | 25.65 |
| 9 | 0.7487 | 0.3816 | 6.70 | 3.441 | 0.71 | 15.25 | 0.363 | 10.07 | 51.89 |

Table 6-3 Predicted performance degradation based on the measured geometry deterioration

| Time | Efficiency | Pressure rise coefficient | Degradation efficiency % | Degradation Pressure rise coefficient % | Mass flow at stall kg/s | Degradation of stall mass flow % | Pressure rise coefficient at stall | Stall Margin % | Degradation of stall margin % |
|---|---|---|---|---|---|---|---|---|---|
| 0 | 0.797 | 0.394 | 0 | 0 | 0.608 | 0 | 0.339 | 14.86 | 0 |
| 2.2 | 0.78 | 0.387 | 2.13 | 1.77 | 0.608 | 0 | 0.348 | 18.53 | 0 |
| 4.6 | 0.765 | 0.379 | 4.01 | 3.80 | 0.658 | 8.22 | 0.338 | 11.1 | 25.27 |
| 6.9 | 0.751 | 0.369 | 5.77 | 6.34 | 0.685 | 12.66 | 0.333 | 8.54 | 42.48 |
| 9 | 0.74 | 0.3605 | 7.15 | 8.50 | 0.6995 | 15.04 | 0.326 | 6.8 | 54.21 |

Table 6-4 Predicted performance degradation based on the predicted geometry deterioration

| Time | Efficiency | Pressure rise coefficient | Degradation efficiency % | Degradation Pressure rise coefficient % | Mass flow at stall kg/s | Degradation of stall mass flow % | Pressure rise coefficient at stall | Stall Margin % | Degradation of stall margin % |
|---|---|---|---|---|---|---|---|---|---|
| 0 | 0.802 | 0.389 | 0 | 0 | 0.5966 | 0 | 0.33582 | 16.92 | 0 |
| 2.2 | 0.7859 | 0.3784 | 2.00 | 2.738 | 0.6021 | 0.92 | 0.32875 | 16.7 | 1.3 |
| 4.6 | 0.7676 | 0.3662 | 4.29 | 5.855 | 0.6599 | 10.62 | 0.32995 | 11.95 | 29.37 |
| 6.9 | 0.7475 | 0.3533 | 6.79 | 9.17 | 0.7038 | 17.96 | 0.32366 | 7.66 | 54.71 |
| 9 | 0.7264 | 0.3402 | 9.42 | 12.55 | 0.7384 | 23.76 | 0.31482 | 5.64 | 66.62 |

## 6.5 DISCUSSION

The results based on the first procedure using Bonham – Howell, figure 6-3 shows large difference from the experimental results at low mass flow rate, this is attributed to an under prediction of the end wall losses. However, the percentage of the performance drop at design mass flow does compare well with experiment figure 6-4.

The second procedure based on Lieblein and Koch-Smith correlations gave good results for the efficiency figure 6-5, and fairly good results for the pressure rise coefficient.

The prediction of the performance degradation using the predicted geometry deterioration revealed similar trend for the measured performance drop, figure 6-6, but it tends to give higher degradation for the last periods of sand ingestion. This is attributed to the slight difference between predicted and measured geometry

deterioration, also because the erosion doesn't vary proportionally with time as proved experimentally.
According to the erosion experiments, it was demonstrated that only at high particle concentration of MIL-E 5007E sand, that there are significant changes in performance for a short time of running. In general the predicted degradation in performance for a period of 9 hours of sand particle ingestion (mass of 14.7 kg) shows good agreement between the efficiency curves as compared to experiments. Figure 6-7 depicts a loss in efficiency of 6.7 % (measured) and 7.15 % (predicted). But for the pressure rise coefficient, figure 6-8, these values are 3.4% (measured), 8.5% (predicted). For the stall margin in figure 6-9, the difference in degradation is 51.9 % (measured), and 54.2% (predicted). Also, it is evident that the stall point was successfully predicted by Koch graphical correlations for stall onset.

The degradation percentages of adiabatic efficiency and pressure rise may be integrated in the simulation programs for gas turbines and aeroengines to determine the effect of sand ingestion on the propulsive performance like one presented by Ghenaiet (2000).

## 6.6 CFD COMPUTATION FOR THE ERODED BLADE

The geometry of the eroded blade was obtained by means of a five-axis CNC digital machine 'Bosto-Matic'. A fine stylus probe 0.5mm was used to generate a batch of measured points on the rotor blade, after interpolation of the data over a three dimensions mesh, ten profile sections of the eroded blade were generated, figure 6-10.

TASCflow code was run for the eroded blade geometry in order to assess the flow pattern after blade erosion. Due to the removal of material from the blade tip corner and increased tip clearance, early separations are evident. The pressure contours on the pressure and suction sides show a different trend from the original rotor blade close to the leading edge. This variation is due to flow leakage around the tip corner, which tends to redistribute the static pressure, figure 6-11. The comparison between figure 6-12a and 6-12b shows that due to the shortening of the tip chord and rounding of the leading edge of the rotor blade, the stagnation point moved backward on the pressure side. As a result, the velocities have higher incidences around the leading edge. Due to an increase of tip clearance higher rate of flow leaks over the tip of the blade, figure 6-13, with a higher region of circulation around the leading edge. The static pressure distribution around the tip section shows high stagnation area that shifted back on the pressure side of rotor blade with a relatively unloaded part of the pressure side, figure 6-14b. The increased leakage of the flow from the pressure to suction side, which mixes out with the annulus wall boundary layer induced a large circulation flow area, figure 6-15a compared to figure 6-15b. The static pressure distribution around the tip of blade is plotted near design mass flow, at high mass flow and near the stall, figures 6-16 to 6-18. All of them show a reduction of the area of pressure loading between the pressure surface and suction surface. At low mass flow the pressure area tends to have a flat shape corresponding to lower lift coefficient and an initiation of blade stall inception.
CFD prediction for aerodynamic performance shows net drop of efficiency and pressure rise coefficient of 7.5% and 8.5% respectively. The comparison with the experimental

results (within 2.8% and 5% errors for pressure rise coefficient and efficiency) does show acceptable results. The stall point was found around mass flow rate 0.72 kg/s as shown by figure 6-19.

*Lift coefficient loss*

The lift coefficient is related to the area delimited by the pressure distribution on the pressure and the suction surface. As discussed previously, the reduction of the blade chord and the blunting of the leading edge do affect the stagnation point and incidence angle, which affects the circulation around the profile and consequently the lift coefficient.

$$C_L = \frac{L}{\frac{1}{2}\rho W_\infty^2 A} \qquad 6\text{-}68$$

Which can be calculated by considering the pressure distribution around the profile and a unity blade span, as follows:

$$C_L = \frac{\int_0^1 chp_+ d\left(x/c\right) - \int_0^1 chp_- d\left(x/c\right)}{\frac{1}{2}\rho W_\infty^2 A} \qquad 6\text{-}69$$

If the upstream velocity is almost constant, then the loss in the lift coefficient can be related to pressure area only, which is computed using Simpson integration method. The percentage change for the lift coefficient after blade erosion is given by.

$$\Delta C_L\% = 100\left[1 - \frac{C_{L_e}}{C_L}\right]$$

The results obtained at design mass flow show a reduction of 5.6% of the lift coefficient near tip and 1.2% at mid span. It is obvious that even the mid section chord reduced slightly, the static pressure varied considerably within the blades due to strong flow leakage, figure 6-11.

## 6.7 TIME OF LIFE PREDICTION

The degradation of the blade geometry was related to the time of operation model in the trajectory code. As a result a relationship between the drop in aerodynamic performance function of time of operation was reached, where particle concentration is a parameter. The value of 10% reduction in adiabatic efficiency was used as the basic criterion for estimating the time of life.

The trajectory code and the performance degradation simulation program were run for a wide range of sand particle concentrations. Where lower value of concentration 25 $mg/m^3$ was based on 95% filtration efficiency of a particle separator, when a helicopter

engine inlet is subjected to dust concentrations of order of 500 mg/m$^3$ (Johannes et al, 1995). For illustration, the numerical simulation resulted in a reduction of 1.52 % of tip clearance and 0.031 % of the mean chord within three hours of sand ingestion.

Figures 6-20 and 6-21 illustrate the degradation of efficiency and pressure rise coefficient as function of time of operation at different concentrations. The slope of curves representing the percentage decrease in efficiency and pressure rise tends to increase exponentially with concentration. The predicted time of life, figure 6-22 was based on the predicted degraded geometry obtained from the trajectory code. The expected lifetime at different concentration levels is as follows:

- At a high concentration (775 mg/m$^3$), the lifetime is 9.2 hours after consuming 15.1 kg of sand.
- At a mean concentration (420 mg/m$^3$), the lifetime is 18 hours after ingestion of 16.8 kg of sand.
- At a low concentration (159 mg/m$^3$), the lifetime is 93.5 hours after ingestion of 21.5 kg of sand.
- At a very low concentration (25 mg/m$^3$), the lifetime is 349 hours after ingestion of 20.3 kg of sand.

The interpolated lifetime curve for the cast aluminium rotor blades based on 10% reduction in adiabatic efficiency tends to follow an exponential decay, given by the following expression.

$$t_{life\_al} = A_1 \cdot e^{\left(-c/\alpha 1\right)} + A_2 \cdot e^{\left(-c/\alpha 2\right)} \qquad 6\text{-}70$$

Where the constants are:

$A_1 = 431$

$A_2 = 22.4$

$\alpha_1 = 91$

$\alpha_2 = 860$

To study the effect of the material hardness on the rotor blades geometry degradation and the subsequent drop in aerodynamic performance, the methodology was repeated for an axial fan rotor made from stainless steel 510. The correlation of erosion rate for this material is given by Tabakoff, (1987), appendix D. The optimum erosion angle for this type of material is 20degree (Feng and Ball, 1999). Because, the hardness of the stainless steel is much higher than the aluminium material, the rate of erosion predicted at the optimum erosion angle is very low (1/37) as compared to aluminium rate, as consequence the degradation in the geometry takes longer. The simulated lifetime for a wide range of sand particle concentrations give the following results:

- At a high concentration (775 mg/m$^3$), the lifetime is 1940 hours.
- At a mean concentration (420 mg/m$^3$), the lifetime is 3125 hours.
- At a low concentration (159 mg/m$^3$), the lifetime is 8900 hours
- At a very low concentration (76.5 mg/m$^3$), the lifetime is 15000 hours.
- At a very low concentration (30 mg/m$^3$), the lifetime is 64000 hours.

The predicted lifetime of the stainless steel rotor blades follows the following exponential decay.

$$t_{life\_st} = B_1 \cdot e^{\left(-c/\beta 1\right)} + B_2 \cdot e^{\left(-c/\beta 2\right)} \qquad 6\text{-}71$$

$B_1 = 2.79E5$

$B_2 = 1.47E4$

$\beta_1 = 17.6$

$\beta_2 = 305.2$

The respective Brinell hardness for the aluminium and stainless steel taken from handbook of material (1992) and the mechanical properties data (1972) are as follows.

$HB_{al}$ =110
$HB_{st}$ =205

The general lifetime equation including the hardness of material is derived by interpolation as follows.

$$t_{life} = 1.158\left(\frac{HB}{HB_{al}} - 1\right)\left[B_1 \cdot e^{\left(-c/\beta 1\right)} + B_2 \cdot e^{\left(-c/\beta 2\right)}\right] + \left(2.158 - 1.158\frac{HB}{HB_{al}}\right)\left[A_1 \cdot e^{\left(-c/\alpha 1\right)} + A_2 \cdot e^{\left(-c/\alpha 2\right)}\right]$$

6-72

## 6.8 CONCLUSIONS

The developed program for the determination of the axial fan stage aerodynamic performance involving a mean line method with more appropriate loss correlations, was extended to predict the degradation of aerodynamic performance due to sand particle ingestion. This predictive capability uses an erosion fault model based on chord length reduction, and increase of tip clearance and roughness. The losses in performance are attributed to the increase in tip clearance, reduction in chord line and blunting of blade leading edge.

The variation of the flow incidence angle due to leading edge blunting was very difficult to model, because it depends on the position of the stagnation point. Nevertheless, in the current work, the variation in incidence was related simply to a

shortening of the blade chord and to an increase of stagger angle. The complex shape after erosion of the leading edge above the two thirds of blade height was shown to cause high flow leakage around the tip of blades, with a defect of lift coefficient and reduction of stall margin.
The results after incorporating Lieblein and Koch-Smith correlations show that, this method can be successfully utilised to predict the axial fan performance degradation. The results of these simulations indicate that erosion causes a drop of pressure rise coefficient, adiabatic efficiency and surge margin. The comparisons with experimental results are generally good.

The lifetime of the axial fan was found to follow an exponential decay, depending on the concentration level. An expression for lifetime involving particle concentration and material hardness was derived, which can be applied for similar types of turbomachines.

In general the application of particle trajectory, rebound characteristics and erosion model to predict blade material loss indicated that, it could also be successfully utilised to obtain parameters useful for performance degradation simulations. This program, within the overall methodology as presented thoroughly in this thesis, constitutes an economic tool to predict performance degradation due to sand ingestion at early phases of design, also, gives an idea on the operating range and limitations of a new fan design prototype.

As long as this program gave good results for a single stage fan, it needs some improvements to be extended to multistage compressor performance degradation based on the stacking method, which is recommended for future developments.

# CHAPTER 7

# GENERAL CONCLUSIONS

## 7.1 REVIEW AND CONCLUSIONS

The study of the axial fan performance degradation due to erosion by sand particle ingestion is presented in this thesis. This study has been undertaken both theoretically and experimentally to obtain a clearer understanding of the flow pattern through the axial fan stage, the mechanism governing sand particle ingestion, particle trajectories and the resulting erosion, blade geometry deterioration and performance degradation. A general methodology has been developed and validated for the impact locations, erosion patterns and aerodynamic performance degradation.

The three dimensional trajectory code which was developed as part of this study for the simulation of the particle dynamics, adopted a Lagrangian model, which accounts for turbulence effect. The governing equations of particle motion were solved in a stepwise manner using the seventh order Runge-Kutta Fehlberg method. The tracking of particles and their corresponding flow properties were based on the finite element interpolation method. The prediction of blade material erosion used the particle trajectory results and an existing semi empirical erosion model corrected for the case of cast aluminium material. The computational domain involved inlet guide vanes and an axial rotor with extended upstream and downstream domains. The flowfield was solved separately using the CFD code TASCflow, which gave all information required by the trajectory code. Flow phenomena, like secondary flow, tip leakage, tip vortex and boundary layer, which are directly included within the flowfield solution are known to affect considerably the dynamics of particles as discussed earlier in the review chapter. For the simulation of aerodynamic performance degradation due to blade geometry deterioration a mean line method that used a fault model based on blade chord reduction, tip clearance increase and surface roughness was developed. A method for predicting the life expectancy for this type of turbomachinery was also presented and extended for a harder material.

The experimental work was divided into two types of tests; the local injection tests were intended to generate qualitative erosion patterns due to local injections of sand particles (narrow bandwidth 150-300 micron), in order to validate the trajectory code results. The particle concentrations and velocities were measured at several points using a laser transit anemometer. The release velocities as measured were used as initial values for the computation of particle trajectories. Secondly, the global injection tests using sand particle (0-1000 micron MIL-E5007E) were carried out near the design point in order to assess the axial fan stage aerodynamic performance reduction and to validate the prediction method based on the mean line method and erosion fault model. The injector

venturi tube positioned upstream of the test rig intake was designed to deliver air and particle mixture, which simulates severe operating conditions.
The main conclusions and observations that have emerged in the course of the present study can be summarised in the following points:

- The predicted trajectories corresponding to the initial three heights of local injection for the narrow bandwidth (150-300micron) sand particles show a noticeable deviation from the mean flow path due to the particle spread, which is also clear from the predicted concentration and the measured particle velocity and concentration. High numbers of impacts with maximum erosion were predicted near the leading edge and tip region due to its direct exposure to sand particles that acquire an important circumferential velocity. The trajectories show tip particles migrating from pressure to the suction side and in the process, induced tip erosion, which was also evident from the signs of wear that appeared on the blades of the tested rotors. The distinctive erosion patterns from the simulation of particle trajectories at different heights of sand injection are generally in good agreement with experiments. The erosion patterns near the leading edge and near the tip of the pressure side were successfully predicted, but less near the mid-chord tip region where the greater erosion area is further away from the tip and extends towards the root. The rotor blade suction surface is subjected to intense impacts near the leading edge, because of the negative incidence angle of the particles at the rotor inlet, but no evidence of erosion on the remaining of the rotor blade suction side, which agree well with the test erosion patterns.

- The prediction of erosion pattern obtained with global sand injection depicts high number of impacts occupying a large portion of the rotor blade leading edge and along a strip near the tip of the blade pressure side, this was supported by the test erosion pattern. The global injection tests for long duration of running at high concentration of MIL-E5007E sand particles revealed net leading edge loss of material over the leading edge tip corner with a rounding of the rotor blade. The tip clearance increased markedly, with a developed burr on the tip towards the blade suction side. The eroded mass and the rate of erosion exhibit an initial phase of incubation, followed by a plateau function of the time of running for the low concentrations. However, at a severe concentration, the mass eroded and the rate of erosion continue to increase because of the nature of sand particles. After a duration of 9 hours the tip clearance increased by 65.7% (predicted 76%) and the tip chord reduced by 10.4 % (predicted 7.17%). The large loss of material around the blade tip corner and its blunting affected the flow angle of attack and caused the stall point to shift at a higher mass flow, with a decrease of the pressure rise and efficiency. The erosion results based on prediction and measurements demonstrated that the maximum values of the rotor blade erosion are generally larger than for IGV blades. The tests showed clear evidence of impacts on the IGV trailing edge and over an area of the trailing edge tip corner, which were also predicted. The simulation results found for erosion rate and geometry deterioration are comparable to experimental results. The difference is due the ignored debris erosion and to the erosion correlation itself.

- From a parametric study for turbulence and fragmentation effects, the fragmentation evidently influences the erosion rates prediction and the geometry deterioration. The following values of erosion rate correspond to measured, predicted without and with fragmentation are 0.653mg/g, 0.678mg/g, 0.409mg/g respectively. As

a particle shatters into smaller debris after impacting solid walls, these ones can produce secondary erosion areas. As consequence, fragments should be tracked independently from the main particle paths. When turbulence effect is considered, there is a significant variation in the computed three dimensional trajectories for fine particles, erosion rates and geometry deterioration. A 5% and 11% difference in tip chord and tip clearance respectively occurs when turbulence effects are included.

- A method for predicting the aerodynamic performance for the axial fan stage based on mean line approach and losses correlations was described thoroughly. To quantify the effects of rotor erosion at a high concentration of sand particle (MIL-E 5007E), this method was extended to predict aerodynamic performance degradation. The results compared with experimental data show that Lieblein and Koch correlations performed better than Bonham-Howell method. The results of the simulation indicate that erosion caused the pressure rise, adiabatic efficiency and surge margin to decrease, which agree well with experimental results. For the stall interpretation of the current fan, a diffuser analogy similar to Koch's was used and gave a good prediction for the stall point. The adiabatic efficiency, pressure rise coefficient and surge margin were shown to decrease according to the following percentages; (measured 6.7%, 3.44%, 51.89%) and (predicted 7.15%, 8.5%, 54.21%). The simulation results for performance degradation are in good agreement with experimental findings

- The CFD analysis carried out for the eroded blade depicts a considerable leakage around the tip due to tip clearance increase with a shift of stagnation point due to leading edge blunting, and a redistribution of static pressure over the rotor blade rounding. The erosion damage tends to reduce the aerodynamic lift coefficient. The area representing the pressure loading around the tip section tends to flatten at low mass flow, which is also an indication of stall inception.

- A methodology was developed to estimate the time of life for the axial fan blades. The relationship between the drop in performance function of time of operation was presented graphically, for a range of sand particle concentrations. To simulate the effect of the material hardness on the rotor blade geometry degradation and the consequent drop in aerodynamic performance, this procedure was applied for an axial fan rotor made from stainless steel. The time of life was found to follow an exponential decay, depending on the concentration level and the material properties such as hardness.

In general for particle trajectory simulation, good agreements with experimental measurements were found in terms of the impact locations at the leading edge and along the chord tip region. The effects of particle concentration, turbulence, fragmentation and size of particles were demonstrated for the different studied cases. It may be concluded that the erosion damage can lead to significant reduction in turbomachinery efficiency, pressure rise, surge margin and the time of life due to blade geometry deterioration. The application of the particle trajectory, rebound characteristics and erosion model to predict blade material loss, indicated that it could also be successfully utilised to obtain the parameters necessary in performance degradation simulation. The comparisons with experimental results were generally good. This confirms that, such a methodology can

be successfully extended for other types of turbomachines, and it is very useful for designing compressors working in dusty atmosphere, and also for their health monitoring.

## 7.2 RECOMMENDATION FOR FURTHER CONTINUATION

To enhance the potential of the global predictive methodology as presented throughout this thesis, further improvements should be made to the computation methodology as mentioned in the previous conclusions. The following points warranted further development of this work with some relevant experimental investigations:

- The actual trajectory code uses a sliding interface at the transition interface. However, it is more realistic to adopt a continual moving grid when tracking the particles inside a rotating domain. This will improve the prediction of erosion pattern in the mid-pressure side area where there is difference with the experimental results. Also, the CFD computations must be carried out for the case of unsteady flow corresponding to several rotor-stator relative positions

- The supplement equation of angular momentum for solid particle must be solved to get the particle spin velocity, which produces the Magnus force contributing to the drift force according to Rubinow and Keller (1961). This obviously will improve the impacting condition near walls.

- The fragmentation is an important parameter, when predicting erosion. As particle fragments into smaller debris, new particles produce secondary erosion areas. Consequently, the paths of these fragments should be traced independently from the main particle paths. This would require more memory and computing time. It is worth thinking how to improve the structure of the code to use the parallel programming technique. Further tests are found necessary in order to extend the range of application of the fragmentation correlation and the fragmentation threshold.

- For the performance degradation based on mean line method, it is necessary to introduce the effect of blade leading edge blunting when calculating the reference incidence variation, and also as an extra term for the profile drag coefficient. The implementation of the stacking technique associated with the erosion fault model will extend the ability of the developed procedure to handle more complicated configurations of multistage axial compressors.

# REFERENCES


1. Abbas A.S, Koussa S and Lockwood F.C, 1981, " The prediction of the particle Laden Gas " , 18th Symposium on Combustion pp 1427, the Combustion Institute 1981

2. Abernethy R.B, and Thompson J.W, Jr, 1973, " Handbook of Uncertainty in Gas Turbine Measurements ", AEDC-TR-73-5, Feb 1973

3. Abernethy R.B, 1985, " Precision and Propagation of Error " , Pratt &Whitney Engineering Division, West Palm Beach, Vol 98, " Thrust and Drag its Prediction and Verification – Progress in Astronautics and Aeronautics Martin Summerfield ", Editor in Chief AIAA series, 1985

4. Ahmed N, Forster P and Elder R.L, 1991, " Laser Anemometry in Turbomachines ", IMechE 1991 vol 205

5. Aker G.F and Sararanamutto H.I.H, 1989, " Predicting Gas Turbine Performance Degradation Due to Compressor Fouling Using Computer Simulation Techniques ", ASME Journal of Engineering for Gas Turbines and Power, Vol 111, April 1989, pp 343 – 350

6. Alge T.L and Moehring J.T, 1994, " Modern Transport Engine Experience with Environmental Ingestion Effect " , Propulsion and Energetic Panel (PEP), Symposium held in Rotterdam, the Netherlands, April 1994. AGARD

7. Anderson John. D Jr , 1984, " Fundamentals of Aerodynamics ", Second Edition. New York: McGraw-Hill, 1984

8. Balan C and Tabakoff W, 1984," Axial Flow Compressor Performance Deterioration " , AIAA paper 84 -1208, June 1984

9. Batcho P.F, Moller T.C , Padova C and Dunn M.G, 1986, " Interpretation of Gas Turbine Response Due to Dust Ingestion " , DNA TR - 86 - 306 , Sep 1986

10. Batcho Paul, 1987, " Modeling Gas Turbine Deterioration Due to High Levels of Dust Ingestion " , AIAA 87 – 0144

11. Bindon J, 1989, " The Measurements and Formation of Tip Clearance Loss " , ASME Journal of Turbomachinery, vol 110 1989, pp 257-263.

12. Bitter J.G.A, 1963, " A Study of Erosion Phenomena " , Wear, 6 (1963) 5, 169

13. Breitman D.S, Dueck E.G and Habashi W.G, 1985, " Analysis of a Split Flow Inertial

Particle Separator by Finite Element ", Journal of Aircraft vol 22, N°2 Feb 1985

14. Brenner H, 1961," The Slow Motion of a Sphere Through a Viscous Fluid Towards a Plane Surface " , Chem Eng Sci vol 16 242-251, 1961

15. Brown D.J and Hutchinson P, 1979, " The Interaction of Solid or Liquid and Turbulent Fluid Flow Fields – A Numerical Simulation ", Journal of Fluids Engineering, vol 101, pp265-269, 1979

16. Carnahan Brice, Luther H.A and Wilkes James O, 1969 , " Applied Numerical Methods" , John Wiley & Sons, New York: 1969

17. Casey M.V, 1987, " A Mean Line Prediction Method for Estimating the Performance Characteristics of an Axial Compressor Stage " , C264 / 87 IMechE Proceeding 1987

18. Caughey D.A and Jameson A, 1979, " Numerical Calculation of Transonic Potential Flow About Wing Body Combinations " , AIAA Journals, Vol 17, N°2, pp175, 1979, also AIAA paper 77-679

19. Chen P.P and Crowe C.T, 1984, " On the Monte-Carlo Modeling Particle Dispersion in Turbulence " , Proc Int Symposium on Gas-Solid Flows, ASME FED 10 , pp 37-41, 1984

20. Chen X.Q and Pereira J.C.F, 1995, " Predictions of Evaporating Spray in Anisotropically Turbulent Gas Flow ", Numerical Heat Transfer 27, pp 143-162, 1995

21. Chen X and Pereira J.C.F, 1995, " Efficient Computation of Particle Dispersion in Turbulent Flows With a Stochastic Probabilistic Model " , Numerical Heat Transfer A27 , 143 (1995).

22. Connor J.J and Brebbia C.A, 1976, " Finite Element Techniques for Fluid Flow ", London Boston: Newnes-Butterworths, 1976

23. Crosby J.K, 1986, " Factor Relating to Deterioration Based on RR RB211 In Service Performance " , FED-Vol. 37 The AIAA / ASME 4$^{TH}$ Joint Fluid Mechanics Plasma Dynamics, and Lasers Conference Atlanta, Georgia May 12 – 14, 1986

24. Crowe C.T, 1991, " The Sate of Art in The Development of Numerical Models for Dispersed Phase Flows ", Proceeding of International Models for Dispersed Phase Flows ", Tsukuba Japan 1991, pp 49-59

25. Crowe C.T , Sommerfield M and Tsuji M, 1998, " Fundamentals of Gas Particle and Gas Droplet Flow ", CRC Press, Boca Raton, USA 1998.

26. Cumpsty N, 1989, " Compressor Aerodynamics " , Longman Scientific & Technical 1989

27. Denton J.D, 1975, " A Time Marching Method For Two and Three Dimensional Blades Flow " , Aeronautical Research Council R&M 3775 - 1975

28. Denton J.D and Singh U.K, 1979," Time Marching Methods for Turbomachinery Flow Calculation - Part1 Basic Principles and 2 D Applications, and Part II Three Dimensional Flows ", VKI lecture 1979

29. Denton J.D and Cumpsty N.A , 1987, " Loss Mechanisms Turbomachines " , C260/87 IMechE 1987

30. Denton J.D, 1993, " Loss Mechanism in Turbomachines " , The 1993 IGTI Scholar Lecture ASME Journal of Turbomachinery Vol 115, October 1993, pp 621-656.

31. Dodge P.R, 1976, " A Non Orthogonal Numerical Method for Solving Transonic Cascade Flows ", ASME paper 76-GT-63, 1976

32. Dukowicz J.K, 1980, " A particle Fluid Numerical Model for Liquid Sprays " , Journal of Computational Physics, 35, pp229-253, 1980

33. Dulikravich D.S and Caughey D.A, 1980, " Finite Volume Calculation of Transonic Potential Flow Through Rotors and Fans ", FDA-80-03, Report Cornell University March-1980

34. Dunham J and Came P.M, 1970, " Improvements to the Ainley - Mathieson Method of Turbine Performance Prediction " , ASME Paper 70-GT-2 , 1970

35. Dunn M.G, Padova C and Adams R.M , 1983, " Operation of Turbine Engines in Dust Laden Environments " , N88 - 17654 Calspan Advanced Technology Center Buffalo, NY 14225 Research Report Sponsored by Defence Nuclear Agency Contract DNA 001-83-C-0182

36. Dunn M.G , Padova C, Moller .J.E and Adams .R.M, 1987, " Performance Deterioration of a Turbofan and a Turbojet Engine Upon Exposure to a Dust Environment " , ASME Journal of Engineering for Gas Turbine and Power, vol 109, July 1987, pp 336 -343.

37. Dunn M.G , Baran A.J and Miatech J, 1996, " Operating of Gas Turbine Engines in Volcanic Ash Clouds " , ASME Journal of Engineering for Gas Turbines and Power, Vol 118, October 1996 , pp 724 –731

38. Eckardt D, 1986, " Advanced Experimental Techniques for Turbomachinery Development " , MTU Motoren Und Turbines Union Munchen GMBH, Editor David Japikse Concepts ETI Inc Norwich Vermont 05055, USA 1986

39. Edwards V.R and Rouse P.L , 1994, " US Army Rotorcraft Turboshaft Engines Sand and Dust Erosion Considerations " , 83 rd Symposium, Propulsion and Energetic Panels of Erosion, Corrosion and Foreign Object Damage Effect in Gas Turbine 25-8 April 1994

40. Elfekki S, Tabakoff W, 1987, " Erosion Study of Radial Flow Compressor With Splitter " , ASME Journal of Turbomachinery, vol 109 January 1987 pp 62-69

41. Elghobashi S, 1994, " On predicting Particle Laden Turbulent Flows ", Applied Science Research 1994, 52, pp 309- 324

42. El Sayed Abdelazim A.F., Lasser R and Rouleau W.T, 1986, " Effect of Secondary Flow on Particle Motion and Erosion in a Stationary Cascade " , International Journal of Heat and Fluid Flow, vol 7 N° 2 June 1986

43. El Sayed A.F.A.A and Hegazy A, 1995, " An Iterative Procedure for Estimating the Effect of Erosion on Turbine Blades Life Time " , A96 - 26200 Yokohama International Gas Turbine Congress 22-27 1995, vol 3

44. Eroglu H and Tabakoff W, 1990, " Effect of Inlet Flow Angle on The Erosion of Radial Turbine Guide Vanes " , ASME Journal of Turbomachinery, vol 112, Jan 1990, pp 64 –70

45. Eroglu H and Tabakoff W, 1991, " 3D LDV Measurement of Particle Rebound Characteristics " , AIAA Paper 91- 0011, Jan 1991

46. Faddick R.R, " Properties of the phase, 1980, " , FEU Short Course on Fundamentals of Slurry Pipelining Cranfield Institute of Technology UK, June 1980

47. Fehlberg Erwin, 1968, " Classical Fifth, Sixth, Seventh and Eighth Order RK Formulas With Step Size Control " , NASA TR-287 October 1968

48. Feng Z, Ball A , 1999, " The erosion of four materials using seven erodents — towards an Understanding ", Wear 233–235 1999 674–684

49. Fehlberg Erwin, 1969, " Classical R-K Formulas With Step Size Control and Their Application to Some Heat Transfer Problems " , NASA TRR-315, 1969

50. Filbee R.D , 1990, " A Study of Aerodynamics of The Small Scale Contra–Whirl IGV Fan " , PhD Thesis 1990, Cranfield University.

51. Finnie I , 1958, " The Mechanism of Erosion Ductile Metals " , ASME Journal of Applied Mechanics, Vol 25, 1958, pp 527 -532

52. Finnie I , 1960, " Erosion of Surfaces By Solid Particles ", Wear, vol 3 1960 pp 87-103

53. Fitzgerald A. E, Higginbotham D. E, Grabel A, 1981," Basic Electrical Engineering " , McGraw Hill 5TH Edition. New York: McGraw-Hill, c1981

54. Finnie I, Wolak J and Kabil Y, 1967, " Erosion of Metals by Solid Particles " , Journal of Materials, vol 2 N°3, September 1967, pp 682 – 700

55. Fluent 5: user's guide Publication info: Lebanon, NH: FLUENT Incorporated, 1998

56. Ghenaiet A, 2000, " An Approximate Method for Jet Engines Flight Performances Prediction ", 2000–GT–0149 , ASME Paper TURBO EXPO Land Sea & Air 8-11 May 2000 Munich, Germany

57. Ghenaiet A, Elder R.L, Tan S.C, 2001, " Particle Trajectories Through an Axial Fan and Performances Degradation Due to Sand Ingestion ", 2001–GT–0497 , ASME Paper TURBO EXPO Land Sea & Air June 4-6 2001 New Orleans USA

58. Gill M.E, 1981," Description of a Programme for Analysis of Data Arising From a Two Spot Laser Anemometer ", Report November 1981, SME Cranfield Institute of Technology UK

59. Goldman A.J , Cox R.G and Brenner H, 1967, " Slow Viscous Motion of a Sphere Parallel to a Plane Wall _I Motion Through a Quiescent Fluid ", Chem Eng Sci vol 22 637-651, 1967

60. Goodwin J.E, Sage W and Tilly G.P, 1984, " Study of Erosion by Solid Particles ", Proceeding of the Institution of Mechanical Engineers, vol 1984 pt 10 N° 15 1970, pp 279-292

61. Gordon D.W and Korakianitis T, 1998, " The Design of High Efficiency Turbomachinery and Gas Turbines " , Prentice Hall 1998

62. Gosman A.D, Ioannides E, 1983, " Aspects of Computer Simulation of Liquid Fuelled Combustors ", Journal of Energy, Vol 7 N.6 , Nov-Dec 1983

63. Gosman A.D, Ioannides E, Lever D.A and Cliffe K.A, 1980, " A Comparison of Continuum and Discrete Droplet Finite-Difference Models Used in the Calculation of Spray Combustion in Swirling Turbulent Flows " AERE Harwell Rept. TP 865, 1980

64. Gostelow J.P, 1973, " Review of Compressible Flow Theories for Airfoil Cascade " , ASME Journal of Engineering for Power, October 1973, pp 281-292

65. Gostelow J.P, 1984, " Cascade Aerodynamics ", Pergamon Press 1984

66. Grant G and Tabakoff W, 1974 , " Erosion Prediction in Turbomachinery Due to Environmental Solid Particles " , AIAA Paper N° 74-16 AIAA 12th Aerospace Sciences Meeting Washington DC/ Jan 30- Feb1 ,1974

67. Grant G and Tabakoff W, 1975, " Erosion Prediction in Turbomachinery Resulting From Environment Solid Particles " , Journal of Aircraft, Vol 12, N°5 1975 pp 471-478

68. Greitzer E.M, 1988," Flow Instabilities in Turbomachines " , Thermodynamics and Fluid Mechanics of Turbomachinery Edited by A. S. Ucer, P. Stow and CH Hirsch NATO ASI series

69. Habashi W.G, 1980," Numerical Methods of Turbomachinery Recent Advances in Numerical Methods in Fluids ", Vol 1 Pineridge Press Ltd, 1980, pp 245-287.

70. Hafez M, South J and Murman E, 1979, " Artificial Compressibility Methods for Numerical Solution of Transonic Full Potential Equations " , AIAA Journal, Vol.17, 1979, pp838

71. Haider .A and Levenspiel .O, 1989, " Drag Coefficient and Terminal Velocity of Spherical an non-spherical particles " , Powder Technology 58, 63-70 1989

72. Hamed A and Fowler S, 1983, " Erosion Pattern of Twisted Blades by Particle Laden Flows ", ASME Journal of Engineering for Power, Vol 105 October 1983 pp 839-843

73. Hamed A, 1984, " Solid Particle Dynamic Behavior Through Twisted Blades Rows " , Journal of Fluids Engineering, vol 106 / 251 September 1984 , pp 251 – 256

74. Hamed A, Tabakoff W and Mansour L, 1986, " Turbine Erosion Exposed to Particulate Flow " , ASME Paper 86-GT-258

75. Hamed A , 1988a, " Effect of Particle Characteristics on Trajectories and Blade Impact Patterns " , ASME Journal of Fluids Engineering Vol 110 March 1988, pp 33 – 37

76. Hamed A, 1988b, " Introduction of The Dynamics of Two phase Flows " , May 24 27 1988 VKI Lecture Series 1988 – 08 Particulate Flows and Blade Erosion

77. Hamed A, Tabakoff W and Wenglarz R , 1988, " A Particulate Flow and Blade Erosion ",

Von Karman Institute for Fluid Dynamics Lecture Series 1988 - 08 May 1988.

78. Hamed A, 1989, " Influence of Secondary Flow on Turbine Erosion ", ASME Journal of Turbomachinery, vol 111, July 1989, pp 310 - 314

79. Hamed A, Tabakoff W, 1990, " Jet Engines Performance Deterioration ", International Congress of Fluids Mechanics 3 RD 1990 Proceeding vol 2

80. Hamed A and Tabakoff W, 1994," Experimental and Numerical Simulations of the Effects on Ingested Particles in Gas Turbines Engines " , Propulsion and Energetic Panels (PEP) Symposium held in Rotterdam, the Netherlands, April 1994

81. Hamed A, Moy H, 1993" Probabilistic Simulation of Fragment Dynamics and Their Surface Impacts in the SSMEE Turbo-pump ", 115 (2) pp 302-308 June 1993 ASME Journal of Fluid Engineering

82. Harris P.K, 1996, " Erosion in Centrifugal Compressor impellers ", PhD Thesis Cranfield University 1996

83. Hill P and Peterson C, 1965, " Mechanics and Thermodynamics of Propulsion " , Addison - Wesley, New York, 1965 , pp 238 –242

84. Hinze J.O , 1959," Turbulence ", Mc Graw Hill, 1959.

85. Horlock J.H and Lakshminarayan B, 1976, " Secondary Flows: Theory Experiment and Application in Turbomachinery Aerodynamics ", Annual Review of fluid mechanics vol 5, 1976, pp 592-606

86. Horlock J.H, 1973a, " Axial Flow Turbines ", Huntington, N.Y: R.E. Krieger Pub. Co, 1973

87. Horlock J.H, 1973b, " Axial Flow Compressors " , Huntington, N.Y: R.E. Krieger Pub. Co, 1973

88. Howell A.R and Bonham R.P, 1950, " Overall and Stage Characteristics of Axial Flow Compressor " , Internal Combustion Turbines. Proc. IMechE, pp 235 -248, 1950.

89. Howell A.R, Calvert W.J, 1981, " Axial Flow Compressor Performance Prediction by Stage Stacking – Determination of Stage Aerodynamics " , NGTE Report N° R81002 UDC 621.45.037-154, June 1981

90. Humphrey J.A.C, 1990, " Review, Fundamentals of Fluid Motion in Erosion by Solid Particle Impact " International Journal of Heat and Flow, vol 11 N° 3, September 1990

91. Hussein M.F and Tabakoff W, 1973 , " Dynamic Behavior of Solid Particles Suspended by Polluted Flow In a Turbine Stage ", Journal of Aircraft Vol 10 N° 7, 1973 pp334 -340

92. Hussein M.F and Tabakoff W, 1974, " Computation and Plotting of Solid Particle Flow In Rotating Cascades ", Computers and Fluids, Vol 2, 1974

93. Issa R.I, 1986, " Solution of the Implicitly Discretised Fluid Flow Equations by Operator Splitting ", J. Comput Phys, vol 62 pp 40-65.

94. Ives D.C, and Liutermoza J.F, 1976," Analysis of Transonic Cascade Flows Using Conformed Mapping and Relaxation Technique ", AIAA paper 76-370 Ninth Fluid and Plasma Dynamics Conference, San Diego 1976

95. Jansen W and Moffatt, W. C , 1967, " The off Design Analysis of Axial Flow Compressors ", ASME Journal of Engineering for Power, October, 1967, pp 453 – 462

96. Japikse D, 1976, " Review - Progress in Numerical Turbomachinery Analysis ", ASME Journal of Fluids Engineering December 1976, pp 592-606

97. Japikse David, 1986, " Advanced Experimental Techniques in Turbomachinery ", Editor David Japikse , Norwich, Vermont, 05055, USA : Concepts ETI, 1986

98. Japiske D, Baines N.C, 1994, " Introduction to Turbomachinery " Norwich,VE: Concepts ETI and Oxford University Press, 1994

99. Johannes P, Van Der Walt and Alan Nurick, 1995, " Erosion of Dust Filtered Helicopter Turbine Engines - Part I Basic Theoretical Considerations " , Journal of Aircraft , vol 32 No 1 January - February 1995

100. Katsanis T and McNally W.D, 1969, " Revised Fortran Program for Calculating Velocities and Streamlines on a Blade to Blade Stream Surface of a Turbomachine ", NASA TMX-1764, 1969

101. Katsanis T, 1970, " Fortaran Program for Calculating Transonic Velocities On a Blade to Blade Stream Surface of a Turbomachine ", NASA TND-5427, 1970

102. Kerr J.A, 1989, " Final Report to the Helicopter Engine Environmental Protection IPS Contract " , A23A/768 Rolls-Royce plc

103. Koch C.C and Smith L.H Jr , 1976, " Loss Sources and Magnitudes in Axial Flow Compressors " Journal of Engineering for Power July 1976

104. Koch C.C, 1981," Stalling Pressure Rise Capability of Axial Flow Compressor Stages " , ASME Journal of Power, 103 October 1981 645-656

105. Knupp Patrick and Steinberg Stanly, 1994, " Fundamentals of Grid generation ", University of New Mexico, Boca Raton, FL: CRC Press, 1994

106. Kuk V.H.M, Jones P.T.V and Rose M.G, 1994, " Particle Deposition in Gas Turbine Blade Film Cooling Holes " , Propulsion and Energetic Panel (PEP) Symposium held in Rotterdam, the Netherlands, in April 1994

107. Lakshminarasimha A.N and Saravanmuttoo H.I.H, 1986, " Simulation of Fouling Using Stage Stacking Techniques " , AIAA / ASME 4th Joint Fluid Mechanics, Plasma Dynamics and Laser Conference, Atlanta, GA , May 12-14,1986

108. Lakshminarayana B, 1996 " Fluid Mechanics and Heat Transfer of Turbomachines " , John Wiley & Sons 1996.

109. Ledermann W, 1981, " Handbook of Applicable Mathematics ", Volume III, Numerical Methods, pp145 -150 John Wiley & Son 1981

110. Lewis R.I., 1996, " Turbomachinery Performance Analysis " , 1996 Arnold Edition, Great Britain

111. Lieblein S, 1959, " Loss and Stall Analysis of Compressor Cascades ", Journal of Basic Engineering, Transaction of ASME Sept 1959 pp 387-400

112. Lieblein S, 1960, " Incidence and Deviation Angle Correlations For Compressor Cascades " , Journal of Basic Engineering pp 575-586 , September 1960

113. Lieblein S , 1965, " Experimental Flow in Two Dimensional Cascades ", NASA SP-36 Chapter VI

114. Ling Z.A and Huang S.L, 1986, " Particle Trajectories in Full 3D Flow of Turbomachinery ", FED -Vol 37 The AIAA/ASME 4TH Joint Fluid Mechanics Plasma Dynamics, and Lasers Conference Atlanta, Georgia May 12 -14, 1986

115. Lixing Zhou, 1993 , " Theory and Numerical Modelling of Turbulent Gas Particle Flows and Combustion ", Science Press ; CRC Press INC Beijing: Science Press, 1993

116. Logan Earl JR, 1995, " Handbook of Turbomachinery ", Marcel Dekker, Inc New York 1995

117. Mann D.L and Warnes G.D, 1994, " Future Directions in Helicopter Engine Protection System Configuration Turbines " , 83 rd Symposium, Propulsion and Energetic Panels of Erosion, Corrosion and Foreign Object Damage Effect in Gas Turbine 25-8 April 1994.

118. Mason J.S and Smith B.V, 1972, " The Erosion of Bends by Pneumatically Conveyed Suspensions of Abrasive Particles " , Powder Technology 1972, 6, 323-335

119. Mattingly Jack D., Heiser William H, Daley Daniel H, 1987, " Aircraft engine design " New York, N.Y: American Institute of Aeronautics and Astronautics, 1987 AIAA education series

120. McKenzie A.B, 1980, " The Design of Axial Compressor Blading Based on The Tests of a Low Speed Compressor ", Proc. IMechE , vol 194 N° 6 pp 103-111, 1980

121. McKenzie A.B, 1997," Axial Flow Fans and Compressors " , Ashgate 1997

122. Mei R, 1992, " An approximated Expression for the Shear Lift Force On a Spherical Particle at Finite Reynolds Number " , Int, Journal Multiphase Flows 18 , 145-147 ,1992

123. Menguturk M, Gunes D, Erlen M and Sverdrup E.F, 1986," Multistage Turbine Erosion " , ASME Journal of Turbomachinery, Vol 108, Oct 1986, pp 290 -297

124. Miller D.C and Wasdell D.L, 1987, " Off – Design Prediction of Compressor Blade Losses " , C279 / 87 ImechE Proceeding 1987.

125. Montgomery, J.E and Clark, J.M. Jr, 1962, " Dust Erosion Parameters for a Gas Turbine ", SAE paper N 538 June 1962

126. Morsi and Alexander, 1972, " An Investigation of Particle Trajectories in Two Phase Flow System " , Journal of Fluid Mechanics 55 Pt2 1972 pp 193-208

127. Muir D.E, Saravanamuttoo H.I.H and Marshall D.J, 1988, " Health Monitoring of Variable Geometry Gas Turbines for the Canadian Navy " , ASME Journal of Engineering For Power, 1988 , vol 111, N°2, pp 244-250

128. Murray Hammick , 1991, " Report From the Front Sea Kings in Sand " , The Gulf War in Review, International Defence Review 5/ 1991

129. Neilson J.H and Gilchrist A, 1968a, " Erosion by a Stream of Solid Particles " ,Wear, 1968 , 11, 11-122

130. Neilson J.H and Gilchrist A, 1968b, " An Experimental Investigation Into Aspects of Erosion in Rocket Motor Tail Nozzles " , Wear, 1968 , 11, 123-143

131. Ower E and Pankhurst R.C, 1966," The Measurement of Airflow " , 5th Edition Oxford New York: Pergamon Press, [1966]

132. Palmer D.L and Waterman W.F, 1995, " Design and Development Of an Advanced Two Stage Centrifugal Compressor ", Journal of Turbomachinery, vol 117 April 1995 pp 205 - 212

133. Paramour M.D and Jennings P.G, 1993 ," Operational Requirements for Helicopter Engines for UK Services " , 82nd Symposium Propulsion and Energetic Panels on Technologies Requirements for Small Gas Turbines at Canada, October 4-8, 1993 AGARD CP-537

134. Patankar S.V and Spalding D.B, 1972, " A Calculation Procedure for Heat, Mass and Momentum Transfer in Three Dimensional Parabolic Flows ", Int. J. Heat Mass Transfer, Vol 15, pp. 1787-1806

135. Patankar S.V, 1980, " Numerical Heat Transfer and Fluid Flow ", Mc Graw Hill, New York

136. Pearsall I.S , 1963, " The Testing of Axial Flow Fans ", National Engineering Laboratory Report N 95, East Kilbride: National Engineering Laboratory, 1963

137. Perkins H.J and Horlock J.H , 1975, " Computation of Flows in Turbomachine - Finite Elements in Fluids " , Vol 2, John Wiley, 1975 pp 141-157

138. Peterson R.C, 1986, " Design Features for Performance Retention in the CFM56 Engine ", Turbomachinery Performance Deterioration FED - Vol. 37 The AIAA / ASME 4TH Joint Fluid Mechanics Plasma Dynamics, and Lasers Conference Atlanta, Georgia May 12 – 14, 1986.

139. Poti N.D Rabe D.C, 1988, " Verification of Compressor Data Accuracy by Uncertainty Analysis and Testing Methods", Journal of Turbomachinery, April 1988, Vol 110

140. Quinn Ivan, 1999," Investigation Into Erosion on Air Algeria JT8D T1 Blades " , May 1999 LAI, Pratt & Whitney Private Report

141. Rao P.V and Buckley D.H, 1985 , " Characterisation of Solid Particle Erosion Resistance of Ductile Metals Based on Their Properties " , ASME Journal of Engineering for Gas Turbine and Power, Vol 107, 1985, pp 669 - 678

142. Richardson J.H and Smakula F.K, 1979, " Causes of High Pressure Compressor Deterioration in Service ", AIAA/SAE/ASME Paper N79 – 1234 , 15 Joint Propulsion Conference, June 1979, Las Vegas, Nevdaa

143. Robbins W.H and Dugan J.F, 1965, " Prediction of Off -Design Performance of Multistage Compressors ", NASA SP36, 297-310, 1965.

144. Robert B. Abernethy, 1985, " Precision and Propagation of Error " , Pratt &Whitney Engineering Division, West Palm Beach, vol 98 " Thrust and Drag its Prediction and Verification – Progress in Astronautics and Aeronautics Martin Summerfield ", Editor in Chief AIAA series , c1985

145. Robinson C.J, 1982, " A Review of the Effect of Rotor Tip Clearances on Axial Compressor Performance " , Rolls Royce RCR 90830, Jan 1982

146. Rubinow S.I and Keller J.B, 1961, " The Transverse Force on Spinning Sphere Moving in a Viscous Fluid ", Journal of Fluid Mechanics 1961, 11, 447-459

147. Rudinger George, 1976, " Flow of Solid Particles in Gases " , Fundamentals and Applications of Gas-Particle Flow , AGARD, 1976

148. Sage W and Tilly G.P, 1969, " The Significance of Particles Sizes in Sand Erosion of Small Gas Turbines ", JRAeS, Vol 73, May 1969, pp 427-428

149. Schaffler A, 1979, " Experimental and Analytical Investigation of the Effects of Reynolds Number and Blade Surface Roughness on Multistage Axial Flow Compressors " , ASME paper 79-GT-2 April 16, 1979

150. Schlichting H, 1979," Boundary Layer Theory ", 7th Edition Mc Graw Hill , New York, 1979

151. Schodl R, 1974, " On the Development of a New optical Method for Flow Measurements in Turbomachines ", ASME Gas Turbine Conference, Zurich, Switzerland, 1974

152. Schodl R, 1980, " A Laser Two Focus (L2F) Velocimeter For Automatic Flow Vector Measurements In a Rotating Components of Turbomachines ", Journal of Fluids Engineering, Vol 102 , N° 4 Dec 1980 , pp 412-419.

153. Schodl R, 1988, " Optical Techniques for Turbomachinery Flow Analysis ", Institut Fur Antriebstechnik DFVR Koln, Germany Thermodynamics and Fluid Mechanics of Turbomachinery , Edited by A.S Ucer P.Stwo CH. Hirsh, NATO ASI series

154. Schodl R, 1991, " Laser Transit Velocimetry ", DLR Kola, Germany, Laser Velocimetry Lecture Series 1991-05 June 10-14-1991, Von Karman Institute for Fluid Dynamics.

155. Schmucker J and Schaffler A, 1994, " Performance Deterioration of Axial Compressors Due to Blade Defects ", Propulsion and Energetic Panel (PEP), Symposium held in Rotterdam, the Netherlands, April 1994

156. Shepherd DG, 1959, " principles of Turbomachinery " , The Mc Millan Company, New York 1959, pp 177-187

157. Schwind R.G and Mc Millan O.J, 1982, " Blade Erosion Effects on Aircraft Engine

Compressor " , Nelson Engineering and Research, Inc , Report N° 83-16347

158. Shirolkar J.S, Coimbra C.F.M and M.Queiroz Mc Quay, 1996, " Fundamental Aspects of Modeling Turbulent Particle Dispersion in Dilute Flows ", Prog, Energy Combustion Sci. vol 22, pp 363 -399, 1996, Elsevier Science Ltd.

159. Shirolkar J.S and Mcquay M.Q, 1998 , " Probability Density Function Propagation Model for Turbulent Particle Dispersion " , International Journal of Multiphase Flow, vol 24 No 4, pp 663 - 678 , 1998

160. Sirs R.C, 1993, " The Operation of Gas Turbine Engines in Hot and Sandy Condition " , 83rd Symposium, Propulsion and Energetic Panels of Erosion, Corrosion and Foreign Object Damage Effect in Gas Turbine 25-8 April 1994 Technologies Requirements for Small Gas Turbines at Canada, October 4-8, 1993 AGARD CP-537

161. Sommerfeld M and Huber N, 1999, " Experimental Analysis and Modelling of Particle Wall Collisions ", International Journal of Multiphase Flow, 25 (1999) 1457-1489

162. Sommerfeld M., 'Martin Luther Universitat Germany', 2000, " Theoretical and Experimental Modelling of Particulate Flow - Overview and Fundamentals ". Lecture series 2000 – 06, April 3-7 2000, Edited by J-M Buchlin, Von Karman Institute, Belgium

163. Smith L.H Jr , 1970, " Casing Boundary Layer in Multistage Axial Flow Compressors " Flow research on Blading ed L.S DZUNG Elsevier Publishing Amesterdam Netherlands, 1970.

164. Stewart W.L, Witney W.J and Wong R.V, 1960, " A Study of Boundary Layer Characteristics of Turbomachinery Blade Rows and Their Relation to Overall Blade Losses ", ASME Trans Series D. J Basic Eng vol 82, 1960

165. Tabakoff W, Grant G and Ball R, 1974, " An experimental Investigation of Certain Aerodynamic Effects on Erosion " , AIAA Paper 74 -639 1974

166. Tabakoff W , Hosny W and Hamed A, 1976, " Effect of Solid Particles on Turbine Performances " , ASME Journal of Engineering for Power, Jan 1976, pp 47 -52

167. Tabakoff W and Hamed A, 1977, " Aerodynamic Effects on Erosion In Turbomachinery " , ASME Paper N°70, 1977 Joint Gas Turbine Congress, Tokyo 22-27 May 1977

168. Tabakoff W, Kotwak R and Hamed A, 1979 ," Erosion Study of Different Materials Affected by Coal Ash Particles " , Wear Vol 52,1979 PP 161-173

169. Tabakoff W , Hamed A and Balan C , 1980, " Performance Deterioration of an Axial Flow Compressor Stage With Presence of Solid Particles ", Proceeding of The 5Th International Symposium on Airbreathing Engines, 1980

170. Tabakoff W and Balan C , 1981, , " Effects of Solid Particles Suspended In Fluid Flow Through an Axial Flow Compressor Stage " , Paper N° 75 , International Symposium On Air Breathing Engines, February 16-18 1981, Bangalore , India

171. Tabakoff W and Hamed A, 1983, " Turbomachinery Performance Deterioration and Retention " , Von Karman Institute for Fluid Dynamics, Lecture Series 1988-08 , May 24 - 27, 1988

172. Tabakoff W and Balan C, 1983a, " A Study of the Surface Deterioration Due to Erosion ", ASME Journal of Engineering For Power, Vol 105, Oct 1983, pp 834-838

173. Tabakoff W and Balan C, 1983b, " Effect of Sand Erosion on the Performance Deterioration of A Single Stage Axial Flow Compressor " AIAA 83-7053

174. Tabakoff W and Balan C, 1983c, " Effect of Sand Erosion on the Performance Deterioration of A Single Stage Axial Flow Compressor ", Proceeding of the Sixth International Symposium on Air Breathing Engines, June 6-10, 1983 Paris, France

175. Tabakoff W, 1984, " Review Turbomachinery Performance Deterioration Exposed to Solid Particulate Environment ", ASME Journal of Fluids Engineering, Vol 106, June 1984, pp 125 –134

176. Tabakoff W, 1986, " Study of Single Axial Performance Deterioration " , AIAA/ASME 4TH Joint fluid Mechanics May, 12 – 14 ,1986

177. Tabakoff W and Hamed A, 1986, " The Dynamics of Suspended Solid Particles on Two Stage Gas Turbine ", ASME Journal of Turbomachinery vol 108, October 1986 pp 298-302.

178. Tabakoff W, 1987, " Compressor Erosion and Performance Deterioration " , ASME Journal of Fluids Engineering Vol 109 , September 1987 pp 297 –306

179. Tabakoff W and Hamed A, 1988, " Temperature Effect on Particle Dynamics And Erosion in Radial Inflow Turbine " , ASME Journal of turbomachinery, vol 110, April 1988, pp 259 –264

180. Tabakoff W, 1988, " Turbomachinery Erosion Evaluation and Erosion Test Results for Different Alloys " ,Von Karman Institute for Fluid Dynamics , Lecture Series.

181. Tabakoff W, Lakshminarasimha A.N and Pasin M, 1990, " Simulation of Compressor Performance Deterioration Due to Erosion " , ASME Journal of Turbomachinery, Vol 112, January 1990, pp 79– 83

182. Tabakoff W, Hamed A and Murugan D.M, 1996, " Effect of Target Materials on the Particle Restitution Characteristics for Turbomachinery Application ", Journal of Propulsion and Power Vol 12 N°2 March - April 1996.

183. Tan S.C, 1984, " A Computer Code to Predict Particle Trajectories In a Three-dimensional Gas Turbine Intake " , MSc thesis, Cranfield Institute of Technology, 1983-84

184. Tan S.C, 1988, " A Study of Particle Trajectories in a Gas Turbine Intake " , PhD Thesis Cranfield University, January 1988

185. Tan S.C and Elder R.L, 1992, " Assessment of Particle Rebounds and Fragmentation Characteristics ", Progress Report, Cranfield University 1992.

186. Tan S.C, Harris P.K and Elder R.L, 1994, " Particle Trajectories in Gas Turbines " , 83rd Symposium, Propulsion and Energetic Panels of Erosion, Corrosion and Foreign Object Damage Effect in Gas Turbine 25-8 April 1994

187. Tan S. C, Elder R.L, Harris P.K, 1994, " Unique Test Facility For Rebound Factor ", paper 94-GT-350 Presented at ASME Conference, The International Gas Turbine and Aeroengine Congress and Exposition , Hague Netherlands June 13-16, 1994

188. TASCflow code manual, 1995, " Theory Documentation ", ASC 1995, Advanced Scientific Computing Ltd, Waterloo Canada

189. Tilly G.P, 1969, " Sand Erosion of Gas Turbines Engines " , Note For the Turbomachinery Sub-Committee of The Aeronautical Research Council, ARC-30948, 1969

190. Tilly G.P and Sage W, 1970, " The Interaction of Particles and Material Behaviour in Erosion Process ", Wear, vol 16 (1970) pp 447-465

191. Tilly G.P, 1973, " A Two Stage Mechanism of Ductile Erosion " , Wear, 1973, 23, 87-96

192. Tilly G.P, 1974 ," Particle Erosion of Ductile Metals ", Wear 27, 1974

193. Torobin L.B and Gauvin W.H, 1961, " The drag Coefficient of Single Spheres Moving in Steady and Accelerated Motion in a Turbulent Fluid " , AIChEJ vol 7 615-619, 1961

194. Versteeg H.K, Malalasekera W, 1995," An Introduction to Computation Fluid Dynamics The Finite Volume Method ", Longman Group Ltd 1995

195. Ucer A.S, Stow P and Hirsch C.H, 1989," Thermodynamics and Fluid Mechanics of Turbomachinery ", volume 1and 2, NATO ASI Series

196. Ulke A, Rouleau W.T, 1976," Effects of Secondary Flows on Turbine Blade Erosion". ASME paper N76-GT-74 , March 21-25.

197. Upton A.W.J, 1974, " Axial Flow Compressor and Turbine Blade Fouling ", First Symposium in Gas Turbine Operations and Maintenance, National Research Council of Canada, Oct

198. Wakeman T and Tabakoff W, 1983, " Effect of Particle Rebound Characteristics on Erosion of Turbomachinery Components " , ASME Paper N 83-GT-169

199. Wallis R.A, 1961, " Axial Flow Fans Design and Practice " , George Newnes London 1961

200. Wallis R.A, 1968, " A Rationalised Approach to Blade Element Design, Axial Flow Fans " , Inst of Eng, Australia Conference on Hydraulic and Fluid Mechanics, 1968

201. Wallis R.A , 1972, " The Development of Blade Sections for Axial Flow Fans " , Mechanical and Chemistry Engineering. Trans I.E Augst , vol MC8 N°2 pp 111-116, November 1972

202. Wenglarz R.A, 1982, " Boundary Layer Effects on Impingement and Erosion " , Proc 17th Annual Cavitation and Poly-Phase Flow Forum, ASME Fluids Eng. Conf, St Louis, June 7-11, 1982

203. White F.M, 1991 , " Viscous fluid flow ", New York: McGraw-Hill, 1991

204. Wiedenroth W , 1978, " Experimental Work on the Transportation of Solid Liquid Mixture Through Pipelines and Centrifugal Pumps " , Proc 5th International Conference on

Hydraulic Paper A2 BHRA Fluid Engineering Cranfield UK 1978

205. Wright P.I and Miller D.C, 1991, " An improved Compressor Performance Model ", C423 / 028 IMechE Proceeding 1991

206. Wulf Ray H, Kramer W.H and Paas J.E, 1980, " CF6-6D Jet Engine Performance deterioration " , NASA/CR-159786 NASA, 1980

207. Zaita Anthony V, Buley Greg and Karlsons Glen, 1997, " Performance Deterioration Modelling in Aircraft Gas Turbine Engines " , ASME 97-GT-278 Presented at the International Gas Turbine Gas Turbine & Aeroengine Congress & Exhibition, June 2 -5 1997

208. Zhong Yan, Minemura Kiyoshi, 1996, " Measurement of Erosion Due to Particle Impingement and Numerical Prediction of Wear in Pump Casing ", Wear 199 (1996) 36-44

209. Zhuang Y, Wilson J.D and Lozowski E.P, 1989, " A Trajectory Simulation Model For Heavy Particle Motion in Turbulent Flow " , ASME Journal of Fluids Engineering vol 111 pp 492-494, 1989

210. Yakhot V, Orszag S. A, Thangam S, Gatski T.B and Speziale C.G, 1992 ," Development of a Turbulence Model For Sheer Flows By a Double Expansion Technique ", Physics and Fluids vol 4 N7 1992

*Standardisation*

211. BS1042 , " Methods For the Measurements of Fluids in Pipes ", BS 1042-2.1:1983

212. BS848, " Fans for General Purposes Part 1 ,1997, " Performance Testing Using Standard Airways Amendment 1997

213. " A Compressor Routine Test Code ", National Gas Turbine Establishment Peystock Hants, Report N° R246 : HMSO, 1961

214. BS4999 PART3 , " Testing of Electrical Motors ",1987

215. " Flow Through a Suden Enlargement of Area in a Duct " ESDU 72011, 1981

216. Robert B. Ross, 1992, " Metallic Materials Specifications Handbook " , Fourt edition Chapman & Hall

217. US Department of Defense, 1979, " Aerospace Structural Materials Handbook ", Mechanical Properties DATA center. A DOD Materials information center 1979

# APPENDICES

# APPENDIX A

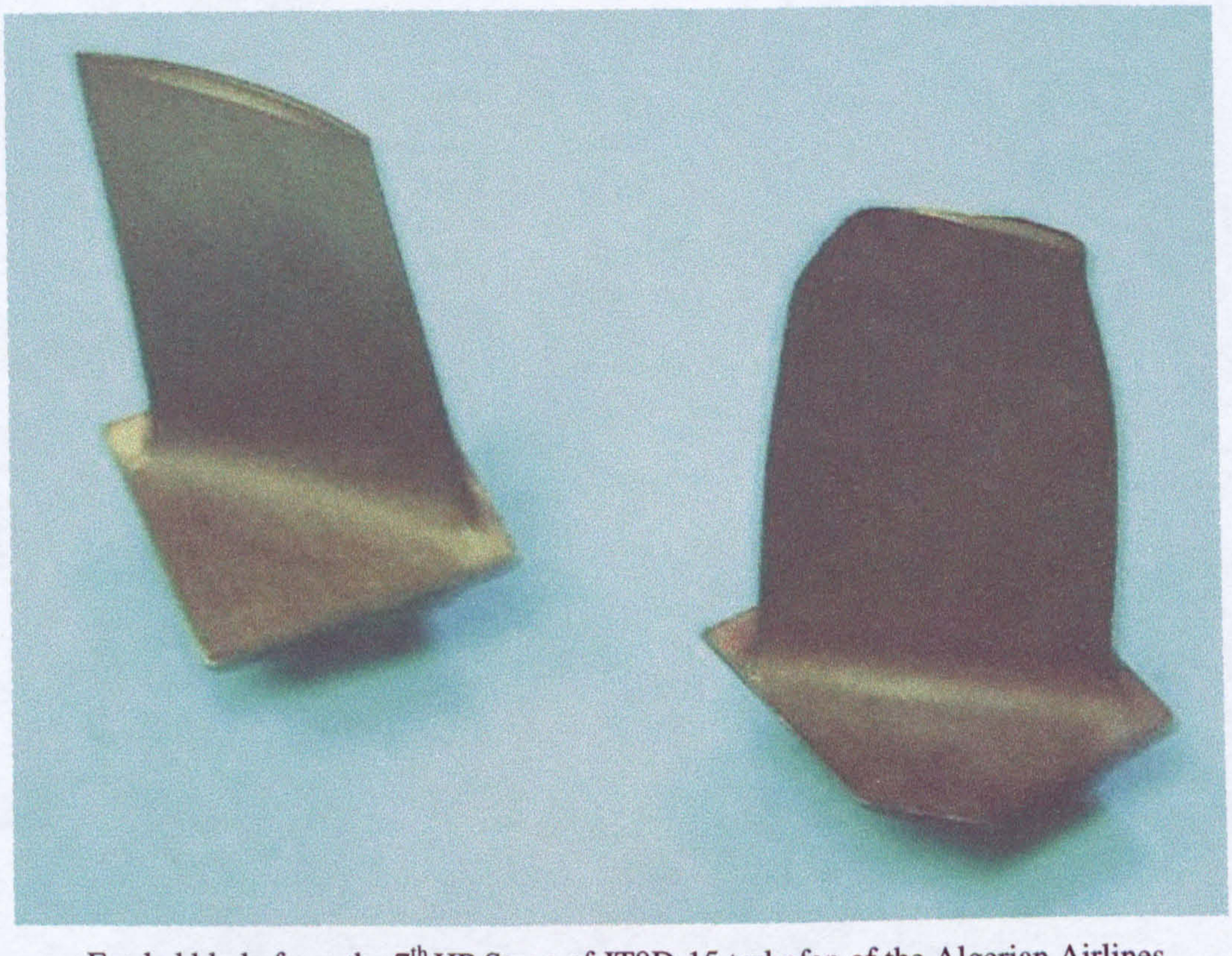

Eroded blade from the 7th HP Stage of JT8D-15 turbofan of the Algerian Airlines

# APPENDIX B

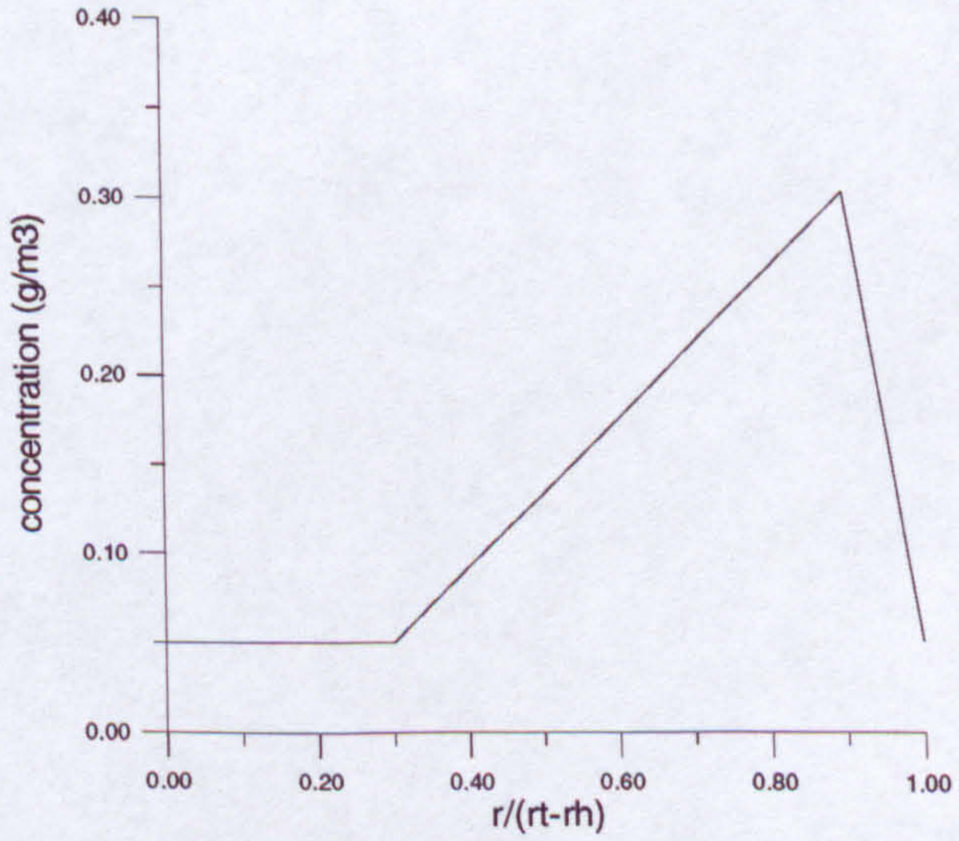


Concentration profile used by Rolls-Royce

# APPENDIX C

Restitution ratio as published by Tabakoff and Hamed (1996).

- *Aluminum 2024*

$$V_{R2}/V_{R1} = 0.93551 - 0.05710\ \beta_1 + 2.28628 \cdot 10^{-3} \beta_1^2 - 3.72484 \cdot 10^{-5} \beta_1^3 + 2.04537 \cdot 10^{-7} \beta_1^4$$

$$\beta_{R2}/\beta_{R1} = 2.68321 - 0.12570\ \beta_1 + 2.54388 \cdot 10^{-3} \beta_1^2 - 1.59472 \cdot 10^{-5} \beta_1^3$$

$$\sigma\left(V_{R2}/V_{R1}\right) = 0.94778 - 0.09407\ \beta_1 + 3.52115 \cdot 10^{-3} \beta_1^2 - 5.30096 \cdot 10^{-5} \beta_1^3 + 2.74714 \cdot 10^{-7} \beta_1^4$$

$$\sigma\left(\beta_{R2}/\beta_{R1}\right) = 1.47251 - 0.06238\ \beta_1 + 1.01706 \cdot 10^{-3} \beta_1^2 - 5.56946 \cdot 10^{-6} \beta_1^3$$

- *AM355 Steel Alloy*

$$V_{R2}/V_{R1} = 0.65810 - 0.00877\ \beta_1 + 0.11954 \cdot 10^{-3} \beta_1^2 - 7.80954 \cdot 10^{-7} \beta_1^3$$

$$\beta_{R2}/\beta_{R1} = 1.68634 - 0.06447\ \beta_1 + 1.35709 \cdot 10^{-3} \beta_1^2 - 8.70497 \cdot 10^{-6} \beta_1^3$$

$$\sigma\left(V_{R2}/V_{R1}\right) = 1.18002 - 0.12245\ \beta_1 + 4.64885 \cdot 10^{-3} \beta_1^2 - 7.04471 \cdot 10^{-5} \beta_1^3 + 3.66273 \cdot 10^{-7} \beta_1^4$$

$$\sigma\left(\beta_{R2}/\beta_{R1}\right) = 1.19593 - 0.05191\ \beta_1 + 0.97339 \cdot 10^{-3} \beta_1^2 - 6.11656 \cdot 10^{-6} \beta_1^3$$

- *Titanium 6A1-4V*

$$V_{R2}/V_{R1} = 0.69188 - 0.02853\ \beta_1 + 1.42919 \cdot 10^{-3} \beta_1^2 - 2.79351 \cdot 10^{-5} \beta_1^3 + 1.72736 \cdot 10^{-7} \beta_1^4$$

$$\beta_{R2}/\beta_{R1} = 1.74714 - 0.06766\ \beta_1 + 1.51846 \cdot 10^{-3} \beta_1^2 - 1.05152 \cdot 10^{-5} \beta_1^3$$

$$\sigma\left(V_{R2}/V_{R1}\right) = 0.57854 - 0.04287\ \beta_1 + 1.47111 \cdot 10^{-3} \beta_1^2 - 2.17213 \cdot 10^{-5} \beta_1^3 + 1.14850 \cdot 10^{-7} \beta_1^4$$

$$\sigma\left(\beta_{R2}/\beta_{R1}\right) = 1.15135 - 0.03620\ \beta_1 + 0.42888 \cdot 10^{-3} \beta_1^2 - 1.29912 \cdot 10^{-6} \beta_1^3$$

- *RENE 41*

$$V_{R2}/V_{R1} = 1.27999 - 0.09240\ \beta_1 + 3.55440 \cdot 10^{-3} \beta_1^2 - 5.59992 \cdot 10^{-5} \beta_1^3 + 3.01229 \cdot 10^{-7} \beta_1^4$$

$$\beta_{R2}/\beta_{R1} = 1.82366 - 0.06673\ \beta_1 + 1.31411 \cdot 10^{-3} \beta_1^2 - 8.07624 \cdot 10^{-6} \beta_1^3$$

$$\sigma\left(V_{R2}/V_{R1}\right) = 0.95330 - 0.08655\ \beta_1 + 3.01769 \cdot 10^{-3} \beta_1^2 - 4.32717 \cdot 10^{-5} \beta_1^3 + 2.16709 \cdot 10^{-7} \beta_1^4$$

$$\sigma\left(\beta_{R2}/\beta_{R1}\right) = 1.52139 - 0.06741\ \beta_1 + 1.16752 \cdot 10^{-3} \beta_1^2 - 6.78918 \cdot 10^{-6} \beta_1^3$$

Measured restitution factors and variance for Aluminum material
due to Tan (1992)

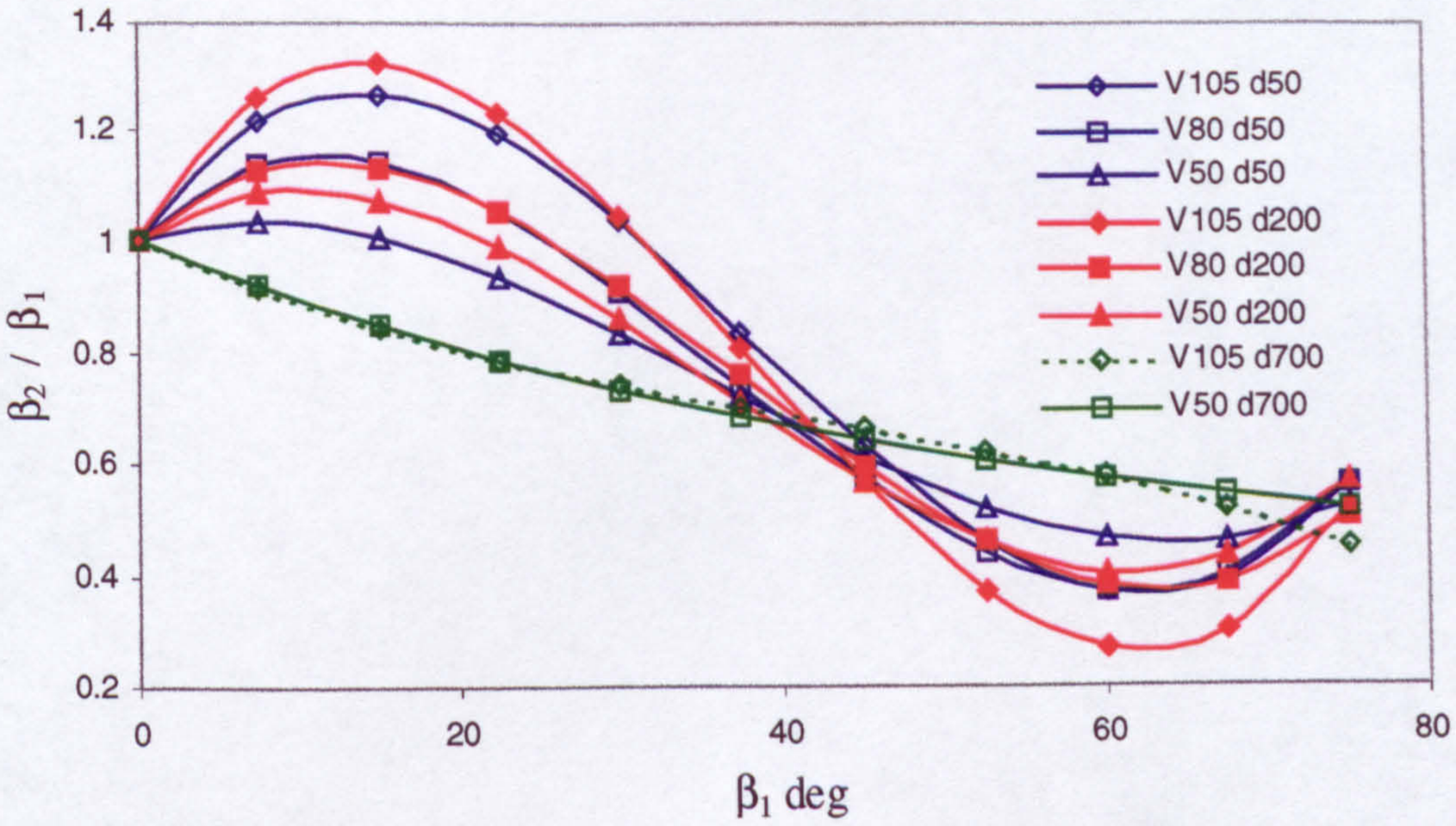


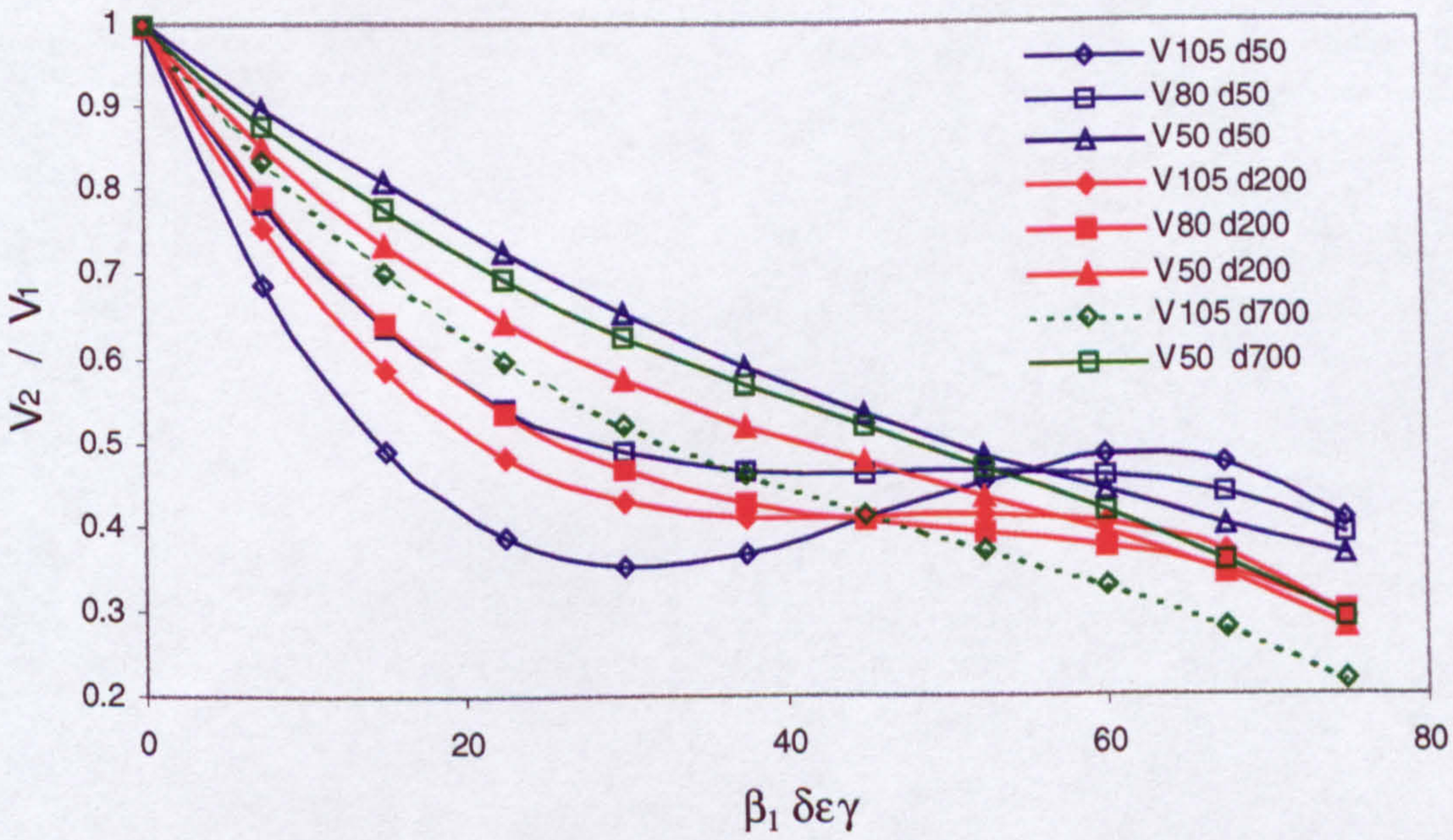


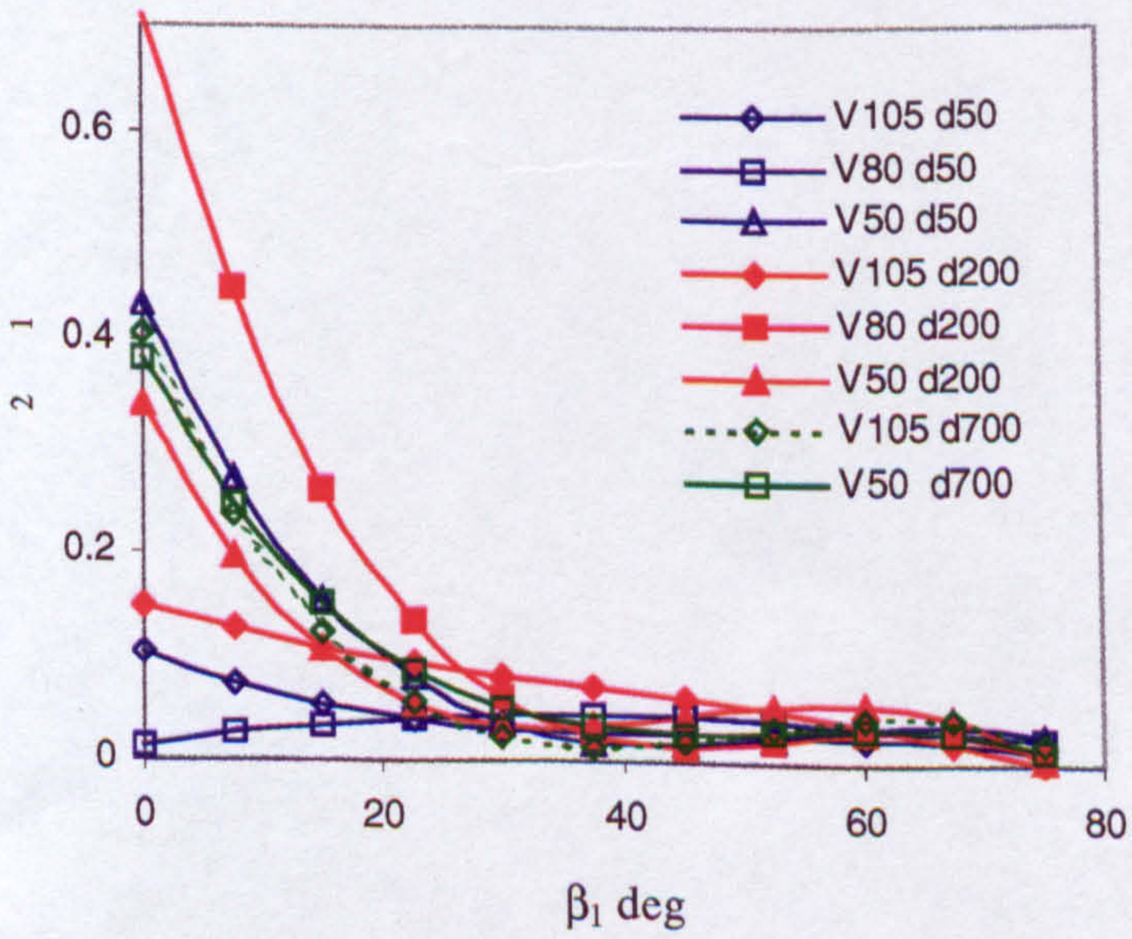


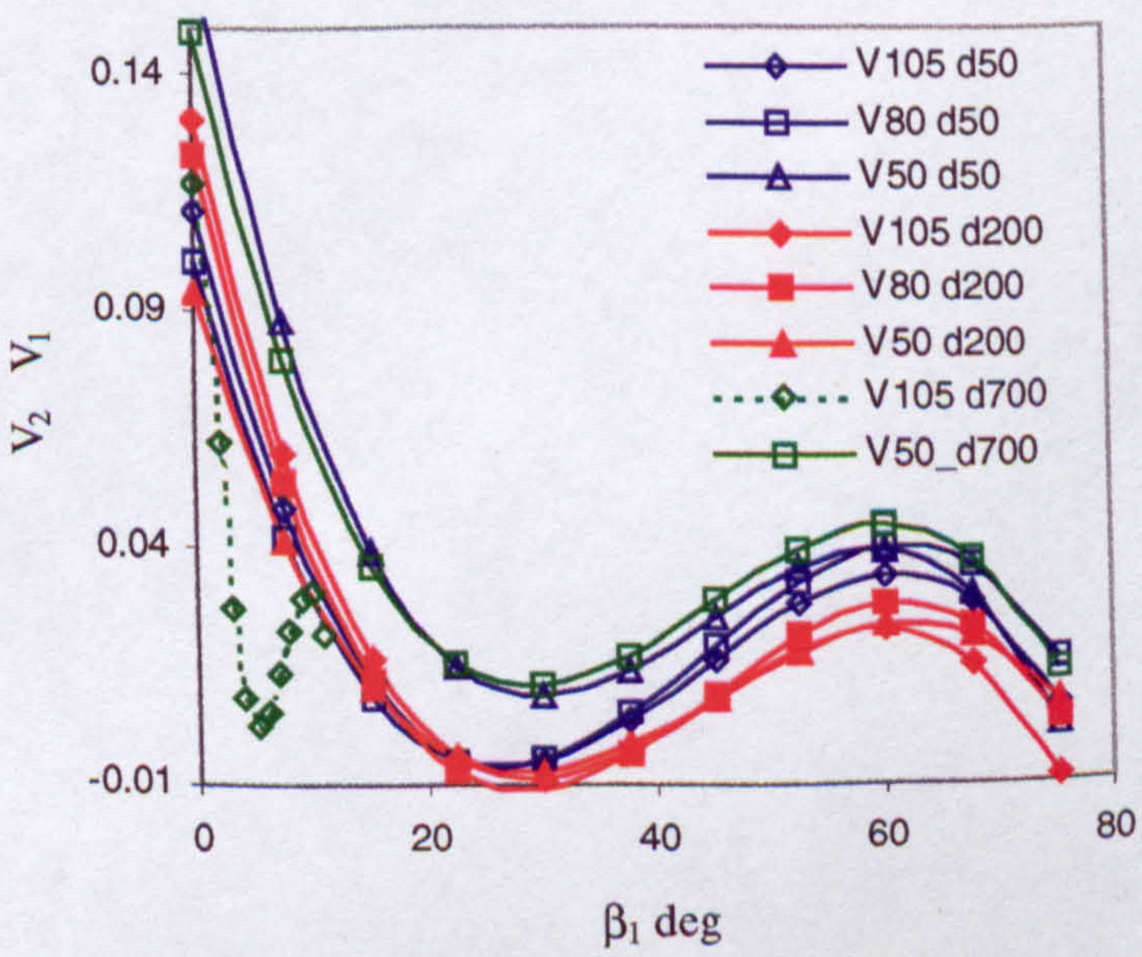

# APPENDIX D

Erosion rate correlation due to Grant and Tabakoff (1974), this parameter is given in (mg/g) milligrams of removed material by grams of impacting quartz particles.

$$\varepsilon = K_1 f(\beta_1)\left(V_{1T}^2 - V_{2T}^2\right) + f(V_{1N})$$

$$f(\beta_1) = \left[1 + C_K\left(K_2 \sin\left(\frac{90^o}{\beta_0}\right)\beta_1\right)\right]^2 \qquad C_K \begin{cases} 1 & if \ \beta_1 \le 2\beta_0 \\ 0 & if \ \beta_1 \rangle \ 2\beta_0 \end{cases}$$

$\beta_0$ is the angle of maximum rate of erosion

The second term in this equation is obtained from an experimental curve fitting as.

$$f(V_{1N}) = K_3 (V_1 \sin\beta_1)^{\alpha}$$

Where, $K_1$, $K_2$, $K_3$, material constants

$\alpha$ is determined at 90 degrees impact angle, with a value equal 4

The first term of this expression can also be written as.

$$= K_1 f(\beta_1) V_1^2 \cos^2\beta_1 \left(1 - R_T^2\right)$$

$$R_T = 1 - 0.0016 V_1 \sin\beta_1$$

For the 2024-aluminium alloy these constants are as the following.

$K_1$ $3.67\ 10^{-6}$
$K_2$ 0.585
$K_3$ $6\ 10^{-12}$
$K_4$ 0.0016

For hard alloys like titanium and stainless steel, Tabakoff (1974) gave modifications to Grant (1974) correlation. The maximum erosion rate angle is 25 degree.

$$f(\beta_1) = \left[1 + C_K K_2 \psi\right]^2 \qquad C_K \begin{cases} 1 & if \ \beta_1 \le 2.66\beta_0 \\ 0 & if \ \beta_1 \rangle \ 2.66\beta_0 \end{cases}$$

$$\psi = [\sin \phi\beta_1]^{0.1} \quad if \quad \beta_1 \le \beta_0$$

$$[1 - \sin \phi(\beta_1 - \beta_0)]^3 + \frac{1}{3}[\sin 2\gamma(\beta_1 - \beta_0)] + \xi \qquad if \quad \beta_1 \rangle \beta_0$$

$$\phi = {}^{90}\!/_{1.66\,\beta_0}$$

$$\gamma = {}^{90}\!/_{\beta_0}$$

$$\xi = 0.7[0.138 + 0.5\sin \gamma\beta_1 - 0.212\cos 2\gamma\beta_1\ ]$$

The constants are given as following

| 410 stainless steel | 6AL-4VT Titanium alloy |
|---|---|
| $K_1 = 0.5225\ 10^{-5}$ | $K_1 = 0.367\ 10^{-5}$ |
| $K_2 = 0.2668$ | $K_2 = 0.2365$ |
| $K_3 = 0.549\ 10^{-12}$ | $K_3 = 0.856\ 10^{-12}$ |
| $K_4 = 0.0017$ | $K_4 = 0.0016$ |

The experimental data (Tabakoff, 1987) was used to obtain the following empirical equation for the erosion mass parameter defined for 510 stainless steel at different impacting velocities and impingement angles for quartz particles (165micron)

$$\varepsilon = K_1\left[1 + CK\left(K_{12}\sin\left(\frac{90}{\beta_0}\beta_1\right)\right)\right]^2 V_1^2\cos^2\beta_1\left(1 - R_T^2\right) + K_3\left(V_1\sin\beta_1\right)^4$$

$$R_T = 1 - 0.0016V_1\sin\beta_1$$

$$CK = 1 \quad \beta_1 \le 2\beta_0$$

$$CK = 1 \quad \beta_1 > 2\beta_0$$

$$K_1 = 0.5225 \times 10^{-5}$$

$$K_{12} = 0.266799$$

$$K_3 = 0.549 \times 10^{-12}$$

The Brinell hardness BHN according to the reference handbook of material (1992) and the mechanical properties data (1972) for these materials are:

| Material | Hardness BHN |
|---|---|
| 2024 Aluminium | 110 |
| 410 stainless steel | 205 |
| 6AL-4VT Titanium | 352 |

The next curve gives the erosion rate for different materials among them the stainless steel 304 when eroded by the silica 180-250 micron, reference (Feng and Ball, 1999). The maximum erosion angle is close to 20 degree

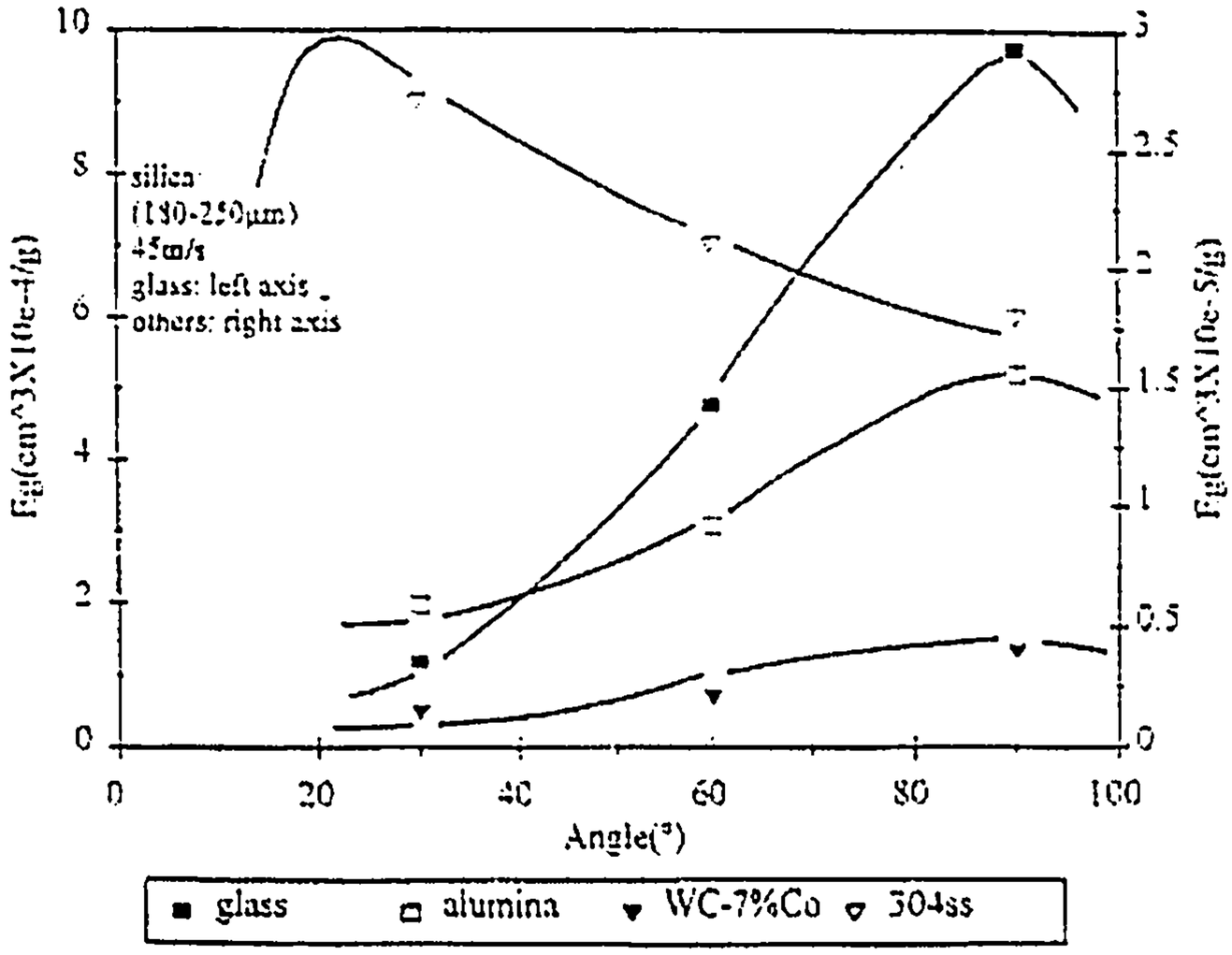

# APPENDIX E

Four categories of test airways are commonly used for axial fan testing facilities in conformity to British standard BS848.

- Type A free inlet, free outlet
- Type B free inlet, ducted outlet
- Type C ducted inlet, free outlet
- Type D ducted inlet, ducted outlet

The type D installation is subdivided into four categories of fan set-ups

- A test installation with a common segment outlet duct and outlet anti-swirl device and with inlet duct simulation.
- A test installation with outlet duct anti-swirl device, without common segment outlet and outlet duct and with inlet duct simulation.
- A test installation with common segment outlet duct and outlet anti-swirl device and common segment inlet duct.
- A test installation with outlet duct simulation without anti-swirl device

<u>Pressure and temperature measurements for axial fans</u>

When a probe is placed in an airway, the accuracy of measurements depend on the flow velocity. The measured temperature is usually bit closer to the stagnation values. In order to measure the mean stagnation temperature, normally one or several probes mounted on radial immersion rake should be located at different positions symmetrically situated from the diameter centre. The number of probes should never be less than six, for the purpose of averaging (HMSO, 1961). If air velocity is low and the annular section is small, one temperature probe can be placed in the centre of the flow passage (BS848, 1997). Care must be exercised in using temperature measurements to calculate stage efficiencies for low-pressure ratio machine. Small temperature measuring errors including that of the thermocouple wire can impact the accuracy of the small temperature difference measurements across low-pressure ratio turbomachinery. Some of errors are due to flow fluctuation and due to the thermal energy transferred from the measured point by heat conduction down the probe stem and by radiation to surrounding surfaces. Good testing requires minimising the level of heat rejection through an appropriate choice of the environmental and test temperature. Radiation heat transfer can be minimised by placing a shield over the thermocouple. In addition, a small vent at the rear of the probe is used to balance the heat loss with thermal energy from the fluid by convective heat transfer. The shielded probes can also reduce the free stream velocity resulting in a higher recovery of temperature.

The static pressure in the standardised airways is an average of four wall tapings readings. Circumferential static pressure tapings are good indicators of flow velocity uniformity. Typically static pressure tap are installed in constant area ducts away from abrupt bends and area changes. A great care must be exercised to assure that the taps are

burr free. When a separated flow is present in the vicinity of the static pressure taping, if the eddies possess an appreciable dynamic head in a direction normal to the surface, then the flush surface of the drill give an erroneous result. As consequence, it needs special rounding shape at the end (Wallis, 1961). The bore diameter of a taping is 1.5mm. The change of area must be progressive to the capillary tubes and the rapid fluctuations of the manometer reading should be limited by damping, so that the average reading is within 1%.

The total pressure at the rotor outlet may be measured directly or indirectly. In the first possibility, the inlet total pressure should be based upon an area mean total pressure obtained by using total pressure sensors located at specific streamwise station relative to the blading. An accurate measurement requires that both inlet and exit total pressure be recorded. This normally includes multiple individual rakes, which are equally spaced around the circumference. Typically, three to four rakes are installed for the inlet measurement. However, cell ambient condition can be used as inlet flow conditions if the test rig includes a well designed inlet bellmouth that is coupled with a short duct. Stage discharge total pressure radial immersion rakes are normally located as close as possible to the test stage exit plane. The rakes are normally located less than a chord length downstream of the trailing edge. In order to get a more representative pressure average, the positions of the individual rakes are indexed equally across the blade passage so that the different wake flow properties are equally measured. Typical rakes will include between five and eight individual pressure sensors per rake (Logan, 1995).

In other situations, the static pressure is measured by averaged four static pressure holes, then by using the mass flow rate the value of the total pressure is calculated. When using a traversed total pressure probe, the measurement errors become significant close to the solid wall, it is frequently necessary to eliminate data close to the wall and to extrapolate instead, or use a correction factor.

# APPENDIX F

## Transit Laser Anemometer

Two different forms of laser anemometers are available in flow measurements, the laser Doppler anemometer and an alternative design, which is known by several names; transit time of flight, L2F and two spot. The laser transit anemometer that eventually evolved to find application in turbomachines is very much associated with Shodl (1974). A transit laser anemometer consists mainly of three components; a transmitting device by which laser beams are directed to a measuring point in the flow, where the probe volume is formed figure F-1. And a receiving device, which is aligned with the probe volume in order to detect the scattering light from the particles passing through an electronic device, which processes the photo-multiplier signals and delivers velocity and turbulence information. The two spot laser generates in the measuring volume two parallel highly focused light beams, figure F-2, which make a light gate in which a particle passing through, produces two successive pulses. This system has the advantage over the Doppler system, because it provides a shorter probe length (Gill, 1981), allowing measurement to be taken closer to solid surfaces. The beam's narrowest diameter is about 10 micron with a separation distance between the two beam axis about 0.2 to 0.4mm (Schodl, 1988).

In order to register the double pulse of scattered light it is necessary, however, that the plane containing the laser beams be parallel to the flow direction, consequently it is possible to determine the flow direction.

The principle of the transit laser anemometer is based on measuring the time between successive start and stop pulses figure F-3, which are stored in memory. The start signal for the time measurement is produced by photomultiplier 1, which receives the scattered light from the first laser beam. Photomultiplier 2, which is aligned with the second beam, yields the stop signal. After amplification of both signal discriminators produce an output logic pulse which can be triggered at their maximum independent of the signal amplitudes and rise-time, figure F-4. As a result a spectrum of a number of measured time intervals versus time of flight is obtained from one focused beam to another (Schodl, 1980), (Eckardt, 1986). The scattered light from each beam is received by a photo-multiplier tube PMT, and the pulses are passed to a multi-channel analyser figure F-7 to build-up a histogram of the transit times of particles, which contains certain amount of noise generated by particles and by flare from solid surfaces. The intensity of the scattered light depends fundamentally upon the size and the shape of a particle. The motion of particles less than 0.5 micron transcripts all flow behaviour.

Taking a single measurement of the time interval between scattered light pulses, one is never sure that this is a right measure. Many measured values taken at a certain probe position are necessary, figure F-6, then a resulting histogram of data is plotted with a Gaussian shape. By setting the plane containing the beams to other slightly different angles and by accumulating the same number of particles entering the probe volume, more velocity histograms are obtained as long as the chosen setting angles of the plane are within the range of the velocity angle fluctuations. A probability distribution of beam transit time is established to compute components of the flow, Schodl (1991).

Due to the geometry constraints within a turbomachine, one is obliged in applying an optical back scattering arrangement with a good transmission of the laser light through a

transparent window toward the measuring point and back to the PMT. The requirements for flat windows are to prevent aberration of the optical focusing that is curved windows will act as lens (Ahmed et al, 1991). It is always preferable to try to limit the size of the flat windows to be used without compromising the aerodynamic surface beyond acceptable limits. Flat window installed in the generally highly curved turbomachinery casing generates projection edges, which should be small to avoid flow disturbances. It was found for the most critical measuring point close to the hub, a cone angle of less than 10 degree is required to avoid edges greater than 0.2mm.

The most important restriction on the application of laser anemometers is the background radiation generated by laser light reflections at the hub and at the casing window. If it is possible to chose a large angle of observation with respect to the axis of the incident beams, the background radiation may be reduced. The L2F system has been operated as close as 0.3 millimetres to the shroud in a rotating compressor passage as reported by reference (Schodl, 1988).

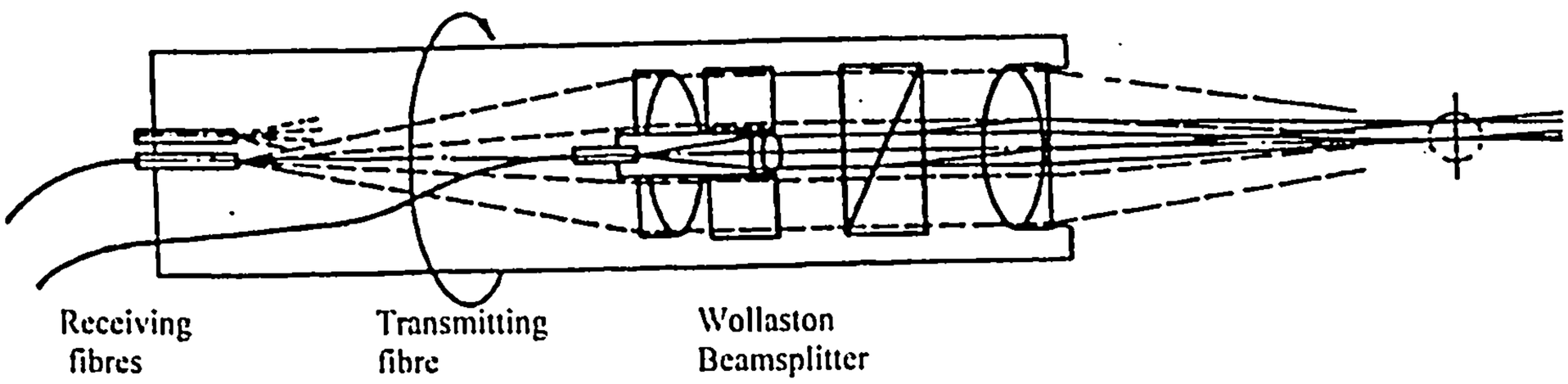


Figure F-1 Block diagram of the fibre L2F probe

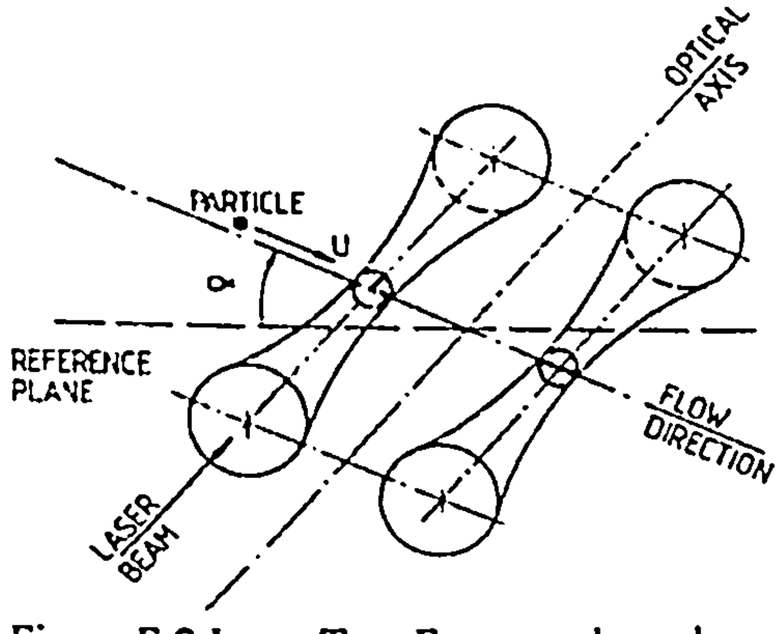


Figure F-2 Laser Two Focus probe volume

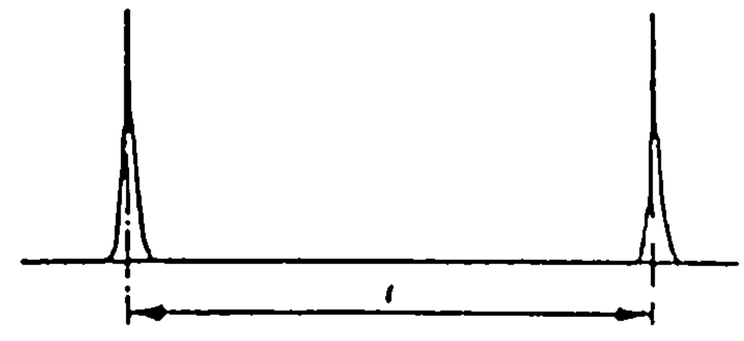


Particle passing through both beams gives rise to double pulse

Figure F-3 Two beams pulses

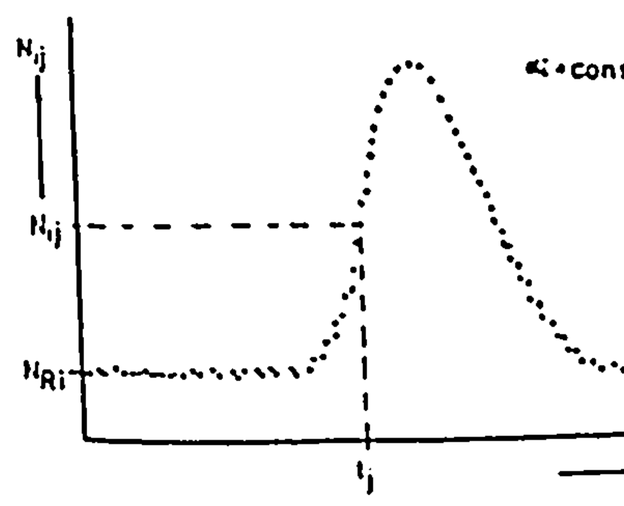


Figure F-4 Histogram of transit times of flight

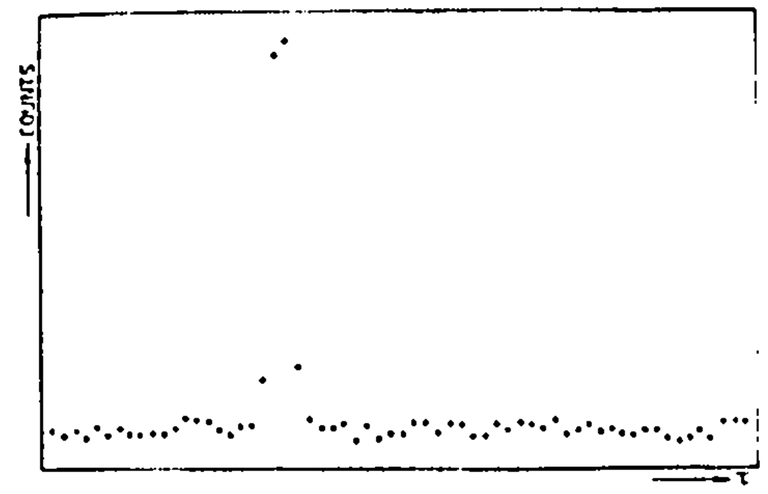


Figure F-5 Histogram of few sampling particles

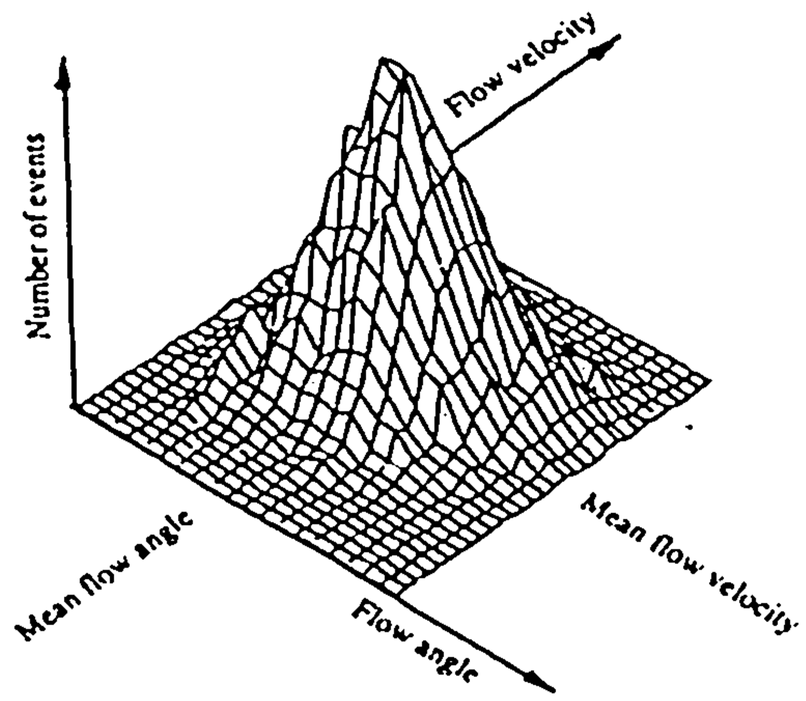


Angle and velocity distribution

Figure F-6 Two dimensional histogram

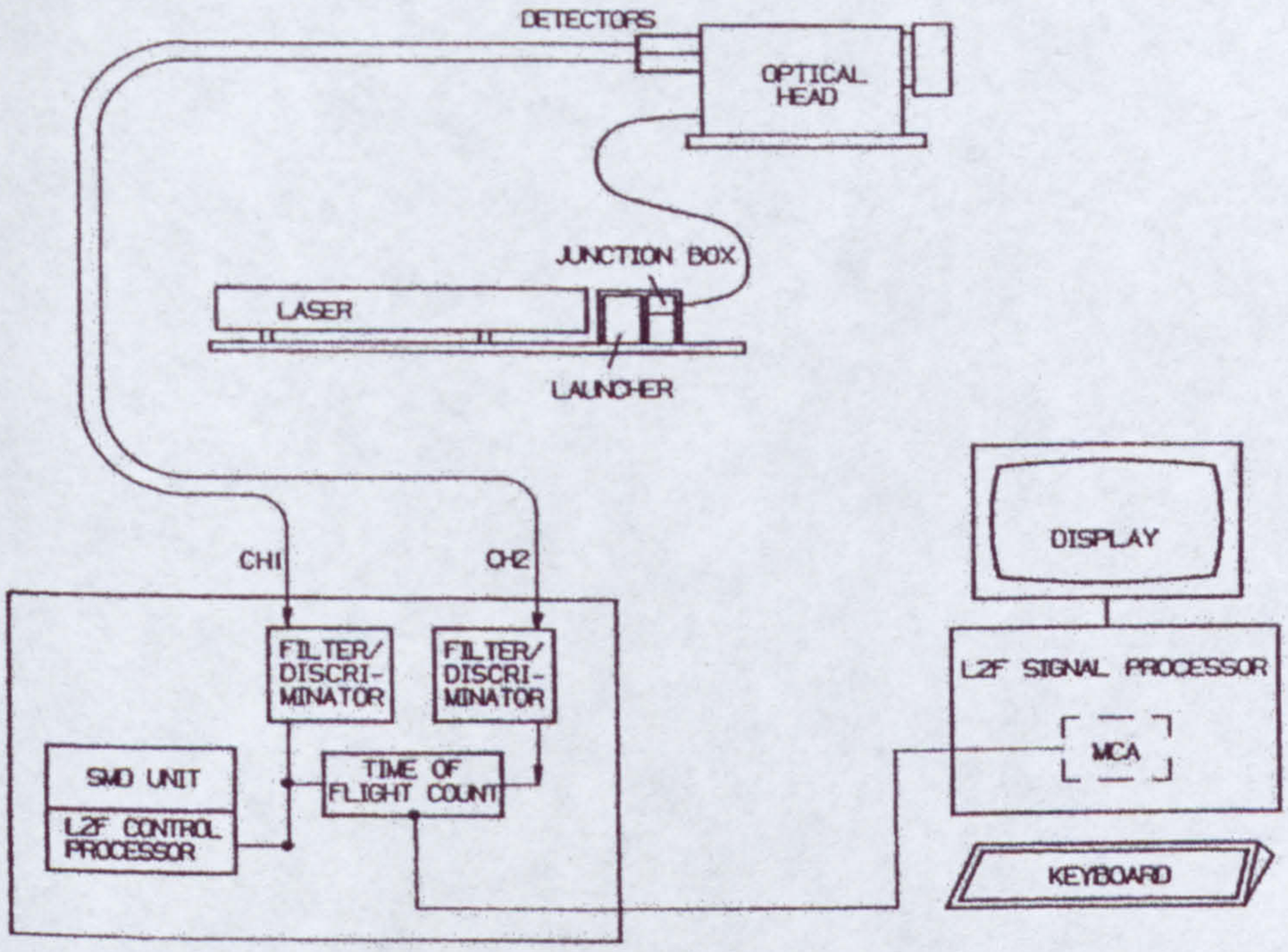


Figure F-7 Layout of signals processing

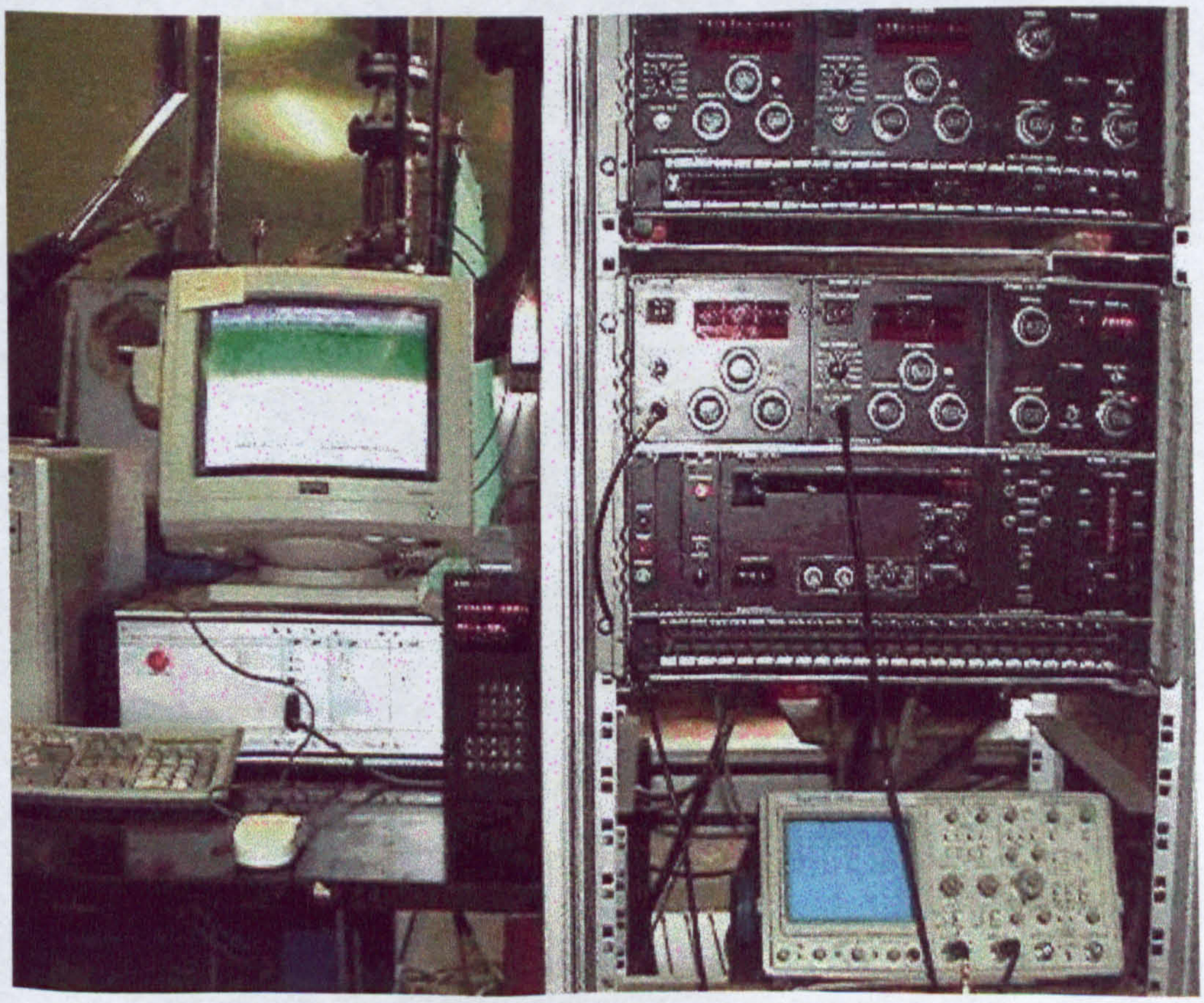

Figure F-8 Control panel and acquisition system with PC

# APPENDIX G

## Determination of the aerothermodynamic parameters

- **Density humidity, and viscosity**

The air density, which includes the air moisture, may be calculated as following.

$$\rho_x = \frac{P_x}{R_w T_x}$$

$$R_w = 287 \Big/ 1 - 0.378 \frac{P_v}{P_a}$$

The vapour pressure is obtained from the following expression when the wet temperature is known, and it lies between 0 °c –150°c.

$$P_v = (P_{sat})_{T_w} - 6.610^{-4} P_{atm}(T_{atm} - T_w)(1 + 0.00115T_w)$$

The saturation pressure is given by

$$P_{sat} = 610.8 + 44.442T_w + 1.4133T_w^2 + 0.027T_w^3 + 2.5566710^{-4} T_w^4 + 2.8916610^{-6} T_w^5$$

The viscosity of air

$$\mu = (17.1 + 0.048T_x)10^{-6}$$

- **Average total pressure when using Pitot tube**

At each measurement point the differential pressure ΔPi across the Pitot static tube is measured. The mean differential pressure at the section, $\Delta P_m$ is a square of the average of the square root of the individual differential pressures ΔPi and is given by the following expression.

$$\Delta P_m = \left[\frac{1}{n}\sum \Delta Pj^{0.5}\right]^2$$

n : number of measurements

The local static temperature may be deduced from the total measured one.

$$T_x = T_{tx}\left(\frac{P_x}{P_x + \Delta P_m}\right)^{\gamma-1/\gamma}$$

- **Fan inlet and outlet pressure**

Assuming total and static pressure with total temperature measured at section 5, where the optimum recovery of static pressure. The stagnation Mach number is calculated by.

$$M_{15}^2 = \frac{4\dot{m}^2}{\pi d^2 \gamma P_{15} \rho_{15}}$$

From which the local Mach number

$$M_5 = M_{15}\sqrt{1+1.217M_{15}^2+1.369M_{15}^4+10M_{15}^6}$$

The correction for compressibility is

$$cop(M_5) = 1 + {M_5^2}/{4} + {M_5^4}/{40} + {M_5^6}/{1600}$$

The stagnation pressure $P_{tFO}$ at the fan outlet is obtained from.

$$P_{tFO} = P_5 + \tfrac{1}{2}cop(M_5)\rho_5 V_5^2\left[1+(\varsigma_{FO-5})_5\right]$$

The stagnation pressure $P_{t2}$ at section 2 upstream of fan inlet can be calculated by.

$$P_{t2} = P_1 + \tfrac{1}{2}cop(M_1)\rho_1 V_1^2\left[1+(\varsigma_{1-2})_1\right]$$

The stagnation pressure $P_{tFI}$ at the fan inlet is calculated by.

$$P_{tFI} = P_2 + \tfrac{1}{2}cop(M_2)\rho_2 V_2^2\left[1+(\varsigma_{2-FI})_2\right]$$

The local friction loss coefficient is given by

$$\varsigma_{1-2} = \Lambda\frac{L_{1-2}}{Dh_{1-2}}$$

The Darcy coefficient

$$\Lambda = 0.005 + 0.42(\mathrm{Re}_d)^{-0.3}$$

The fan total pressure rise

$$\Delta P_{tF} = P_{tFO} - P_{tFI}$$

The fan pressure ratio

$$\Pi_{CF} = {P_{tFO}}/{P_{tFI}}$$

The fan air power.

$$P_{UF} = \frac{m}{\rho_{tFI}}\Delta P_{tF}K_P$$

The fan aerodynamic efficiency is calculated as following, where $P_r$ is net rotor power

$$\eta_{aer} = \frac{P_{UF}}{P_r}$$

$K_P$ coefficient of compressibility.

$$Z_k = \frac{\gamma-1}{\gamma}\frac{\rho_{tFI}P_r}{m\Pi_{tF}} \qquad , \qquad K_p = Z_k\frac{log_{10}\left(1+{\Pi_{tF}}/{P_{tFI}}\right)}{log_{10}\left[1+Z_k{\Pi_{tF}}/{P_{tFI}}\right]}$$

# APPENDIX H

Calibration procedure of the conical intake and the fan characteristics measurements
As shown by *CAL* and *CHARC* flow chart.

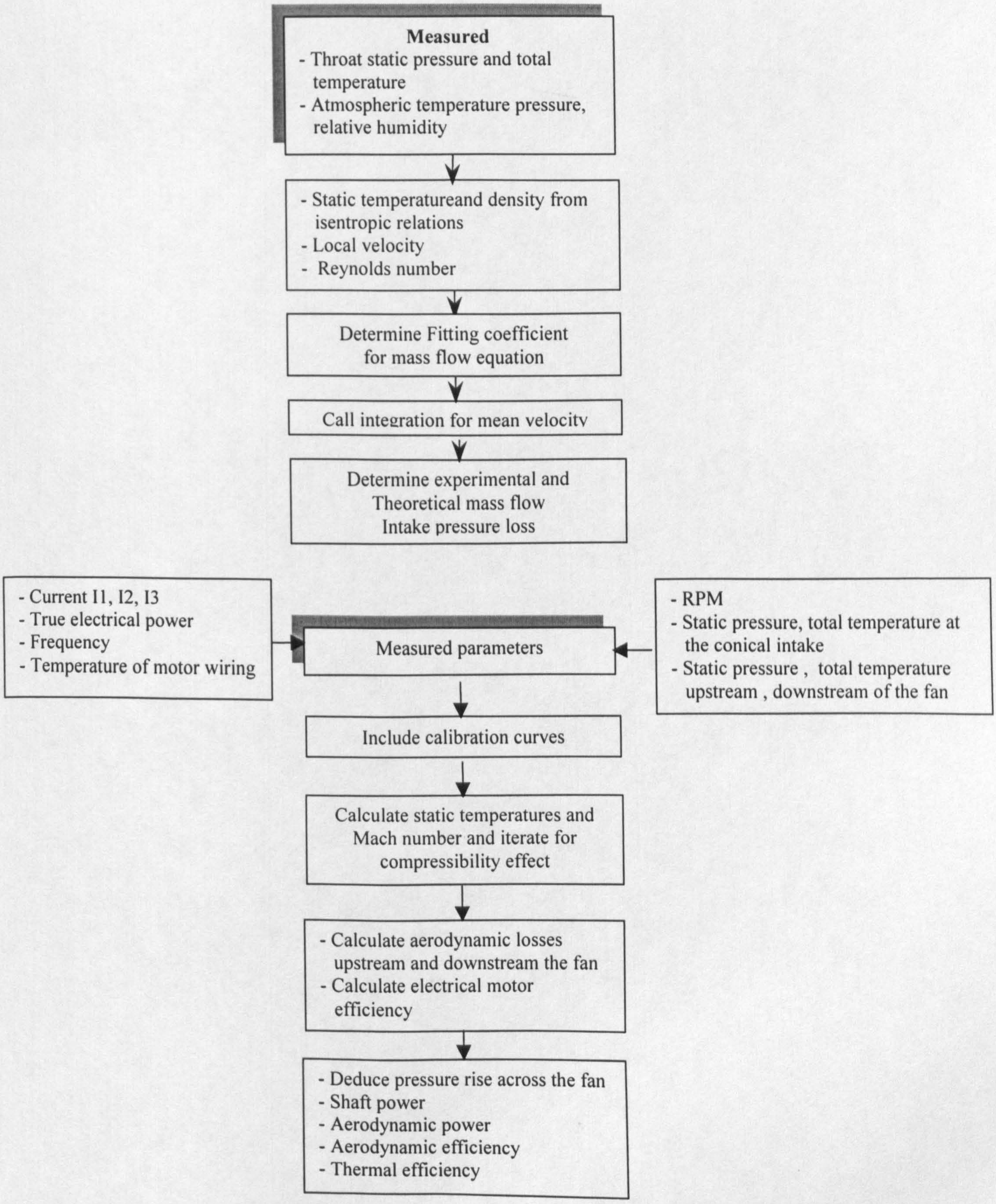

# APPENDIX I

## SUDDEN ENLARGEMENT LOSS

For a fluid flowing along a duct with a sudden enlargement of area a loss of total pressure occurs but the static pressure rises. The recovery plane occurs at about $4D_2$ downstream of the enlargement. From measurement of pressure rise along the wall of larger tube downstream of sudden expansion for different area ratios Ackeret, (1967) indicates that pressure rises of 95% to 97% are obtained after a length $L > 5D_2$.

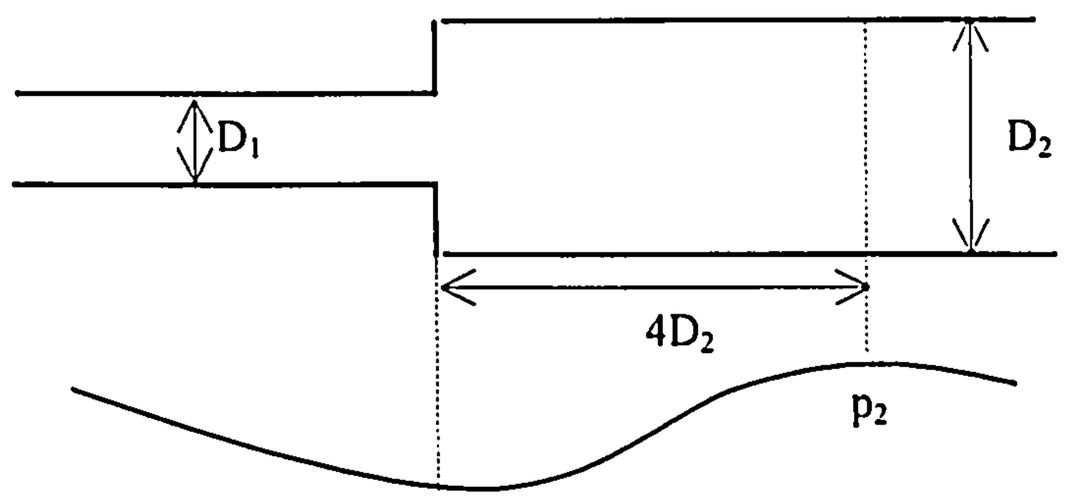


For Reynolds numbers below about 4000, the pressure changes due to sudden enlargement of area in a duct are functions of both Reynolds number and the area ratio of the enlargement, whereas for higher Reynolds the pressure changes depend on area ratio only (ESDU, 1981). For Reynolds number above about 4000, the variation in total pressure loss coefficient follow the theoretical equation known as Borda – Carnot relation, where $\phi = A_1/A_2$..

$$K_{ti} = (1-\phi)^2$$

In incompressible flow the static pressure drop coefficient $K_{si}$ is related to the total pressure loss coefficient by the equation. For Reynolds greater than 4000.

$$K_{si} = 2\phi(\phi - 1)$$

It is common in such cases to use static pressure recovery in referring to static pressure changes.

It is possible to modify the analysis to account for non-uniform velocity profiles by introducing momentum an kinetic energy factors which allow the overall fluxes of momentum and kinetic energy at a cross section to be expressed in terms of the mean velocity. The total and static pressure loss coefficients are then given by.

$$K_{ti} = \beta_1 - 2\phi\alpha_1 + \phi^2(2\alpha_2 - \beta_2)$$

$$K_{si} = 2\phi(\phi\alpha_2 - \alpha_1)$$

# APPENDIX J

## PRECISION AND PROPAGATION OF ERROR DURING MEASUREMENTS

The measurement uncertainty of a parameter is a combination of the bias and precision error.

Precision index S

Bias limit B

Uncertainety U

$$U = B + 2S$$

Error in the measurement is propagated to the parameter through the expression defining such parameter. The effect of the propagation may be approximated with Taylor's series methods.

For a function depending on several parameters

$$f(x_1, x_2, x_3, \ldots, x_n)$$

$$S_f = \left[ \left( \frac{\partial f}{\partial x_1} S_{x1} \right)^2 + \left( \frac{\partial f}{\partial x_2} S_{x2} \right)^2 + \ldots\ldots\ldots + \left( \frac{\partial f}{\partial x_n} S_{xn} \right)^2 \right]^{1/2}$$

$$B_f = \left[ \left( \frac{\partial f}{\partial x_1} B_{x1} \right)^2 + \left( \frac{\partial f}{\partial x_2} B_{x2} \right)^2 + \ldots\ldots\ldots + \left( \frac{\partial f}{\partial x_n} B_{xn} \right)^2 \right]^{1/2}$$

$$U_f = B_f + 2S_f$$

- ***The measured mass flow rate during calibration of the conical air intake***

The measured flow velocity

$$V_i = \sqrt{\frac{2g\rho_w \Delta h_w}{\rho_a}}$$

The actual measured mass flow rate.

$$m = \sum 2\pi \rho_a r_i \Delta r_i V_i$$

$$m = C \sum \left[ r_i \Delta r_i \sqrt{\frac{\Delta h_w P_a}{T_a}} \right]$$

$$C = 2\pi \sqrt{\frac{2g\rho_w}{R}}$$

The precision index $S_m$ for the mass flow rate

$$S_m = \left[ \left( \frac{\partial m}{\partial r_i} S_{r_i} \right)^2 + \left( \frac{\partial m}{\partial \Delta r_i} S_{\Delta r_i} \right)^2 + \left( \frac{\partial m}{\partial \Delta h_w} S_{\Delta hw} \right)^2 + \left( \frac{\partial m}{\partial P_a} S_{P_a} \right)^2 + \left( \frac{\partial m}{\partial T_a} S_{T_a} \right)^2 \right]^{1/2}$$

$$S_m = C \left[ \left( \sum \Delta r_i \sqrt{\frac{P_a \Delta h_w}{T_a}} S_{r_i} \right)^2 + \left( \sum r_i \sqrt{\frac{P_a \Delta h_w}{T_a}} S_{\Delta r_i} \right)^2 + \left( \frac{1}{2} \sum r_i \Delta r_i \sqrt{\frac{P_a}{\Delta h_w T_a}} S_{\Delta hw} \right)^2 + \left( \frac{1}{2} \sum r_i \Delta r_i \sqrt{\frac{\Delta h_w}{P_a T_a}} S_{P_a} \right)^2 + \left( -\frac{1}{2} \sum r_i \Delta r_i \frac{1}{T_a} \sqrt{\frac{P_a \Delta h_w}{T_a}} S_{T_a} \right)^2 \right]^{1/2}$$

By inserting the nominal values and precision errors, the precision index of ( mass flow kg/s) is obtained

The bias limit in mass flow calculation is propagated from the bias limits of the measured variables using the Taylor's series.

$$B_m = \left[ \left( \frac{\partial m}{\partial r_i} B_{r_i} \right)^2 + \left( \frac{\partial m}{\partial \Delta r_i} B_{\Delta r_i} \right)^2 + \left( \frac{\partial m}{\partial \Delta h_w} B_{\Delta hw} \right)^2 + \left( \frac{\partial m}{\partial P_a} B_{P_a} \right)^2 + \left( \frac{\partial m}{\partial T_a} B_{T_a} \right)^2 \right]^{1/2}$$

$$B_m = C \left[ \left( \sum \Delta r_i \sqrt{\frac{P_a \Delta h_w}{T_a}} B_{r_i} \right)^2 + \left( \sum r_i \sqrt{\frac{P_a \Delta h_w}{T_a}} B_{\Delta r_i} \right)^2 + \left( \frac{1}{2} \sum r_i \Delta r_i \sqrt{\frac{P_a}{\Delta h_w T_a}} B_{\Delta hw} \right)^2 + \left( \frac{1}{2} \sum r_i \Delta r_i \sqrt{\frac{\Delta h_w}{P_a T_a}} B_{P_a} \right)^2 + \left( -\frac{1}{2} \sum r_i \Delta r_i \frac{1}{T_a} \sqrt{\frac{P_a \Delta h_w}{T_a}} B_{T_a} \right)^2 \right]^{1/2}$$

By inserting the nominal values and precision errors and bias limit the uncertainty is obtained

- ***The corrected mass flow rate***

$$\dot{m}_c = \dot{m} \frac{Pa_{st}}{P_{tFl}} \sqrt{\frac{T_{tFl}}{Ta_{st}}}$$

$$B_{m_c} = \left[ \left( \frac{Pa_{st}}{P_{tFl}} \sqrt{\frac{T_{tFl}}{Ta_{st}}} B_m \right)^2 + \left( m \frac{Pa_{st}}{2 P_{tFl}} \sqrt{\frac{1}{T_{tFl} Ta_{st}}} B_{T_{tFl}} \right)^2 + \left( - m \frac{Pa_{st}}{P_{tFl}^2} \sqrt{\frac{T_{tFl}}{Ta_{st}}} B_{P_{tFl}} \right)^2 \right]^{1/2}$$

$$S_{m_c} = \left[ \left( \frac{Pa_{st}}{P_{tFl}} \sqrt{\frac{T_{tFl}}{Ta_{st}}} S_m \right)^2 + \left( m \frac{Pa_{st}}{2 P_{tFl}} \sqrt{\frac{1}{T_{tFl} Ta_{st}}} S_{T_{tFl}} \right)^2 + \left( - m \frac{Pa_{st}}{P_{tFl}^2} \sqrt{\frac{T_{tFl}}{Ta_{st}}} S_{P_{tFl}} \right)^2 \right]^{1/2}$$

- ***The shaft power***

$$W_S = W_{RIN}(1 - S)$$

$$W_{RIN} = W_{IN} - 3I^2 R_{S_2} - Fixed\_loss$$

$$B_{W_{RIN}} = \left[ B_{W_{IN}}^2 + \left( -6IR_{S_2} B_I \right)^2 + \left( -3I^2 B_{R_{S2}} \right)^2 + \left( -B_{Fixed\_loss} \right)^2 \right]^{1/2}$$

$$S_{W_{RIN}} = \left[ S_{W_{IN}}^2 + \left( -6IR_{S_2} S_I \right)^2 + \left( -3I^2 S_{R_{S2}} \right)^2 + \left( -S_{Fixed\_loss} \right)^2 \right]^{1/2}$$

$$Fixed\_loss = Motor\_unloaded - 3I^2 R_{S1}$$

$$B_{Fixed\_loss} = \left[ B_{Motor\_unloaded}^2 + \left( -6IR_{S_1} B_I \right)^2 + \left( -3I^2 B_{R_{S1}} \right)^2 \right]^{1/2}$$

$$S_{Fixed\_loss} = \left[ S_{Motor\_unloaded}^2 + \left( -6IR_{S_1} S_I \right)^2 + \left( -3I^2 S_{R_{S1}} \right)^2 \right]^{1/2}$$

The electrical resistance

$$R_H = R_i \frac{234.5 + T_H}{234.5 + T_i}$$

$$B_{R_H} = \left[ \left( \frac{234.5 + T_H}{234.5 + T_i} B_{R_i} \right)^2 + \left( \frac{R_i}{234.5 + T_i} B_{T_H} \right)^2 + \left( -R_i \frac{234.5 + T_H}{(234.5 + T_i)^2} B_{T_i} \right)^2 \right]^{1/2}$$

$$S_{R_H} = \left[ \left( \frac{234.5 + T_H}{234.5 + T_i} S_{R_i} \right)^2 + \left( \frac{R_i}{234.5 + T_i} S_{T_H} \right)^2 + \left( -R_i \frac{234.5 + T_H}{(234.5 + T_i)^2} S_{T_i} \right)^2 \right]^{1/2}$$

The slip factor

$$S = 1 - N/30f$$

- ***The speed of rotation***

As measured by a magnetic pickup via the signal frequency

$$N = 60 f_N$$
$$B_N = 60 B_{f_N}$$
$$S_N = 60 S_{f_N}$$

$$B_S = \left[ \left( \frac{N}{30 f^2} B_f \right)^2 + \left( -\frac{1}{30 f} B_N \right)^2 \right]^{1/2}$$

$$S_S = \left[ \left( \frac{N}{30 f^2} S_f \right)^2 + \left( -\frac{1}{30 f} S_N \right)^2 \right]^{1/2}$$

$$B_{W_S} = \left[ B_{W_{RIN}}^2 + \left( -W_{RIN} B_S \right)^2 \right]^{1/2}$$

$$S_{W_S} = \left[ S_{W_{RIN}}^2 + \left( -W_{RIN} S_S \right)^2 \right]^{1/2}$$

- ***The stage loading factor***

$$\psi = \frac{P_{tFo} - P_{tFi}}{\rho\left(r_t \pi N / 30\right)^2} = \frac{RT_{tFi}\left(\frac{P_{tFo}}{P_{tFi}} - 1\right)}{\left(r_t \pi N / 30\right)^2}$$

$$B_\psi = \left[\left(\frac{\frac{P_{tFo}}{P_{tFi}} - 1}{n^2 N^2} B_{P_{tFi}}\right)^2 + \left(T_{tFi} \frac{\frac{1}{P_{tFi}}}{n^2 N^2} B_{P_{tFo}}\right)^2 + \left(-T_{tFi} \frac{\frac{P_{tFo}}{P_{tFi}^2}}{n^2 N^2} B_{P_{tFi}}\right)^2 + \left(-2T_{tFi} \frac{\frac{P_{tFo}}{P_{tFi}} - 1}{n^2 N^3} B_N\right)^2 + \left(-2T_{tFi} \frac{\frac{P_{tFo}}{P_{tFi}} - 1}{n^3 N^2} B_n\right)^2\right]^{1/2} R\left(\frac{30}{\pi}\right)^2$$

$$S_\psi = \left[\left(\frac{\frac{P_{tFo}}{P_{tFi}} - 1}{n^2 N^2} S_{P_{tFi}}\right)^2 + \left(T_{tFi} \frac{\frac{1}{P_{tFi}}}{n^2 N^2} S_{P_{tFo}}\right)^2 + \left(-T_{tFi} \frac{\frac{P_{tFo}}{P_{tFi}^2}}{n^2 N^2} S_{P_{tFi}}\right)^2 + \left(-2T_{tFi} \frac{\frac{P_{tFo}}{P_{tFi}} - 1}{n^2 N^3} S_N\right)^2 + \left(-2T_{tFi} \frac{\frac{P_{tFo}}{P_{tFi}} - 1}{n^3 N^2} S_n\right)^2\right]^{1/2} R\left(\frac{30}{\pi}\right)^2$$

- ***The fan air power***

$$W_{UF} = \frac{m}{\rho_{tFi}}\left(P_{tFO} - P_{tFi}\right)K_P = mRT_{tFi}K_P\left(\frac{P_{tFO}}{P_{tFi}} - 1\right)$$

$$B_{W_{UF}} = RK_P\left[\left(T_{tFi}\left(\frac{P_{tFO}}{P_{tFi}} - 1\right)B_m\right)^2 + \left(m\left(\frac{P_{tFO}}{P_{tFi}} - 1\right)B_{\rho_{tFi}}\right)^2 + \left(\frac{mT_{tFi}}{P_{tFi}} B_{P_{tFO}}\right)^2 + \left(-\frac{mT_{tFi}P_{tFO}}{P_{tFi}^2} B_{P_{tFi}}\right)^2\right]^{1/2}$$

$$S_{W_{UF}} = RK_P\left[\left(T_{tFi}\left(\frac{P_{tFO}}{P_{tFi}} - 1\right)S_m\right)^2 + \left(m\left(\frac{P_{tFO}}{P_{tFi}} - 1\right)S_{\rho_{tFi}}\right)^2 + \left(\frac{mT_{tFi}}{P_{tFi}} S_{P_{tFO}}\right)^2 + \left(-\frac{mT_{tFi}P_{tFO}}{P_{tFi}^2} S_{P_{tFi}}\right)^2\right]^{1/2}$$

- ***The fan aerodynamic efficiency***

$$\eta_{aer} = \frac{W_{UF}}{W_S}$$

$$B_{\eta_{aer}} = \left[\left(\frac{1}{W_S} B_{W_{UF}}\right)^2 + \left(-\frac{W_{UF}}{W_S^2} B_{W_S}\right)^2\right]^{1/2}$$

$$S_{\eta_{aer}} = \left[\left(\frac{1}{W_S} S_{W_{UF}}\right)^2 + \left(-\frac{W_{UF}}{W_S^2} S_{W_S}\right)^2\right]^{1/2}$$

# APPENDIX K

In the following tables are presented the different coefficients for the polynomials used to interpolatate the NASA data for equation 6-16 of chapter 6

- **Zero camber incidence angle $(I0)_{10}$**

This parameter is function of reference inlet flow angle and it depends on solidity $\sigma$. The following coefficients are used in the interpolating polynomials

| | A0 | A1 | A2 | A3 | A4 | A5 |
|---|---|---|---|---|---|---|
| $\sigma$ =0.4 | -2.7495618E-4 | 0.041815727 | -8.3264007E-4 | 1.9341009E-5 | -1.1015033E-7 | -4.9914661E-10 |
| $\sigma$ =0.6 | 6.3118439E-4 | 0.045288081 | 0.045288081 | -3.7960819E-5 | 6.6548735E-7 | -4.0745803E-9 |
| $\sigma$ =0.8 | 0.0012017764 | 0.079381516 | -0.0013843333 | 4.4778668E-5 | -6.2264018E-7 | 2.8705073E-9 |
| $\sigma$ =1.0 | 7.1482E-4 | 0.079509394 | -2.4191556E-5 | 5.1767706E-6 | -1.4479229E-7 | 8.0731479E-10 |
| $\sigma$ =1.2 | 5.2099707E-4 | 0.11177841 | -0.0017653461 | 6.4195838E-5 | -9.4401486E-7 | 4.5035351E-9 |
| $\sigma$ =1.4 | 7.5718756E-4 | 0.12045801 | -8.346073E-4 | 2.9239802E-5 | -3.9989202E-7 | 1.3861247E-9 |
| $\sigma$ =1.6 | 0.0027656631 | 0.12609334 | 5.0563293E-4 | -3.2990316E-5 | 7.4534003E-7 | -5.817345E-9 |
| $\sigma$ =1.8 | 0.0013823266 | 0.15240684 | -1.9585139E-4 | -1.8726647E-5 | 6.8848089E-7 | -6.3731876E-9 |
| $\sigma$ =2.0 | 0.0042990394 | 0.13868785 | 0.0030694034 | 0.0030694034 | 2.6510243E-6 | -1.7415823E-8 |

- **Slope factor N**

| | A0 | A1 | A2 | A3 | A4 | A5 |
|---|---|---|---|---|---|---|
| $\sigma$ =0.4 | -0.050040793 | -0.0033484557 | -4.3757284E-5 | 7.7760781E-7 | -1.5661422E-8 | 8.8141026E-11 |
| $\sigma$ =0.6 | -0.044930070 | -0.0033938811 | 6.4000583E-5 | -3.392701E-6 | 5.3904429E-8 | -3.4455128E-10 |
| $\sigma$ =0.8 | -0.039928613 | -0.0019609411 | 8.6064977E-6 | -2.1124709E-6 | 4.3742716E-8 | -3.3653846E-10 |
| $\sigma$ =1.0 | -0.039938811 | -2.6879371E-4 | -8.9051573E-5 | 1.2886072E-6 | -6.3374126E-9 | -8.0128205E-11 |
| $\sigma$ =1.2 | -0.030282925 | -7.4088287E-4 | 1.2531323E-5 | -2.5600962E-6 | 5.2192599E-8 | -3.8942308E-10 |
| $\sigma$ =1.4 | -0.025042249 | -4.1359266E-4 | 1.2678467E-5 | -2.2829254E-6 | 4.4689685E-8 | -3.3653846E-10 |
| $\sigma$ =1.6 | -0.020083042 | 5.89088E-4 | -5.9203817E-5 | 5.6854604E-7 | -4.115676E-9 | -4.0064103E-11 |
| $\sigma$ =1.8 | -0.014949009 | 2.865676E-5 | 7.9035548E-7 | -7.3645105E-7 | 4.1885198E-9 | -3.2051282E-11 |
| $\sigma$ =2.0 | -0.010010198 | 8.9117133E-5 | -8.0747378E-6 | 5.8275058E-8 | -1.0307401E-8 | 4.8076923E-11 |

- **Exponent b**

| A0 | A1 | A2 | A3 | A4 | A5 |
|---|---|---|---|---|---|
| 0.96493881 | -9.6719114E-4 | -1.5574009E-4 | 6.9452943E-6 | -1.3854895E-7 | 8.0929487E-10 |

- **Parameter $m_{\sigma=1}$**

| A0 | A1 | A2 | A3 | A4 | A5 |
|---|---|---|---|---|---|
| 0.25006702 | 3.5122378E-4 | 1.5413753E-5 | -5.412296E-7 | 1.0780886E-8 | -4.8076923E-11 |

- **Parameter (K)δt**

| A0 | A1 | A2 | A3 | A4 | A5 |
|---|---|---|---|---|---|
| 1.0822511E-5 | 7.8117424 | 9.3276515 | -63.920455 | 3196.0227 | -13020.833 |

- **Parameter $(\delta 0)_{10}$**

| | A0 | A1 | A2 | A3 | A4 | A5 |
|---|---|---|---|---|---|---|
| σ =0.4 | 8.0128205E-4 | 0.012920017 | -5.5008013E-4 | 2.4865239E-5 | -3.9954837E-7 | 2.3237179E-9 |
| σ =0.6 | 0.0010343823 | 0.020410111 | -9.1313374E-4 | 3.6899038E-5 | -5.8602855E-7 | 3.6057692E-9 |
| σ =0.8 | 0.0013694639 | 0.021490093 | -7.2668998E-4 | 2.8369027E-5 | -3.9481352E-7 | 2.3237179E-9 |
| σ =1.0 | -2.972028E-4 | 0.029874942 | -0.0014225233 | 5.2384178E-5 | -7.1678322E-7 | 3.9903846E-9 |
| σ =1.2 | -4.3706294E-4 | 0.022663462 | -2.9844114E-4 | 6.1771562E-6 | 5.6089744E-8 | -3.2051282E-10 |
| σ =1.4 | -0.0013840326 | 0.023850962 | -4.3811917E-4 | 1.5220717E-5 | -1.0016026E-7 | 7.2115385E-10 |
| σ =1.6 | -0.0020396270 | 0.021346154 | -1.0780886E-5 | -2.076049E-6 | 1.9230769E-7 | -8.0128205E-10 |
| σ =1.8 | -9.6153846E-4 | 0.017797494 | 3.7259615E-4 | -1.3323135E-5 | 3.2415501E-7 | -1.1217949E-9 |
| σ =2.0 | -0.0020104895 | 0.024338287 | -5.7699592E-4 | 2.9778555E-5 | -4.2759324E-7 | 3.525641E-9 |

- **Slope of reference incidence**

| | A0 | A1 | A2 | A3 | A4 | A5 |
|---|---|---|---|---|---|---|
| β1=20 | 0.99795105 | -3.0758089 | 4.4058858 | -3.5561626 | 1.5311772 | -0.26842949 |
| β1 =30 | 0.99879720 | -2.7763823 | 3.4908945 | -2.4317818 | 0.91091200 | -0.14222756 |
| β1 =40 | 0.99915385 | -2.5408077 | 2.9031177 | -1.8193109 | 0.61115967 | -0.086137821 |
| β1 =50 | 0.99981119 | -2.2345408 | 2.1663024 | -1.1362544 | 0.32816142 | -0.042067308 |
| β1 =60 | 1.0000699 | -1.6146503 | 0.45840618 | 0.68090763 | -0.53358100 | 0.11017628 |
| β1 =70 | 0.99997902 | -1.1060012 | -0.40952797 | 1.0792541 | -0.50480769 | 0.072115385 |

# APPENDIX L

The profile loss is related to the defect in the momentum estimated at the blade trailing edge, which is correlated against the equivalent diffusion factor. The general expression for the equivalent diffusion factor is given as follows Smith (1979).

$$D_{eq} = \frac{W_{max}}{W_{OTE}} = \frac{W_m}{W_1}\frac{W_{max}}{W_m}\frac{W_1}{W_{OTE}}$$

The ratio of the throat velocity to inlet velocity is given by

$$\frac{W_1}{W_1}=\left\{(\sin\beta_1 - K_1\sigma\Gamma\cdot)^2+\left[\frac{\cos\beta_1}{A_p^*\left(\frac{\rho_p}{\rho_1}\right)}\right]^2\right\}^{1/2}$$

$$\frac{\rho_p}{\rho_1}=1-\frac{M_x^2}{1-M_x^2}\left[1-A_p^*-K_1\frac{\tan\beta_1}{\cos\beta_1}\sigma\Gamma\cdot\right]$$

$$A_p^* = \left[1 - K_2\sigma\frac{t_{max}}{l}\Big/\cos\beta_m\right]\left(1-\frac{A_{a1}-A_{a2}}{3A_{a1}}\right)$$

$$\Gamma\cdot=\cos\beta_1(\tan\beta_1-\tan\beta_2)/\sigma$$

The maximum suction surface velocity to passage velocity ratio is expressed as following.

$$\frac{W_{max}}{W_t}=1+K_3\frac{t_{max}}{l}+K_4\Gamma\cdot$$

$W_1/W_{OTE}$ This velocity ratio is determined from cascade inlet and exit vector diagram

The different constants are given as follows:

$K_1$=0.2445 $K_2$=0.4458 $K_3$=0.7688 $K_4$=0.6024

# FIGURES 2

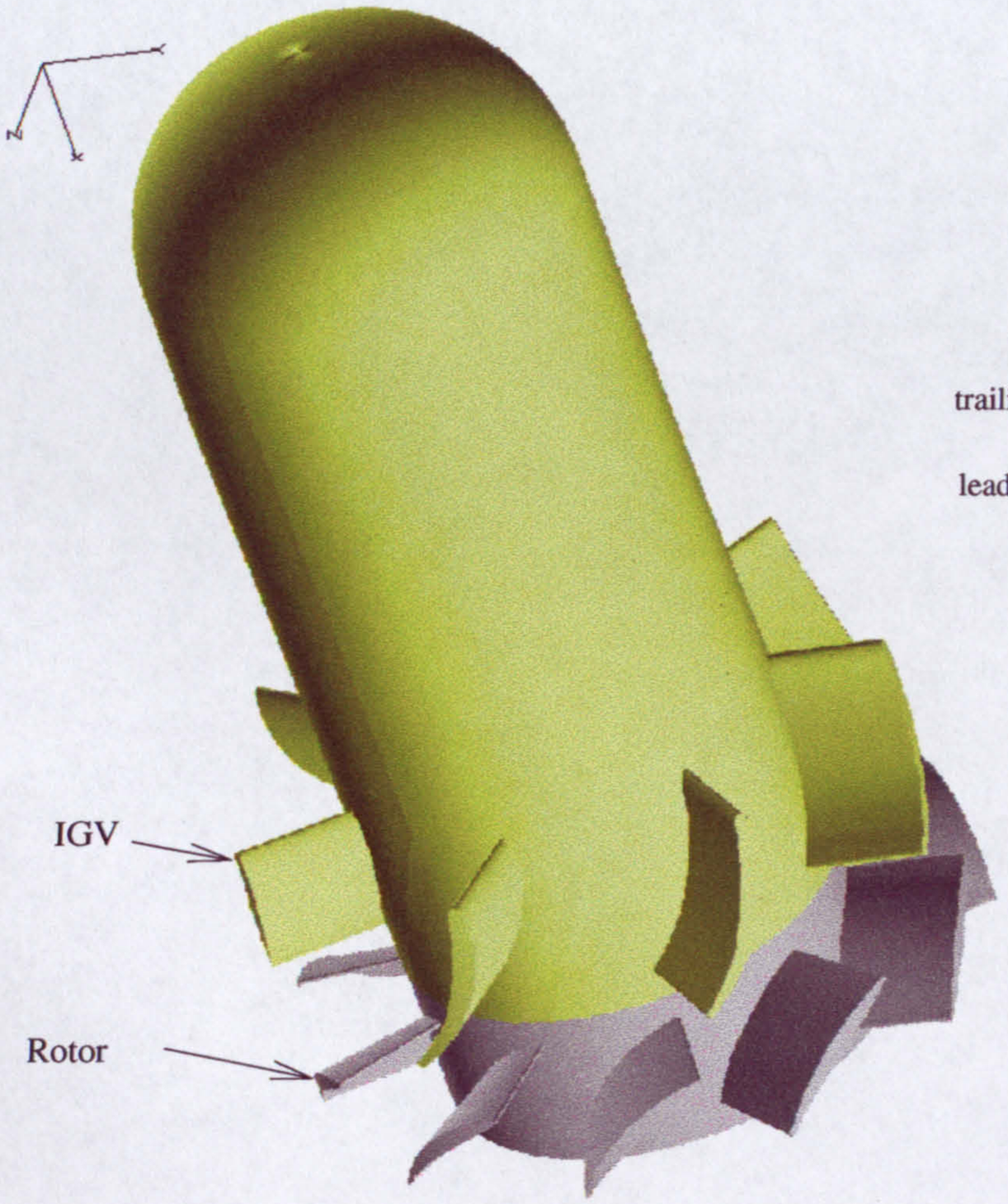


Figure 2-1 Axial fan with an extended nose from IGVs

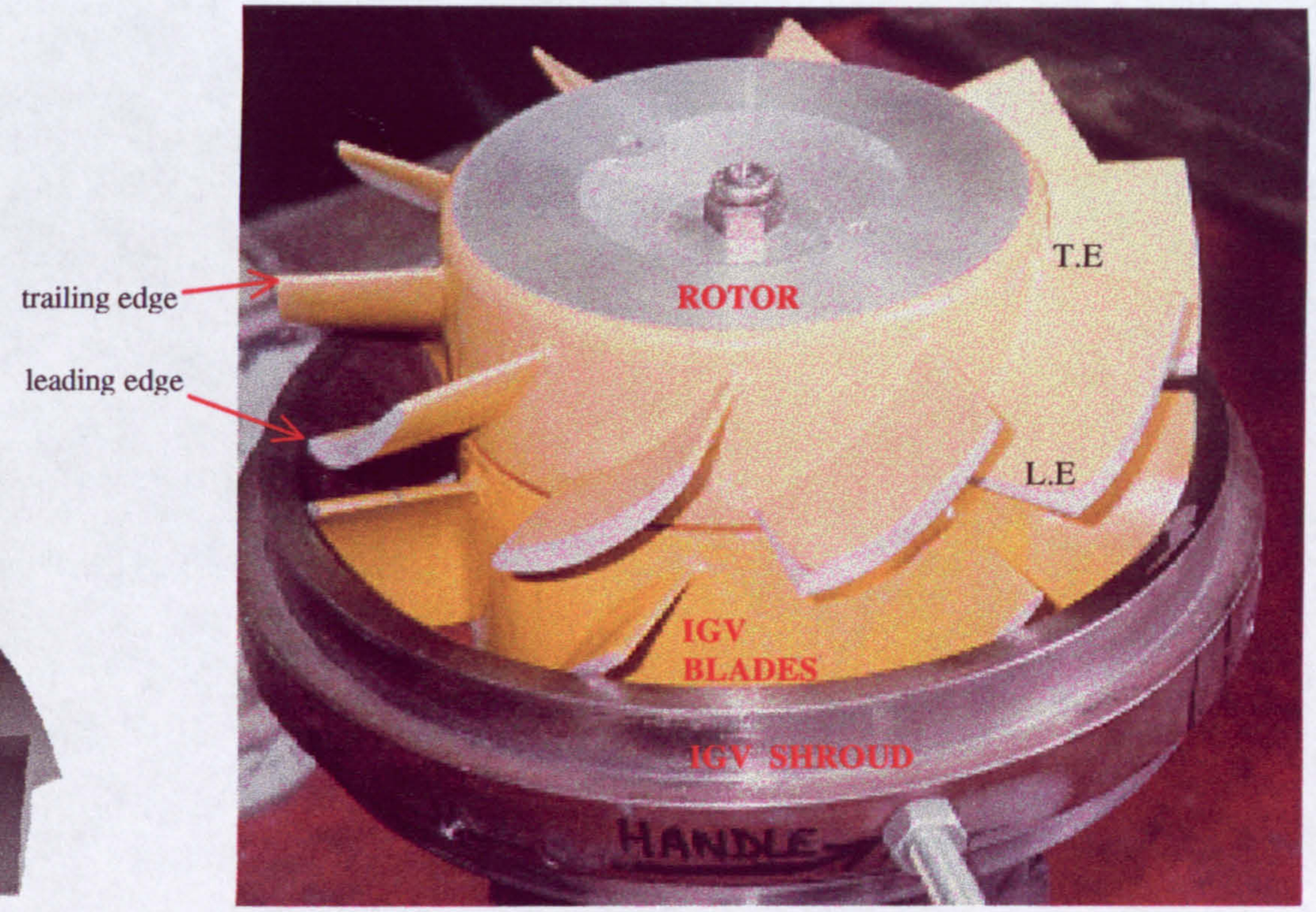


Figure 2-2 Axial fan showing the rotor from the trailing edge

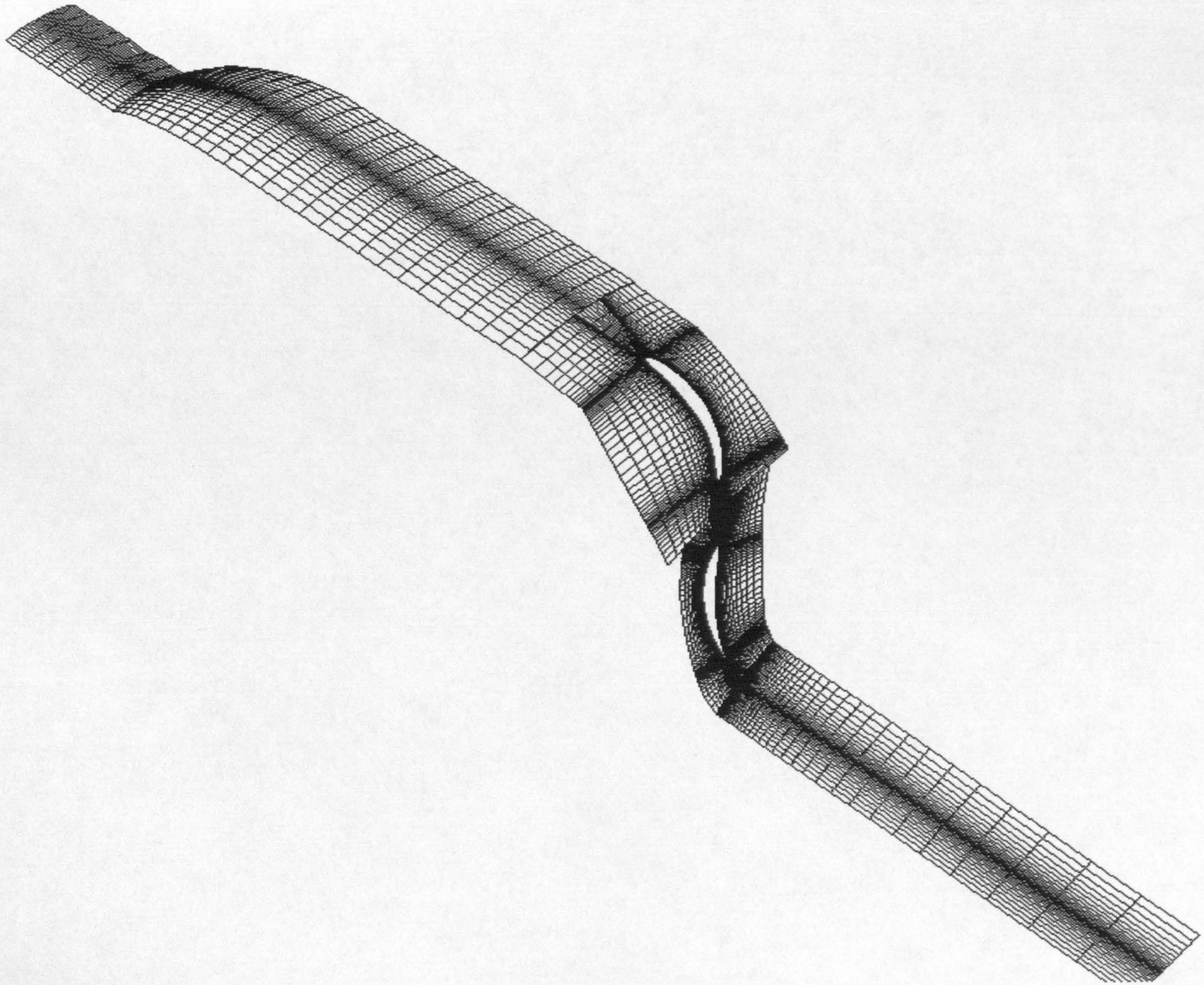

Figure 2-3 Mid span full grid

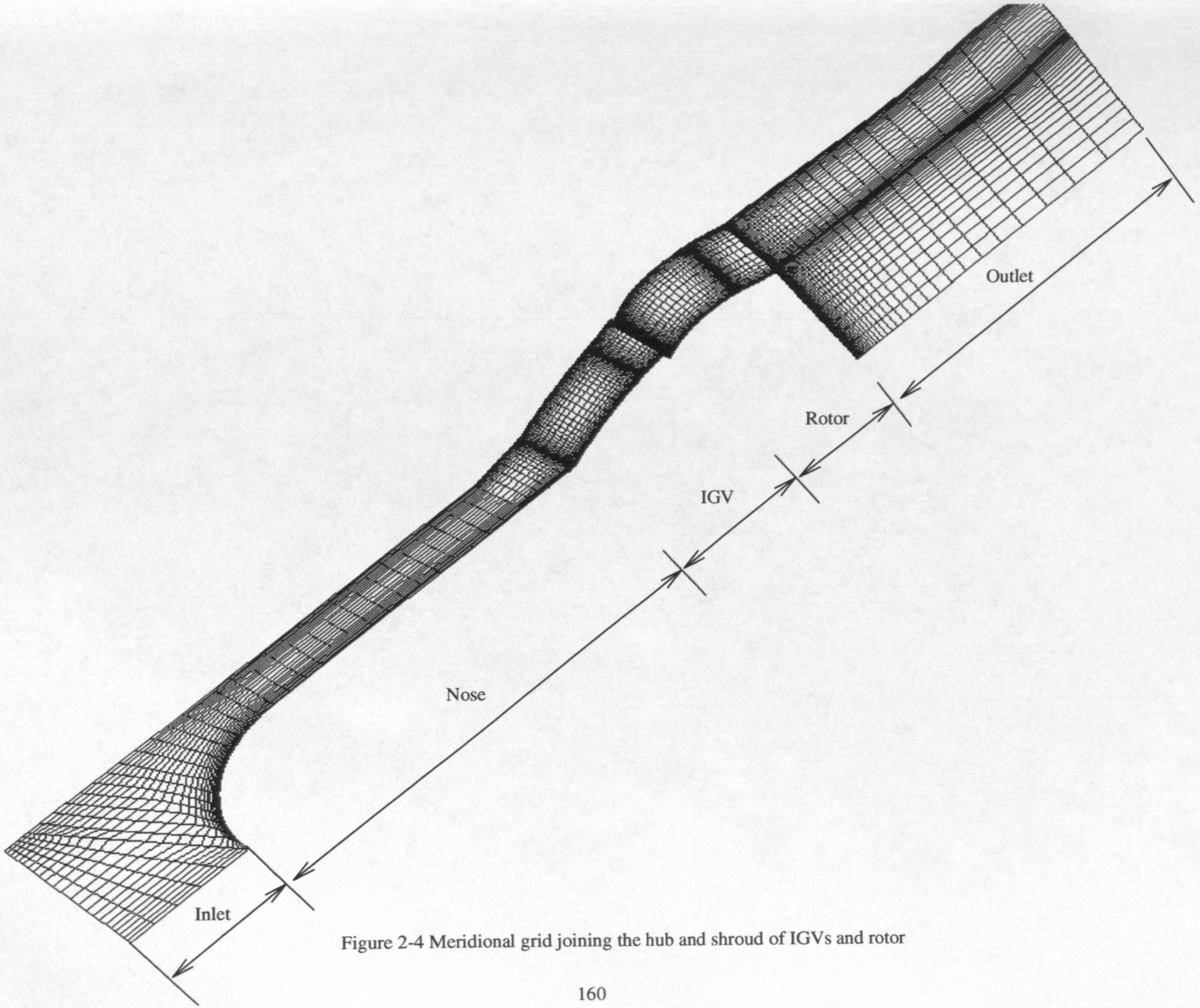


Figure 2-4 Meridional grid joining the hub and shroud of IGVs and rotor

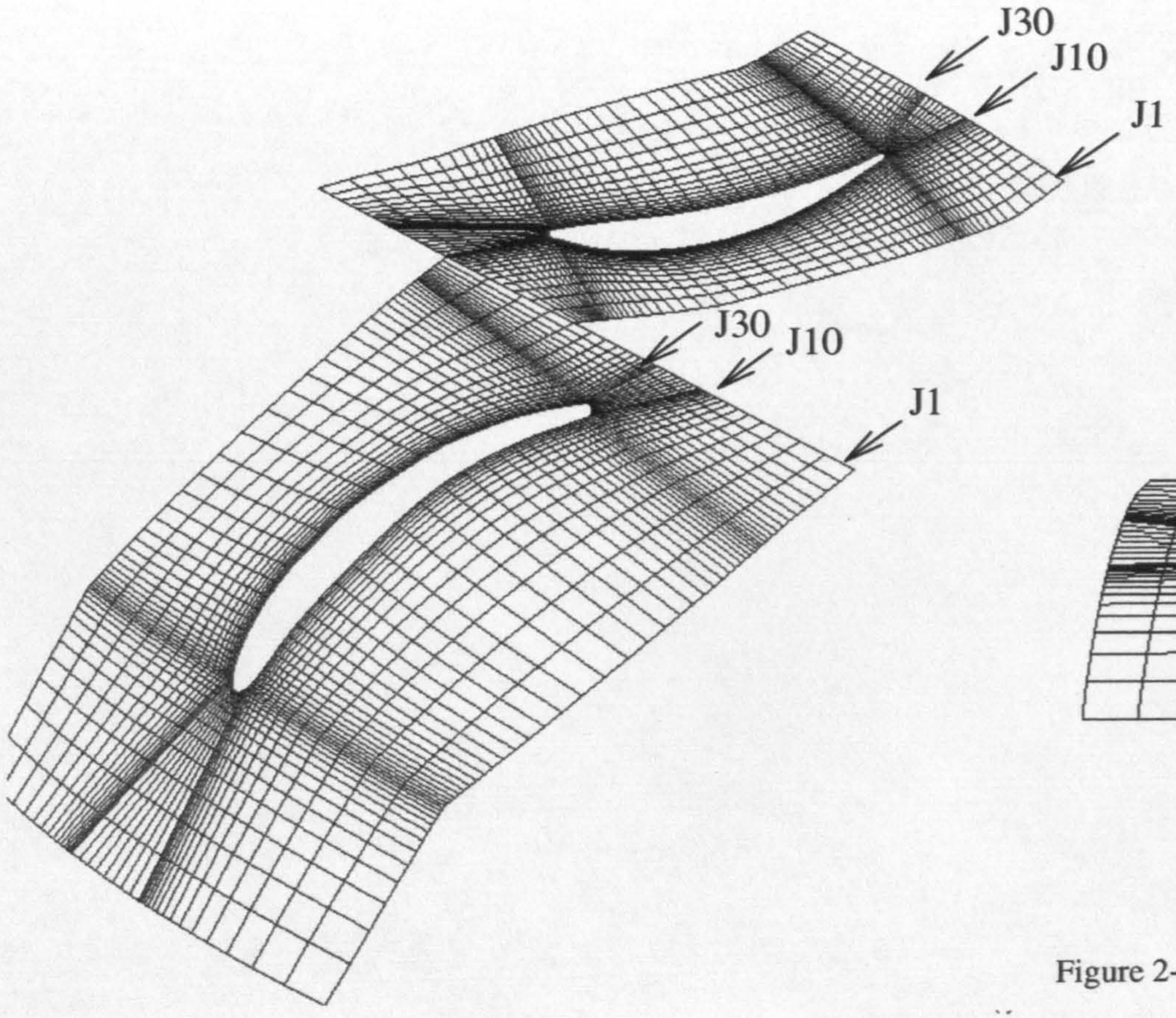


Figure 2-5 Mid span IGV - Rotor grids

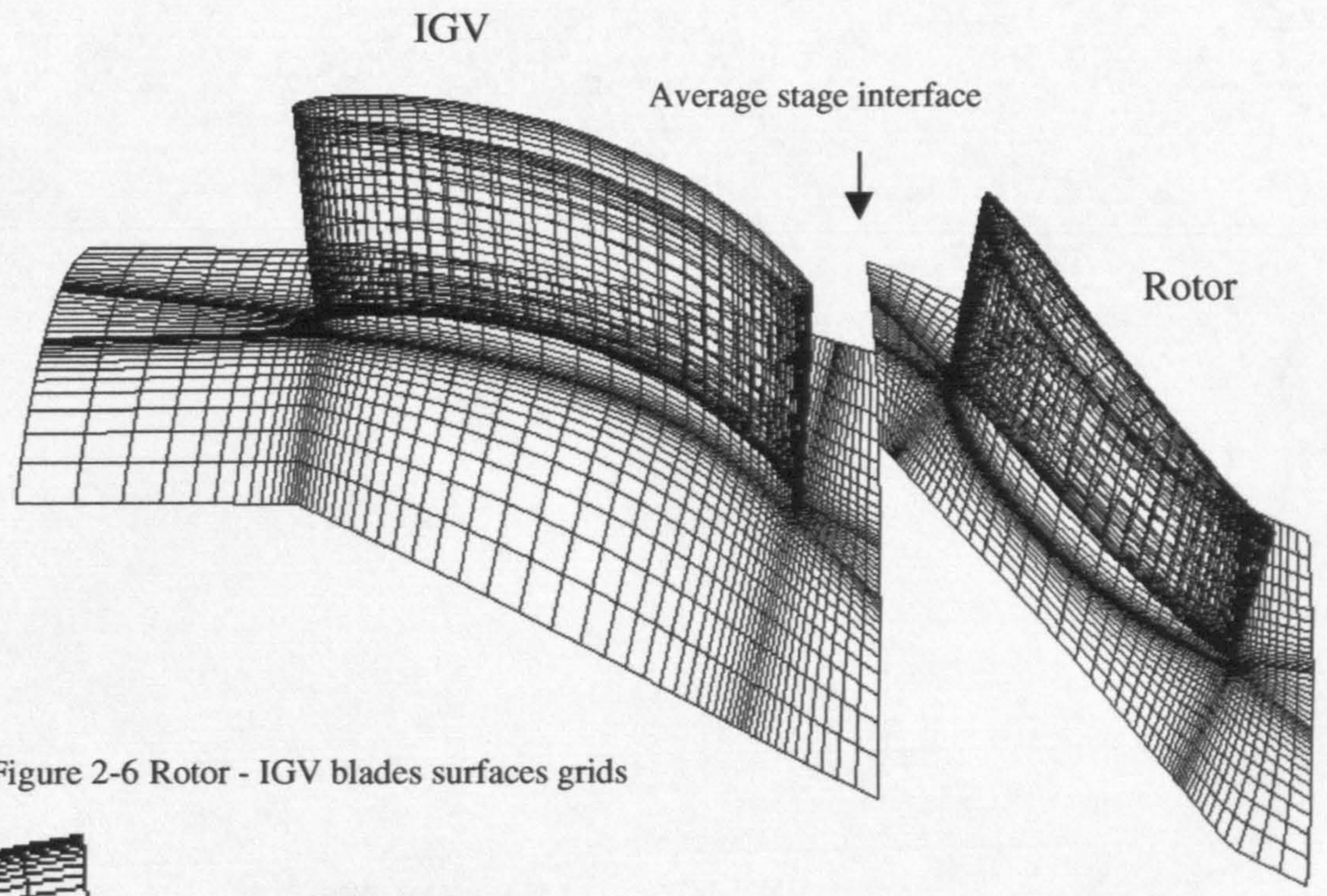


Figure 2-6 Rotor - IGV blades surfaces grids

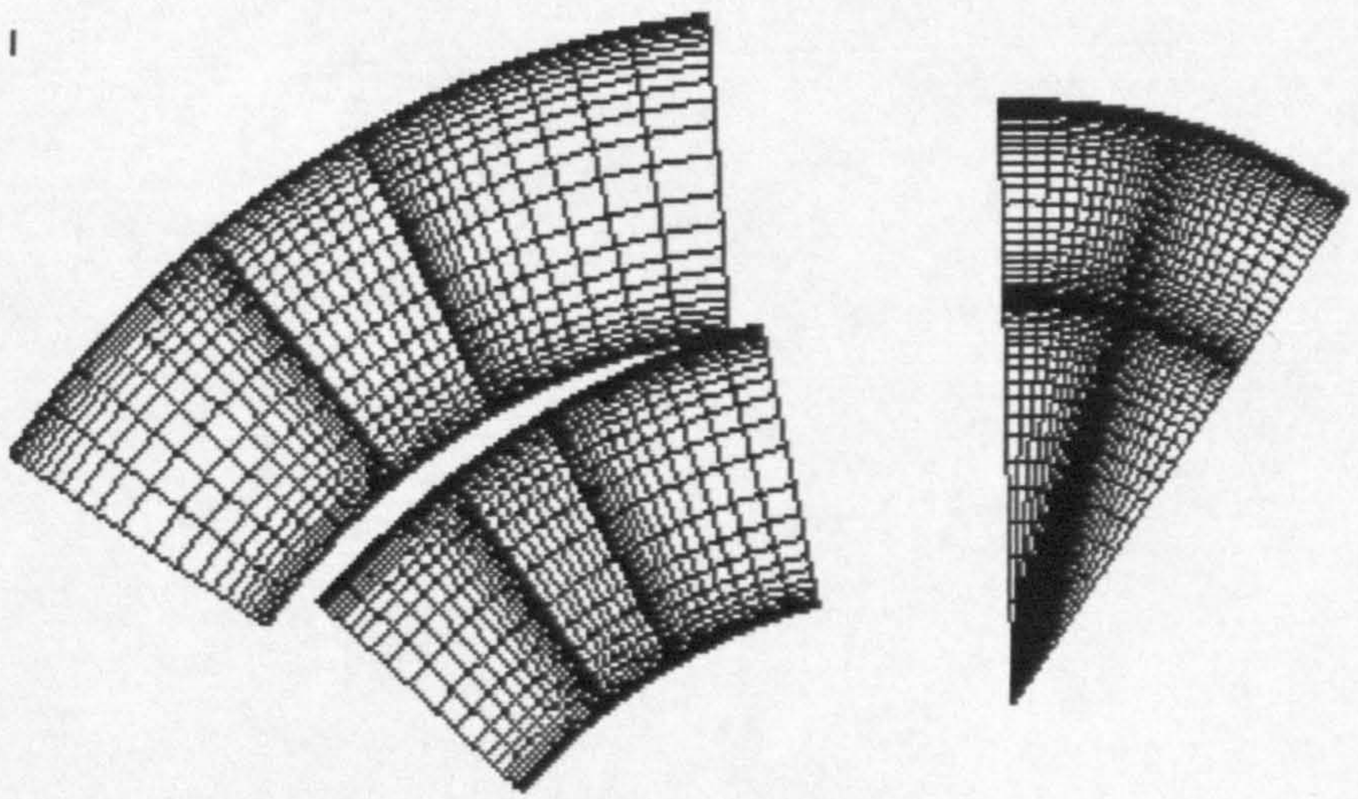

Figure 2-7 Hub to shroud IGV, Rotor and outlet cross section grids

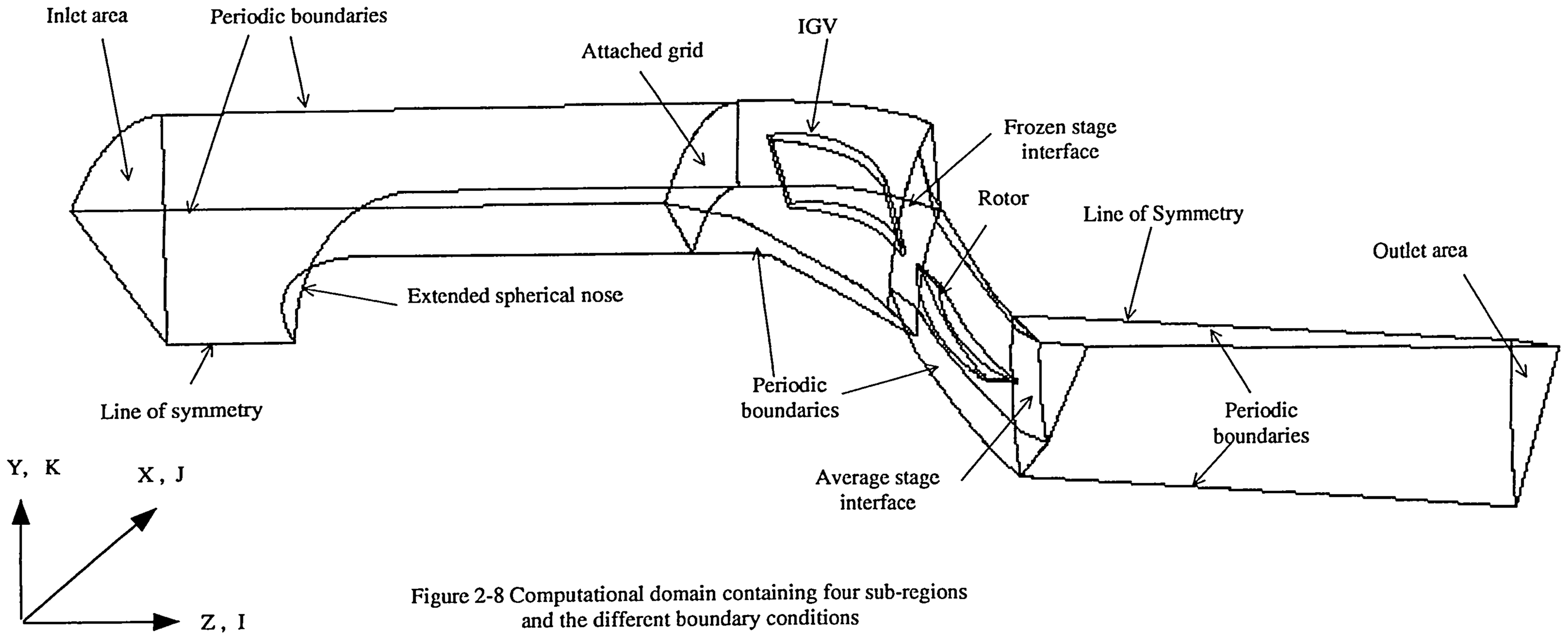


Figure 2-8 Computational domain containing four sub-regions and the different boundary conditions

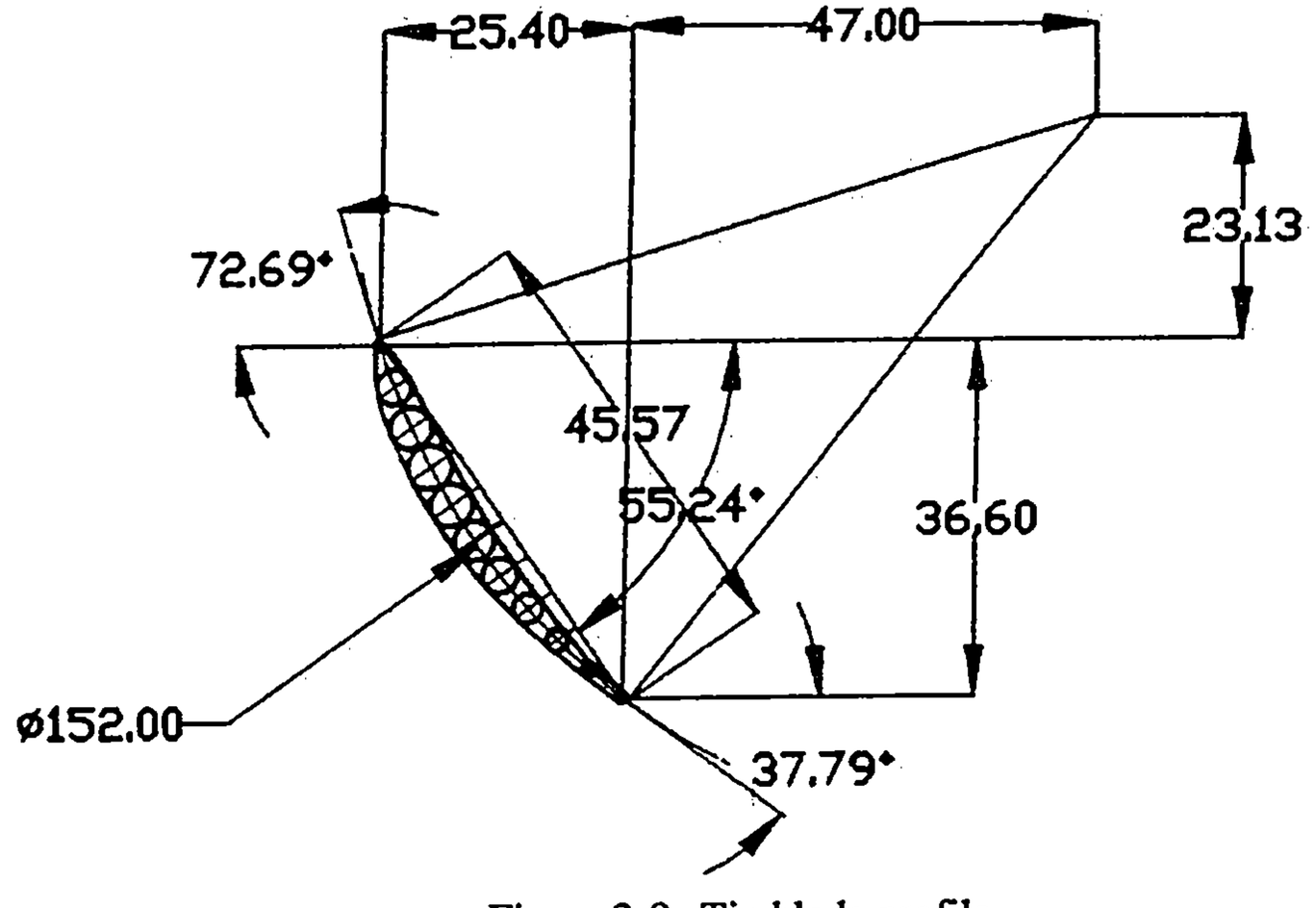


Figure 2-9a Tip blade profile

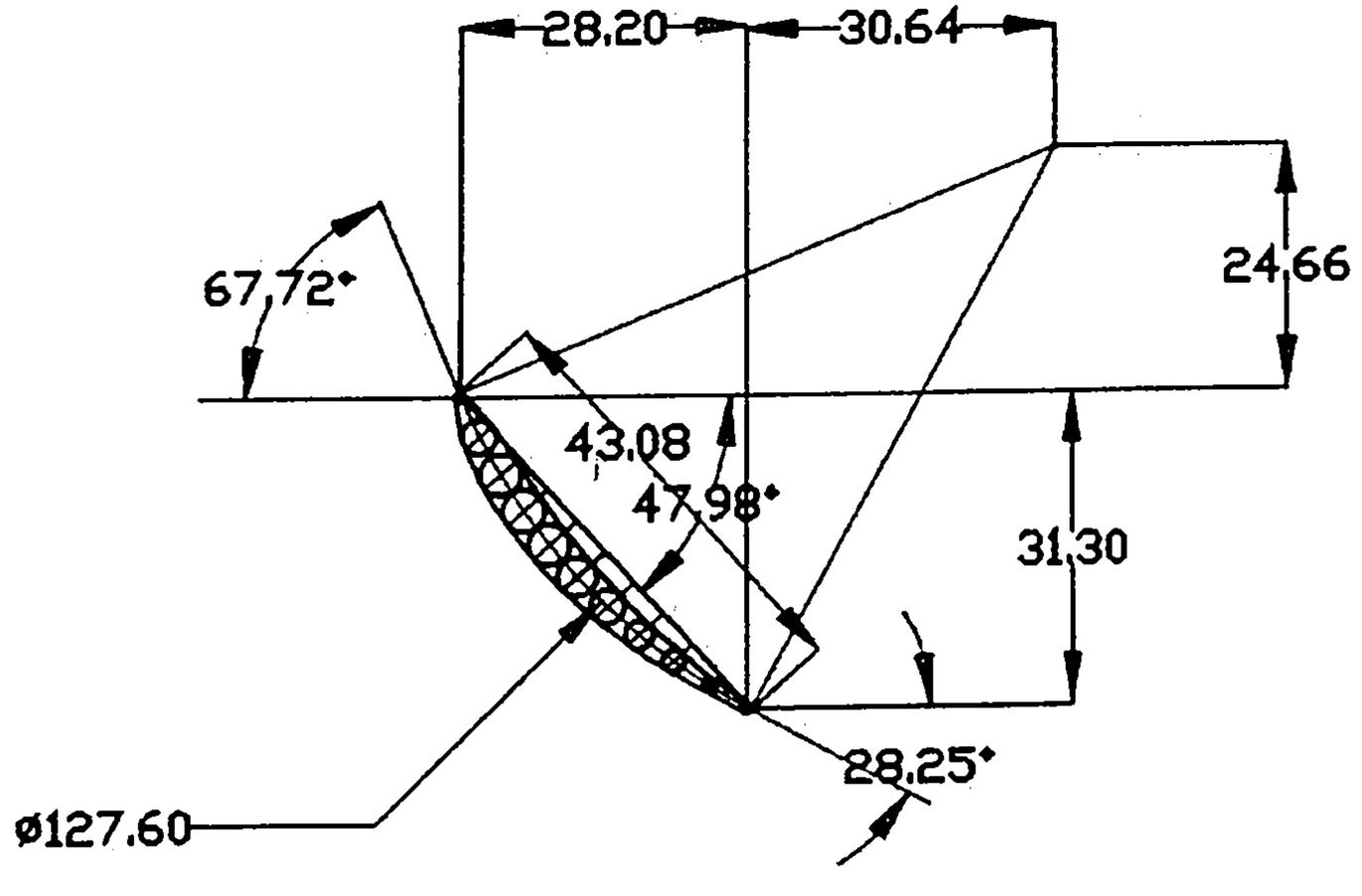


Figure 2-9b Root blade profile

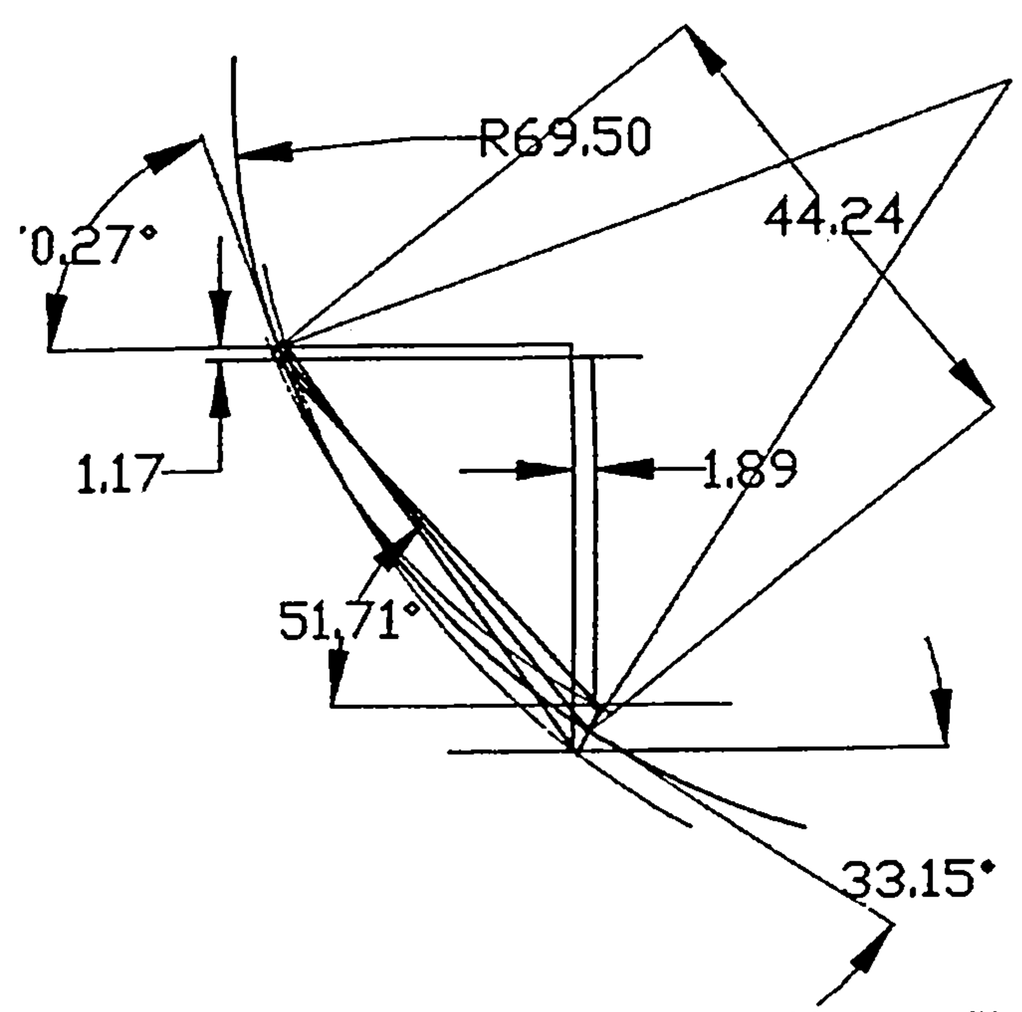


Figure 2-10 Generation of the mean blade profile

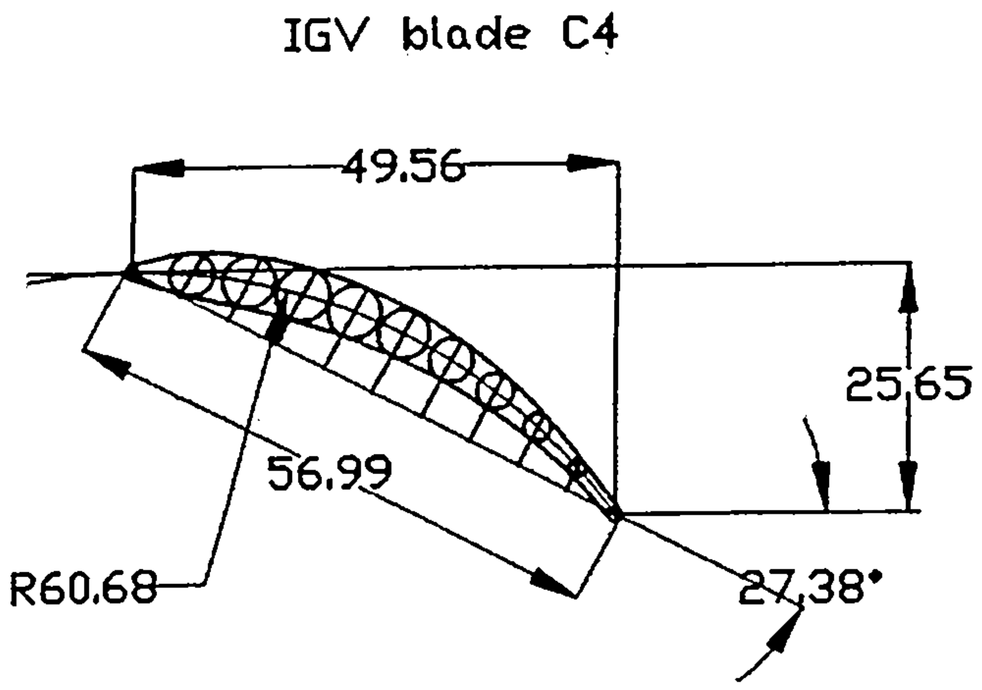


Figure 2-11a IGV C4 blade profile

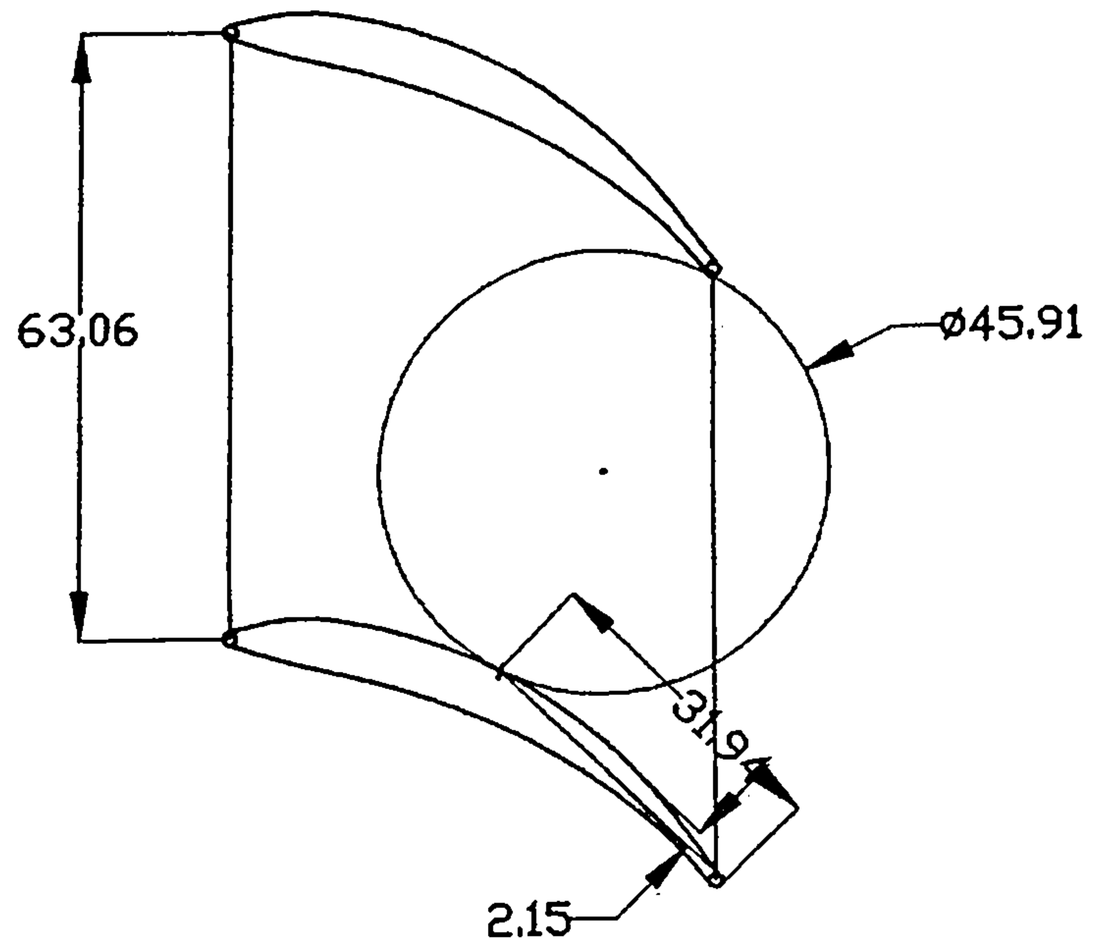


Figure 2-11b IGV cascade geometry

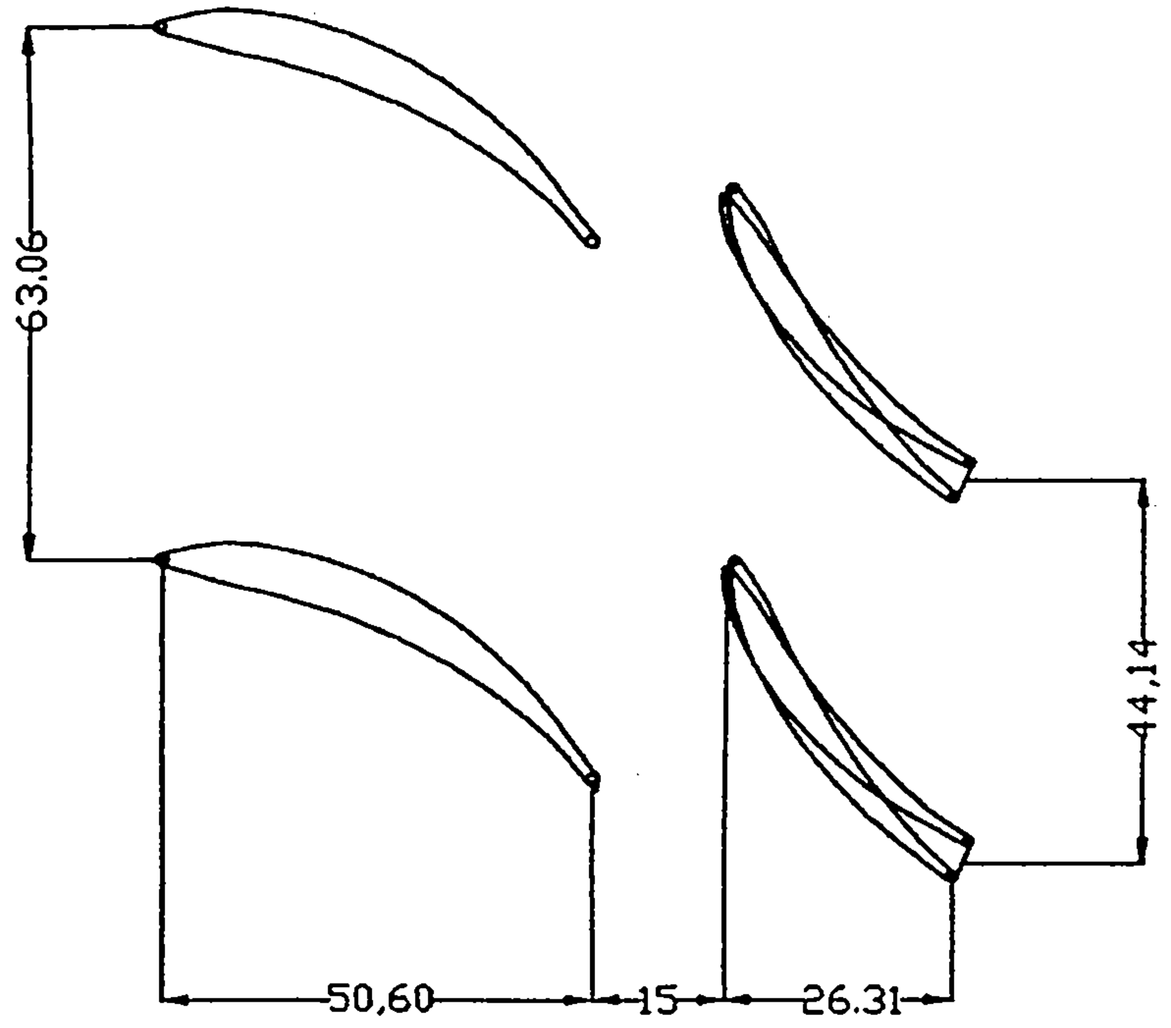


Figure 2-12 Axial fan stage geometrical spacing

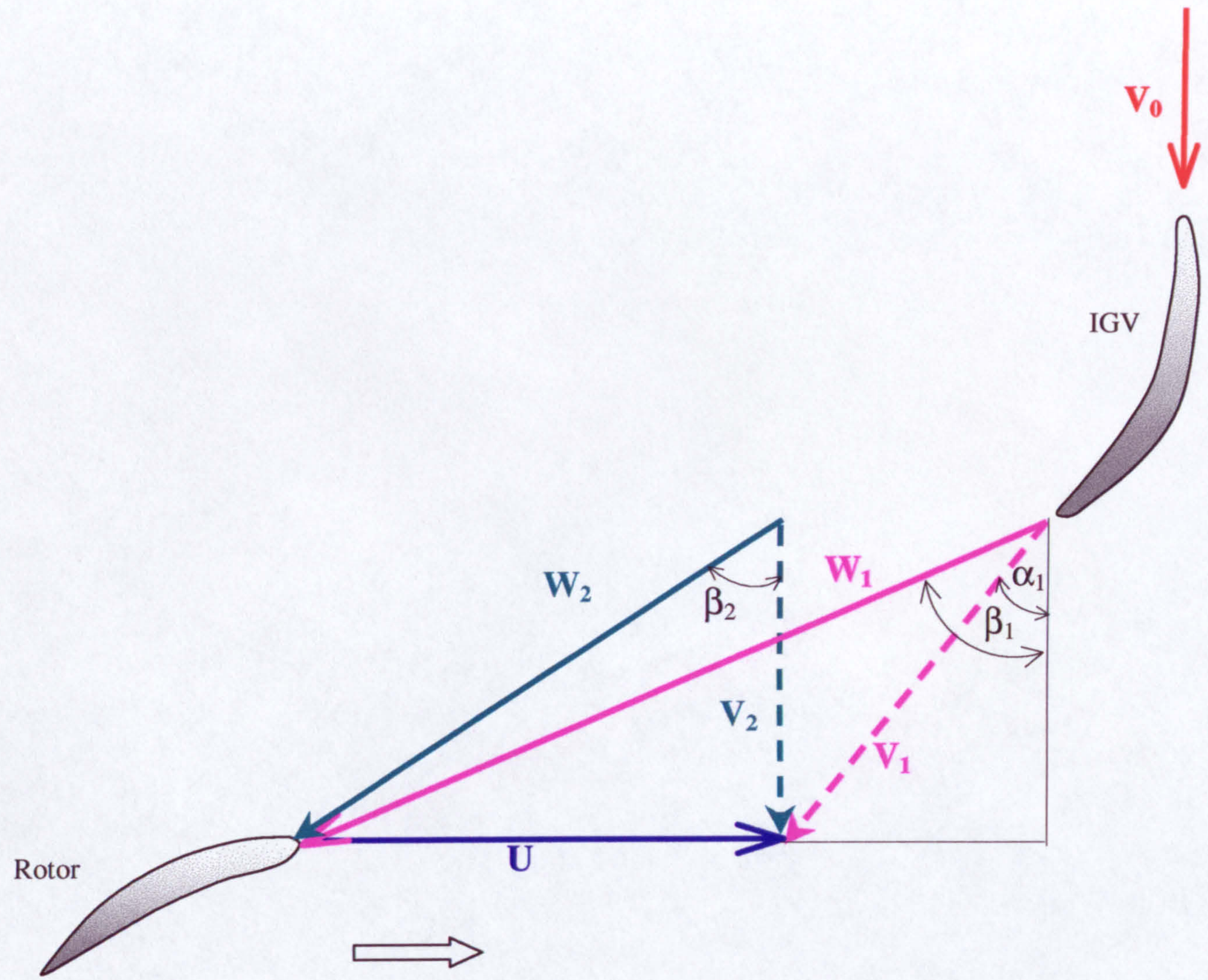


Figure 2-13 Velocity triangles of the axial fan stage at design condition

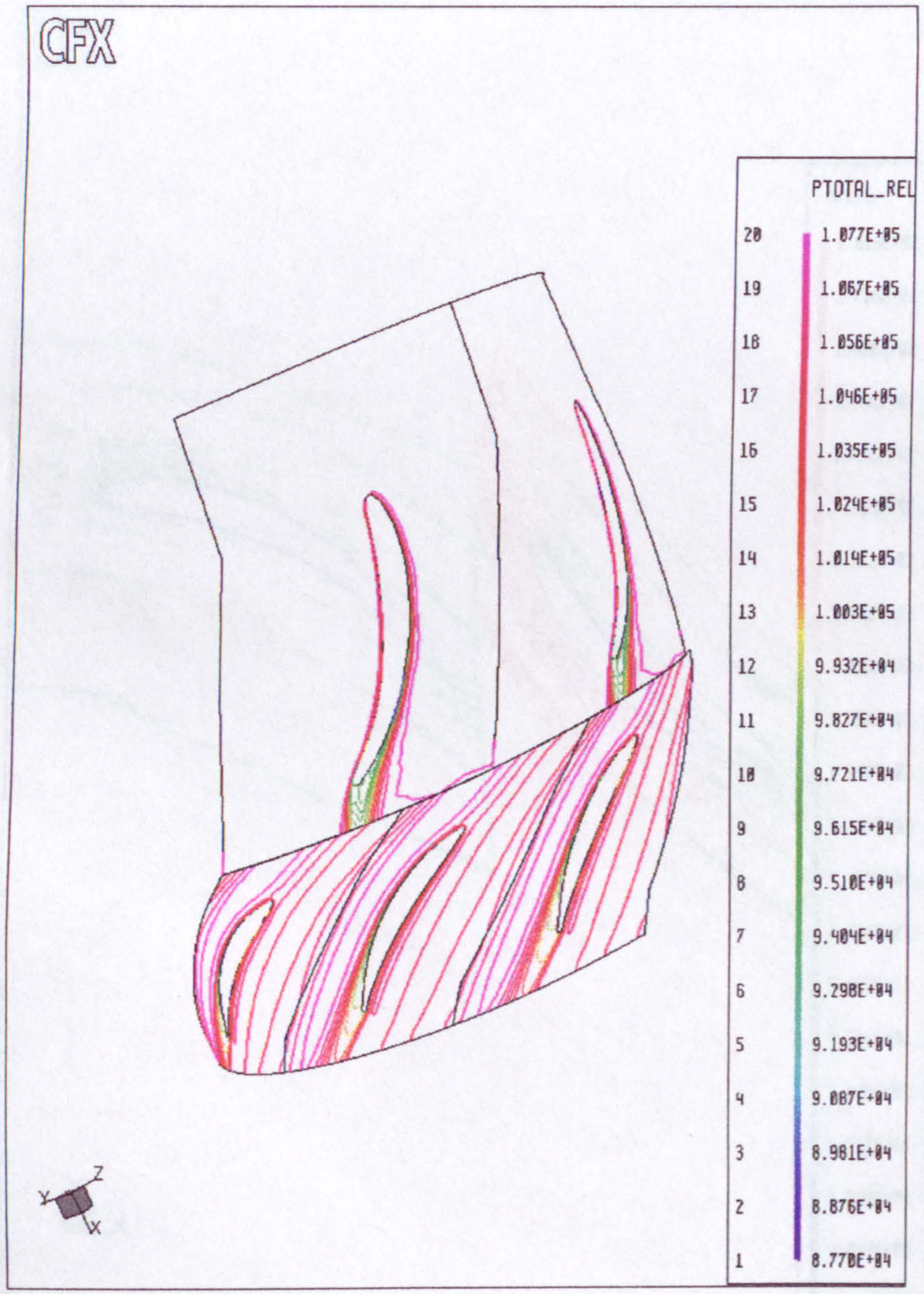


Figure 2-14 Relative total pressure at mid span near design point

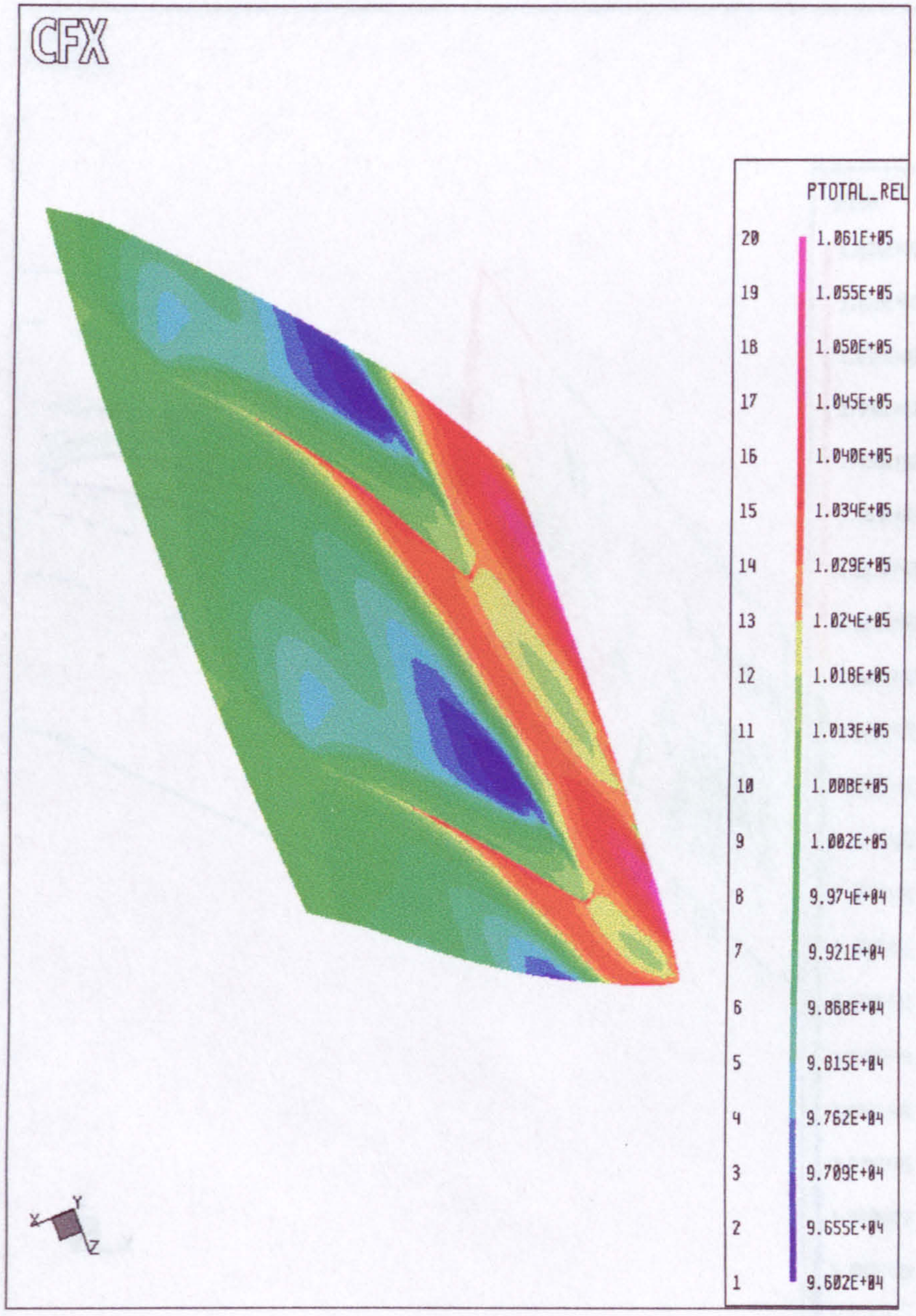


Figure 2-15 Relative total pressure in the tip clearance at design point

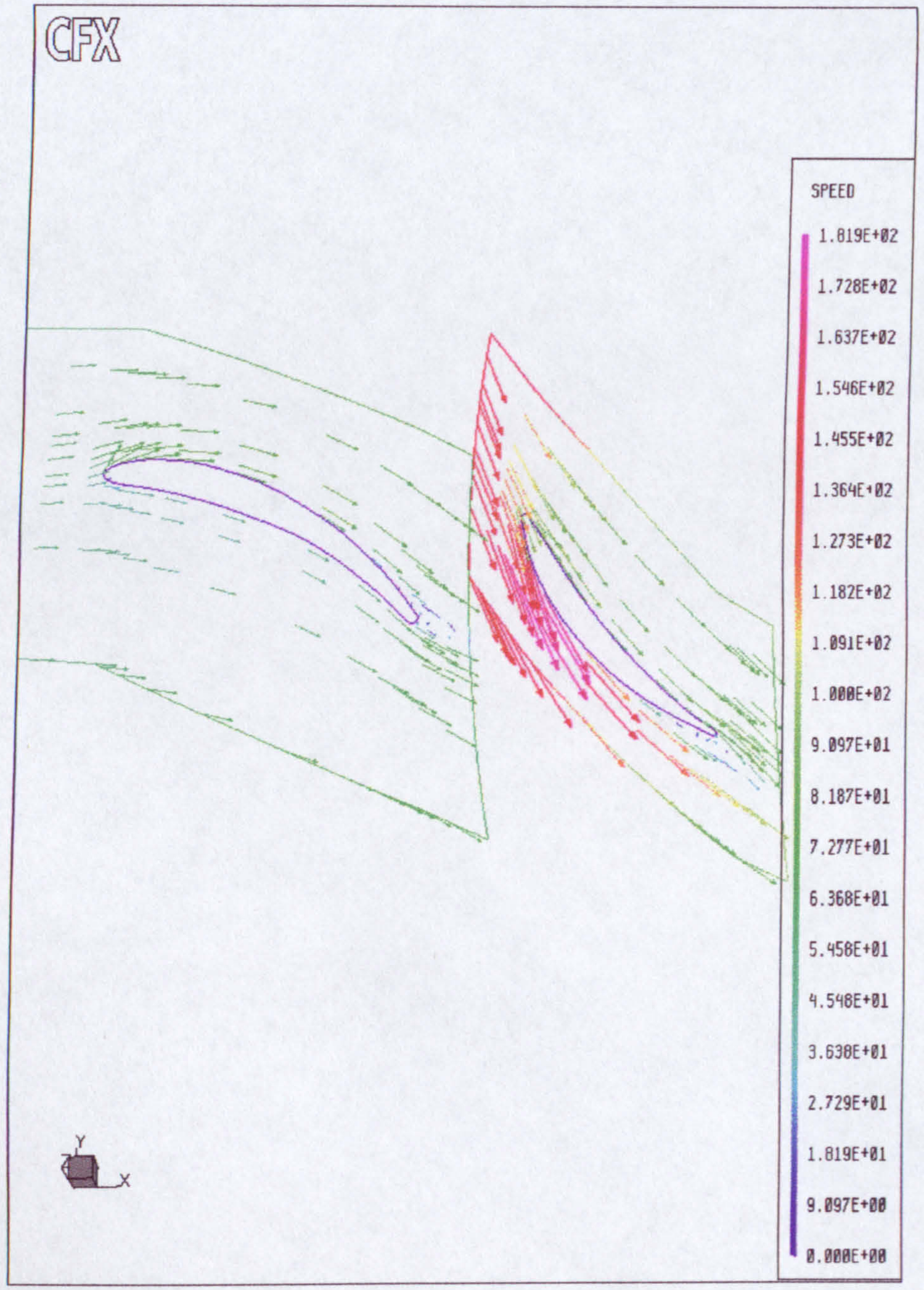


Figure 2-16 Velocity vectors at mid span near design point

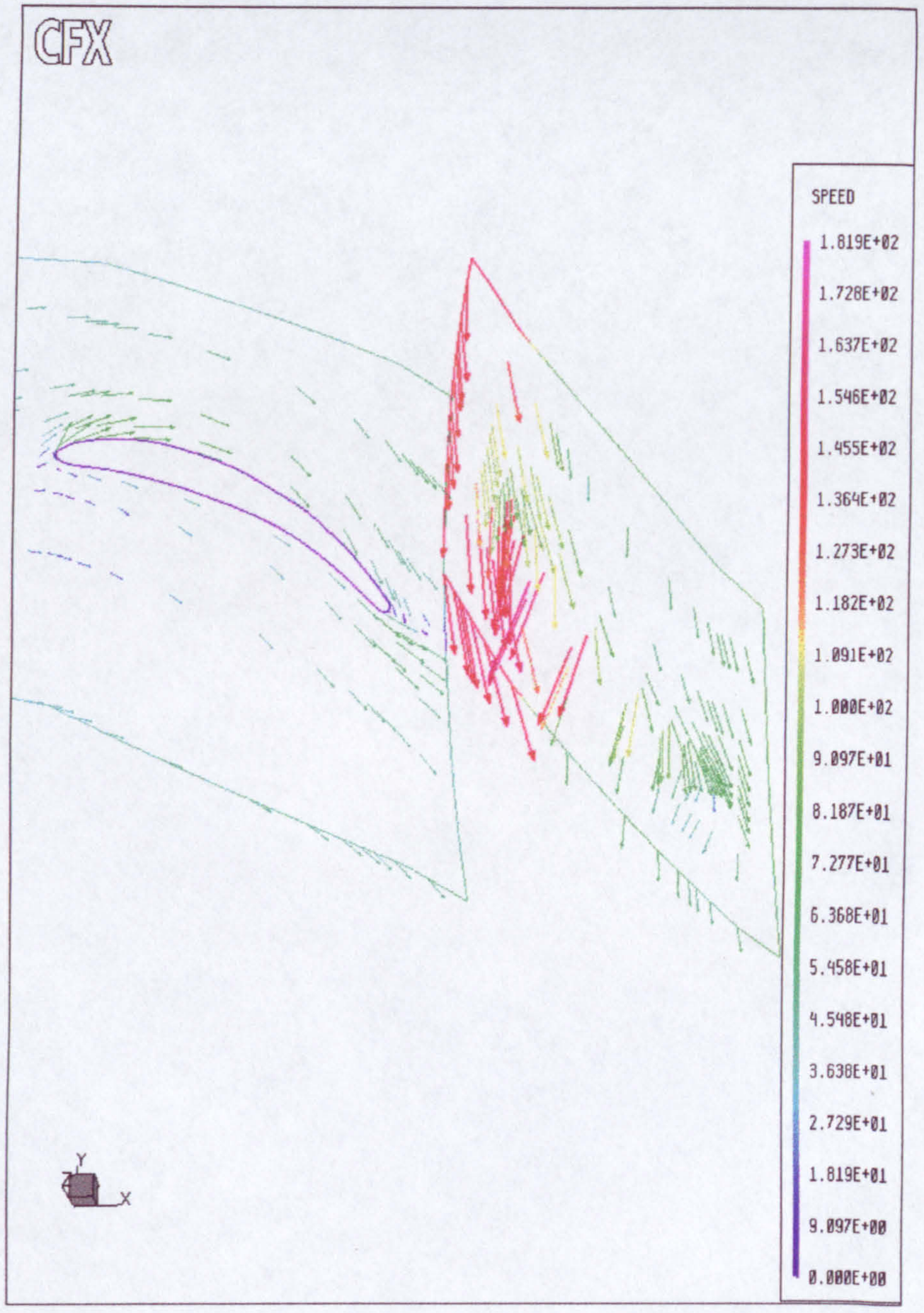


Figure 2-17 Velocity vectors in the tip clearance at the design point

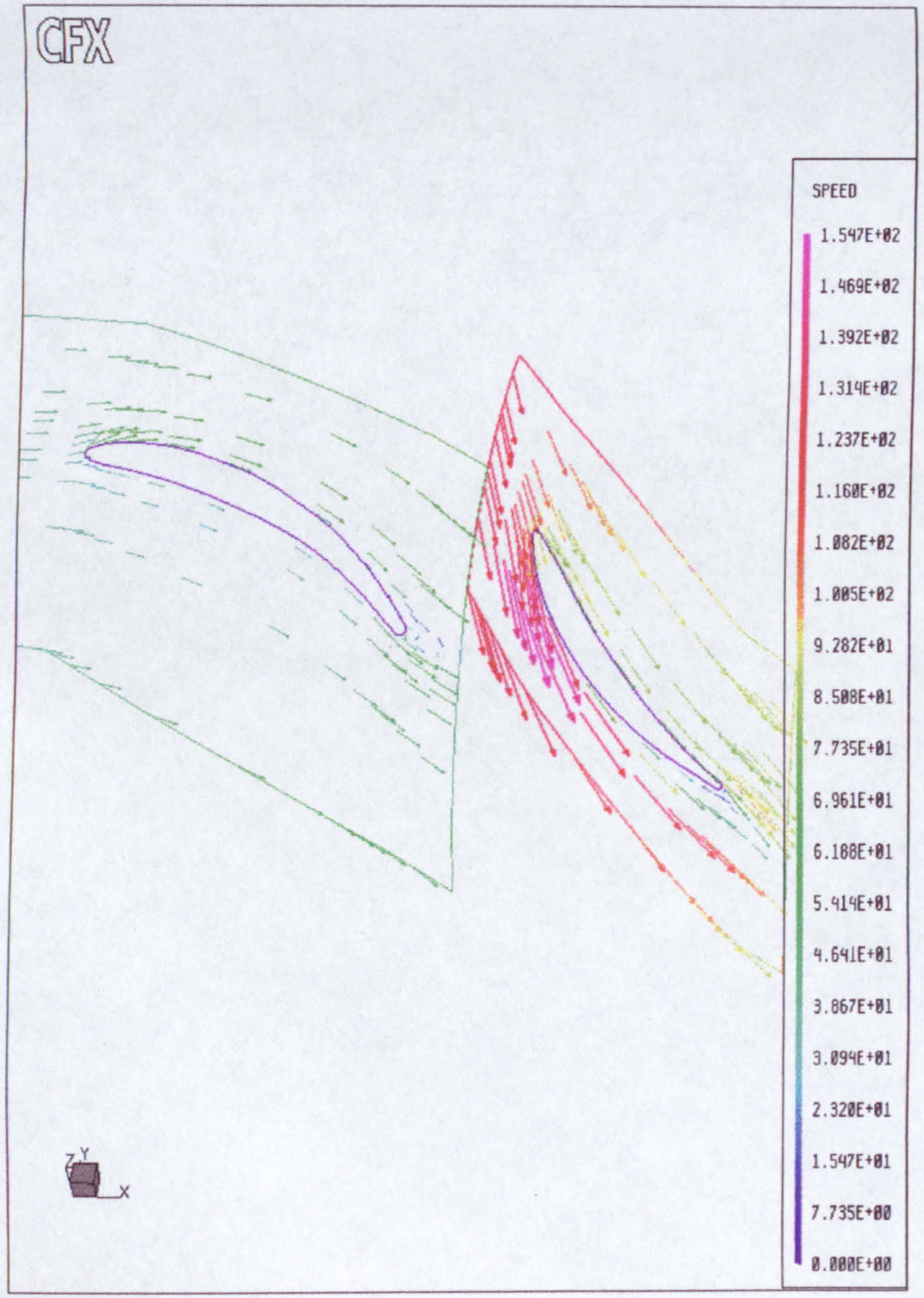


Figure 2-18 Velocity vectors at mid span at low mass flow

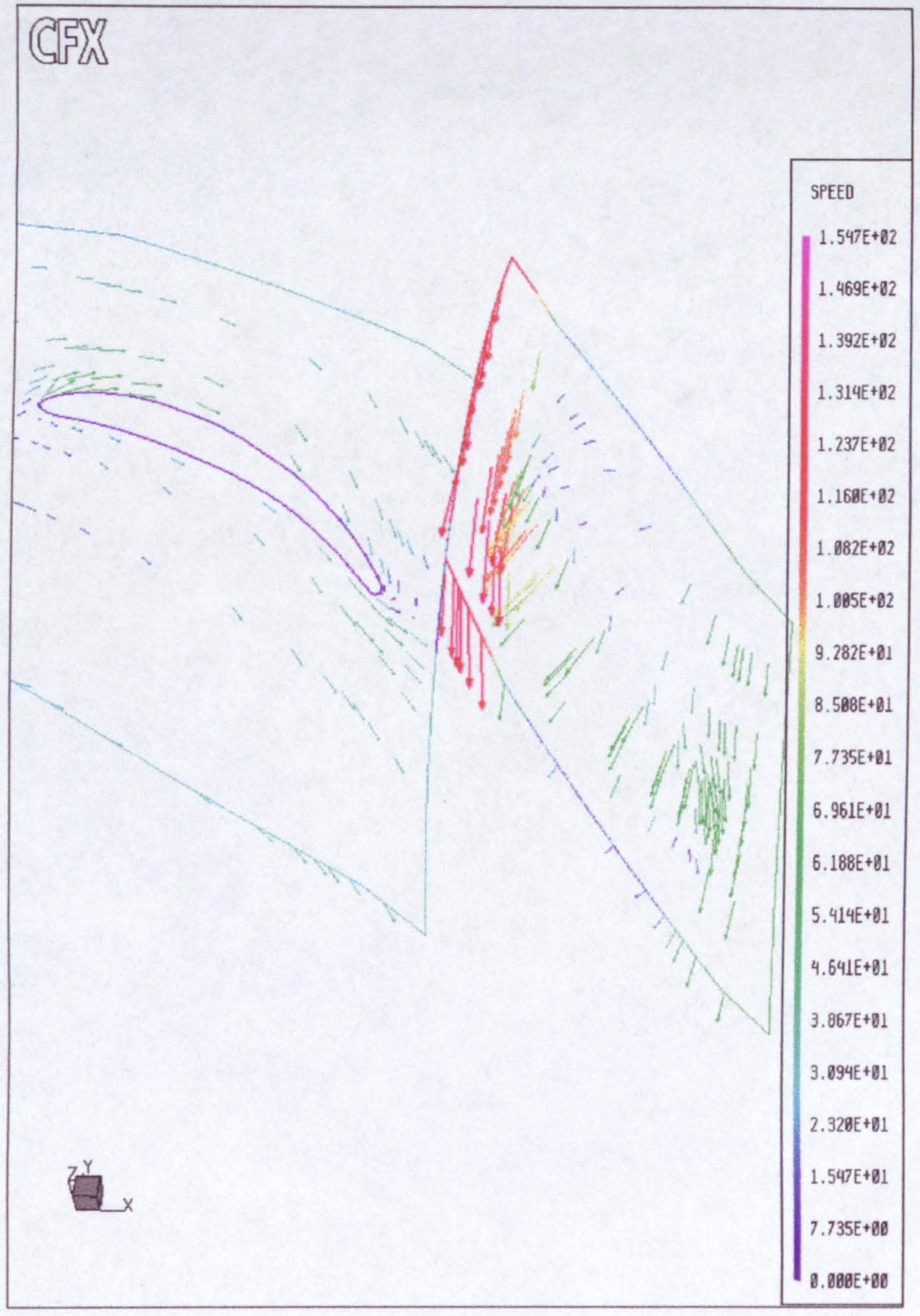


Figure 2-19 Velocity vectors in the tip clearance at low mass flow

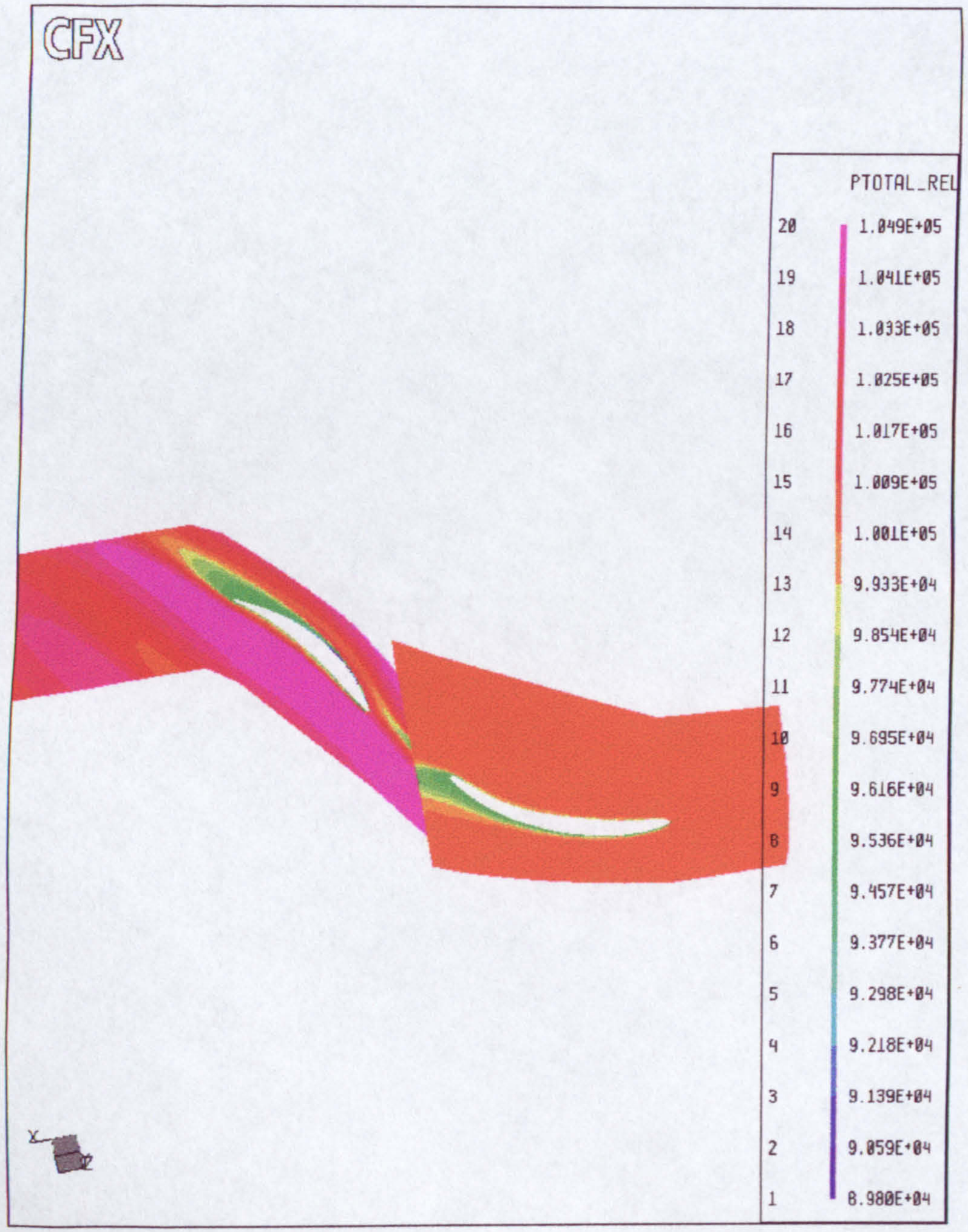


Figure 2-20 Relative total pressure at mid span near design point rotor in the wake of IGV

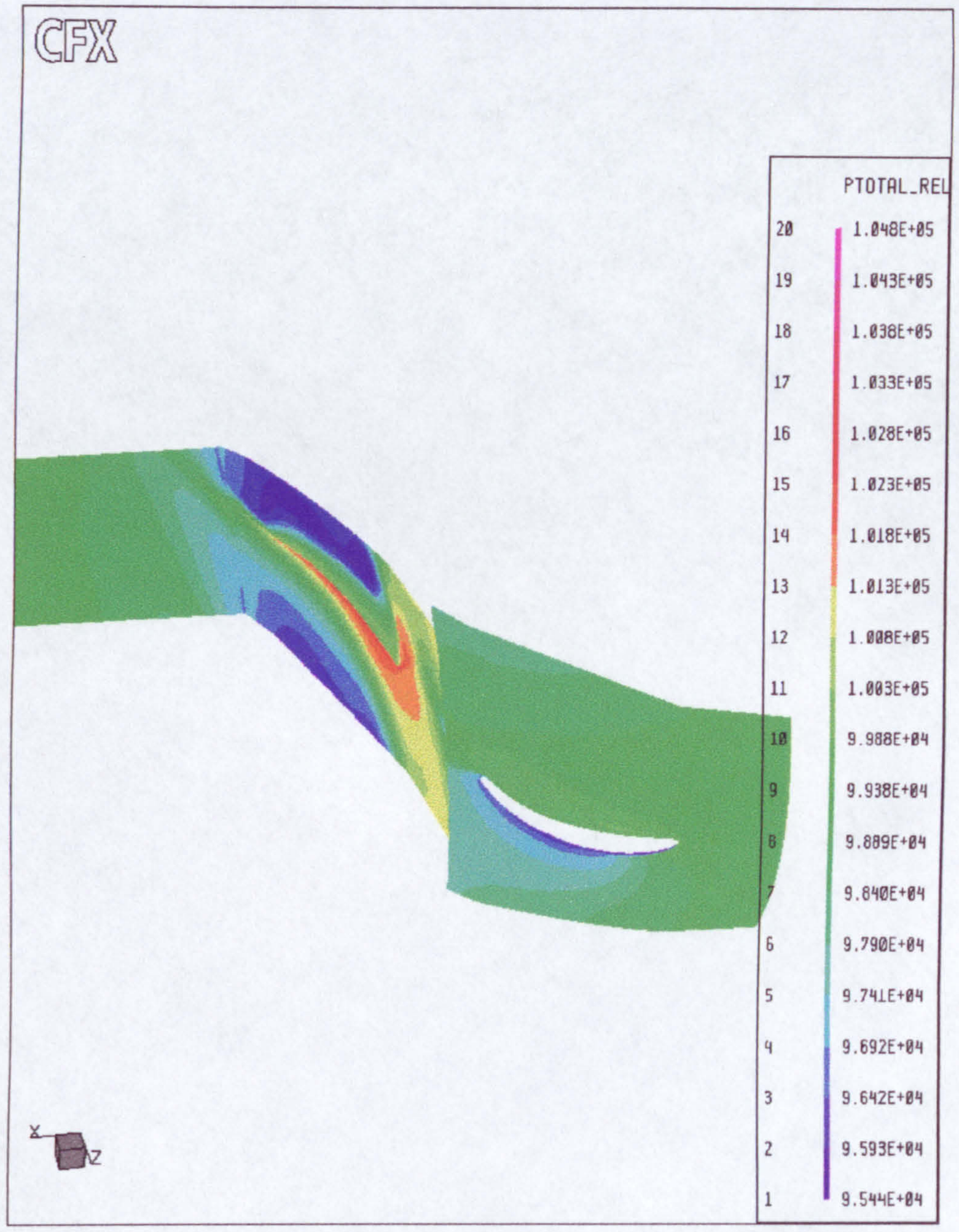


Figure 2-21 Relative total pressure in tip clearance near design point rotor in the wake of IGV

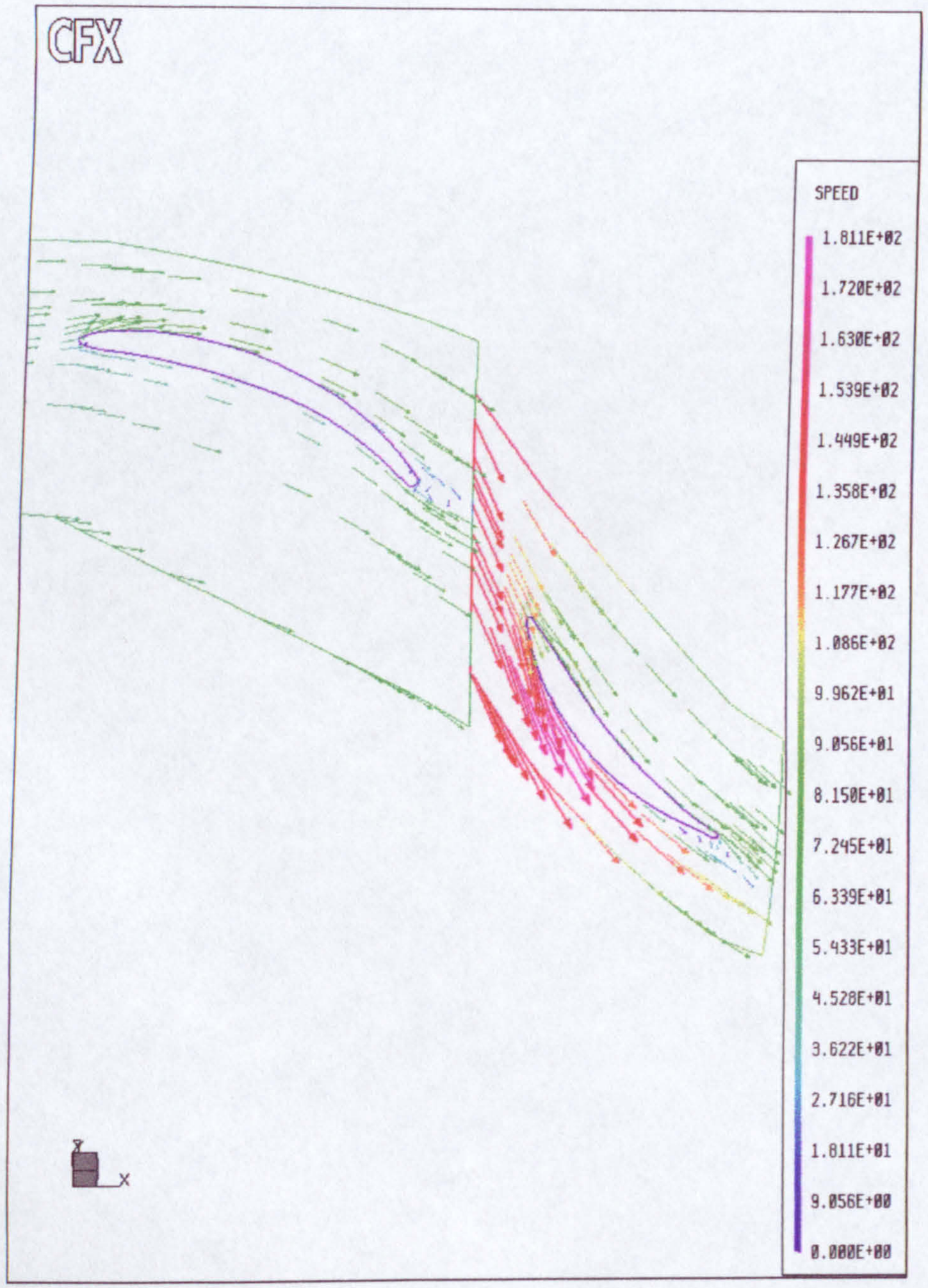


Figure 2-22 Velocity vectors at mid span near design, rotor in the wake of IGV using frozen interface

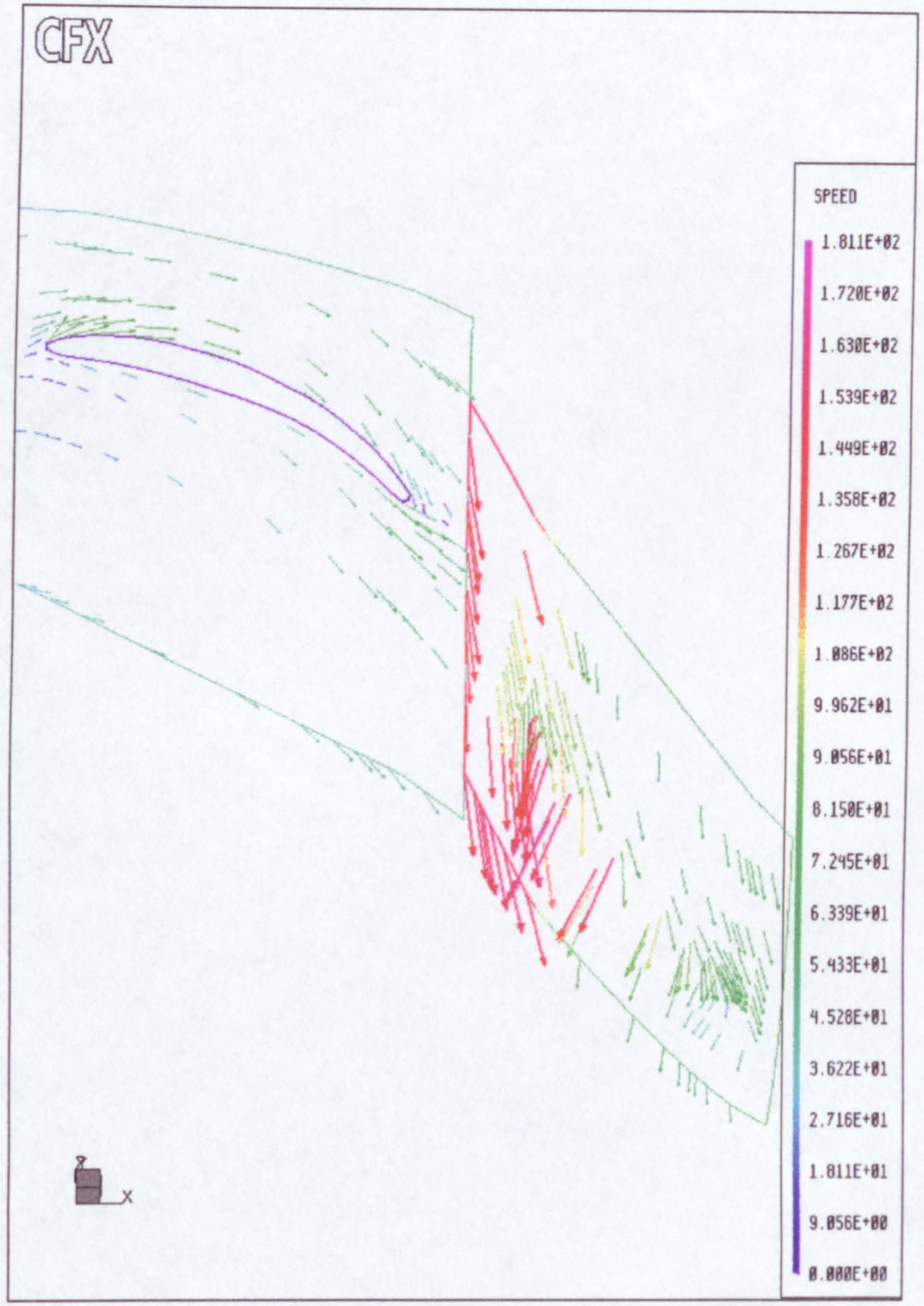


Figure 2-23 Velocity vectors in the tip clearance near design, rotor in the wake of IGV using frozen interface

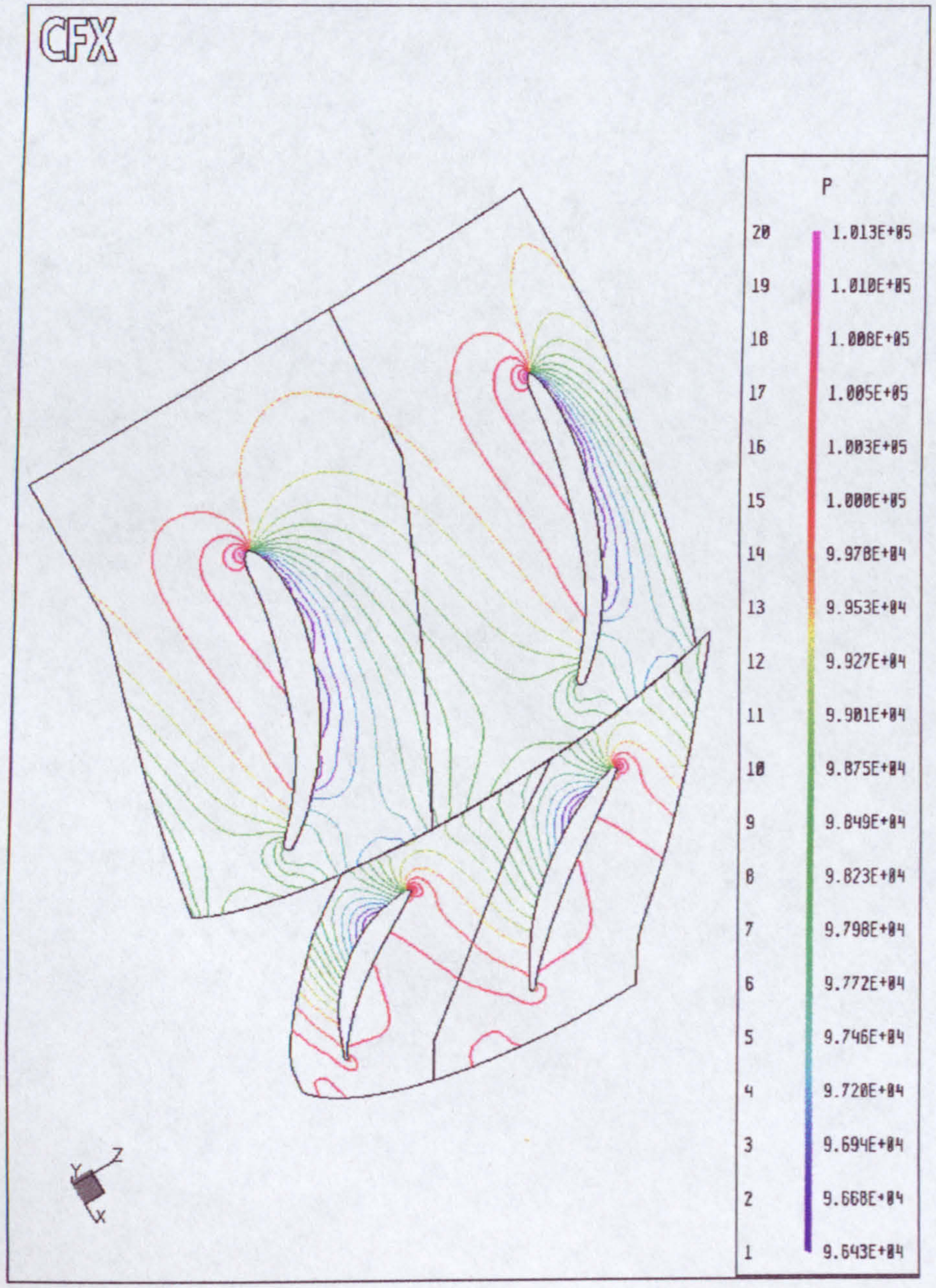


Figure 2-24 Static pressure at mid span near design point

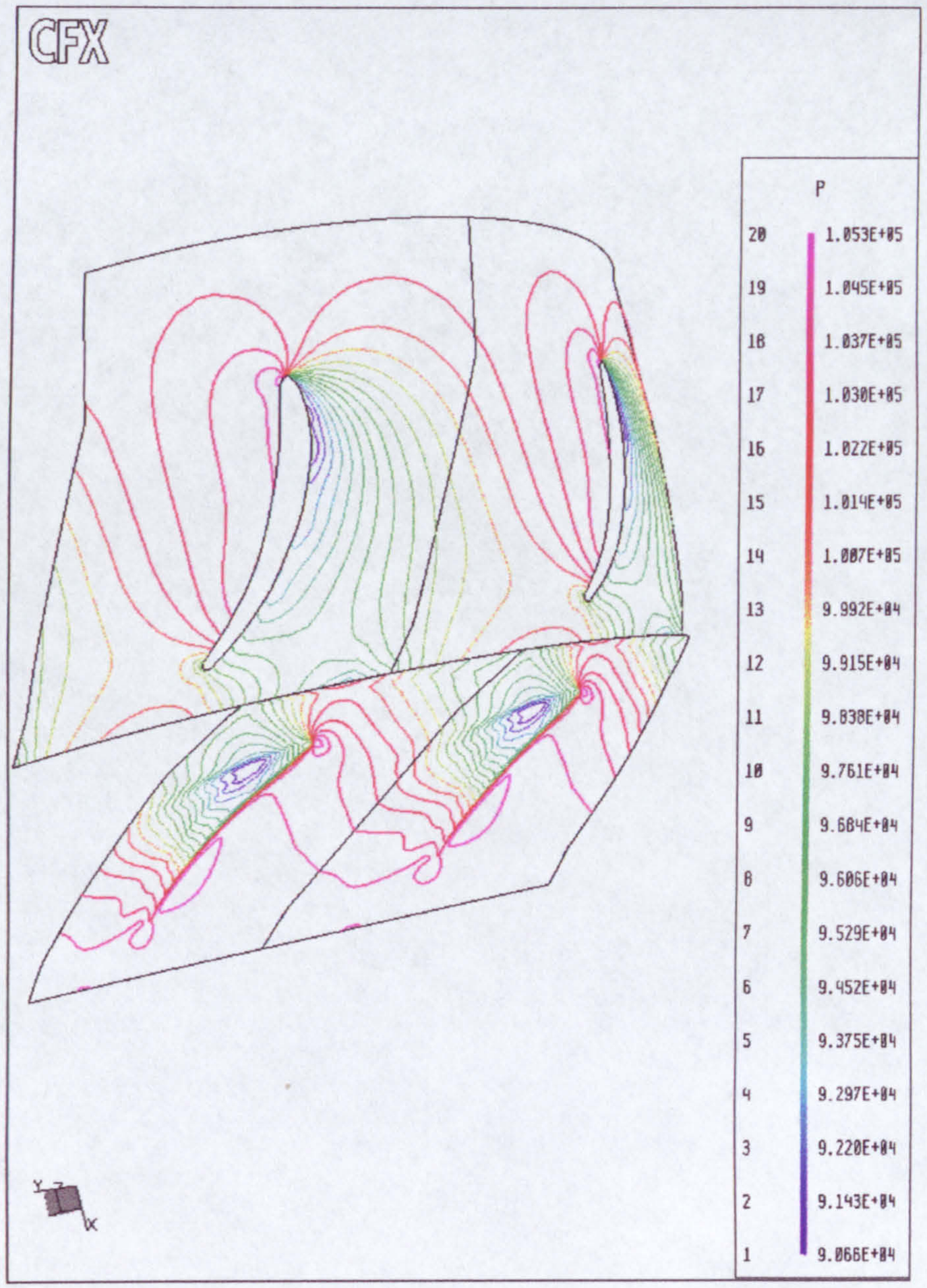


Figure 2-25 Static pressure in the tip clearance near design point

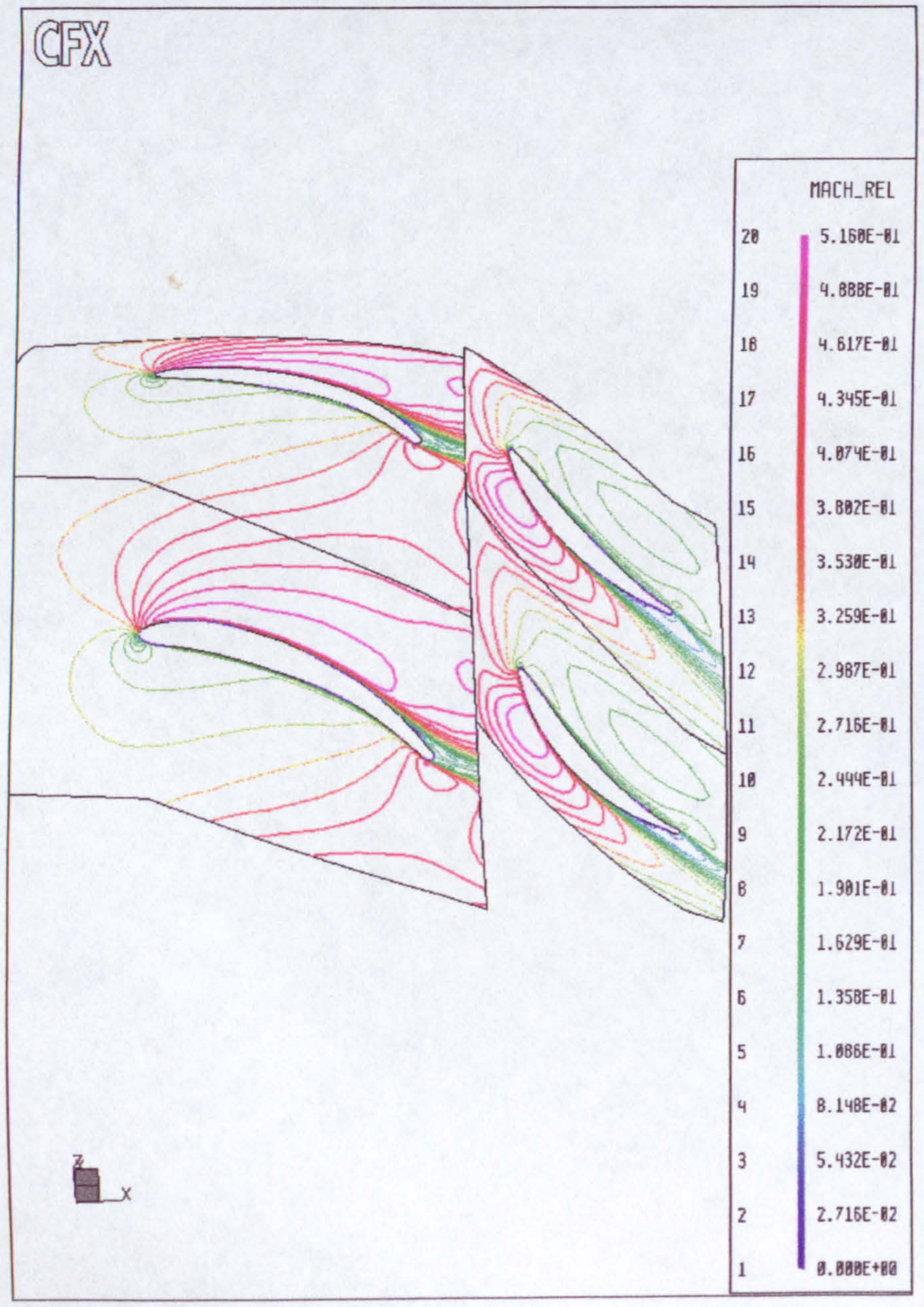


Figure 2-26 Relative Mach number at mid span near design point

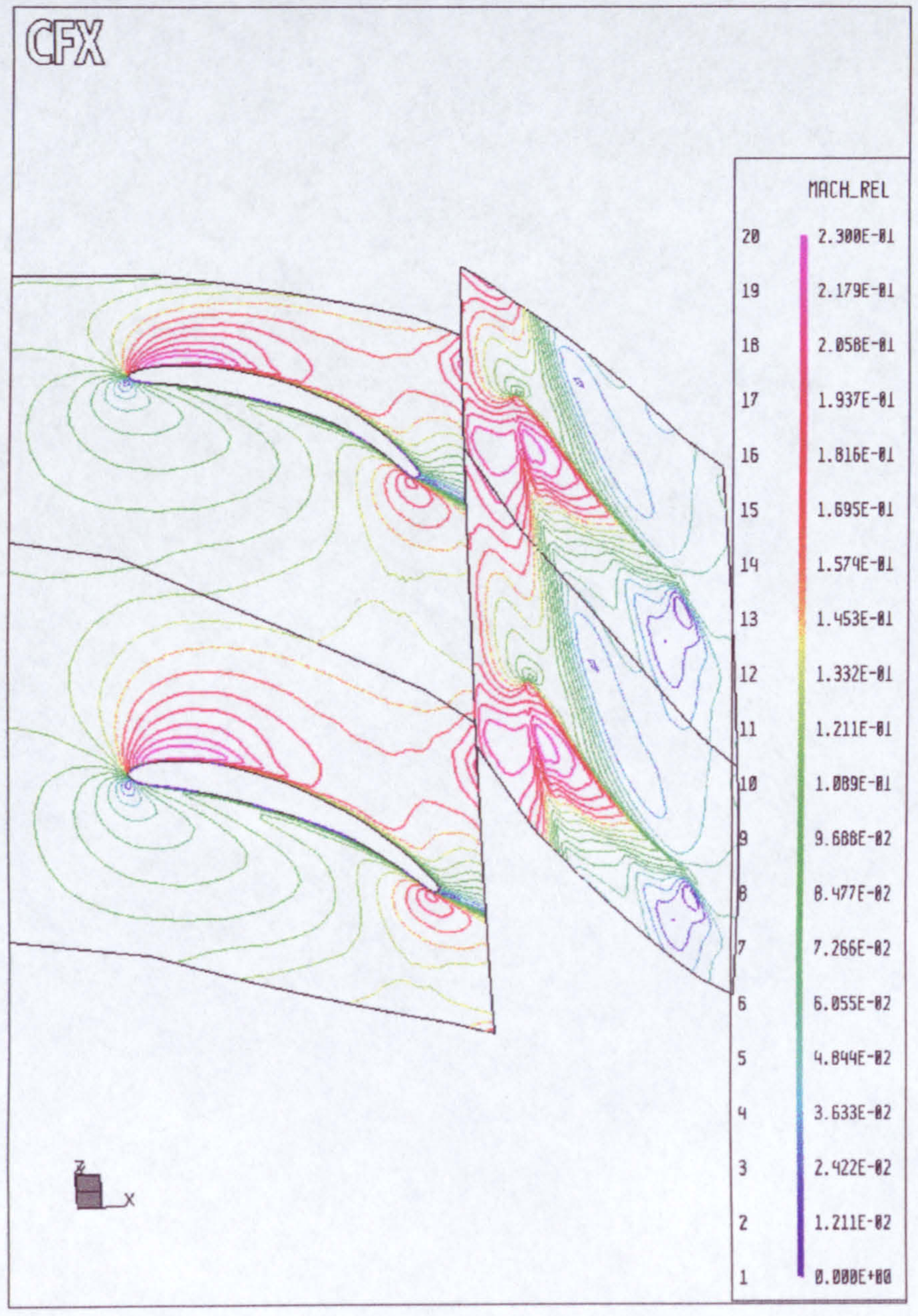


Figure 2-27 Relative Mach number in the tip clearance near design point

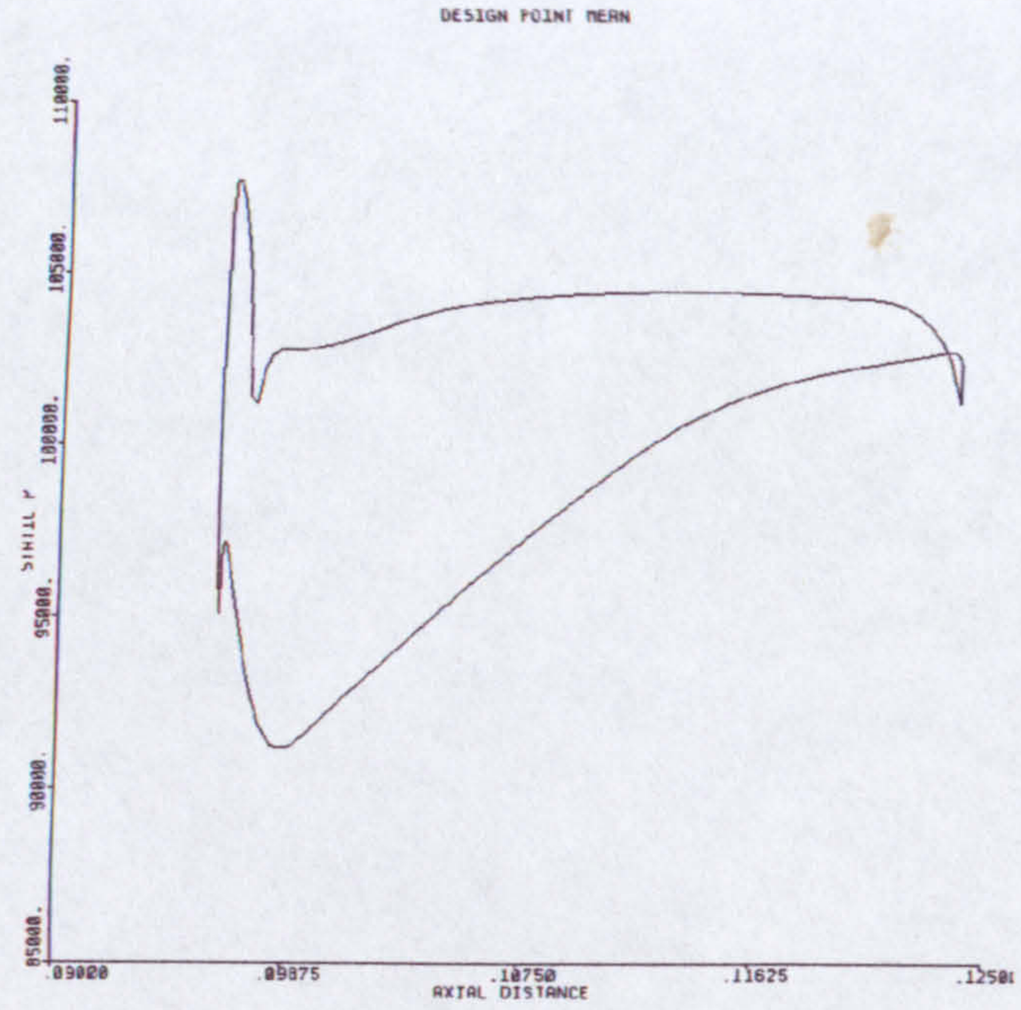


Figure 2-28 Pressure around rotor blade at mid span near design

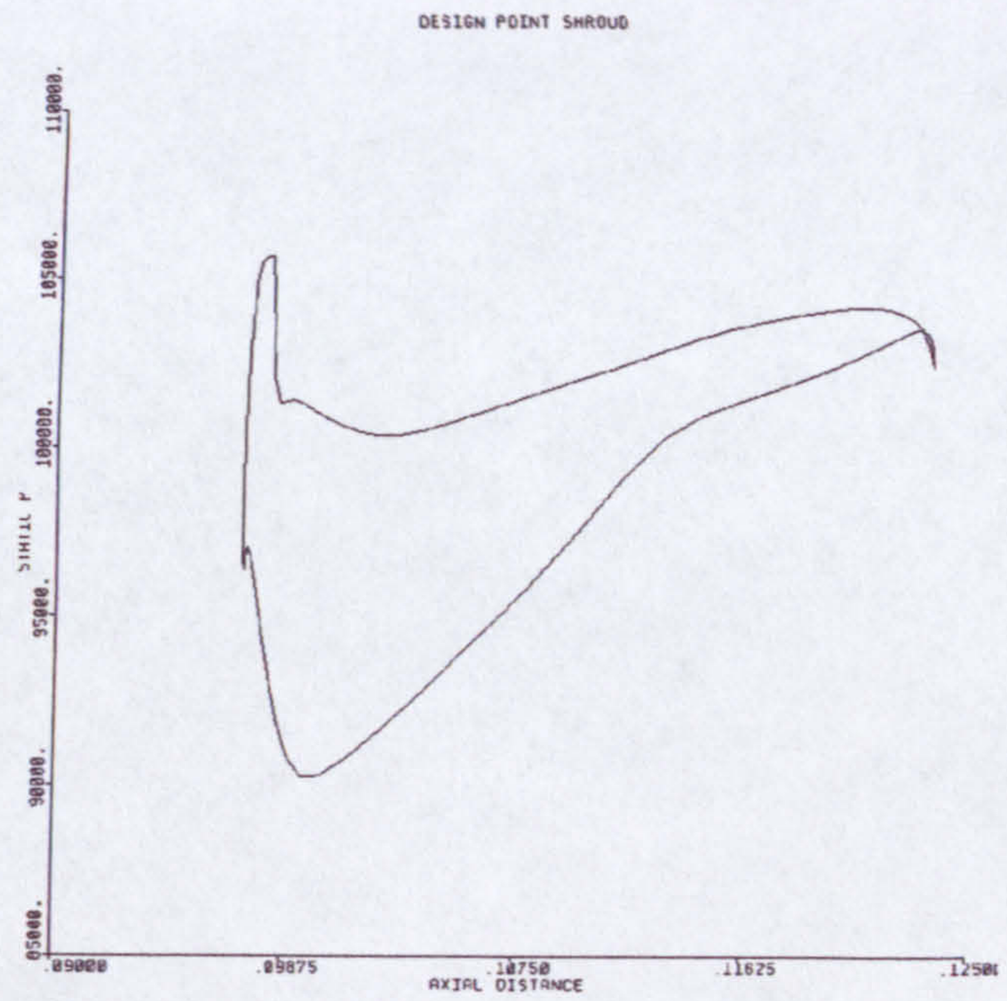


Figure 2-29 Pressure around rotor blade near shroud at design

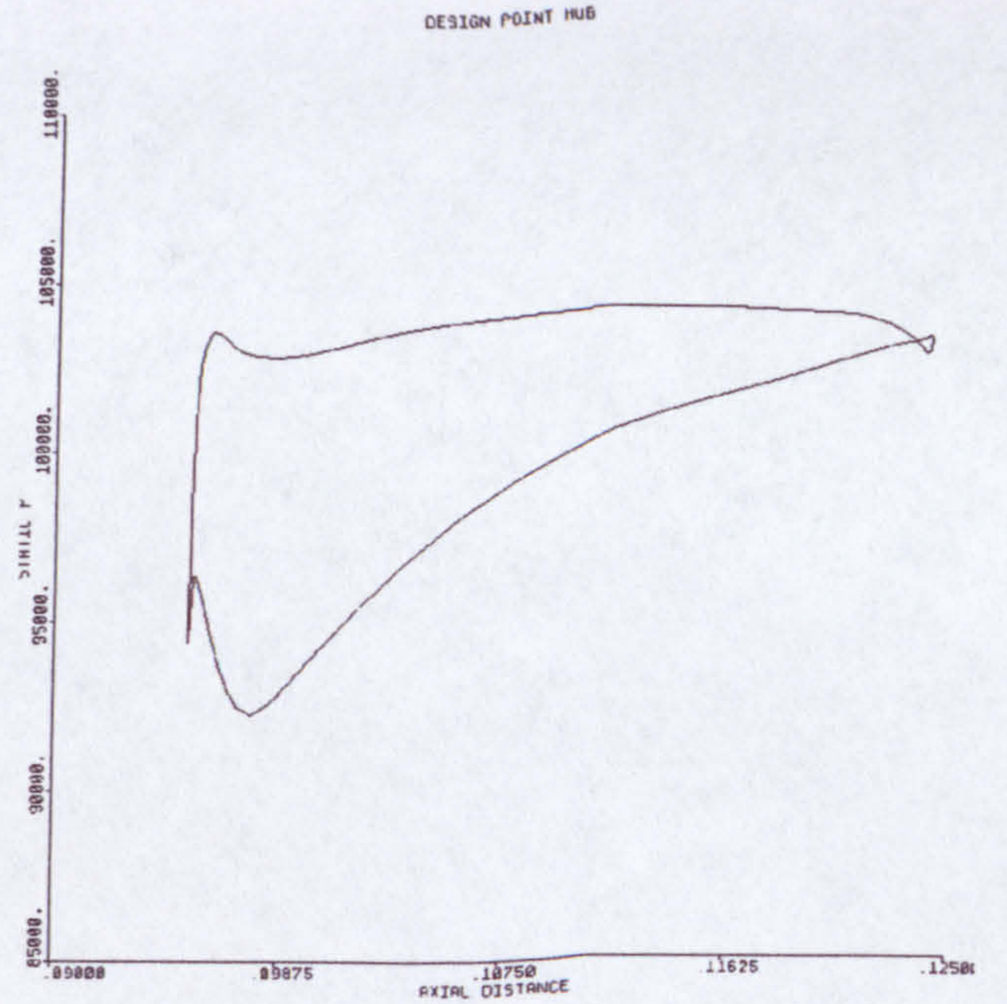


Figure 2-30 Pressure around rotor blade near hub at design

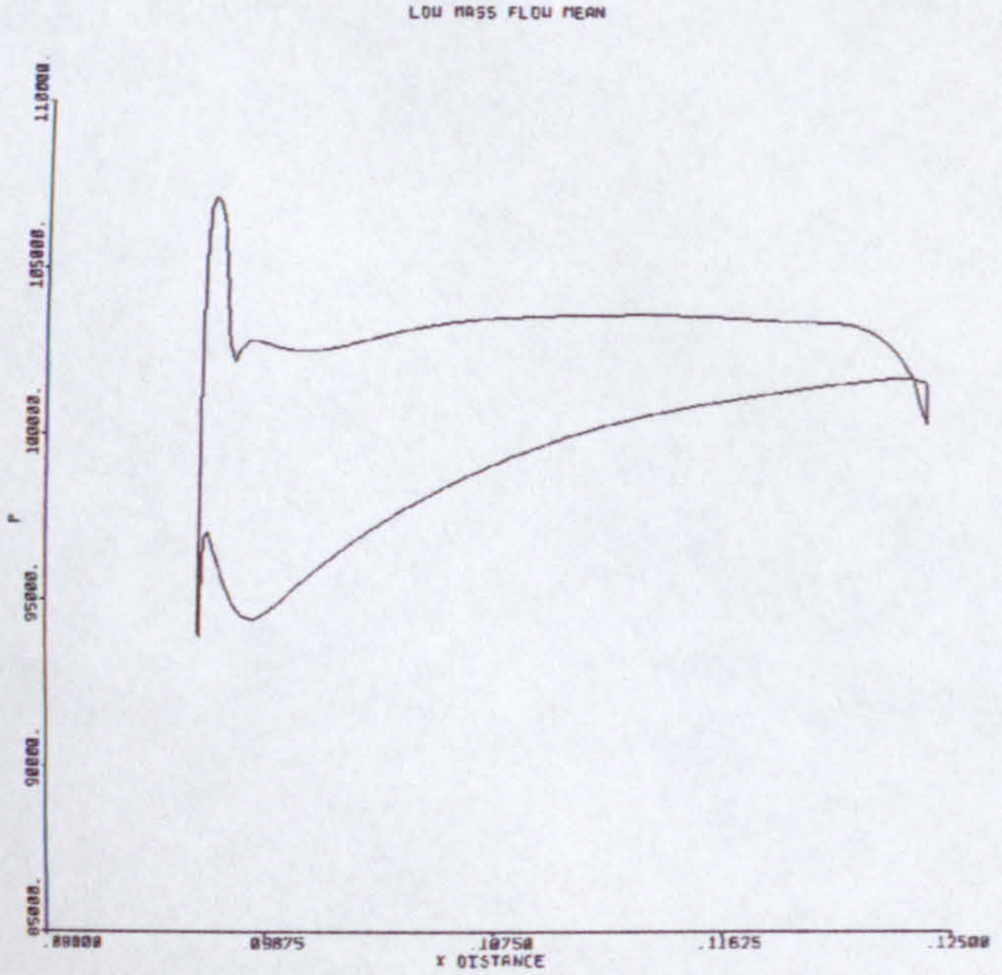


Figure 2-31 Pressure around rotor blade at mid span near surge

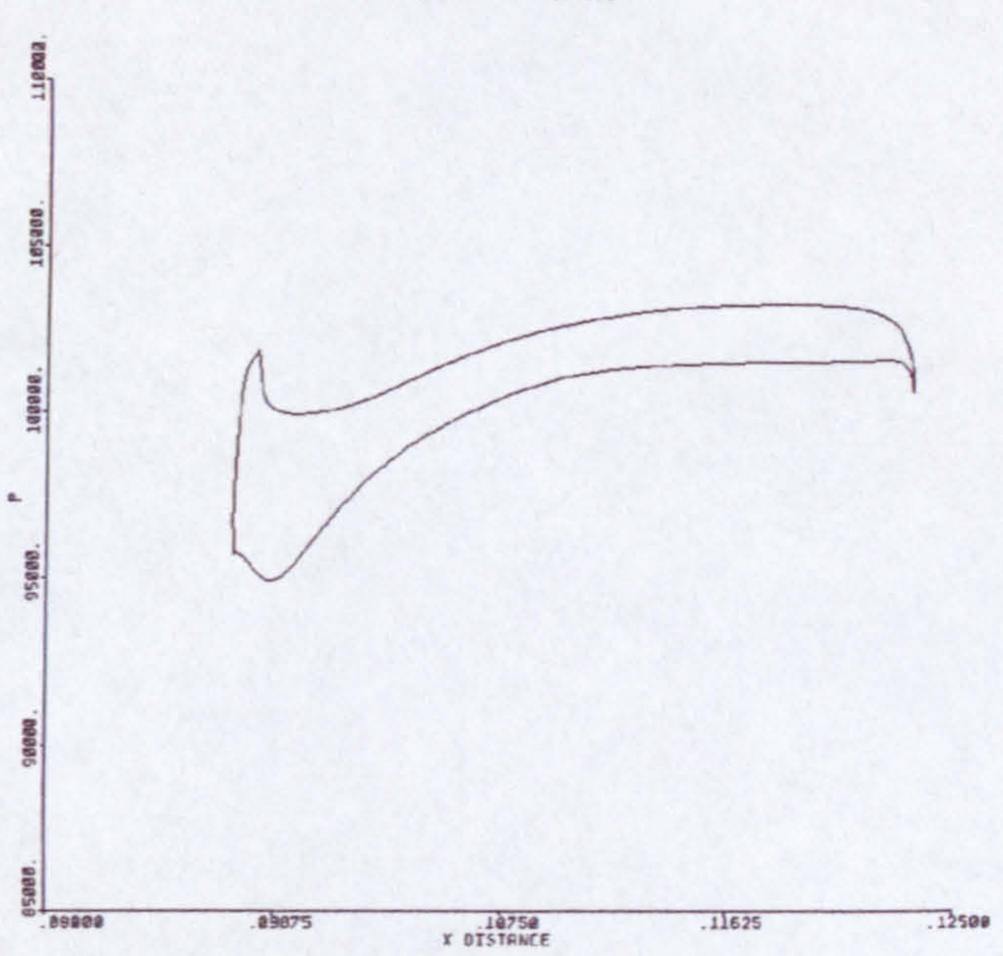


Figure 2-32 Pressure around rotor blade near shroud near surge

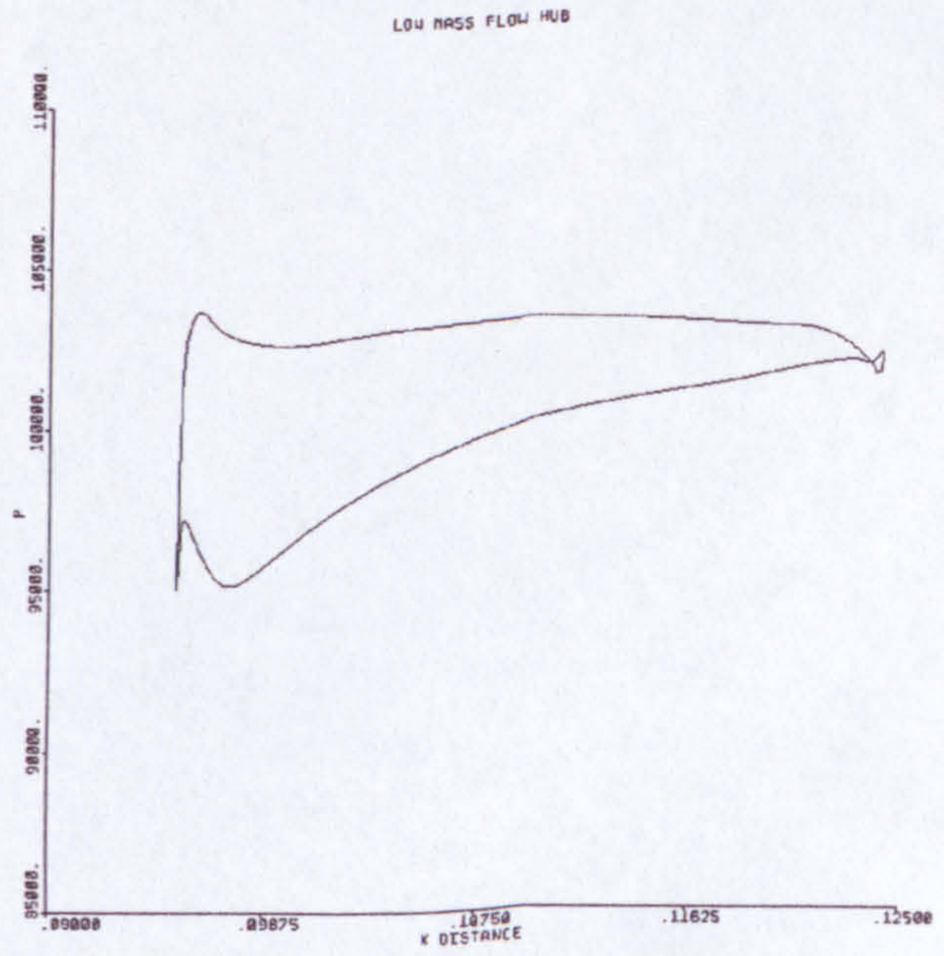


Figure 2-33 Pressure around rotor blade near hub near surge

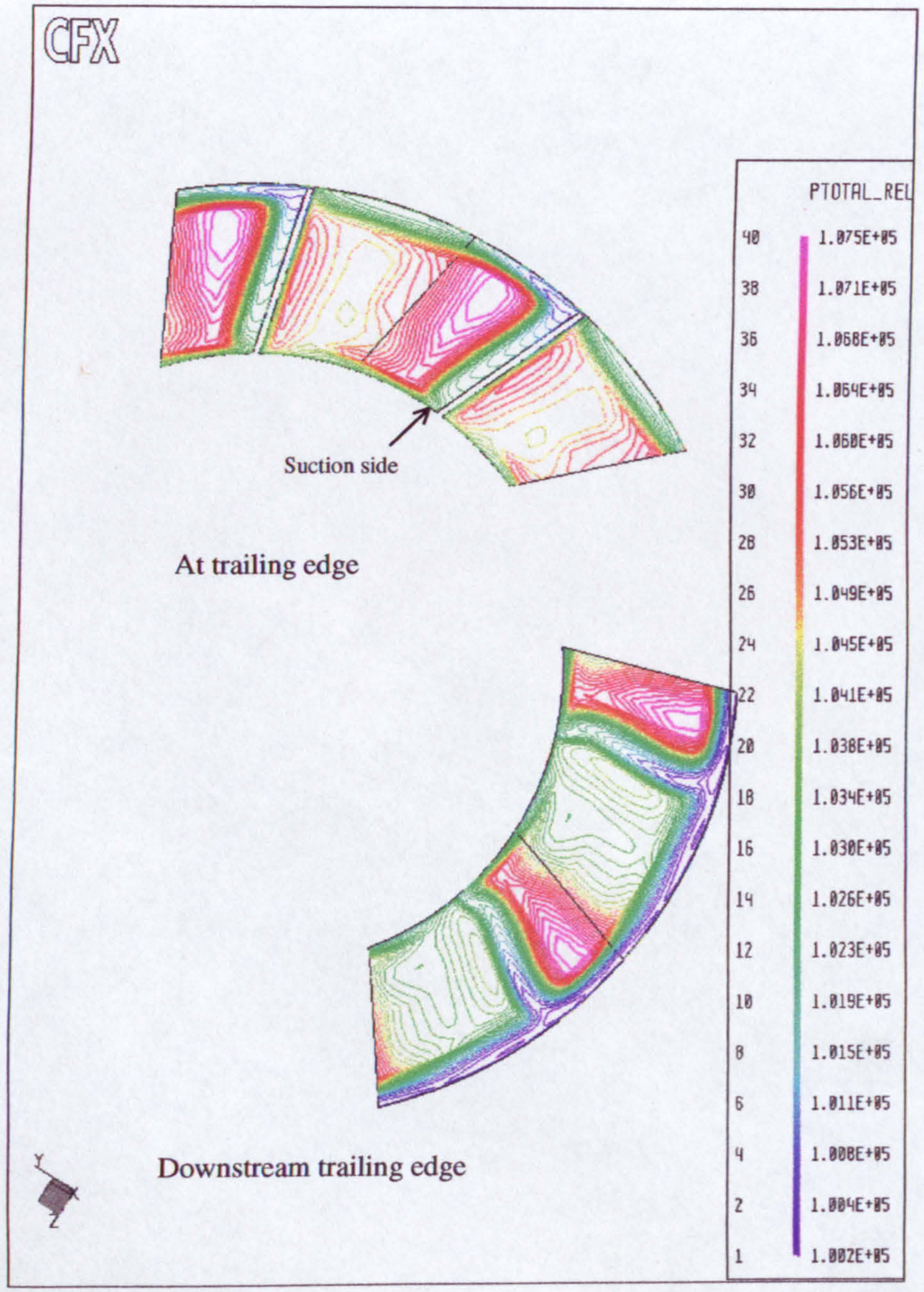


Figure 2-34 Total relative pressure at outlet from rotor near design point

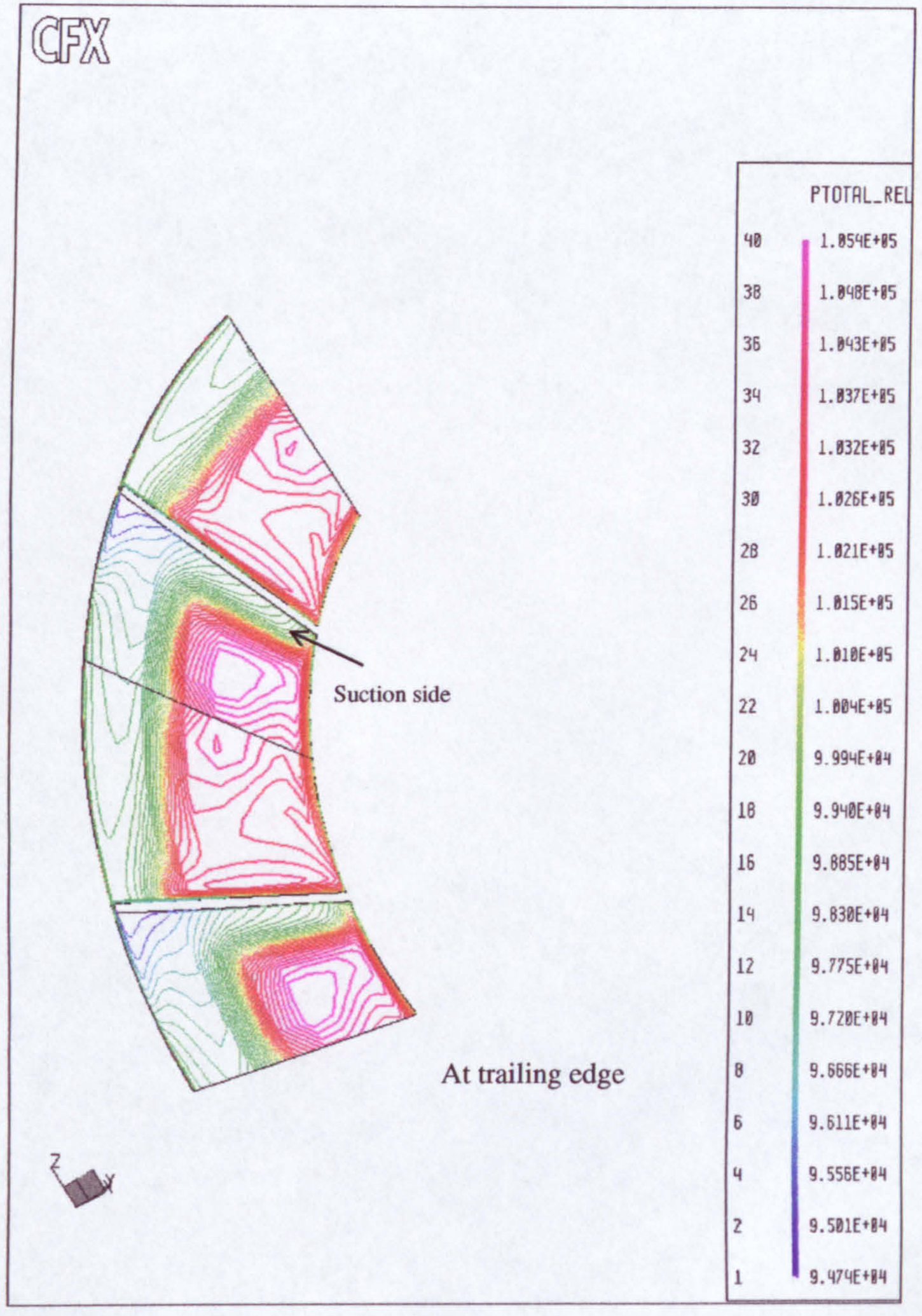


Figure 2-35 Total relative pressure at outlet from rotor at trailing edge near surge

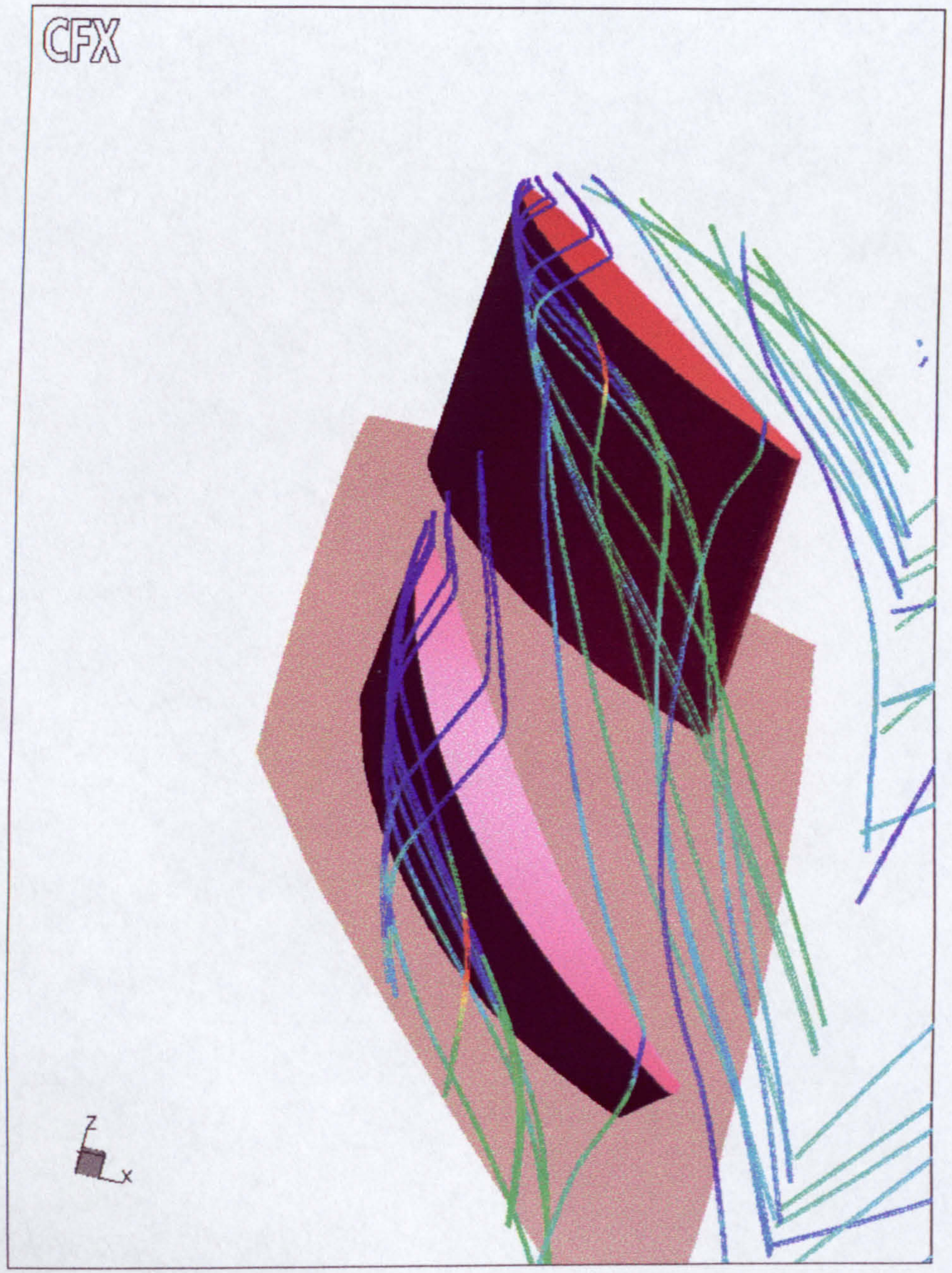


Figure 2-36 Streaklines on the tip of the rotor

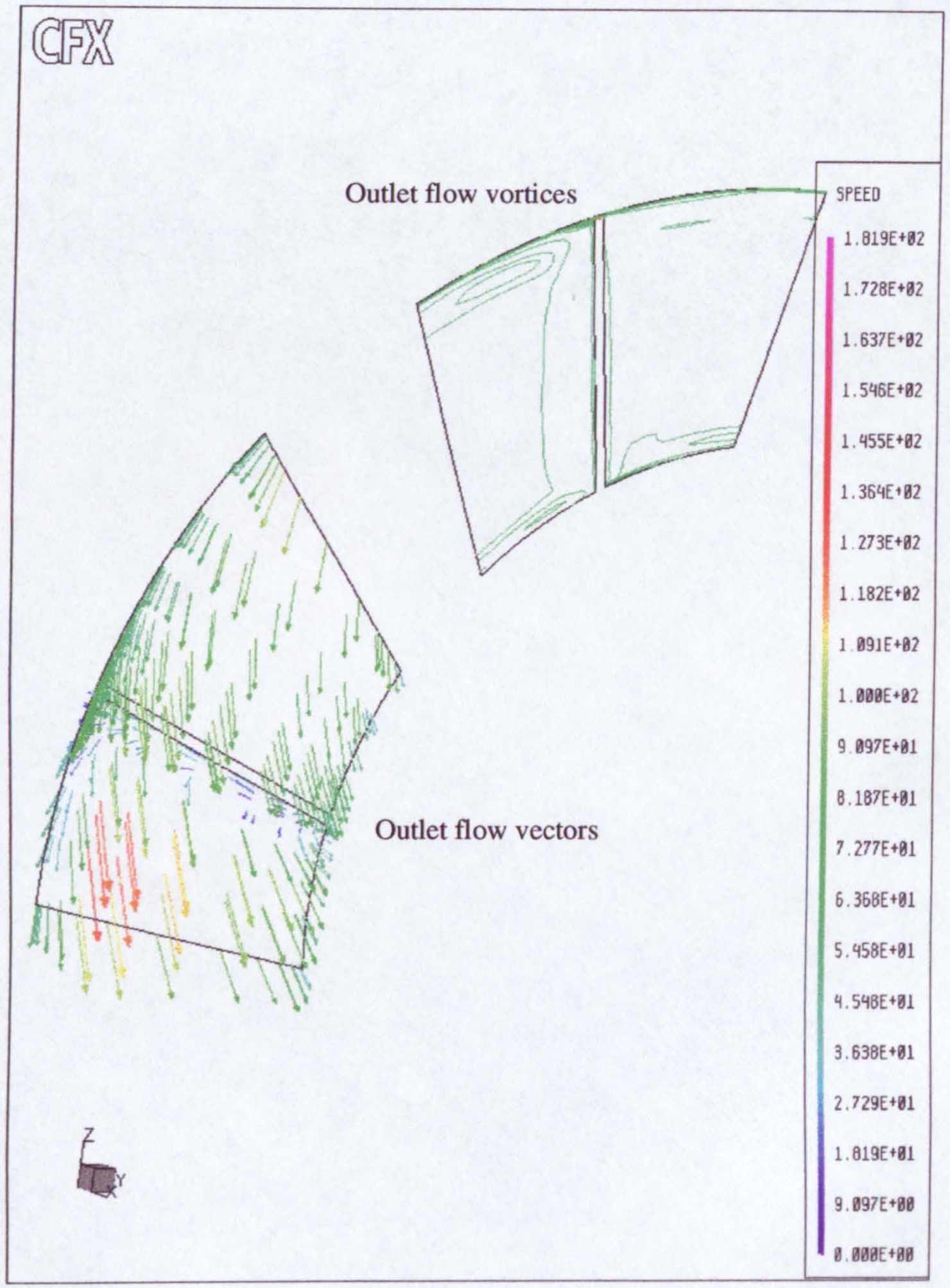


Figure 2-37 Vector velocity from outlet area of the rotor with vorticity

Figure 2-38 Vector plot near the tip

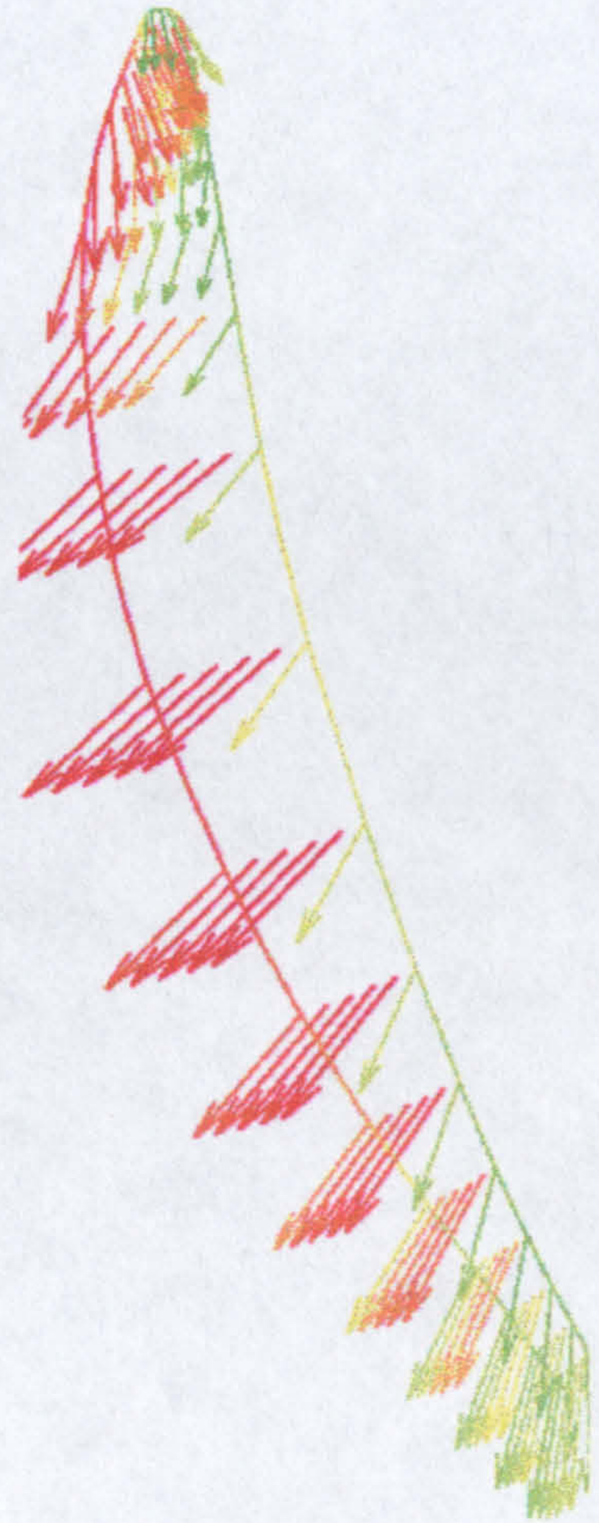

Figure 2-39 Vector plot near the shroud

Figure 2-40 Vector plot near the tip frozen stage

Figure 2-41 Vector plot near the shroud frozen stage

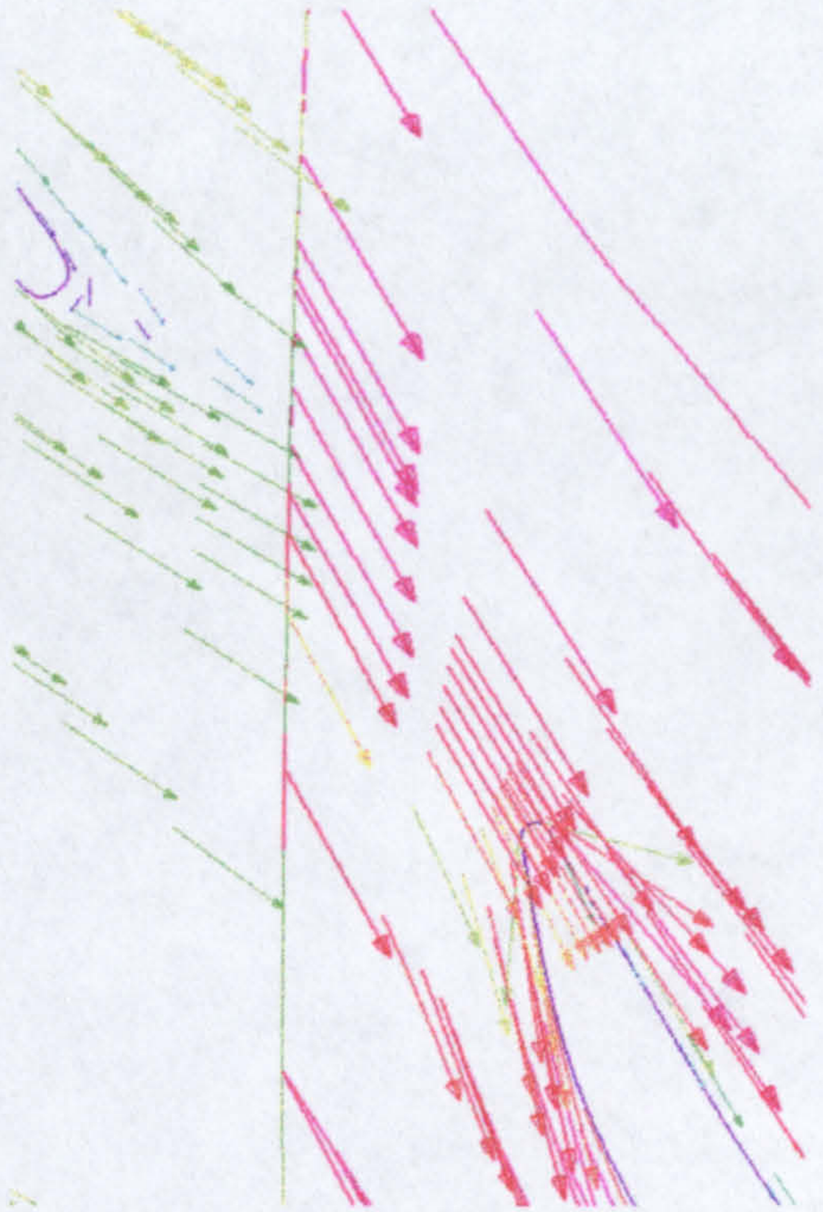

Figure 2-42 Vector plot near The leading edge frozen stage

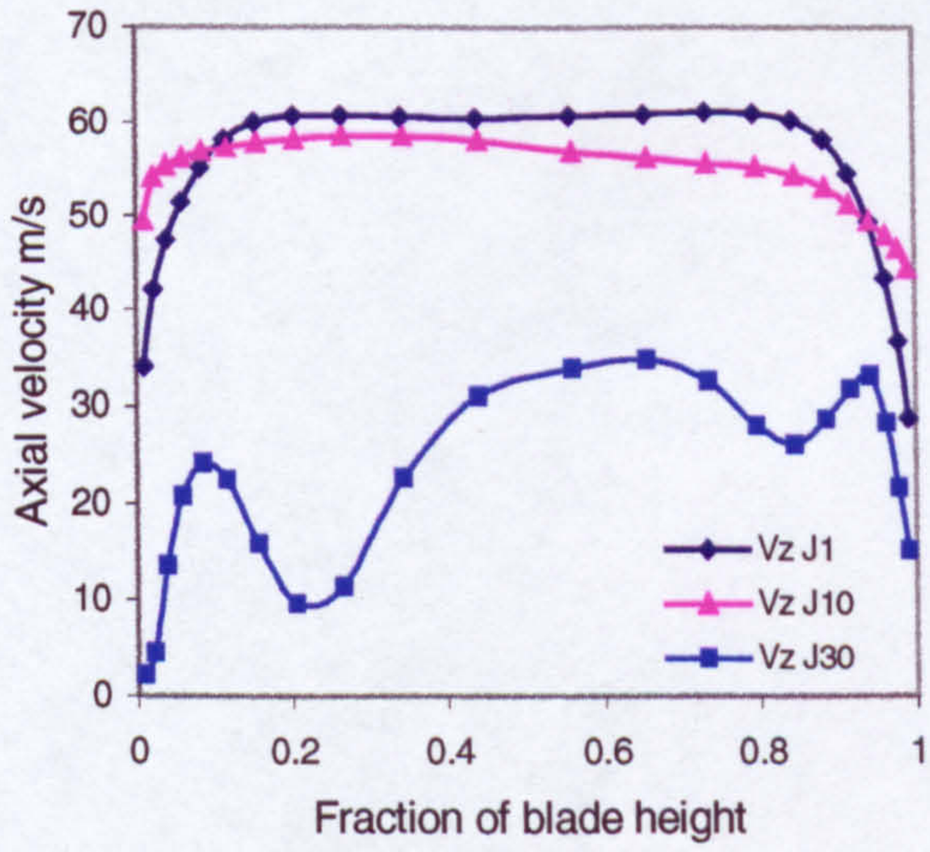


Figure 2-43 Axial velocity along the IGV blade height

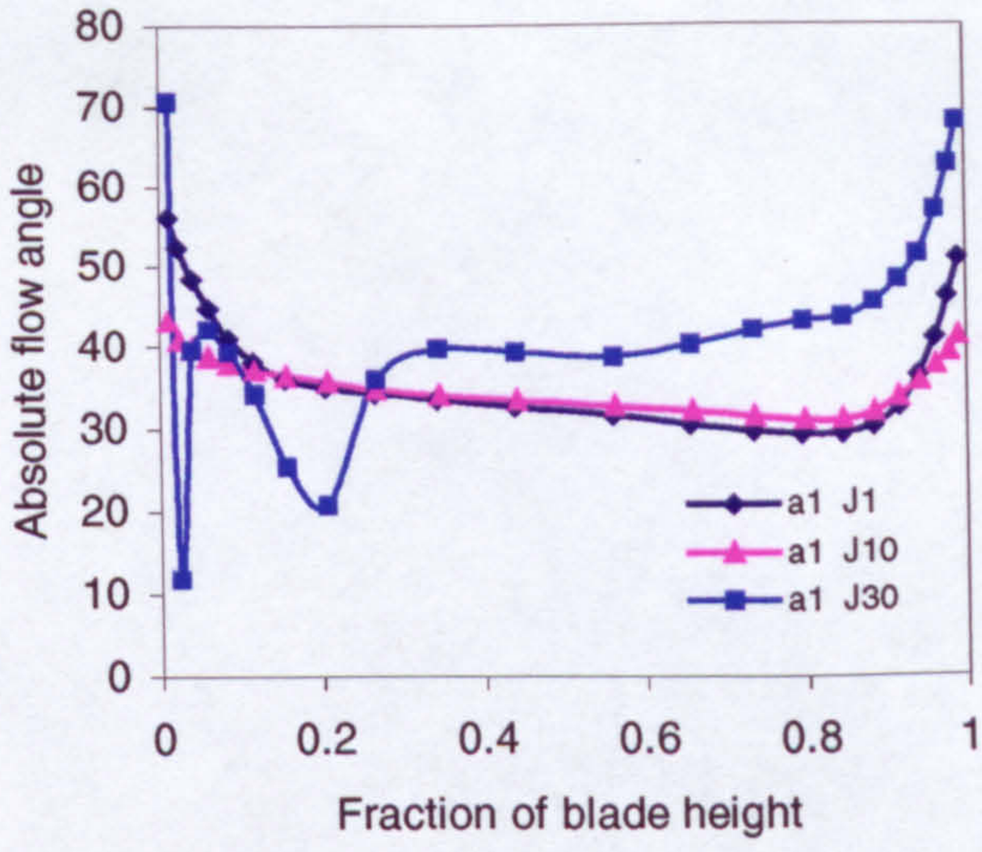


Figure 2-44 Flow angle along the IGV blade height

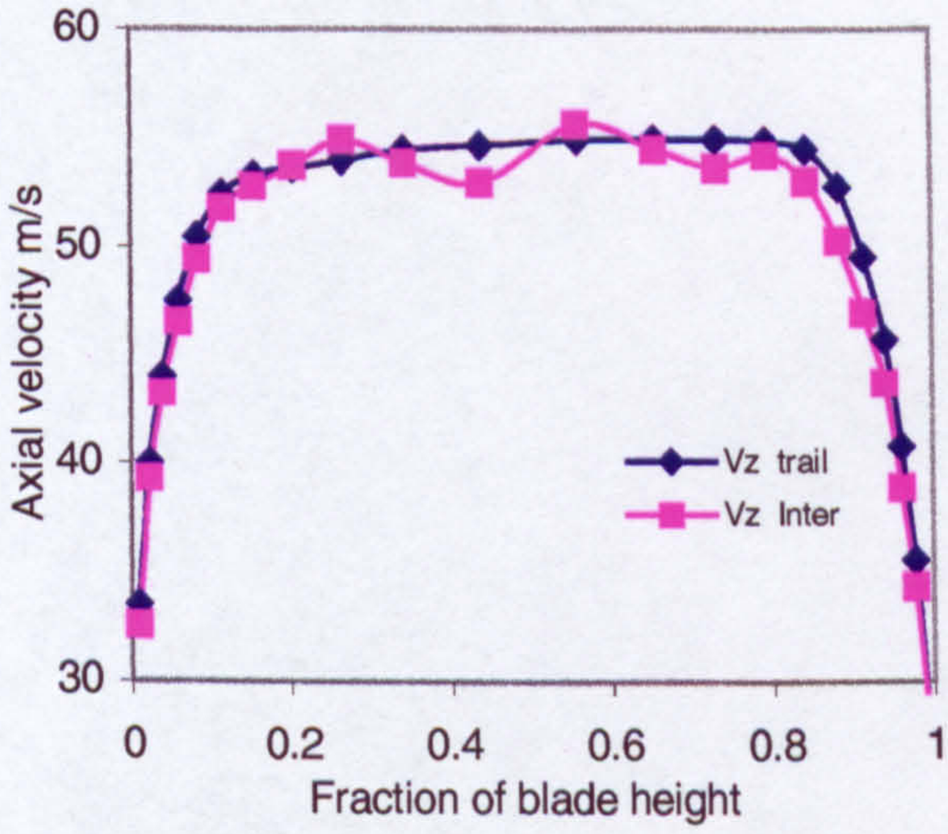


Figure 2-45 Mean axial velocity along IGV blade height

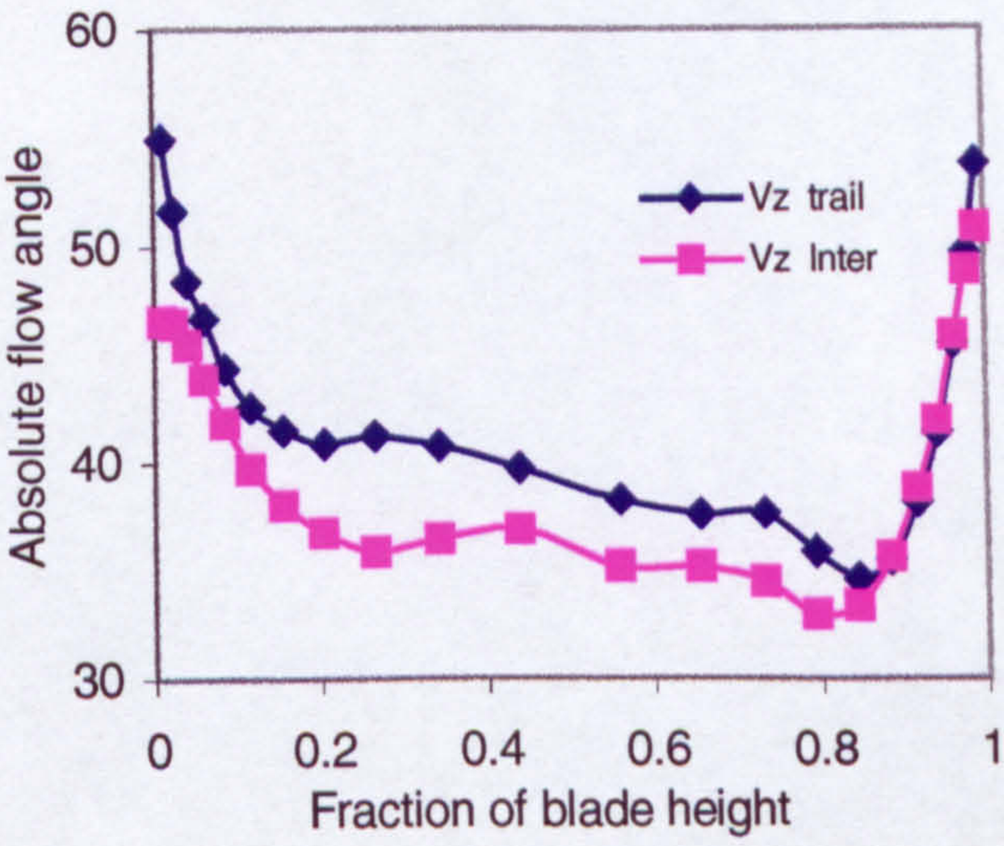


Figure 2-46 Mean flow angle along IGV blade height

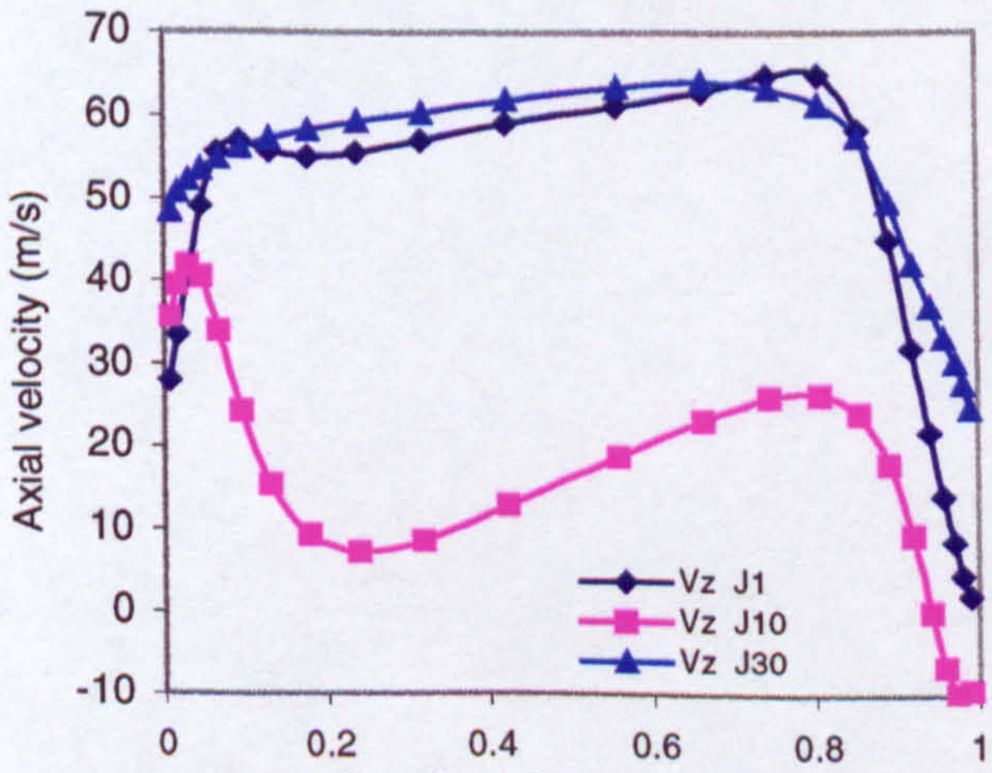


Figure 2-47 Axial velocity along rotor blade height

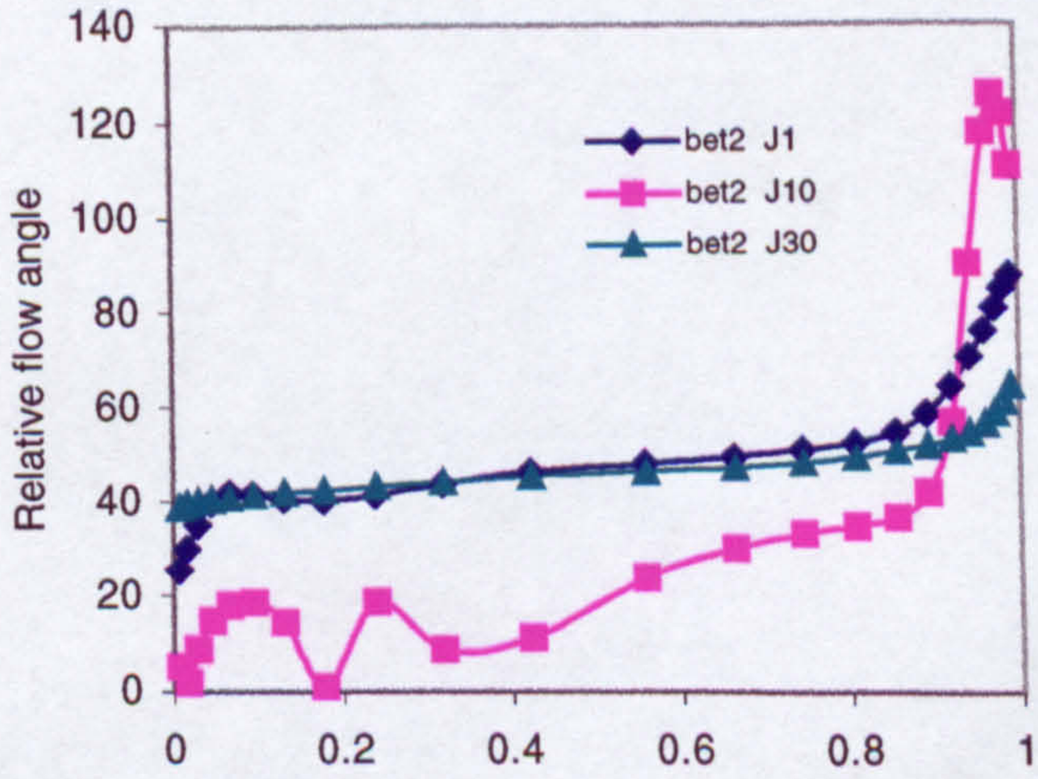


Figure 2-48 Flow angle along the rotor blade height

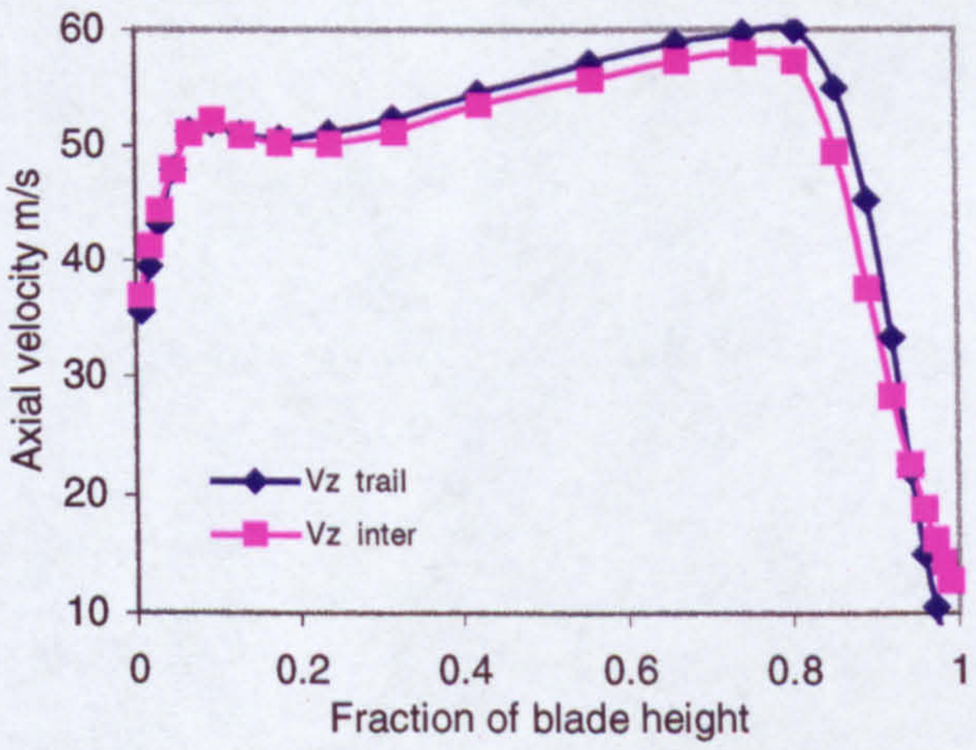


Figure 2-49 Mean axial velocity along rotor blade height

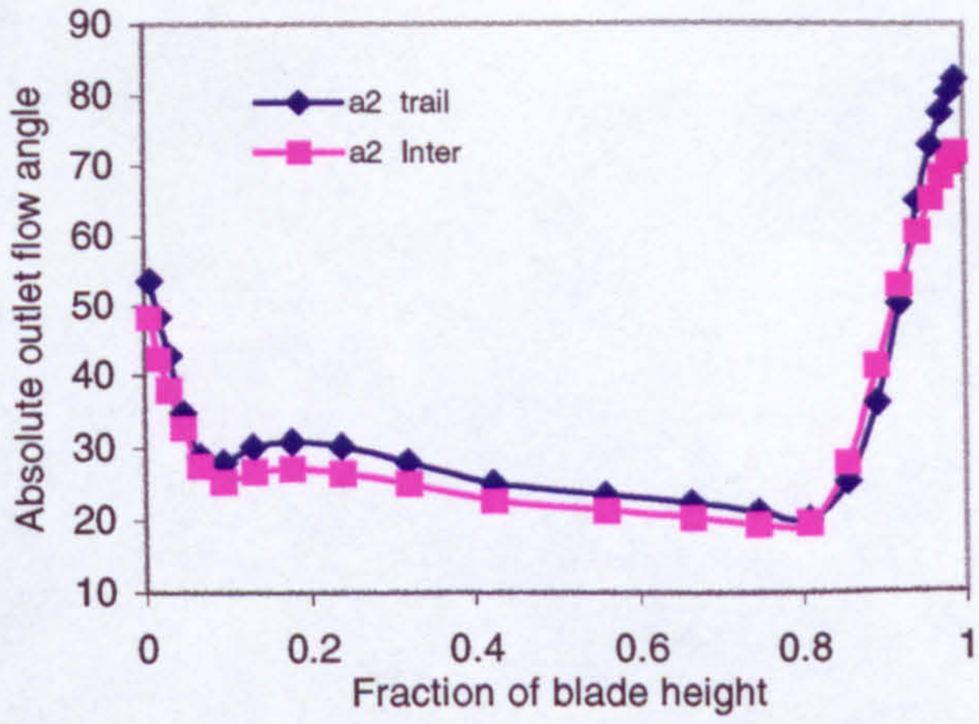


Figure 2-50 Mean flow angle along rotor blade height

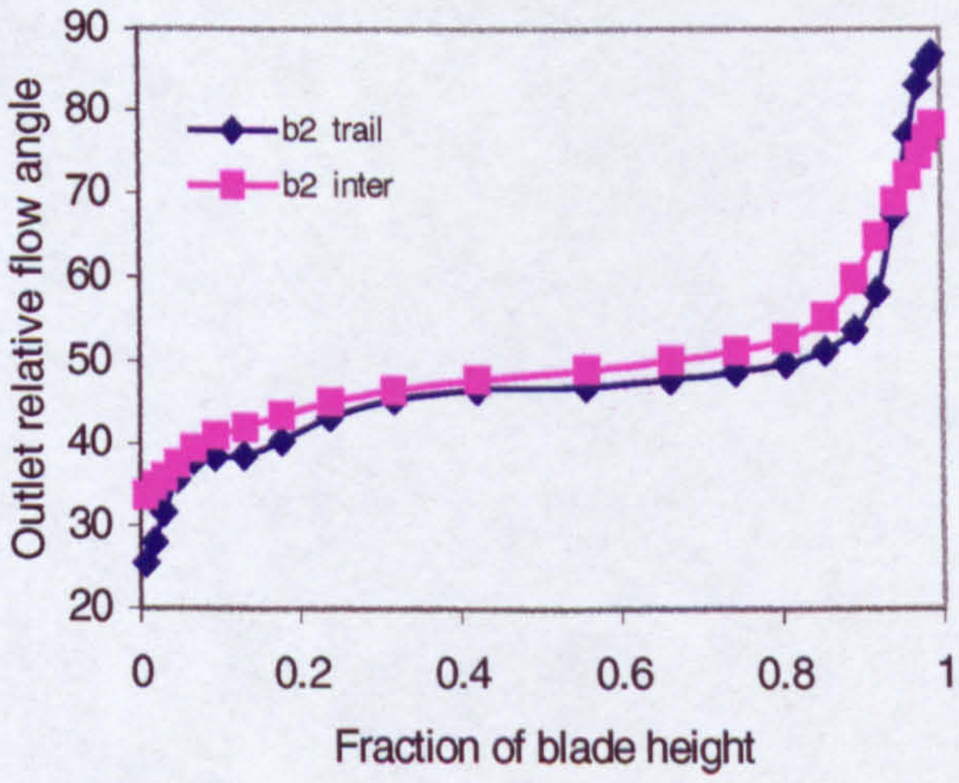


Figure 2-51 Mean outlet angle along rotor blade height

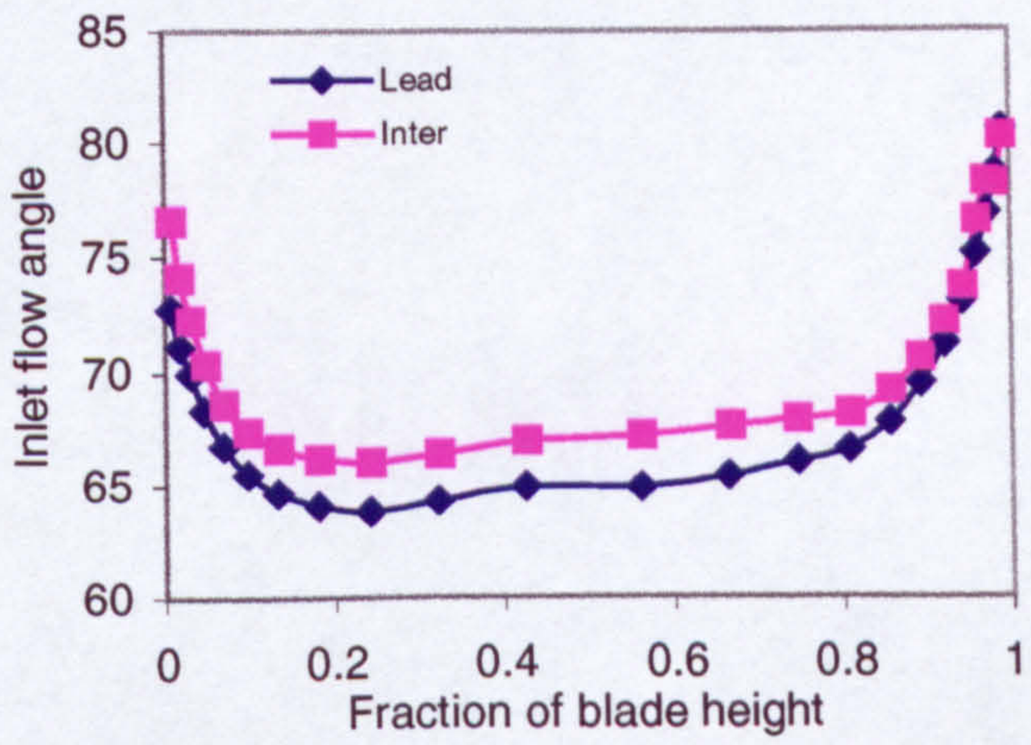


Figure 2-52 Mean inlet angle along rotor blade height

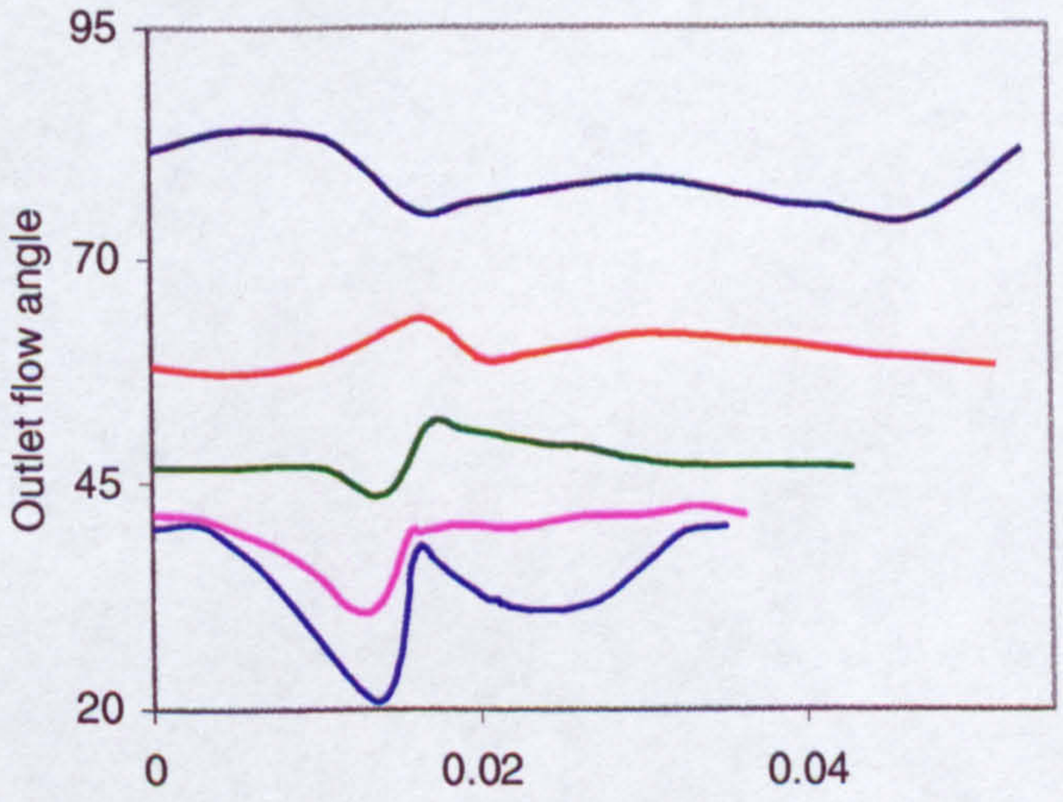


Figure 2-53 Outlet flow angle along rotor blade pitch

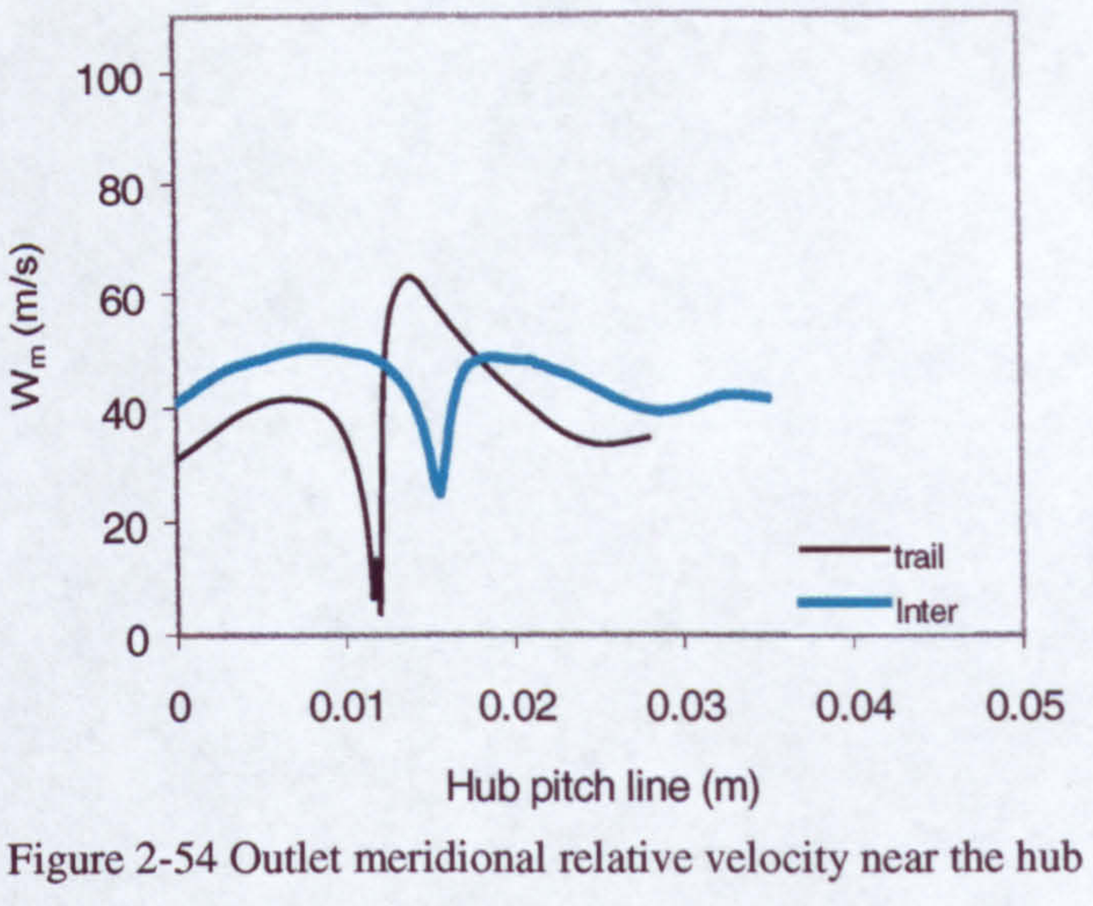


Figure 2-54 Outlet meridional relative velocity near the hub

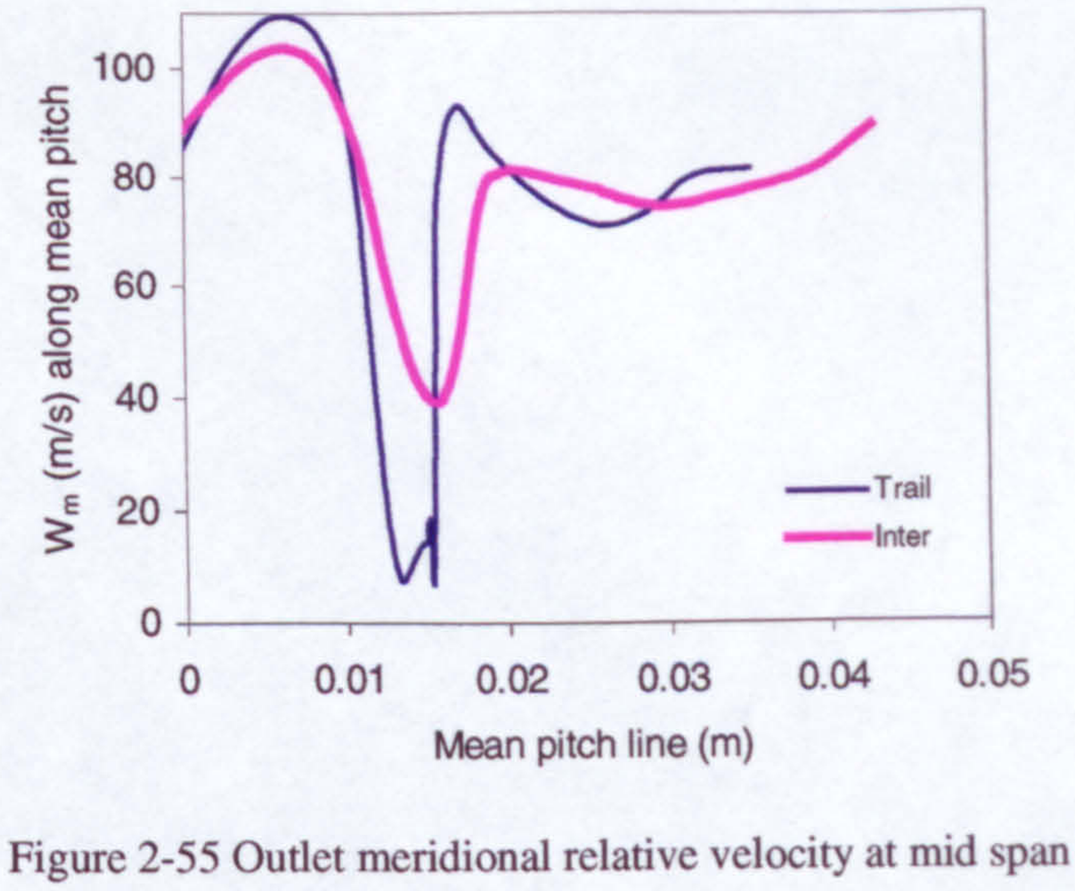


Figure 2-55 Outlet meridional relative velocity at mid span

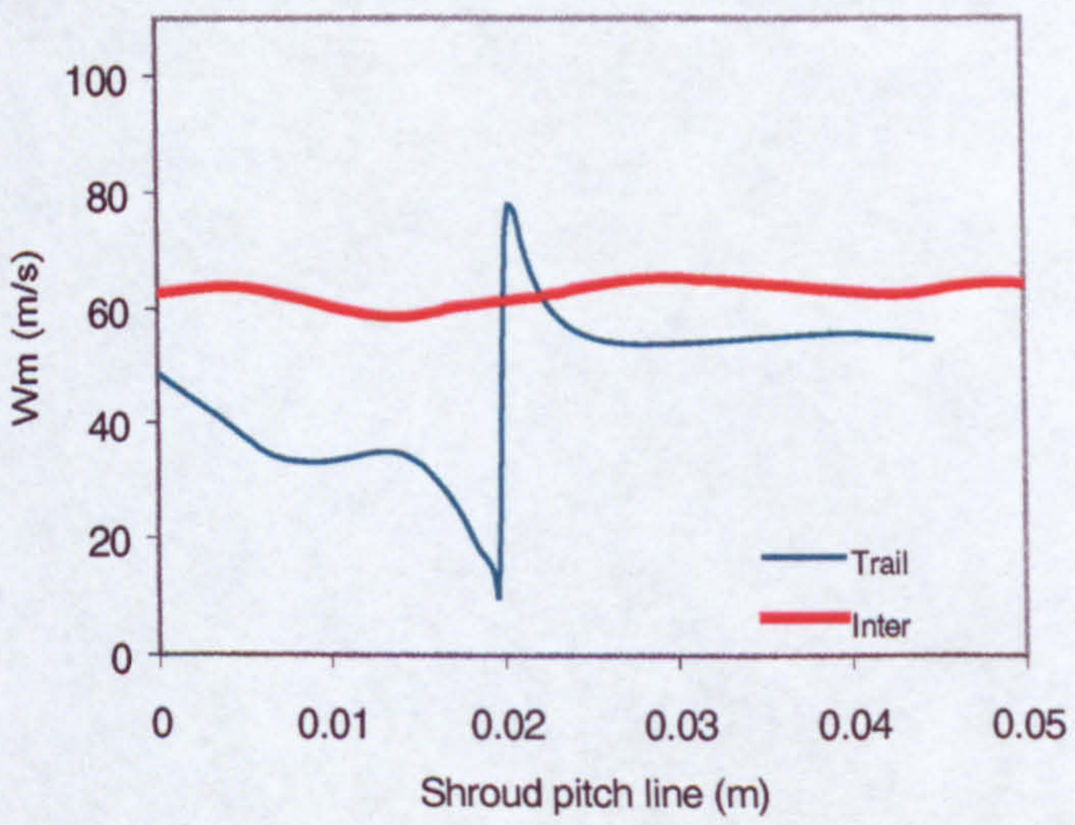


Figure 2-56 Outlet meridional relative velocity near the shroud

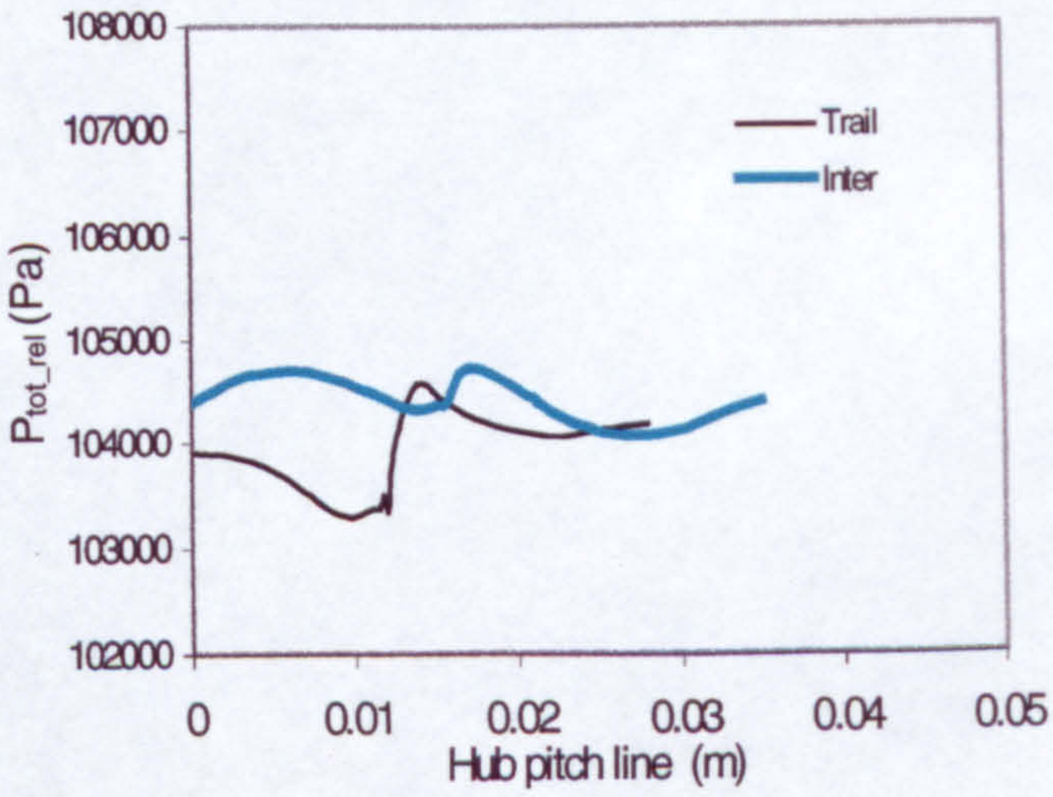


Figure 2-57 Outlet total relative pressure near the hub

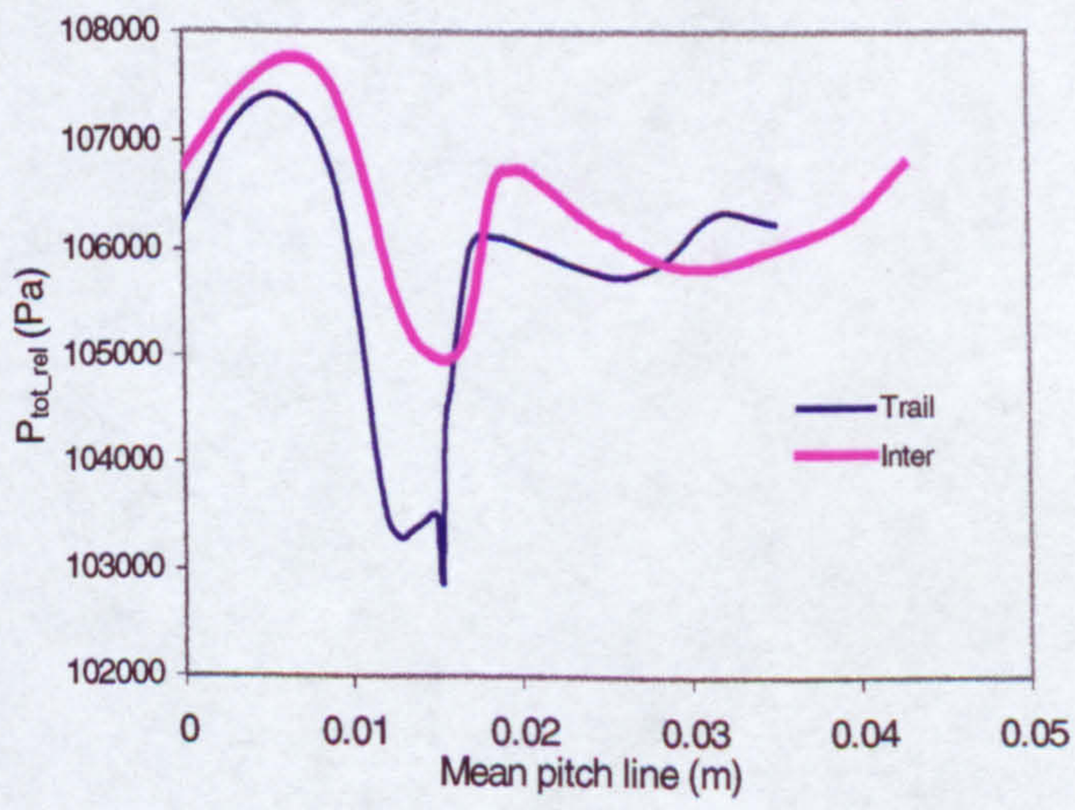


Figure 2-58 Outlet total relative pressure at mid span

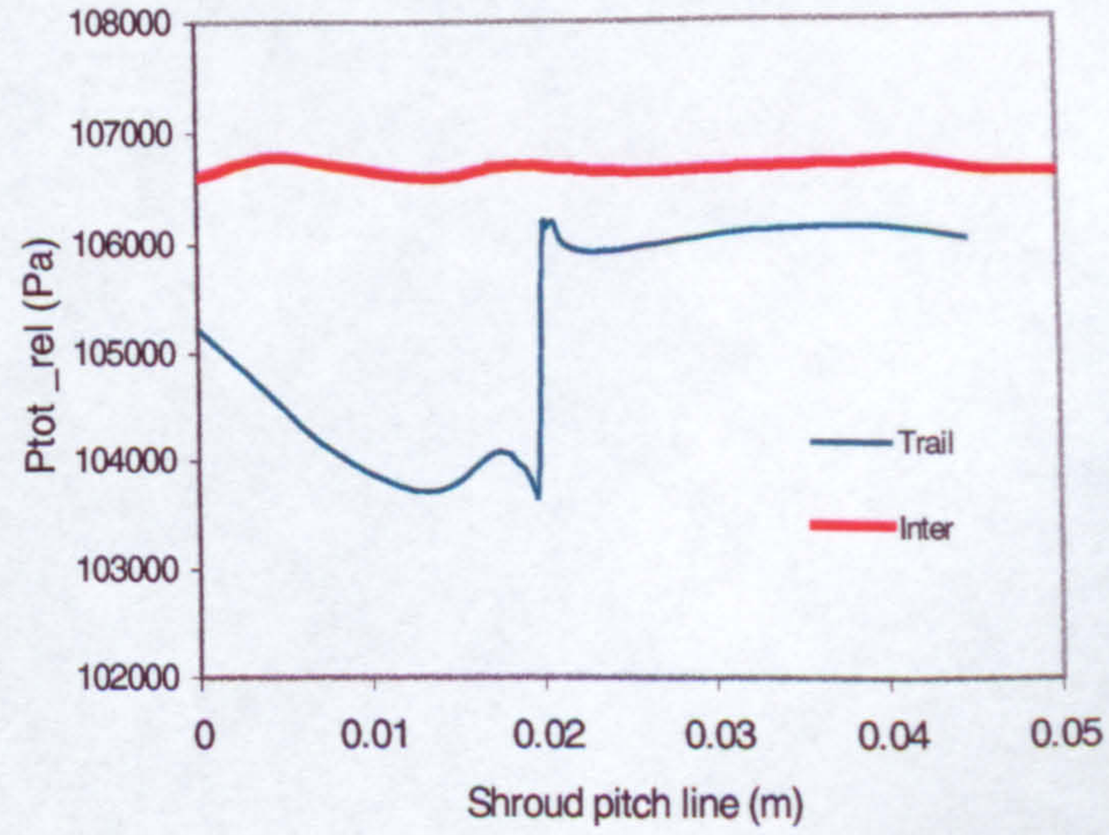


Figure 2-59 Outlet total relative pressure near the shroud

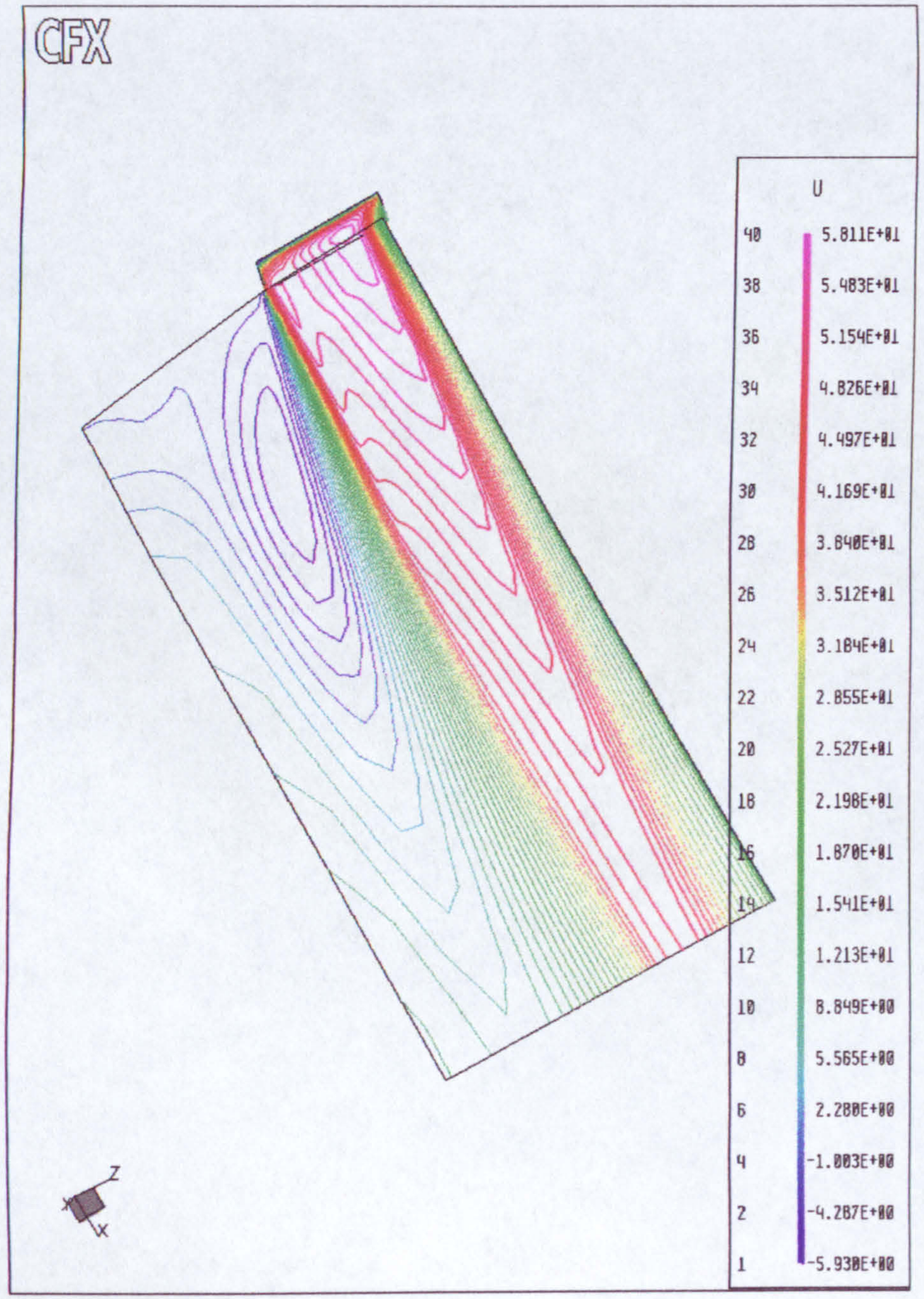


Figure 2-60 Axial velocity in the outlet duct

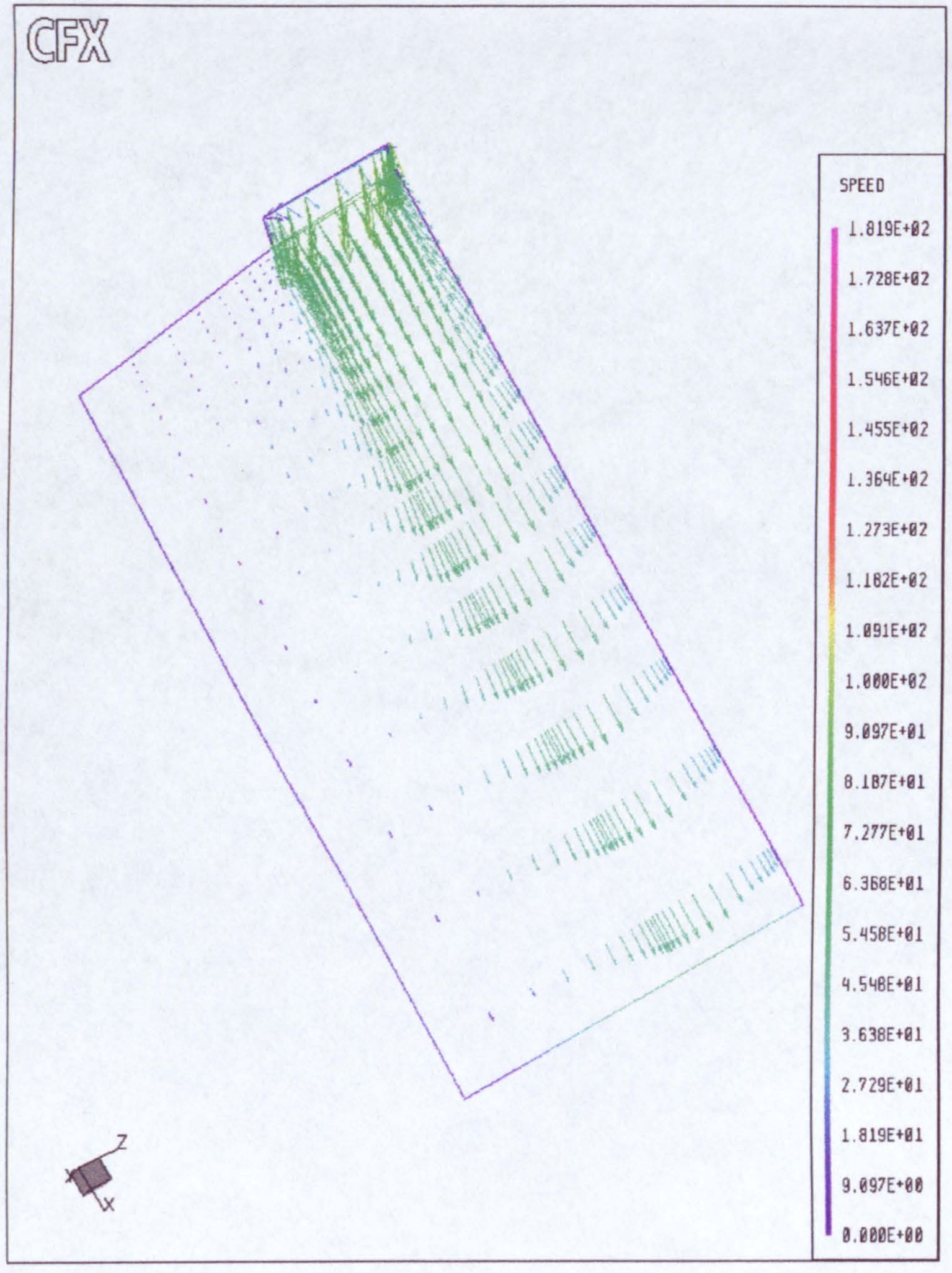


Figure 2-61 Vector velocity in the outlet duct

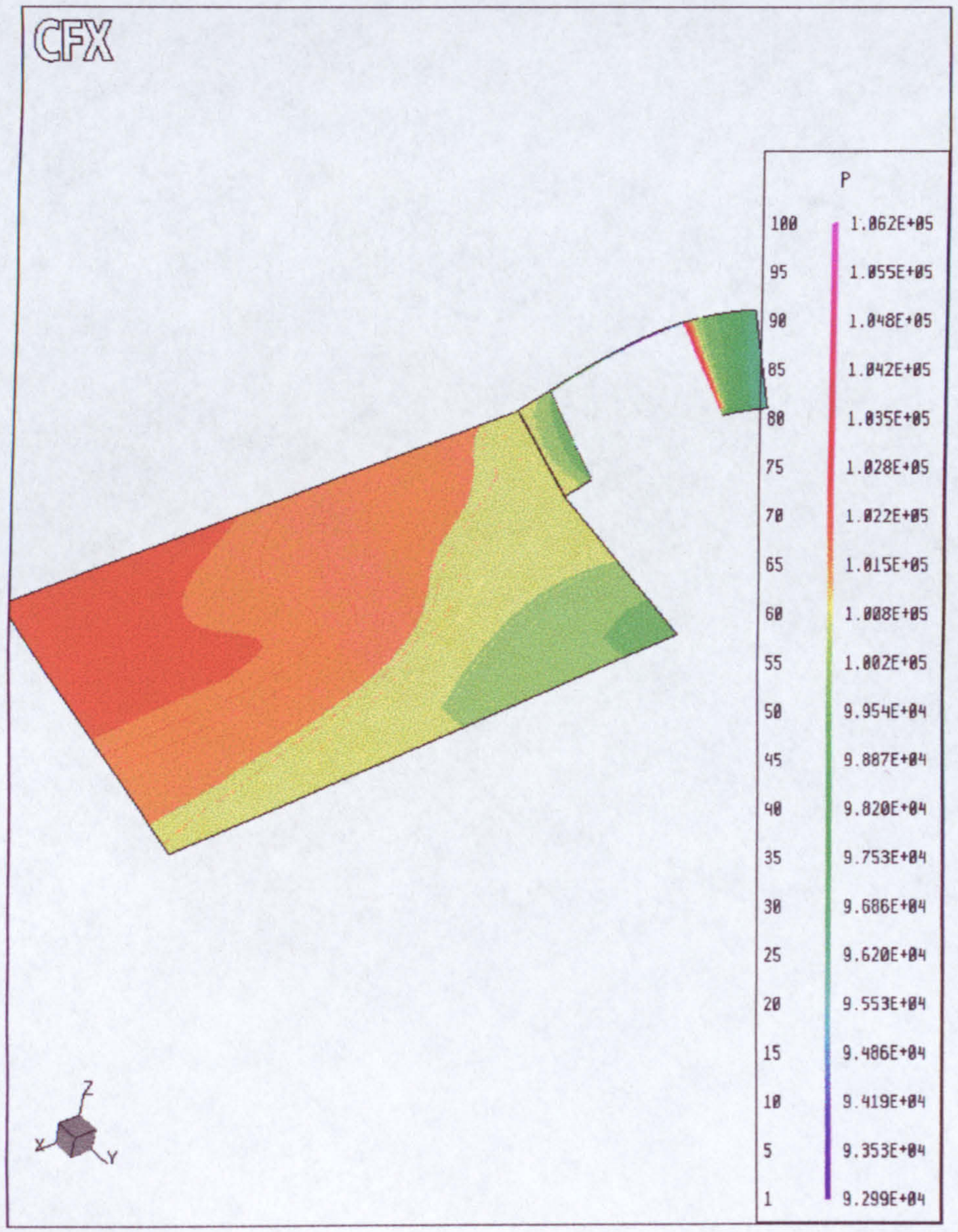


Figure 2-62 Static pressure in the outlet duct

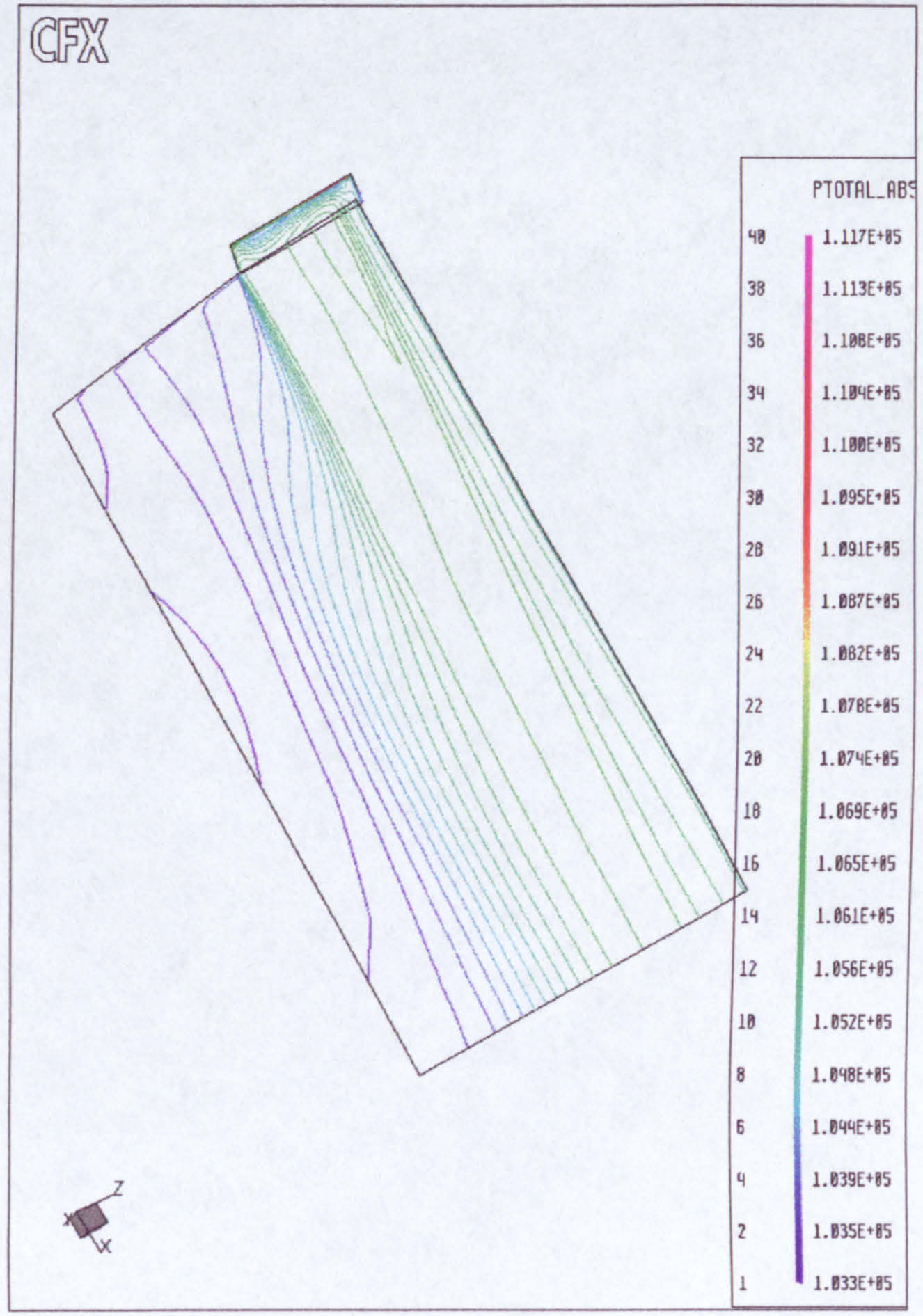


Figure 2-63 Total pressure in the outlet duct

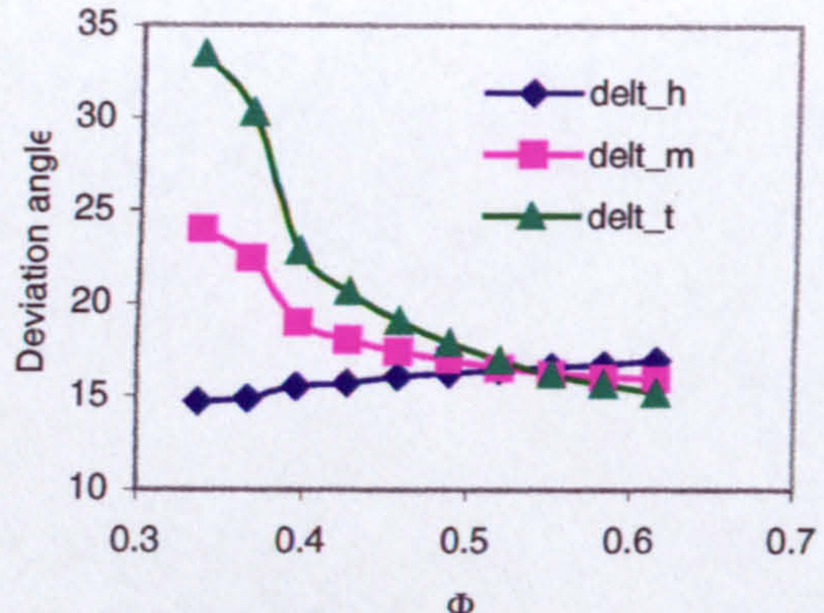


Figure 2-64 Off design rotor deviation angle

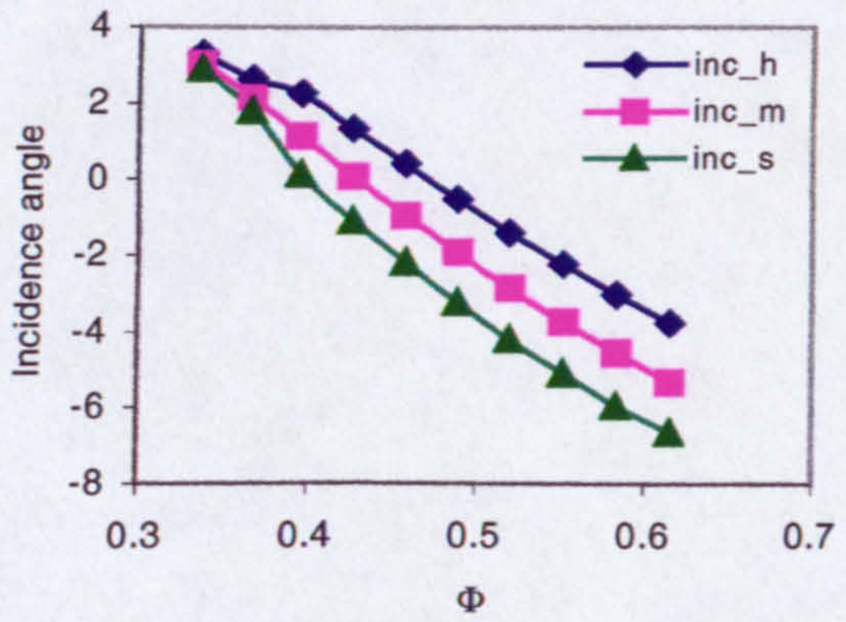


Figure 2-65 Off design rotor incidence angle

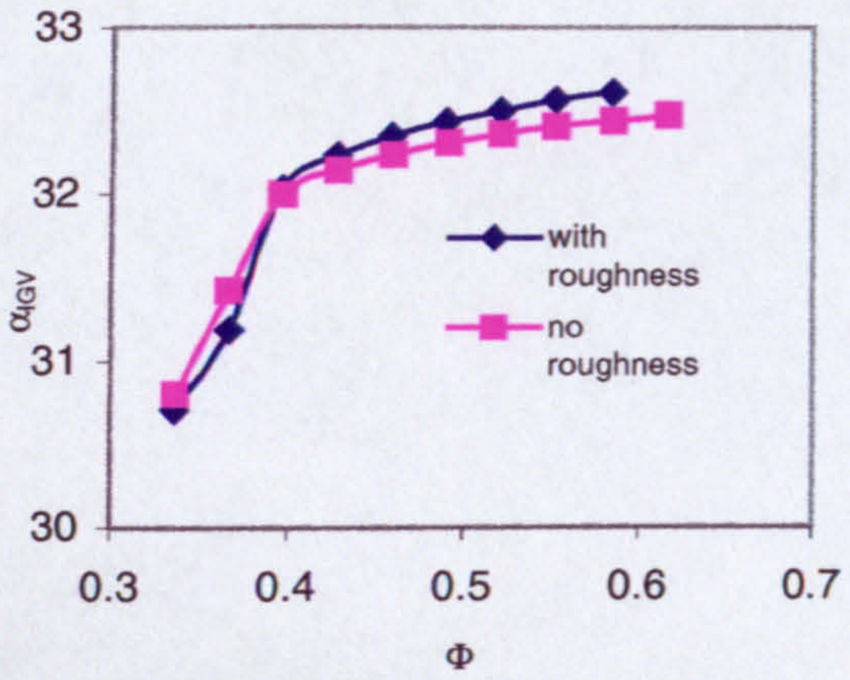


Figure 2-66 Off design IGV outlet flow angle

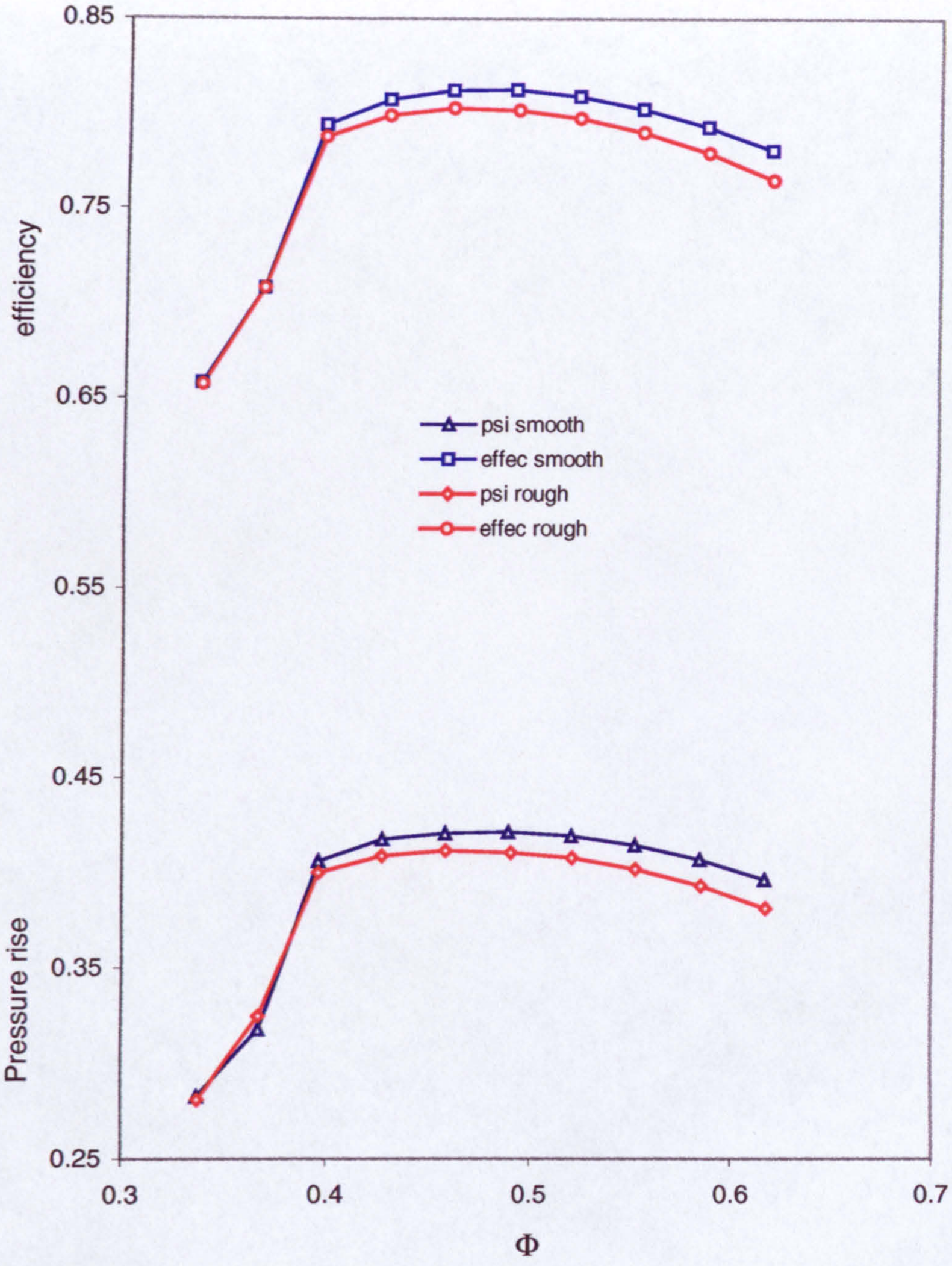


Figure 2-67 Axial fan characteristics

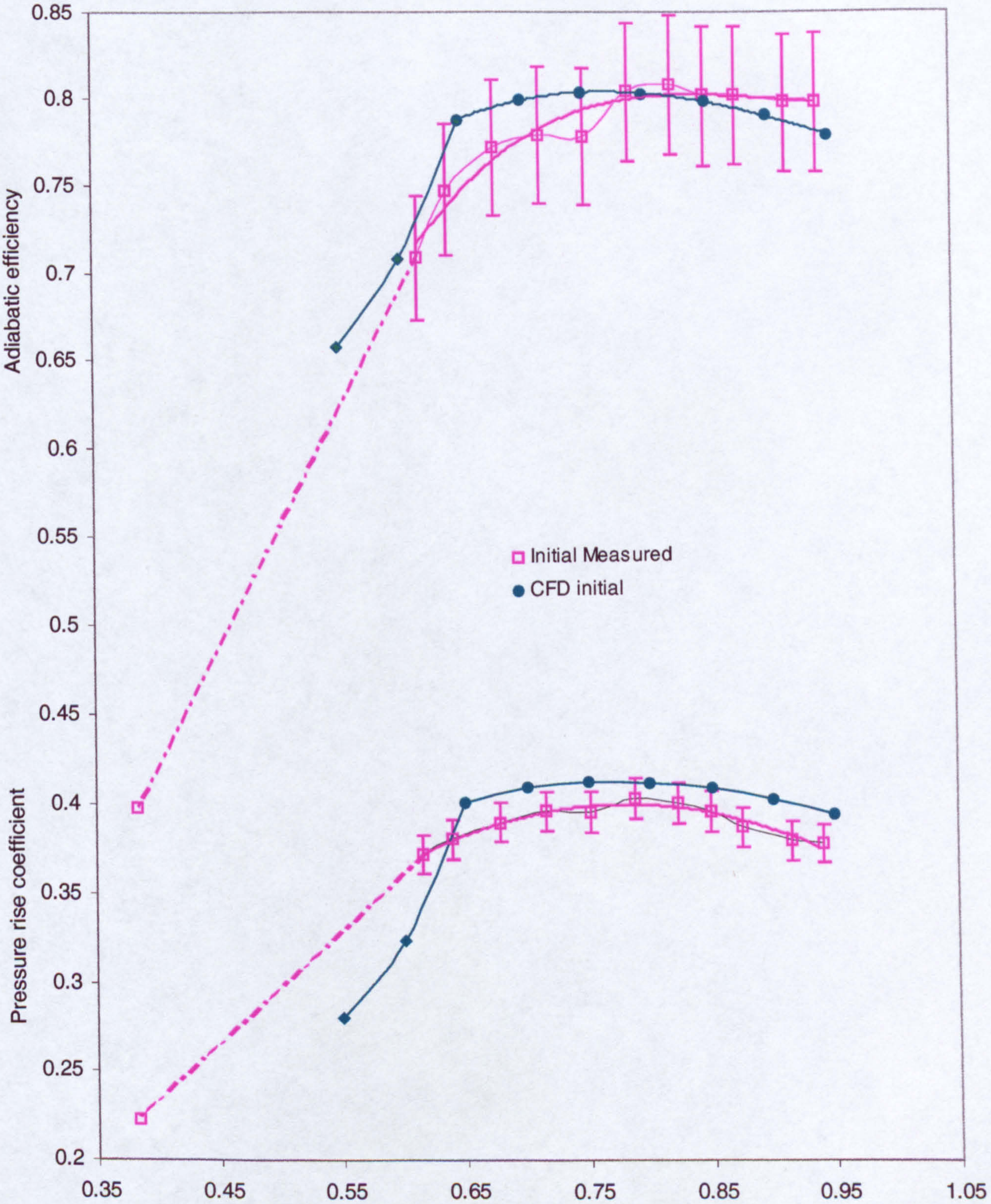


Figure 2-68 Measured and CFD predicted axial fan characteristics

# FIGURES 3

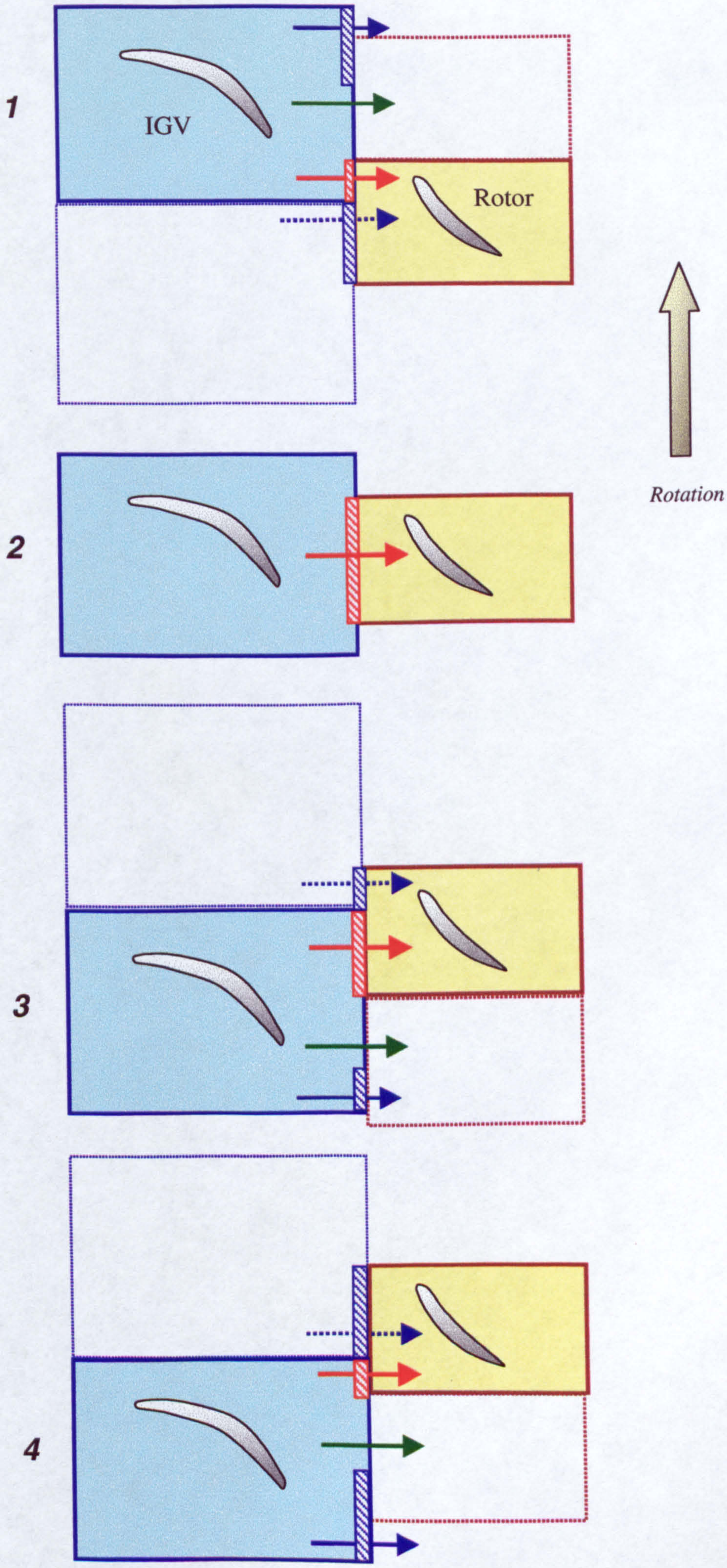


Figure 3-13 IGV and rotor relative positions at the interface plane

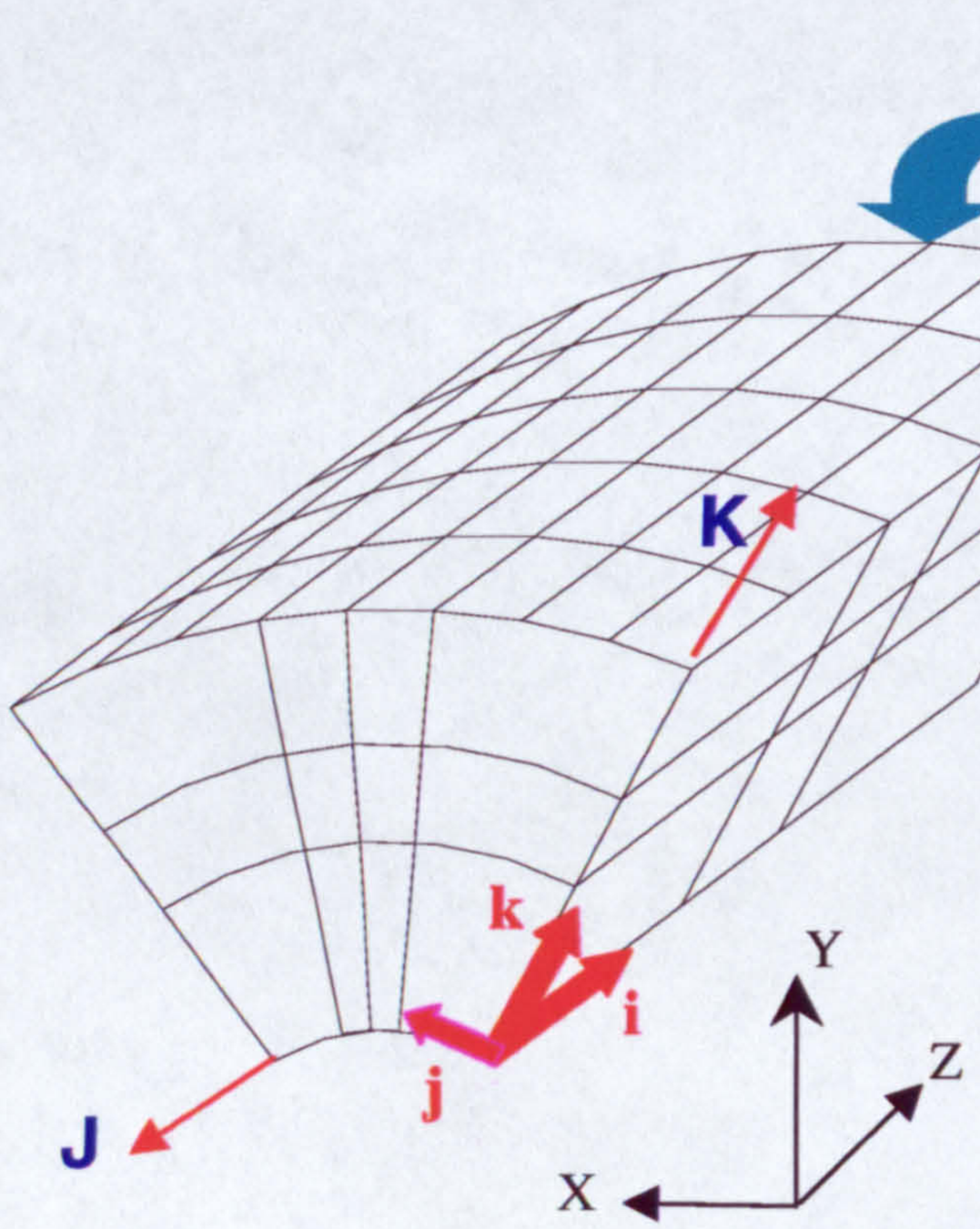


Figure 3-14a Computational domain vertices

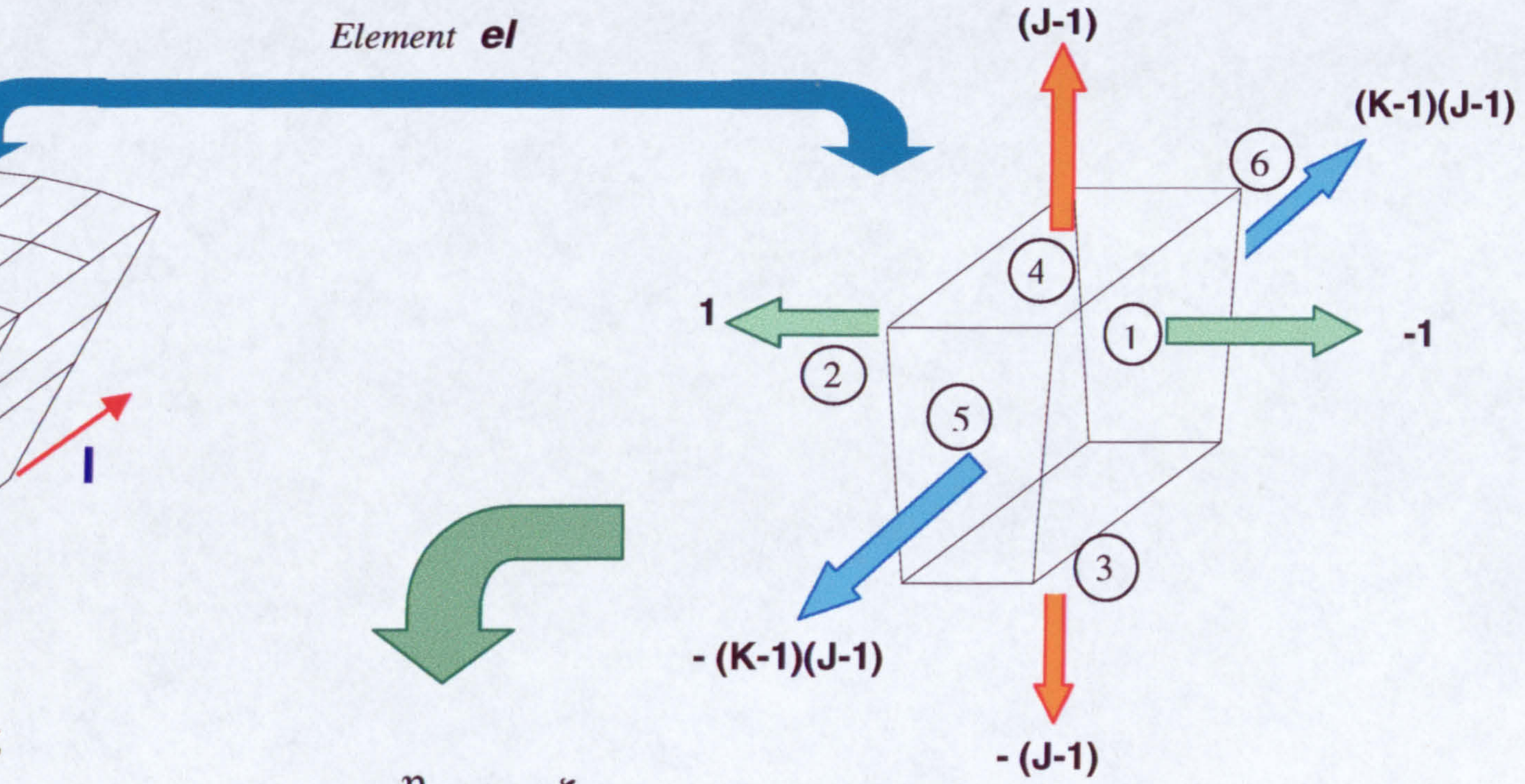


Figure 3-14b Grid element in the physical coordinates
With the directrix values

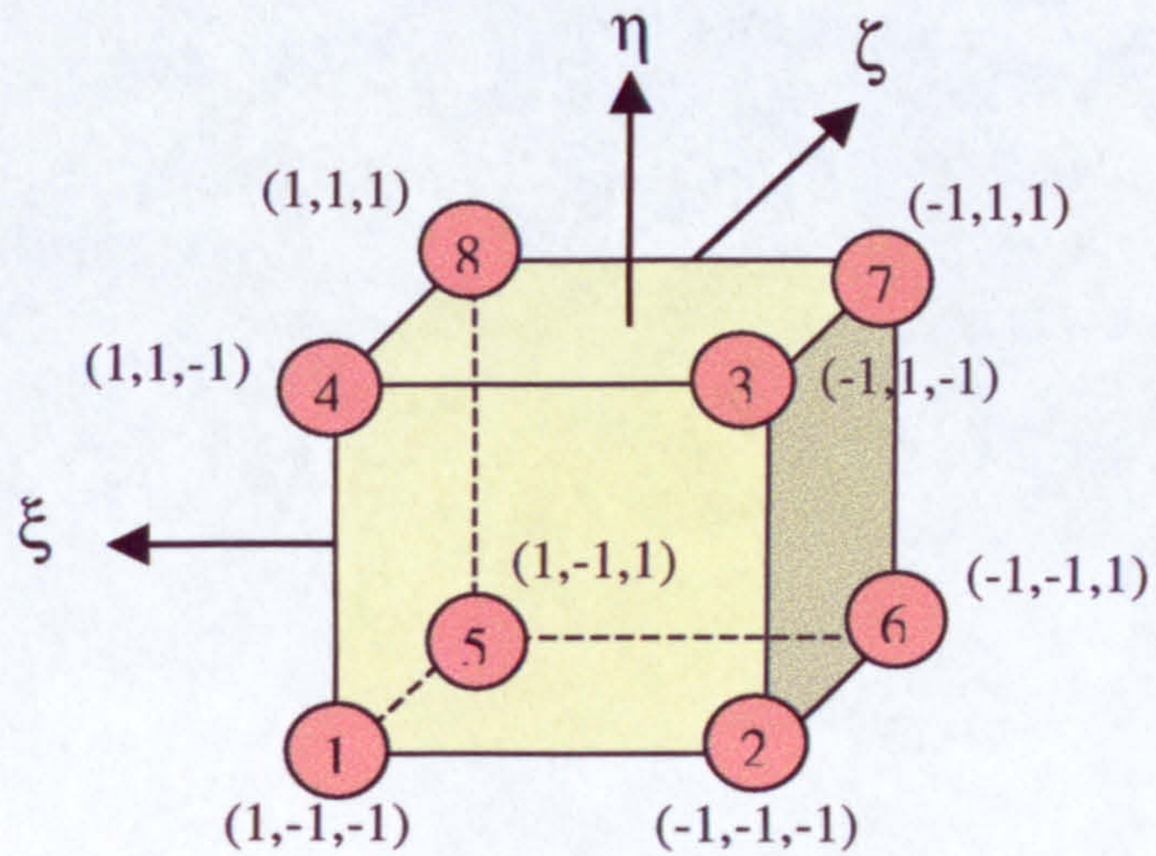


Figure 3-14c Grid element in the natural coordinates

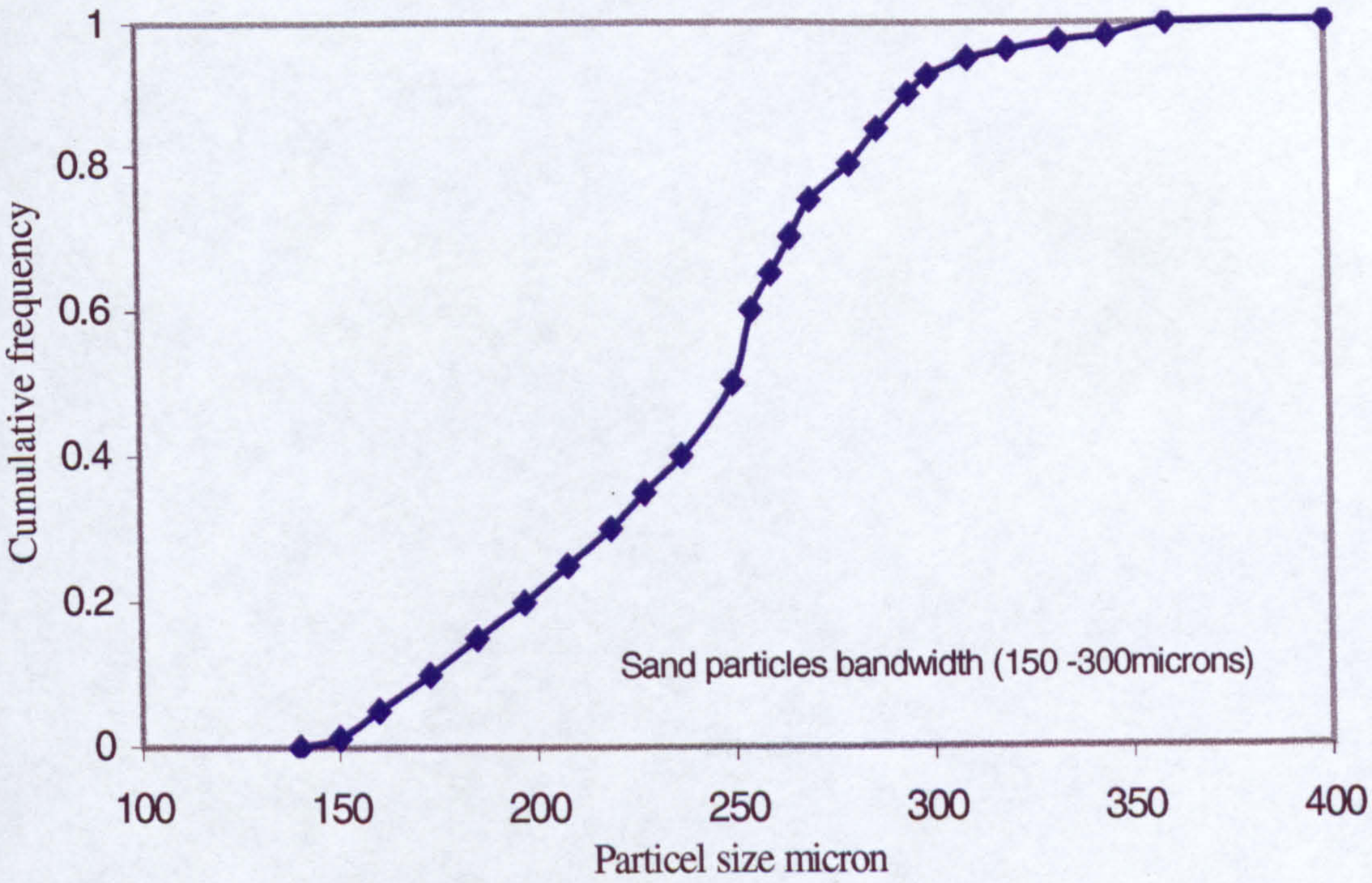


Figure 3-15 Narrow size bandwidth (150 -300microns) sand particles distribution

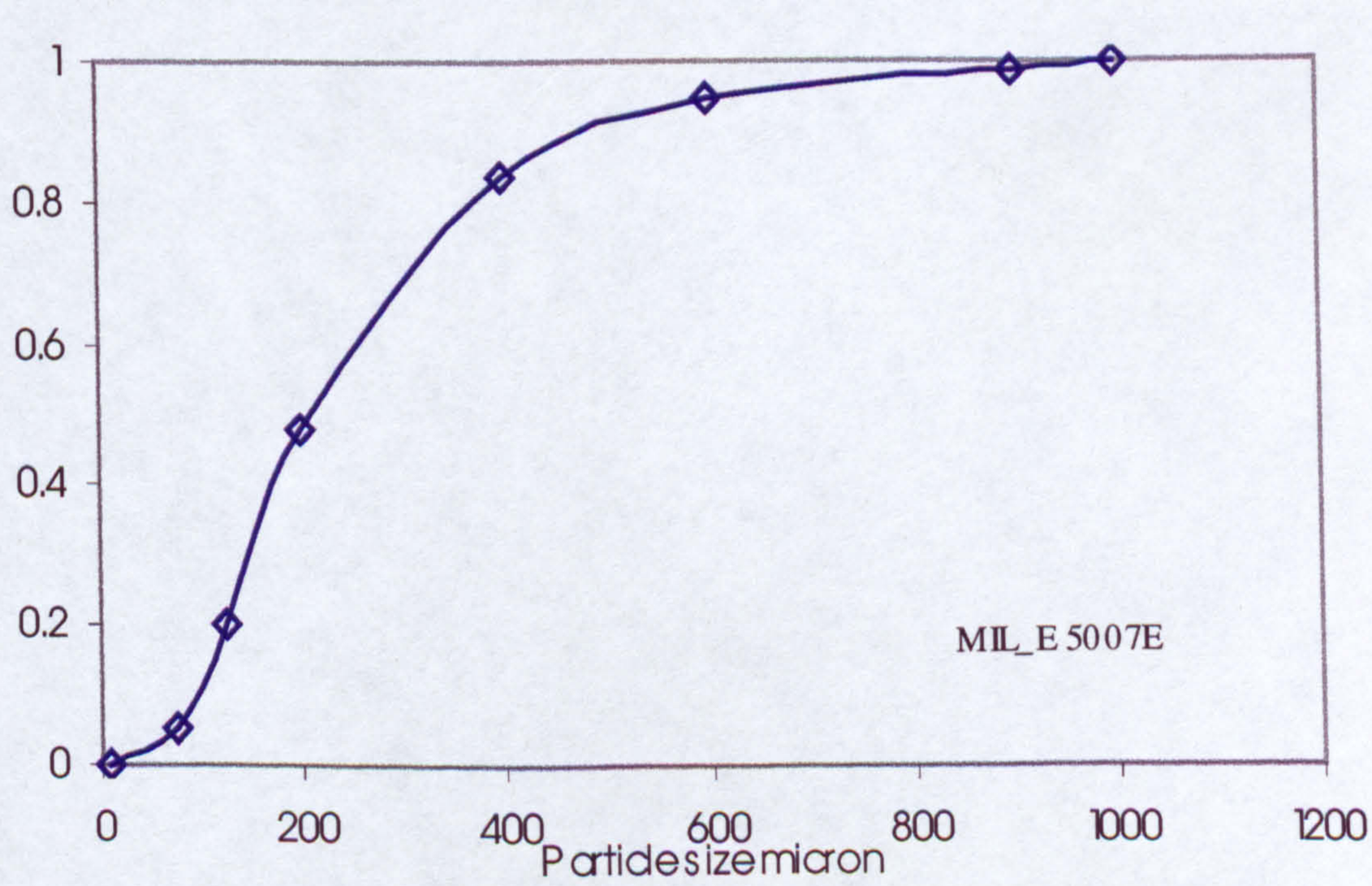


Figure 3-16 MIL_E 5007E 0 -1000 micron particle sand size distribution

Figure 3-17 Trajectories of sand particles (150-300 micron) seeded upstream locally

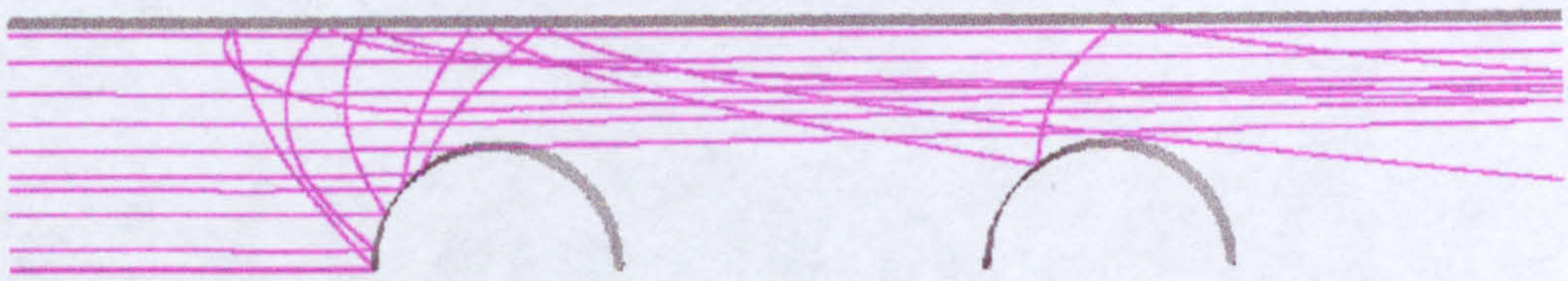

Figure 3-18 Trajectories of sand particles (150-300 micron) seeded upstream globally

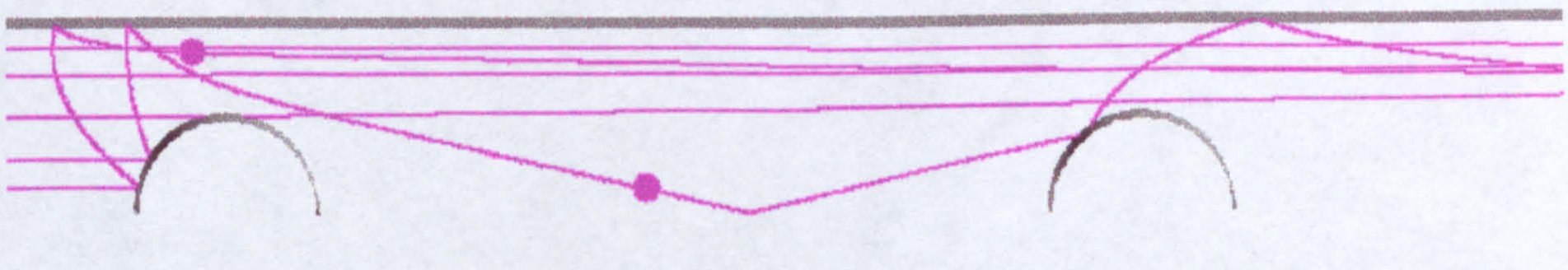

Figure 3-19 Trajectories of (150-300 micron) sand particles seeded upstream globally

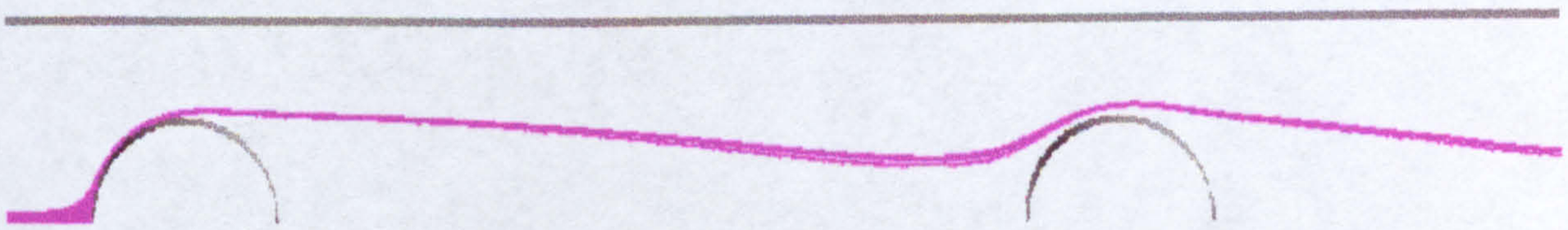

Figure 3-20a Trajectories of 10 micron around half tandem cylinders

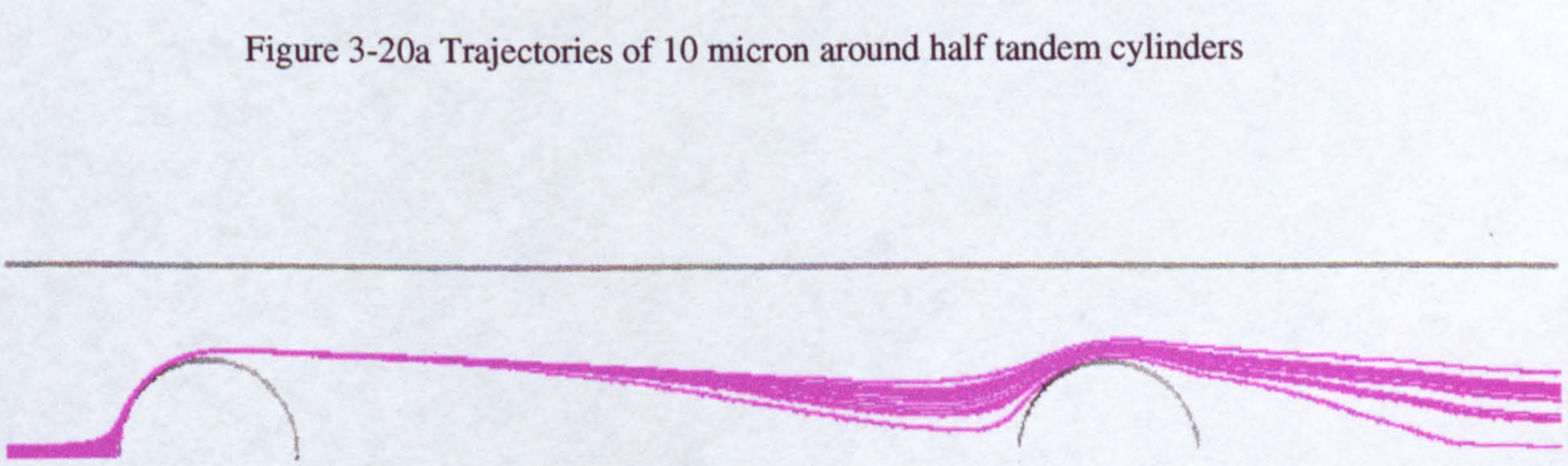

Figure 3-20b Trajectories of 10 micron around half tandem cylinders considering turbulence

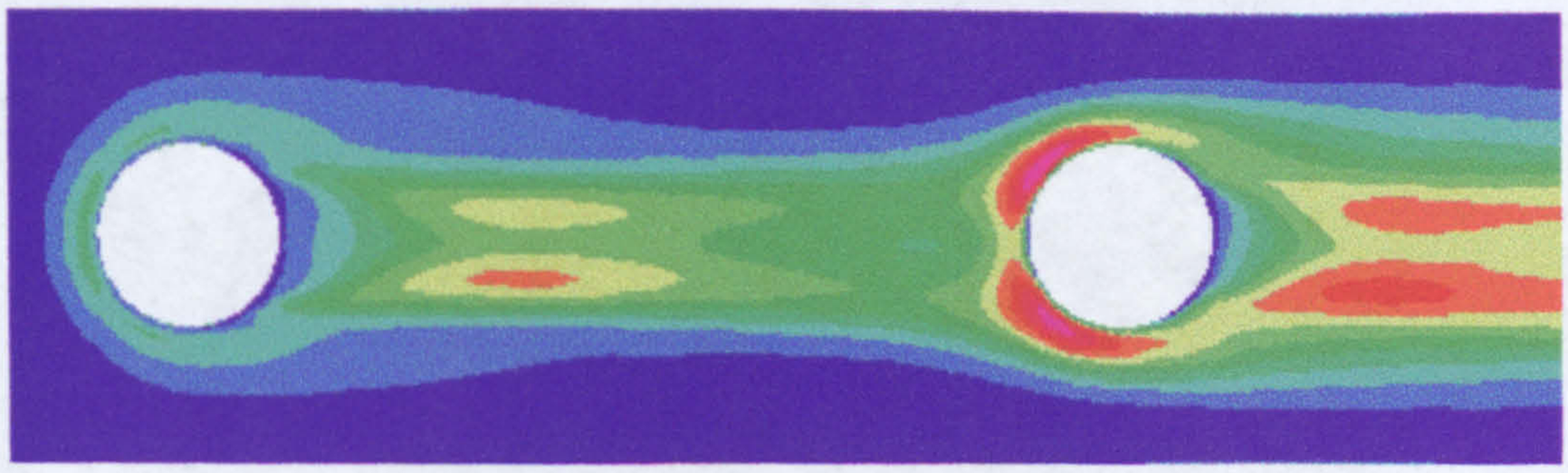

Figure 3-21a Turbulent kinetic energy around tandem cylinders

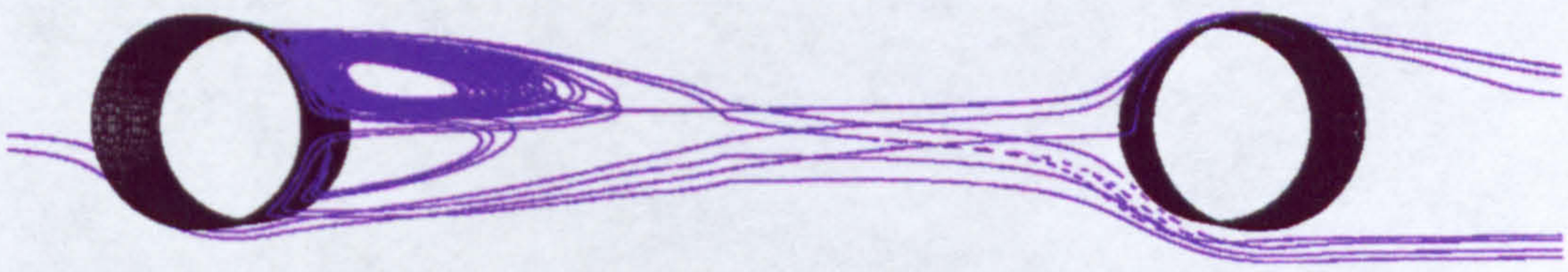

Figure 3-21b Flow streak-lines around tandem cylinders

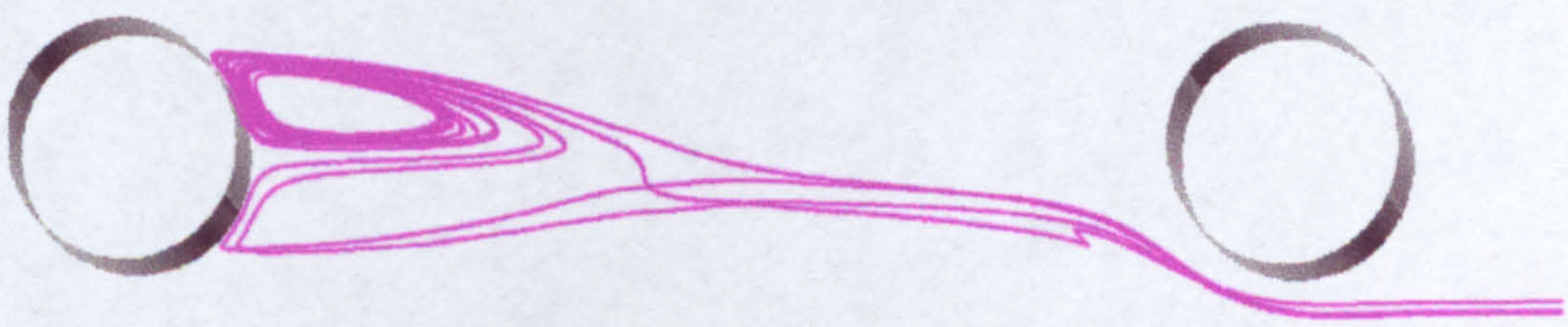

Figure 3-21c Trajectories of 10 micron particles seeded in the wake
of the first cylinder including turbulence effect

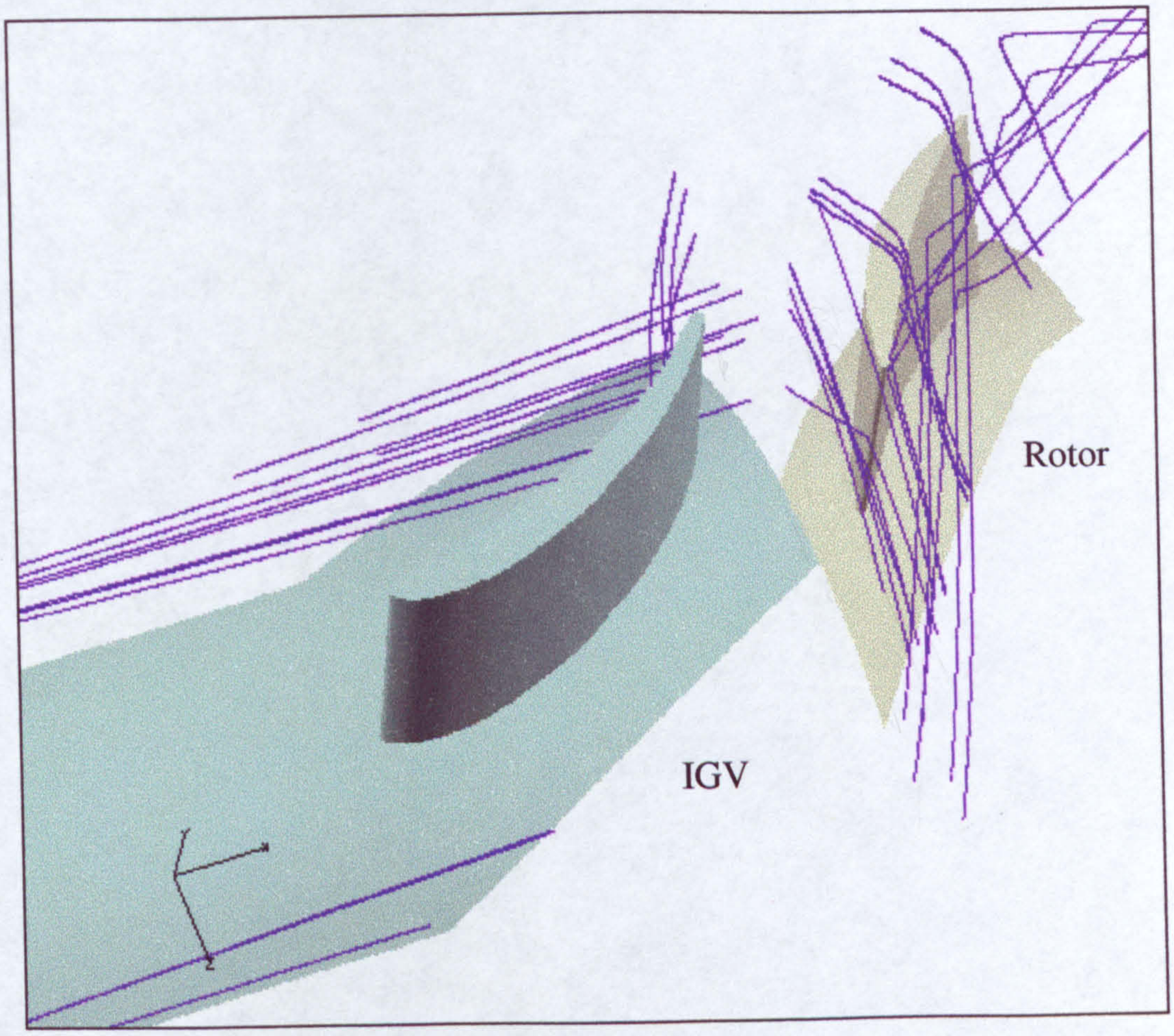


Figure 3-22 Trajectories of (150-300 micron) sand particles injected locally at mid height

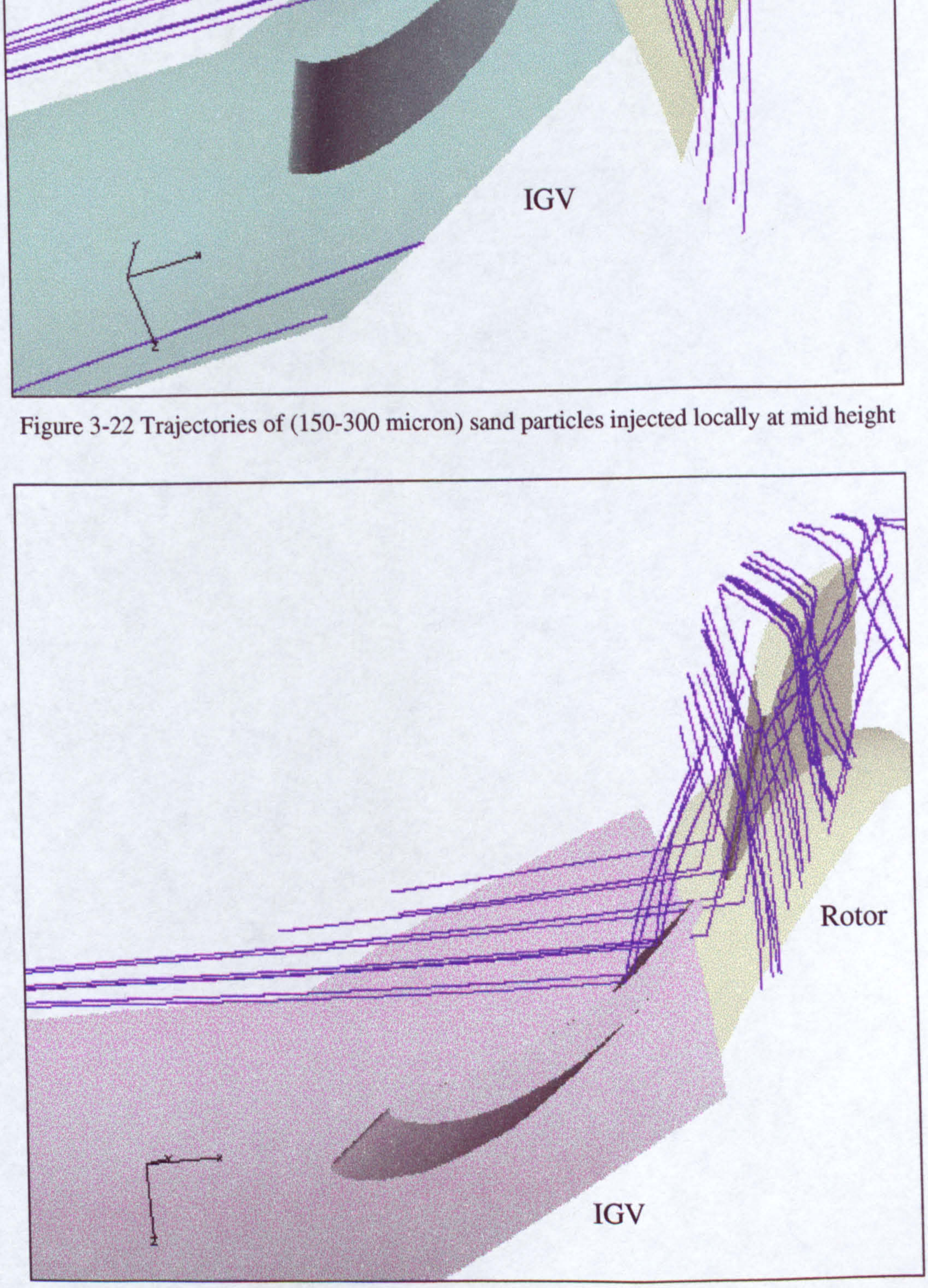


Figure 3-23 Trajectories of (150-300 micron) sand particles injected locally at mid height

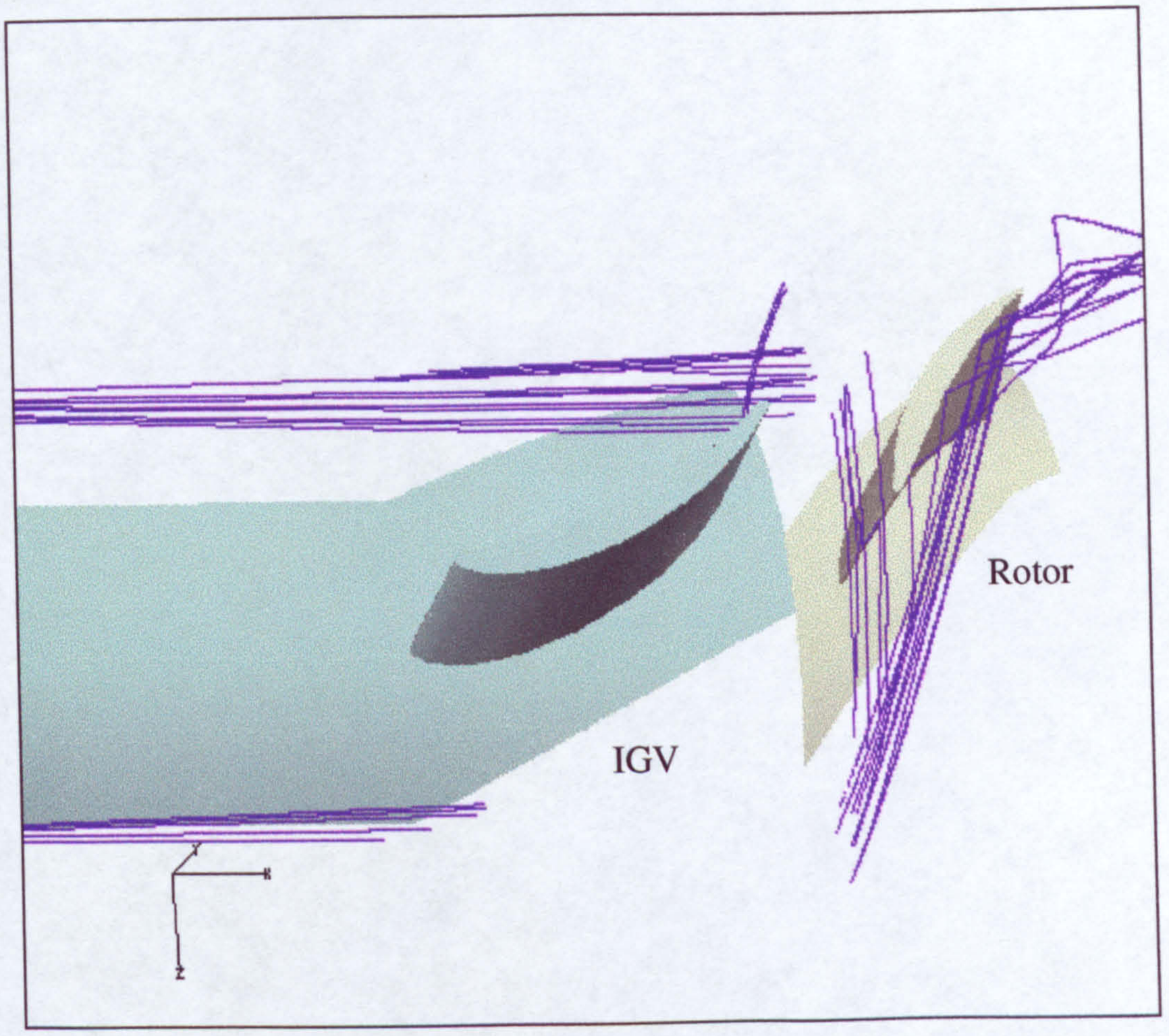


Figure 3-24 Trajectories of (150-300 micron) sand particles injected locally near the tip

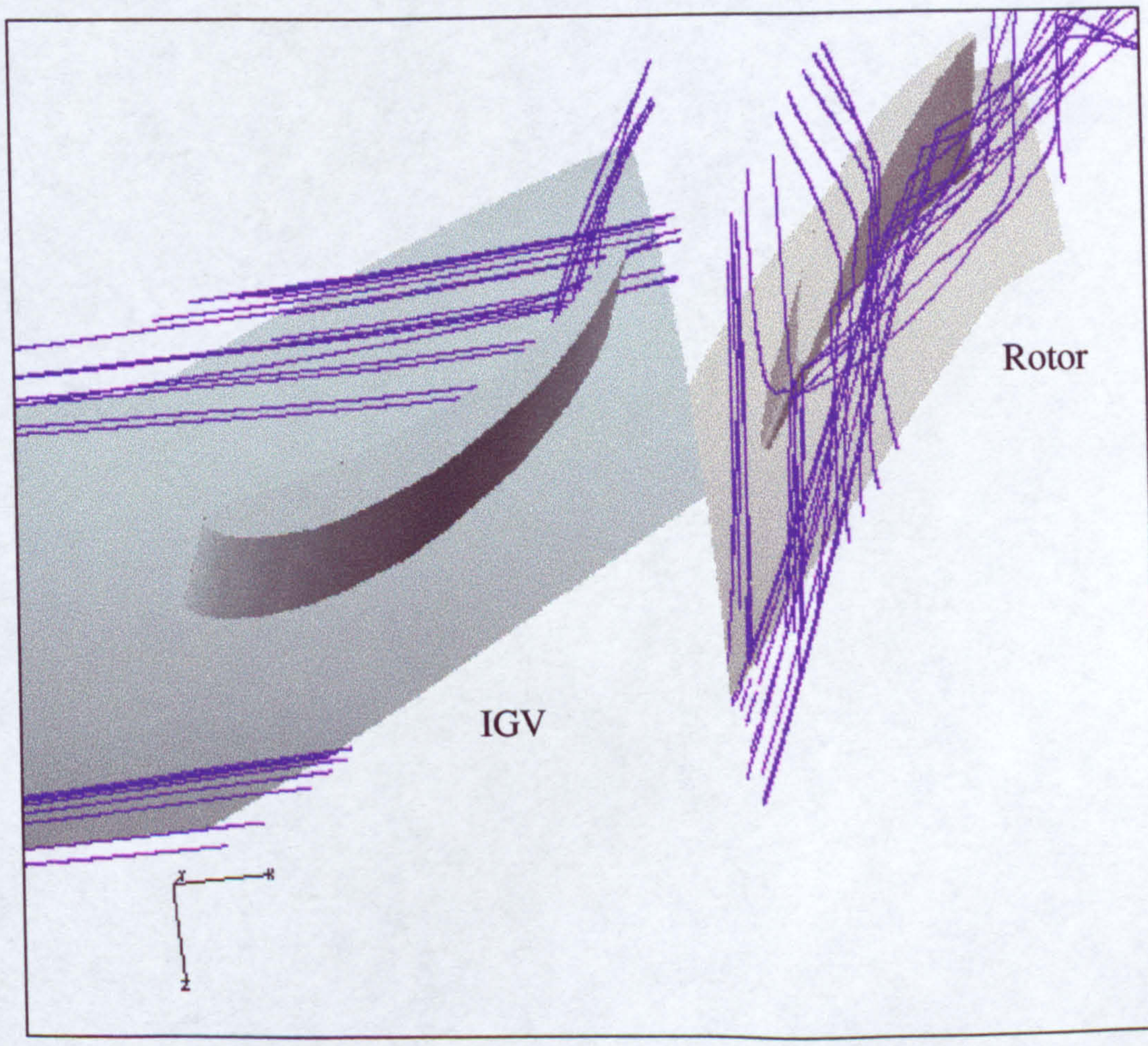


Figure 3-25 Trajectories of (150-300 micron) sand particles injected locally near the hub

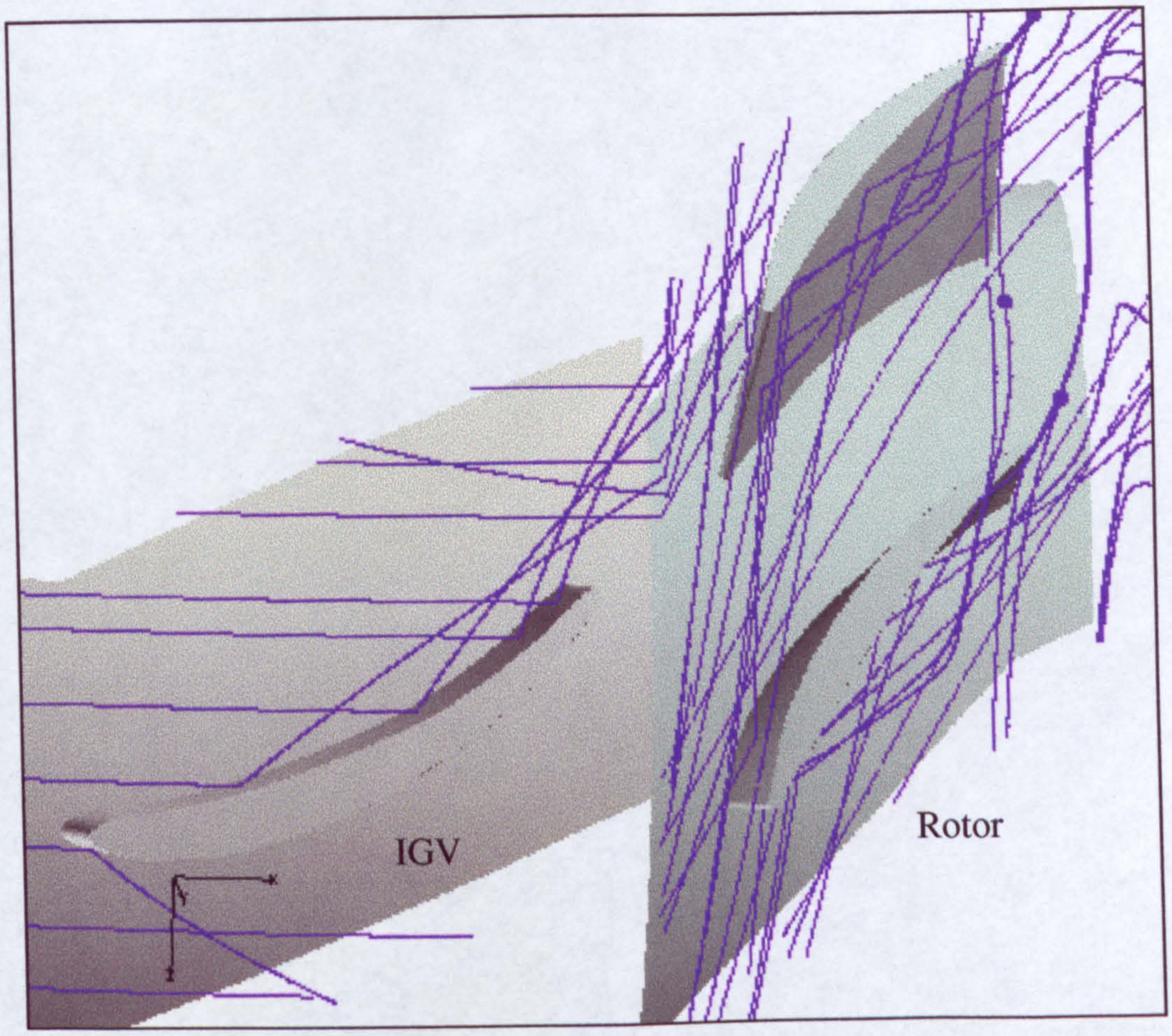


Figure 3-26 Trajectories of (150-300 micron) sand particles seeded globally

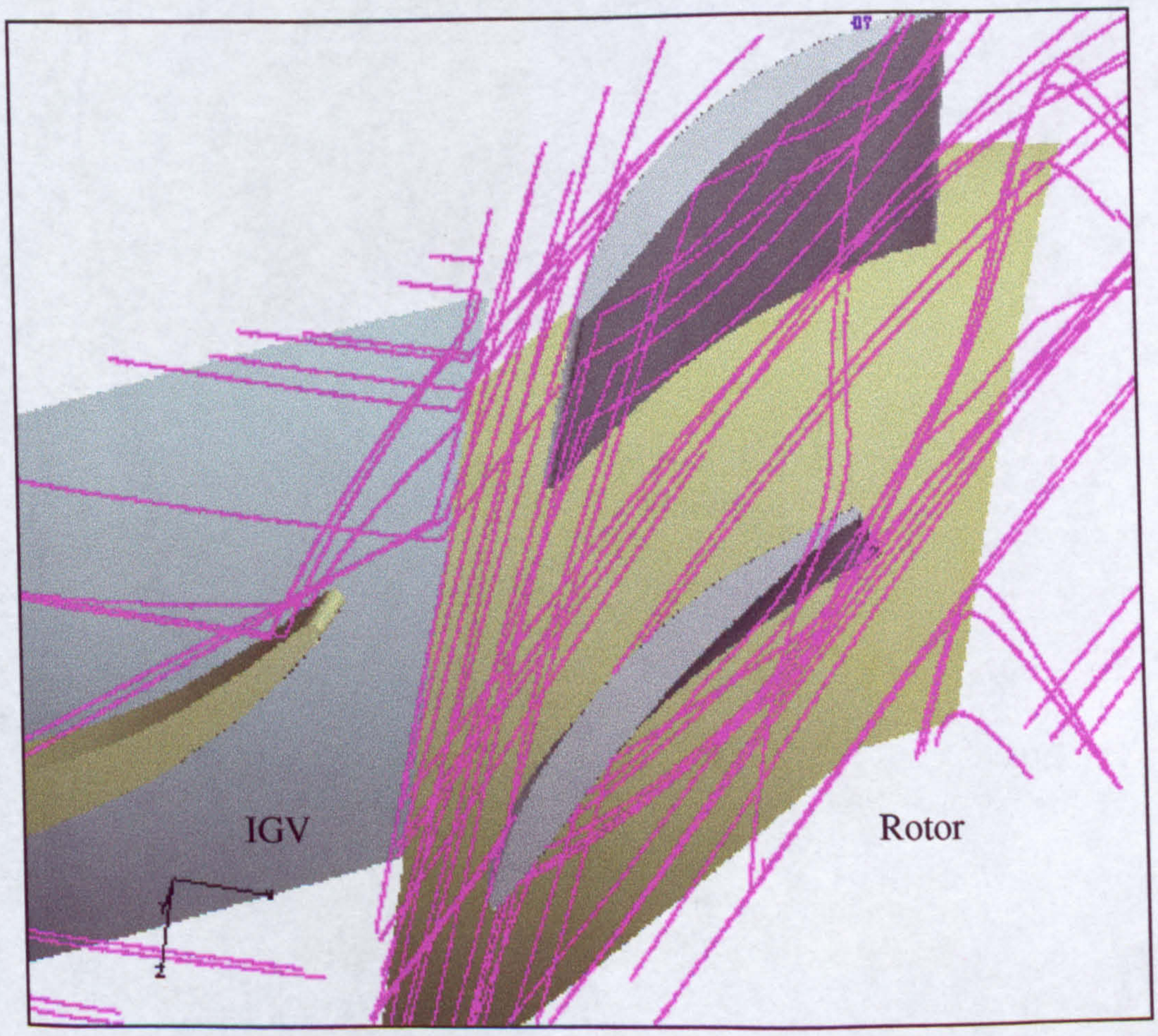


Figure 3-27 Trajectories of MIL-E5007 sand particles seeded globally

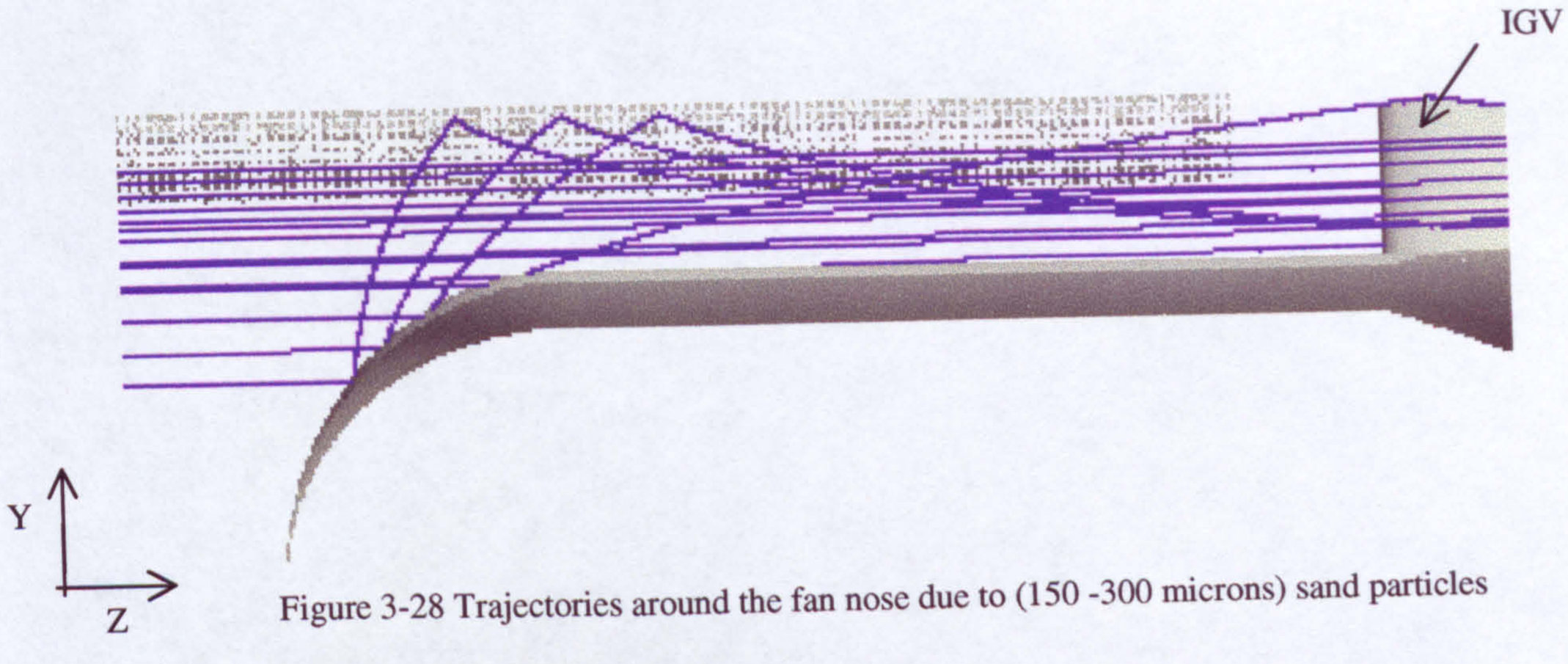


Figure 3-28 Trajectories around the fan nose due to (150 -300 microns) sand particles


Figure 3-29 Trajectories of (150 -300 microns) sand particles between rotor blades and at outlet

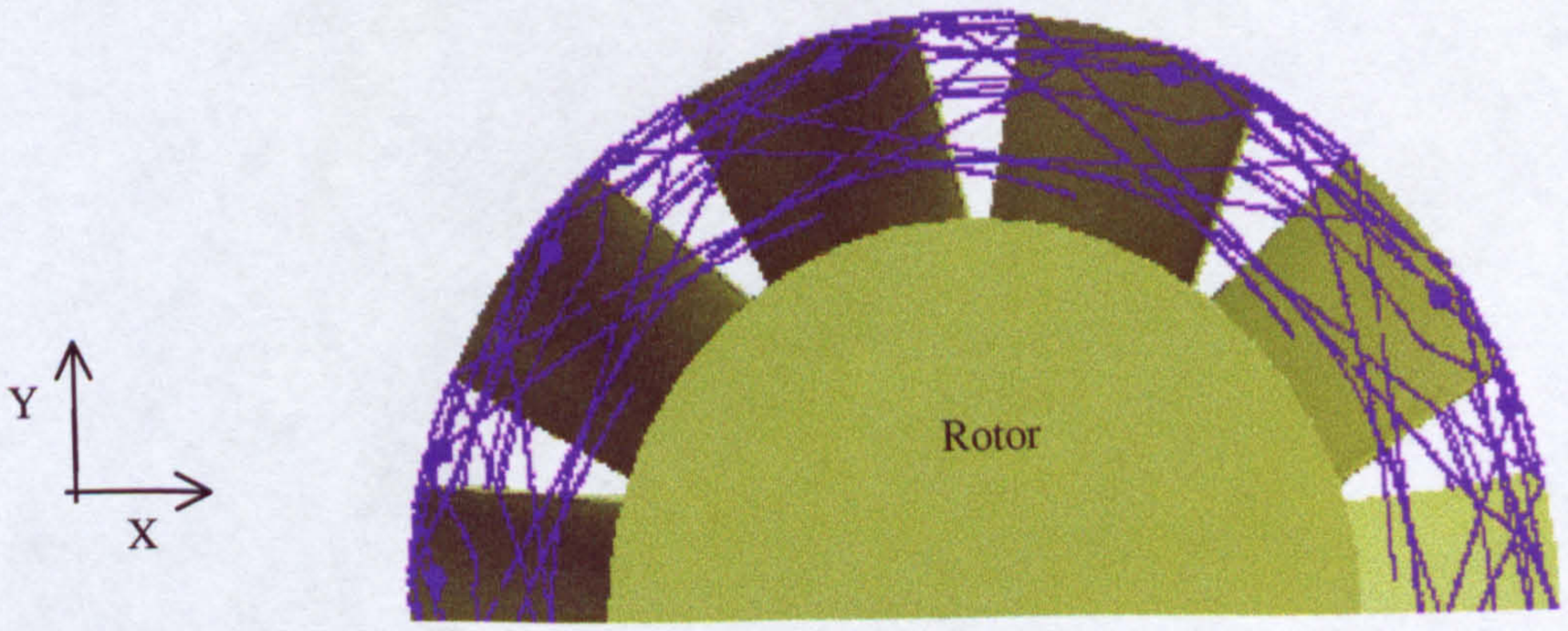


Figure 3-30 Trajectories of (150 -300 microns) sand particles at outlet from the rotor

Figure 3-31 Trajectories of fine particles between rotor blades

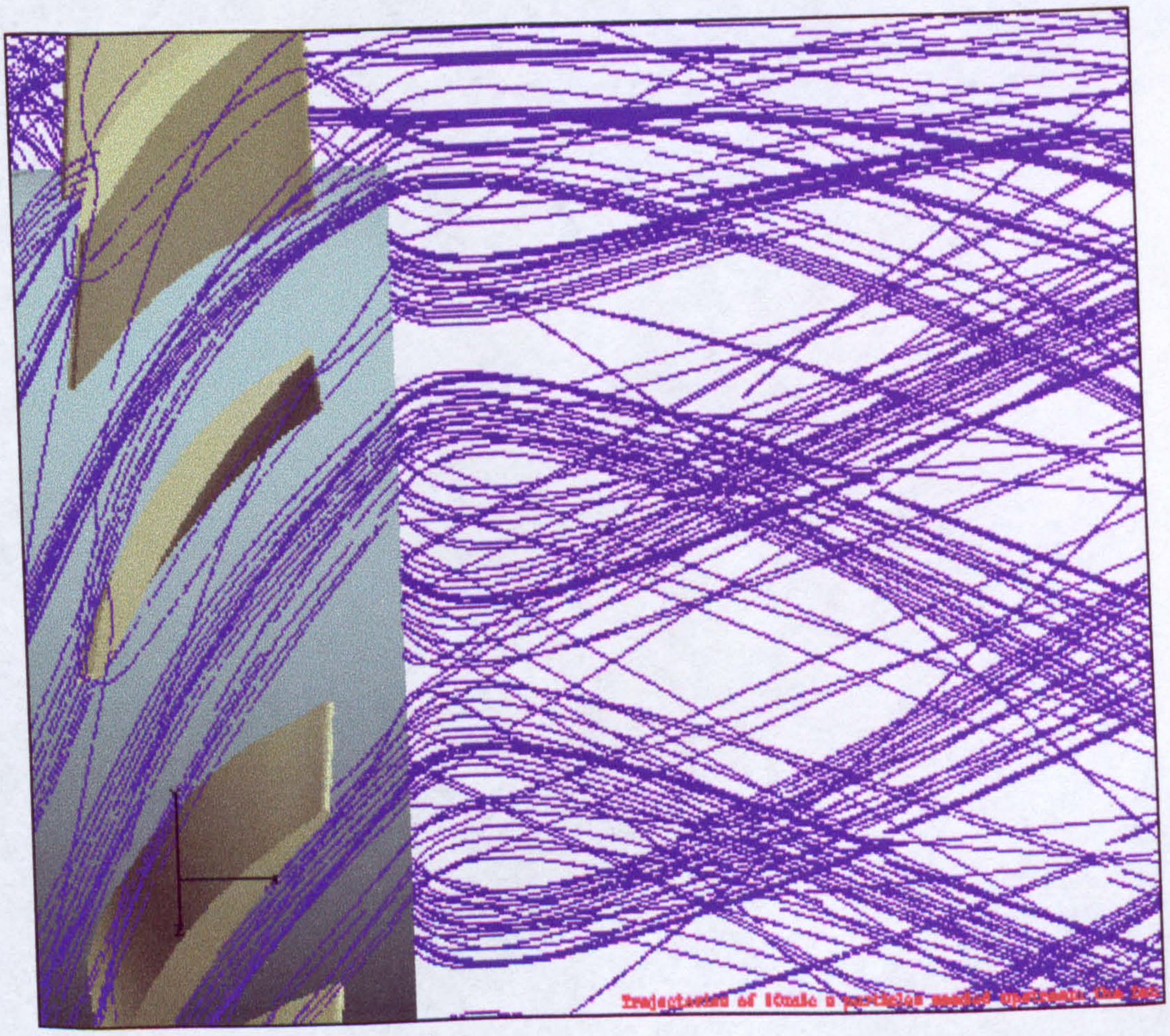

Figure 3-32 Trajectories of fine particles between rotor blades considering turbulence

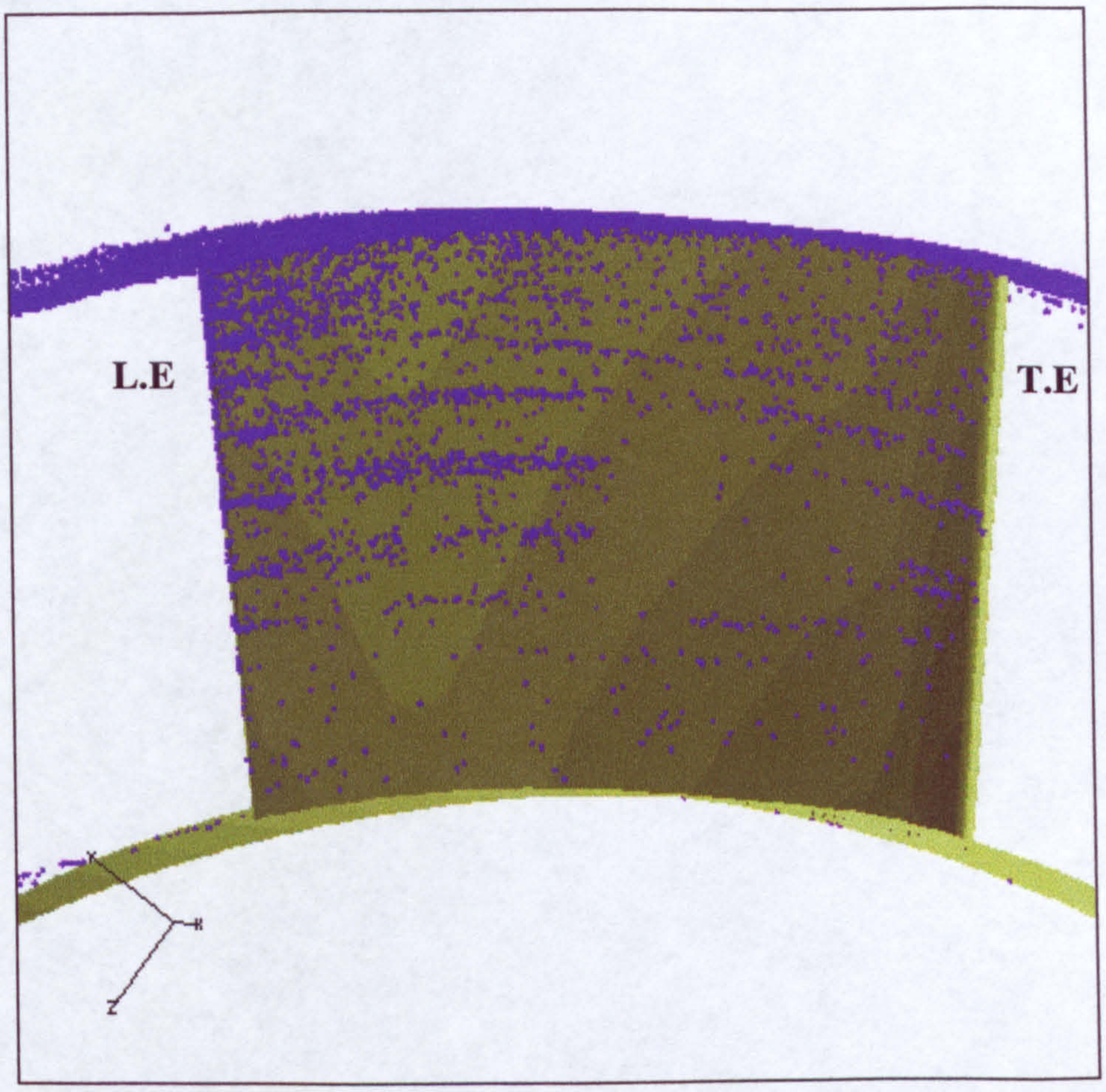


Figure 3-33 Particle impacts on the pressure side of the rotor when seeding at mid height

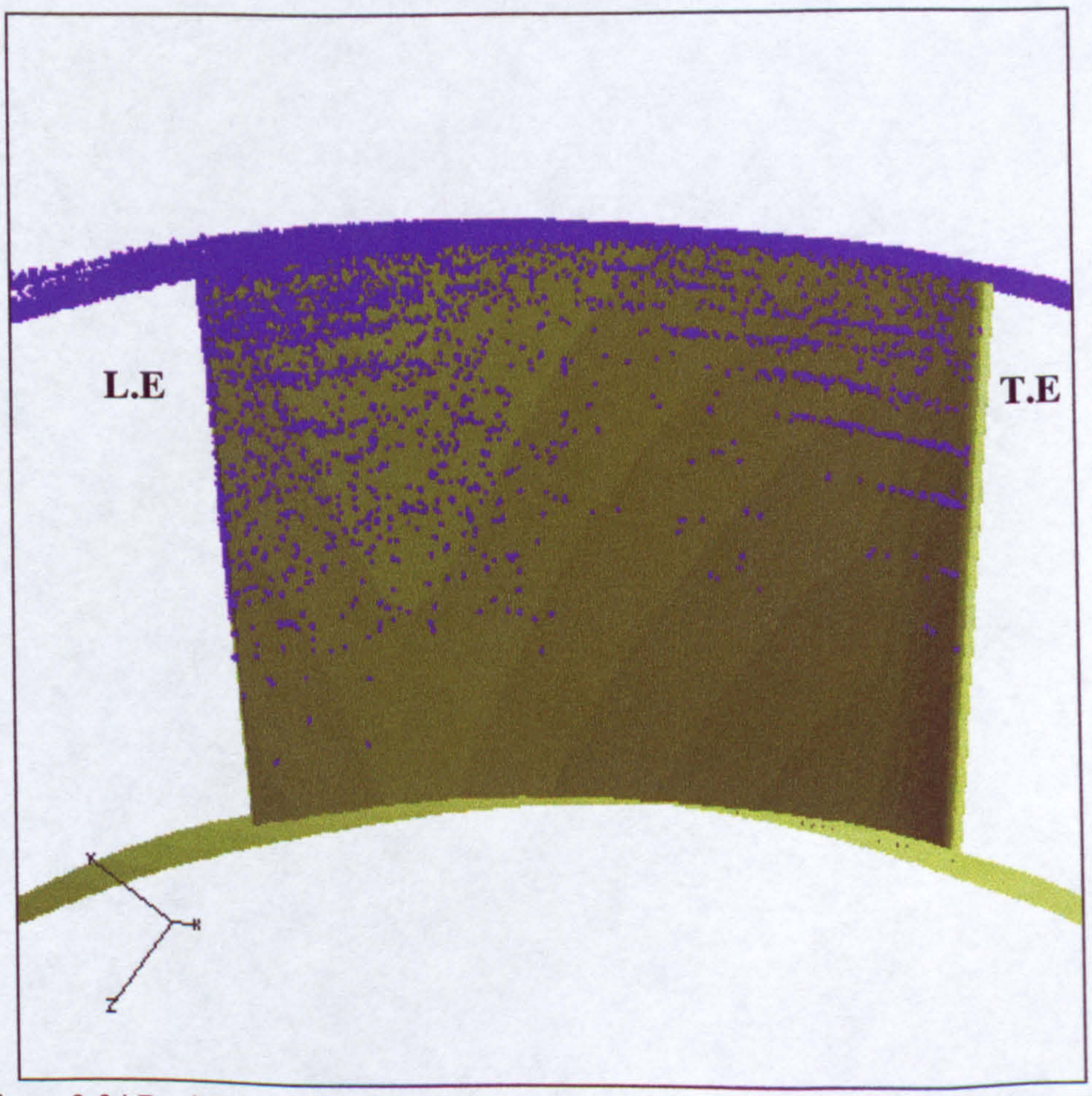


Figure 3-34 Particle impacts on the pressure side of the rotor when seeding near the tip

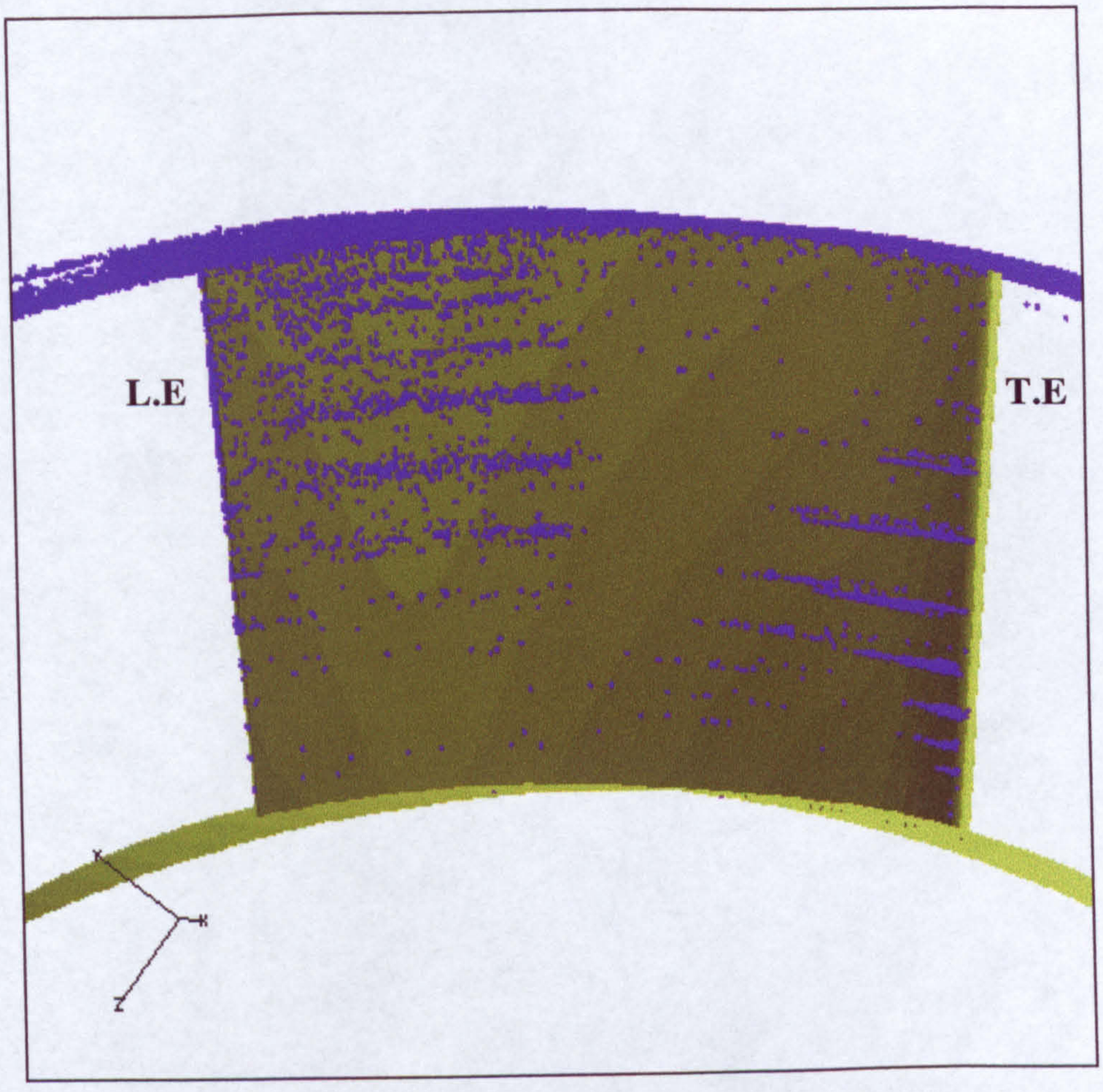


Figure 3-35 Particle impacts on the pressure side of the rotor when seeding near the hub

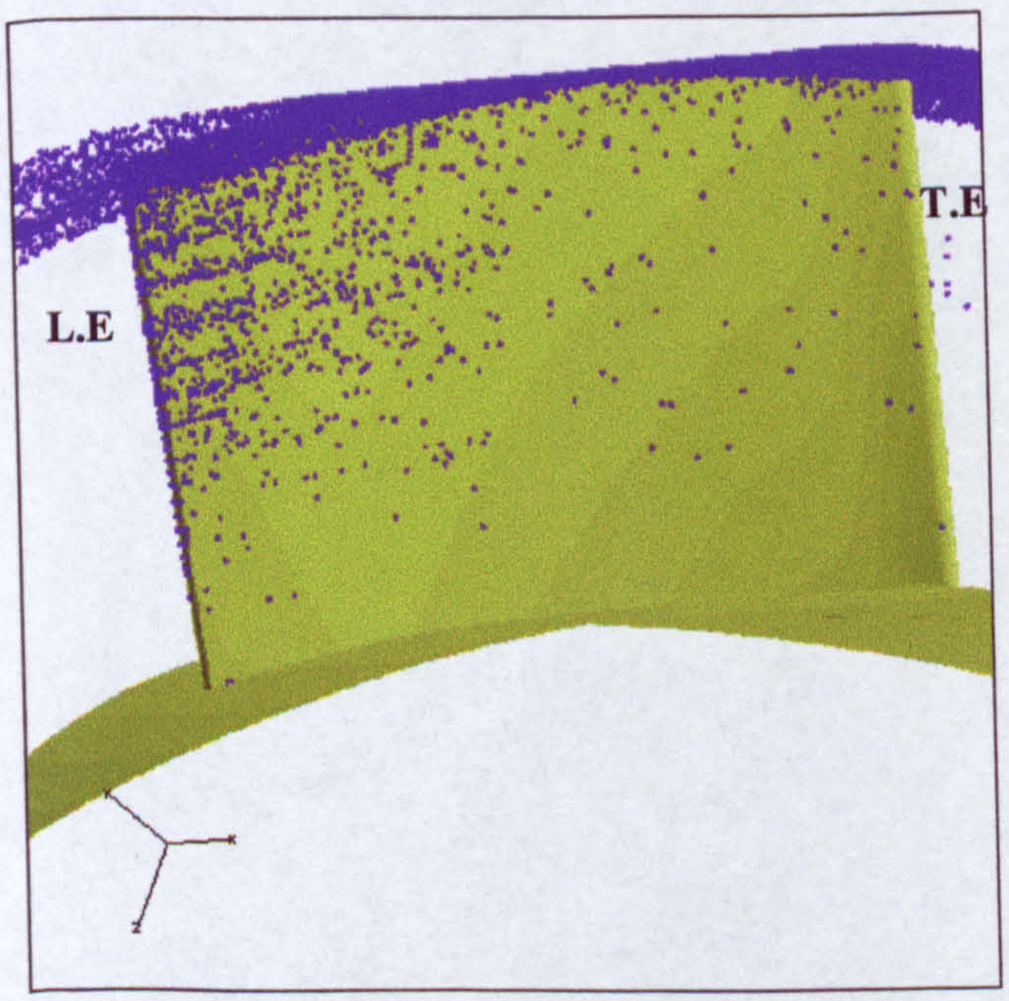


ure 3-36 Impacts on the pressure side due to low concentration of (150-300 microns) sand particles global injection

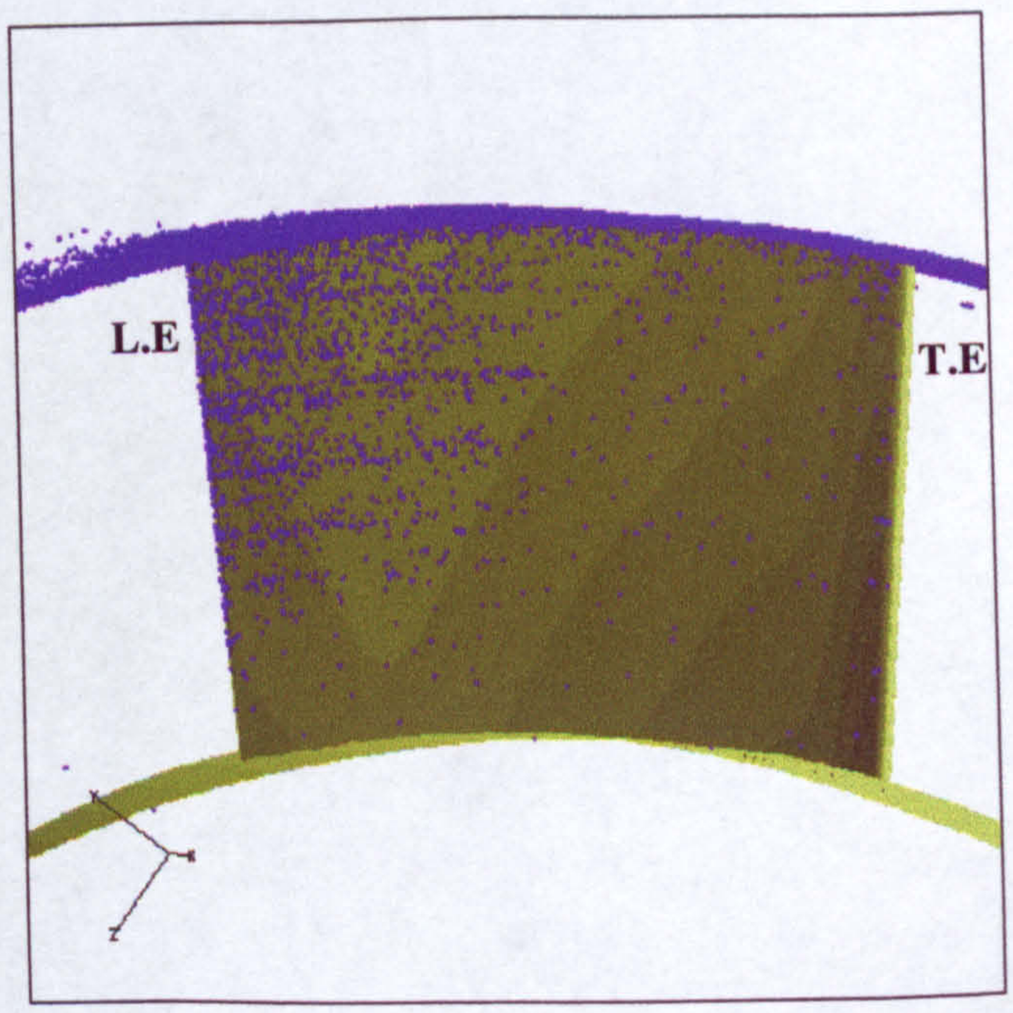


Figure 3-37 Impacts on the pressure due to high concentration of MIL-E 5007E sand particle global injection

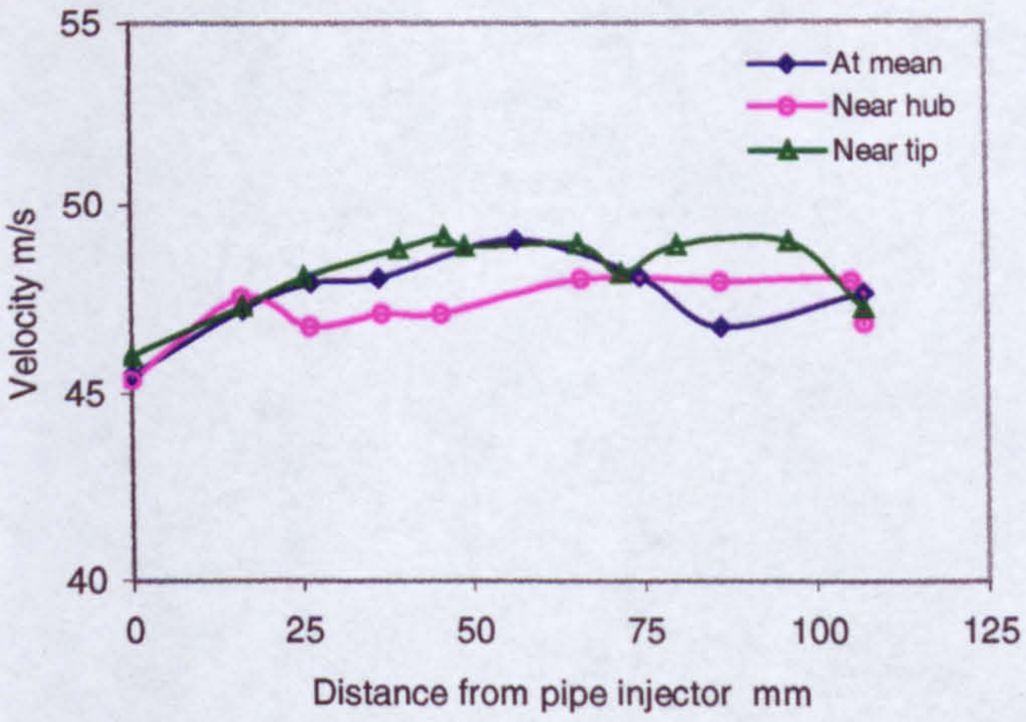


Figure 3-38a Predicted particle velocities from a pipe injector

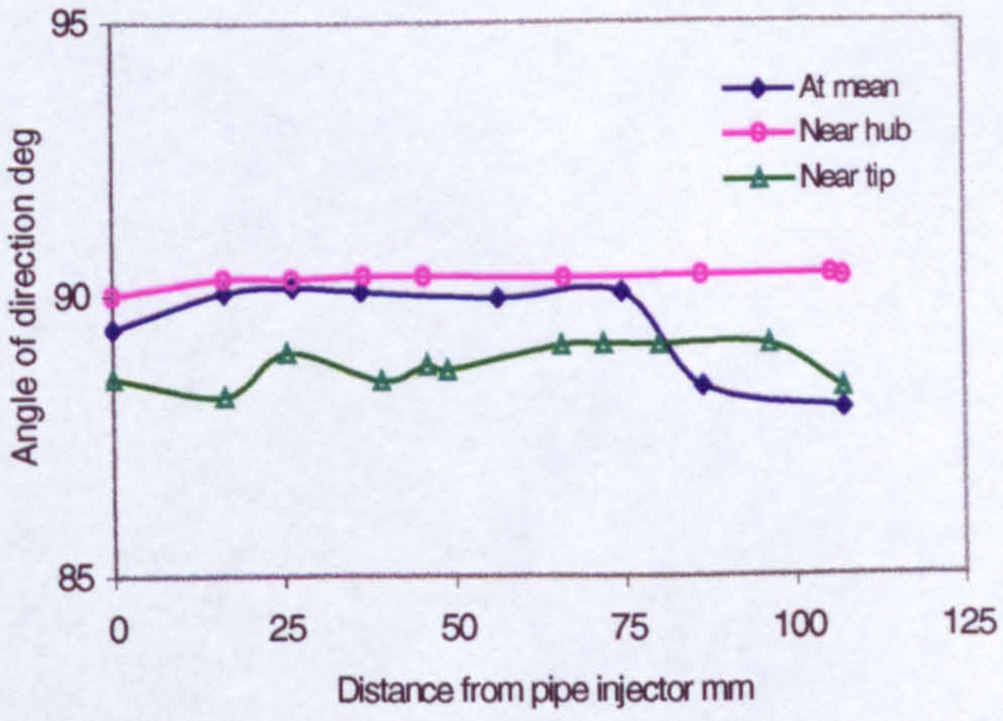


Figure 3-38b Predicted particle angles from a pipe injector

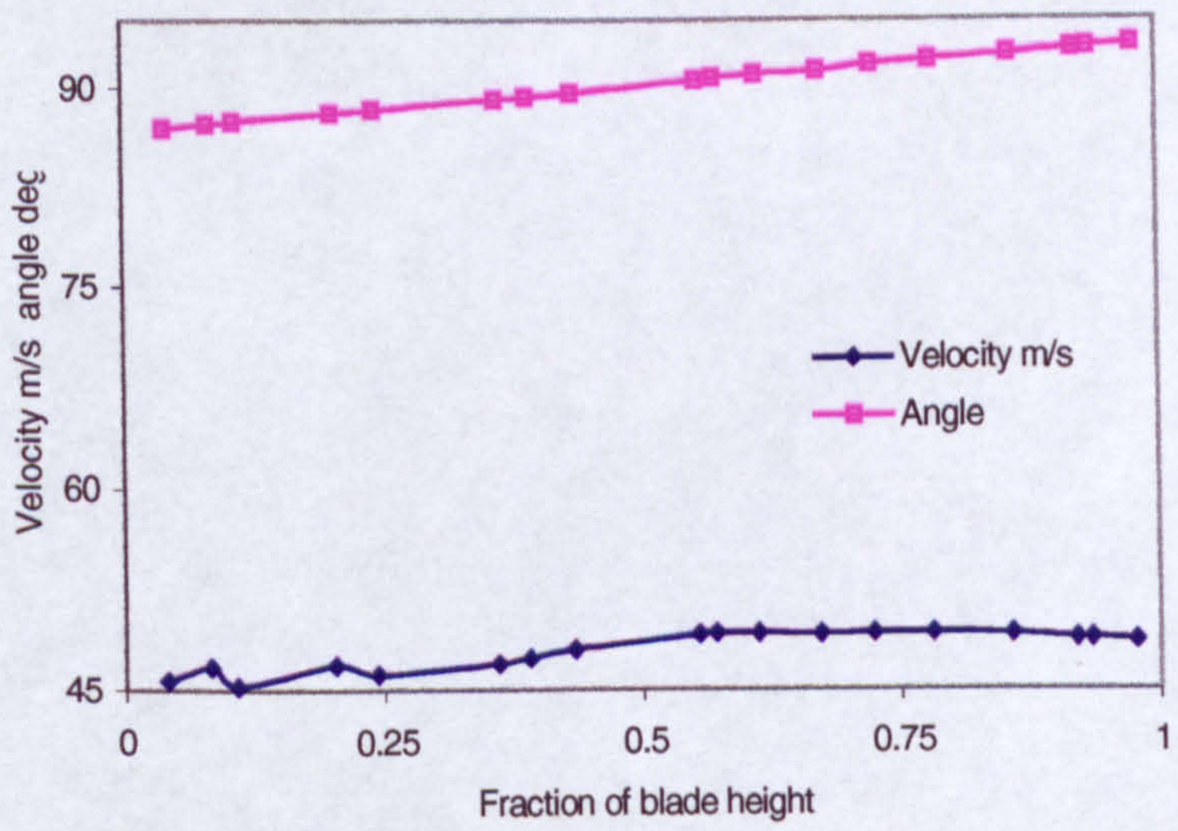


Figure 3-38c Predicted particle velocities across the IGV height

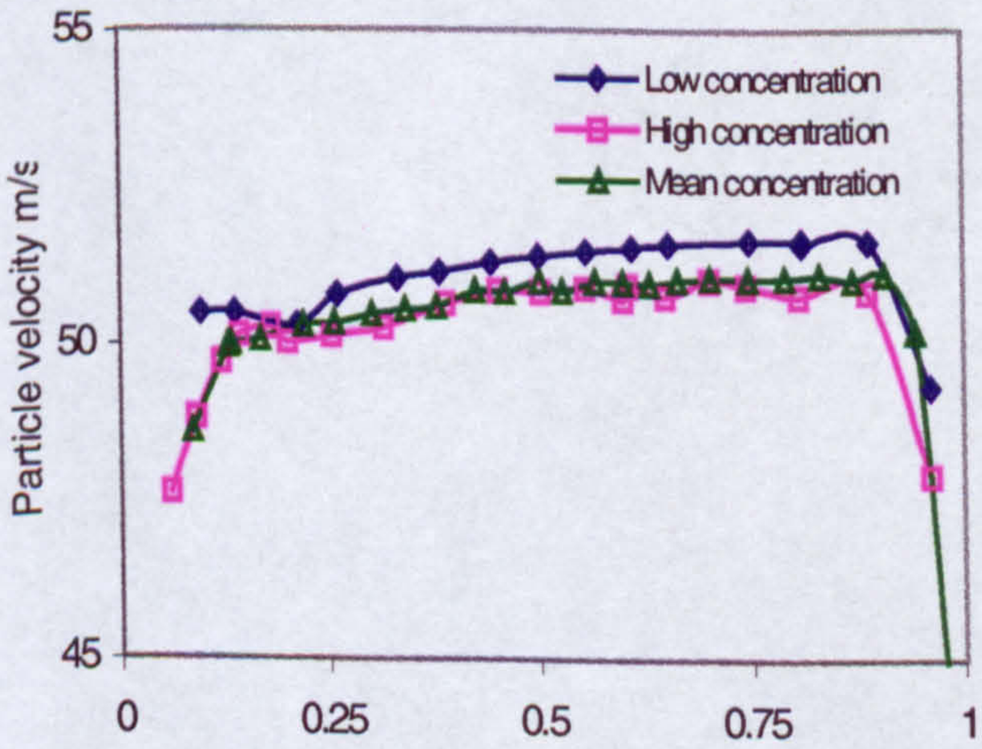


Figure 3-39a Predicted particle velocities across the IGV height

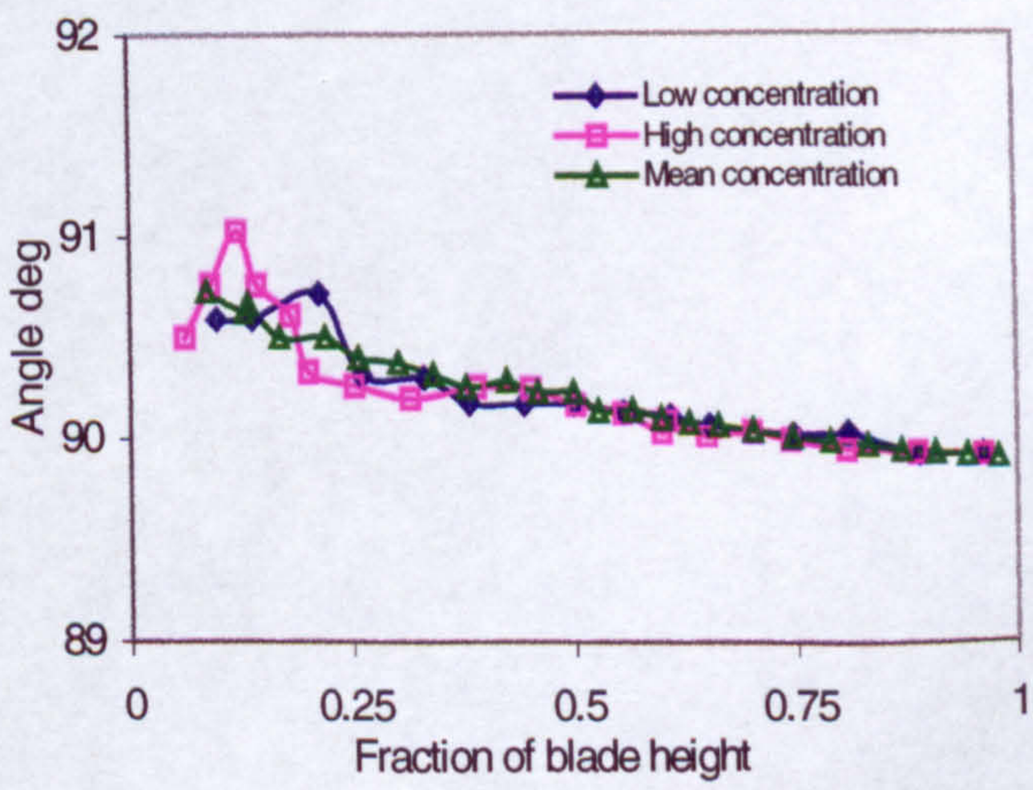


Figure 3-39b Predicted particle angles across the IGV height

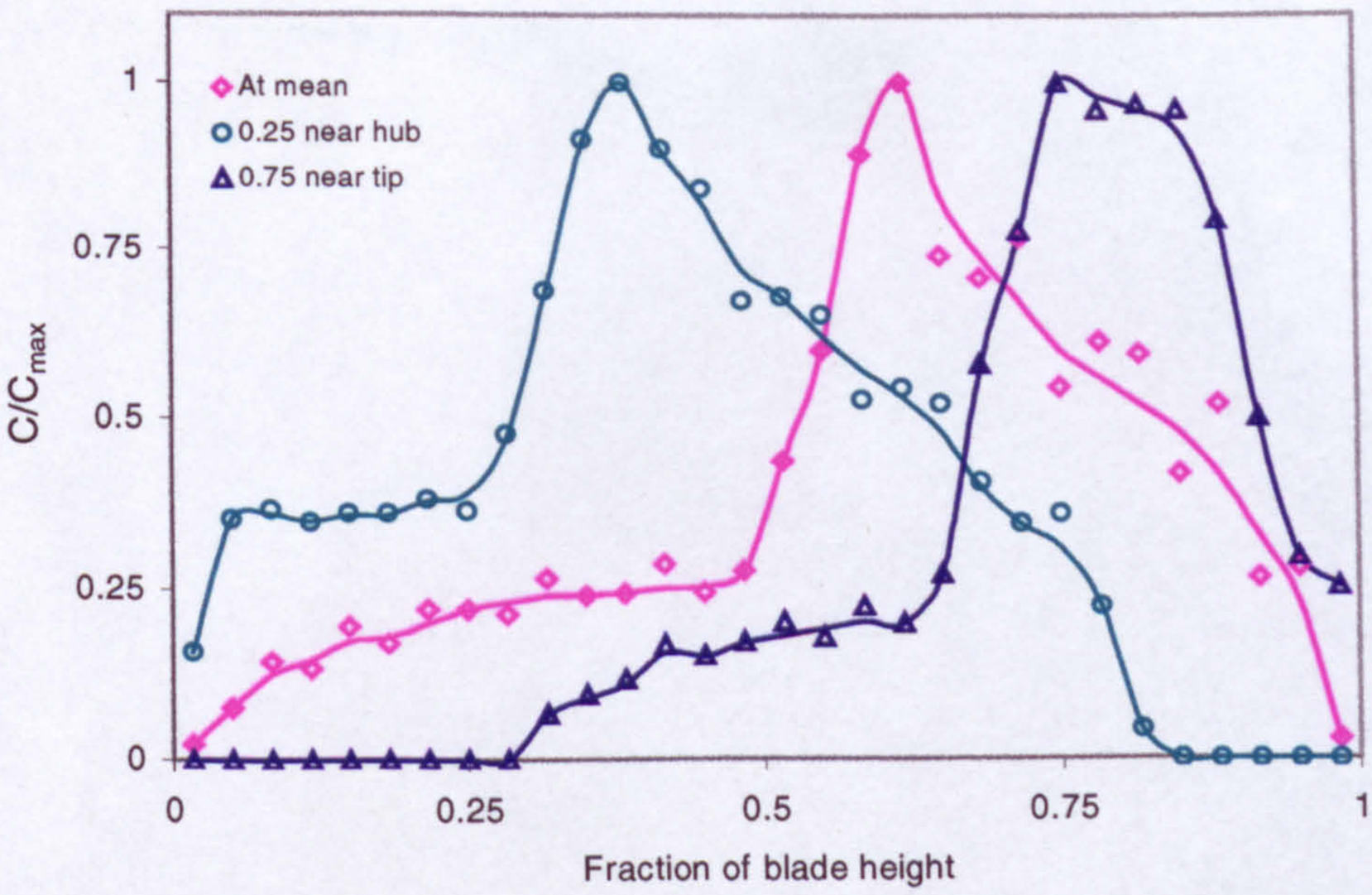


Figure 3-40 Predicted concentration profiles at different height of seeding

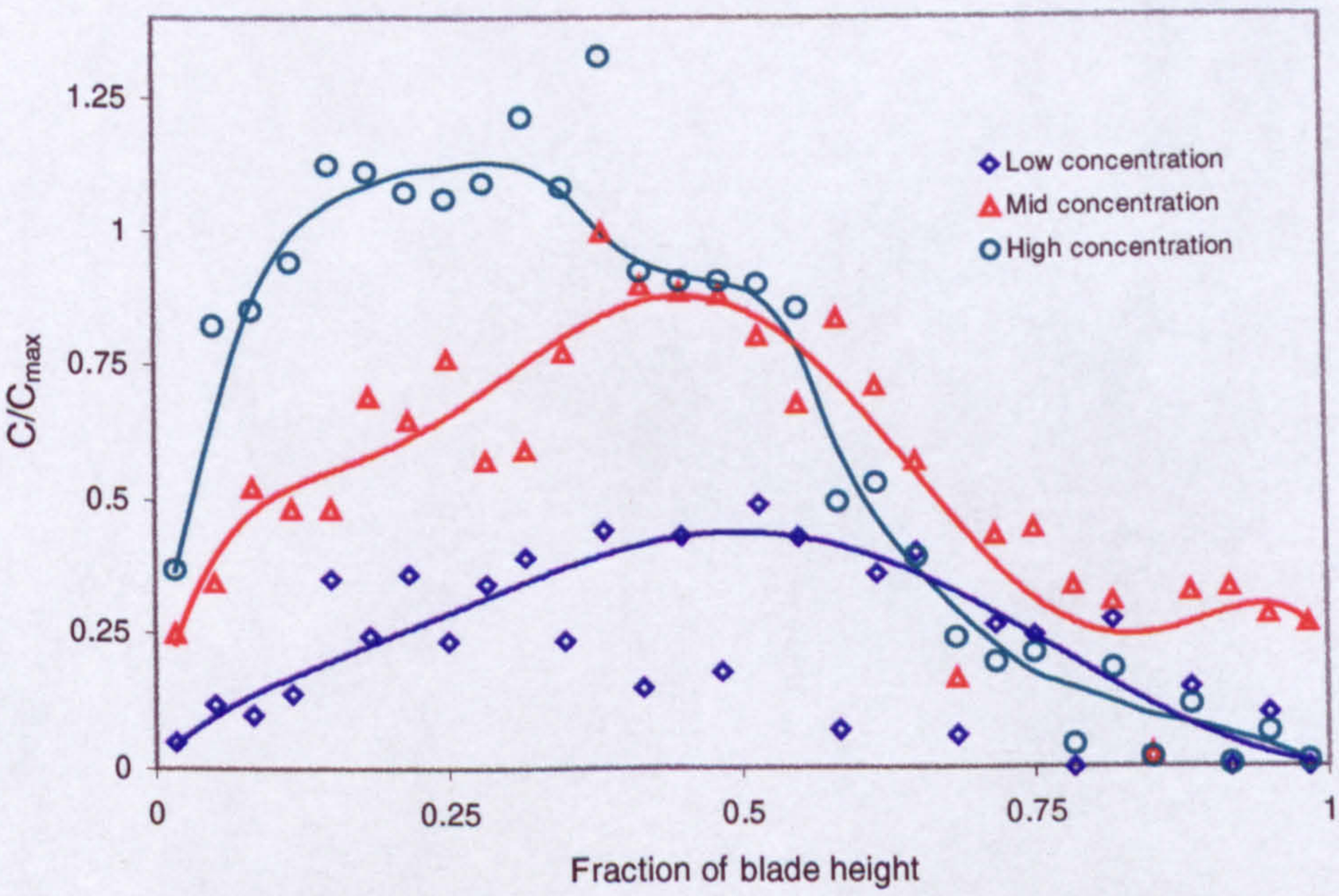


Figure 3-41 Predicted concentration profiles upstream IGV

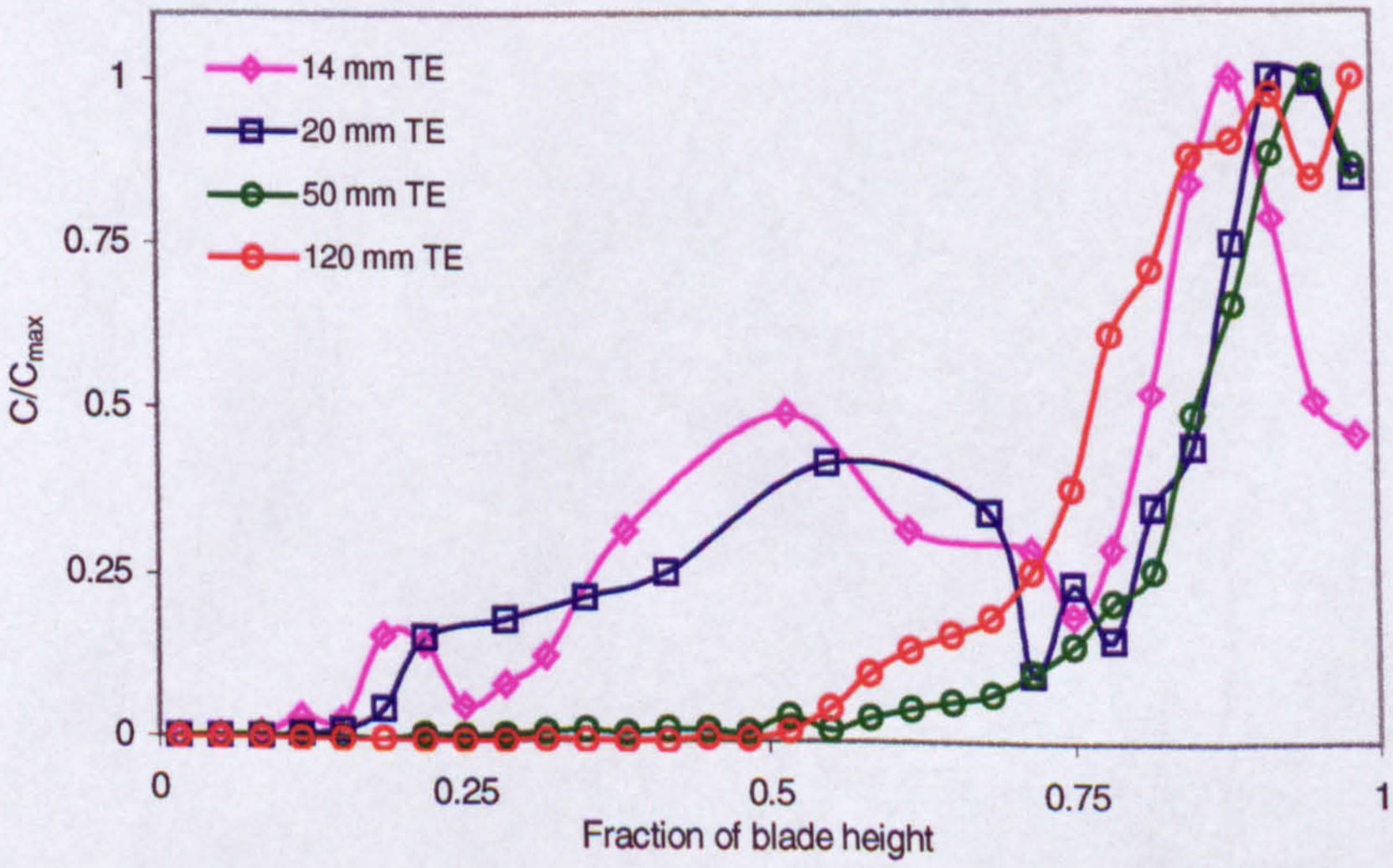


Figure 3-42 Predicted outlet concentration at different axial positions from the rotor outlet

# FIGURES 4

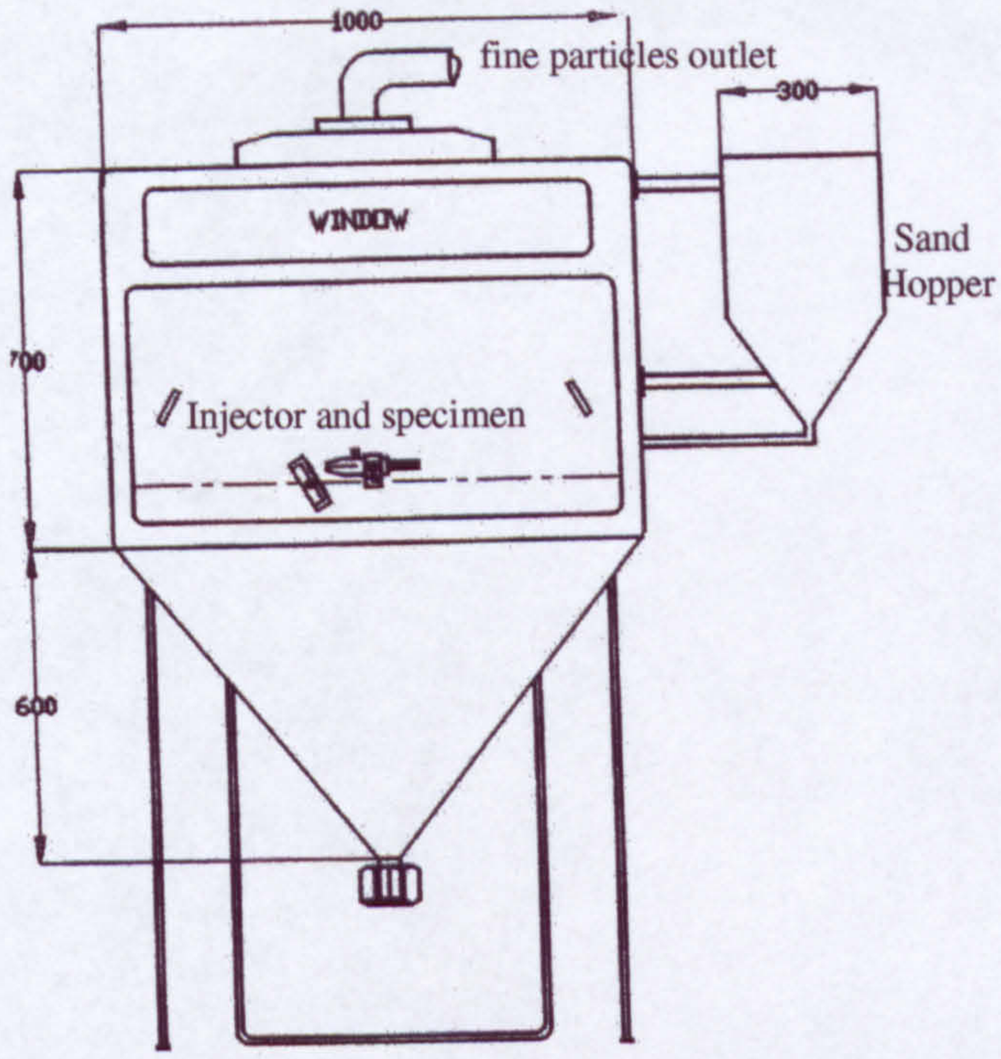


Figure 4-3 Sand blasting rig for erosion testing

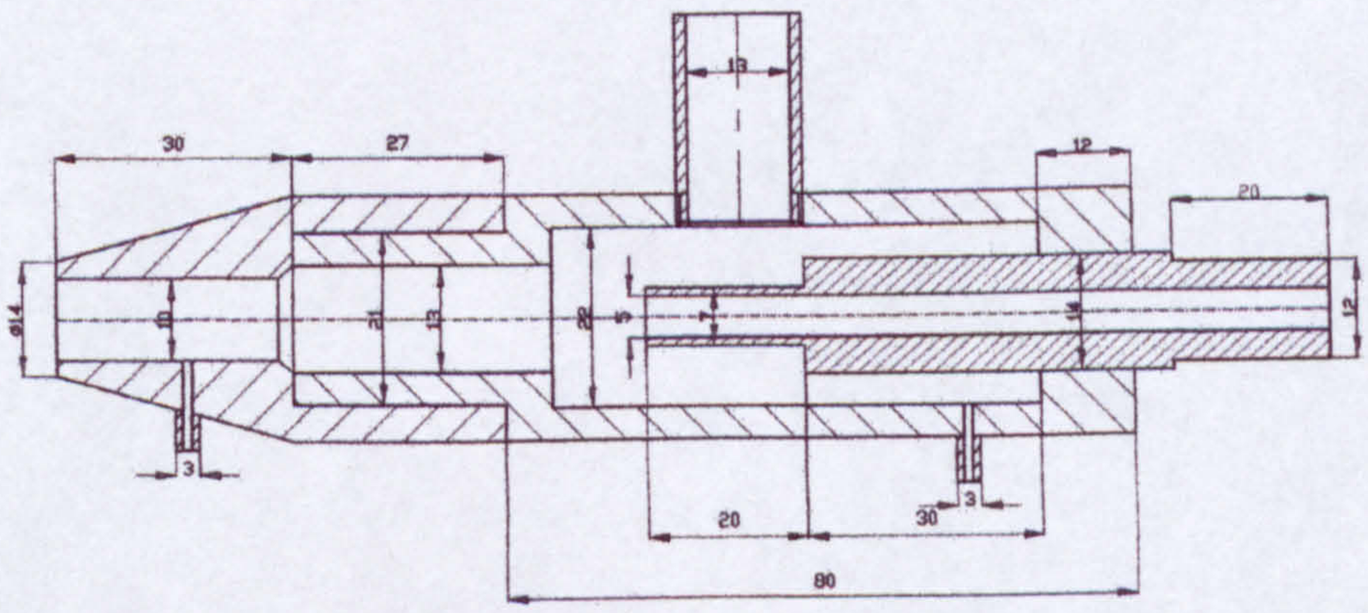


Figure 4-4 Sand particles injector

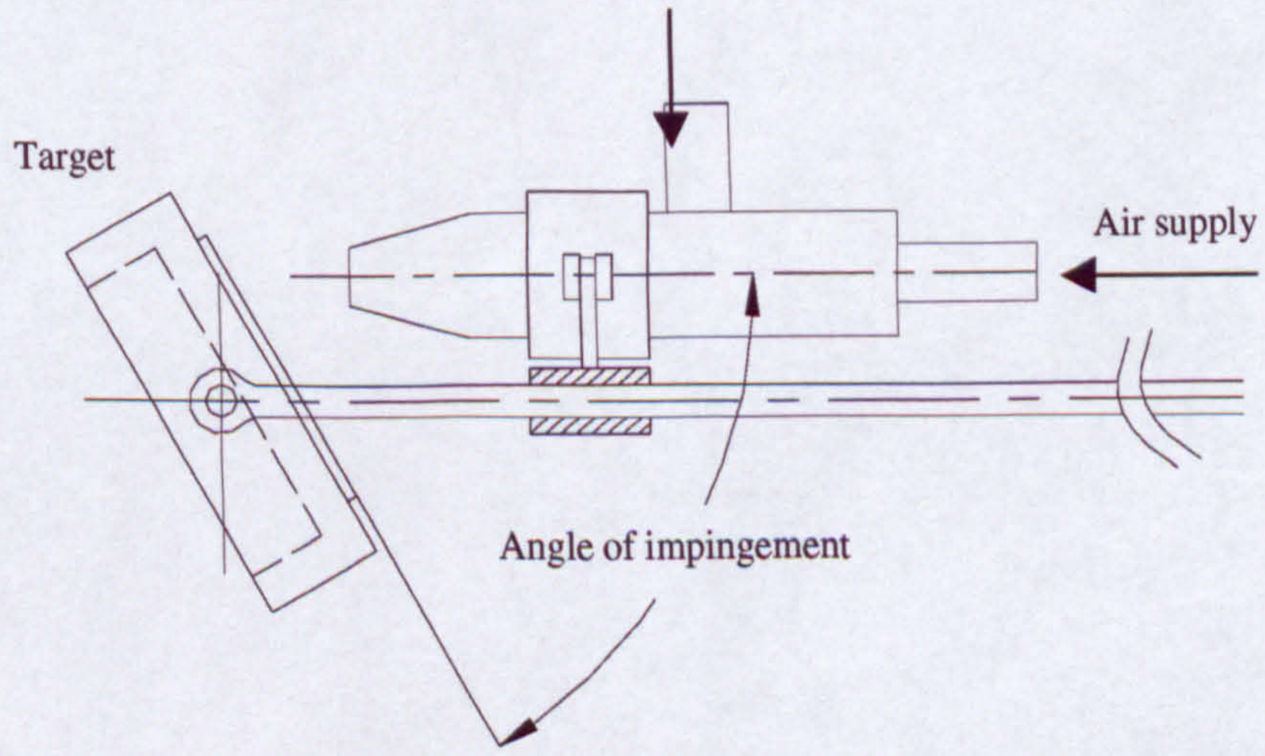


Figure 4-5 Sand particles injector and target assembly

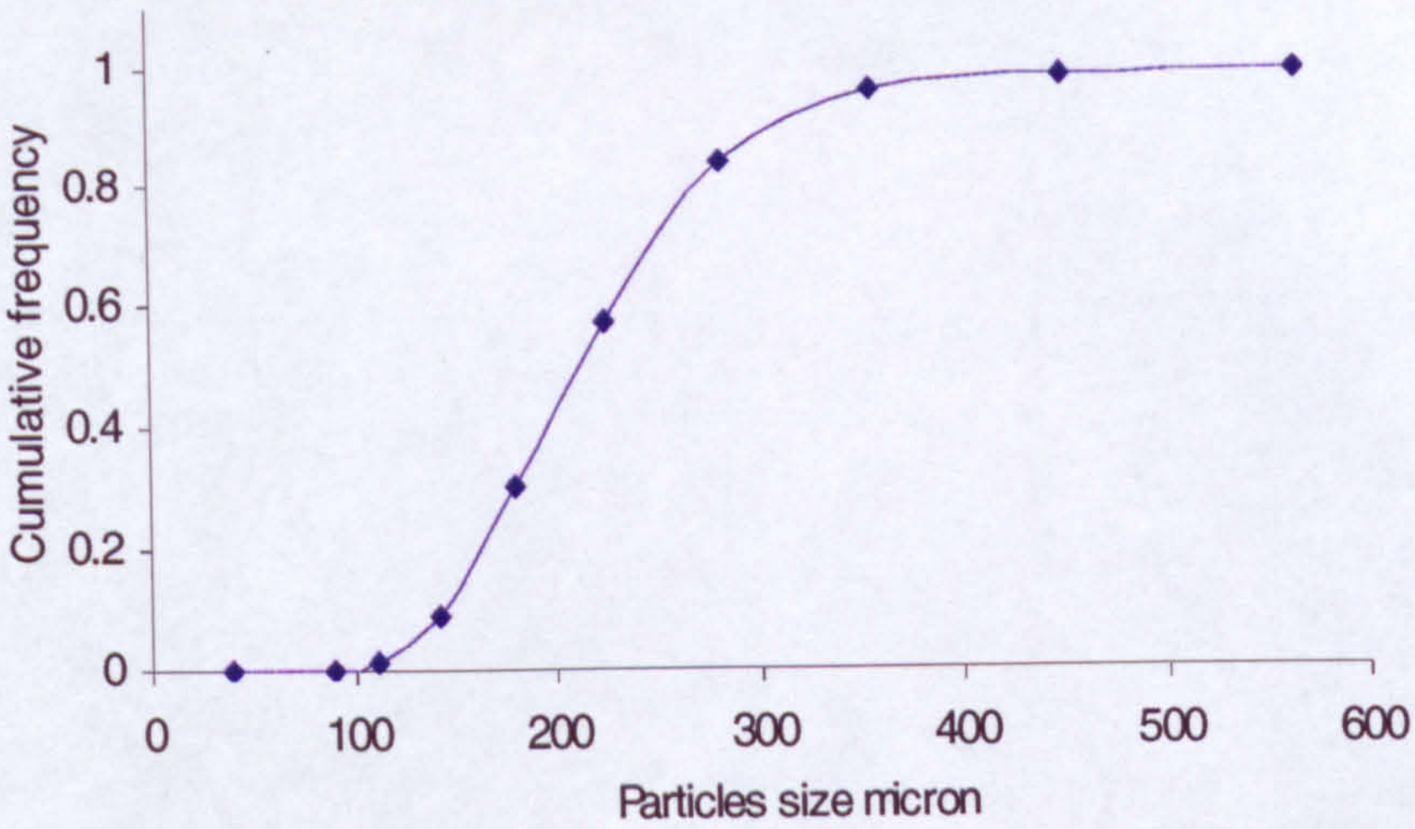


Figure 4-6 Sand particle size distribution used for erosion testing

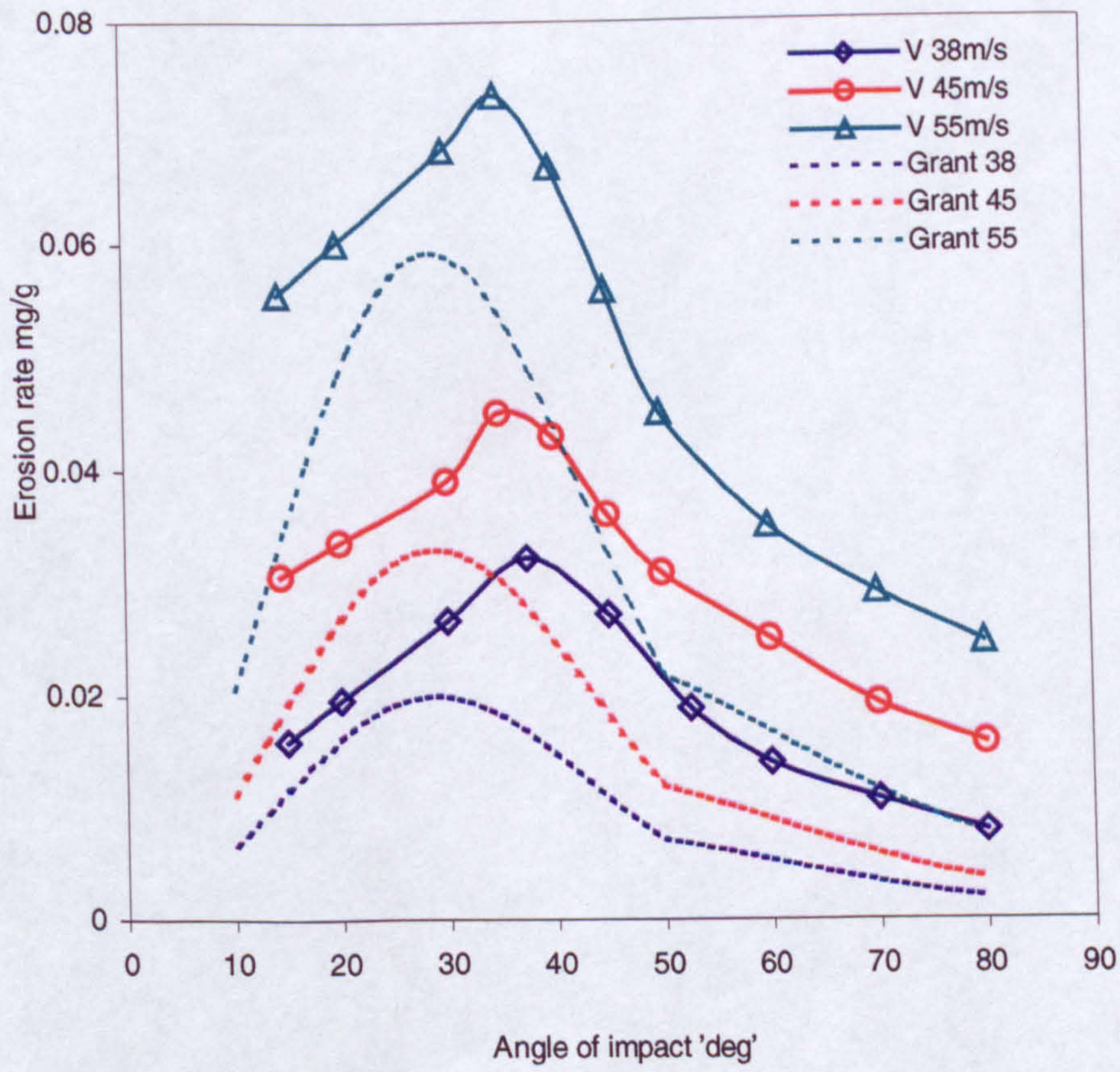


Figure 4-7 Erosion rate of cast aluminium and comparison with Grant correlation


Figure 4-8a Scanning electron micrographs of eroded cast aluminum at angle 30 degree


Figure 4-8b Scanning electron micrographs of eroded cast aluminum at angle 40 degree

18 times scaling

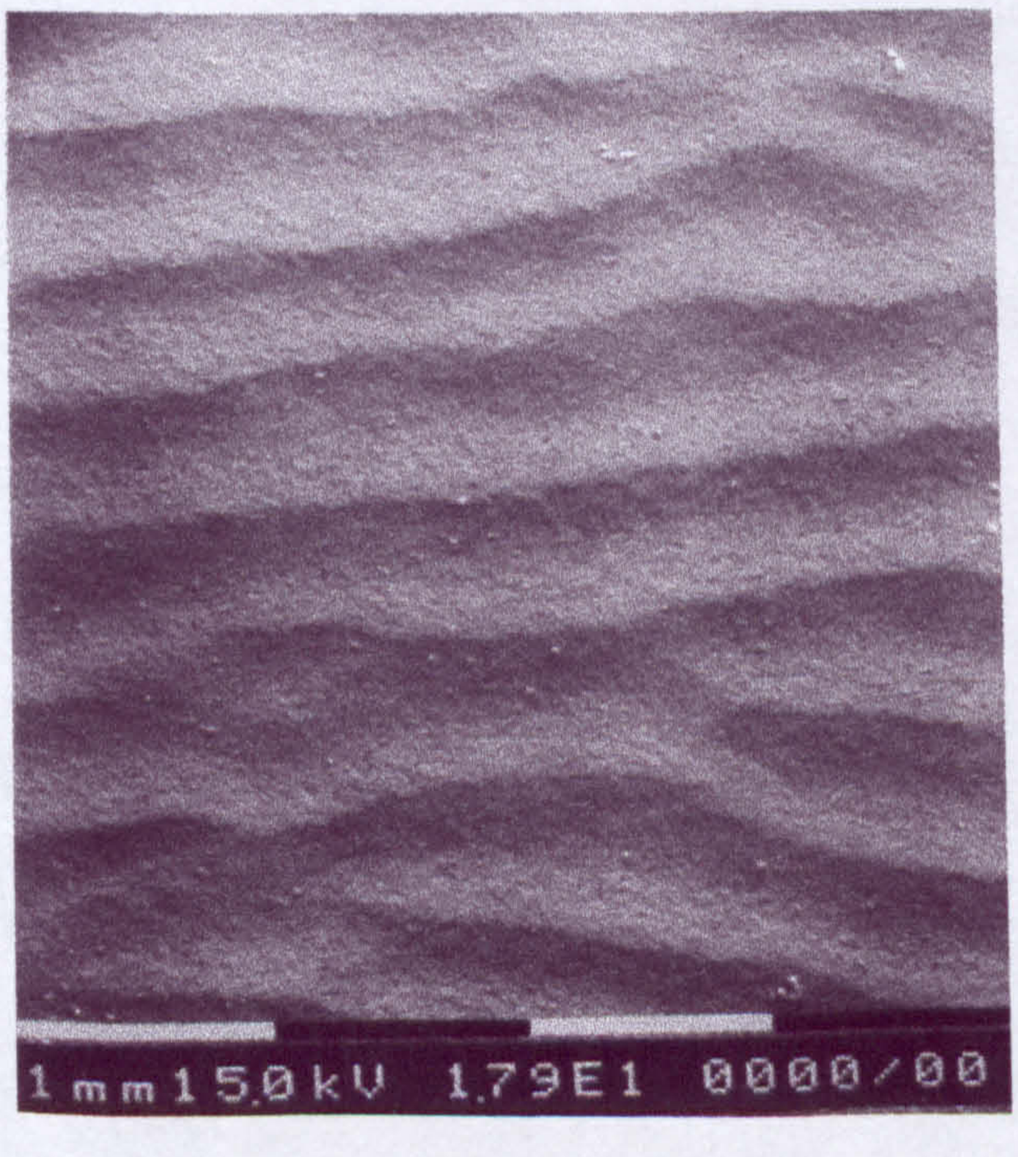


Figure 4-8c Scanning electron micrographs of eroded cast aluminium at angle 60 degree

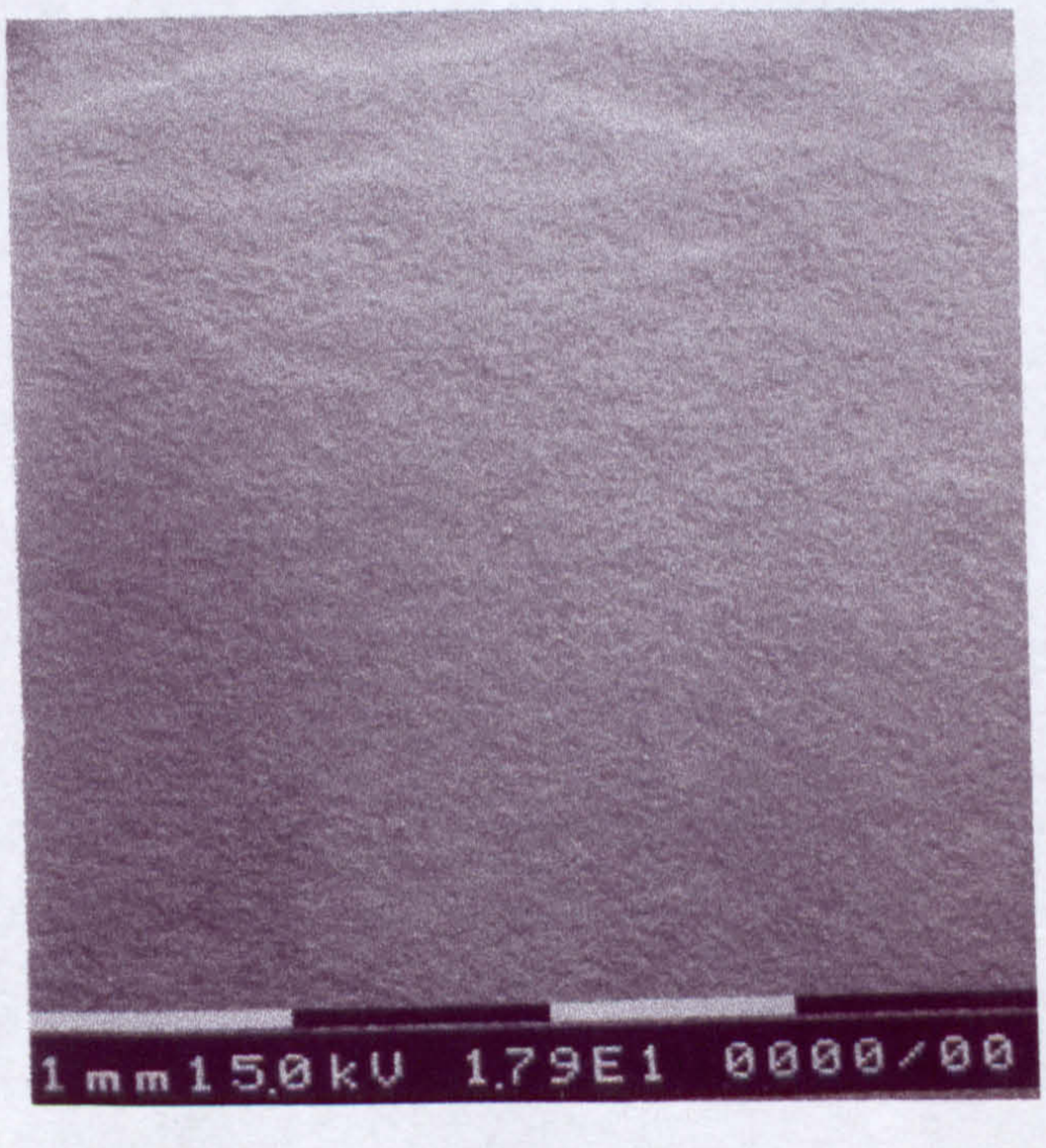


Figure 4-8d Scanning electron micrographs of eroded cast aluminium at angle 80 degree

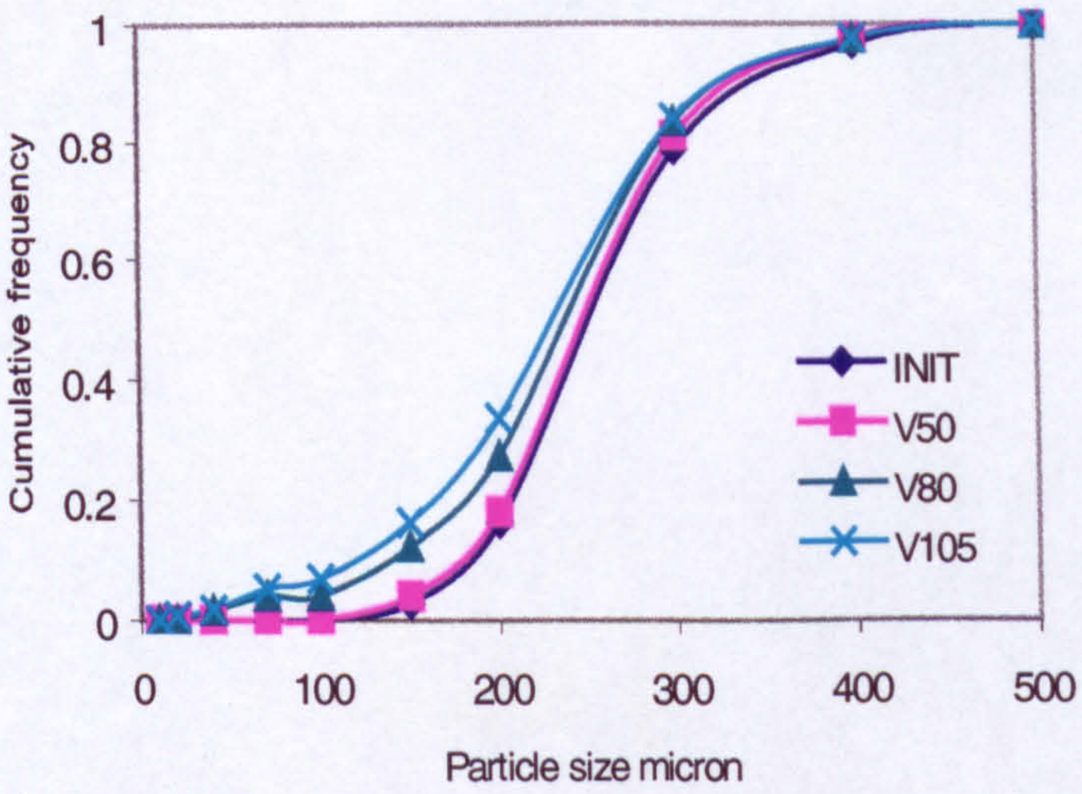


Figure 4-9a Fragmentation of sand particles diameter 180-210 micron at 45 degree angle of impact

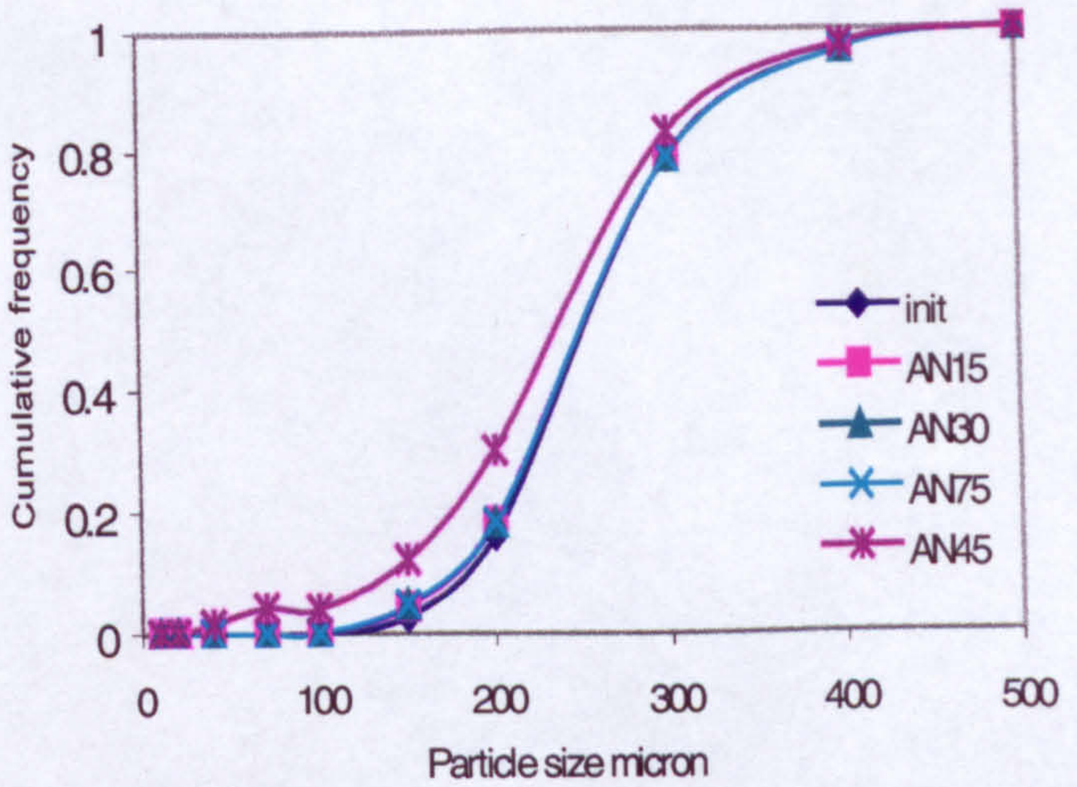


Figure 4-9b Fragmentation of sand particles diameter 180-210 micron at a velocity 80 m/s

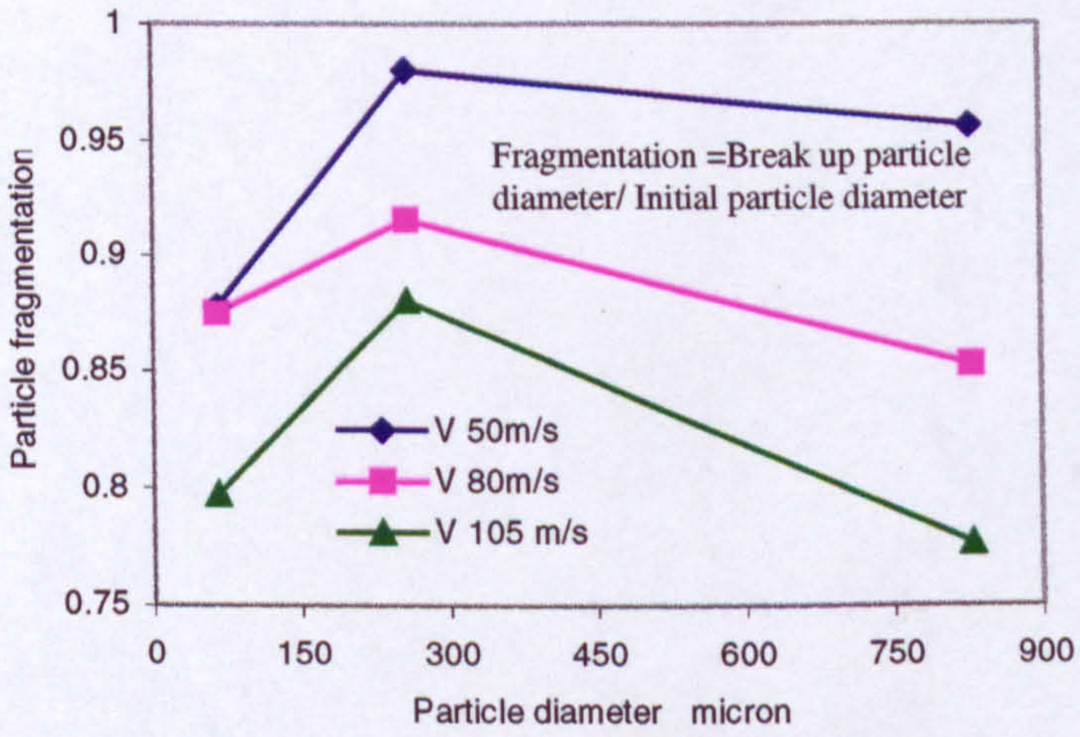


Figure 4-10a Fragmentation function of particle diameter and different impact velocity

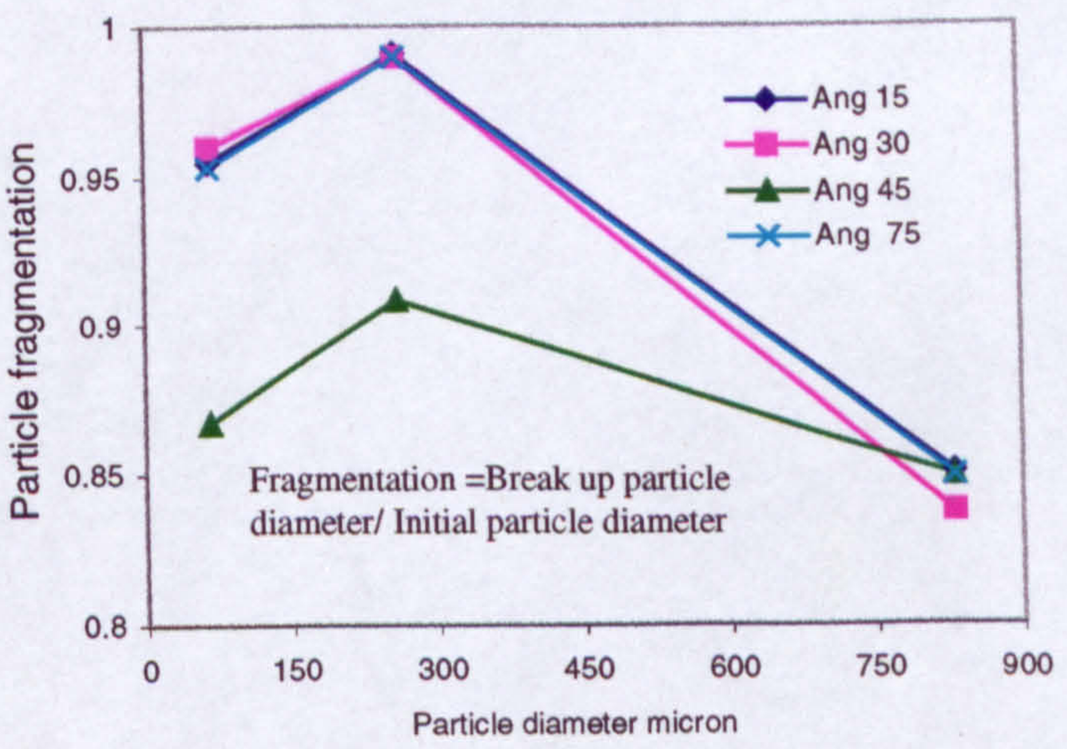


Figure 4-10b Fragmentation function of particle diameter and different impact angle

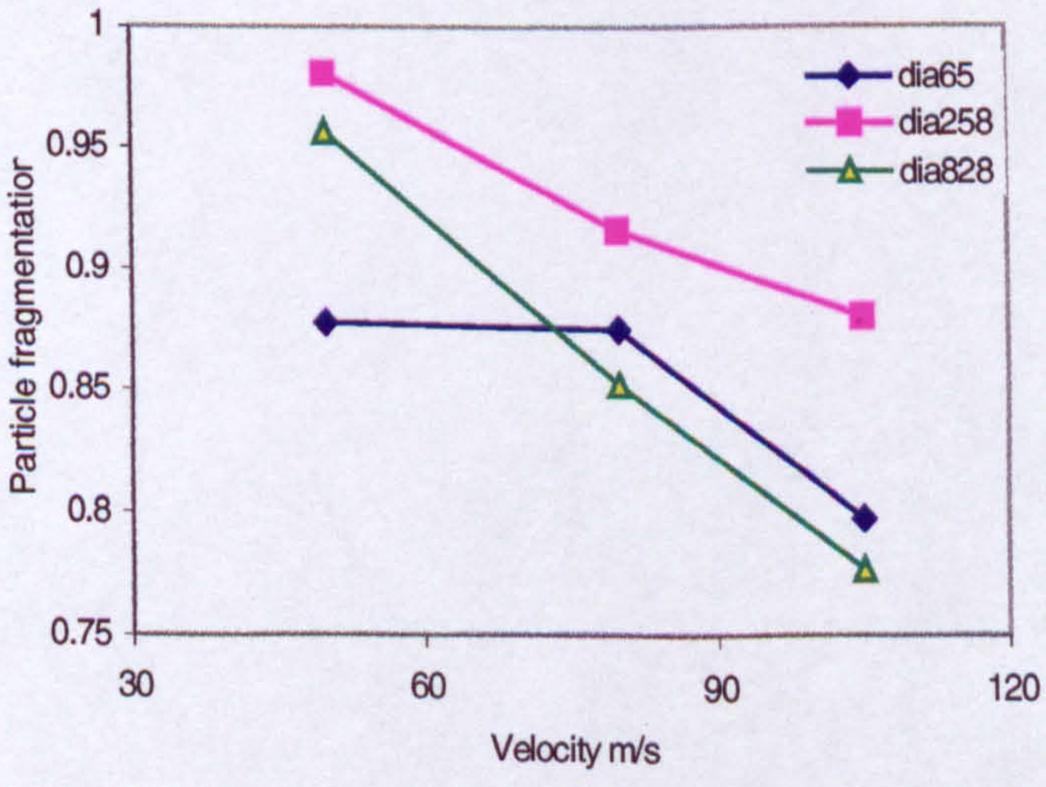


Figure 4-11a Effect of velocity on fragmentation

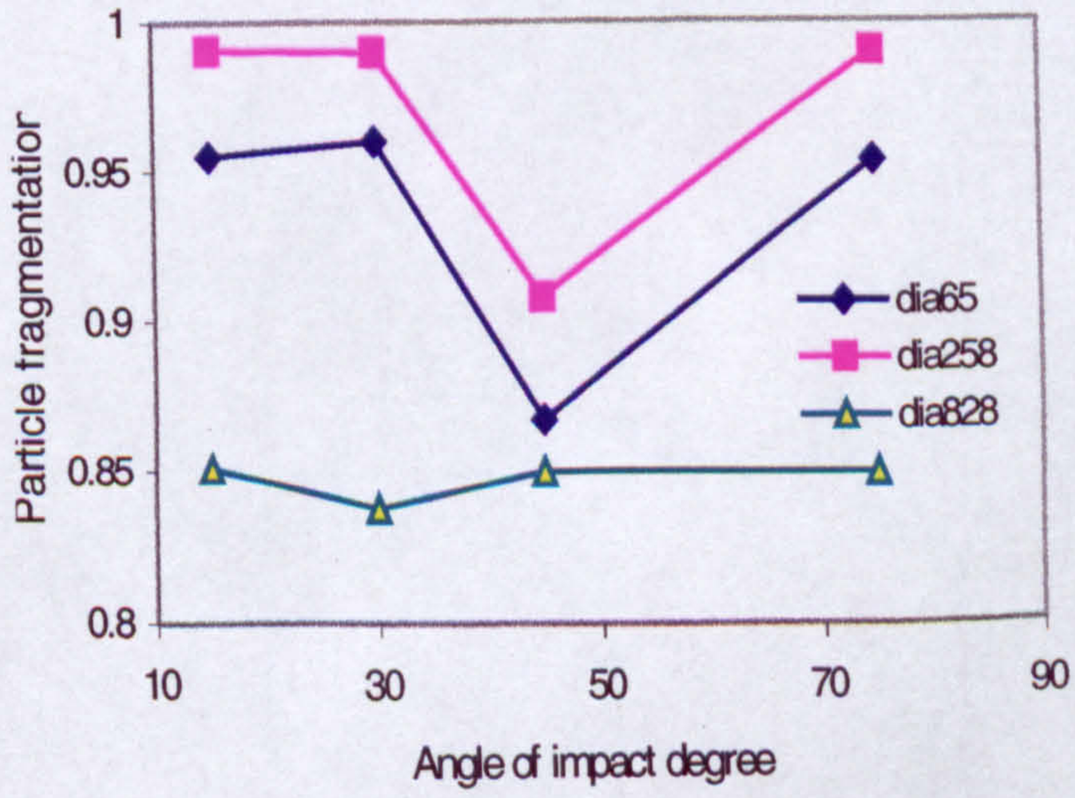


Figure 4-11b Effect of angle of impact on fragmentation

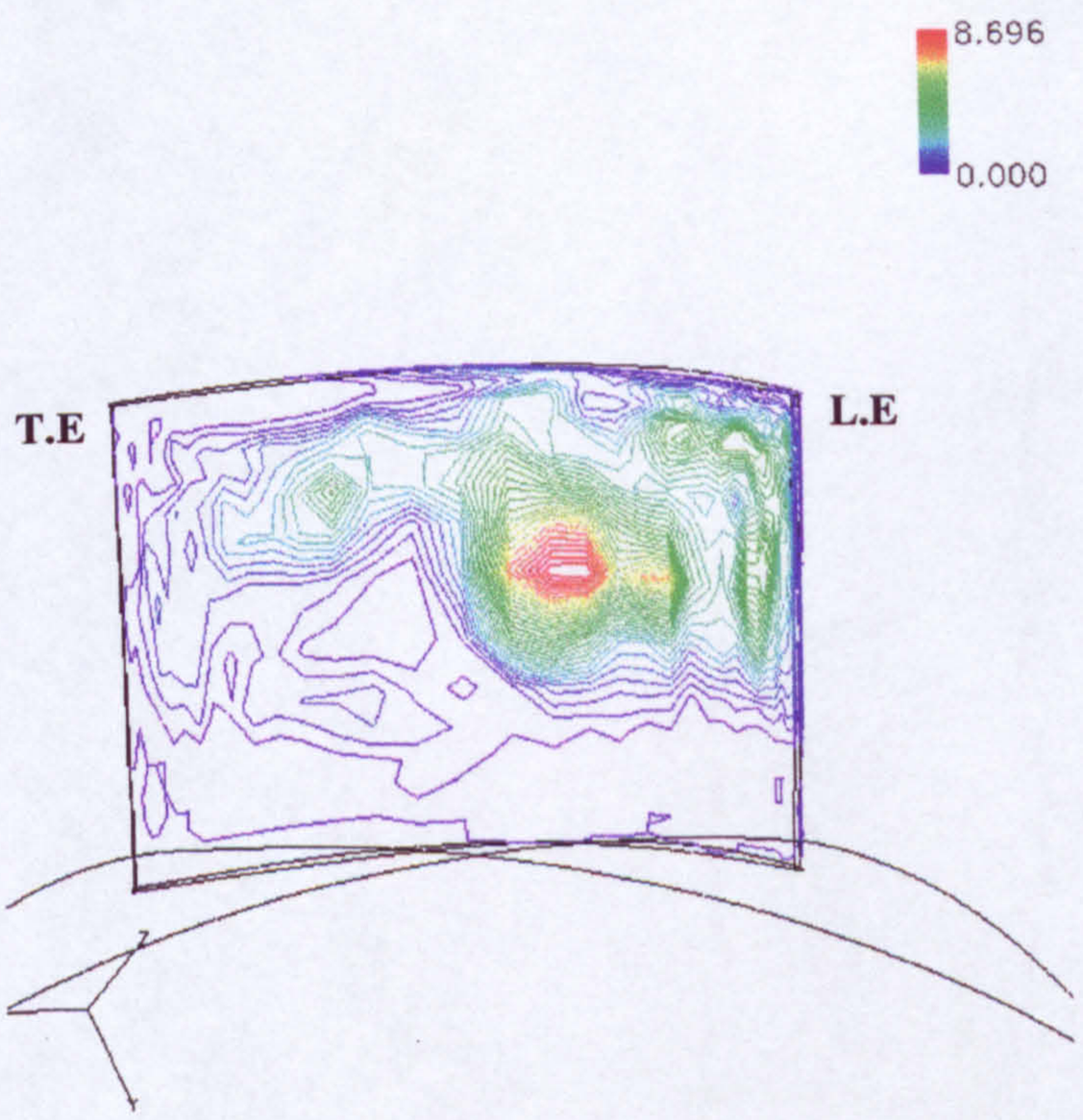


Figure 4-12a Predicted erosion (mg/g) on the pressure side of the rotor, seeding at mid height (150-300 micron) sand particles

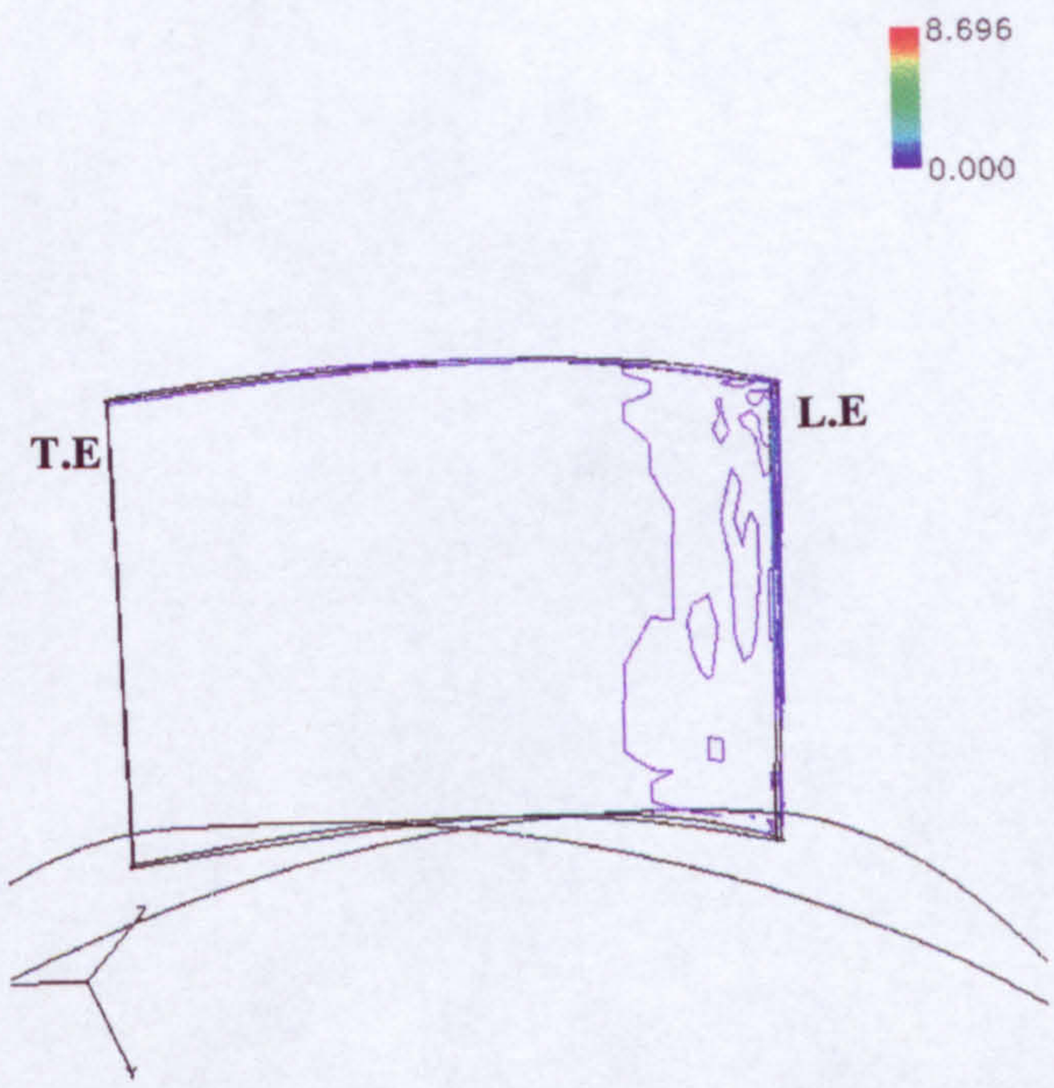


Figure 4-12b Predicted erosion (mg/g) on the suction side of the rotor, seeding at mid height (150-300 micron) sand particles

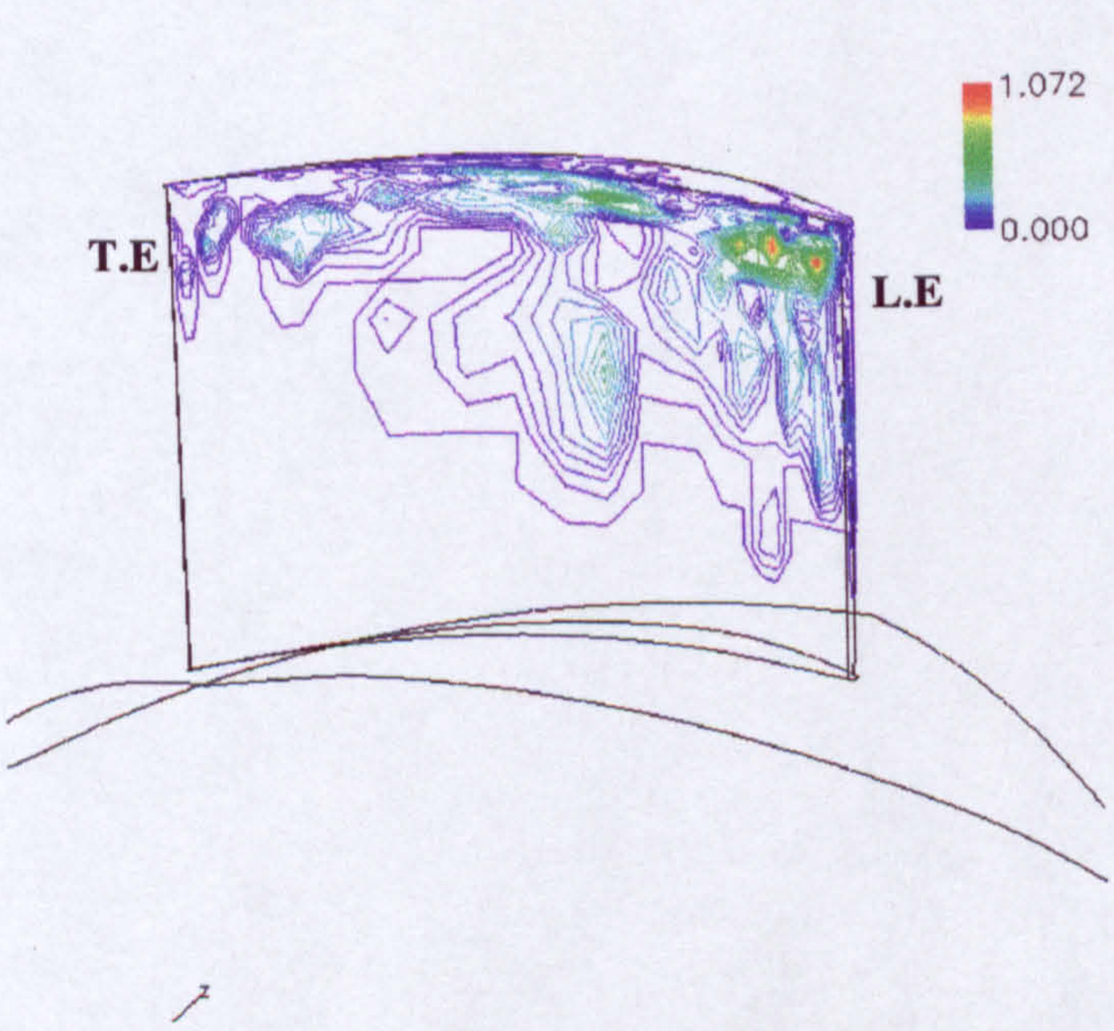


Figure 4-13 Predicted erosion (mg/g) on the pressure side of the rotor, seeding near the tip (150-300 micron) sand particles

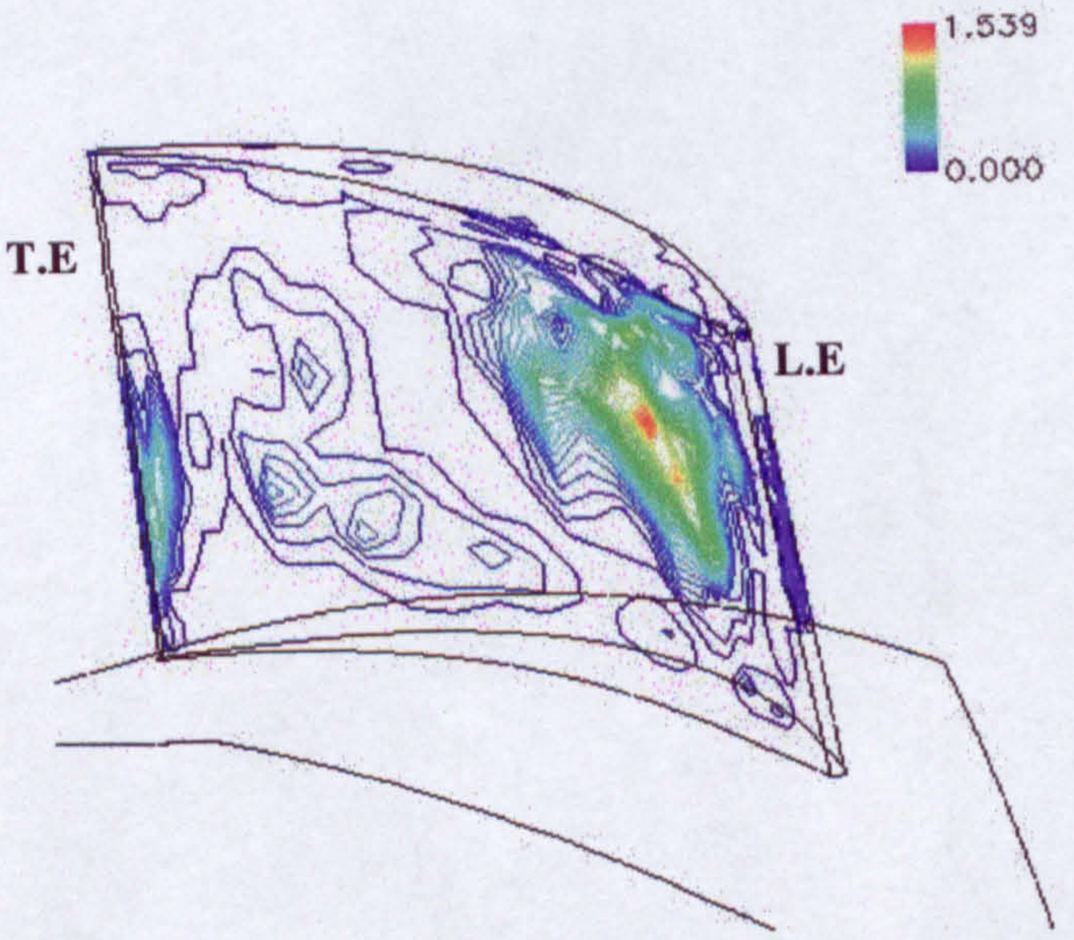


Figure 4-14 Predicted erosion (mg/g) on the pressure side of the rotor, seeding near the hub (150-300 micron) sand particles

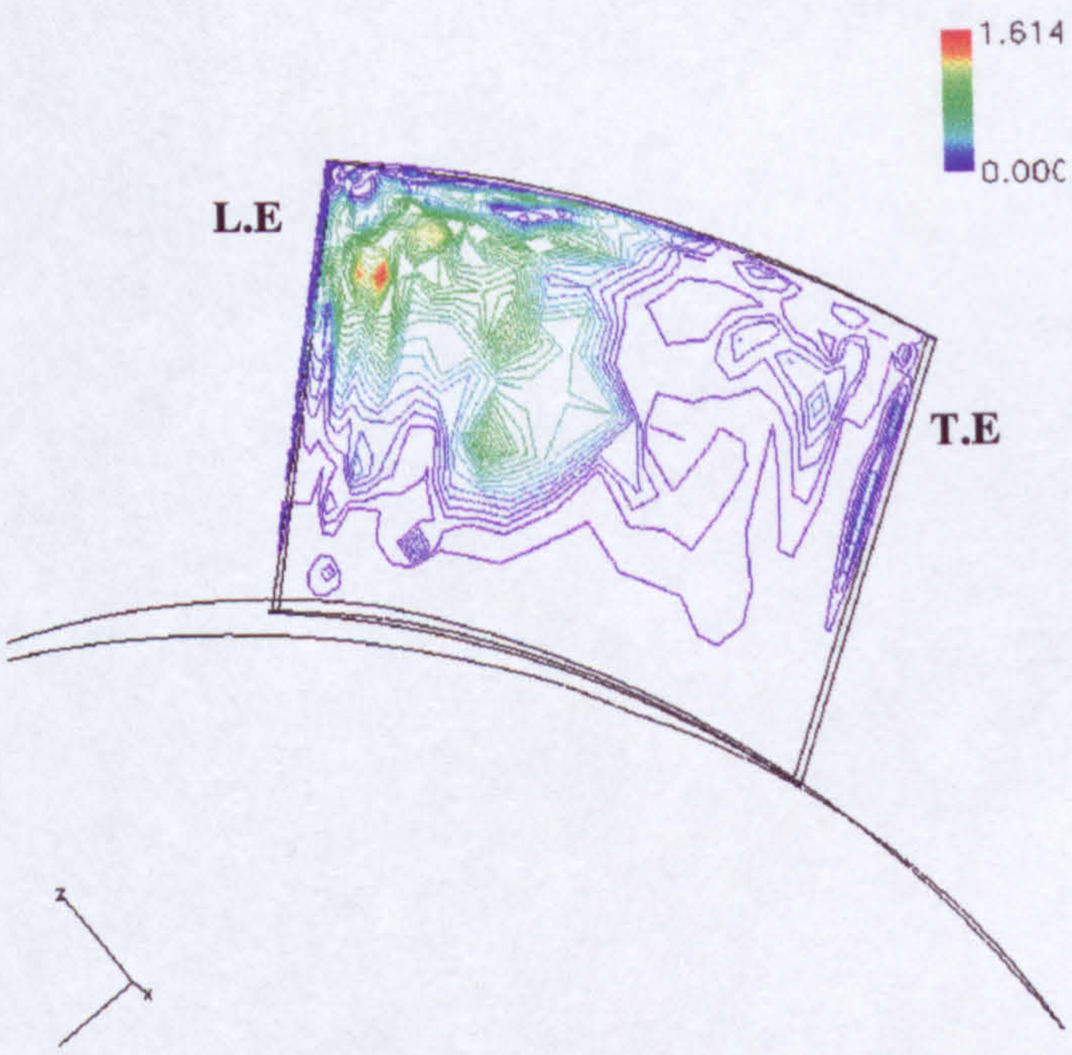


Figure 4-15a Predicted erosion (mg/g) on the pressure side of the rotor, due to global injection of sand particles (150-300 micron) at low concentration

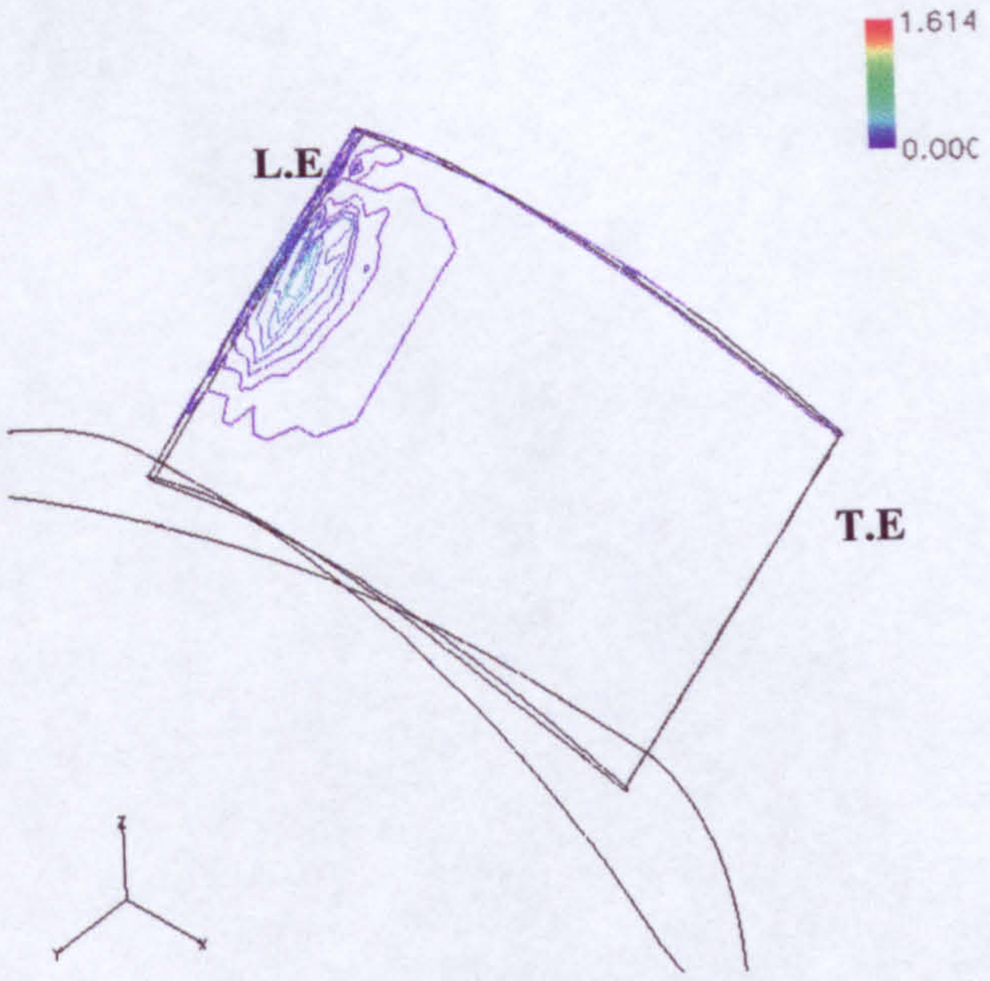


Figure 4-15b Predicted erosion (mg/g) on the suction side of the rotor , due to global injection of sand particles (150-300 micron) at low concentration

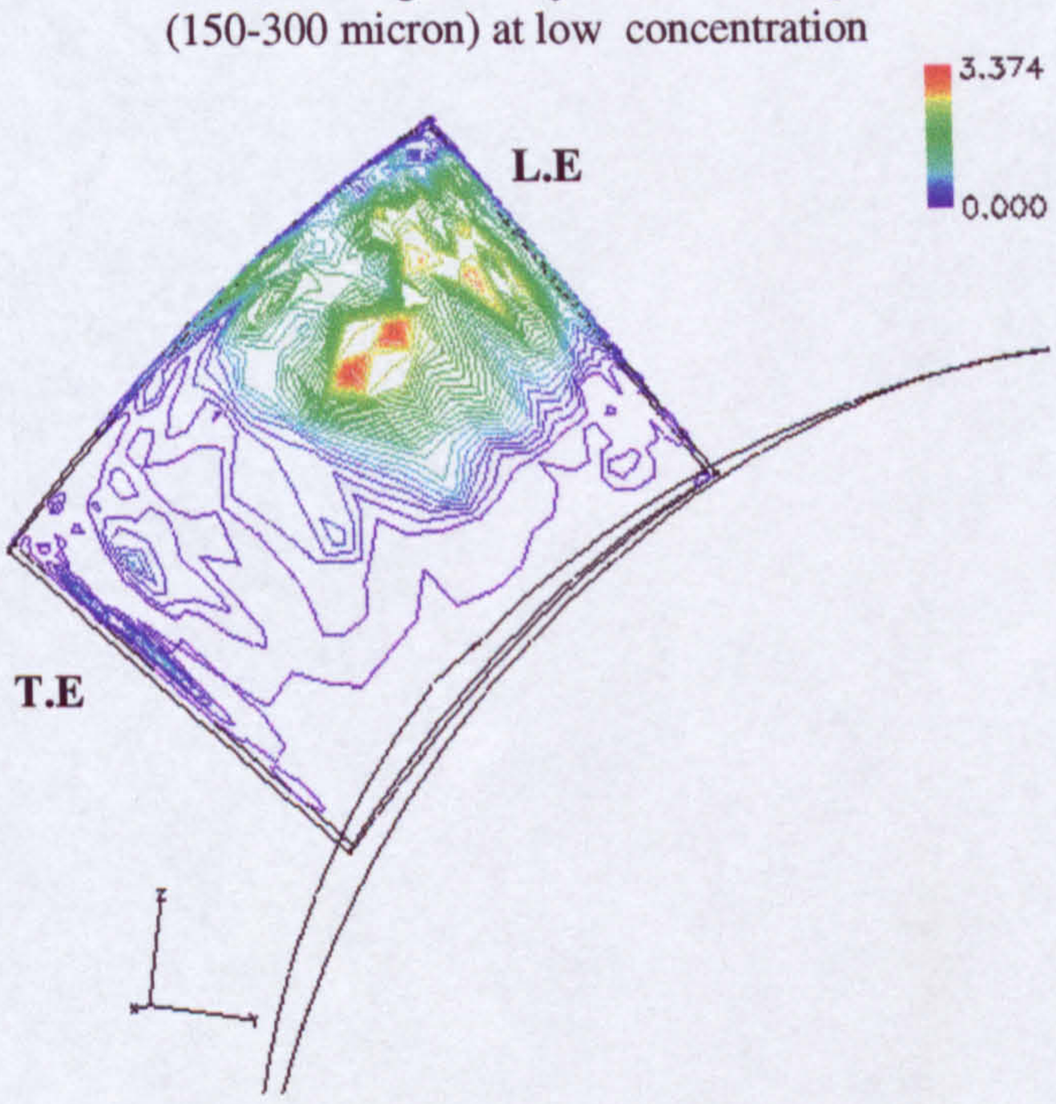


Figure 4-16a Predicted erosion (mg/g) on the pressure side of the rotor, due to global injection of sand particles (150-300 micron) at mean concentration

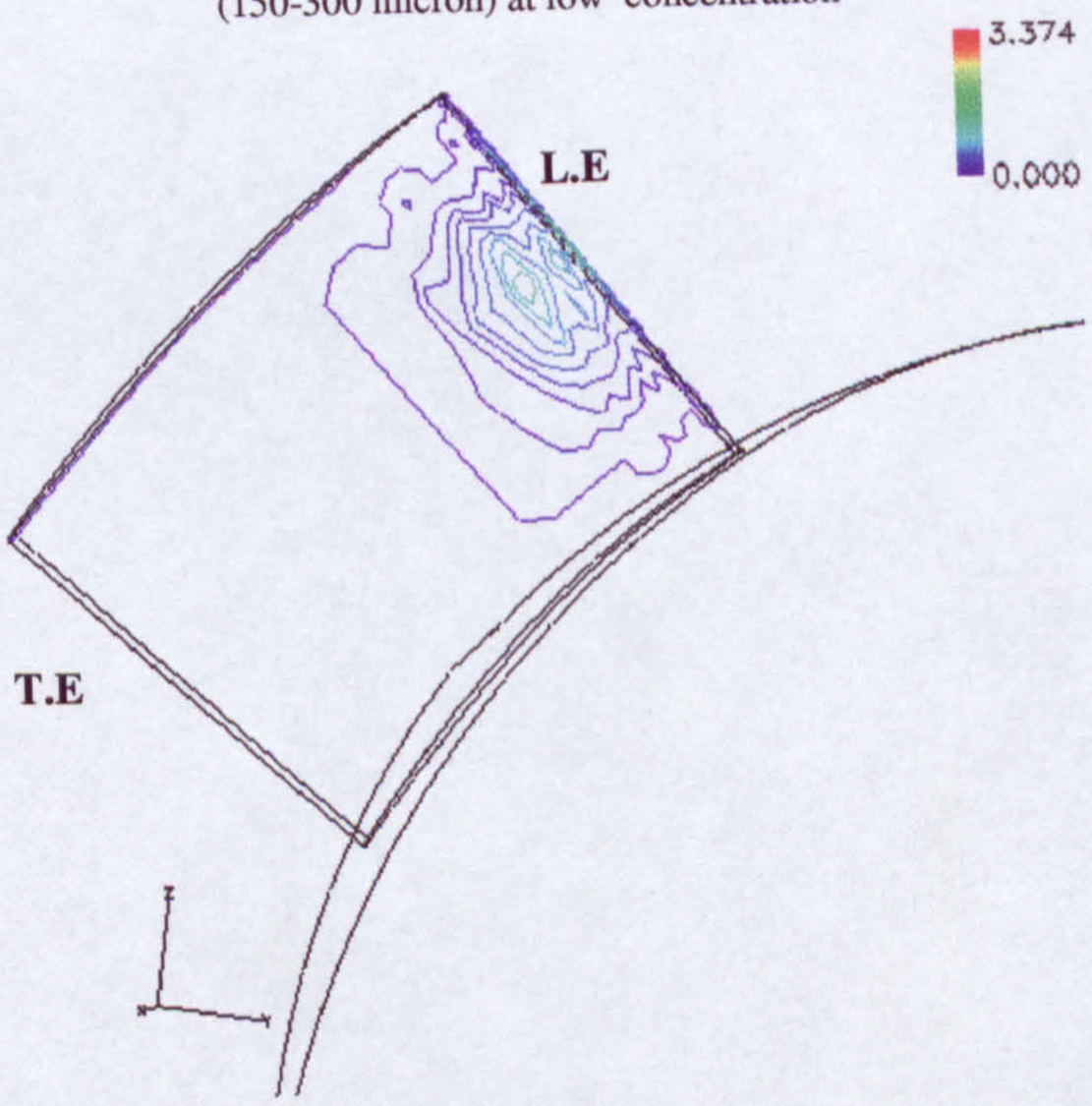


Figure 4-16b Predicted erosion (mg/g) on the suction side of the rotor , due to global injection of sand particles (150-300 micron) at mean concentration

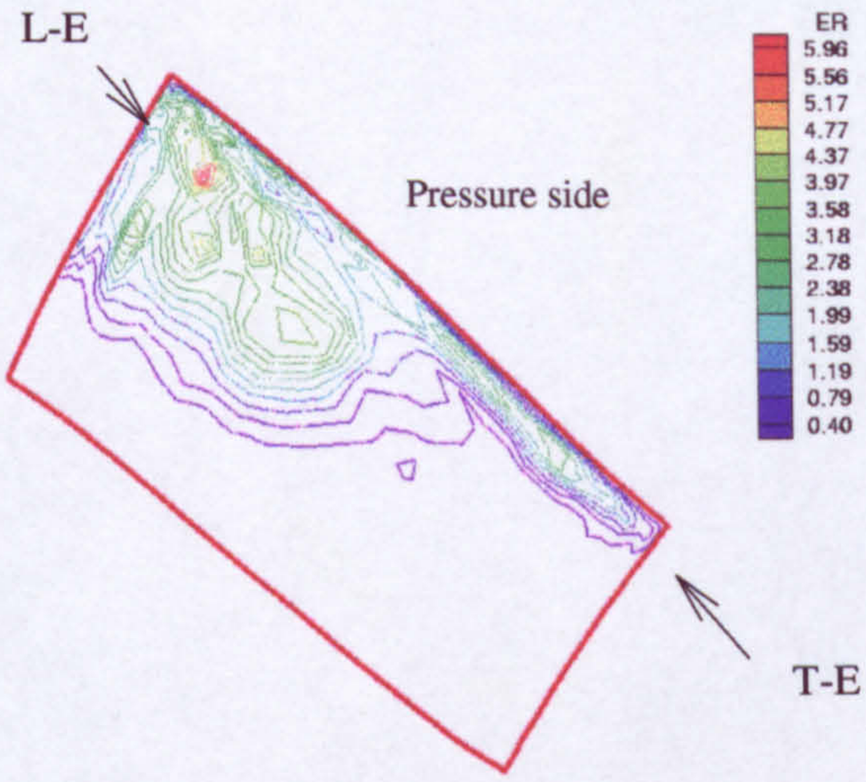


Figure 4-17a Erosion rate on rotor blade pressure side due to global seeding of high concentration of sand MIL-E 5007E

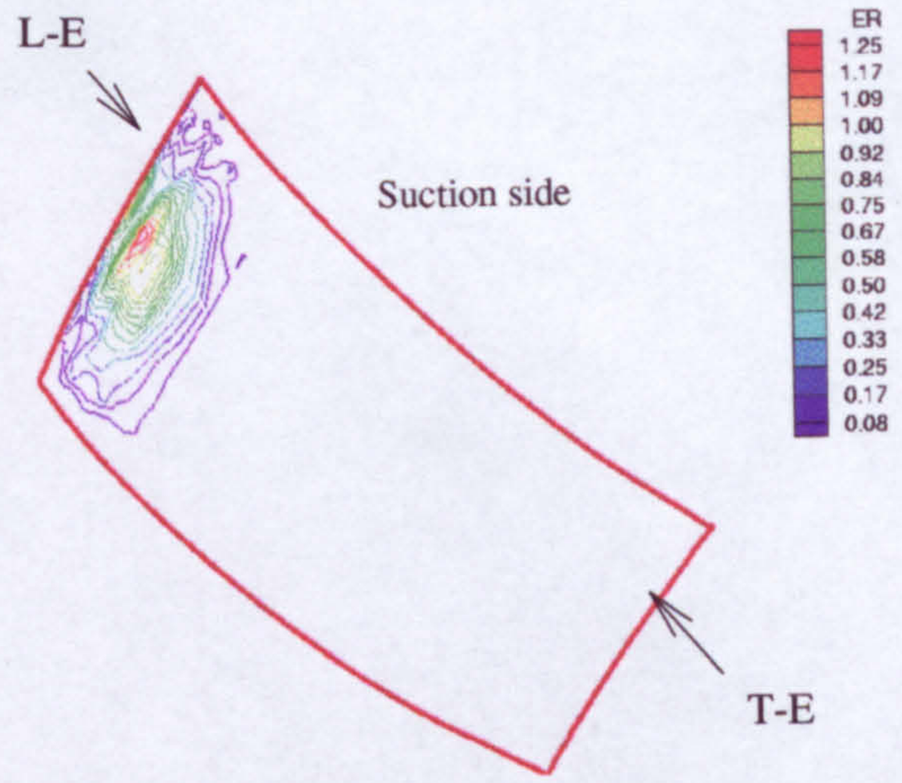


Figure 4-17b Erosion rate on rotor blade suction side due to global seeding of high concentration of sand MIL-E 5007E

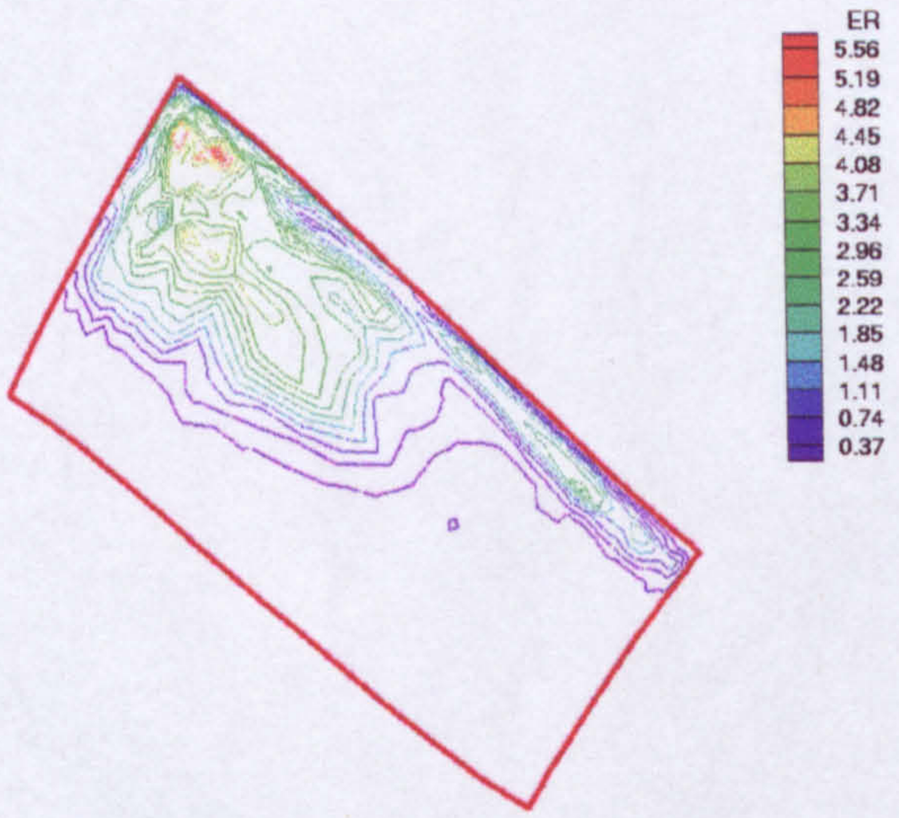


Figure 4-18a Erosion rate on rotor blade pressure side due to global seeding of high concentration MIL-E 5007E sand considering turbulence

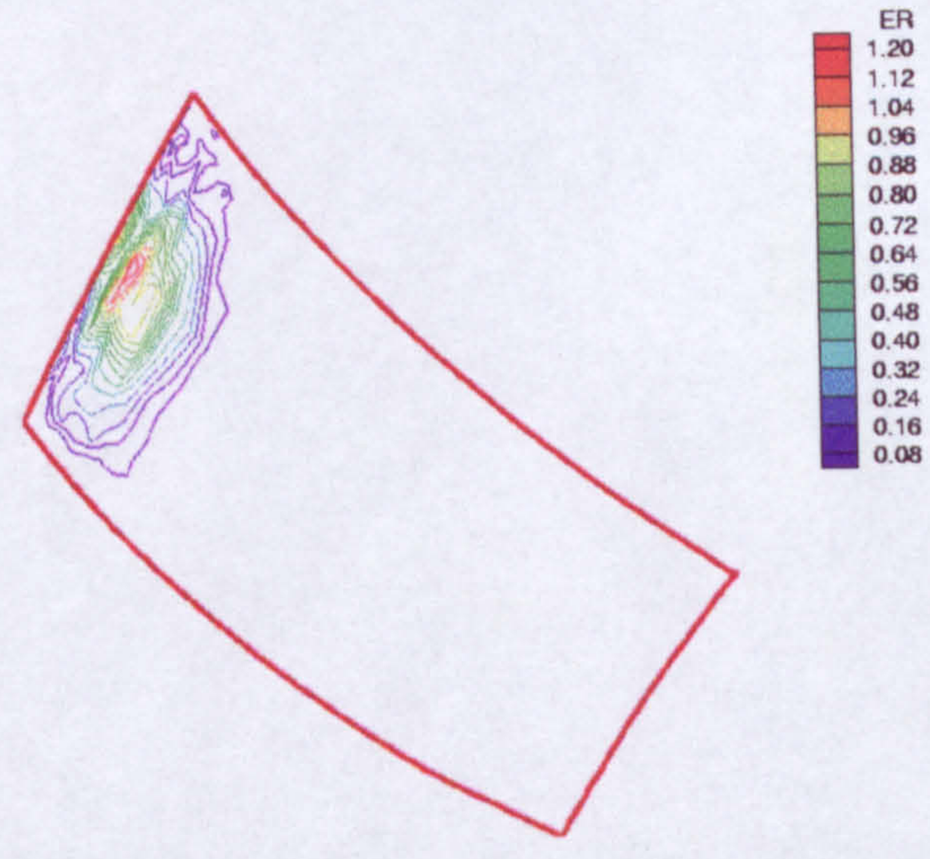


Figure 4-18b Erosion rate on rotor blade suction side due to global seeding of high concentration MIL-E 5007E sand considering turbulence

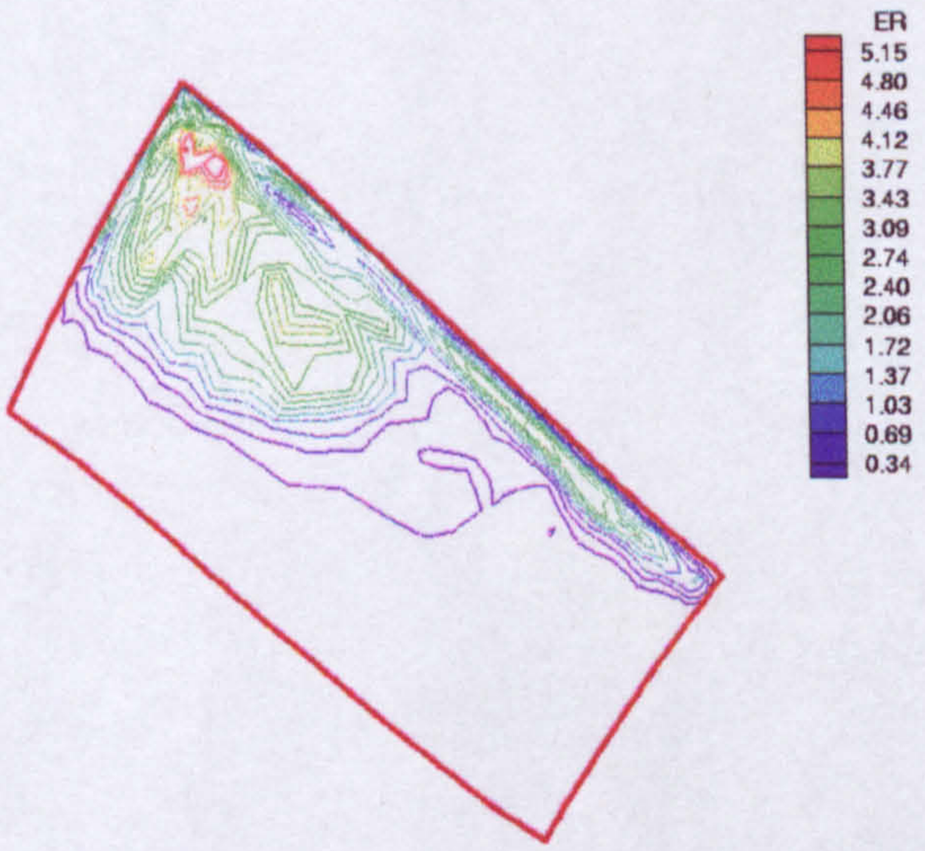


Figure 4-19a Erosion rate on rotor blade pressure side due to global seeding of high concentration MIL-E 5007E without fragmentation

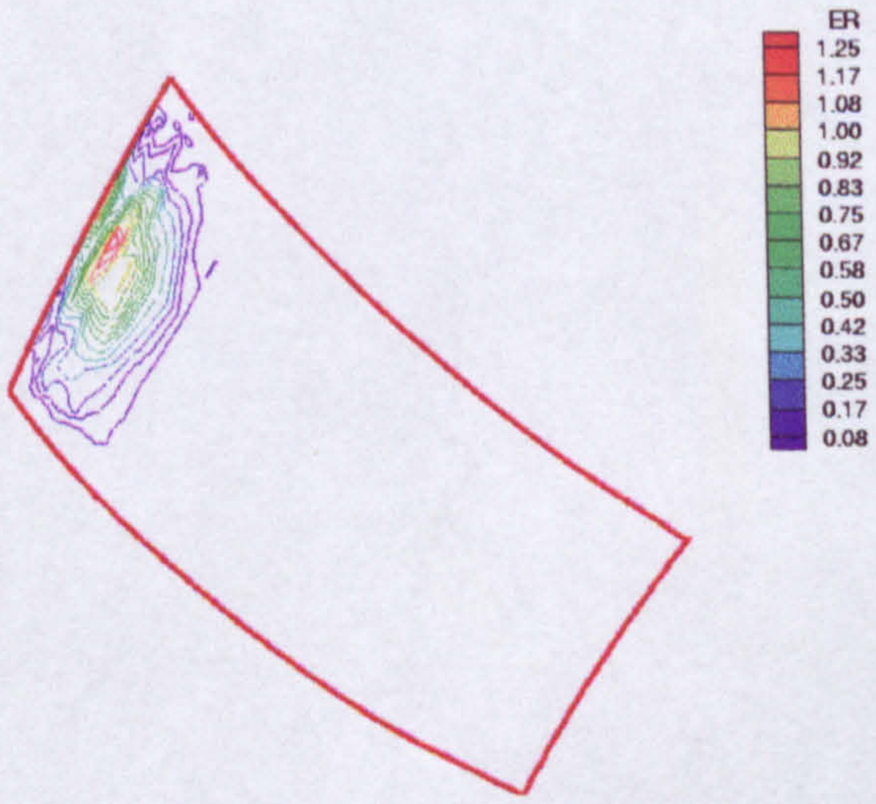


Figure 4-19b Erosion rate on rotor blade suction side due to global seeding of high concentration MIL-E 5007E without fragmentation

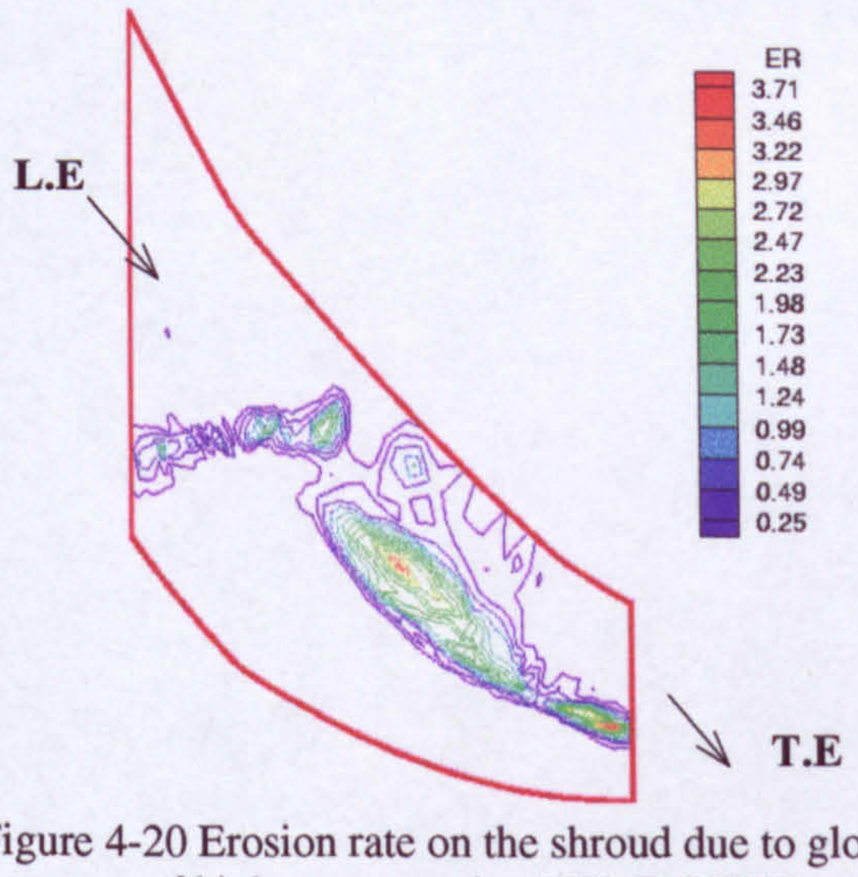


Figure 4-20 Erosion rate on the shroud due to global seeding of high concentration MIL-E 5007E sand

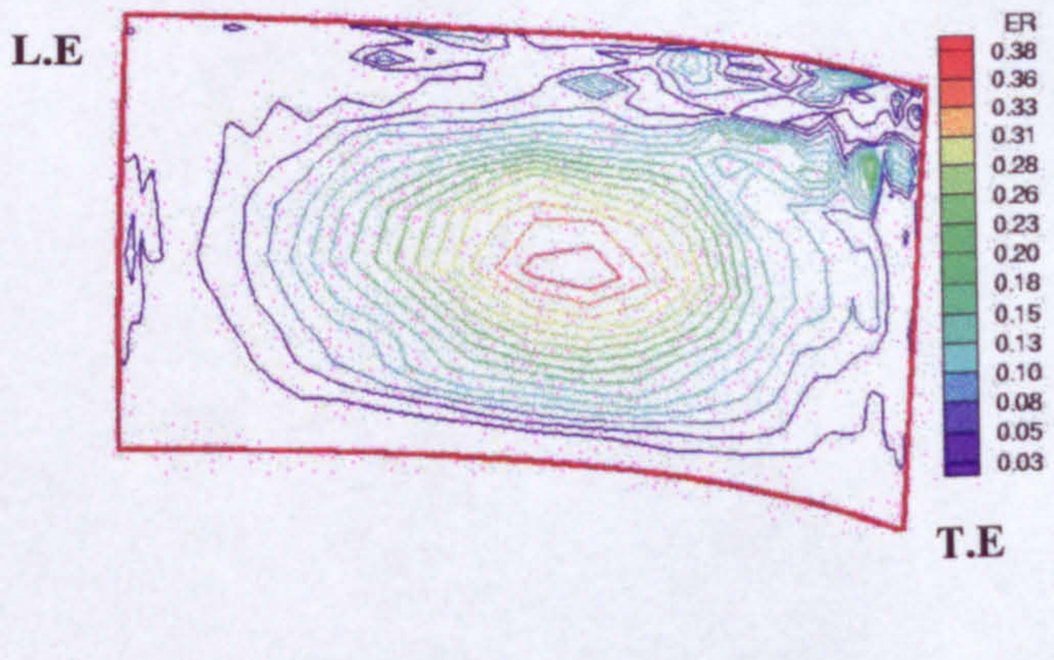


Figure 4-21 Erosion rate on IGV pressure side due to global seeding of high concentration MIL-E 5007E sand

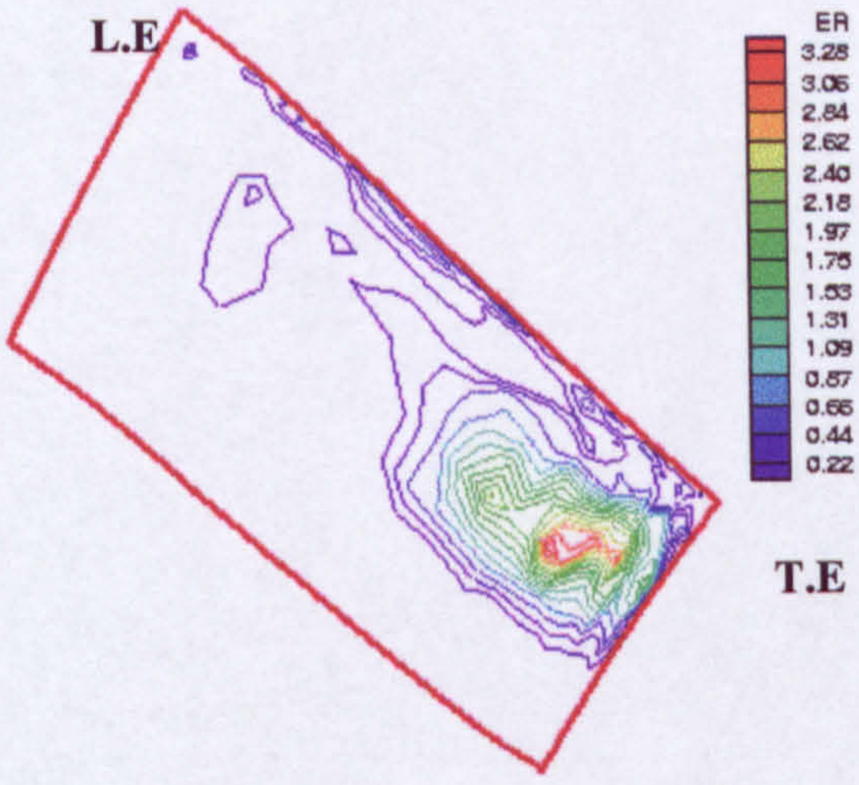


Figure 4-22a Erosion rate on the pressure side of rotor blade due to particles (30 ± 10 micron) at concentration 0.8mg/m$^3$

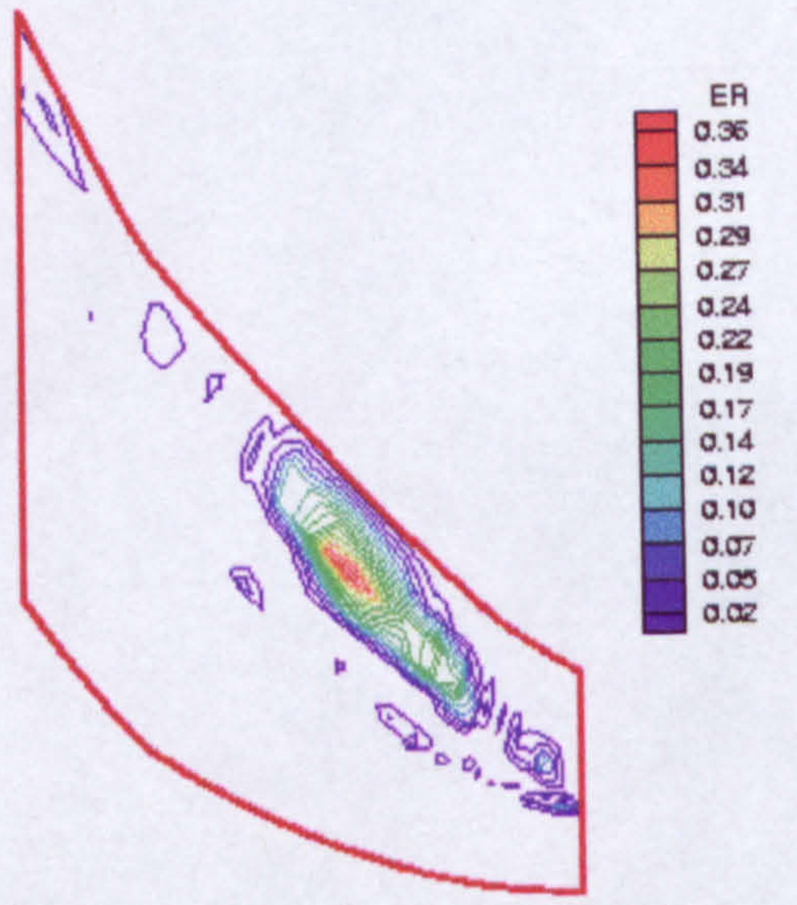


Figure 4-22b Erosion rate on the shroud due to particles (30 ± 10 micron) at concentration 0.8mg/m$^3$

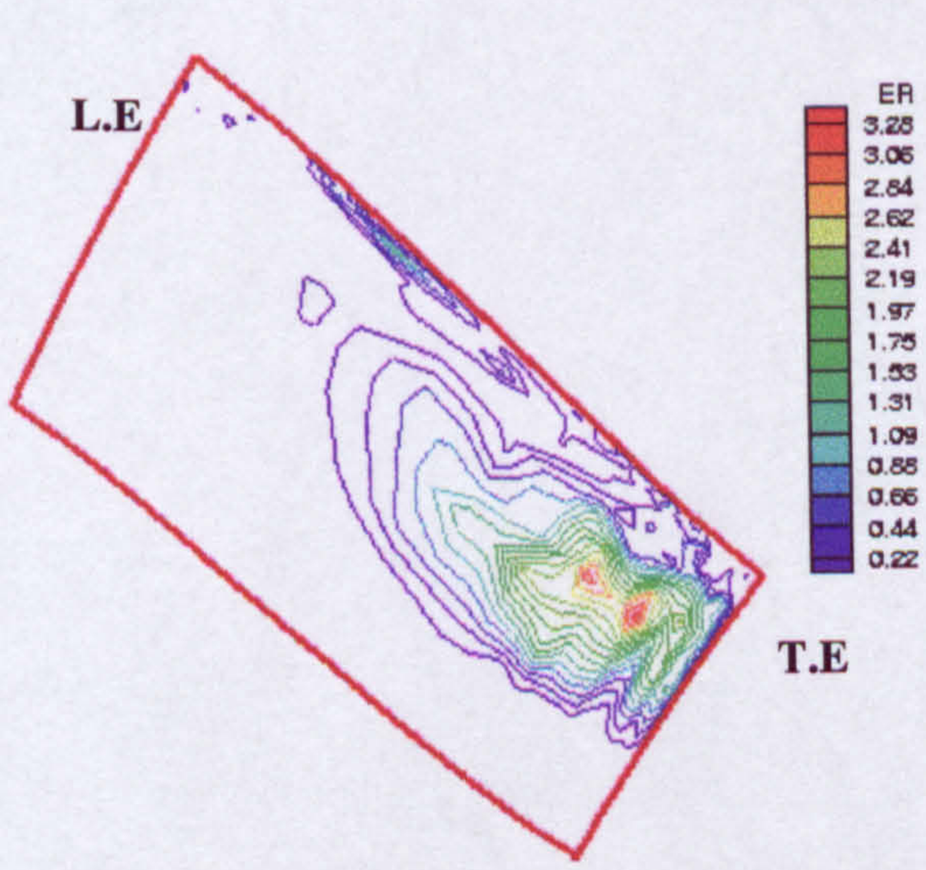


Figure 4-23a Erosion rate on the pressure side of rotor blade due to particles (30 ± 10 micron) at concentration 0.8mg/m$^3$ with turbulence effect

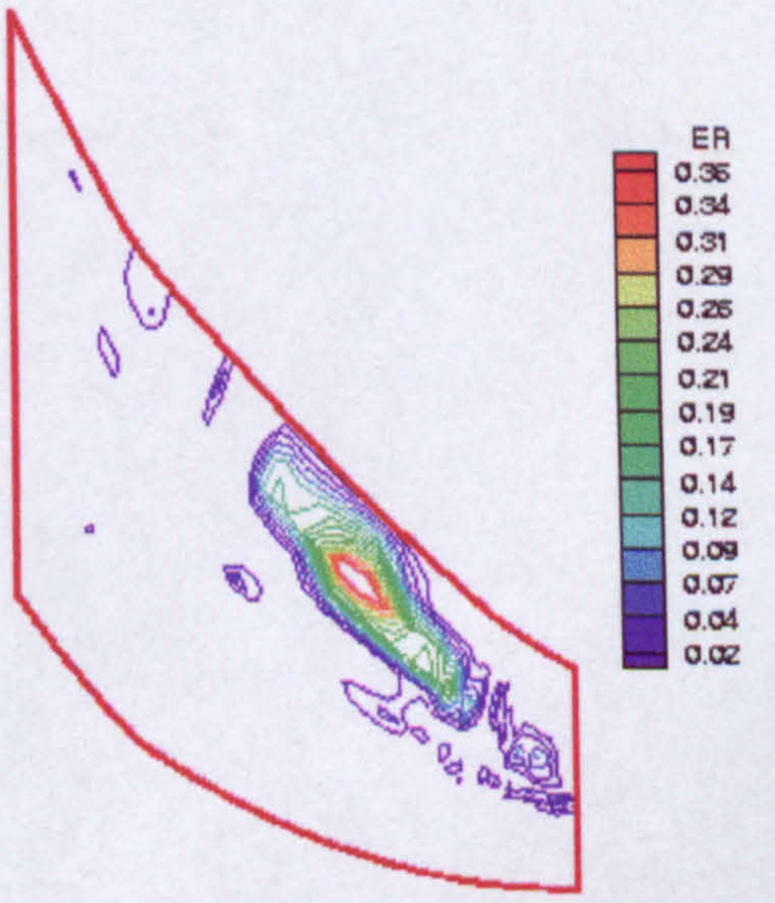


Figure 4-23b Erosion rate on the shroud due to particles (30 ± 10 micron) at concentration 0.8mg/m$^3$ with turbulence effect

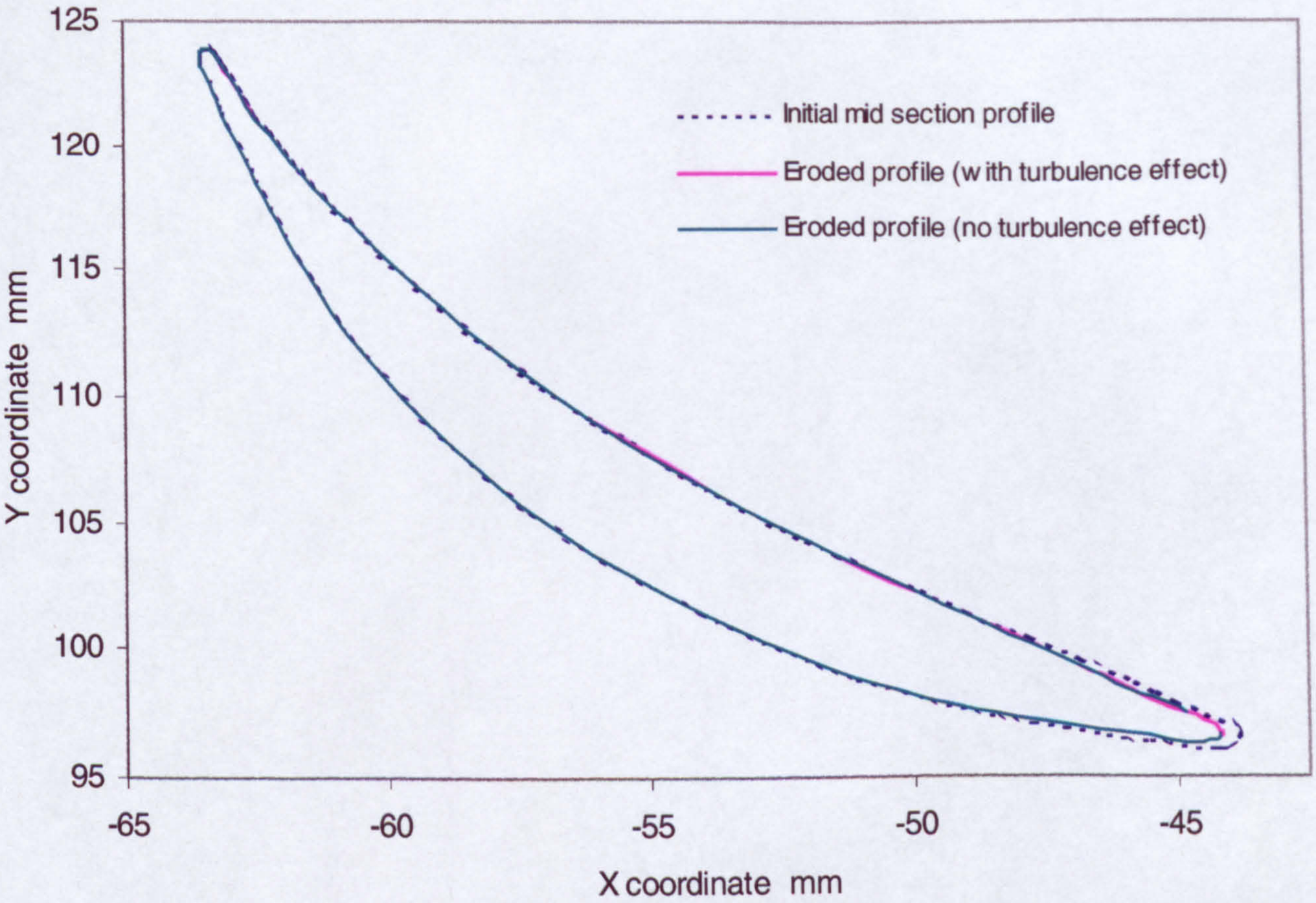


Figure 4-24 Eroded mid section of the rotor blade

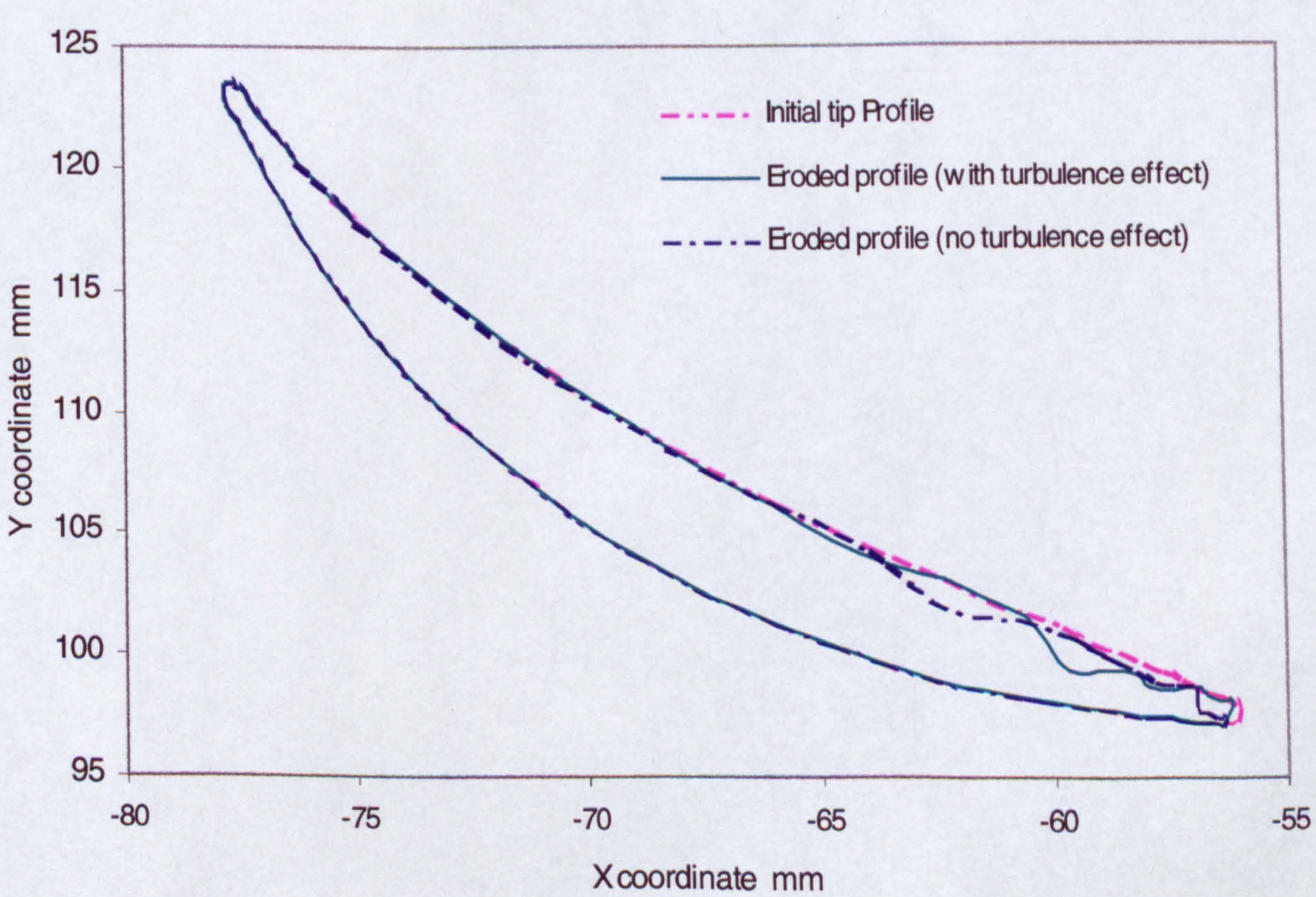


Figure 4-25 Eroded tip section of the rotor blade

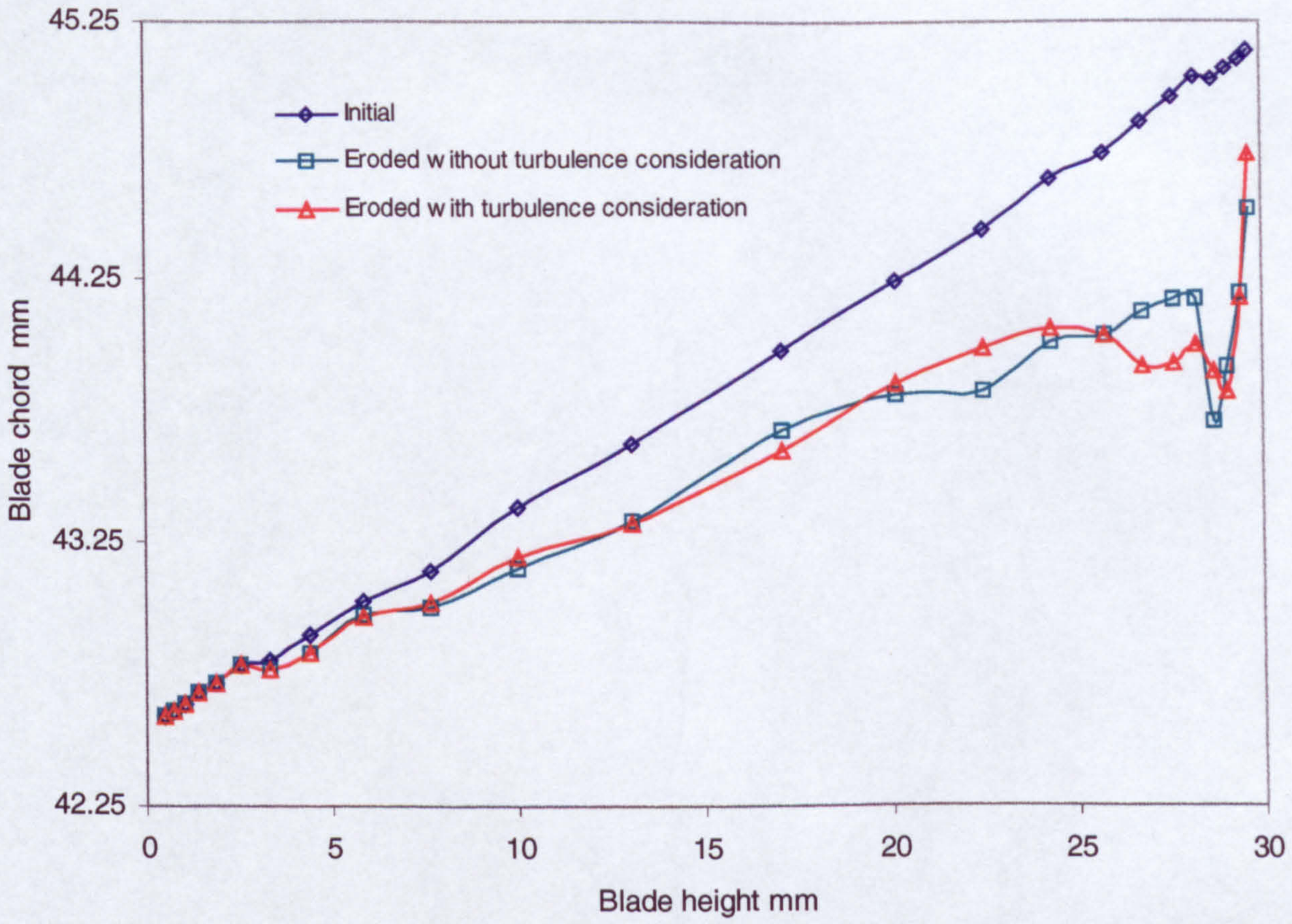


Figure 4-26 Eroded leading edge of the rotor blade

# FIGURES 5

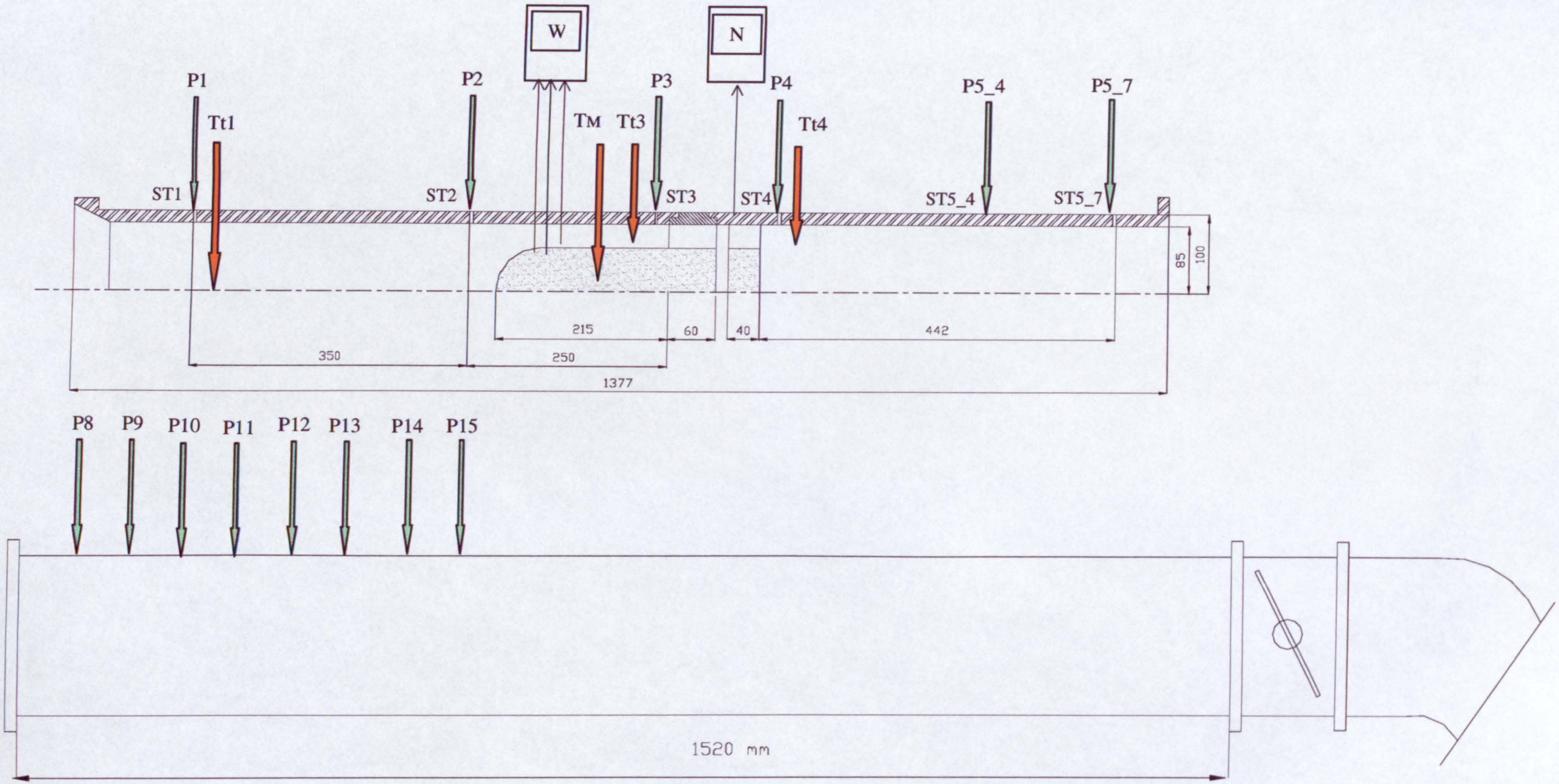


Figure 5-6 test rig measuring points and dimensions

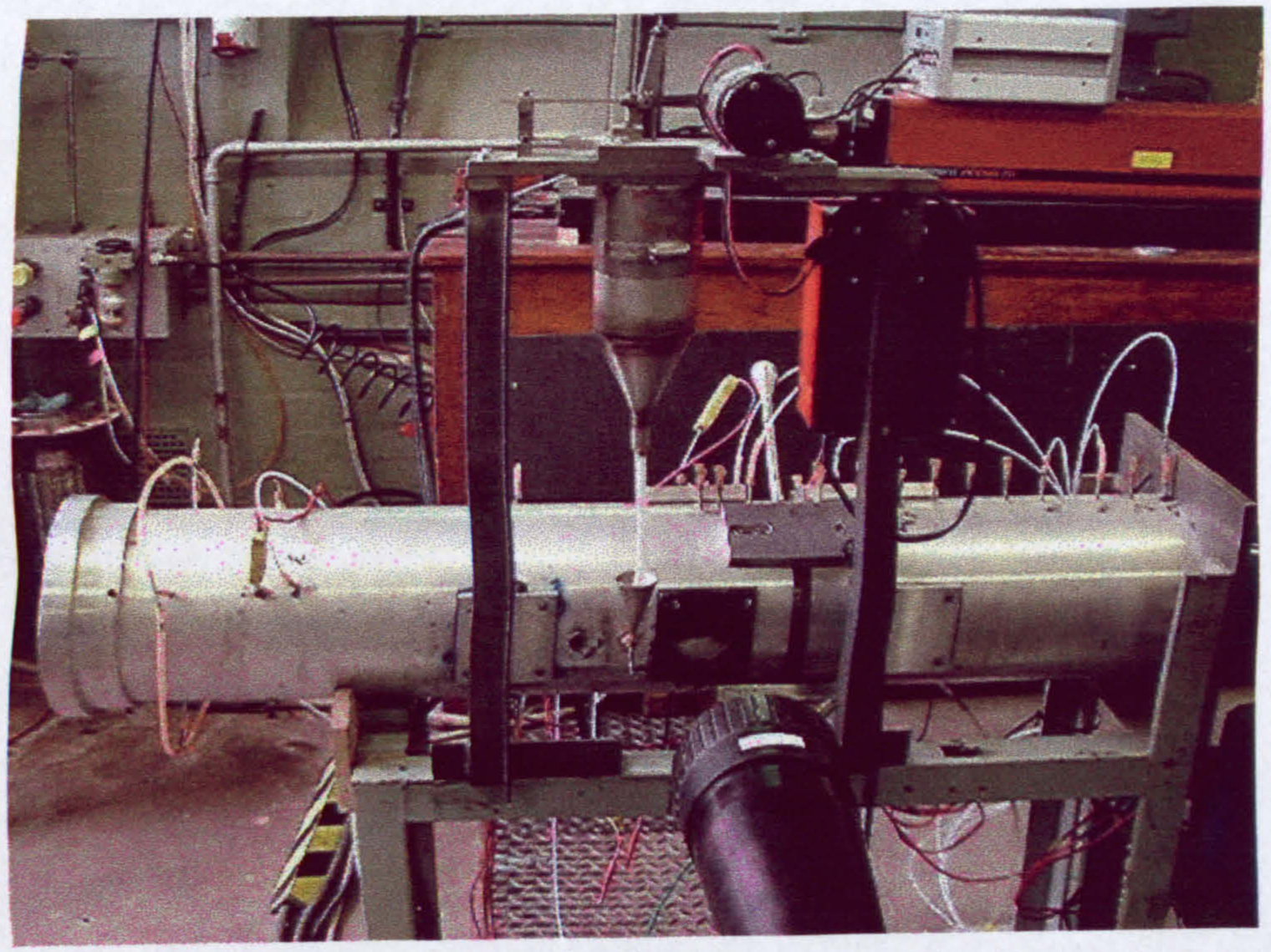

Figure 5-7 Test rig showing local sand injector and laser anemometer

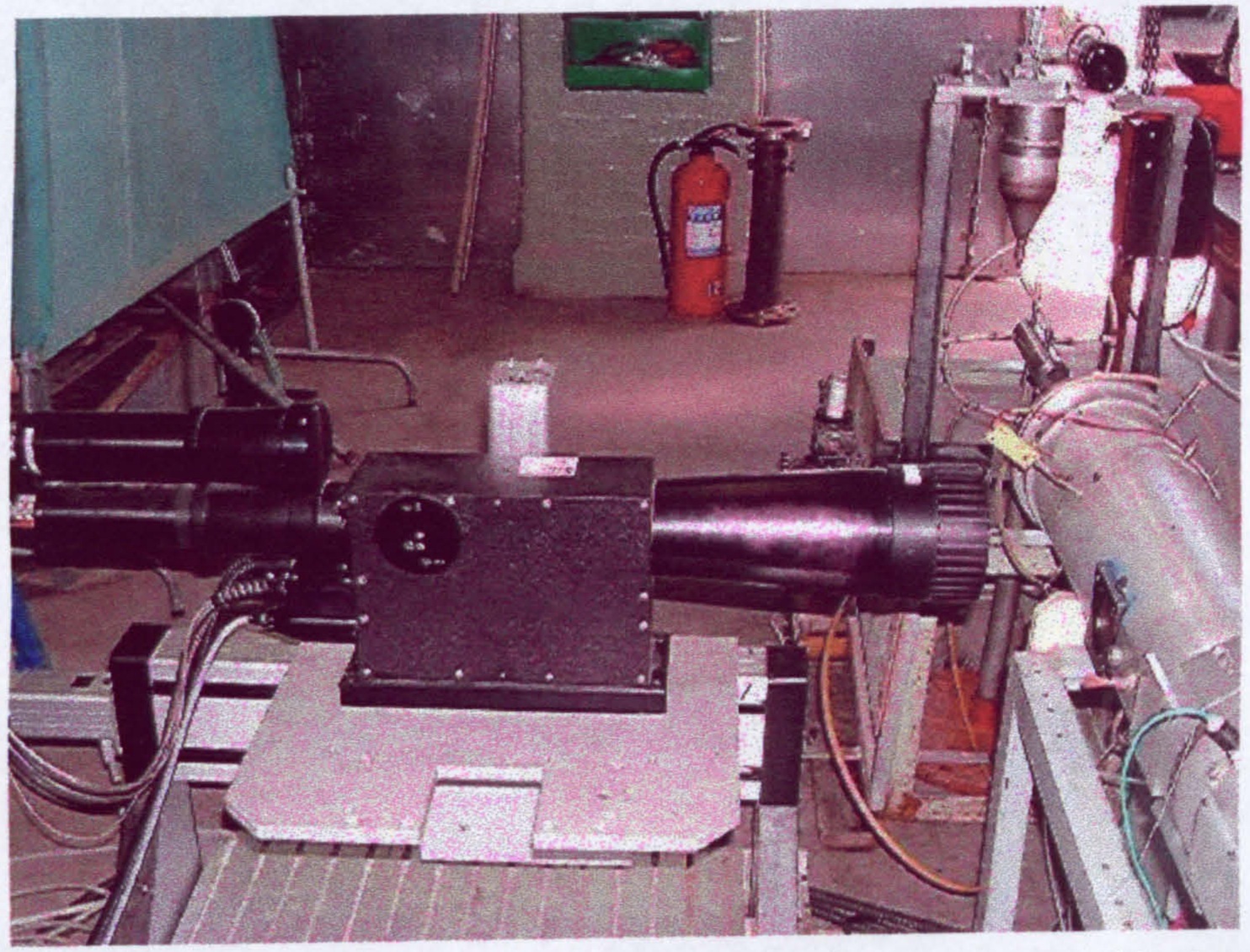

Figure 5-8 Test rig showing global sand injector and laser anemometer -side view

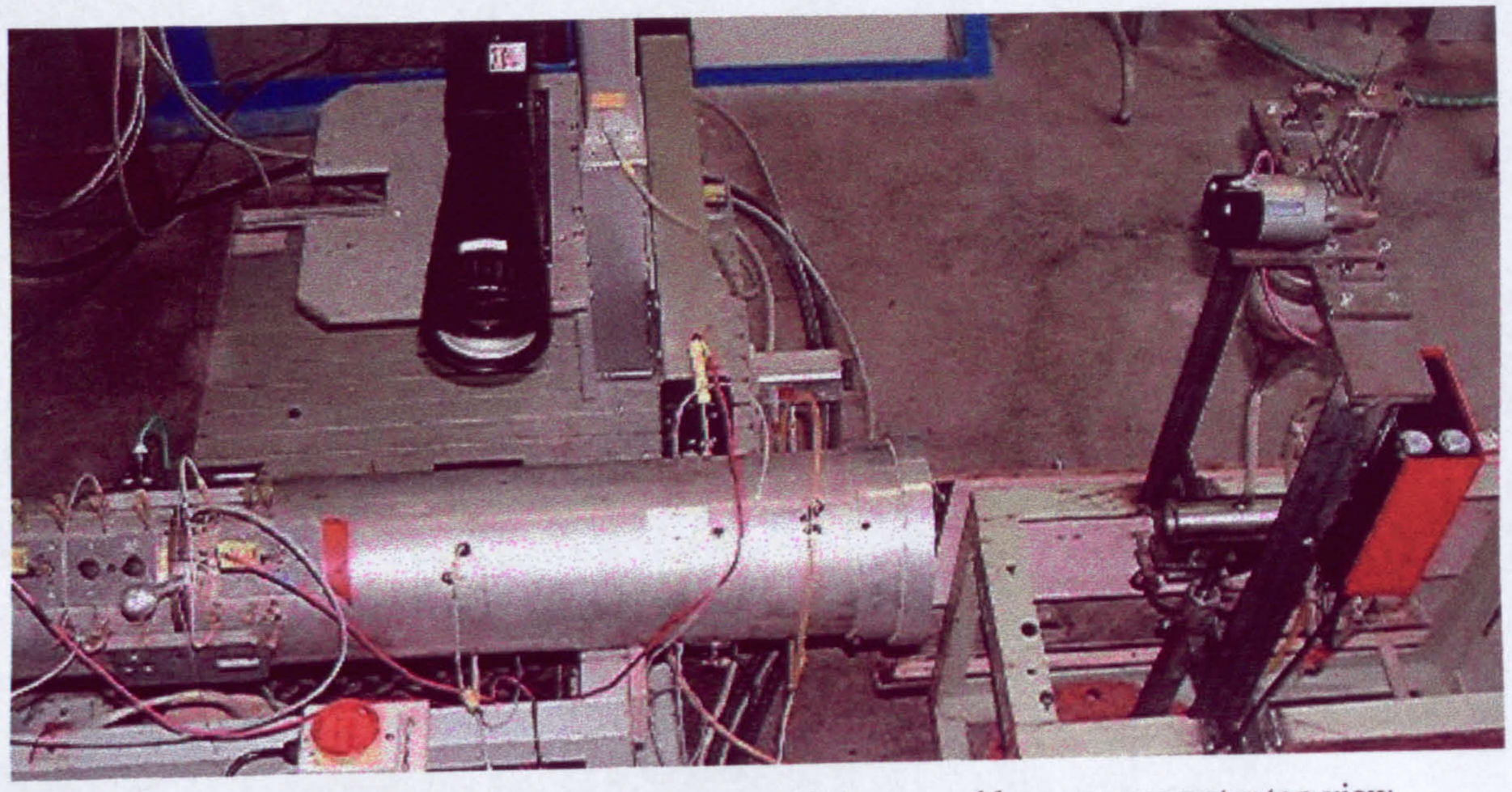

Figure 5-9 Test rig showing global sand injector and laser anemometer top view

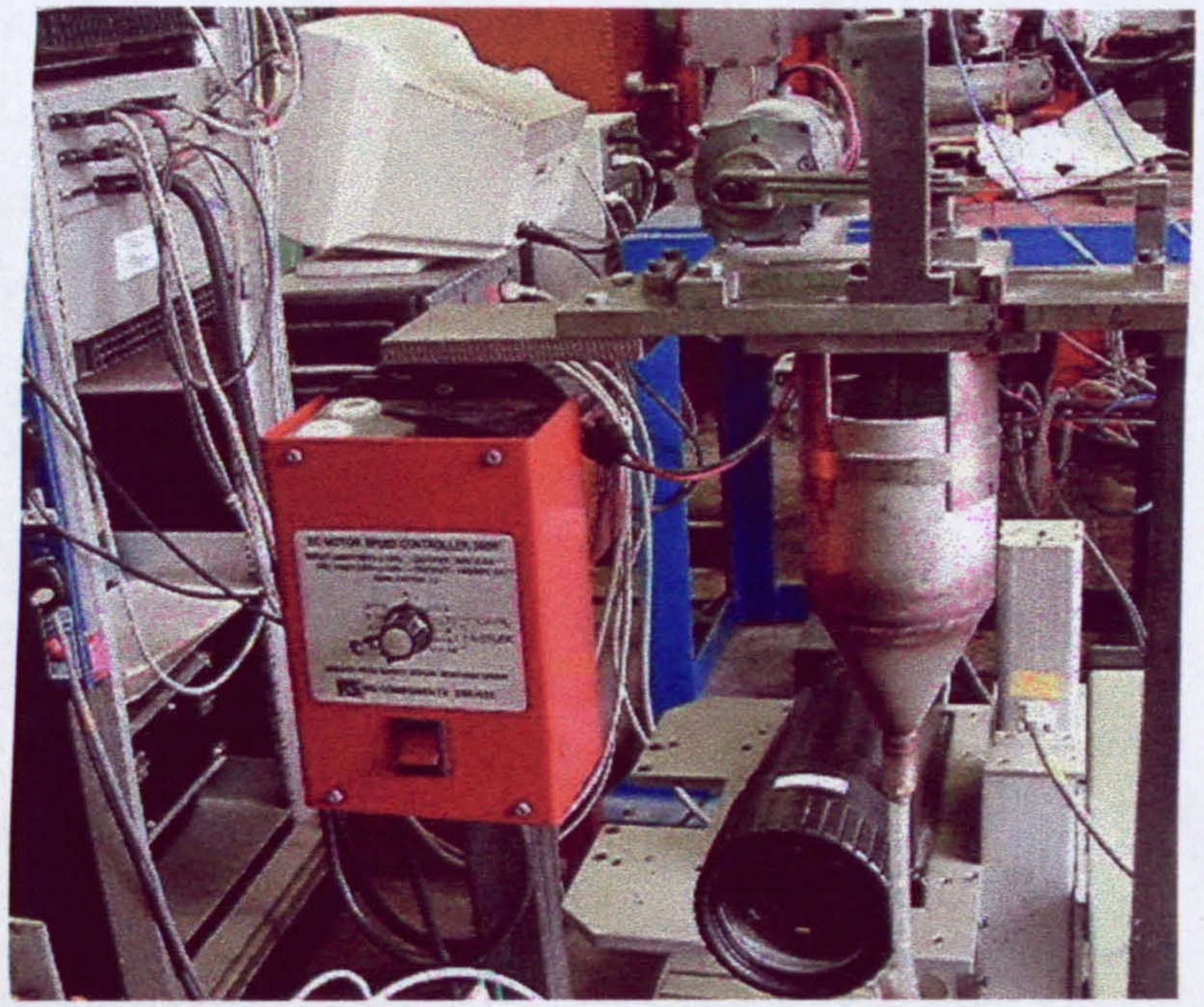

Figure 5-10 Seeding system upstream IGV

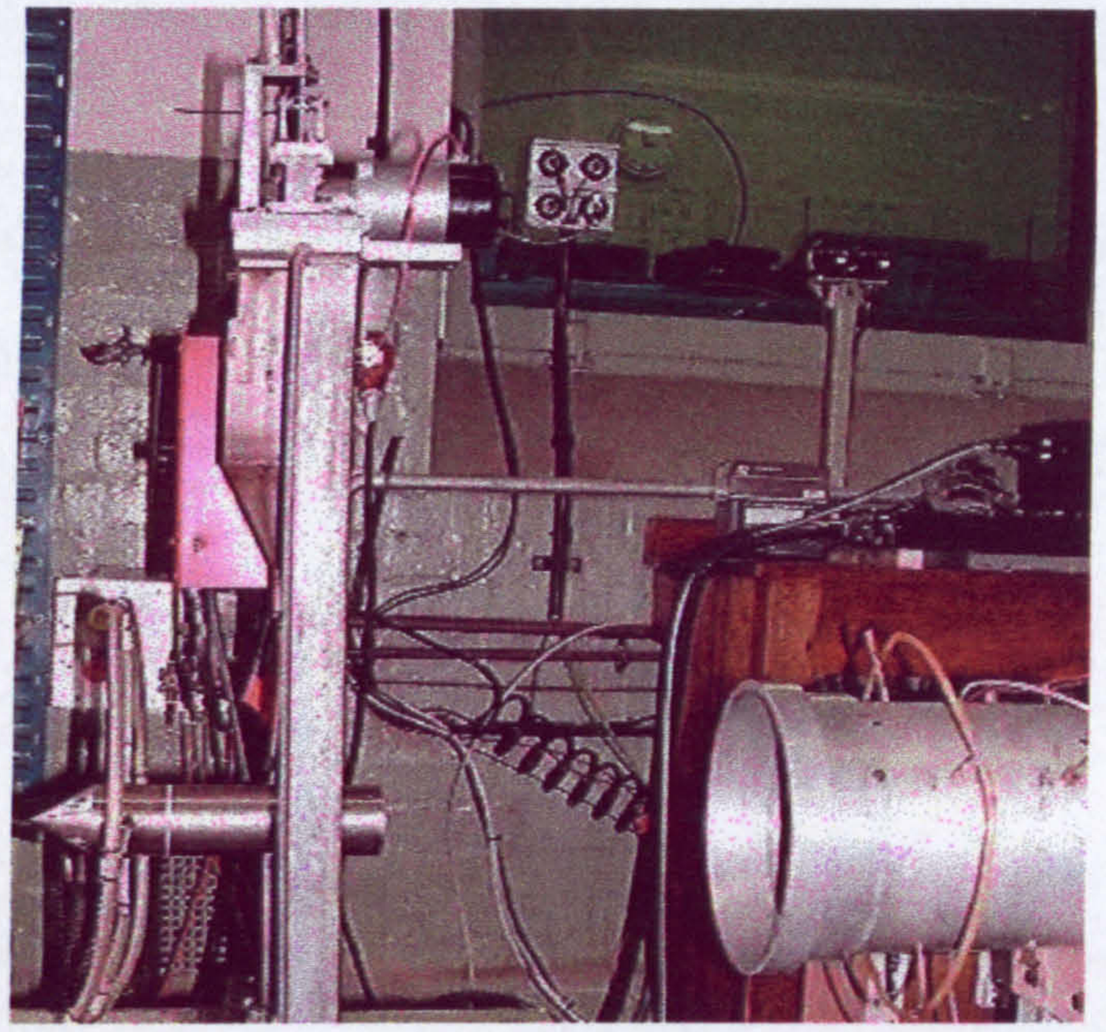

Figure 5-11 Global injector upstream fan inlet

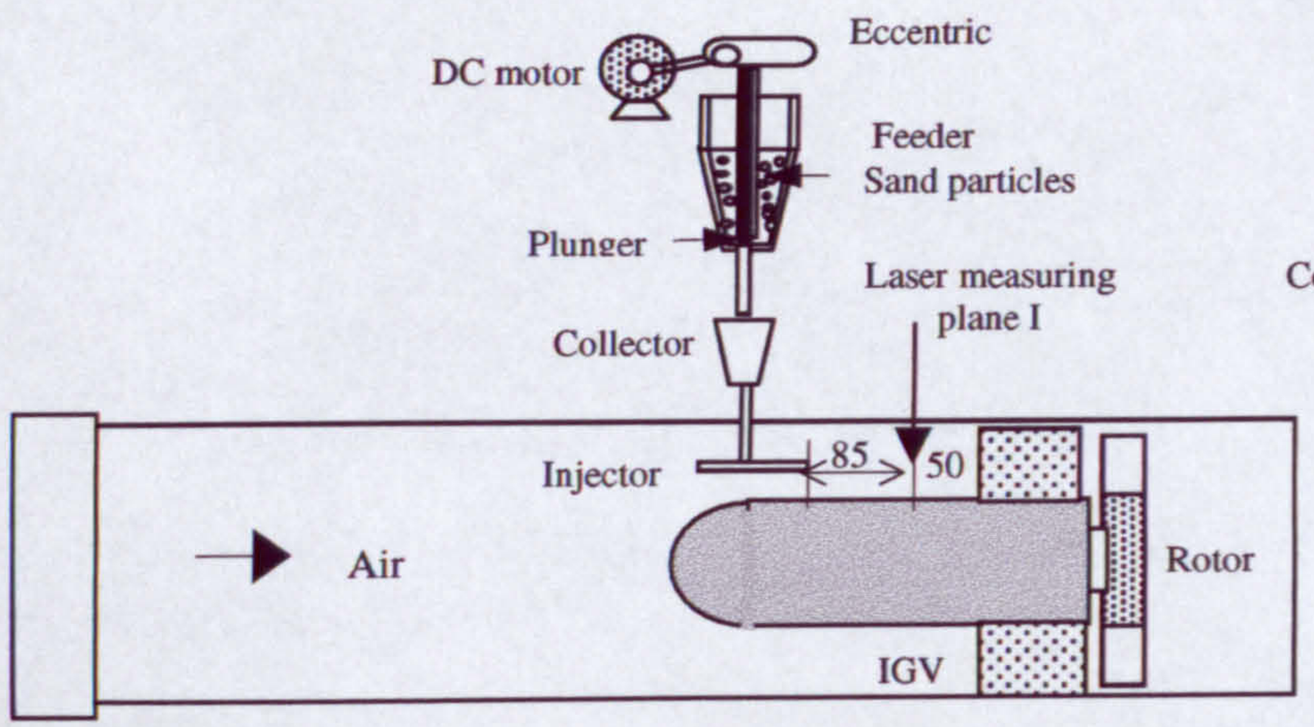


Figure 5-12 Local sand injection erosion test rig

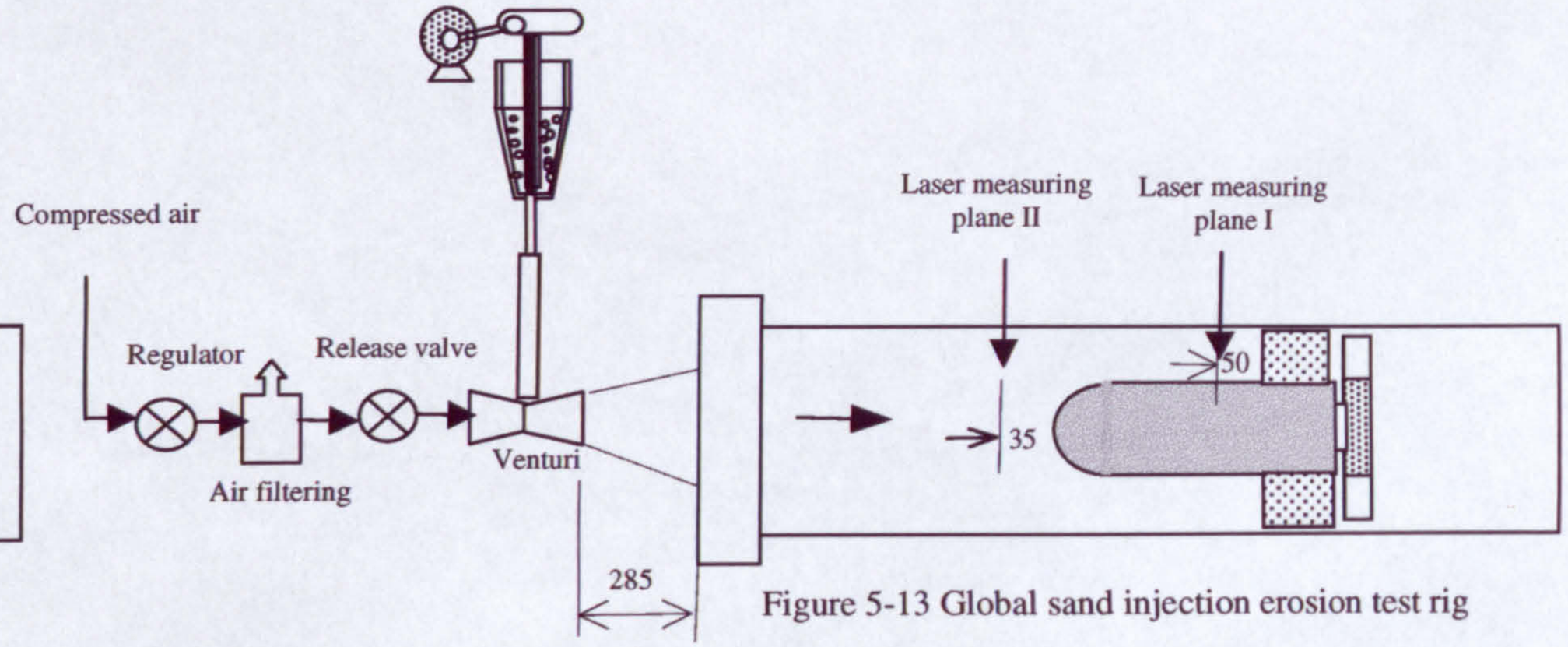


Figure 5-13 Global sand injection erosion test rig

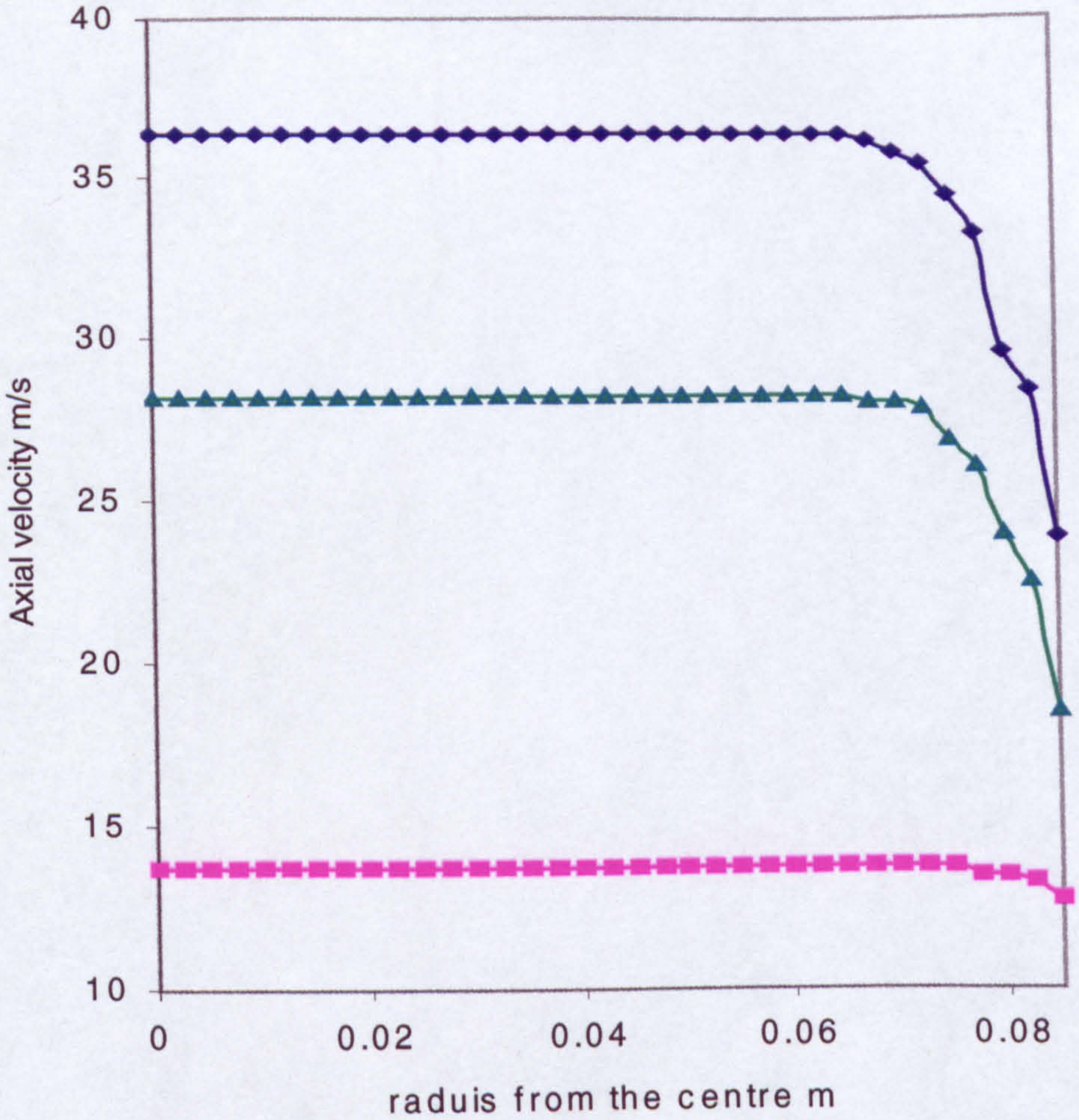


Figure 5-14 Axial velocity profiles across the radius of the conical intake

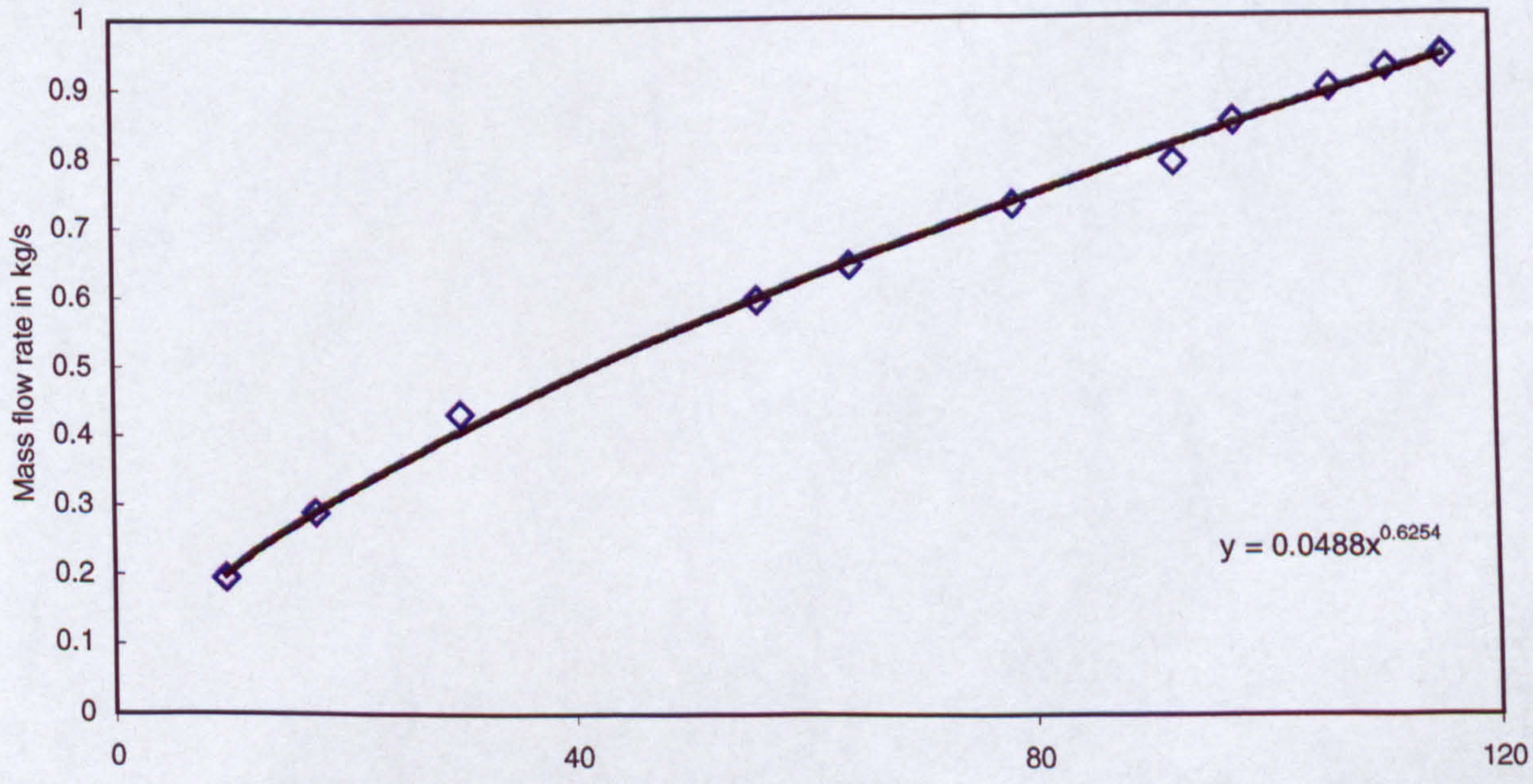


Figure 5-15 Calibration curve of the conical intake

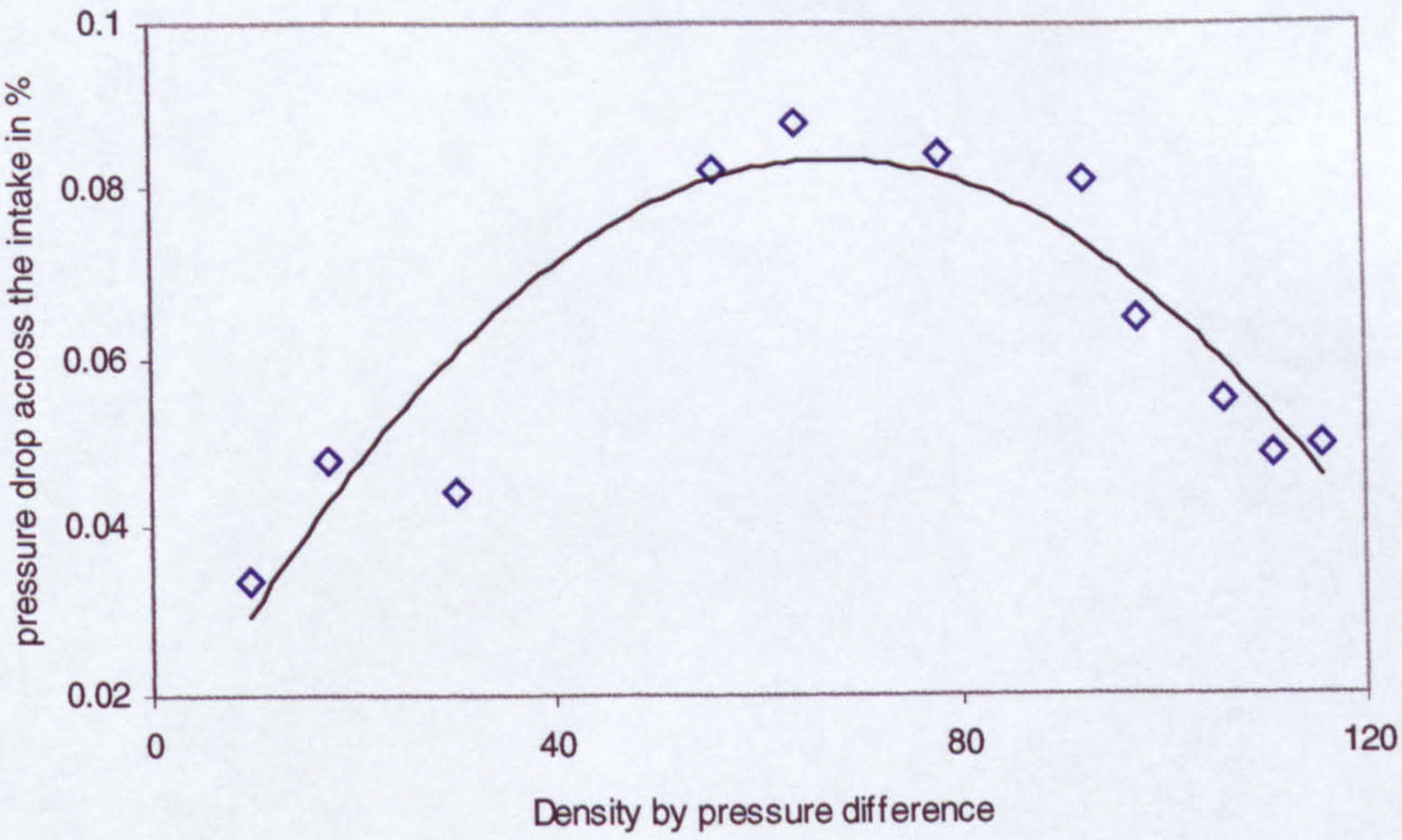


Figure 5-16 Pressure loss of the conical intake

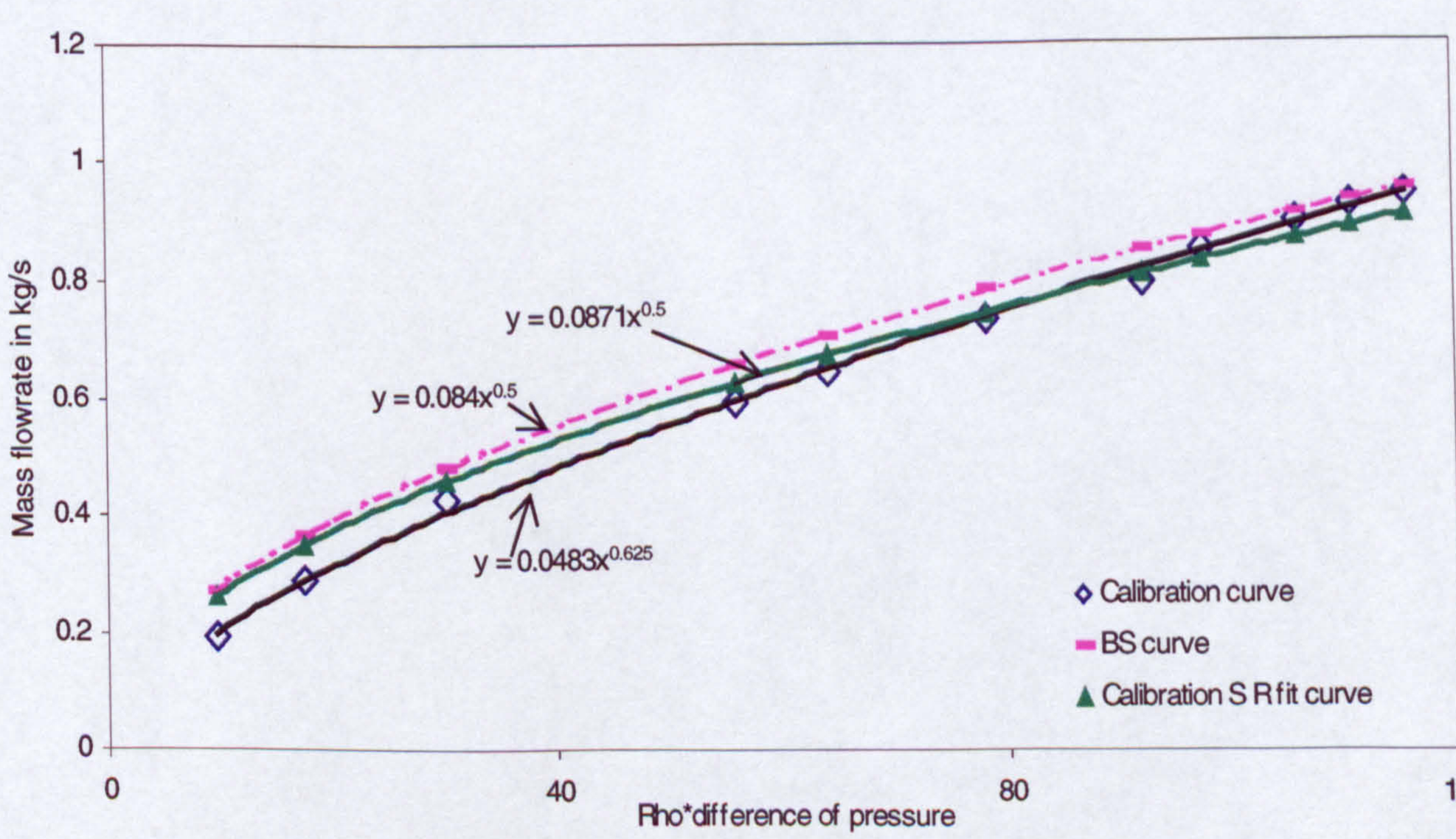


Figure 5-17 Comparison between BS and the calibrated conical intake

Material Stainless steel
Inside roughness Ra 0.8
Outside roughness Ra 1.6

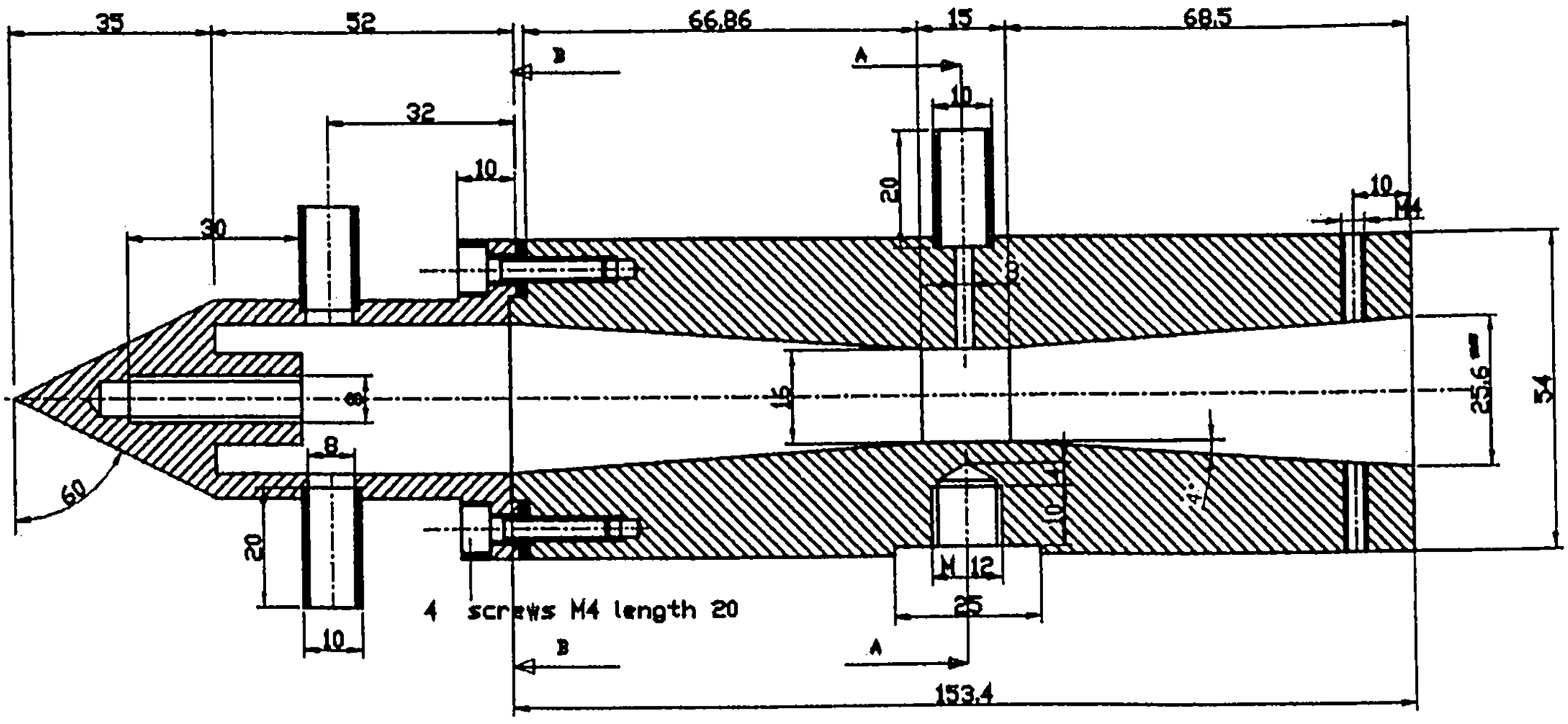


B-B

10 mm tube

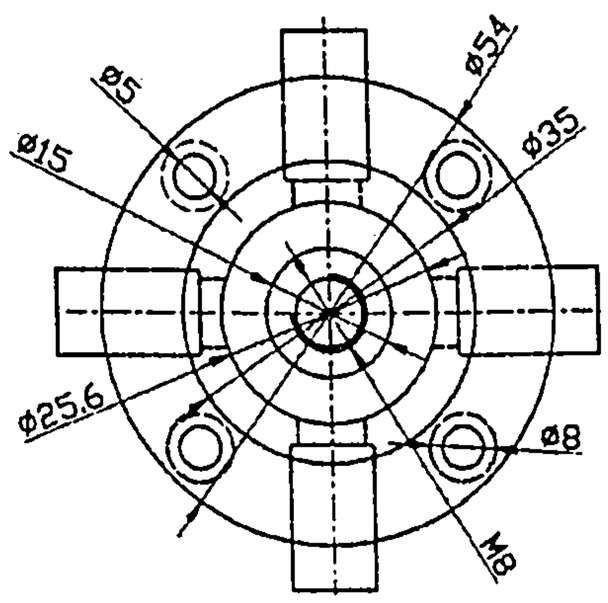


A-A

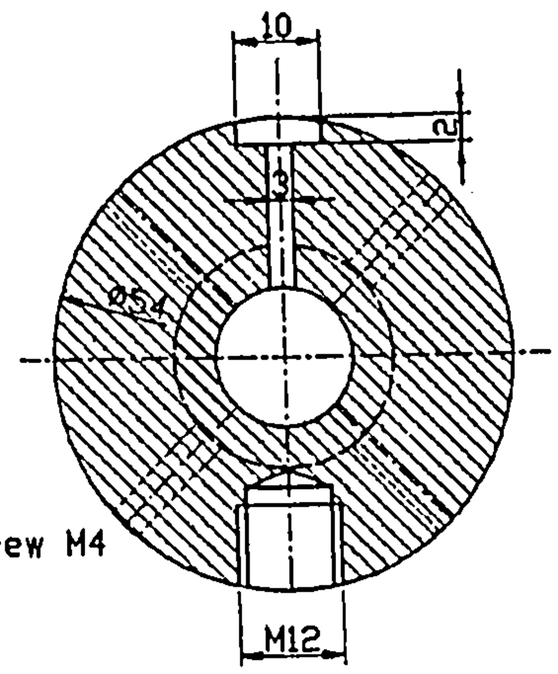


Grup screw M4

Figure 5-18 Venturi injector design drawing

Material Stainless steel
Inside roughness Ra 0.8
Outside roughness Ra 1.6

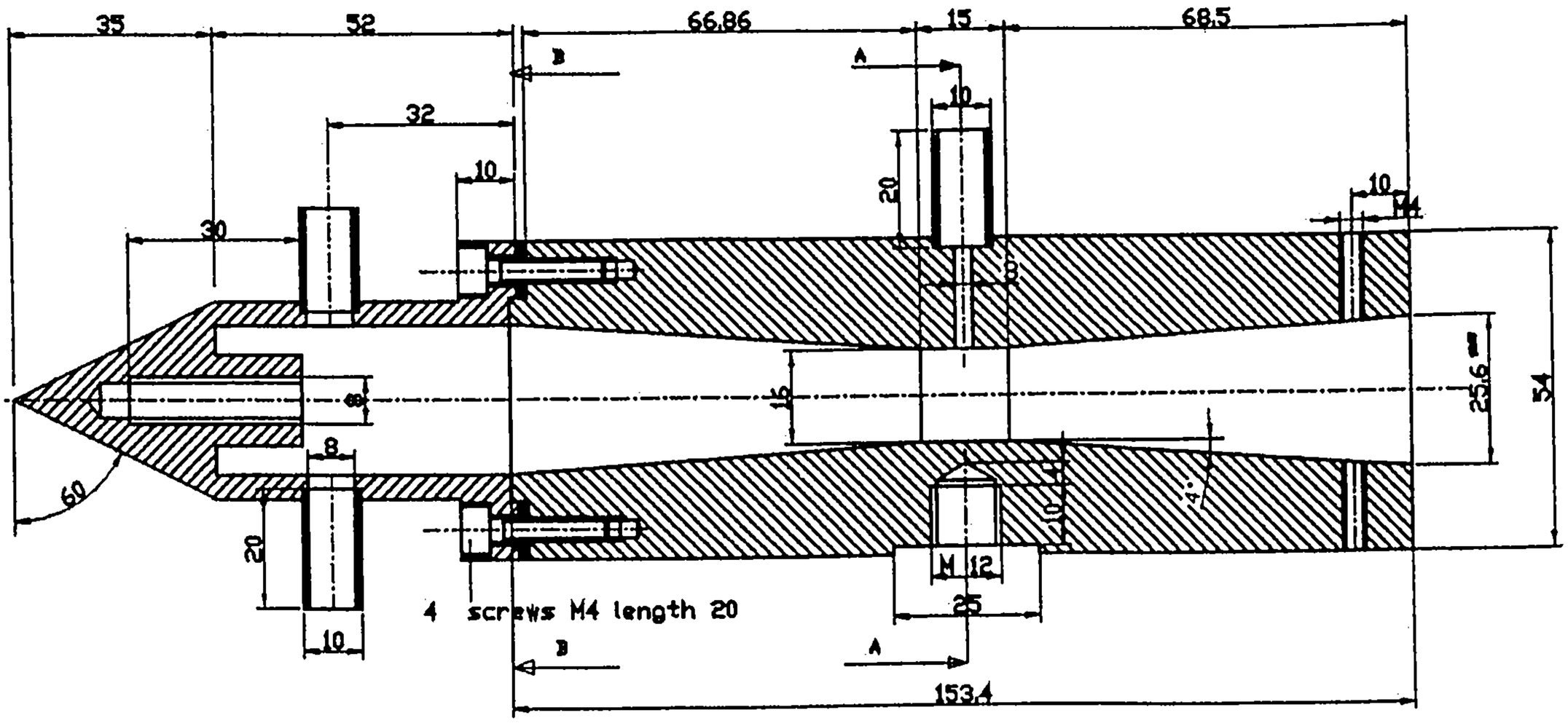


B-B

10 mm tube

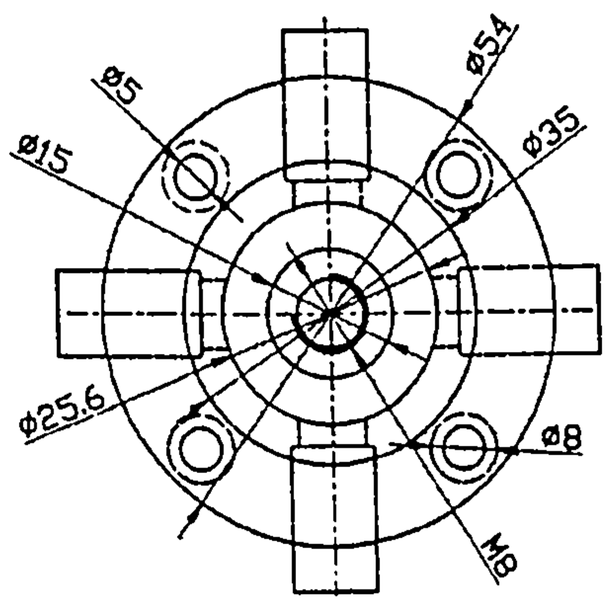


A-A

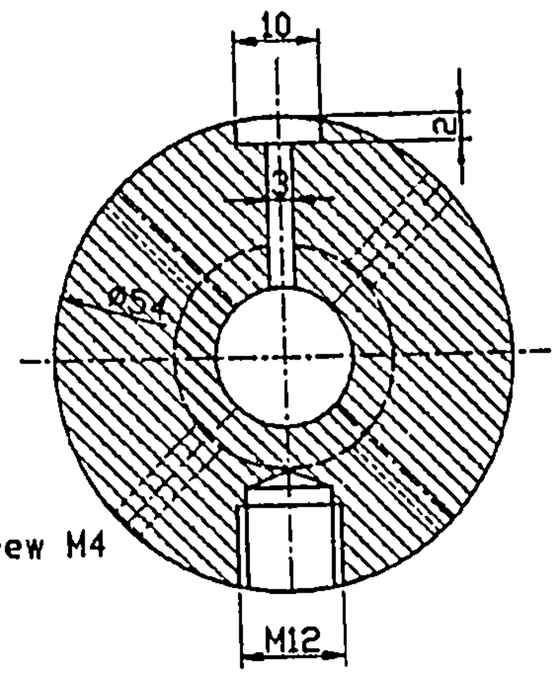


Grup screw M4

Figure 5-18 Venturi injector design drawing

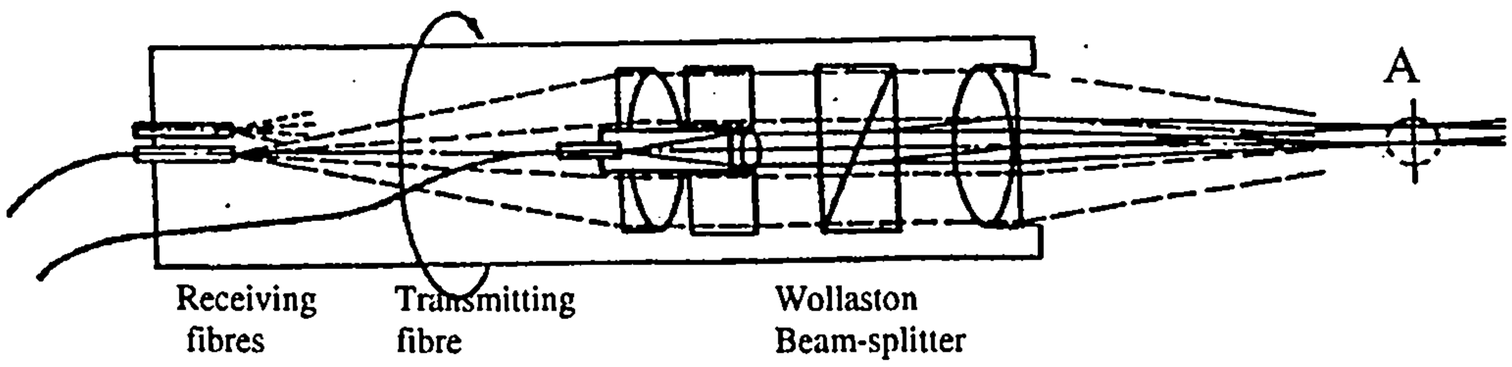


Figure 5-19 Block diagram of the fibre L2F probe

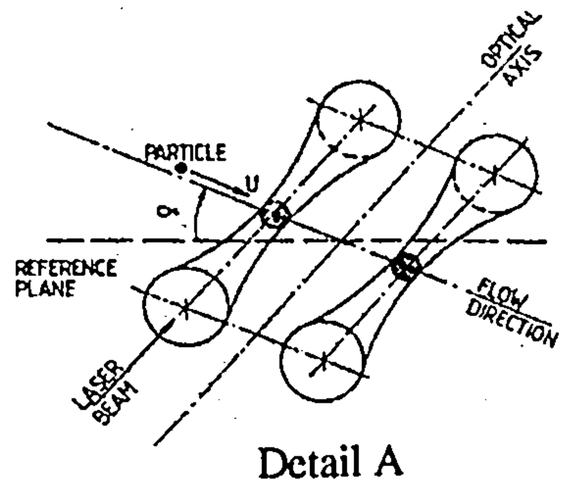


Figure 5-20 Laser two focus probe volume

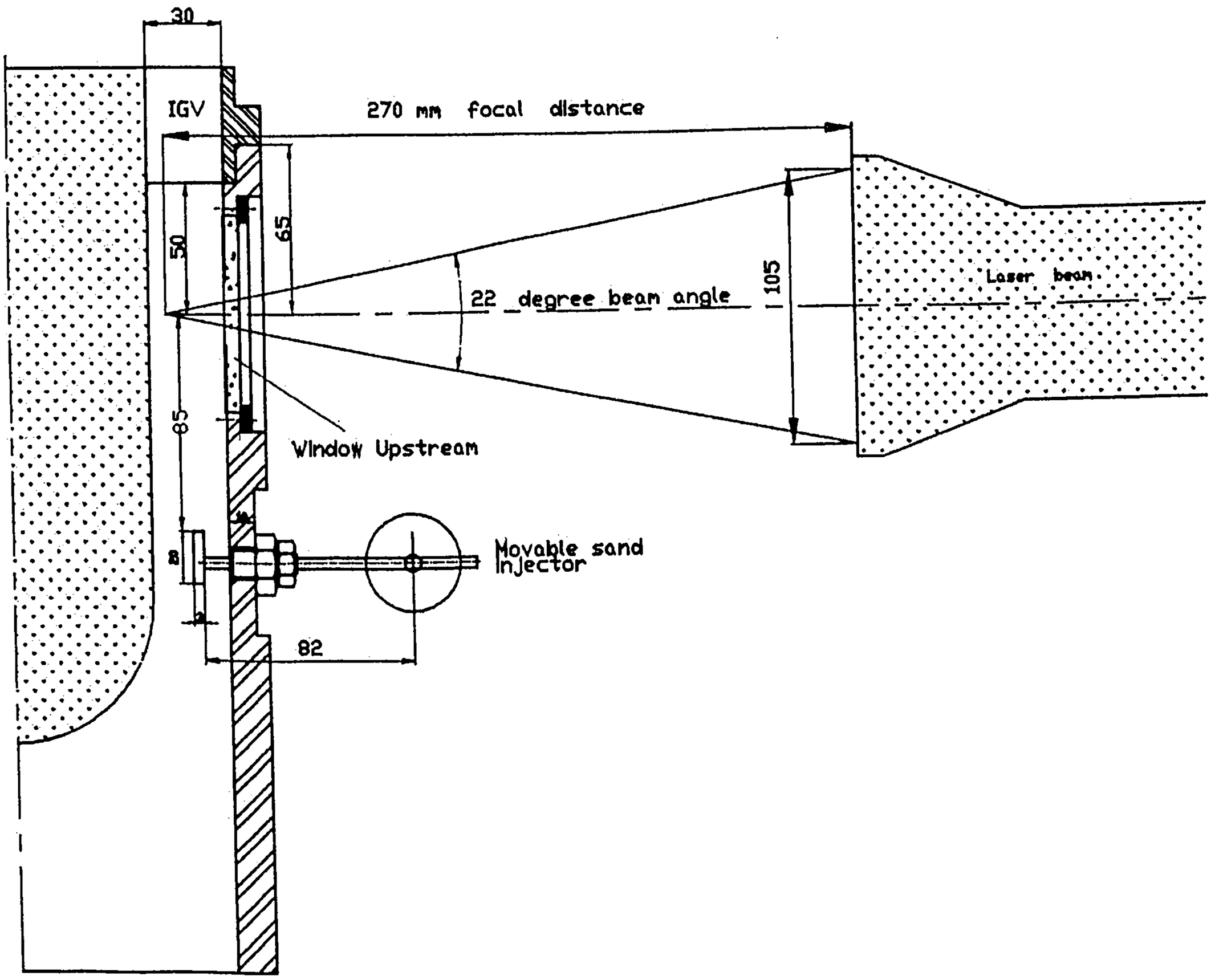


Figure 5-21 Arrangements for the local injector pipe and the transit laser anemometer

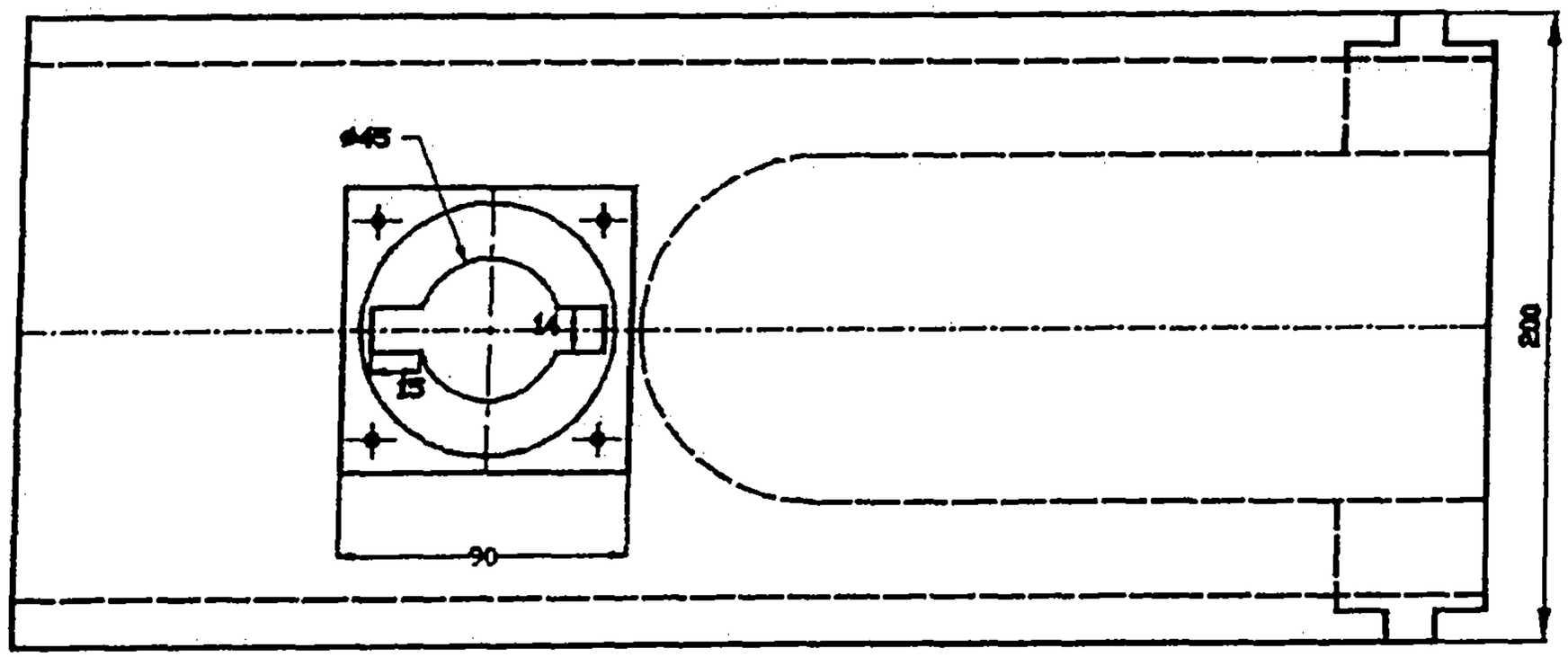


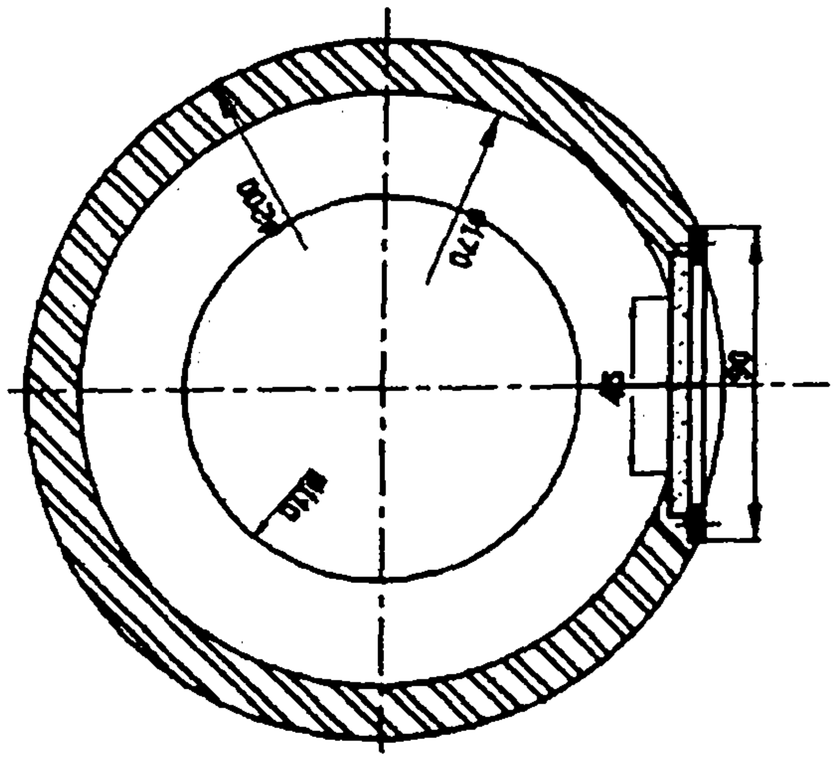


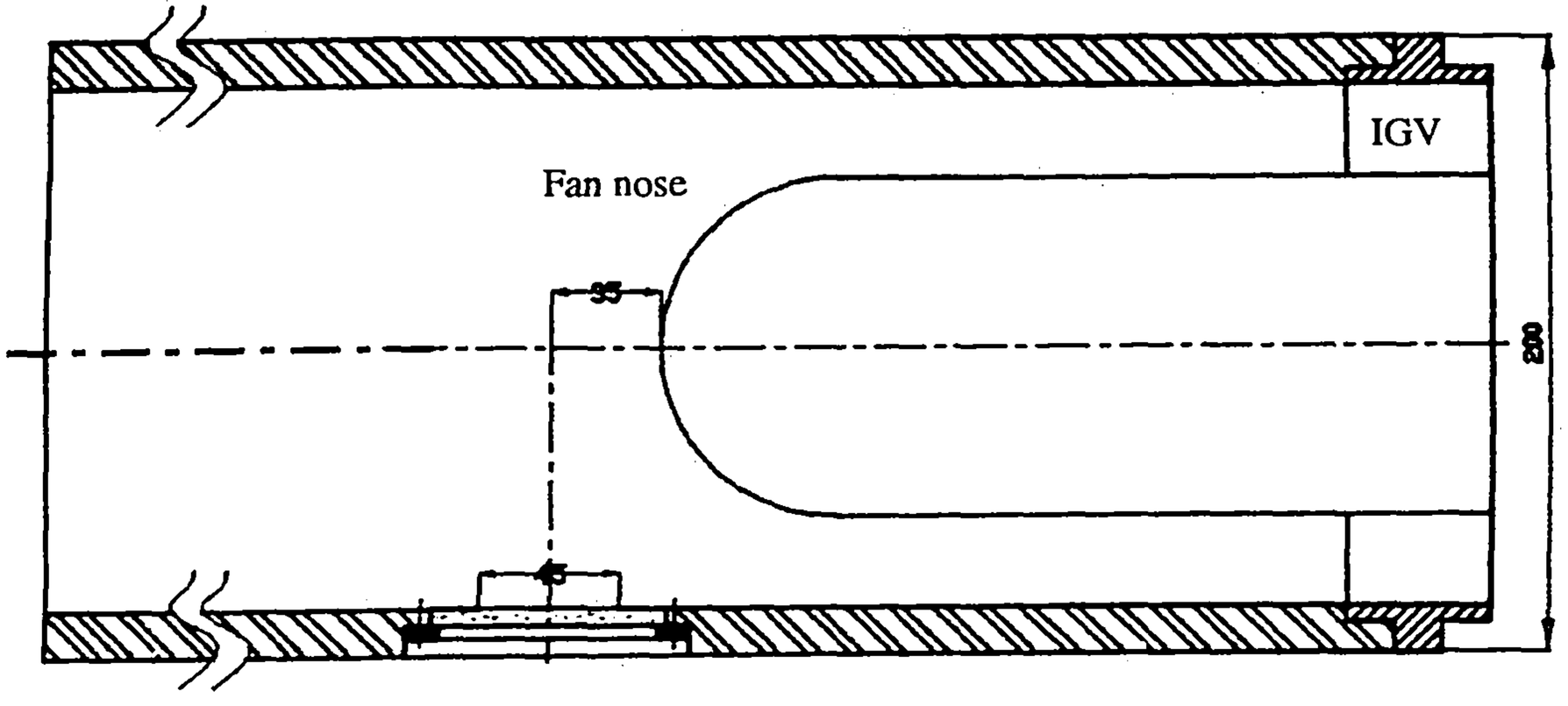


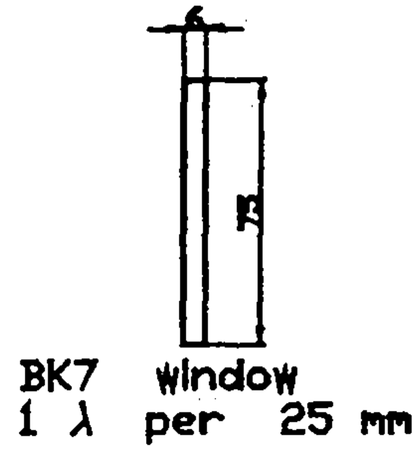


Figure 5-22 Arrangements for the upstream fan nose window

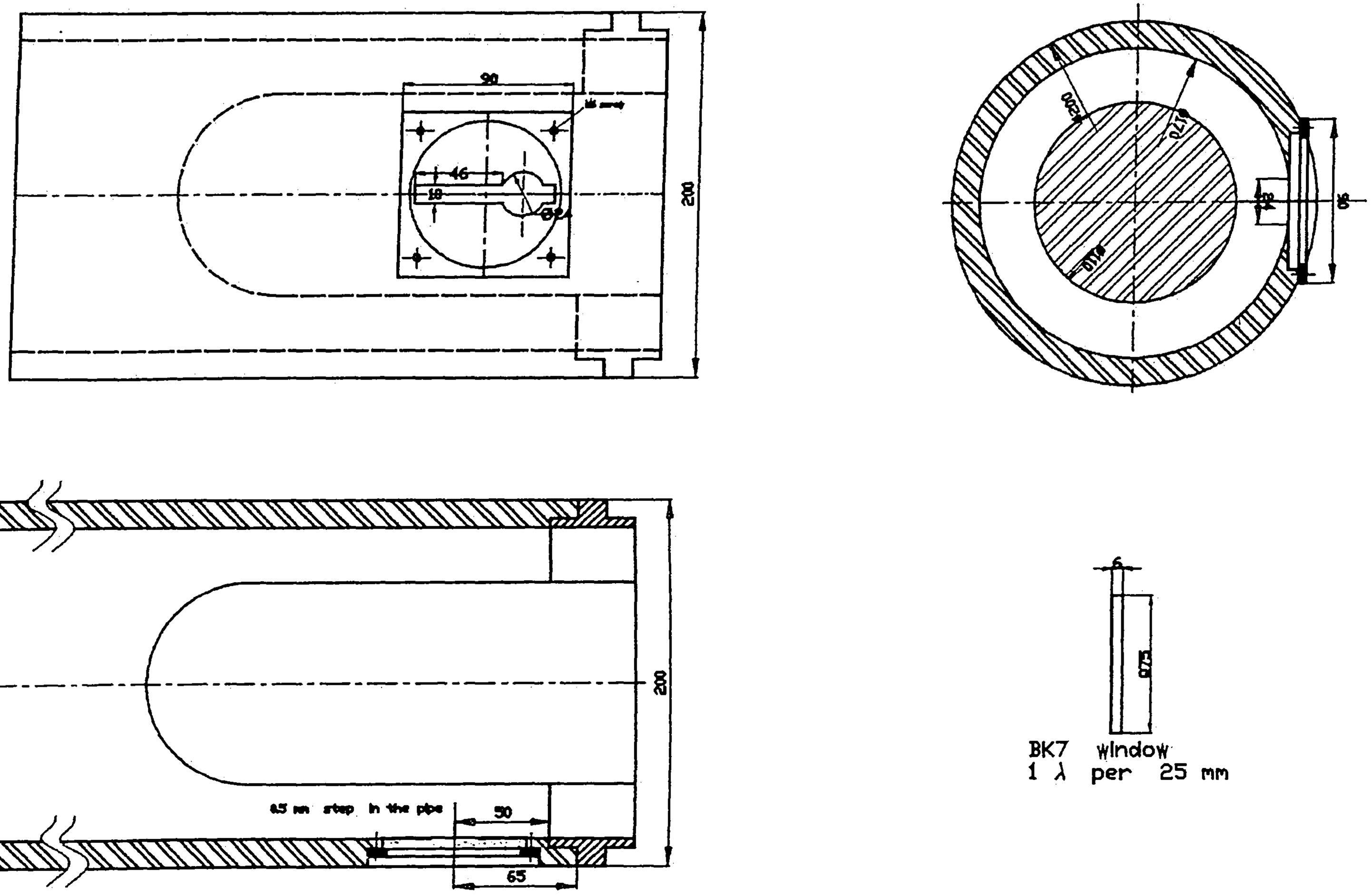


Figure 5-23 Arrangements for the upstream IGV window

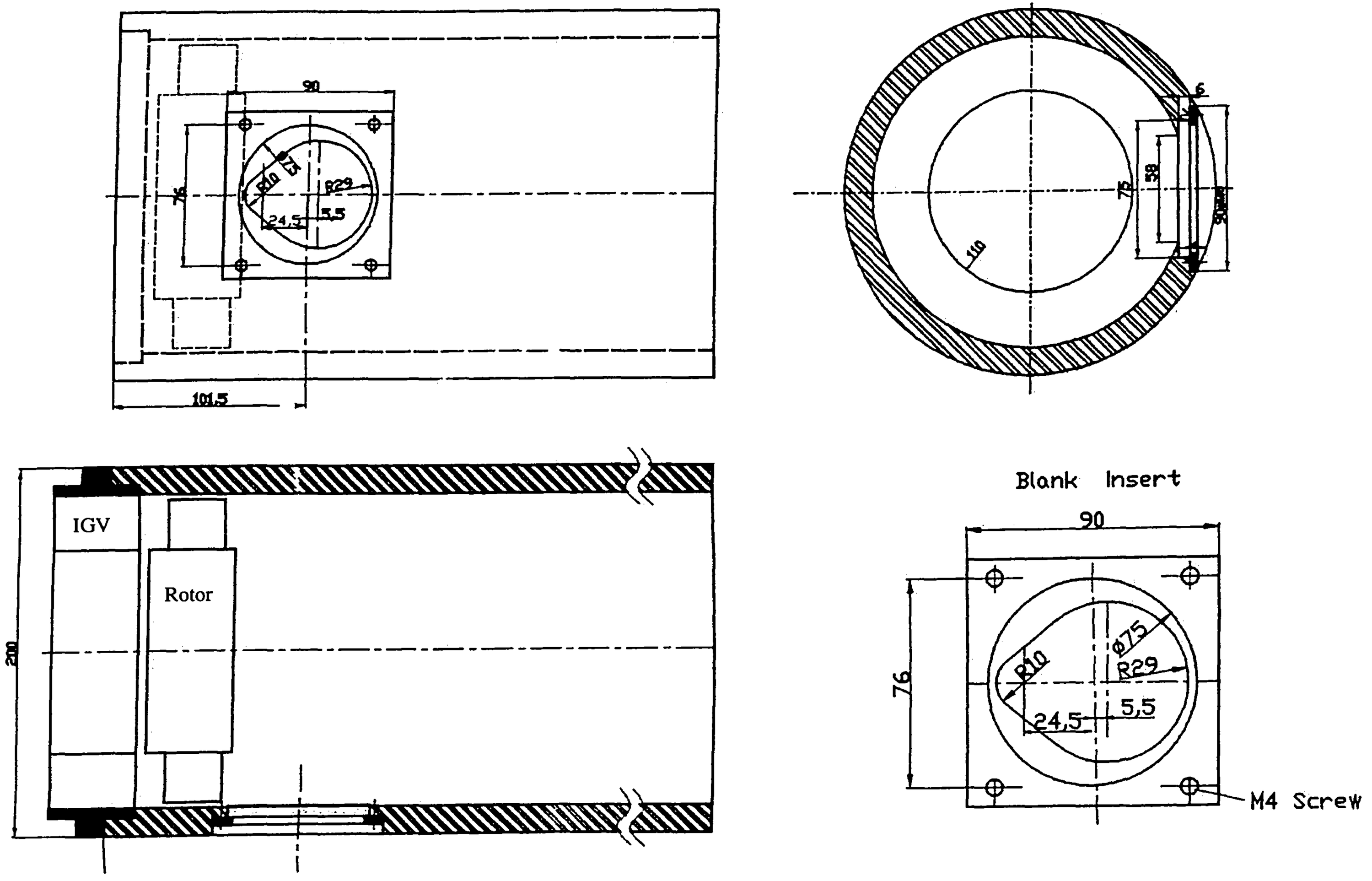


Figure 5-24 Arrangements for the downstream rotor window

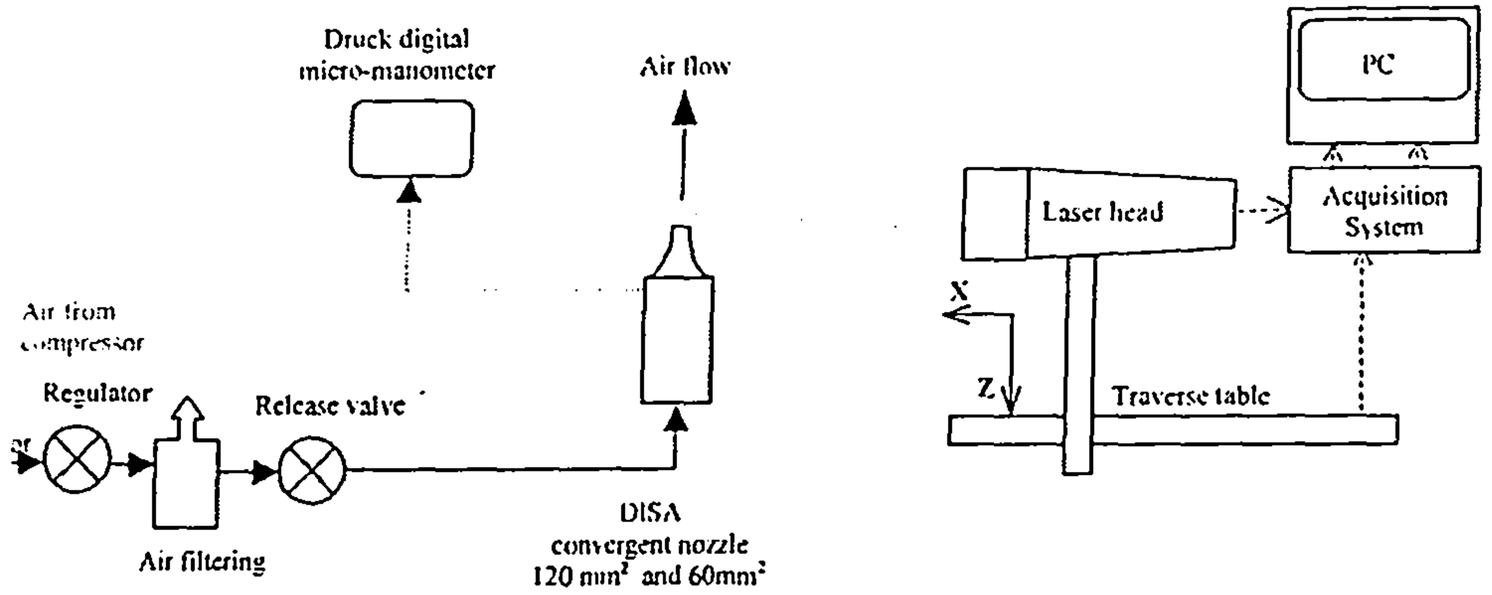


Figure 5-25 Laser calibration using Disa convergent nozzles

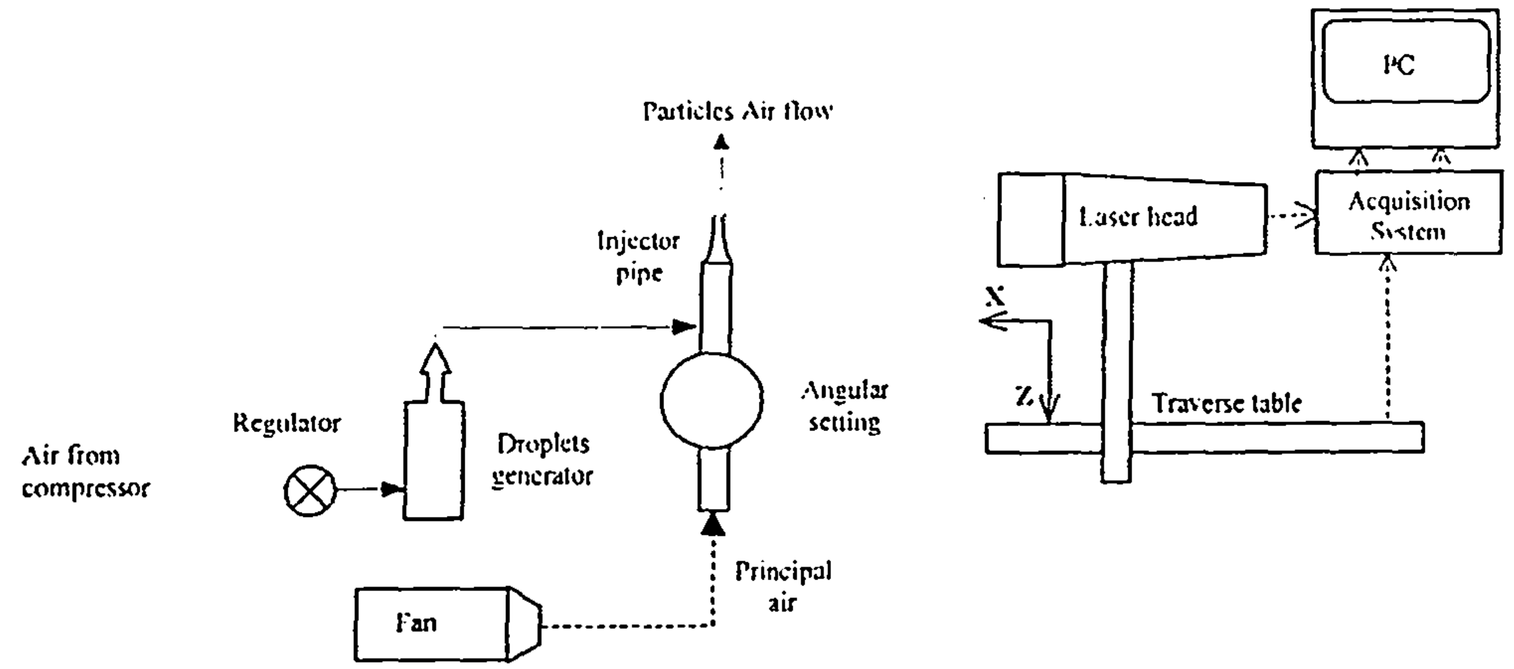


Figure 5-26 Nozzle droplets concentration measurement

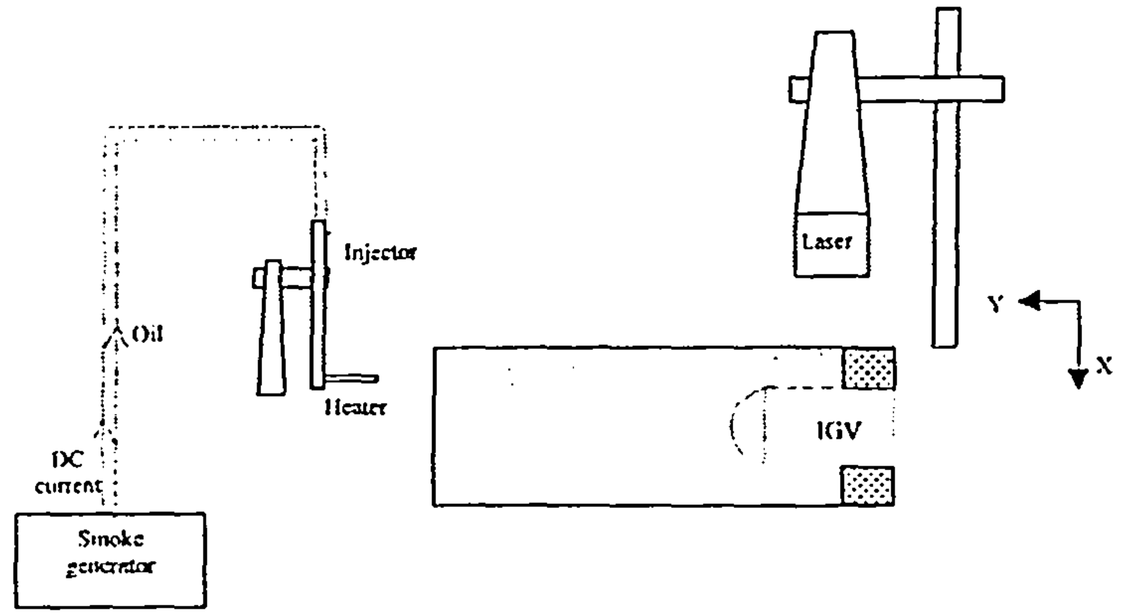


Figure 5-27 Smoke concentration measurement upstream IGV

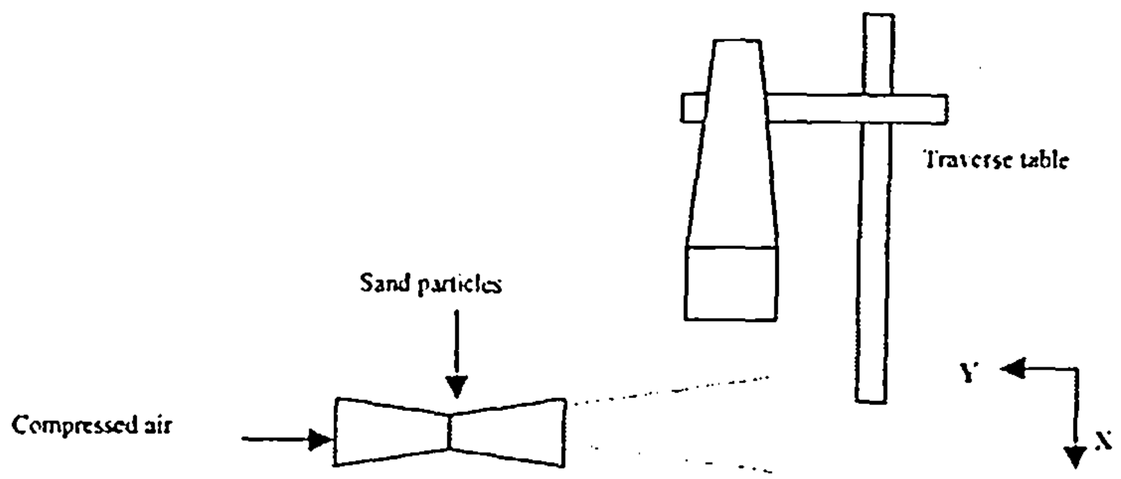


Figure 5-28 Concentration profile measurement from a venturi

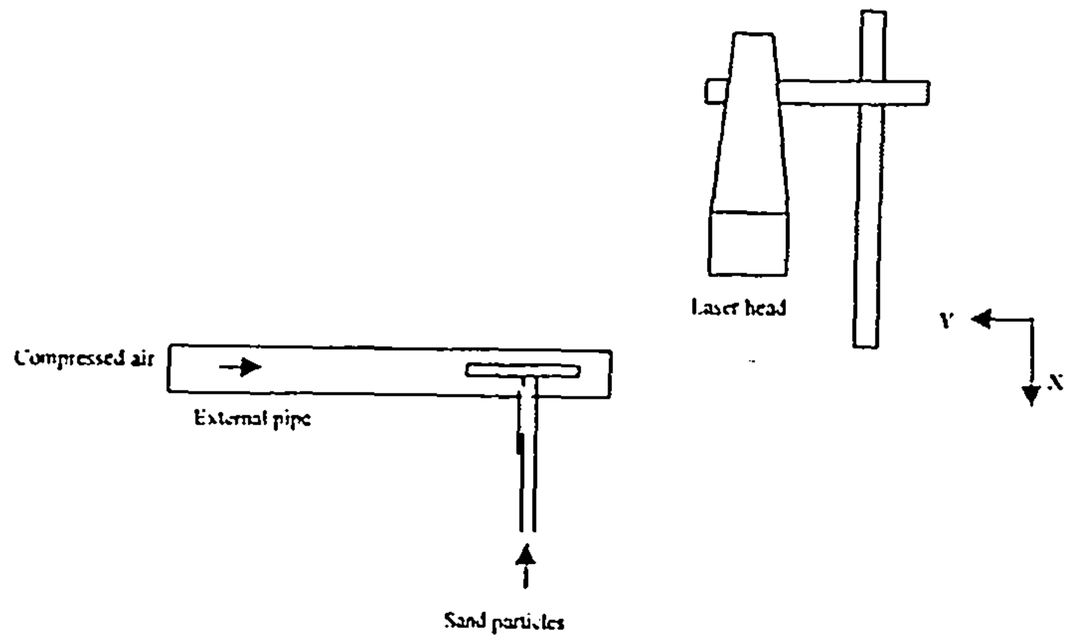


Figure 5-29 Concentration measurement from a pipe injector

Figure 5-30 Calibration of 120mm$^2$ convergent jet nozzle at air pressure 100PSI

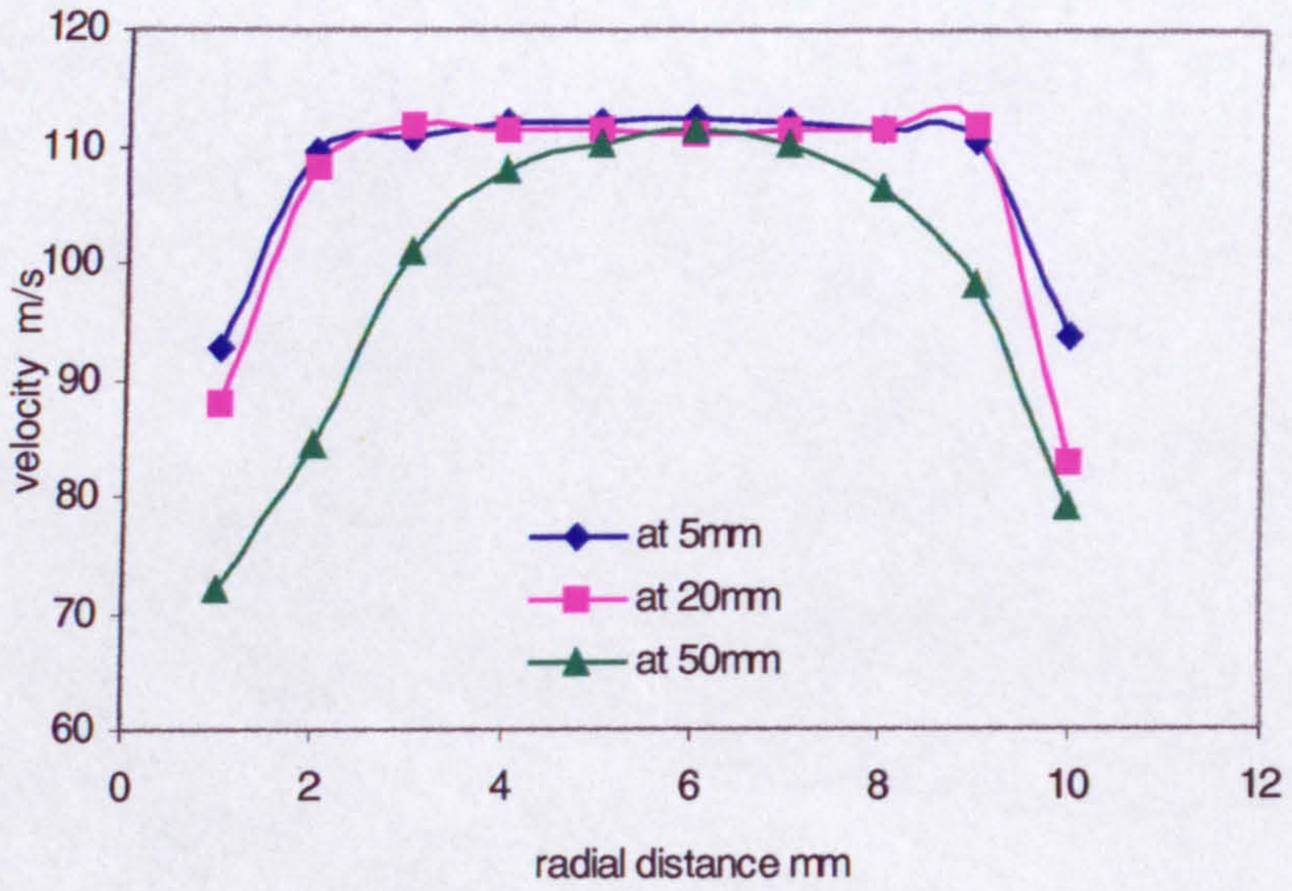


Figure a

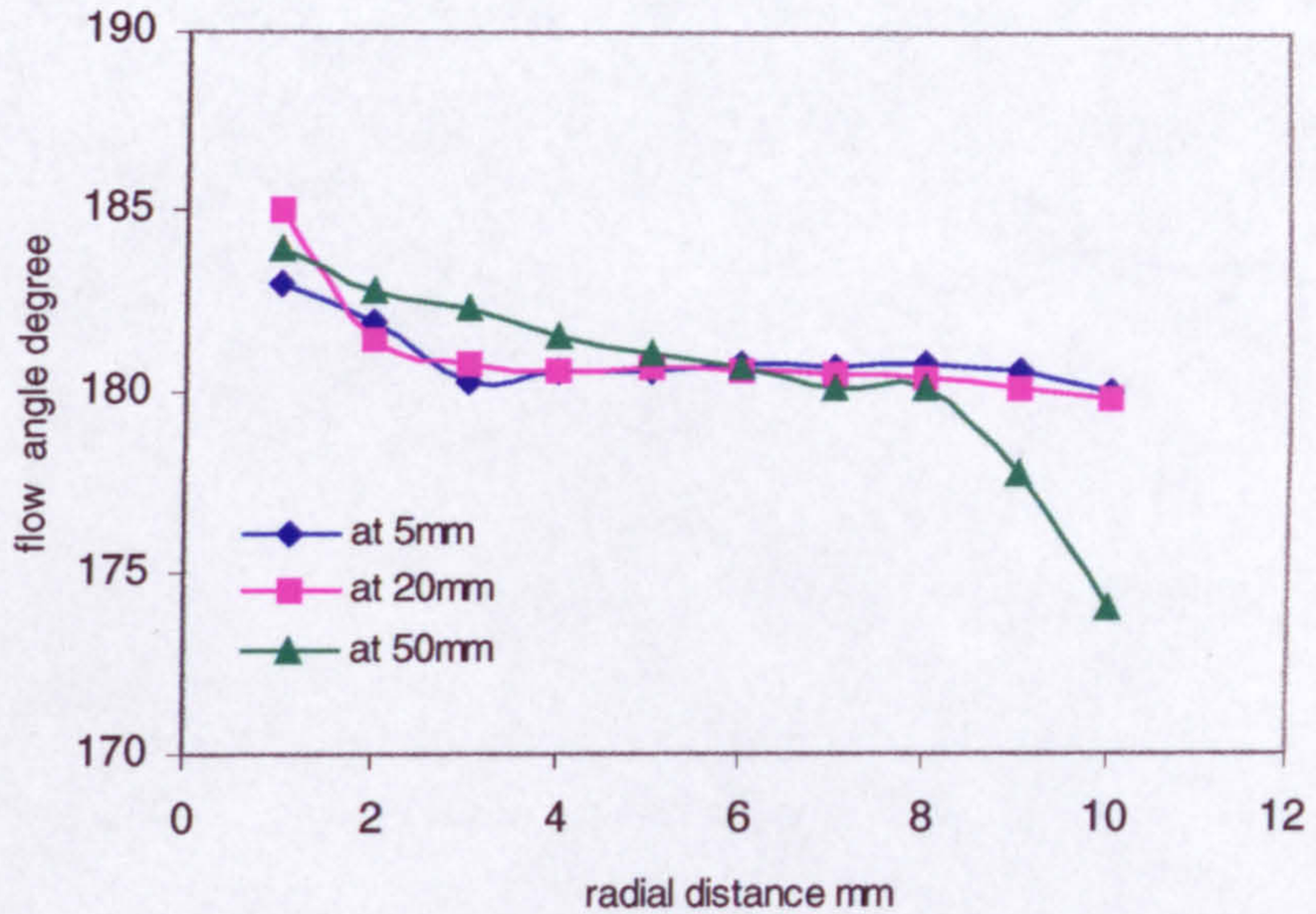


Figure b

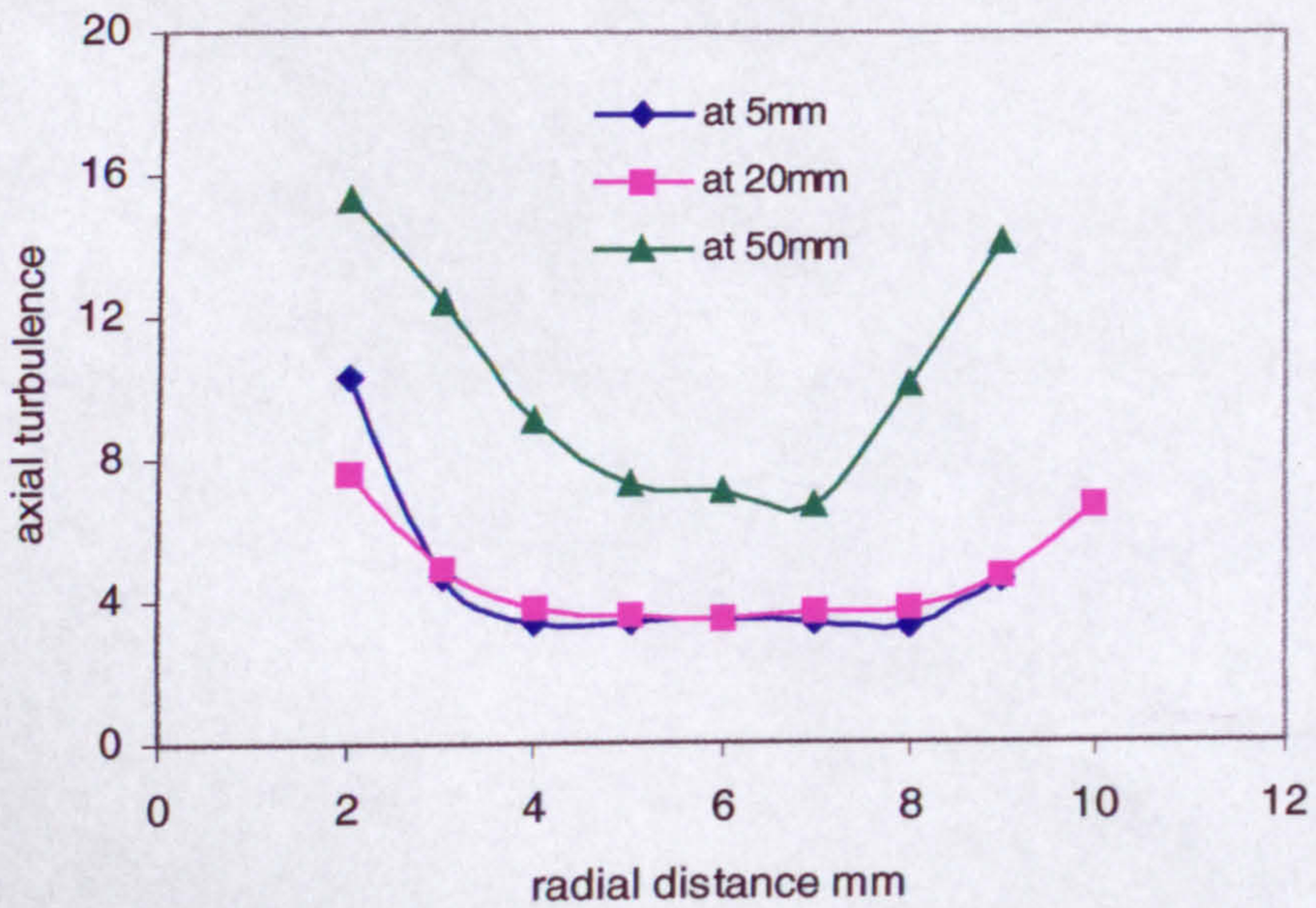


Figure c

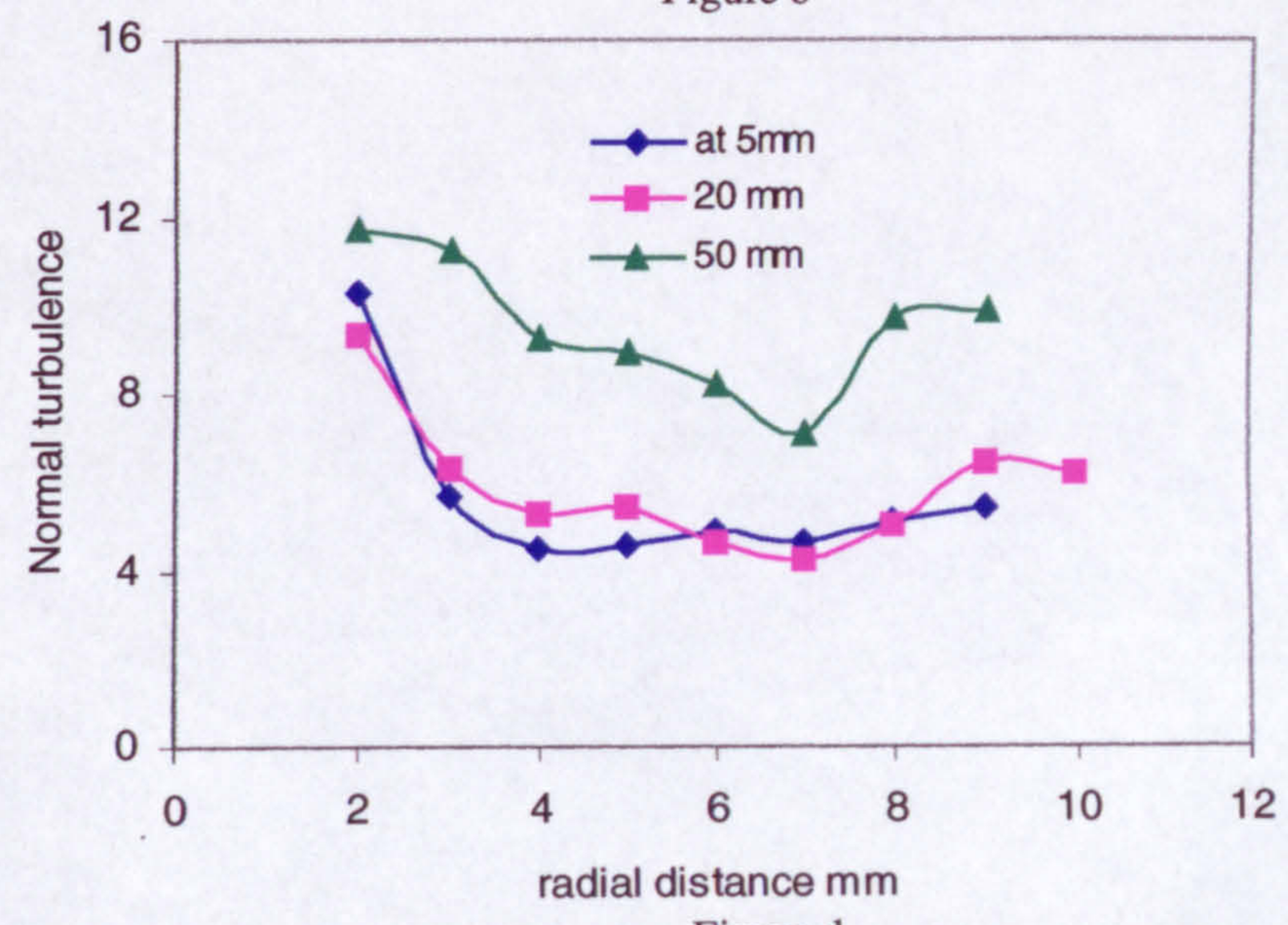


Figure d

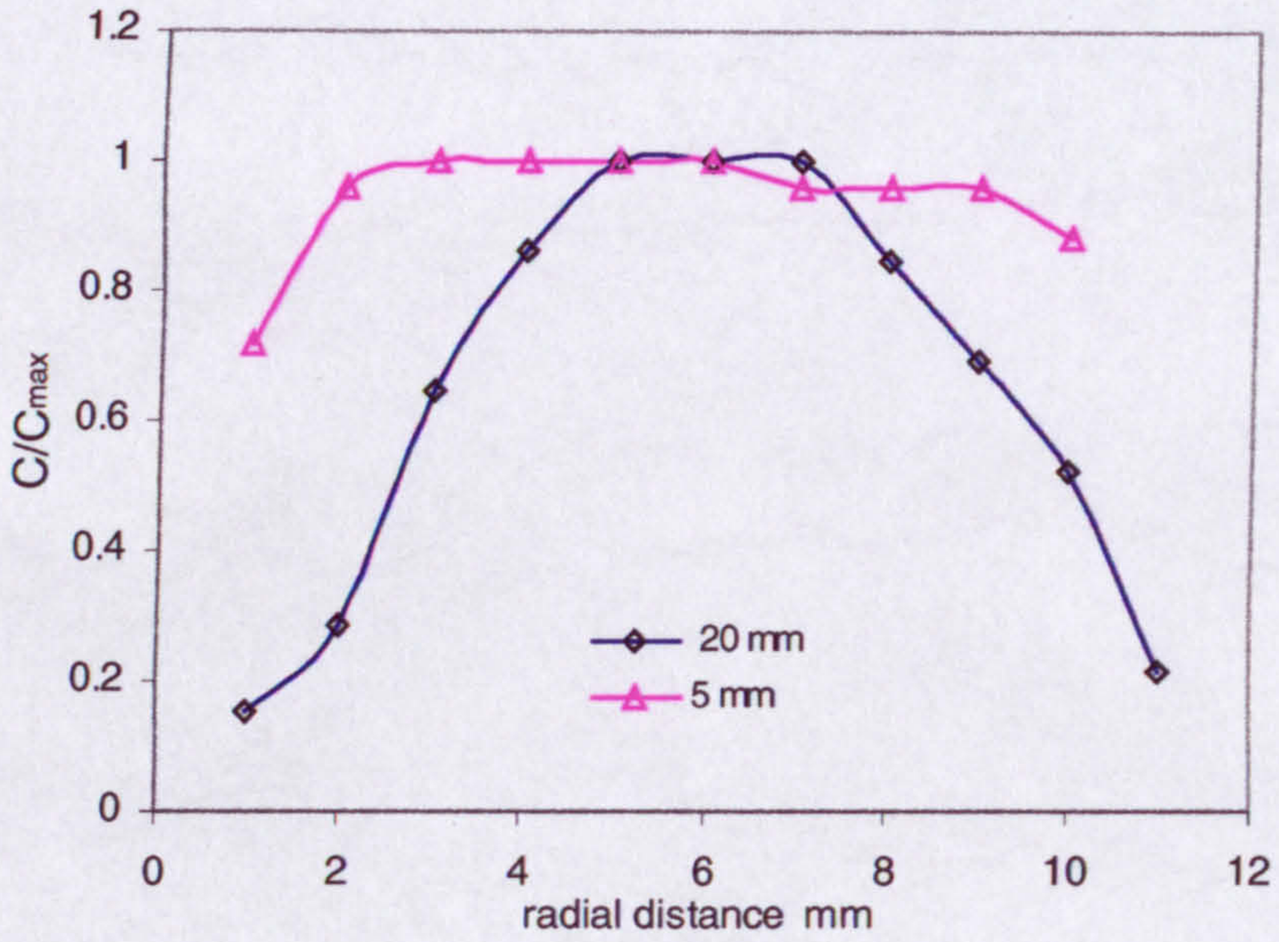


Figure 5-31a Water propanol droplet concentration from a vertical pipe

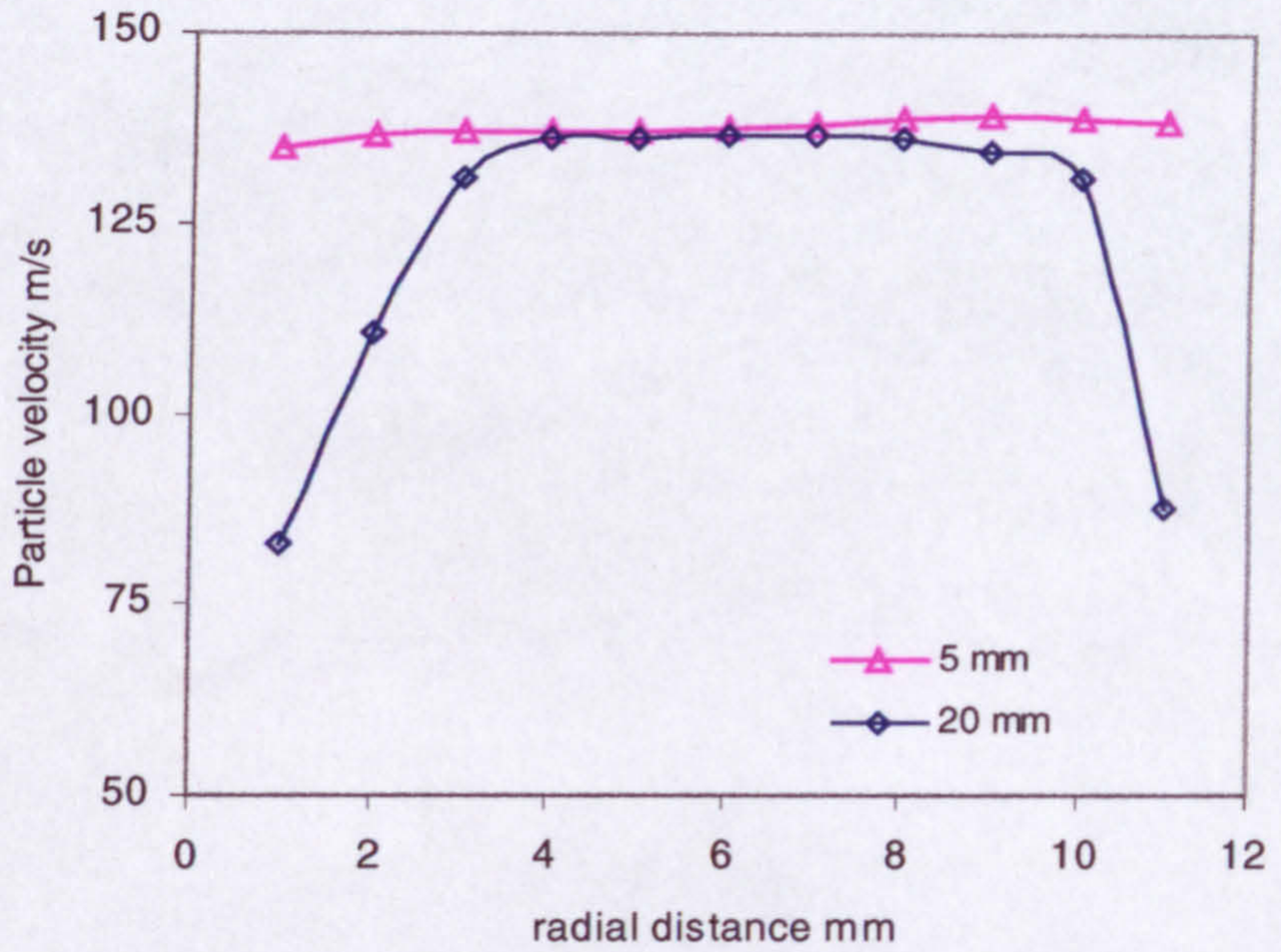


Figure 5-31b Water propanol droplet velocity from a vertical jet pipe

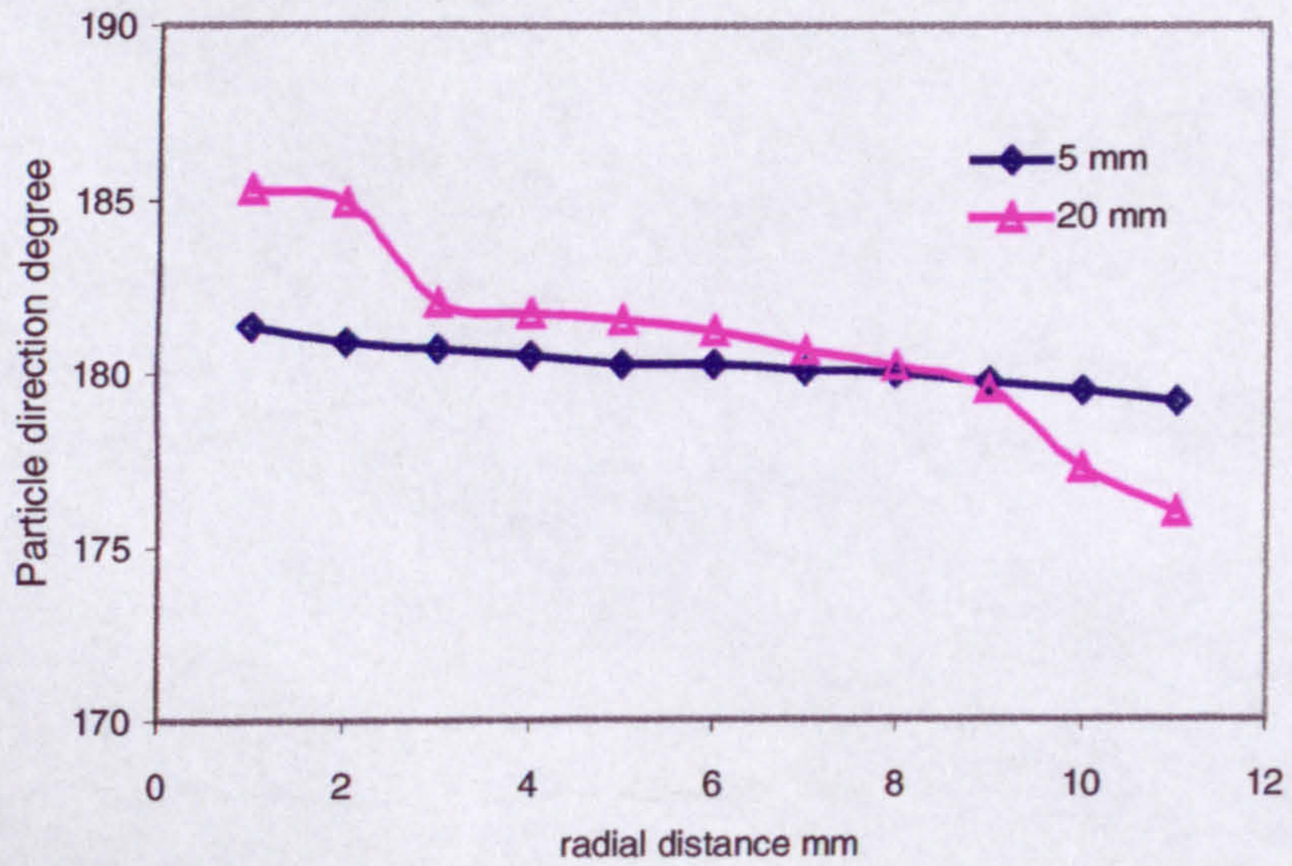


Figure 5-31c Water propanol droplet direction

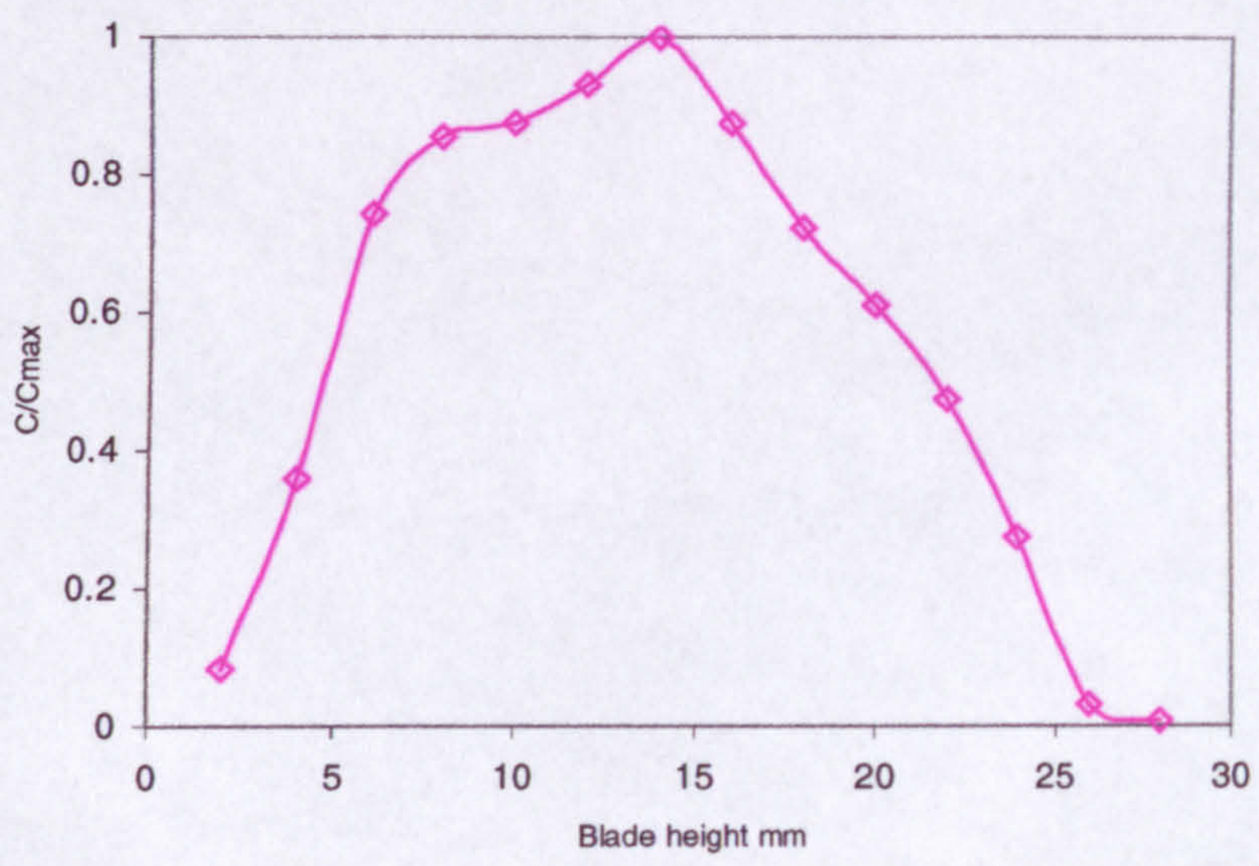


Figure 5-32 Smoke concentration upstream IGV blades

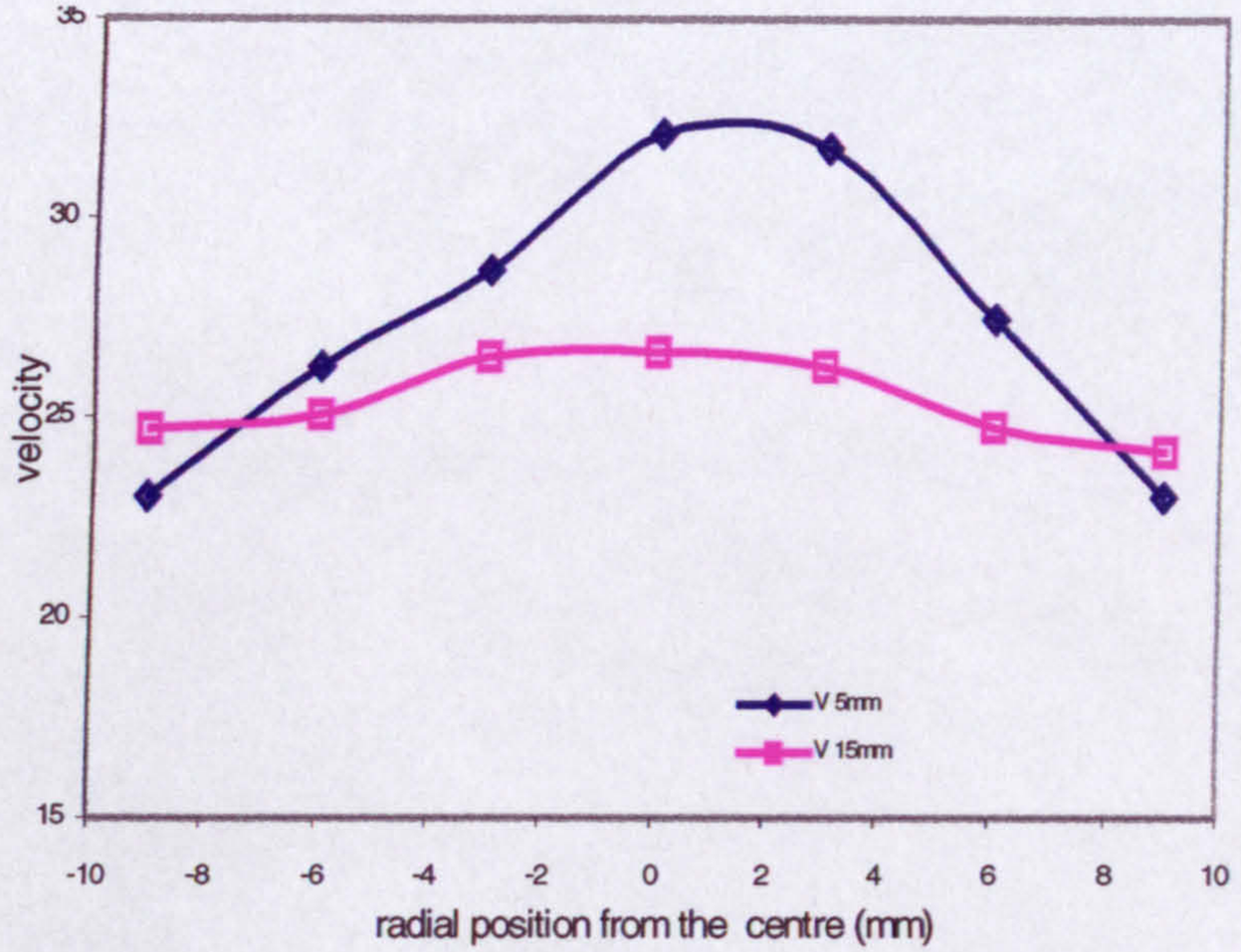


Figure 5-33a Air velocity from venturi injector

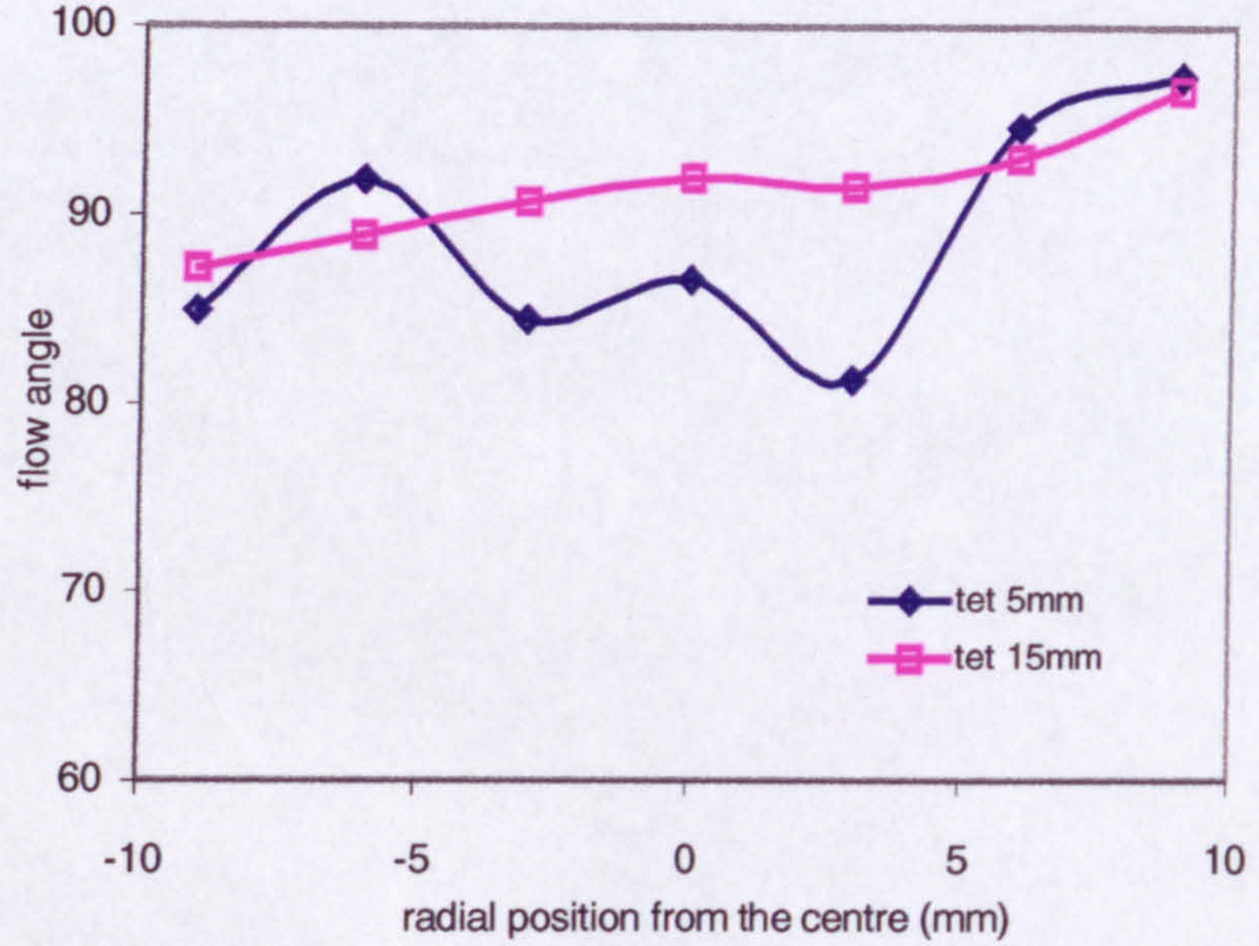


Figure 5-33b Air direction from venturi injector

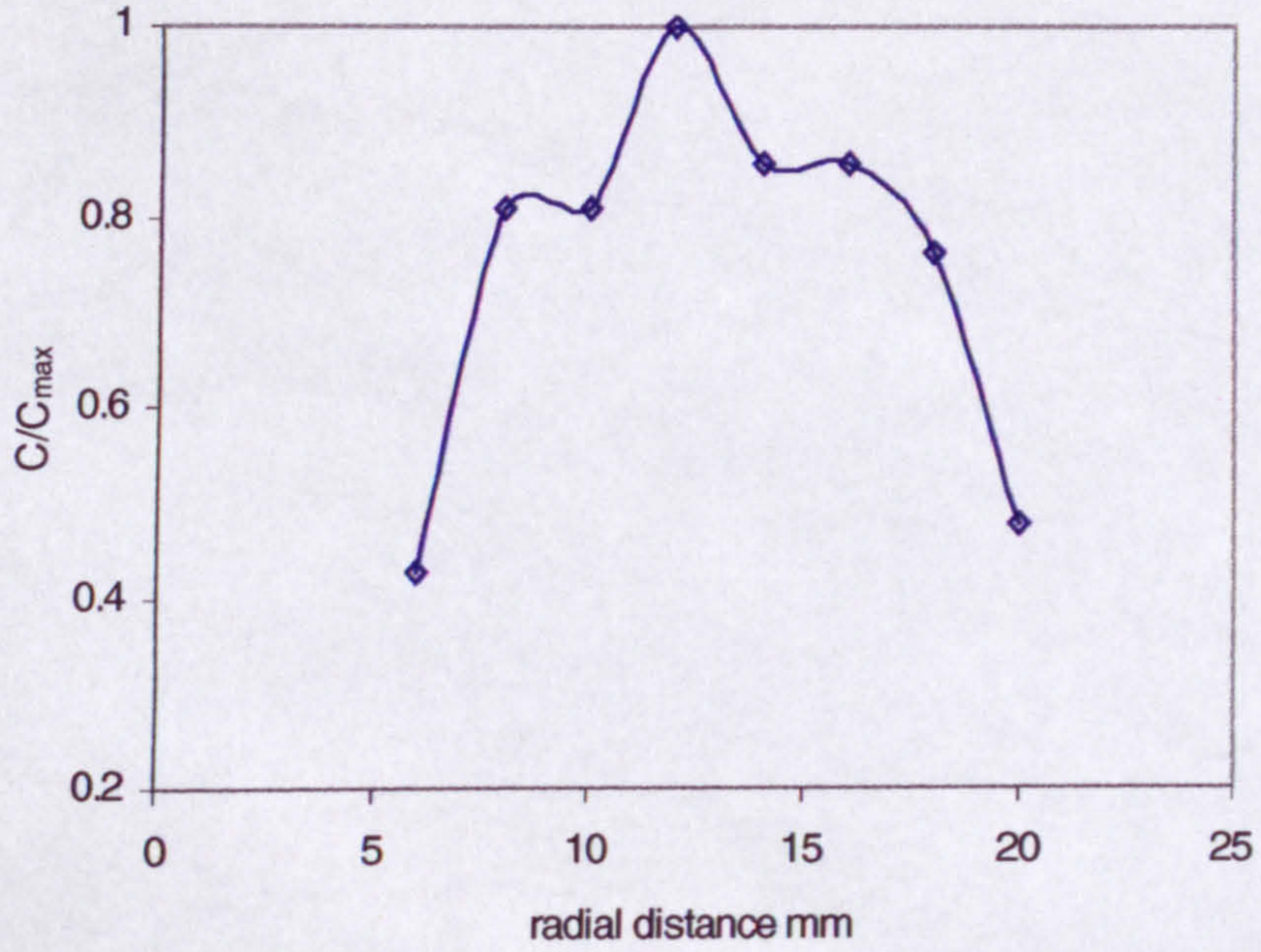


Figure 5-33c Sand concentration from venturi injector

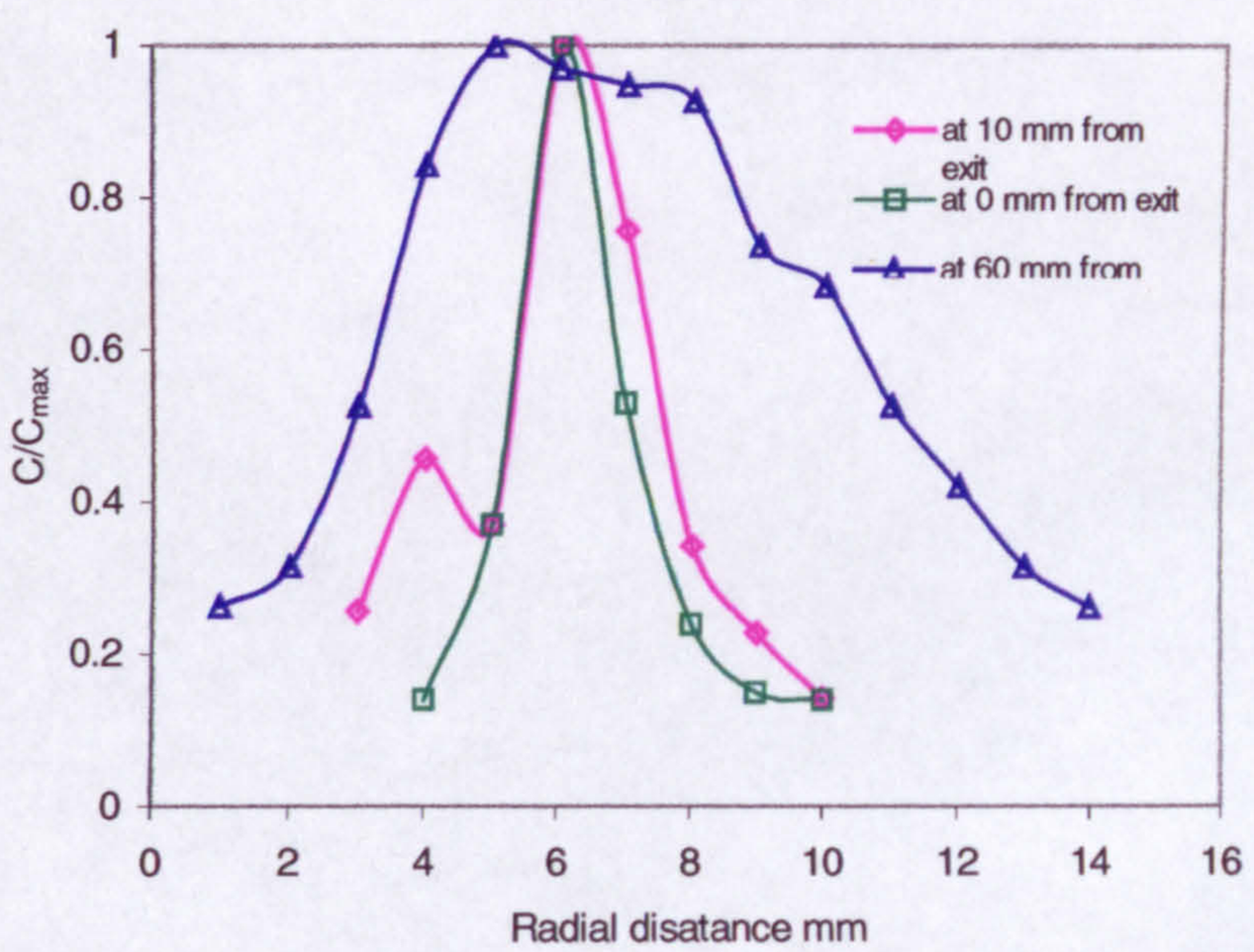


Figure 5-34 Sand concentration from 3 mm pipe injector

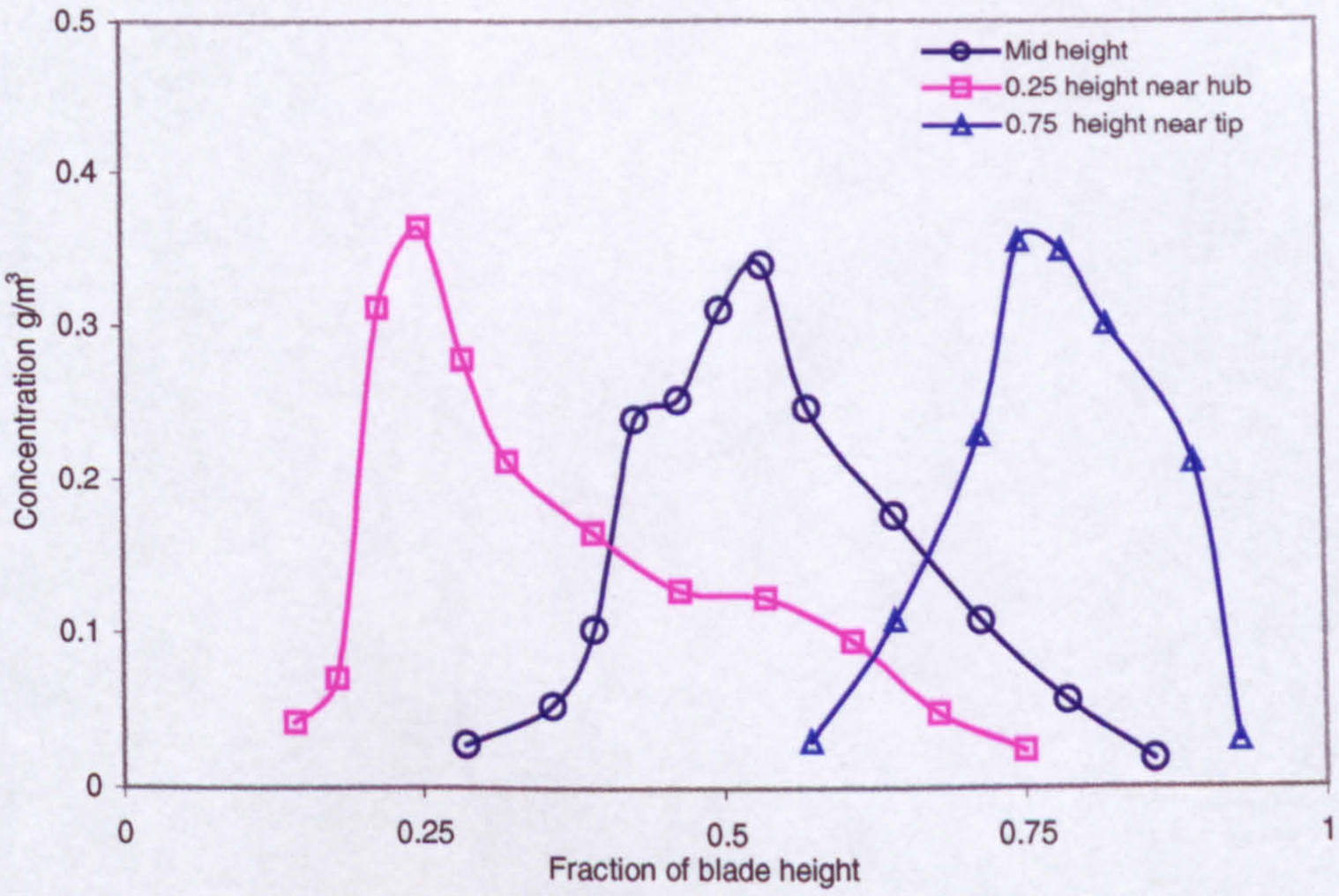


Figure 5-35 Local concentration profiles measured at 85mm from different release heights

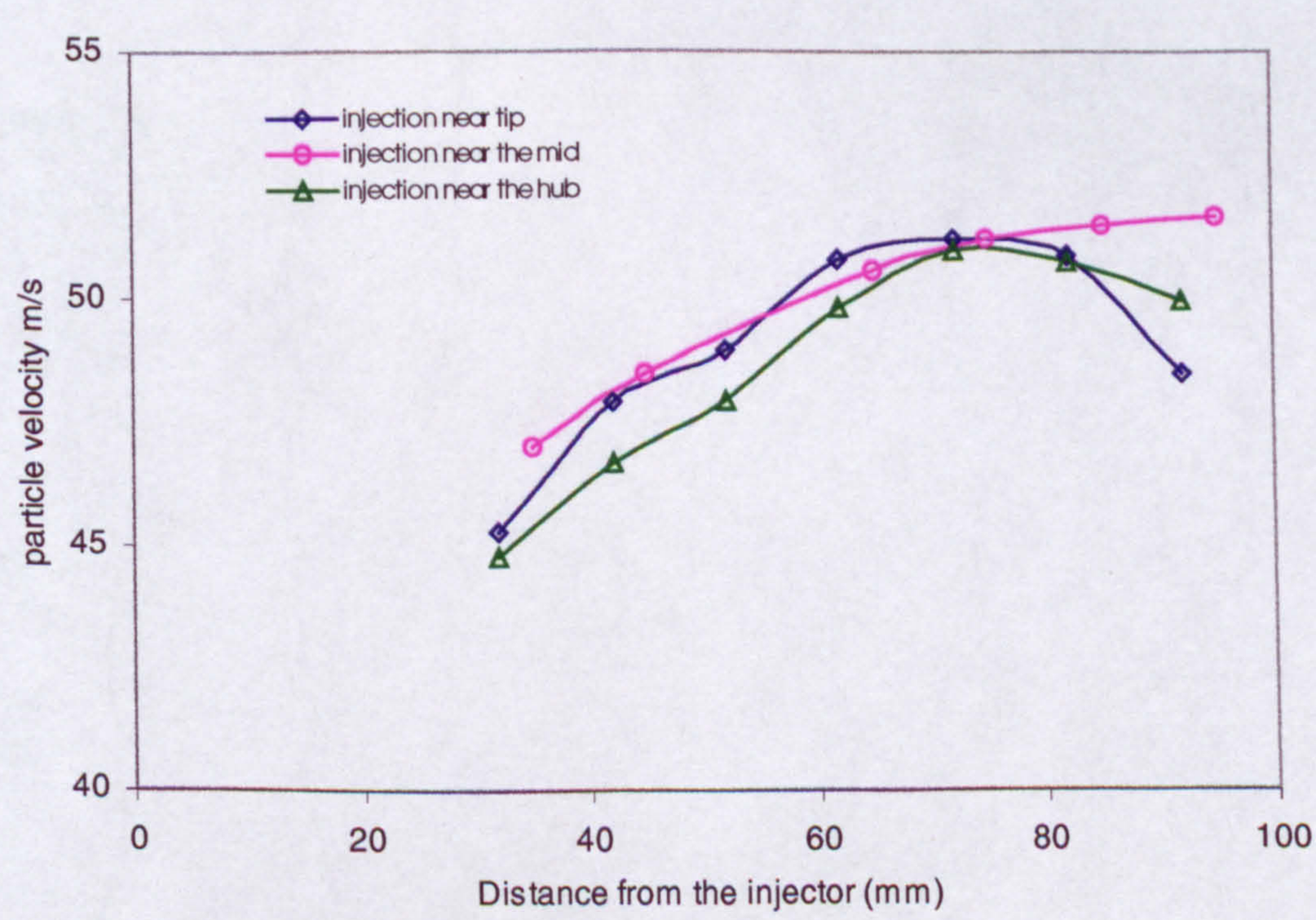


Figure 5-36 Particle velocity measured along seeding line at different release heights

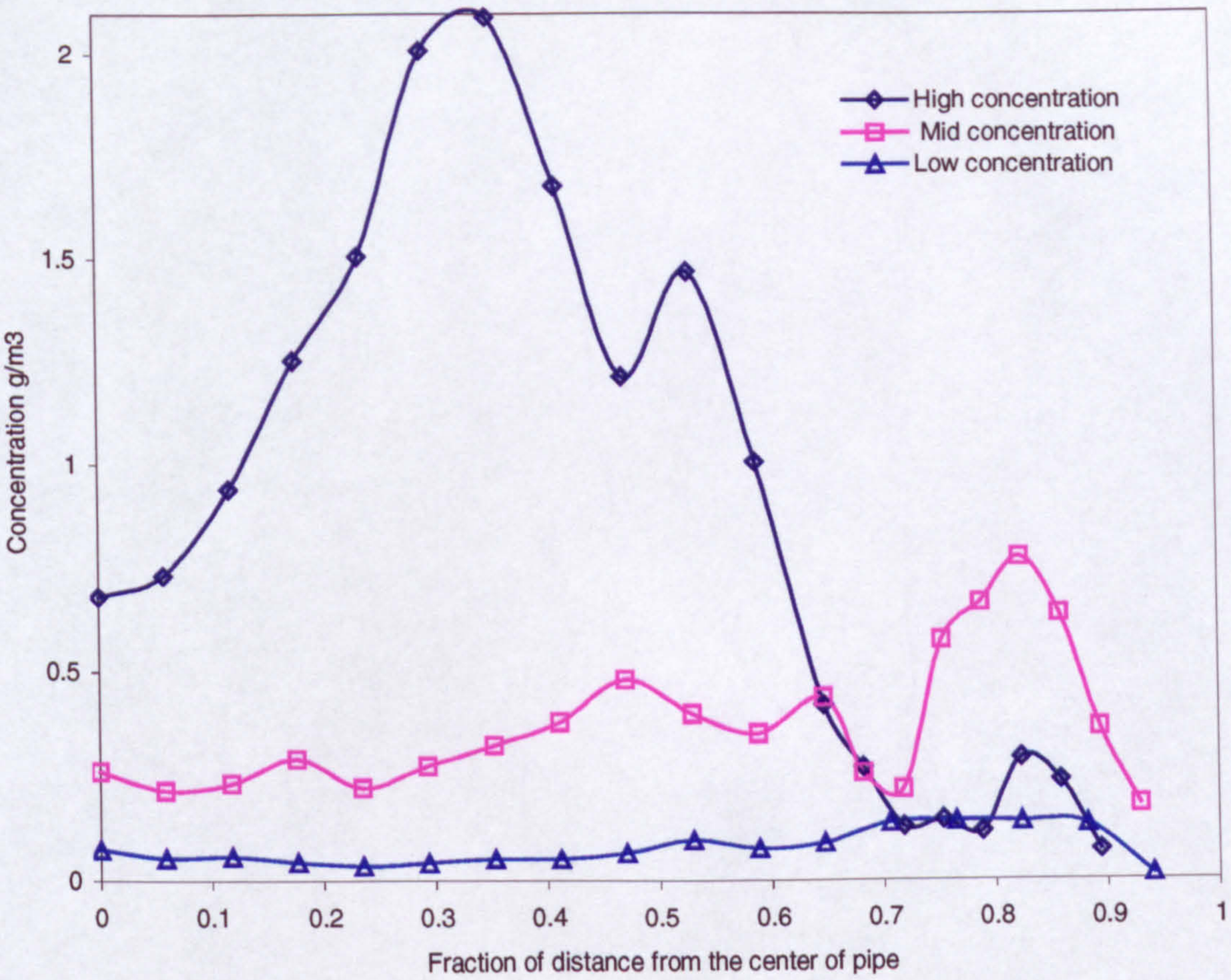


Figure 5-37 Concentration profiles measured at 35 mm from the inlet nose seeding globally

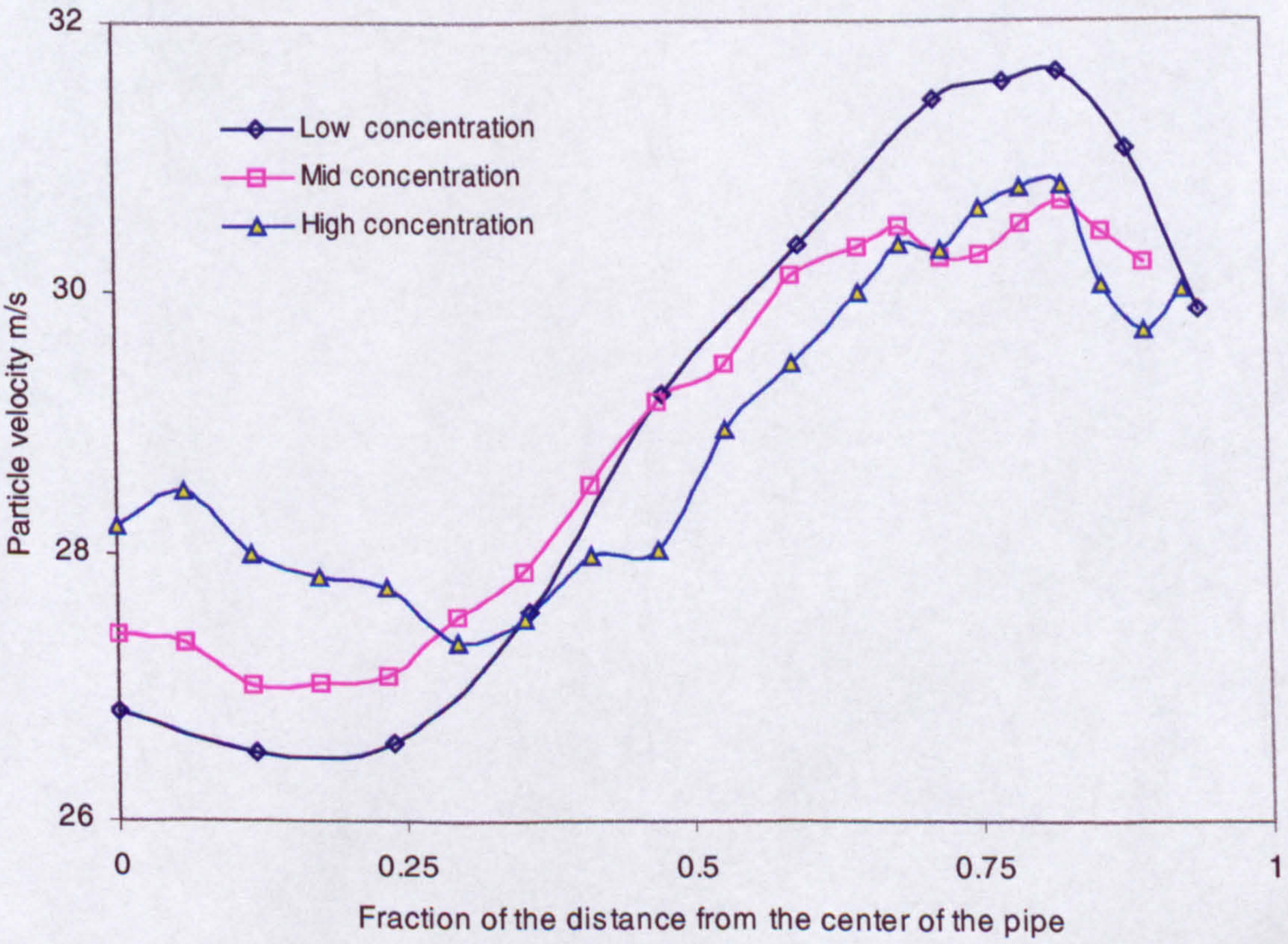


Figure 5-38 Particle velocity measured at 35 mm from the inlet nose seeding globally

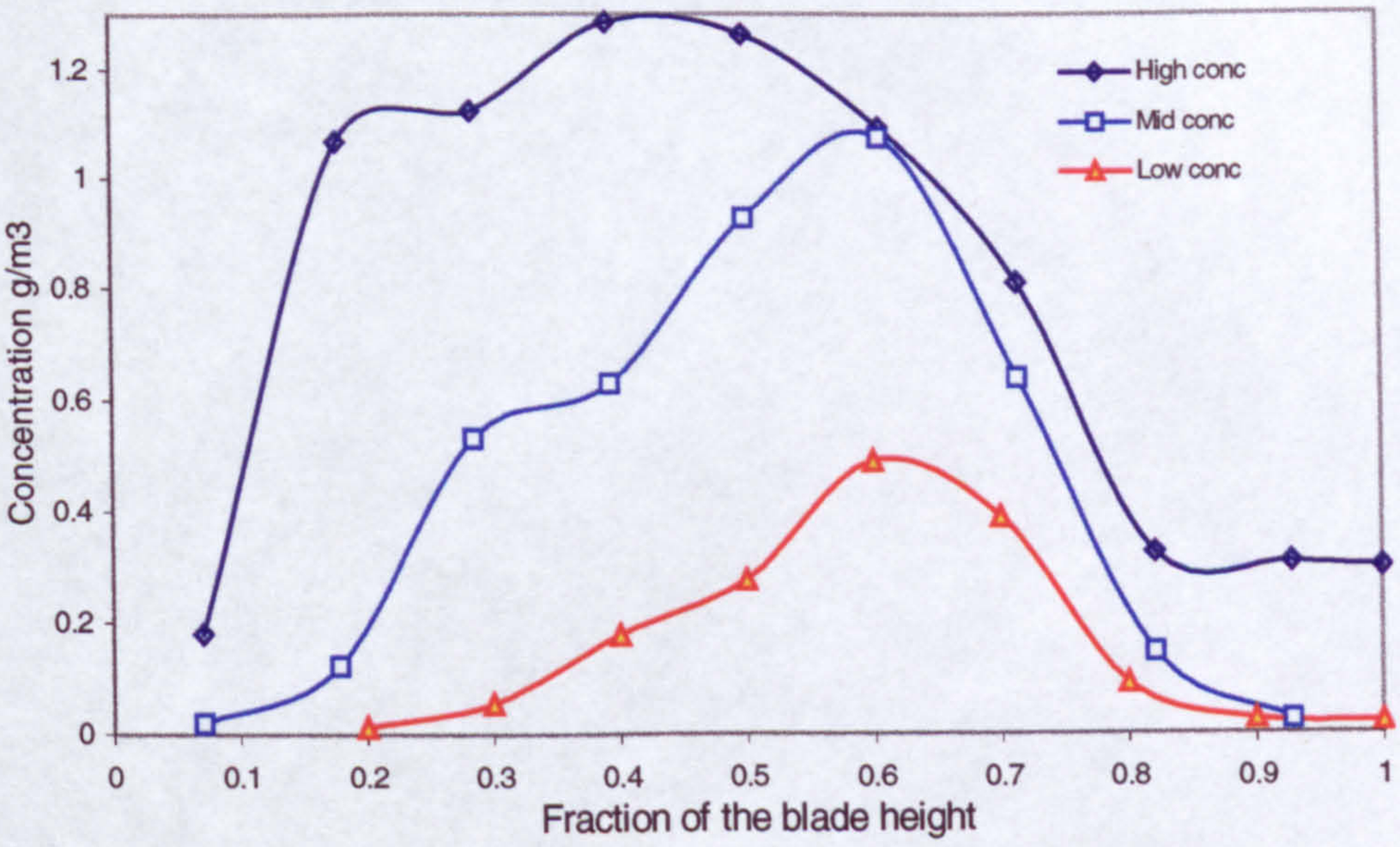


Figure 5-39 Concentration profiles measured at 50 mm from IGV seeding globally

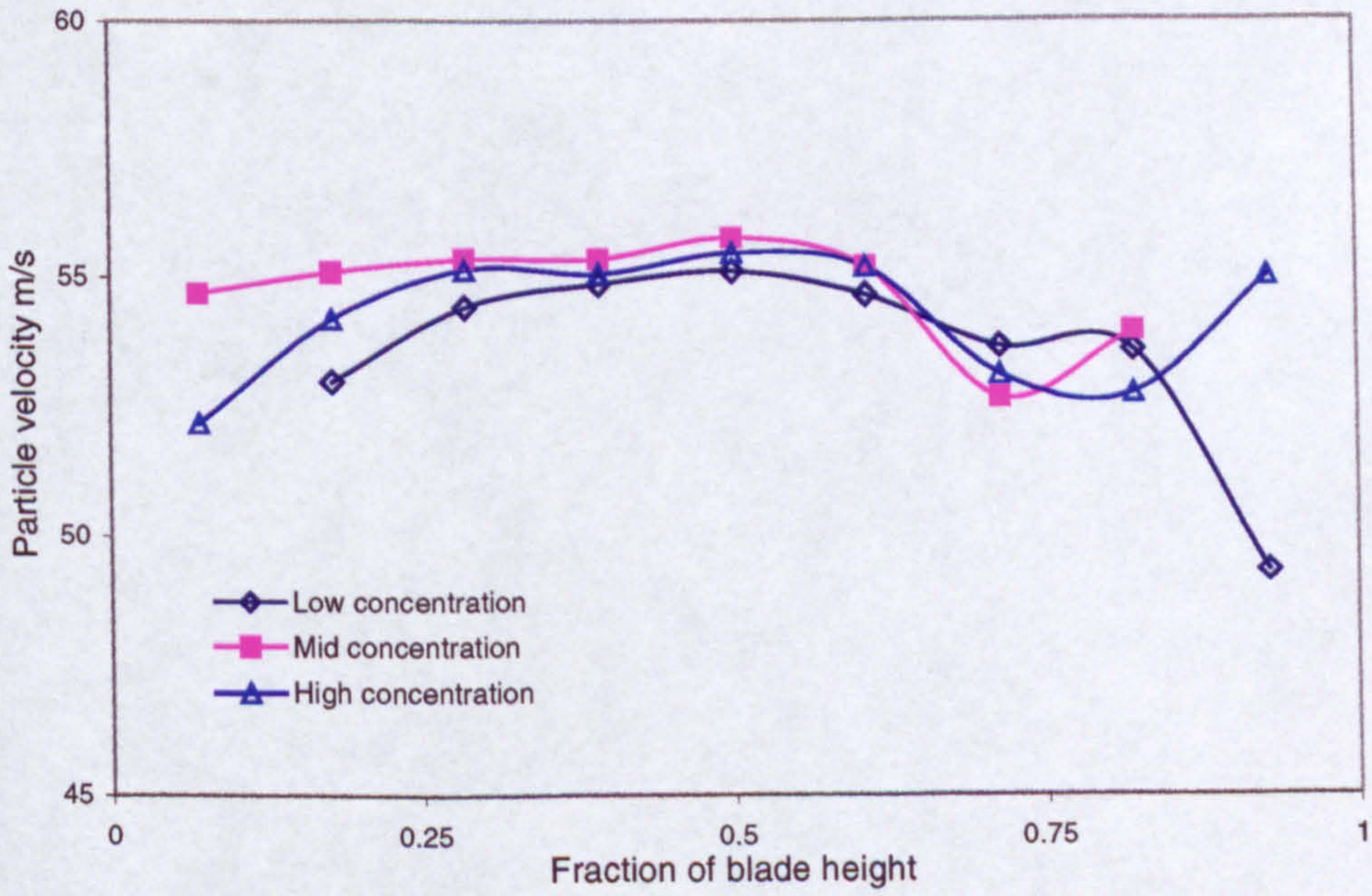


Figure 5-40 Particle velocity measured at 50 mm from IGV seeding globally

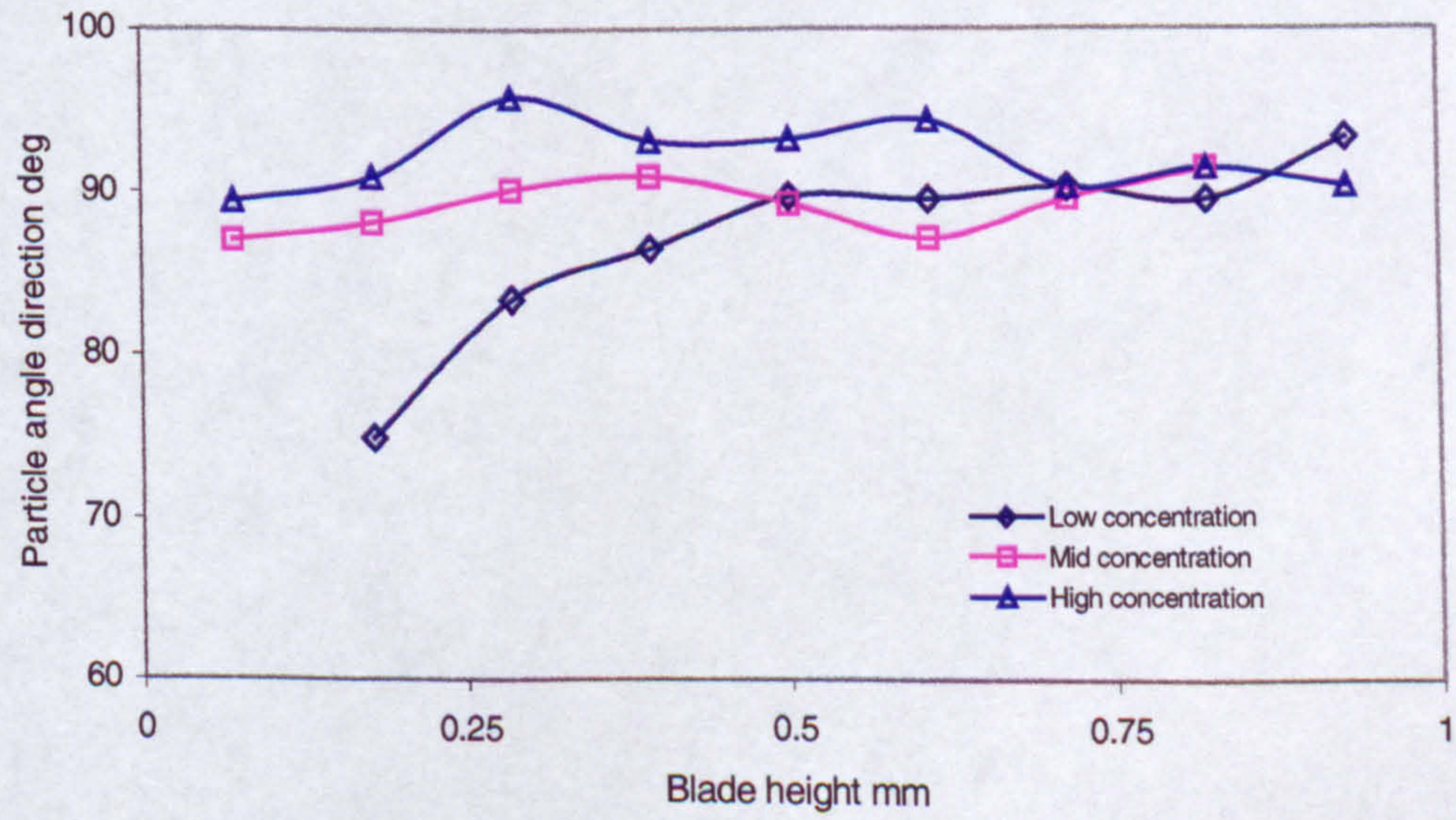


Figure 5-41 Particle angle measured at 50 mm from IGV seeding globally

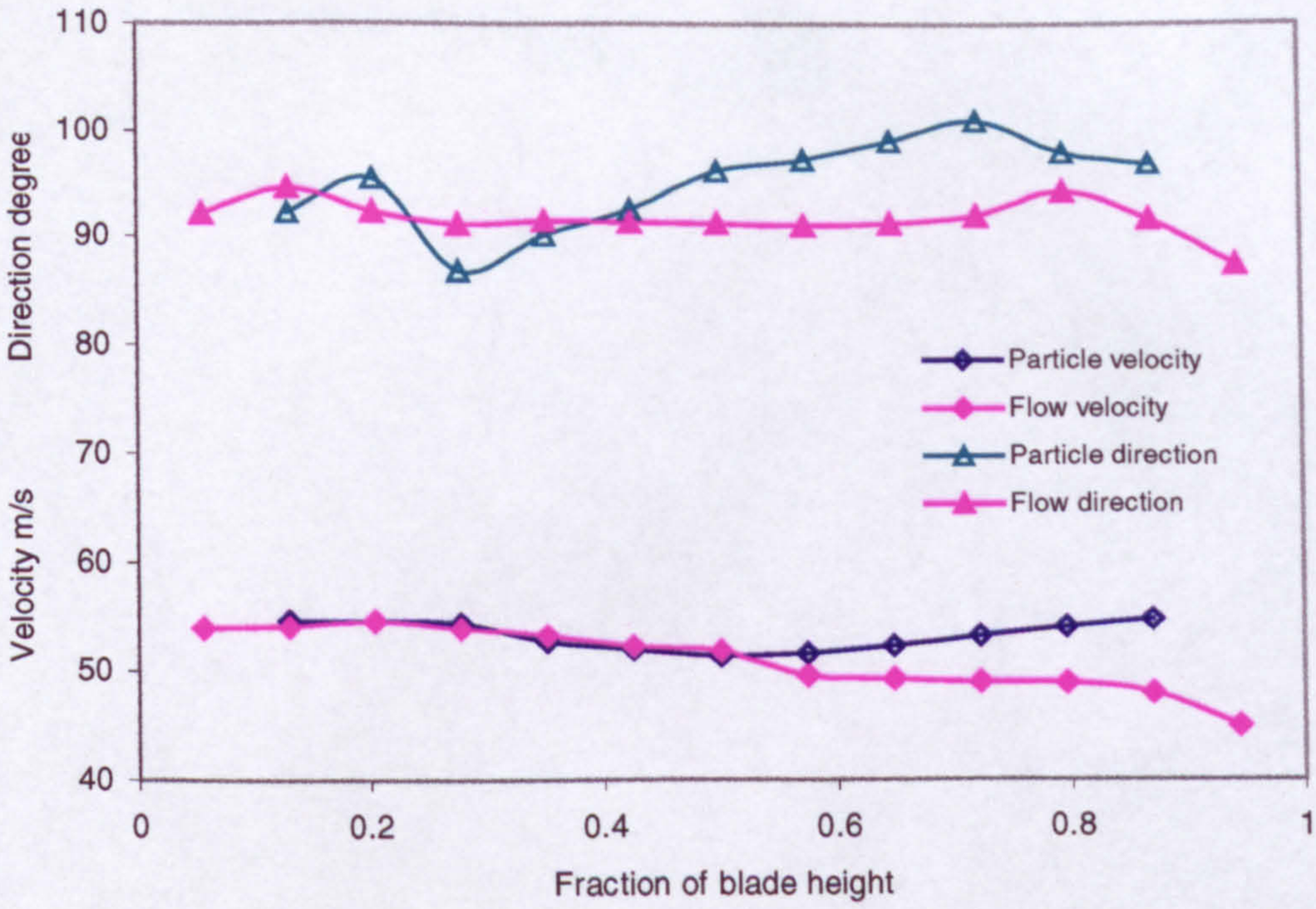


Figure 5-42 Velocity and direction of sand particles MIL-5007E seeding globally compared to airflow velocity at upstream IGV

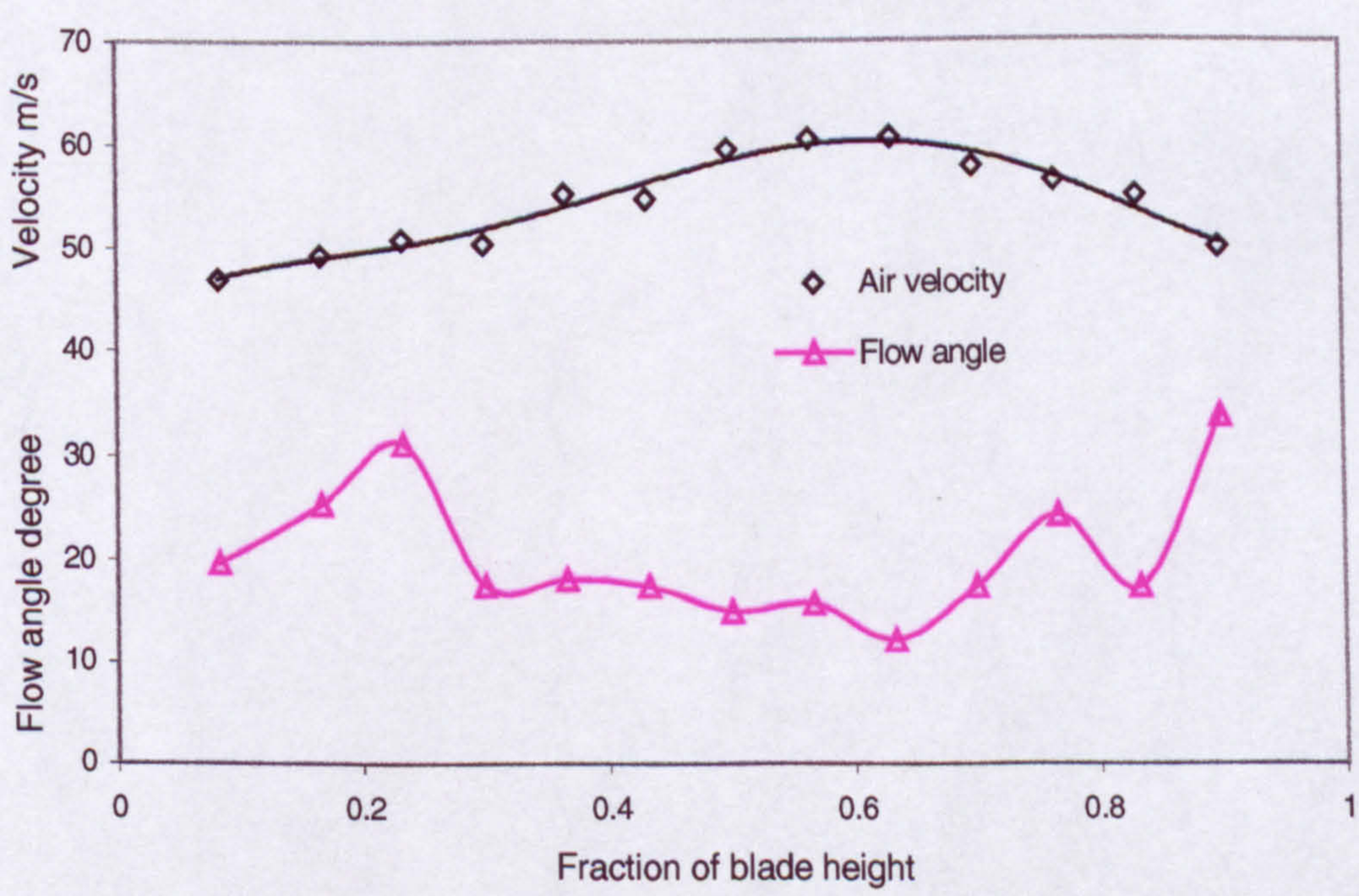


Figure 5-43 Flow velocity and angle at 7 mm downstream the fan rotor

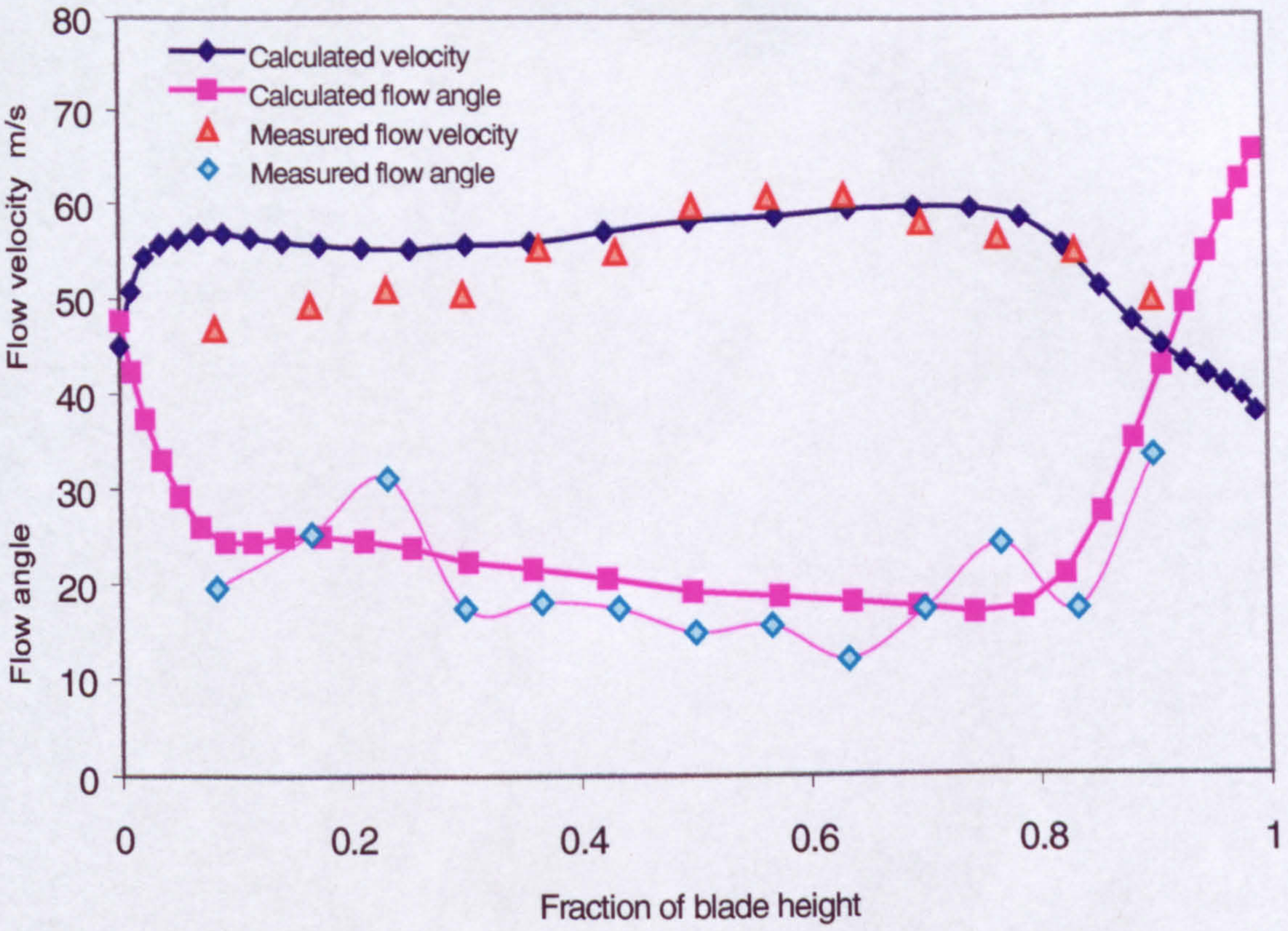


Figure 5-44 CFD and measured flow velocity and angle at 7 mm downstream of the rotor

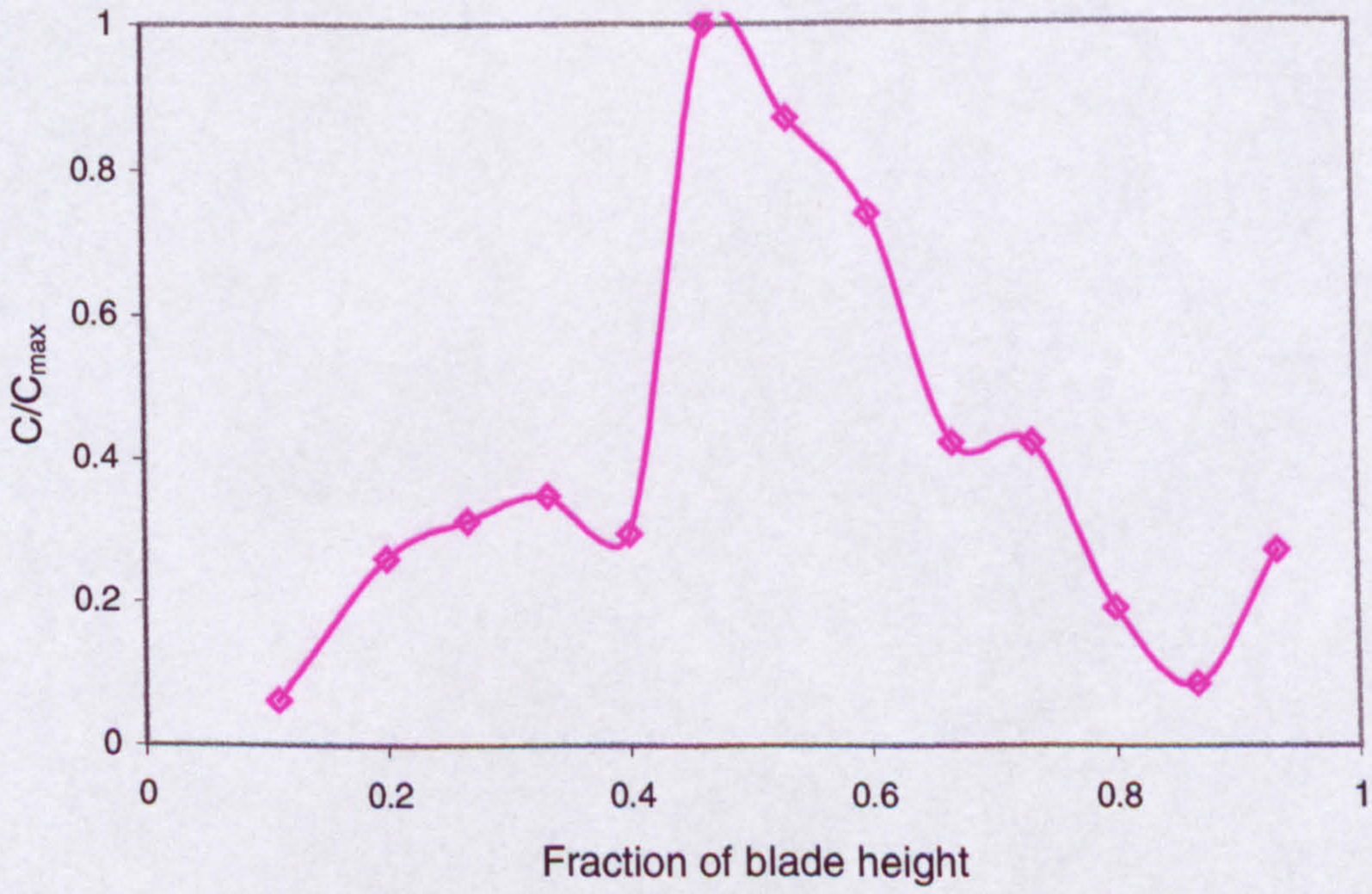


Figure 5-45 Particle concentration at 16 mm downstream the rotor

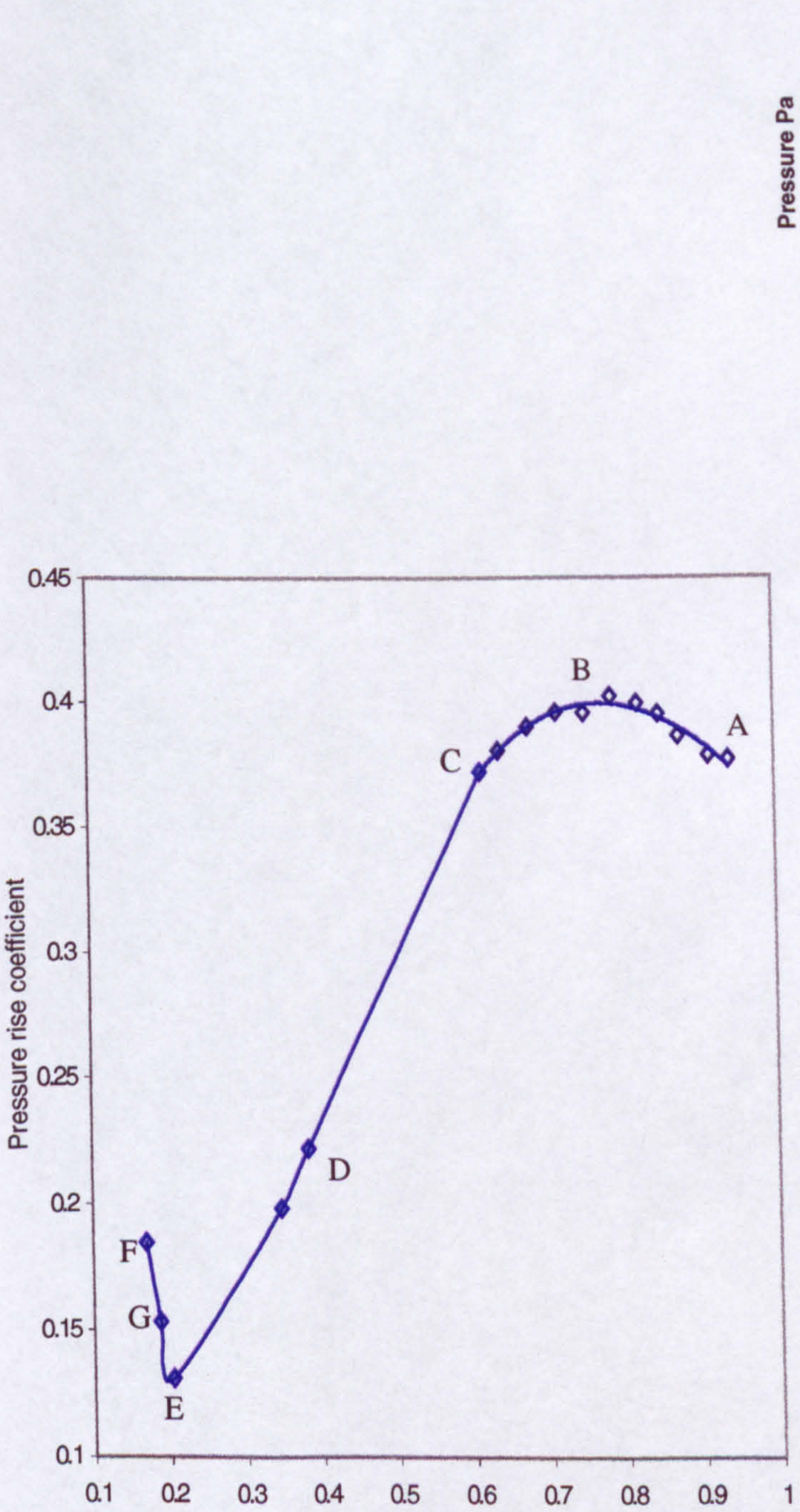


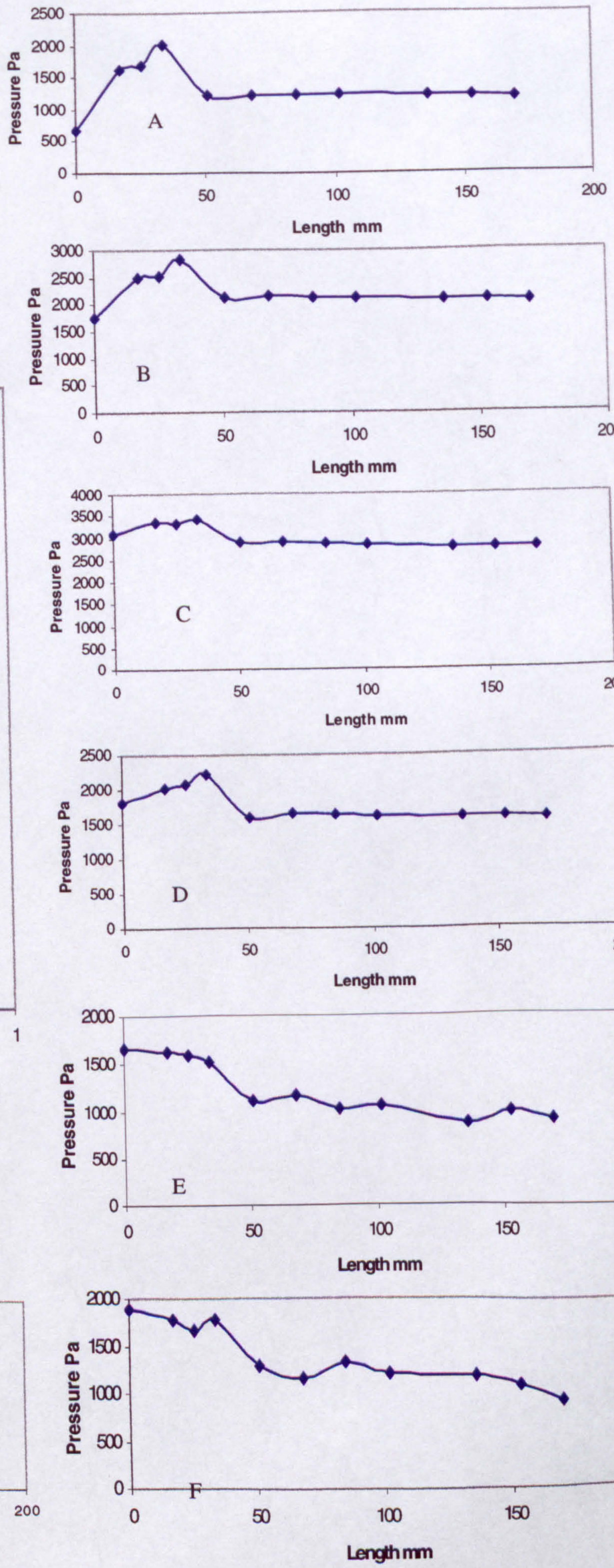


Figure 5-46 Axial fan performance with outlet static pressure distribution

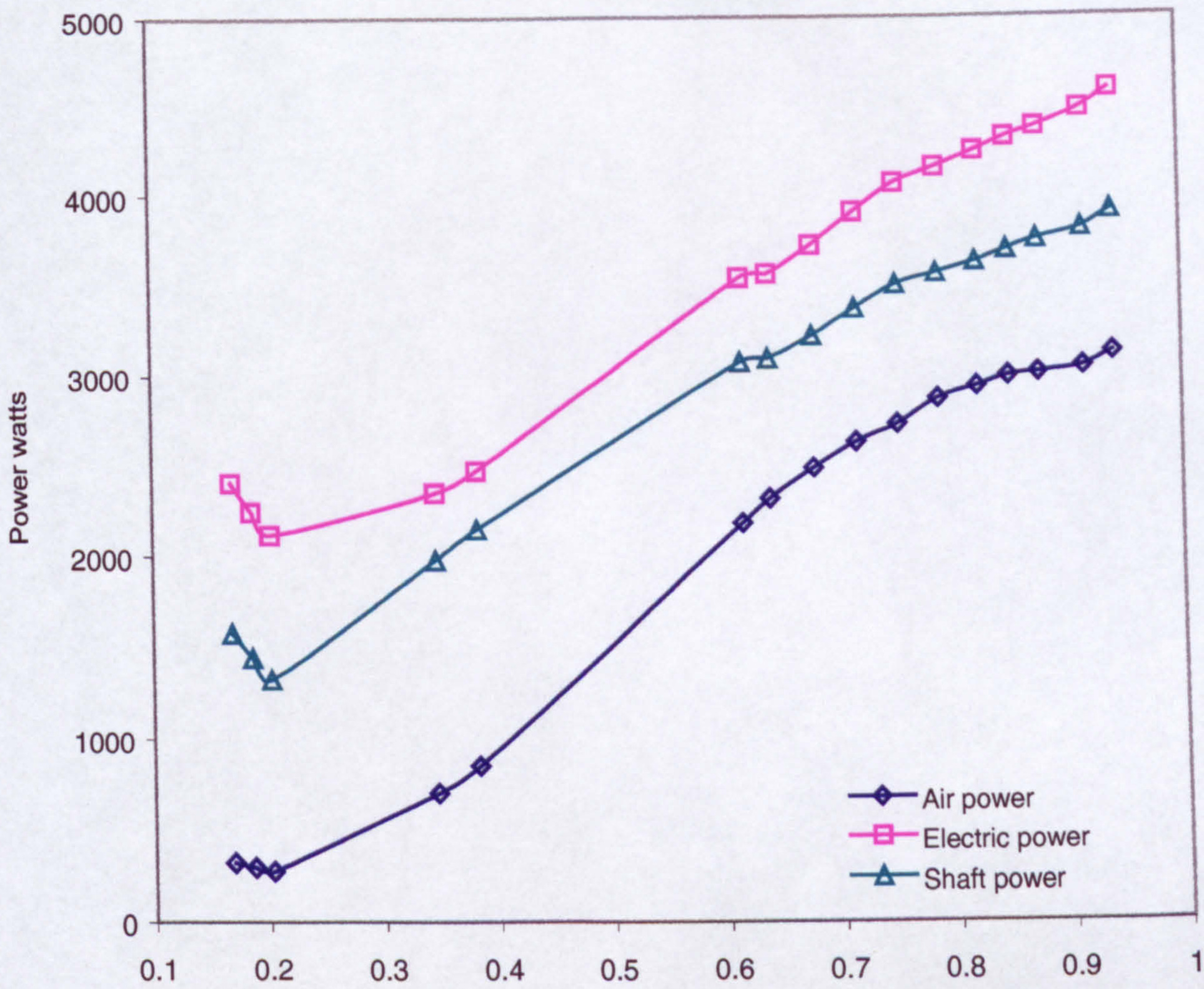


Figure 5-47 Axial fan power measurements

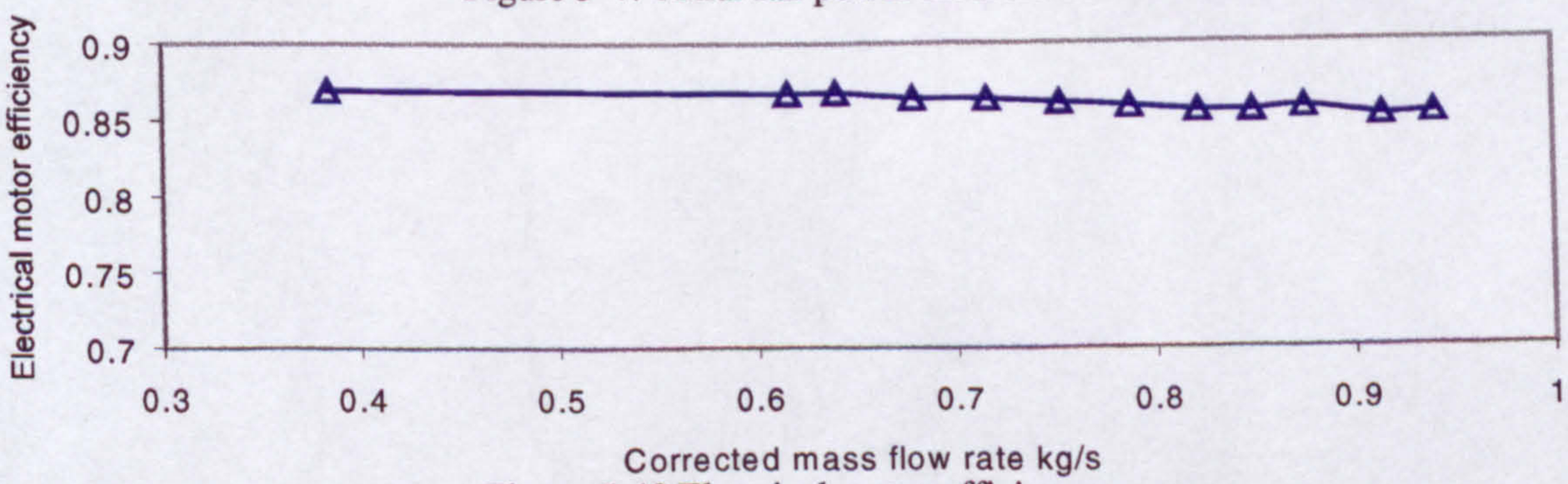


Figure 5-48 Electrical motor efficiency

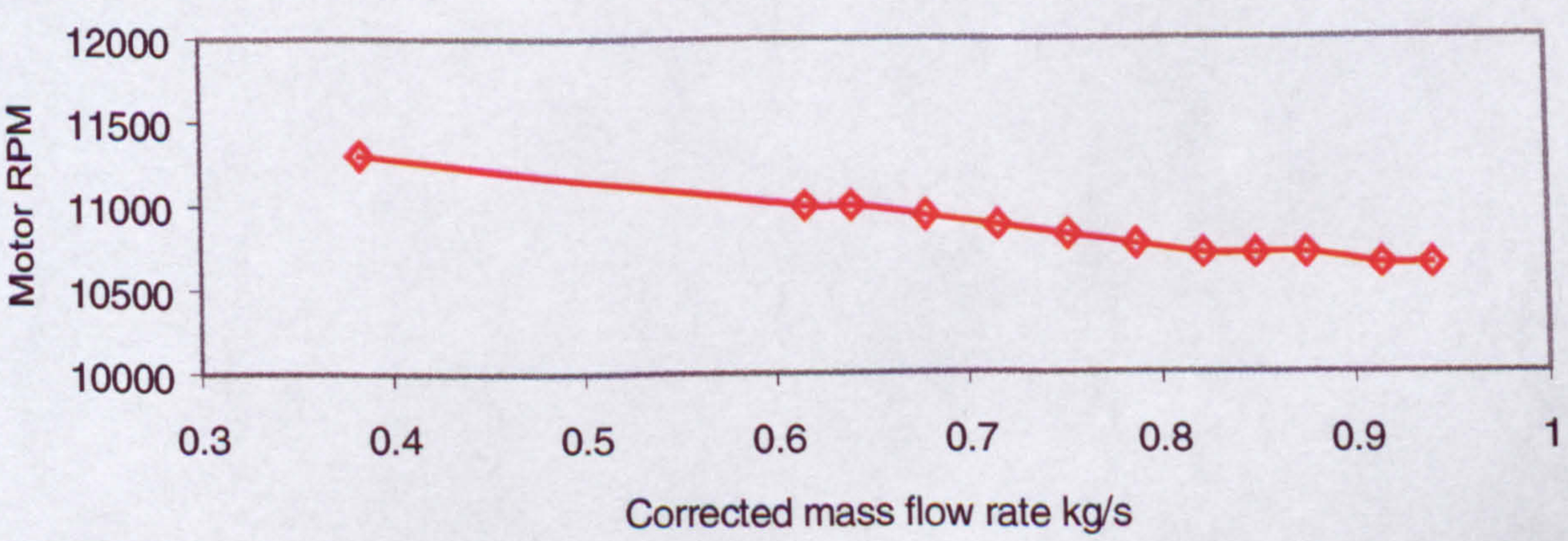


Figure 5-49 Electrical motor speed of rotation

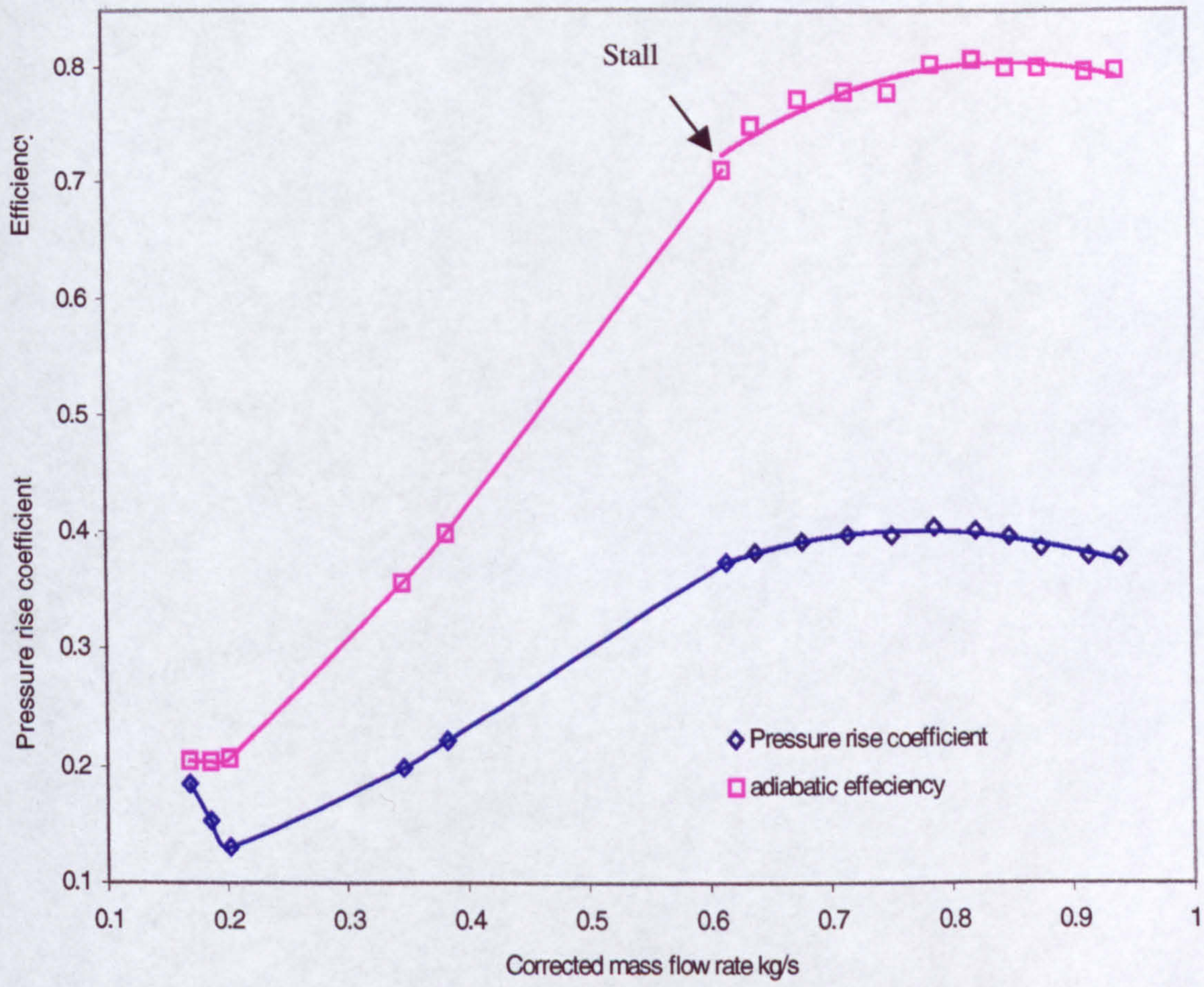


Figure 5-50 Full axial fan measured characteristics

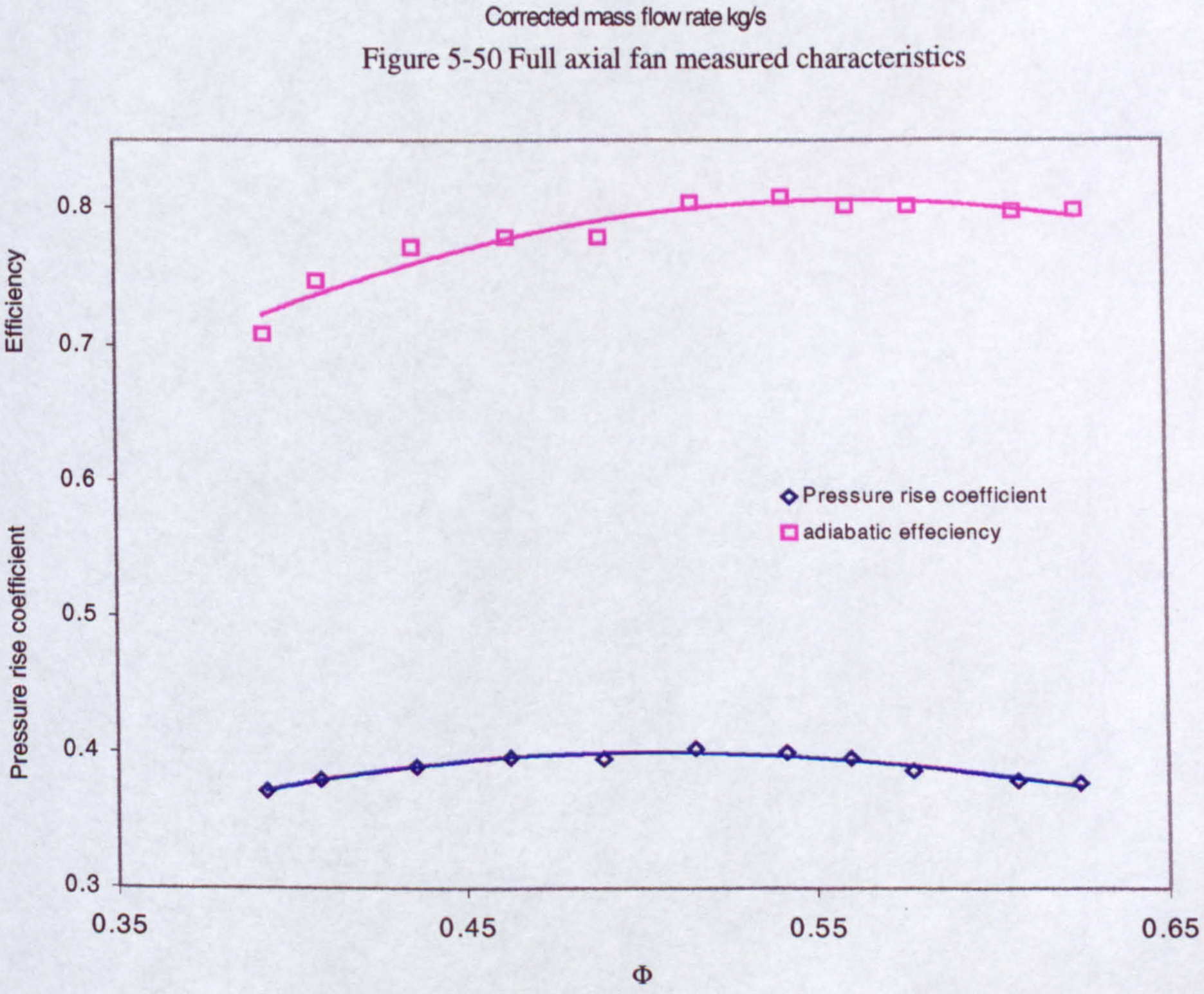


Figure 5-51 Axial fan measured stable characteristics

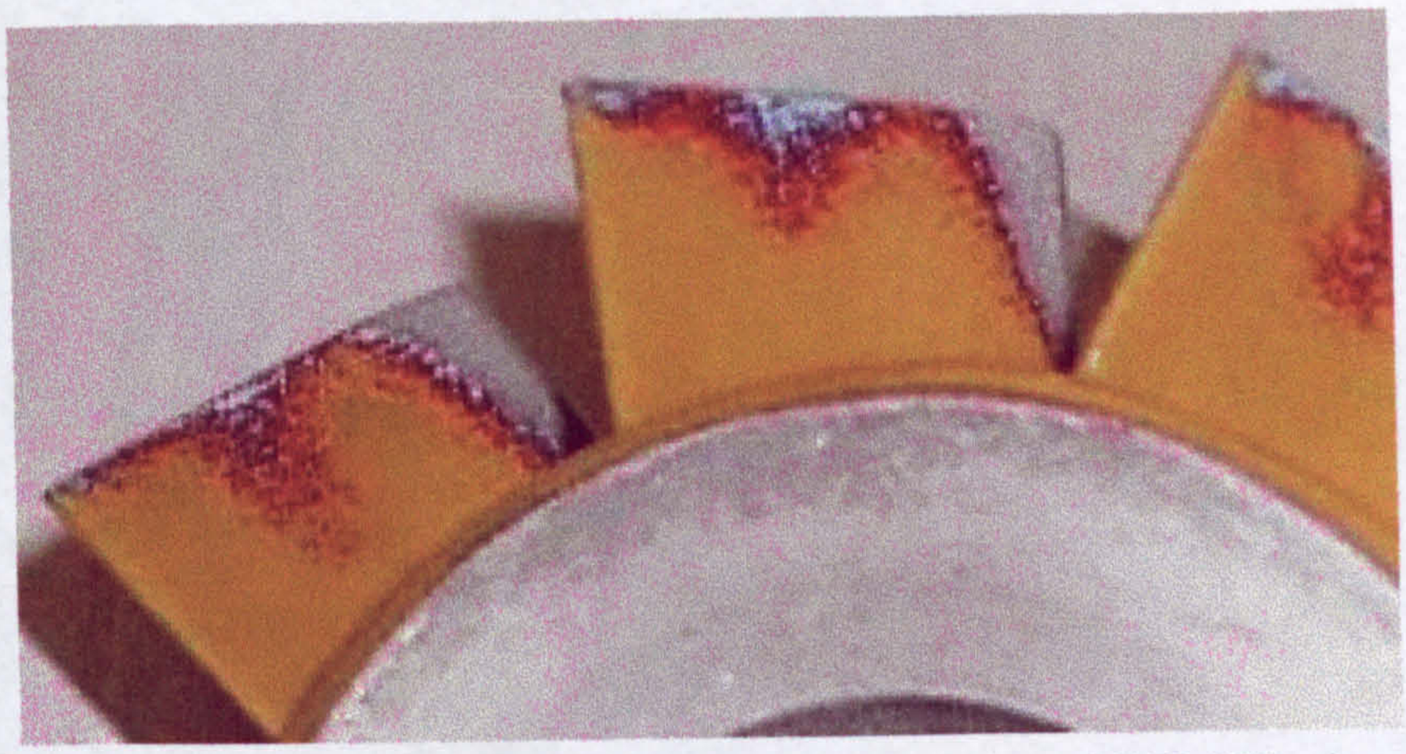

Figure 5-52 Erosion of the pressure side due to injection of (150-300 micron) sand particles at mid-blade height after 1.3h

Figure 5-53 Erosion of the pressure side due to injection of (150-300 micron) sand particles at mid-blade height after 3h

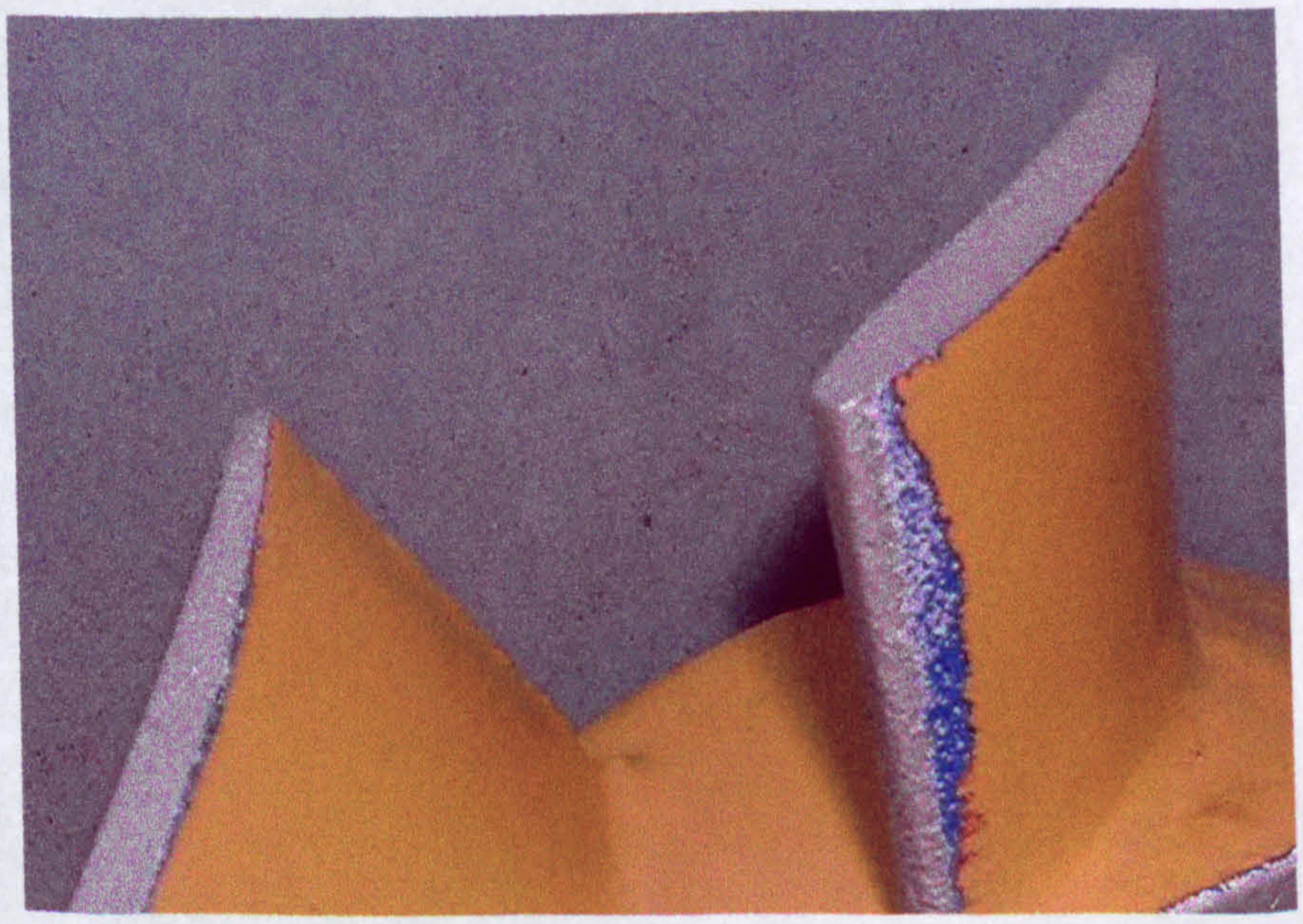

Figure 5-54 Erosion of the suction side due to injection of (150-300 micron) sand particles at mid-blade height after 3h

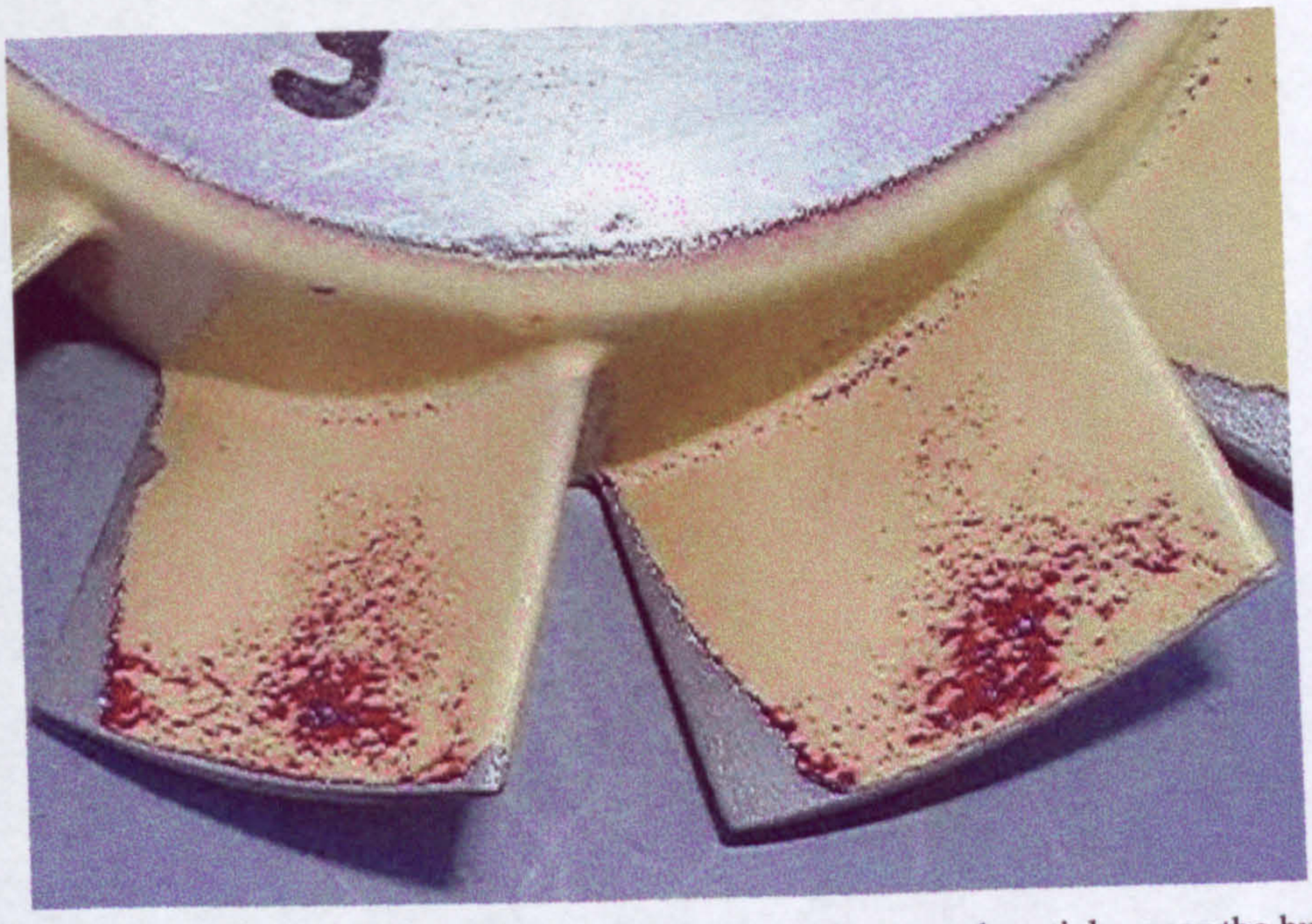

Figure 55 Erosion due to injection of (150-300 micron) sand particles near the hub

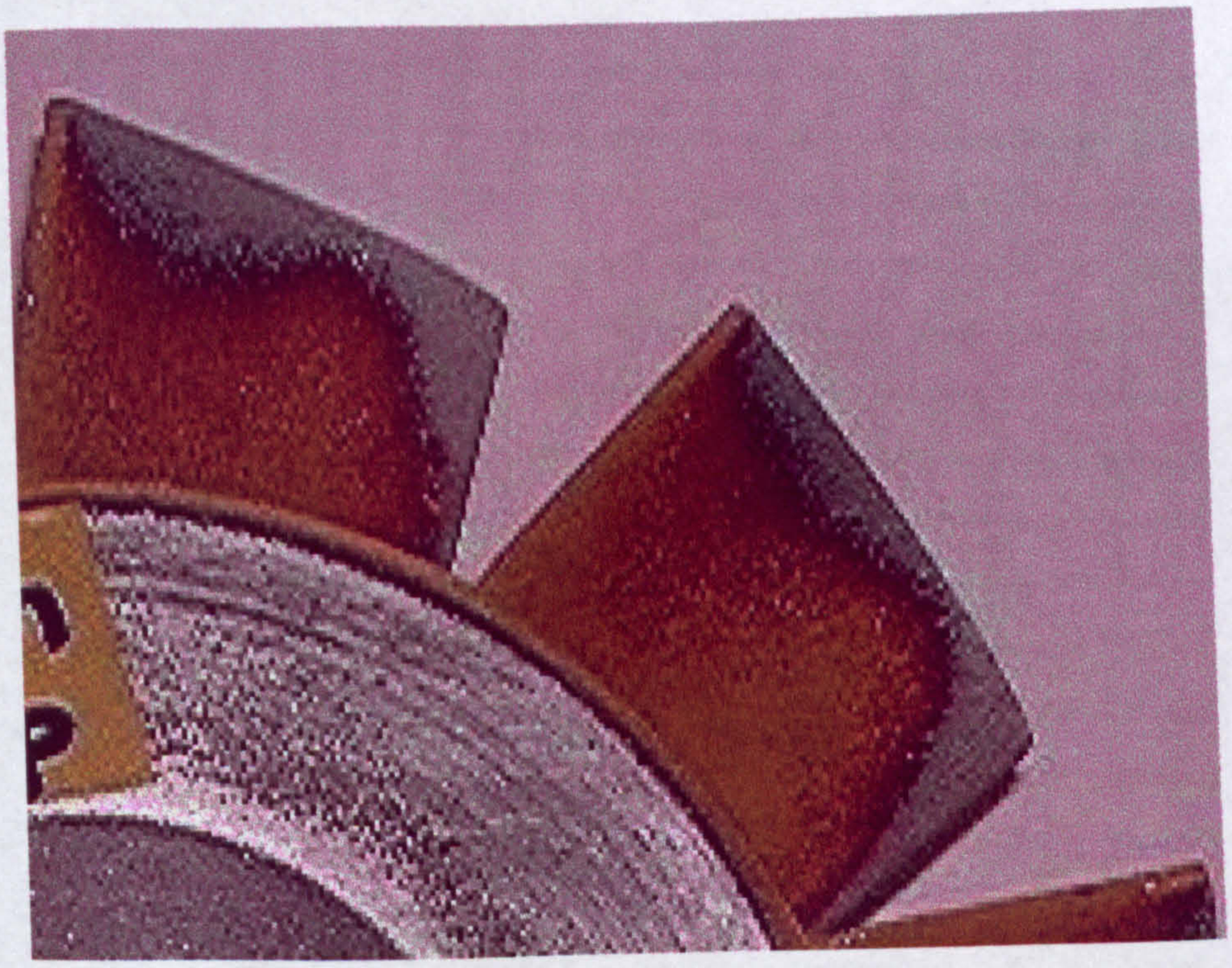

Figure 5-56 Erosion due to injection of (150-300 micron) sand particles near the tip

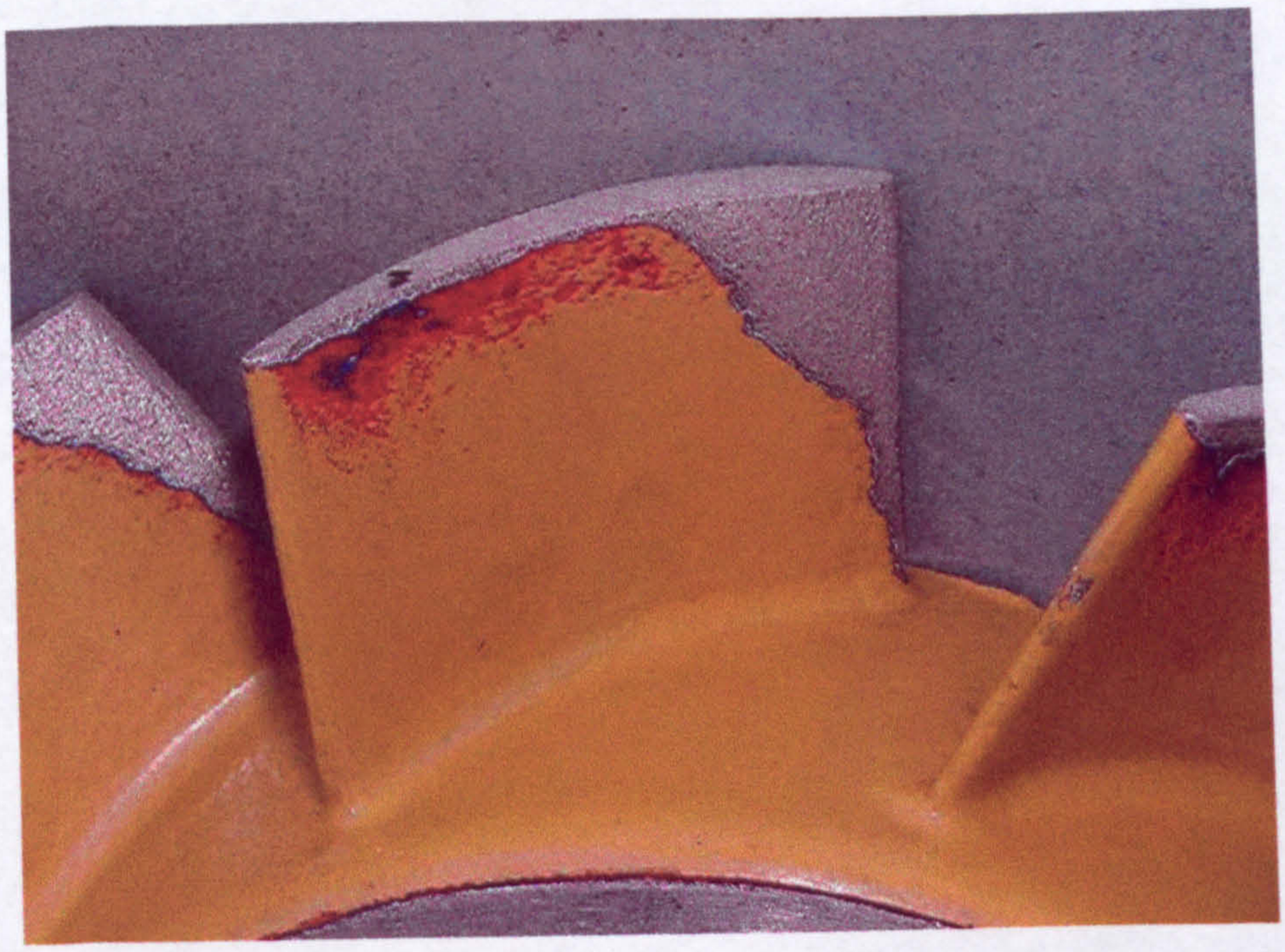

Figure 5-57 Erosion pattern due to global injection of (150-300 micron) sand particles

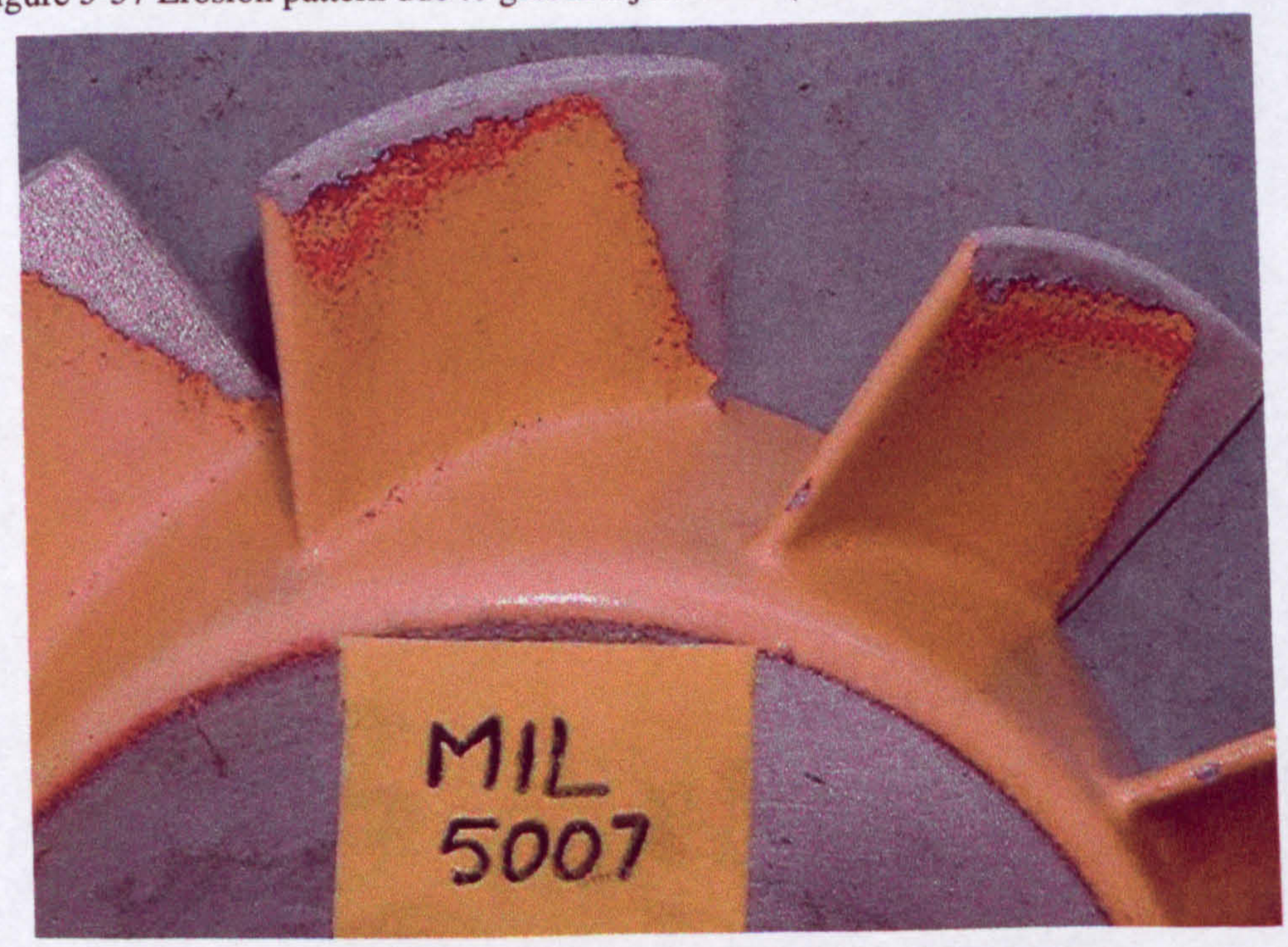


Figure 5-58 Erosion pattern due to global injection of (MIL-E 5007E) sand particles

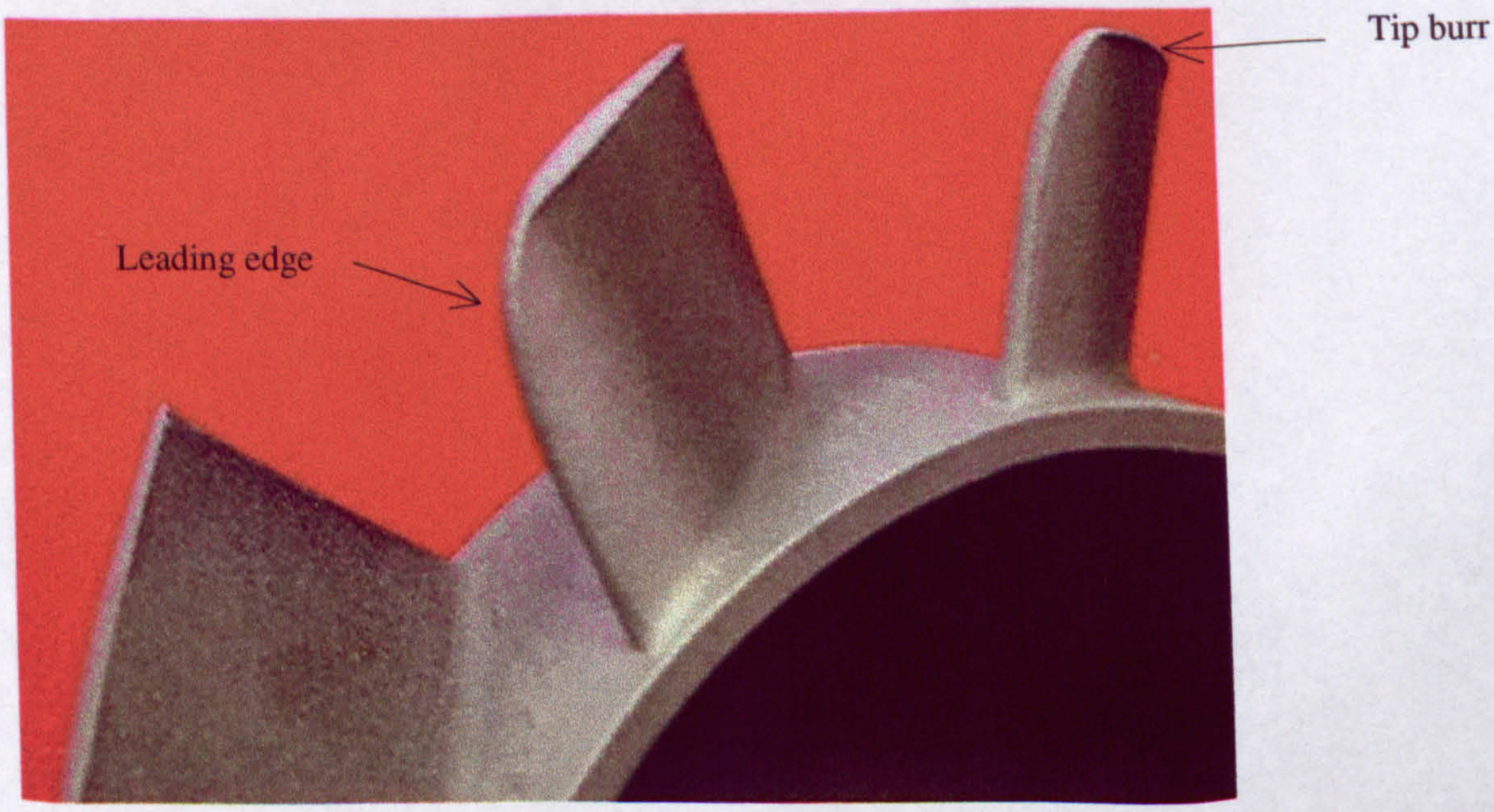


Figure 5-59a Erosion due to global injection (MIL-E 5007E) sand at final step

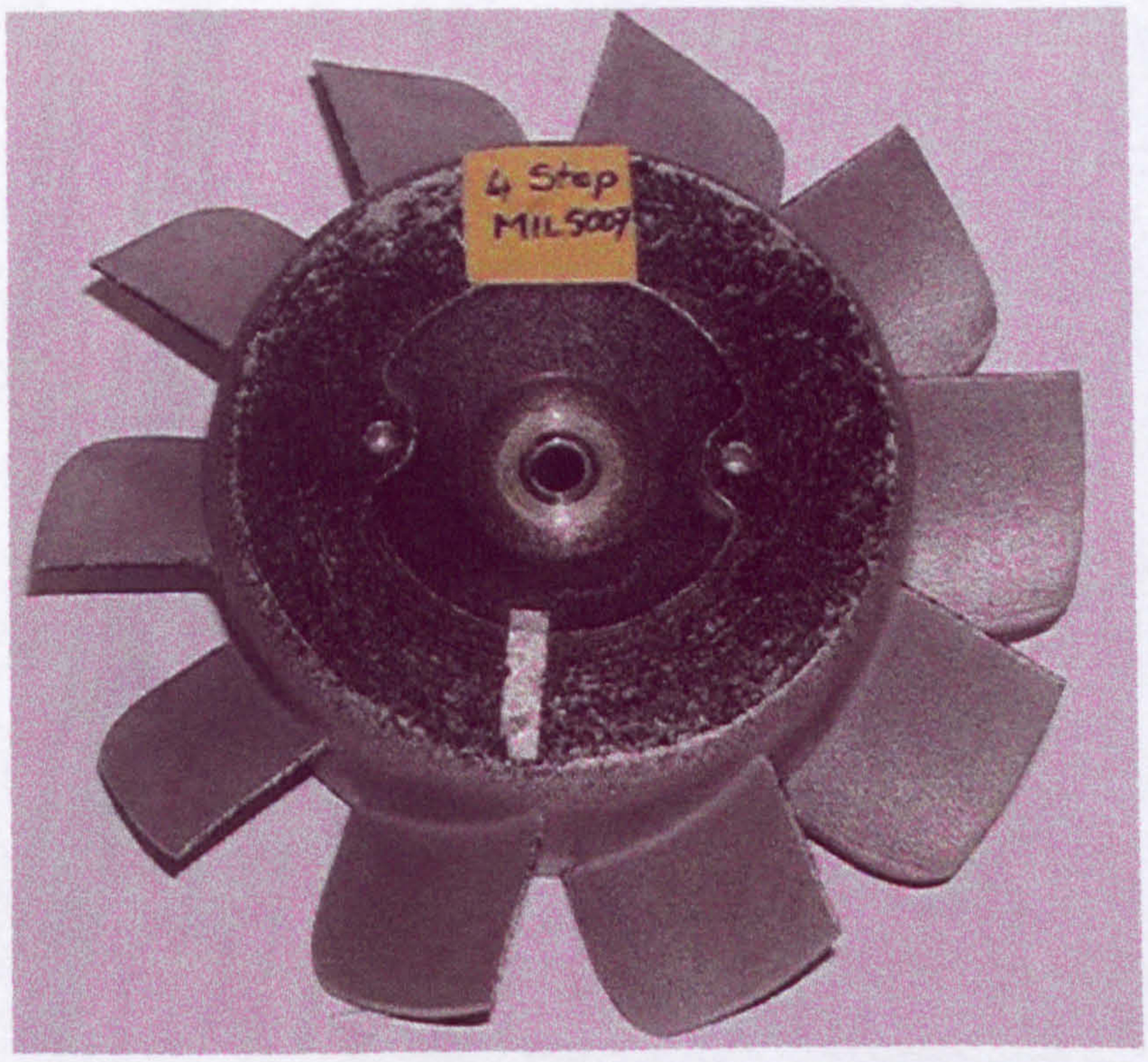


Figure 5-59b Rotor erosion due to high concentration of MIL-E-5007E sand

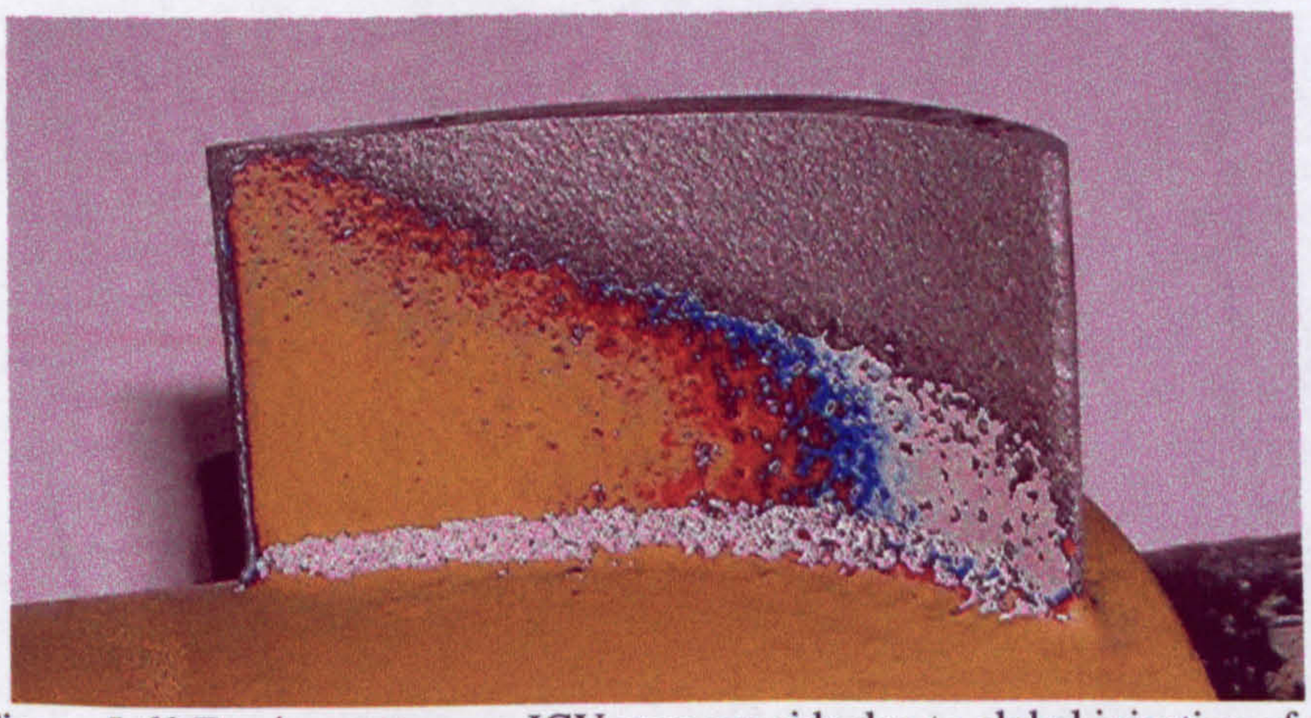

Figure 5-60 Erosion pattern on IGV pressure side due to global injection of sand

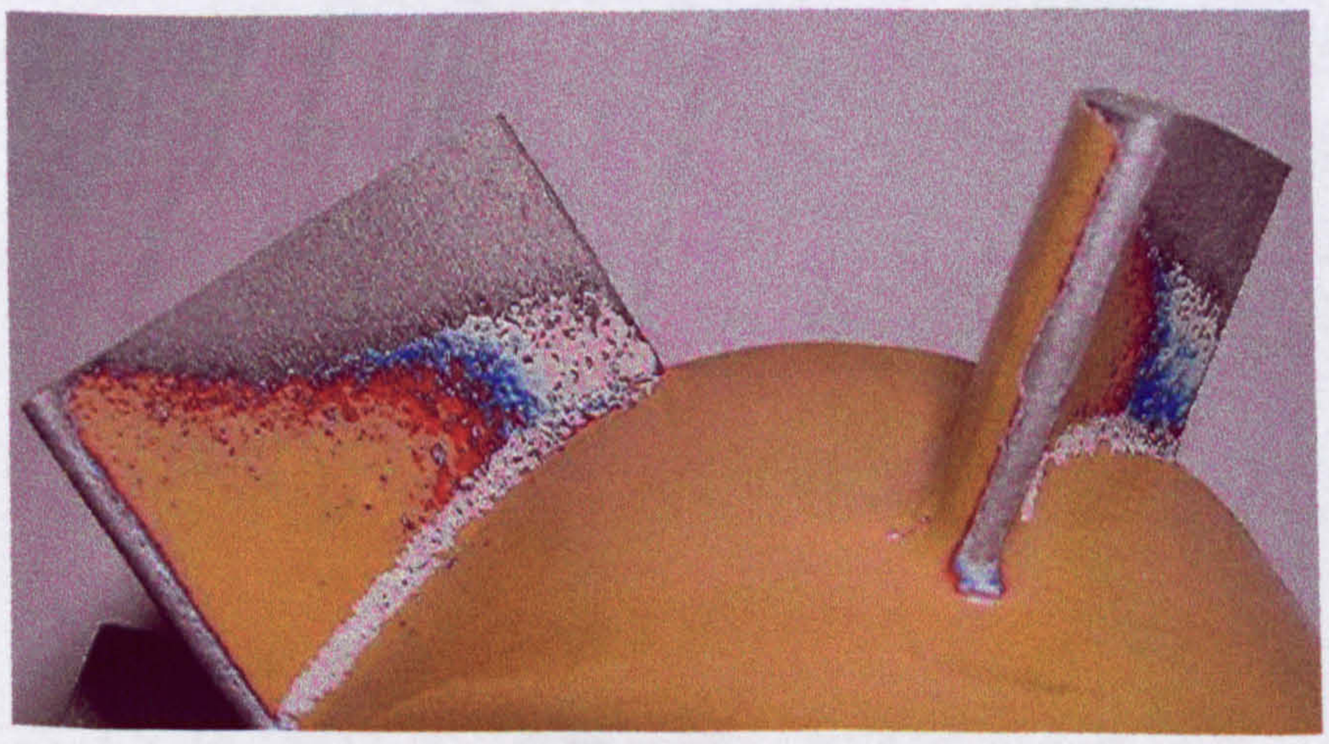

Figure 5-61 Erosion pattern on IGV pressure side and trailing edge due to global injection of sand

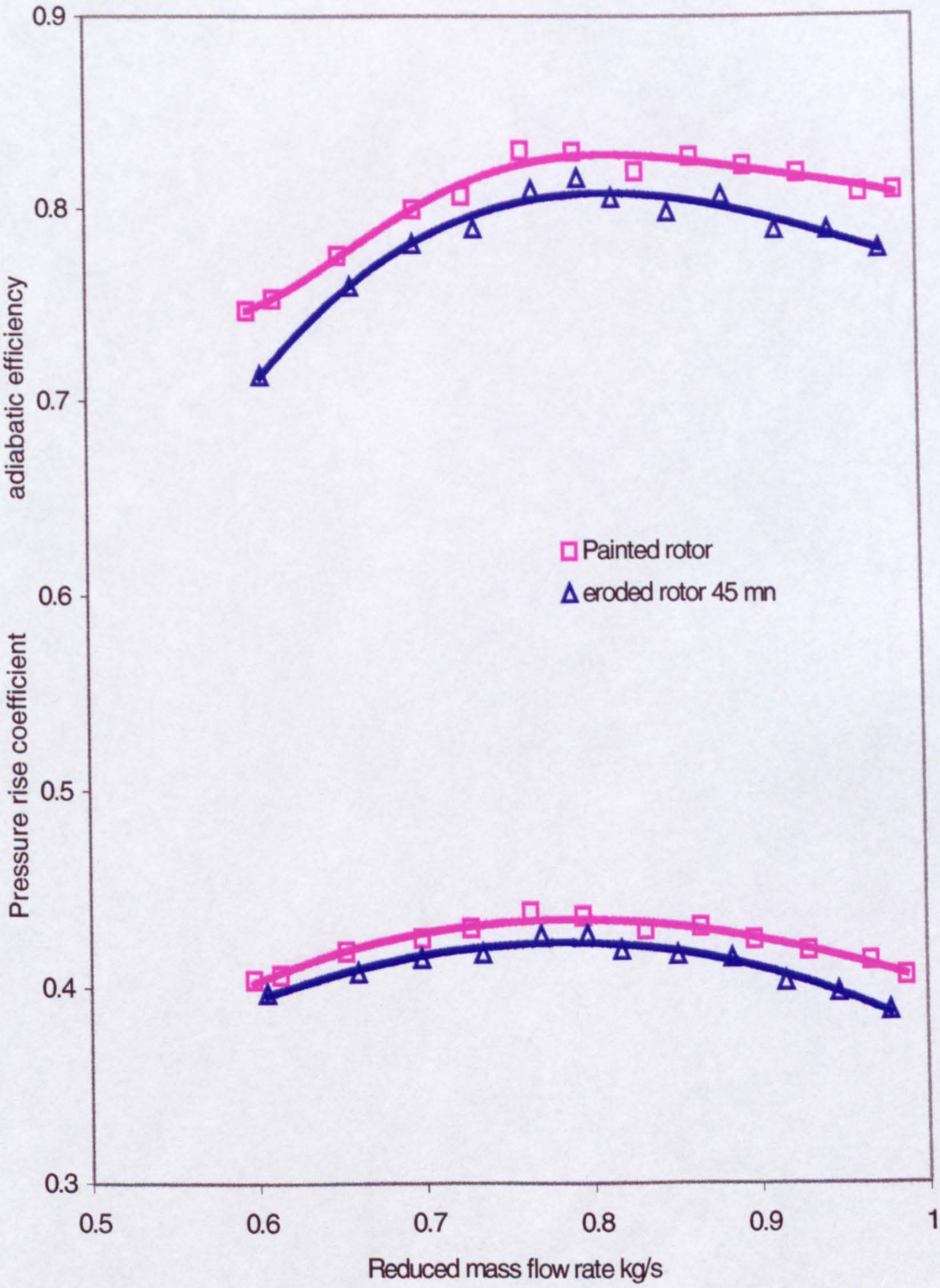


Figure 5-62 Performance degradation of a painted rotor at high concentrations
MIL-E 5007E sand particles

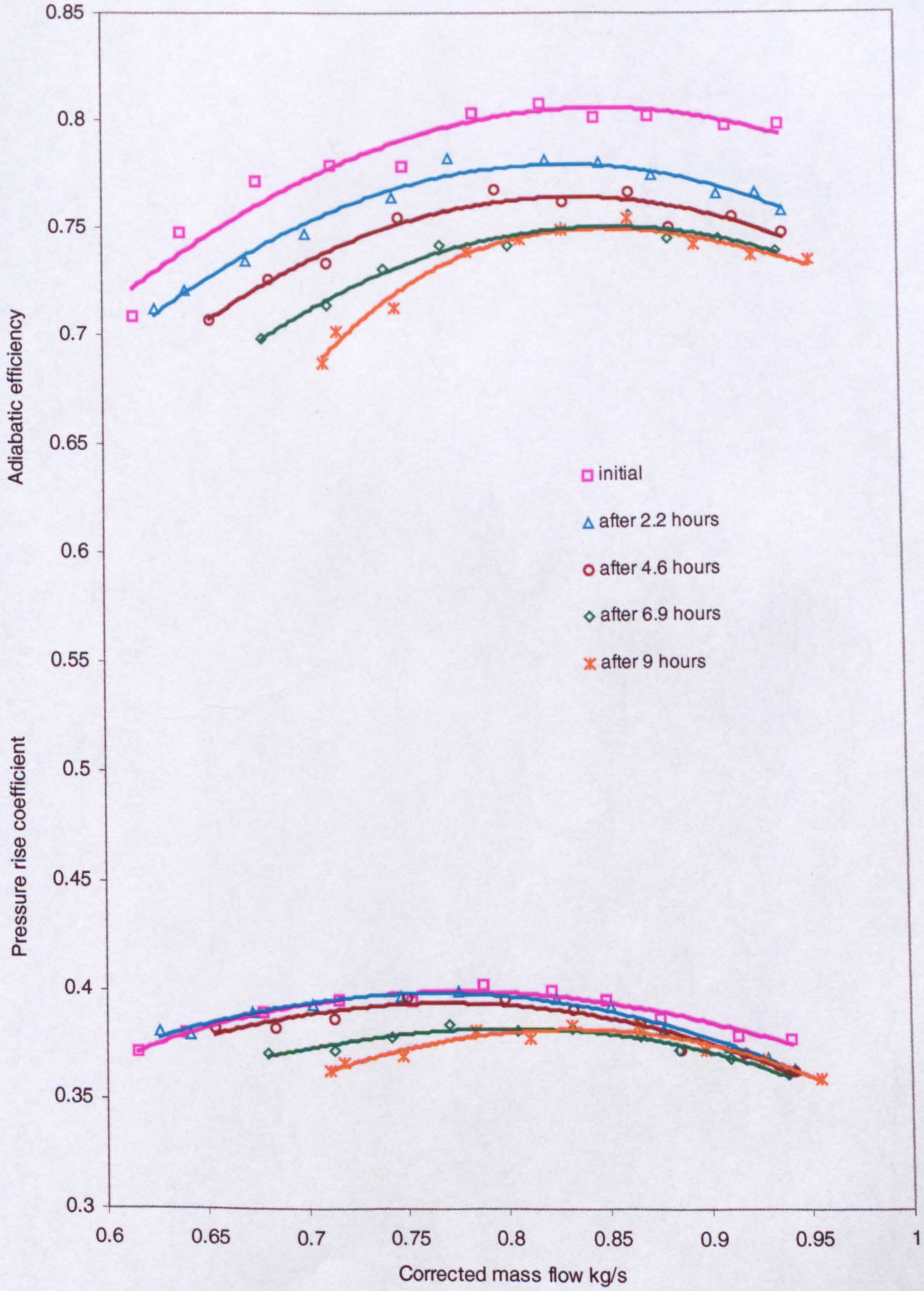


Figure 5-63 Performance degradation due to high concentrations of MIL-E 5007E sand

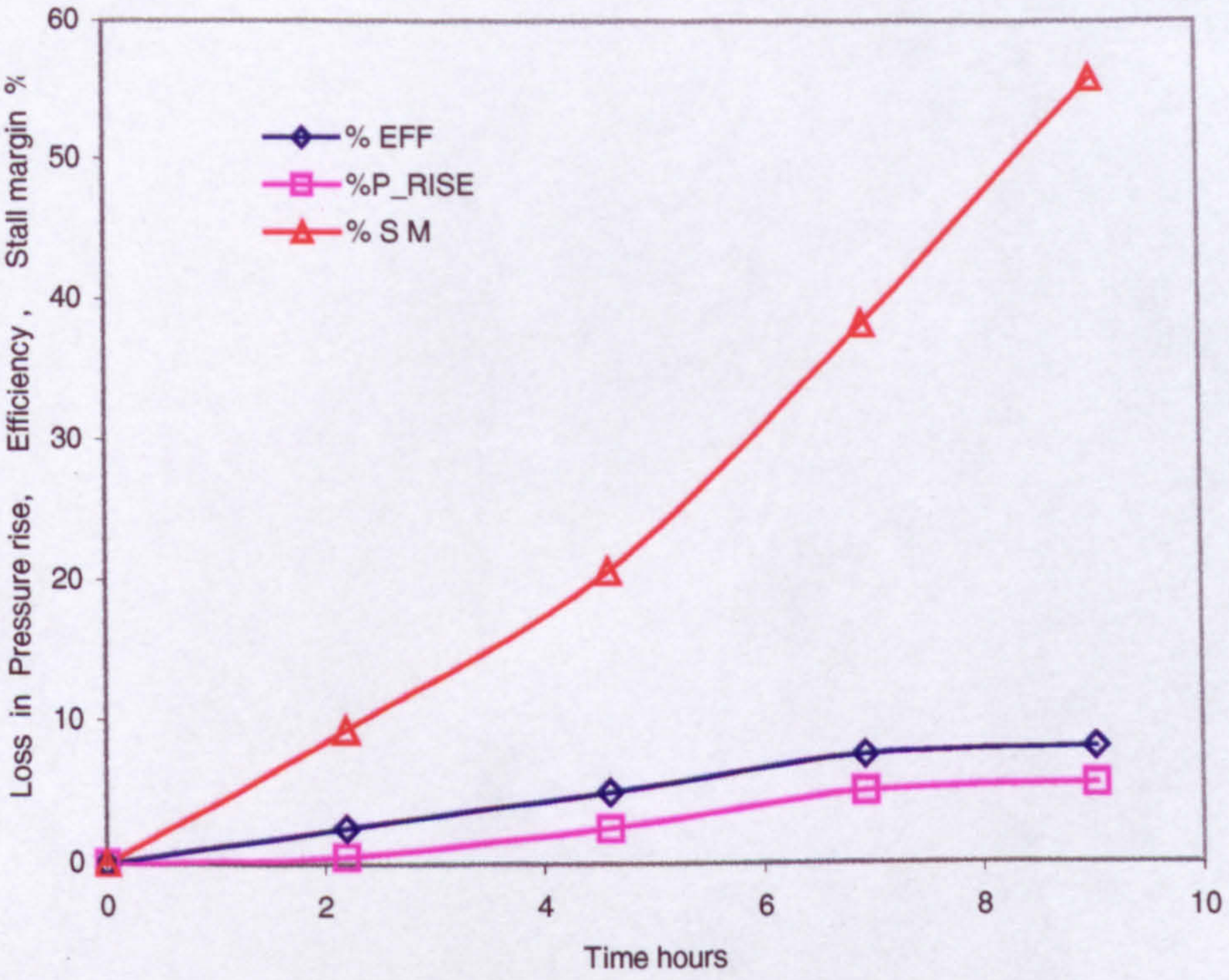


Figure 5-64a Loss in performance due to high concentration MIL-E 5007 E sand with time

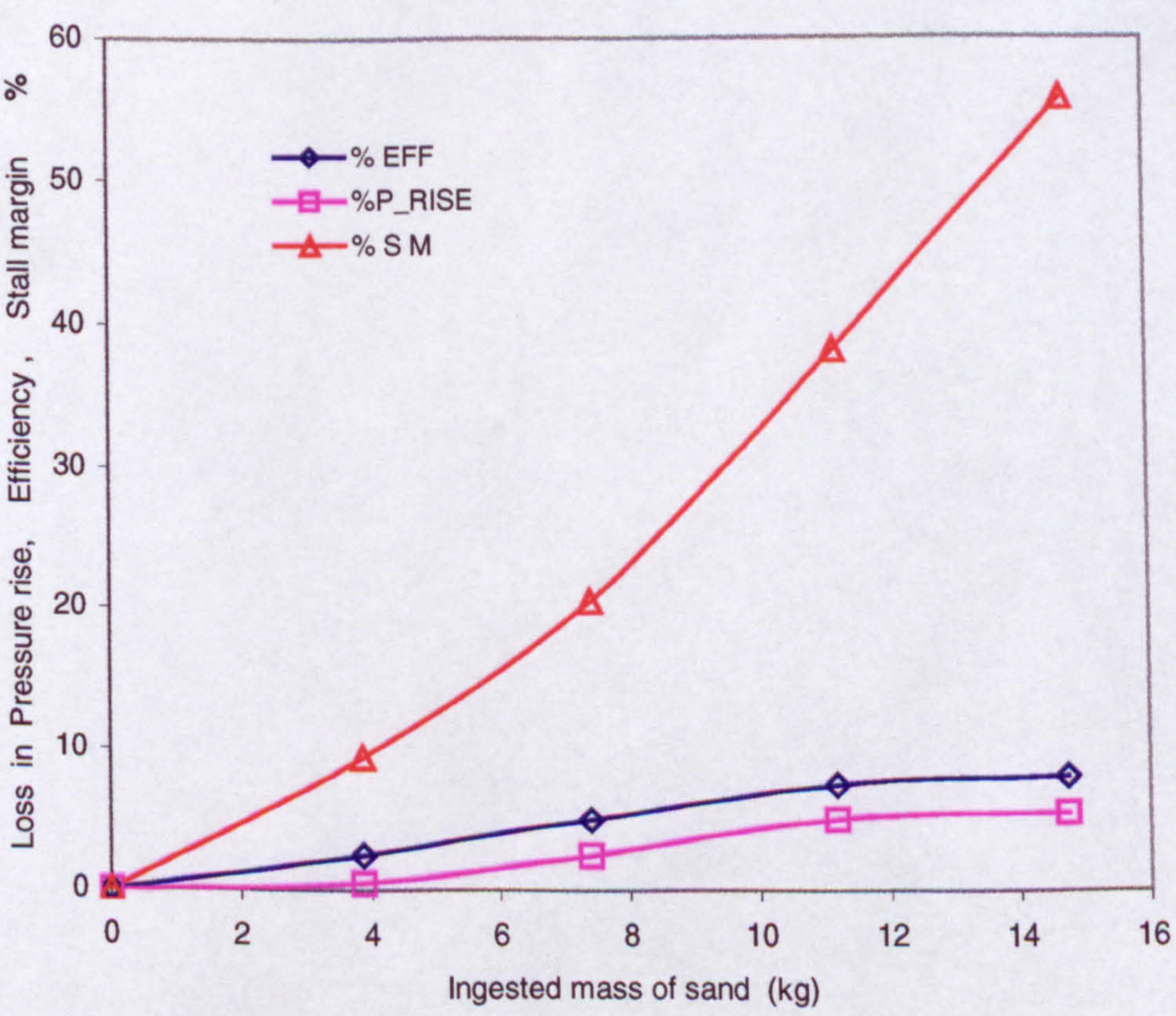


Figure 5-64b Loss in performance with mass of MIL-E 5007E sand at high concentration

Figure 5-65 Variation in tip clearance with ingested mass of sand

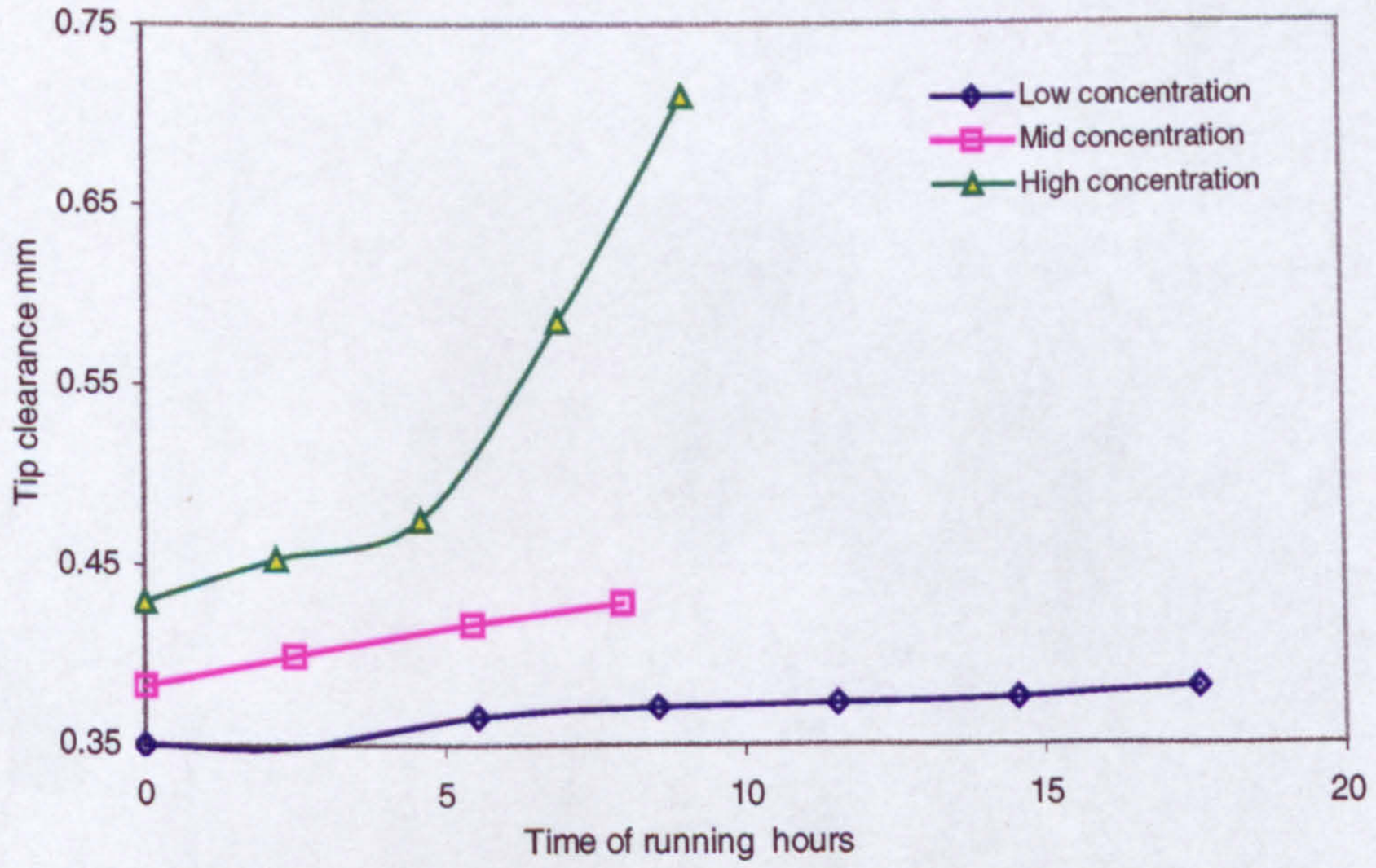


Figure 5-66 Variation of tip clearance with time of running

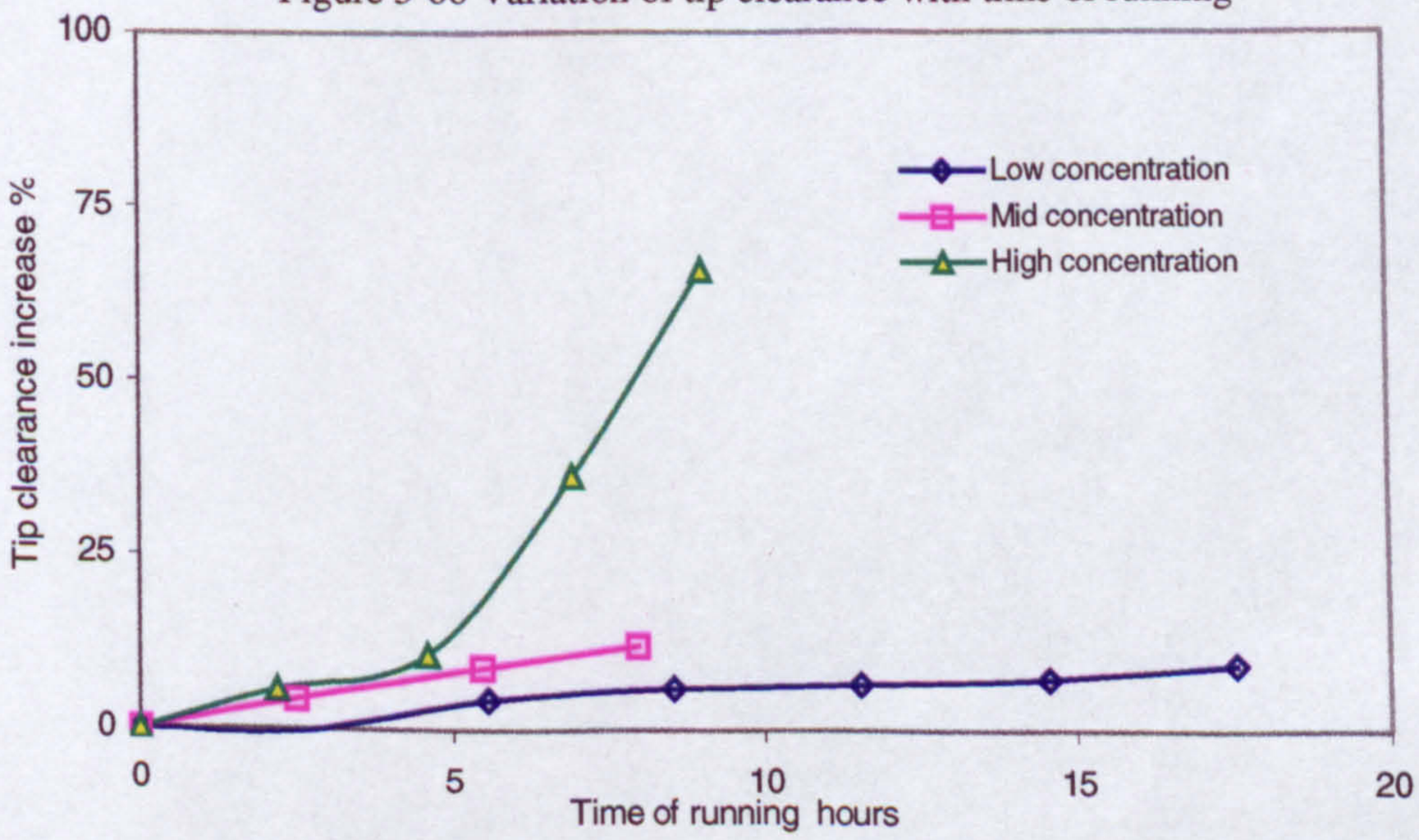


Figure 5-67 Percentage increase in tip clearance with time of running

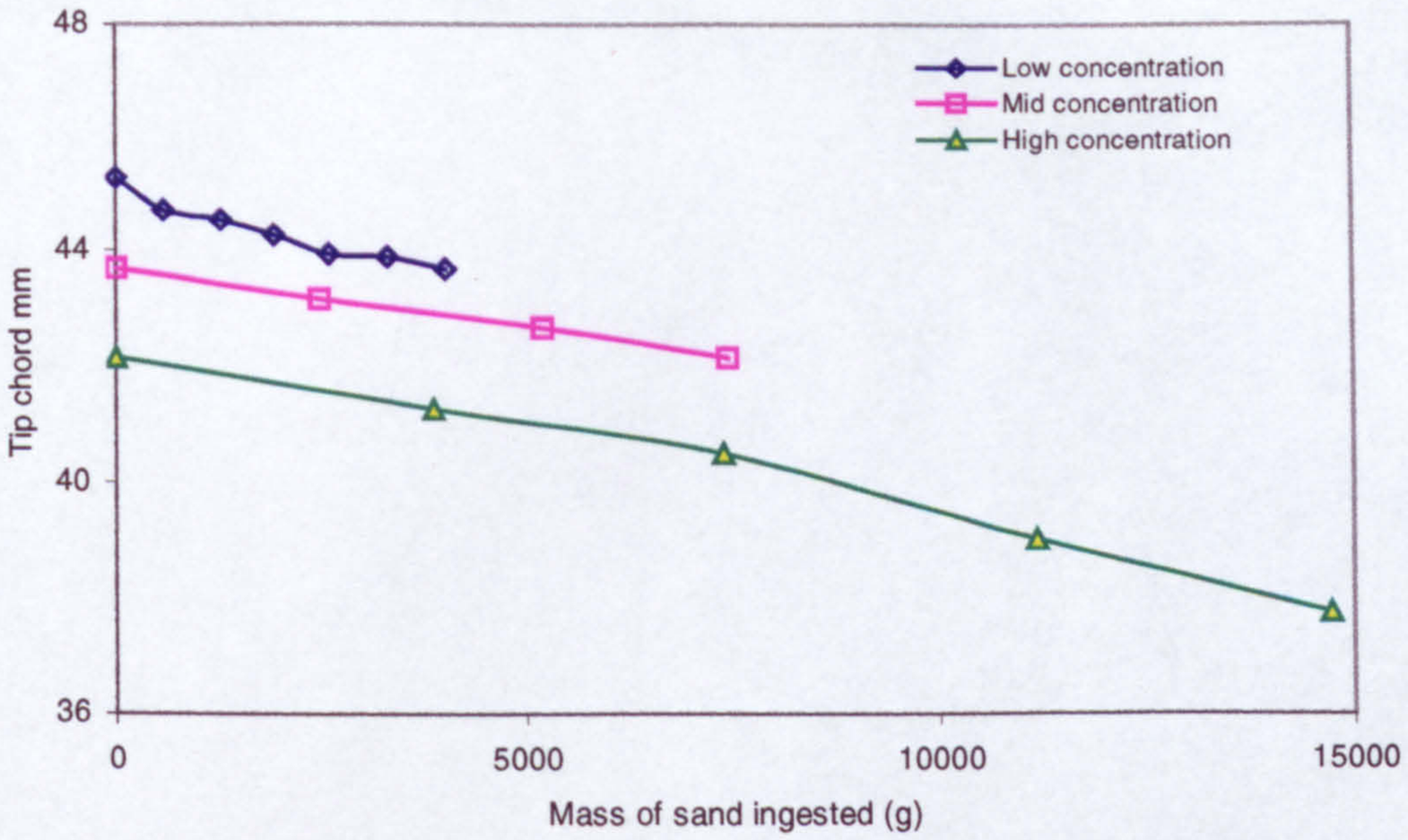


Figure 5-68 Variation in blade tip chord with ingested mass of sand

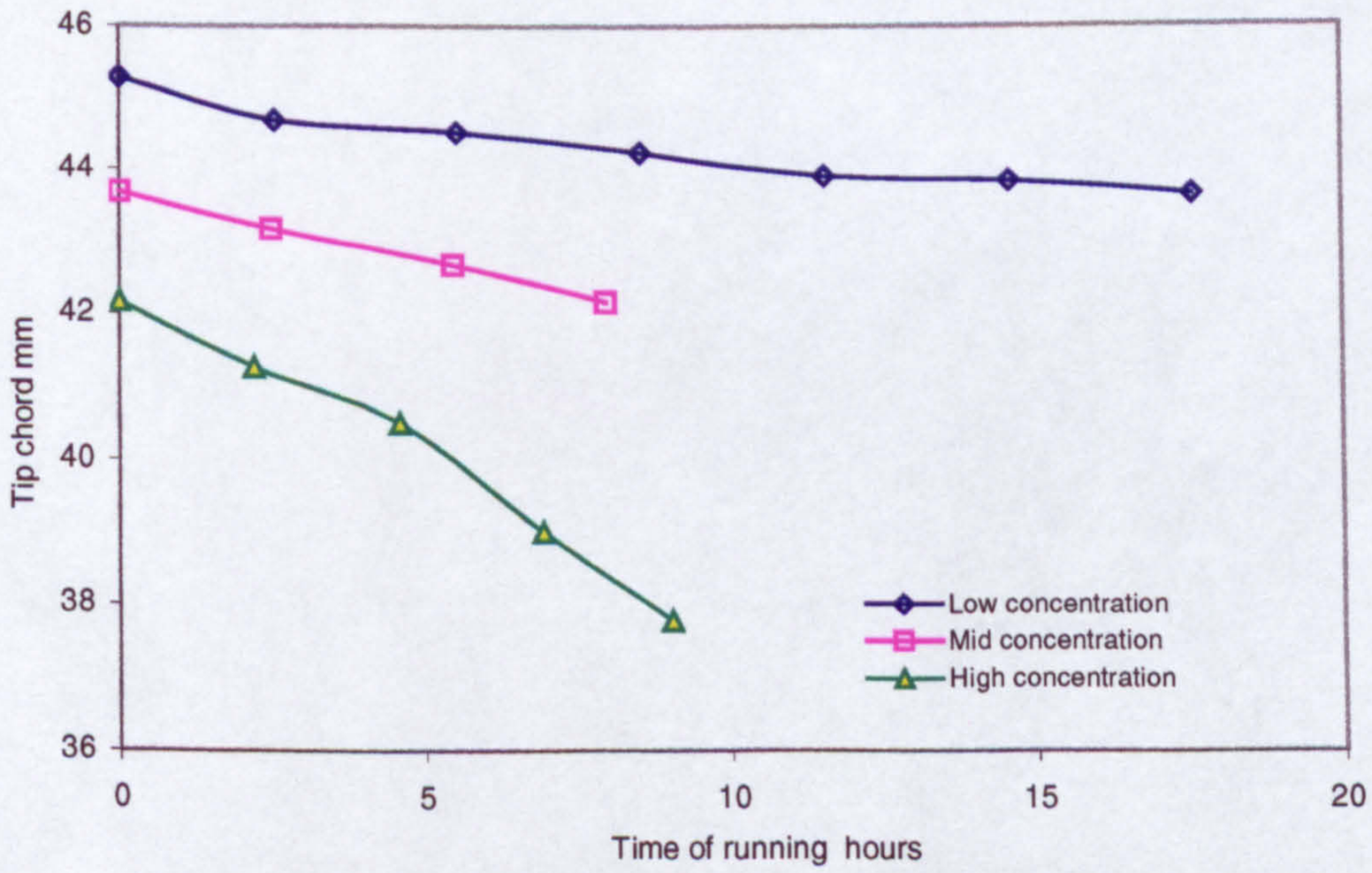


Figure 5-69 Variation in blade tip chord with time of running

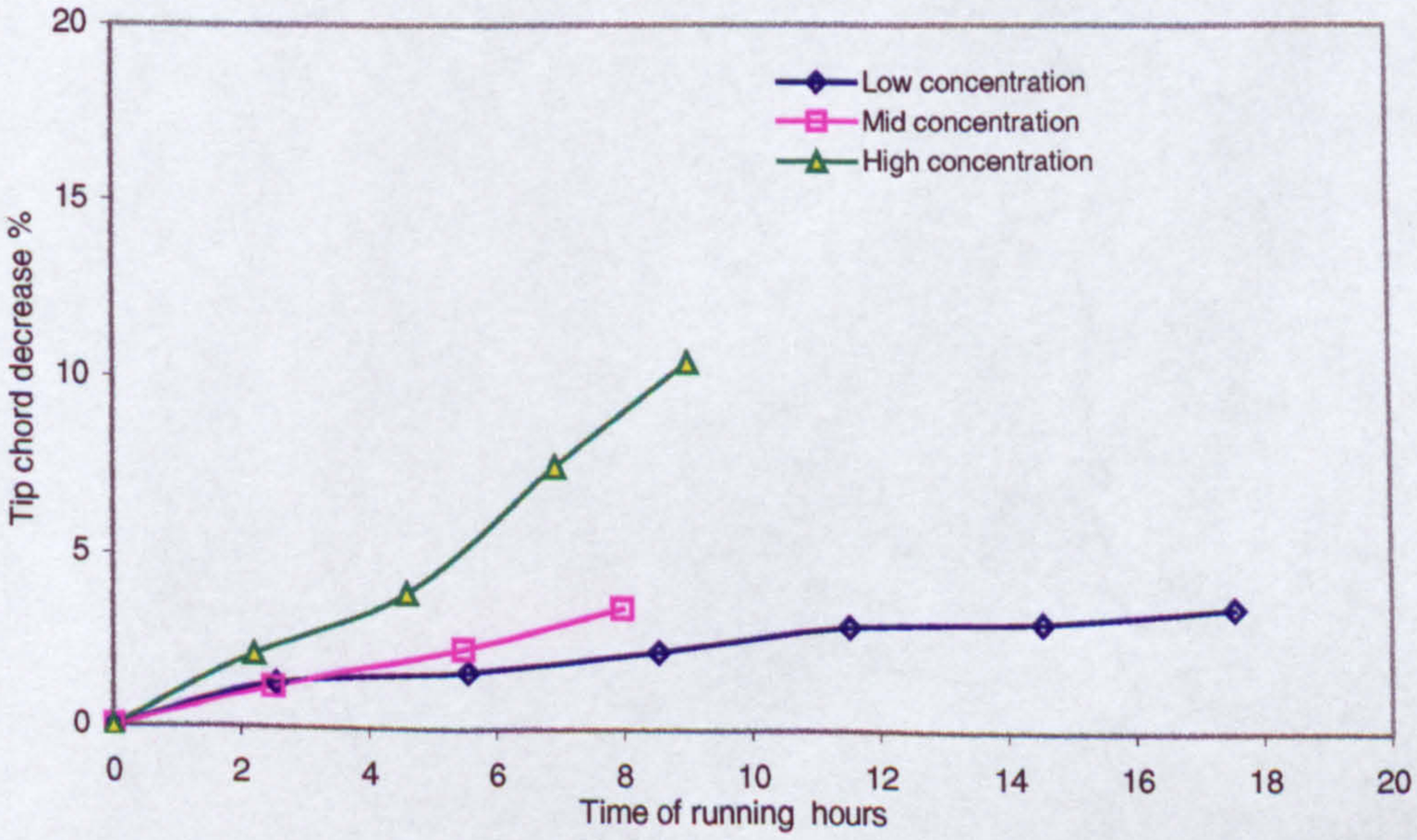


Figure 5-70 Percentage decrease in blade tip chord with time of running

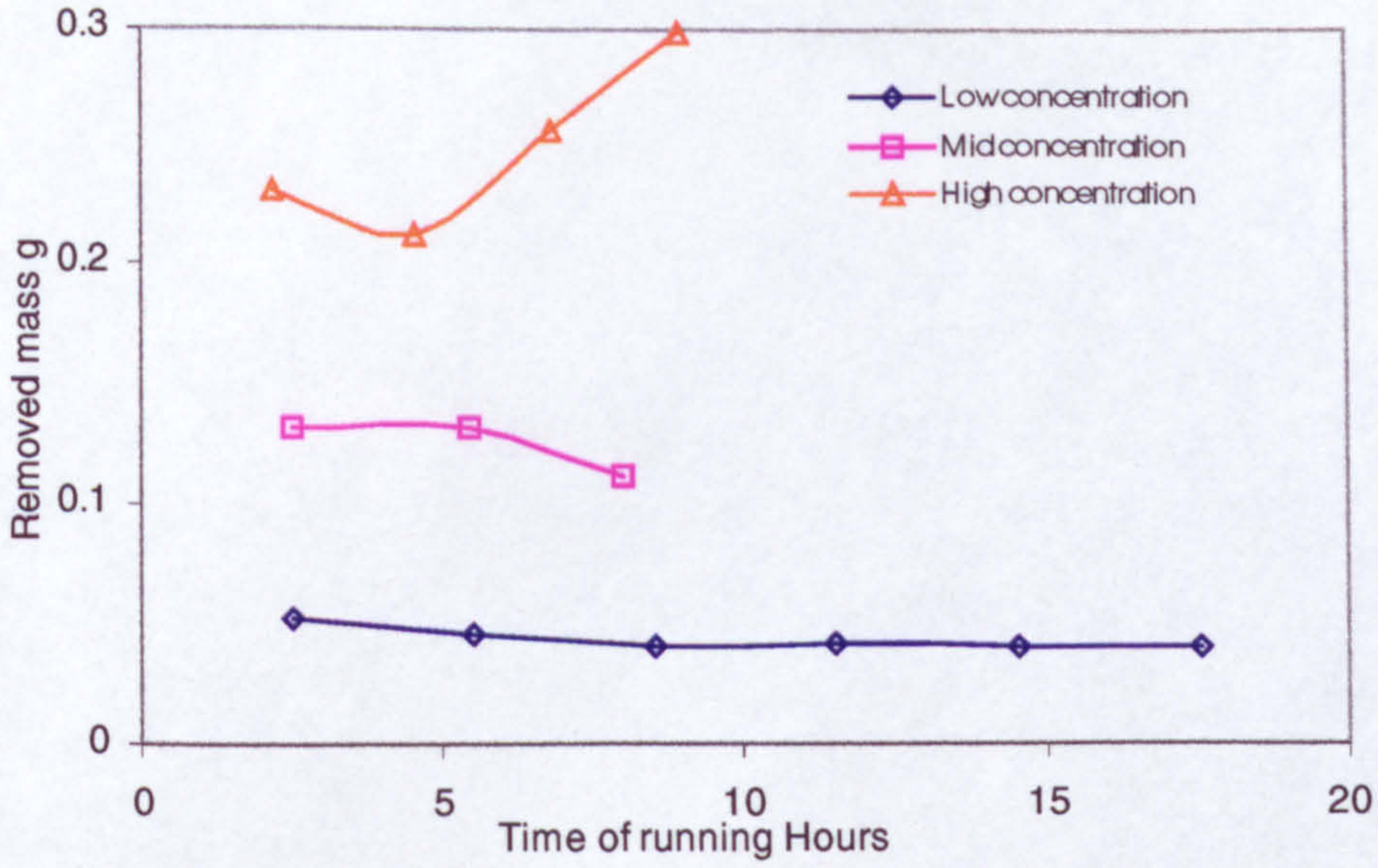


Figure 5-71 Erosion mass per blade with time of running

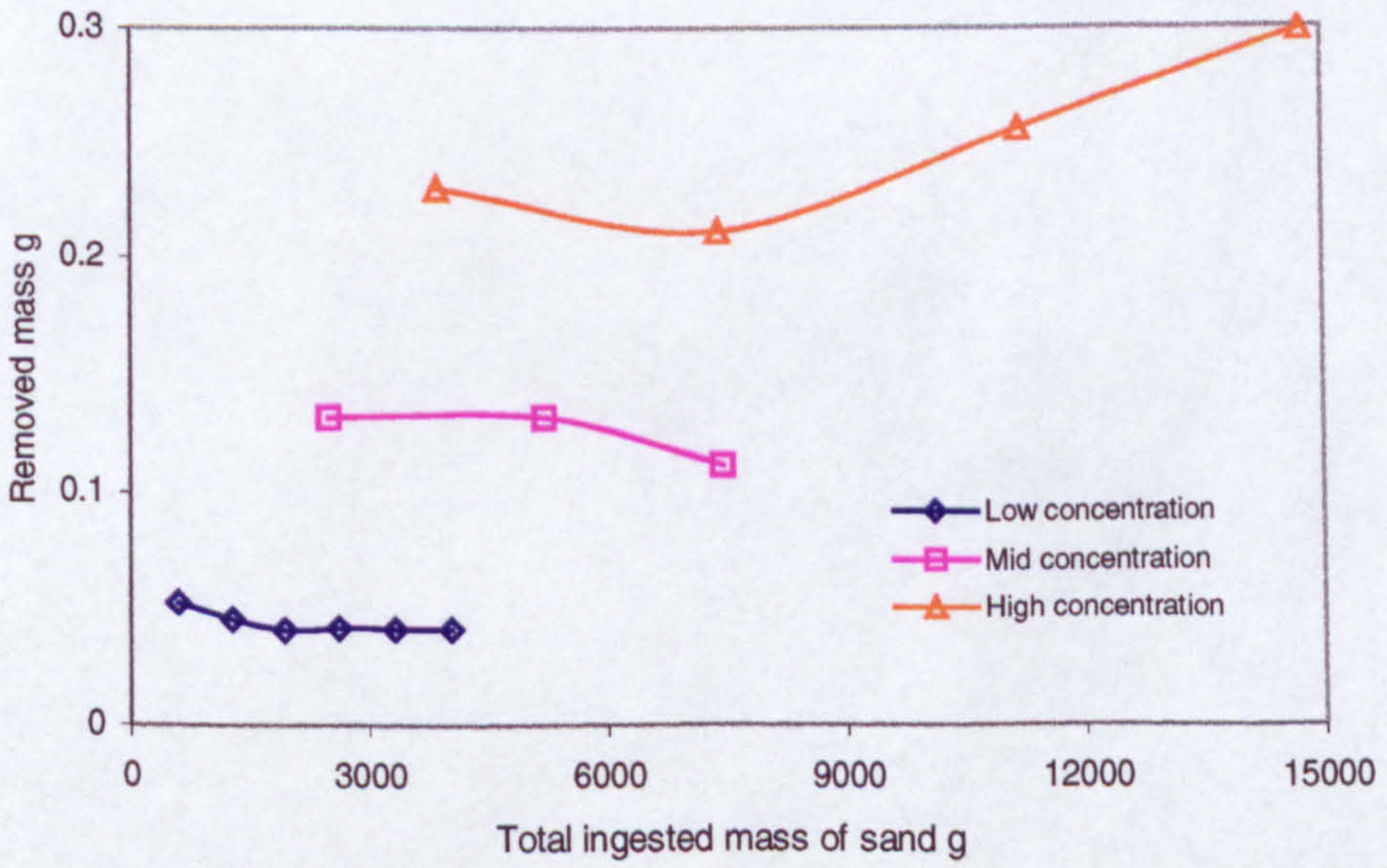


Figure 5-72 Erosion mass per blade with ingested mass of sand

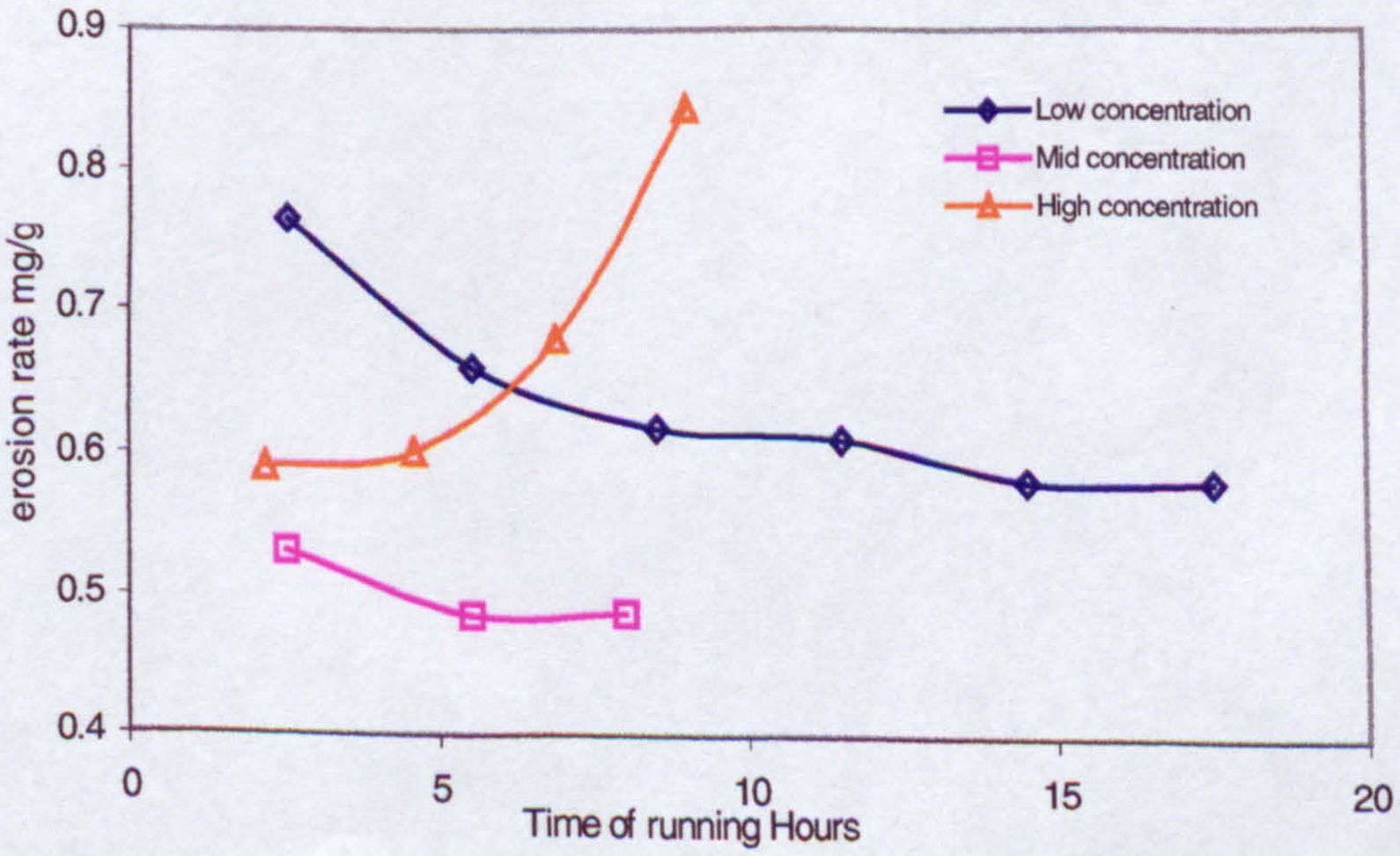


Figure 5-73 Erosion rate per blade with time of running

# FIGURES 6

# and

# APPENDIX M

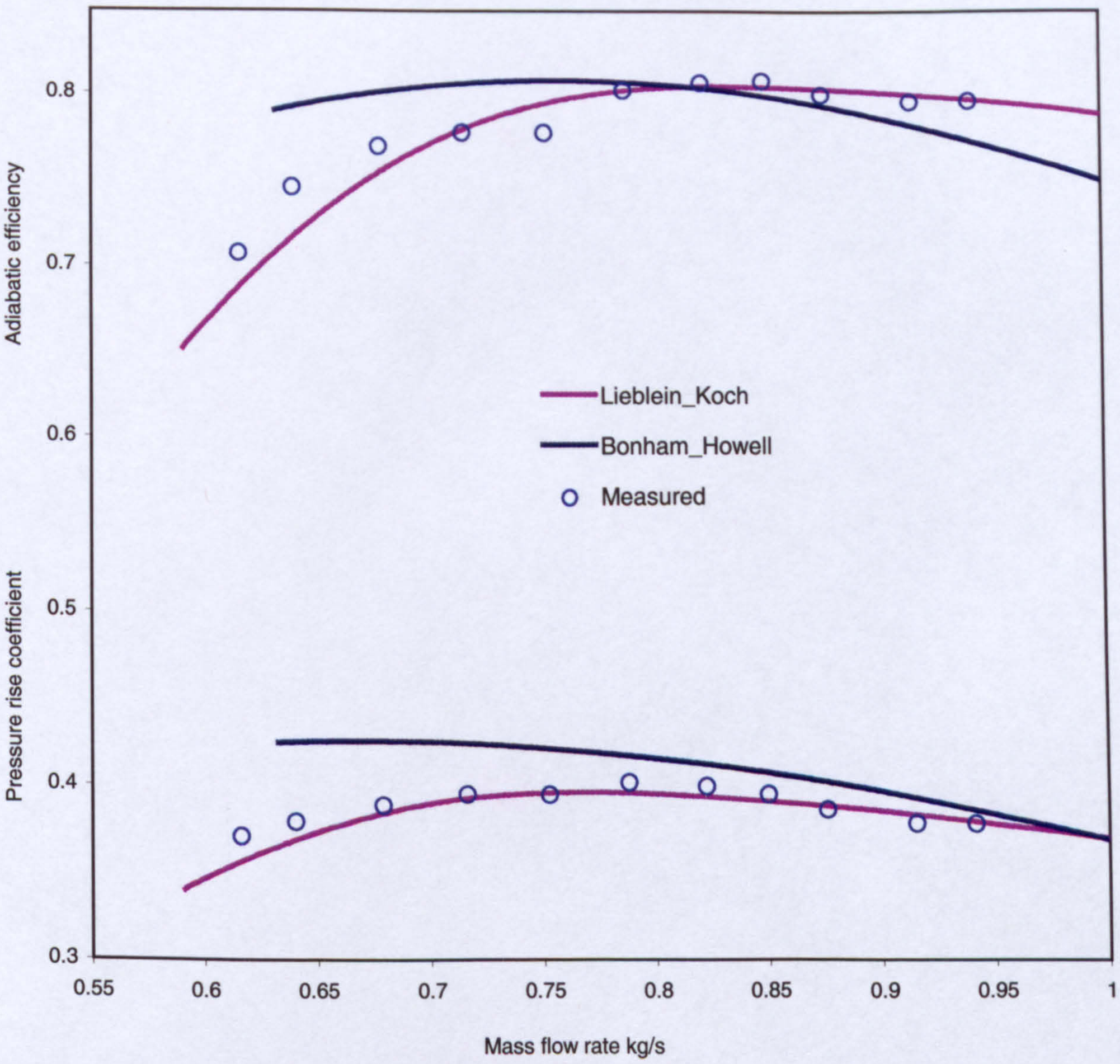


Figure 6-3 predicted characteristics using Bonham-Howell and Lieblein-Koch

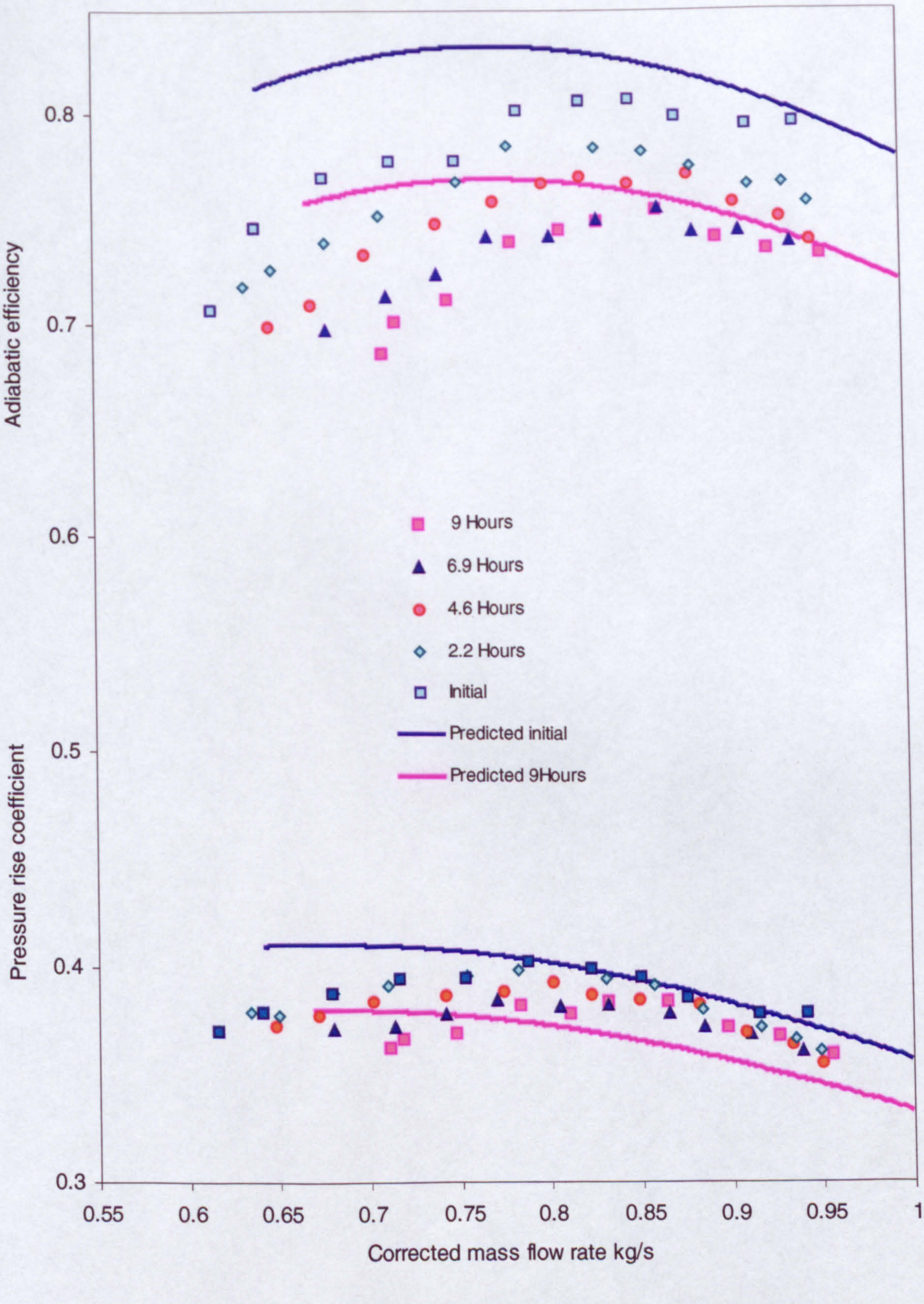


Figure 6-4 predicted characteristics degradation using Bonham-Howell method

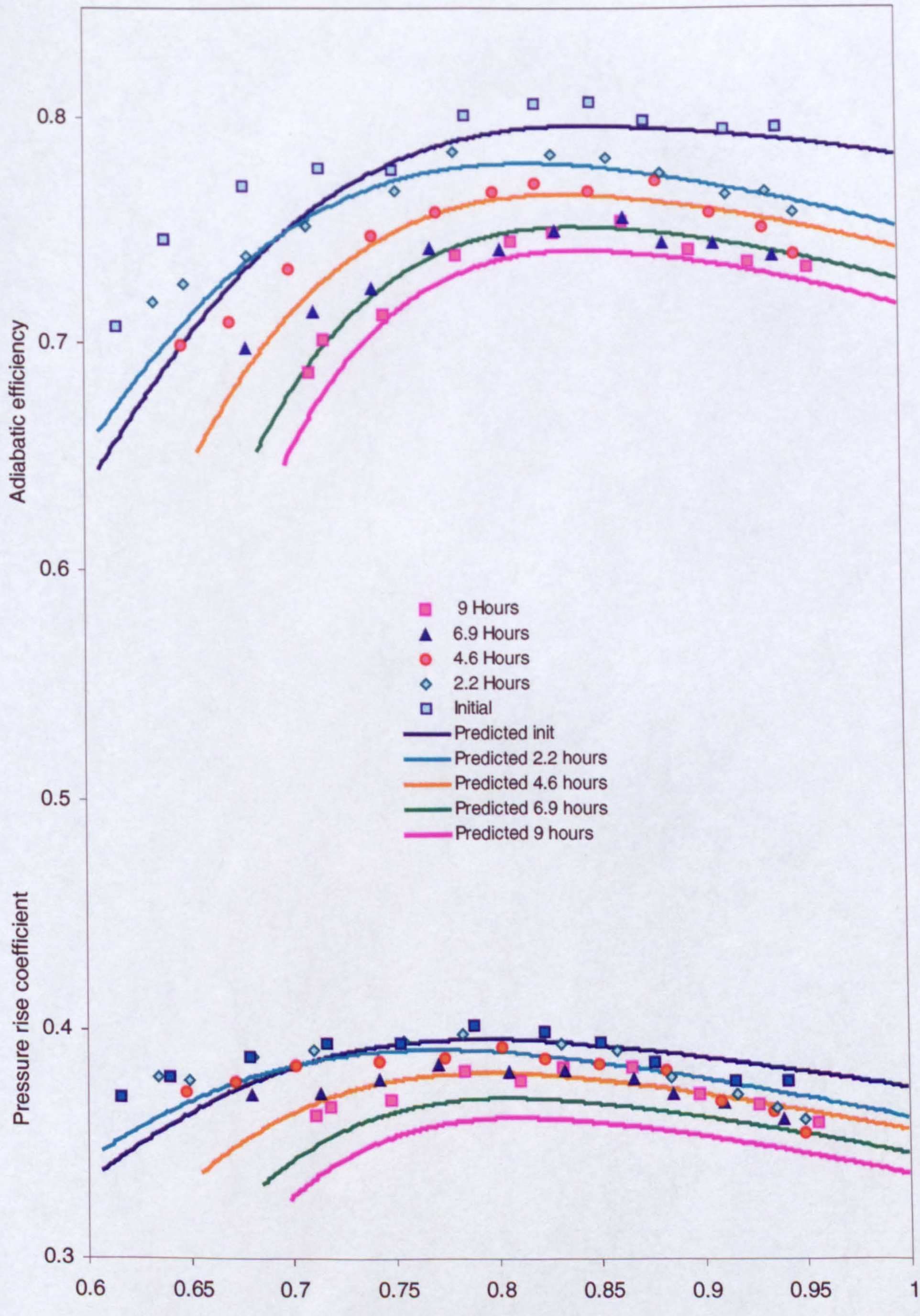


Figure 6-5 predicted characteristics degradation using Lieblein-Koch
Based on the measured geometry changes

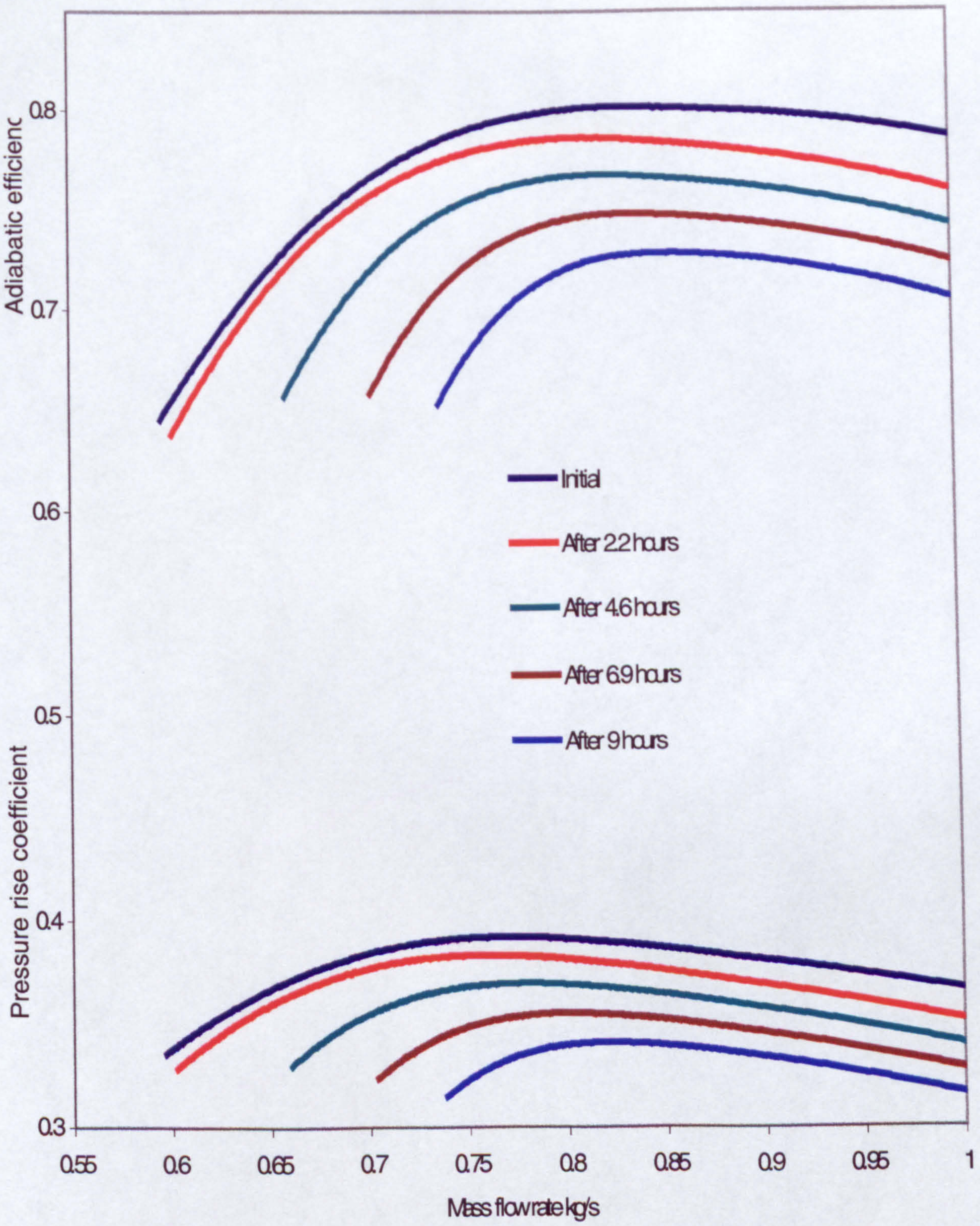


Figure 6-6 predicted characteristics degradation using Lieblein-Koch based on the predicted geometry changes

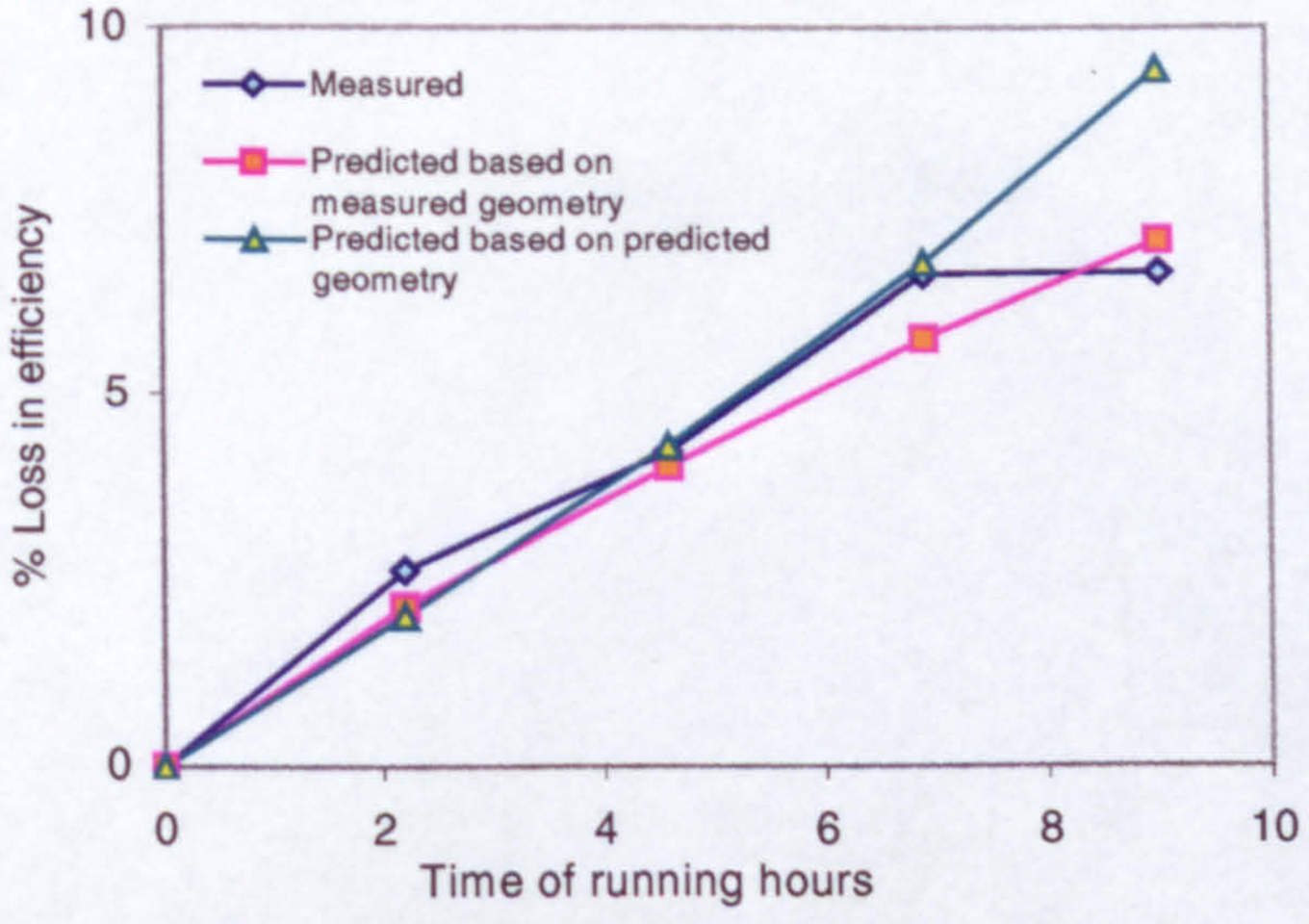


Figure 6-7 Comparison between predicted and measured efficiency degradation

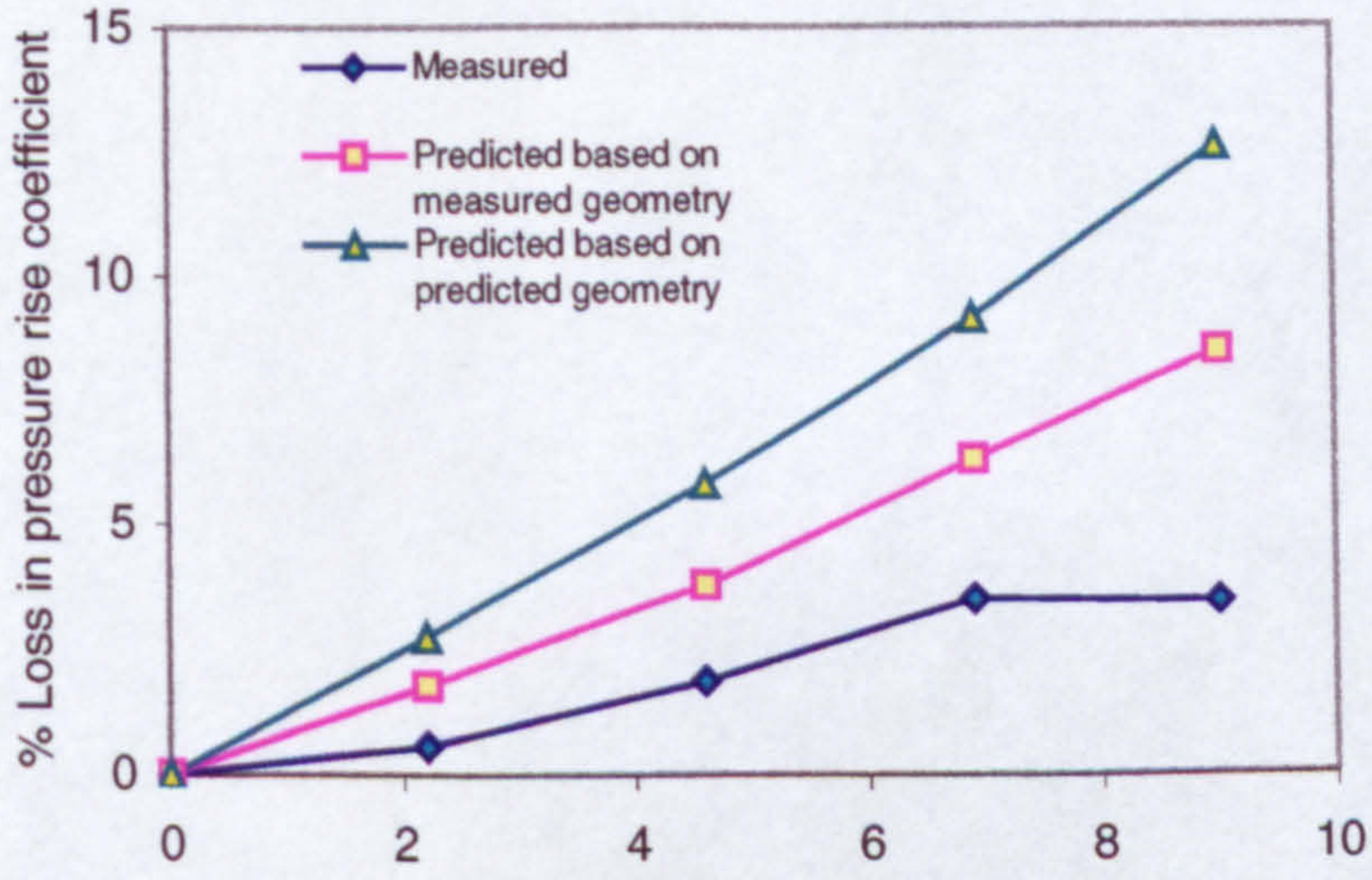


Figure 6-8 Comparison between predicted and measured pressure rise degradation

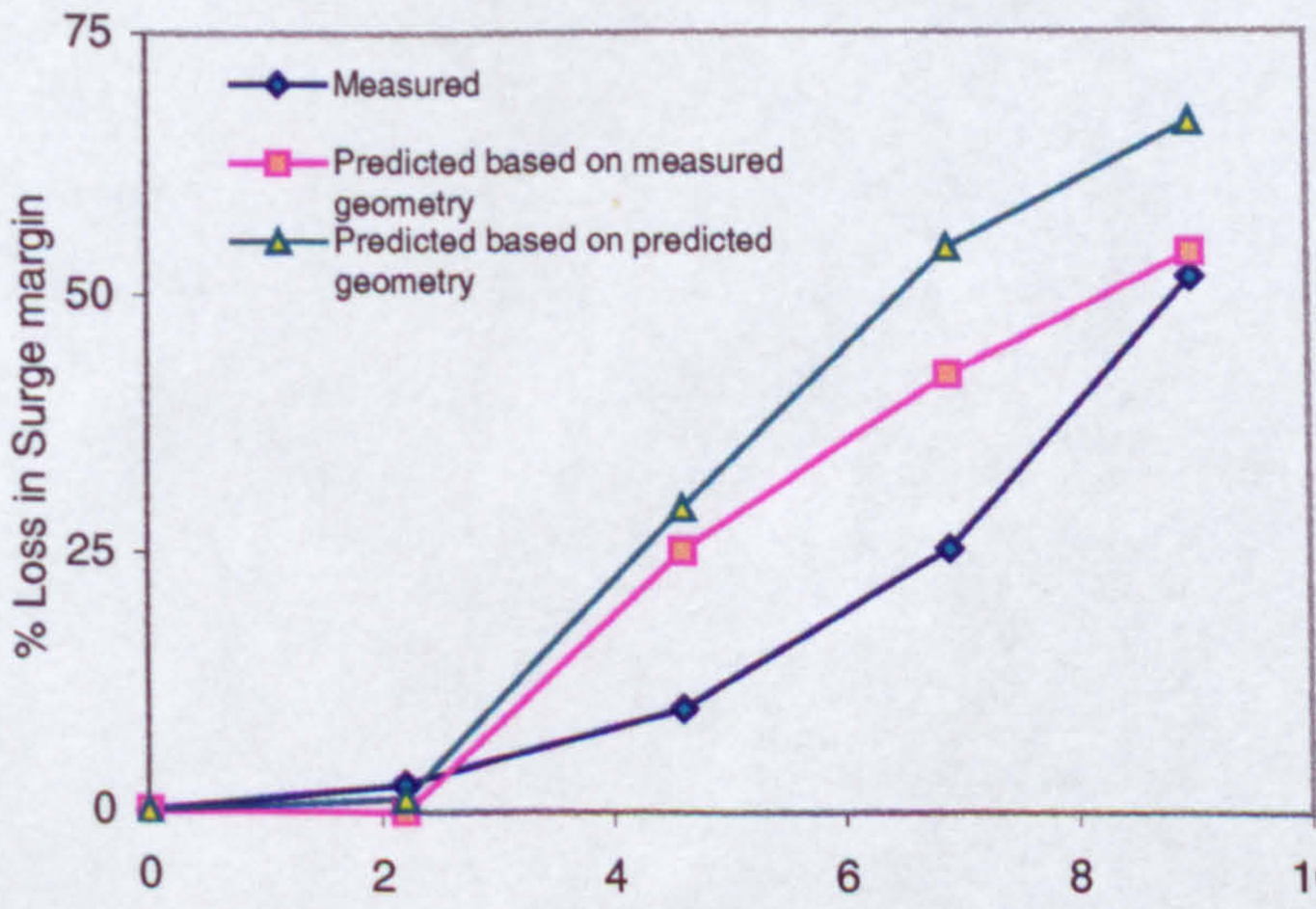


Figure 6-9 Comparison between predicted and measured surge margin degradation

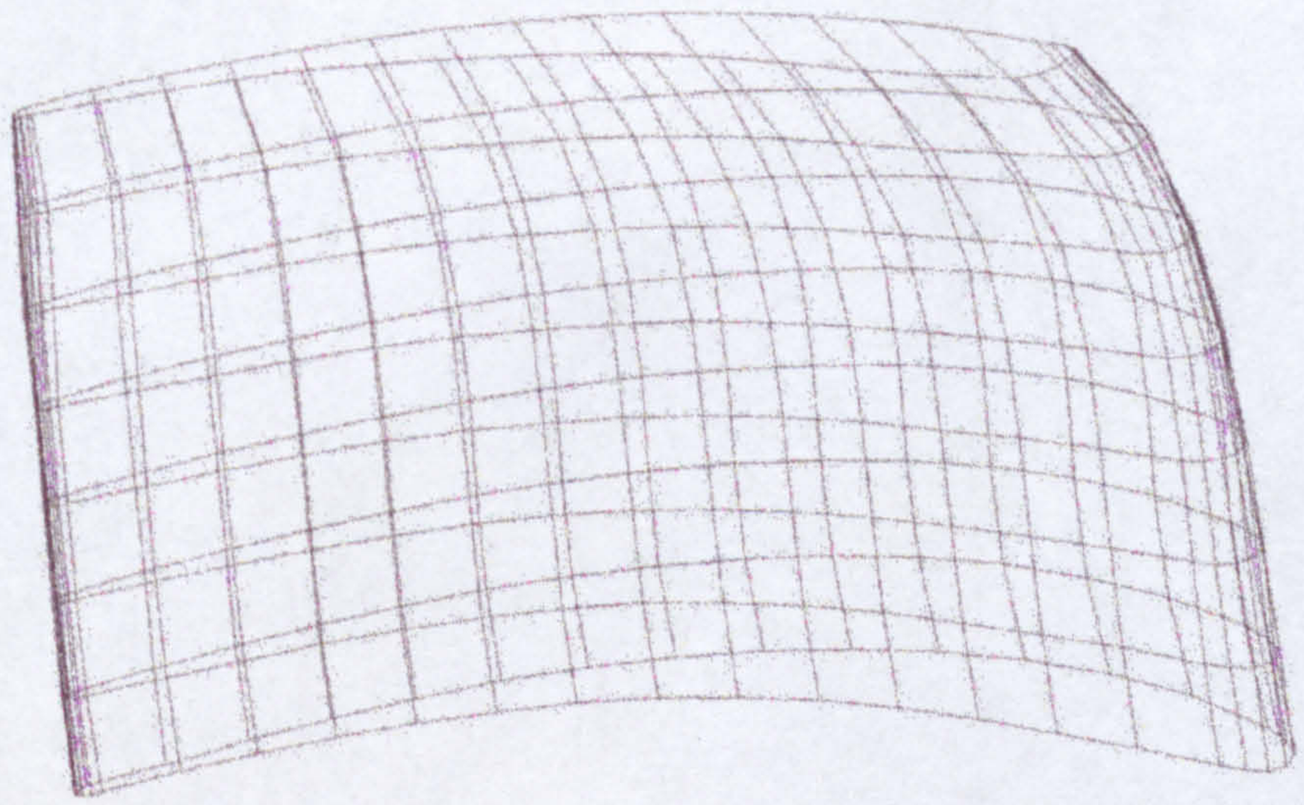

Figure 6-10 Measured geometry of the eroded blade

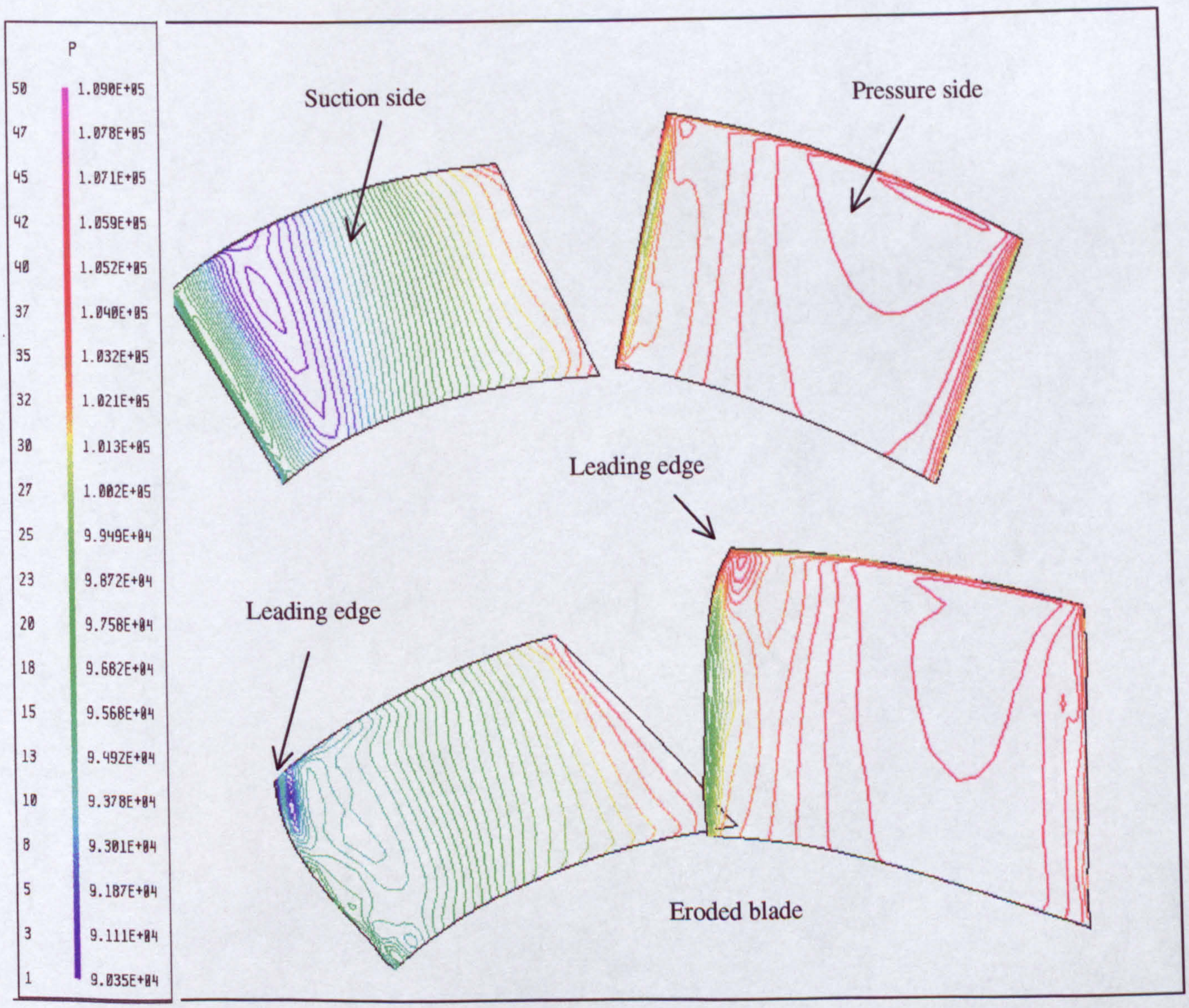


Figure 6-11 Pressure contours on the pressure side and the suction side of the original and the eroded blade

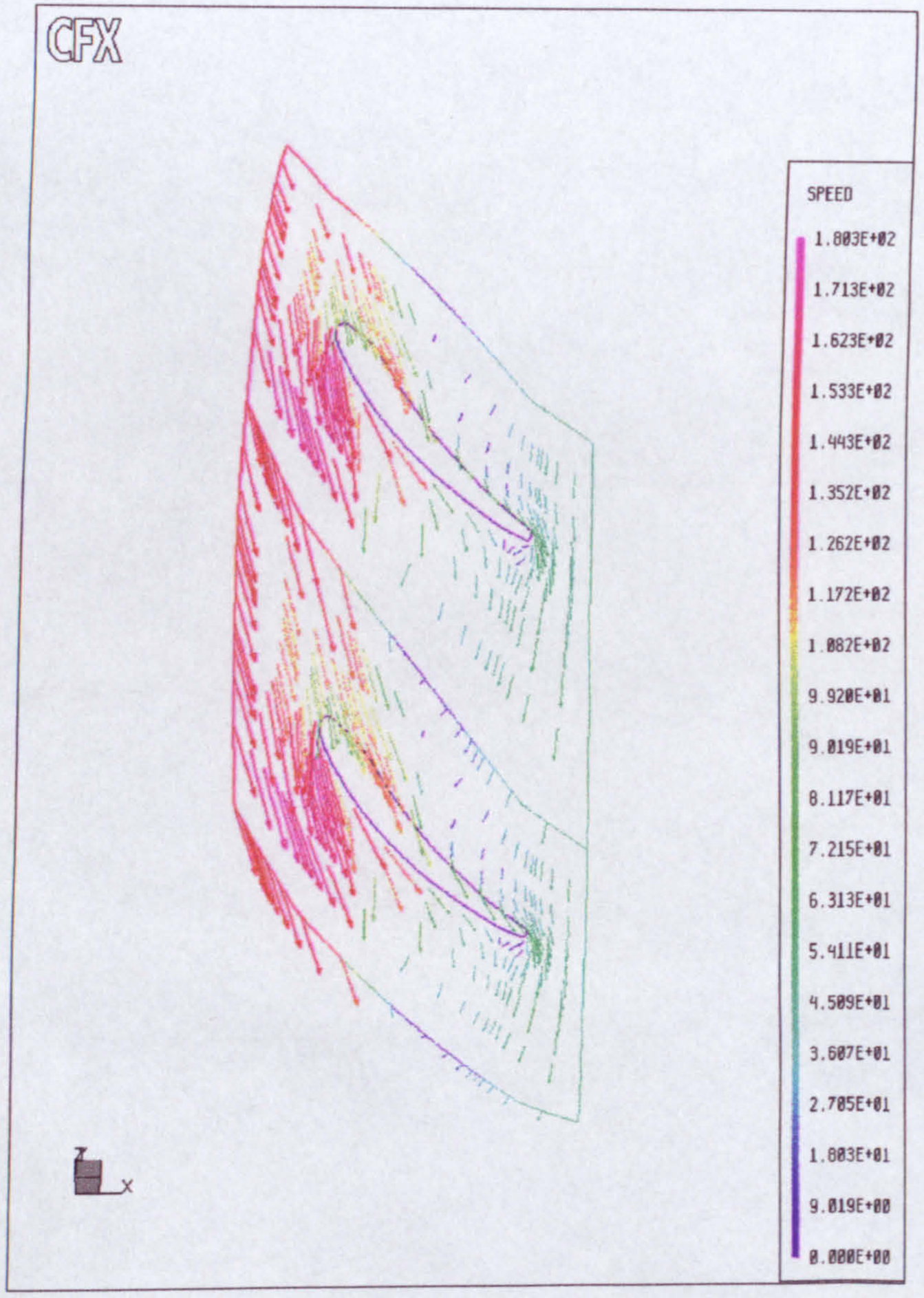


Figure 6-12a Vector plot at the tip of the eroded blade near design point

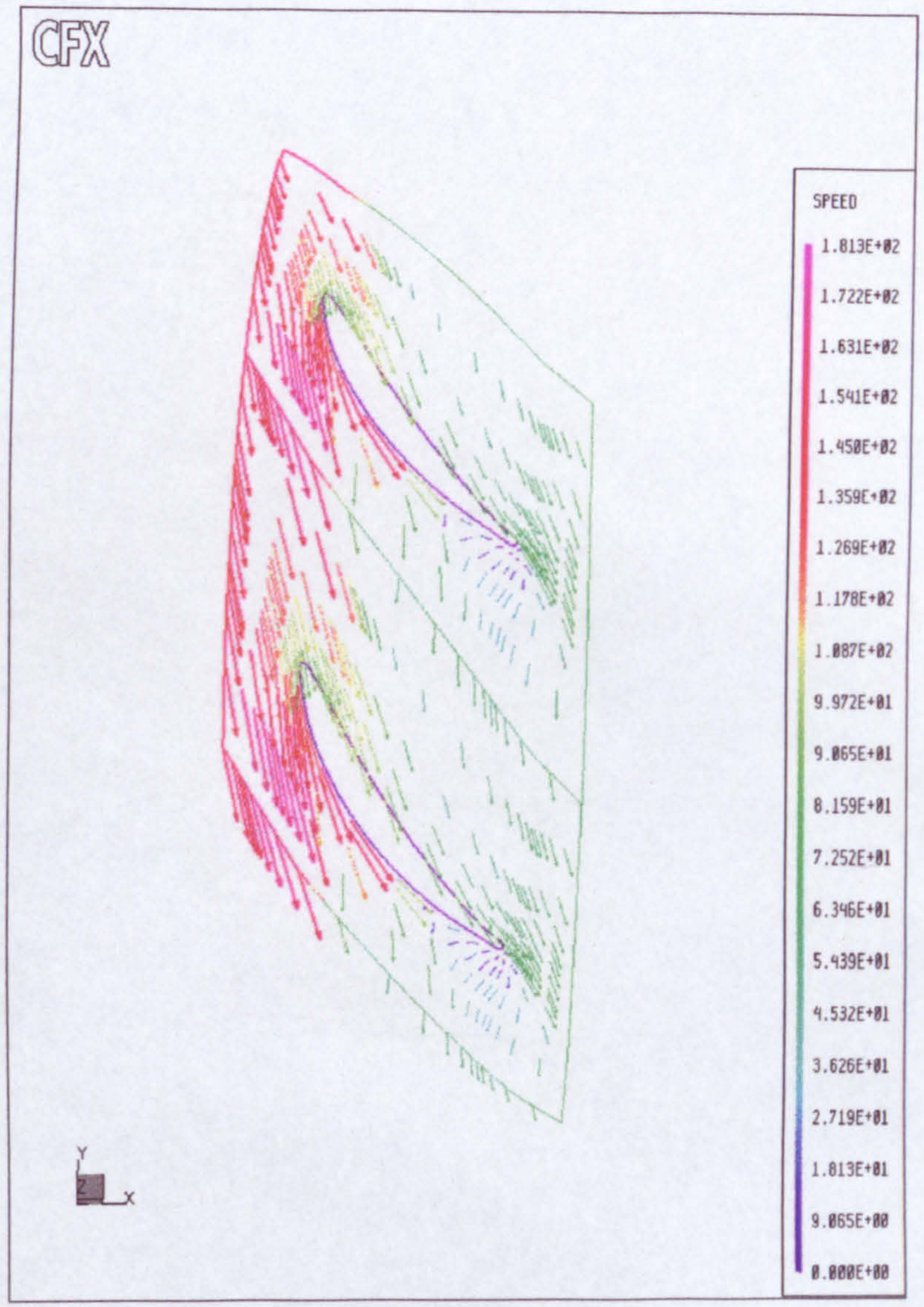


Figure 6-12b Vector plot at the tip of the original blade near design point

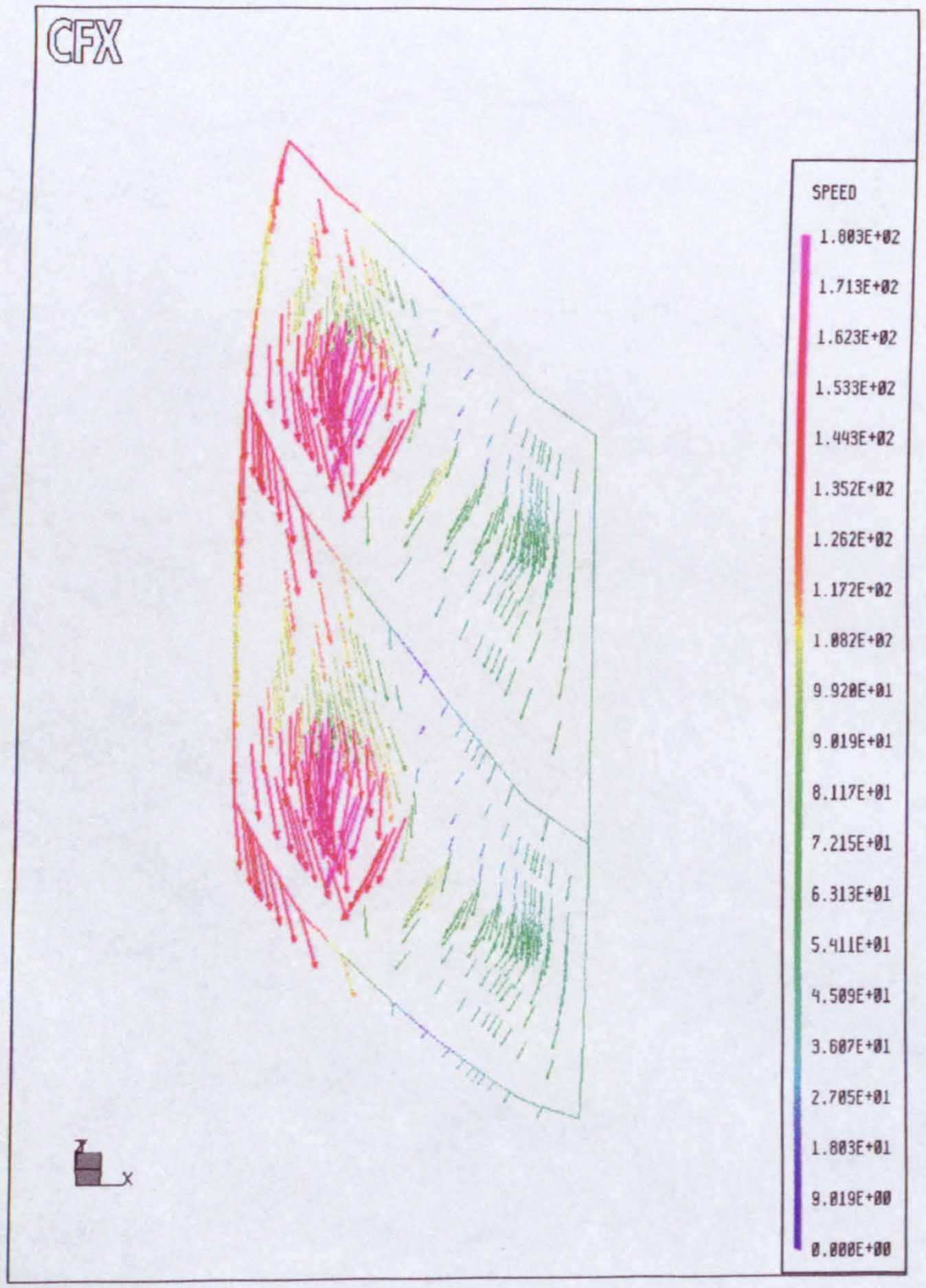


Figure 6-13a Vector plot in the tip region of the eroded blade near design point

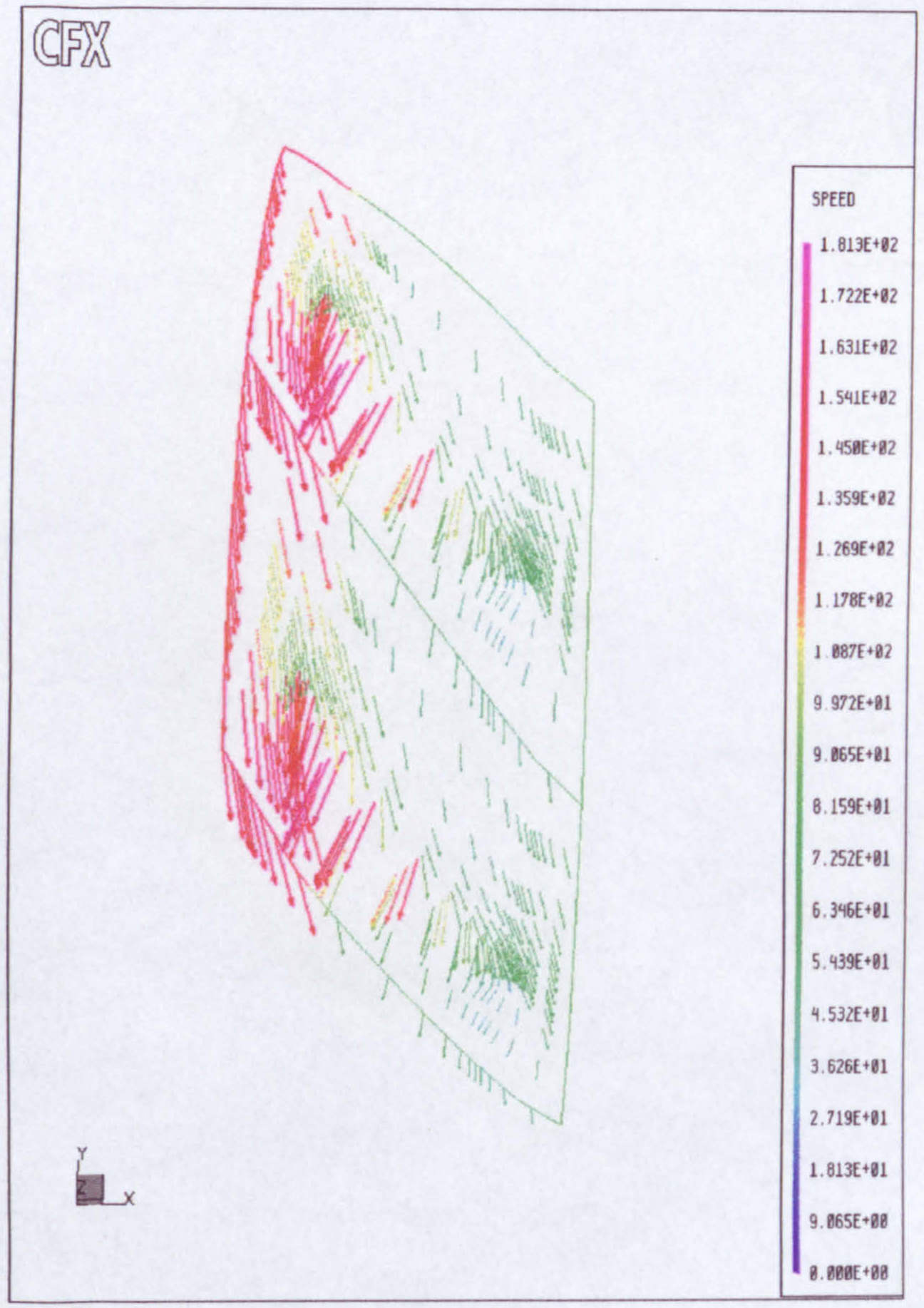


Figure 6-13b Vector plot in the tip region of the original blade near design point

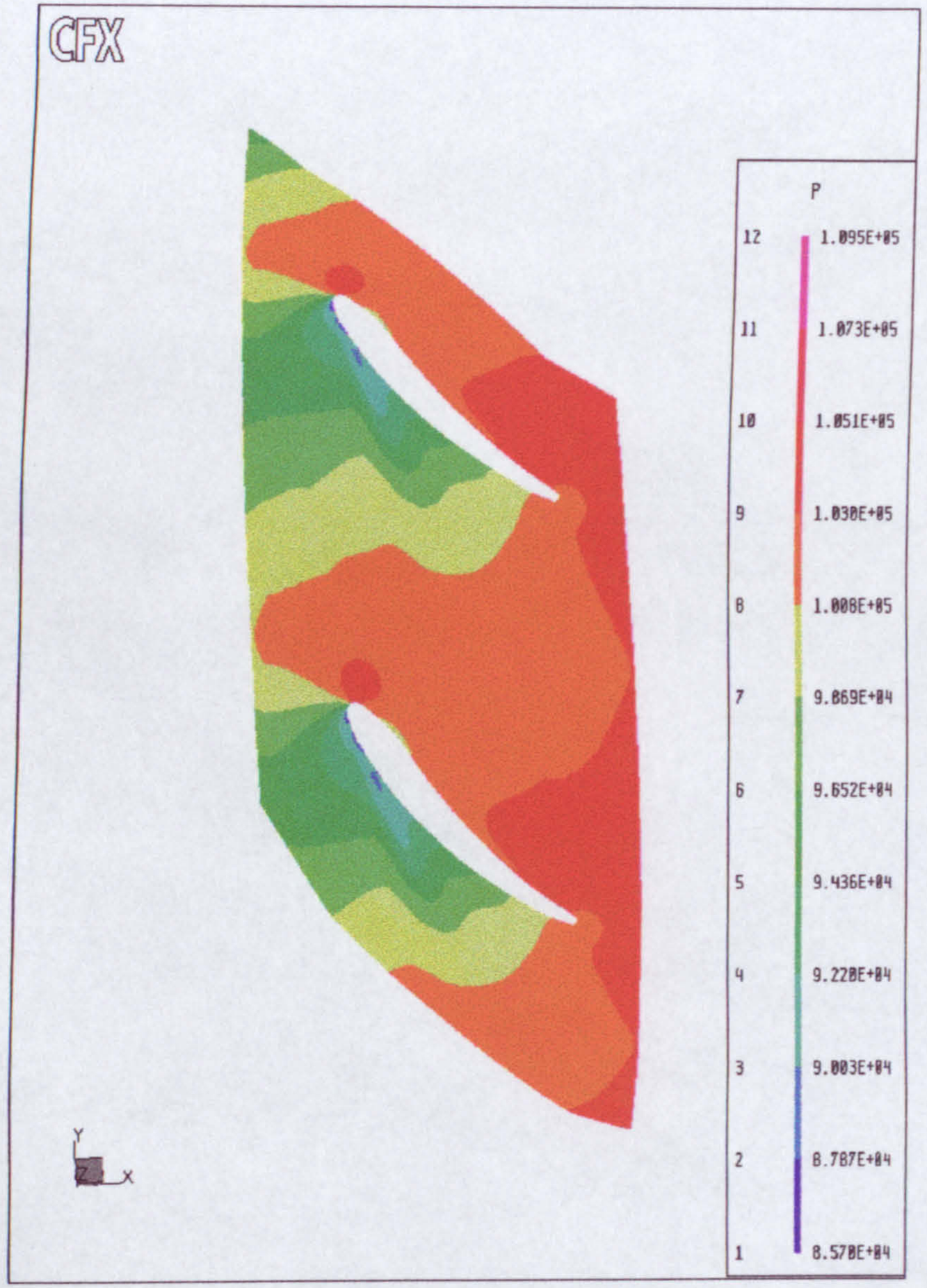


Figure 6-14a Static pressure at the tip of the eroded blade near design point

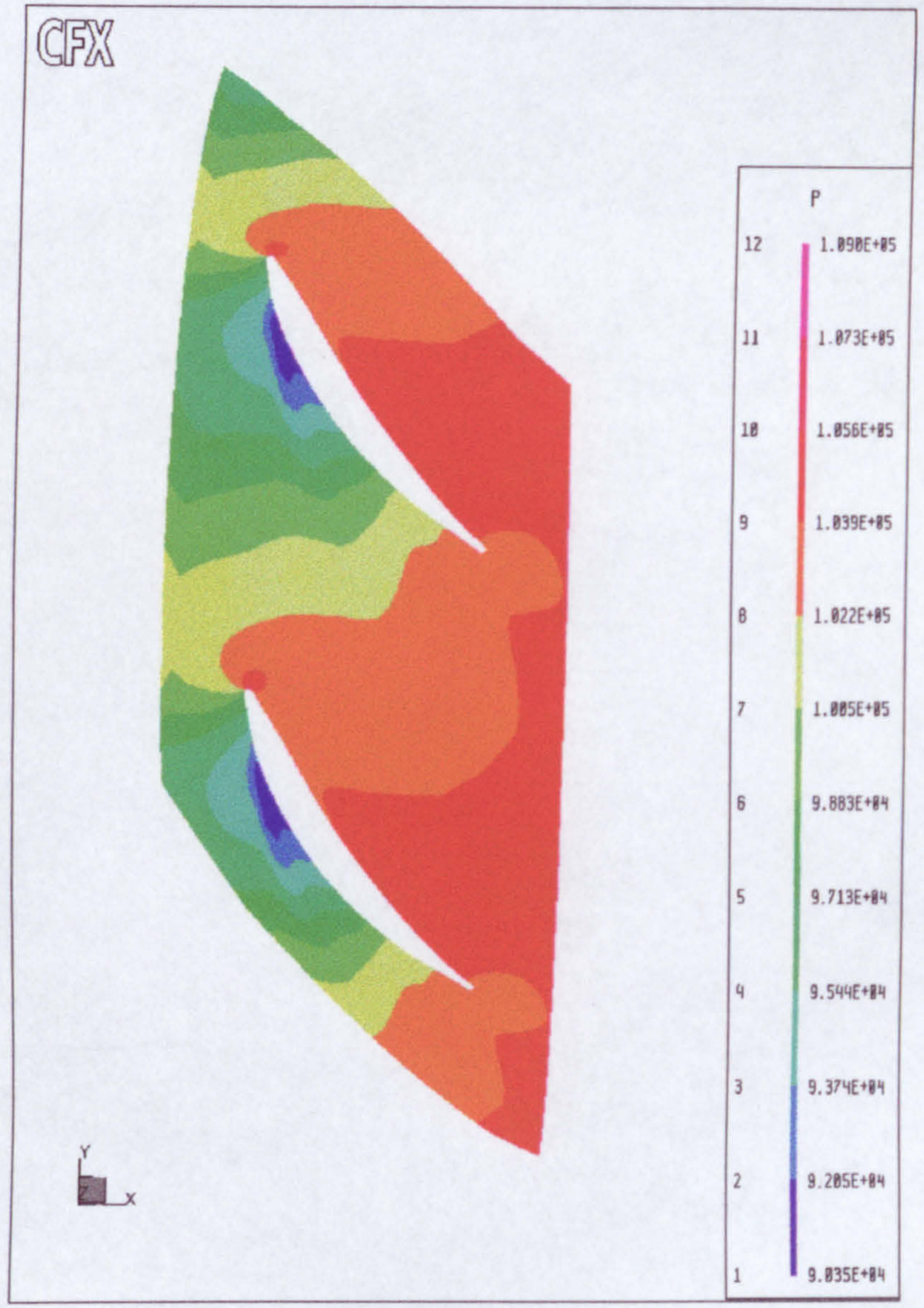


Figure 6-14b Static pressure at the tip of the original blade near design point

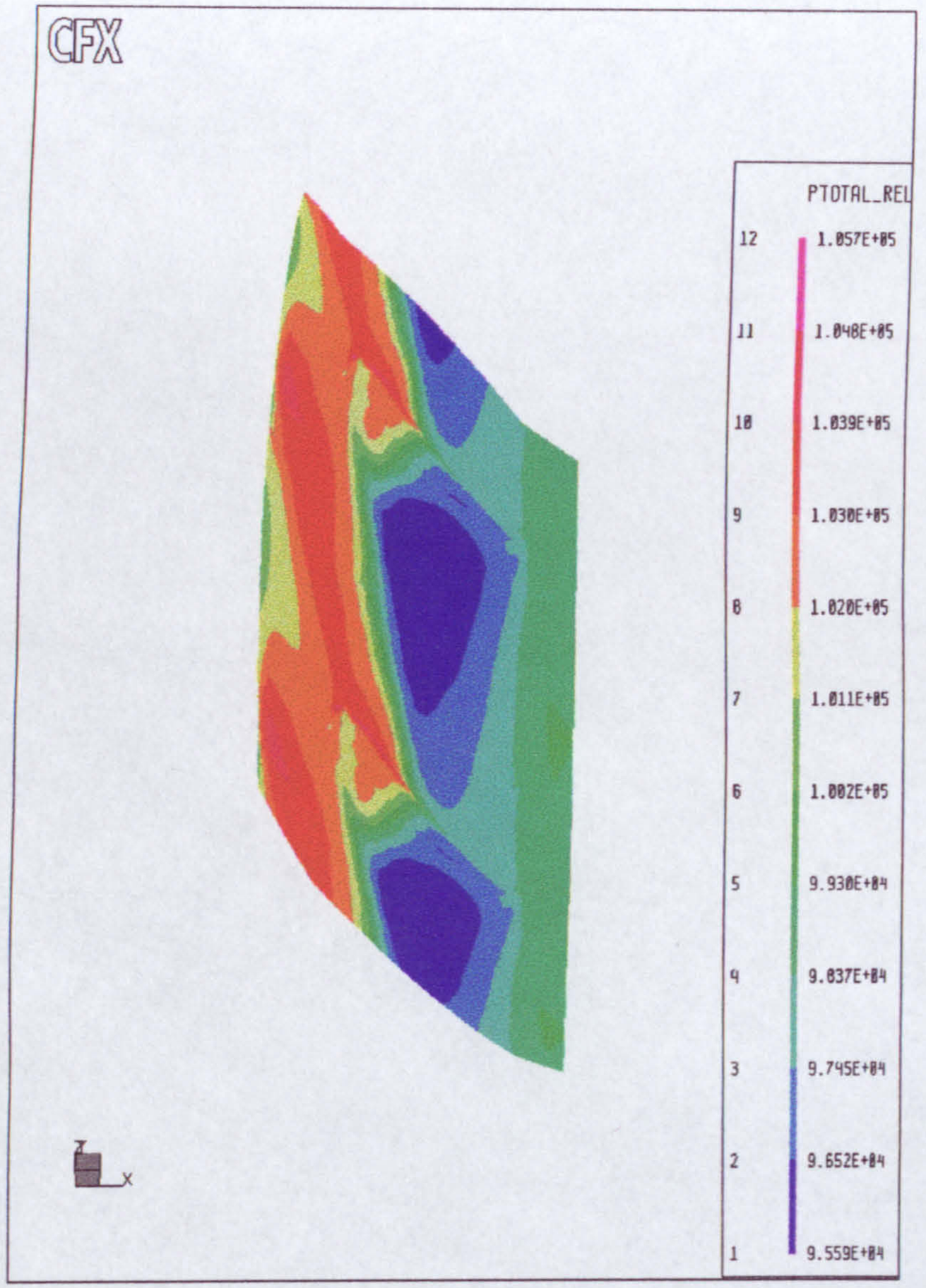


Figure 6-15a Relative total pressure in the tip region of the eroded blade at design point

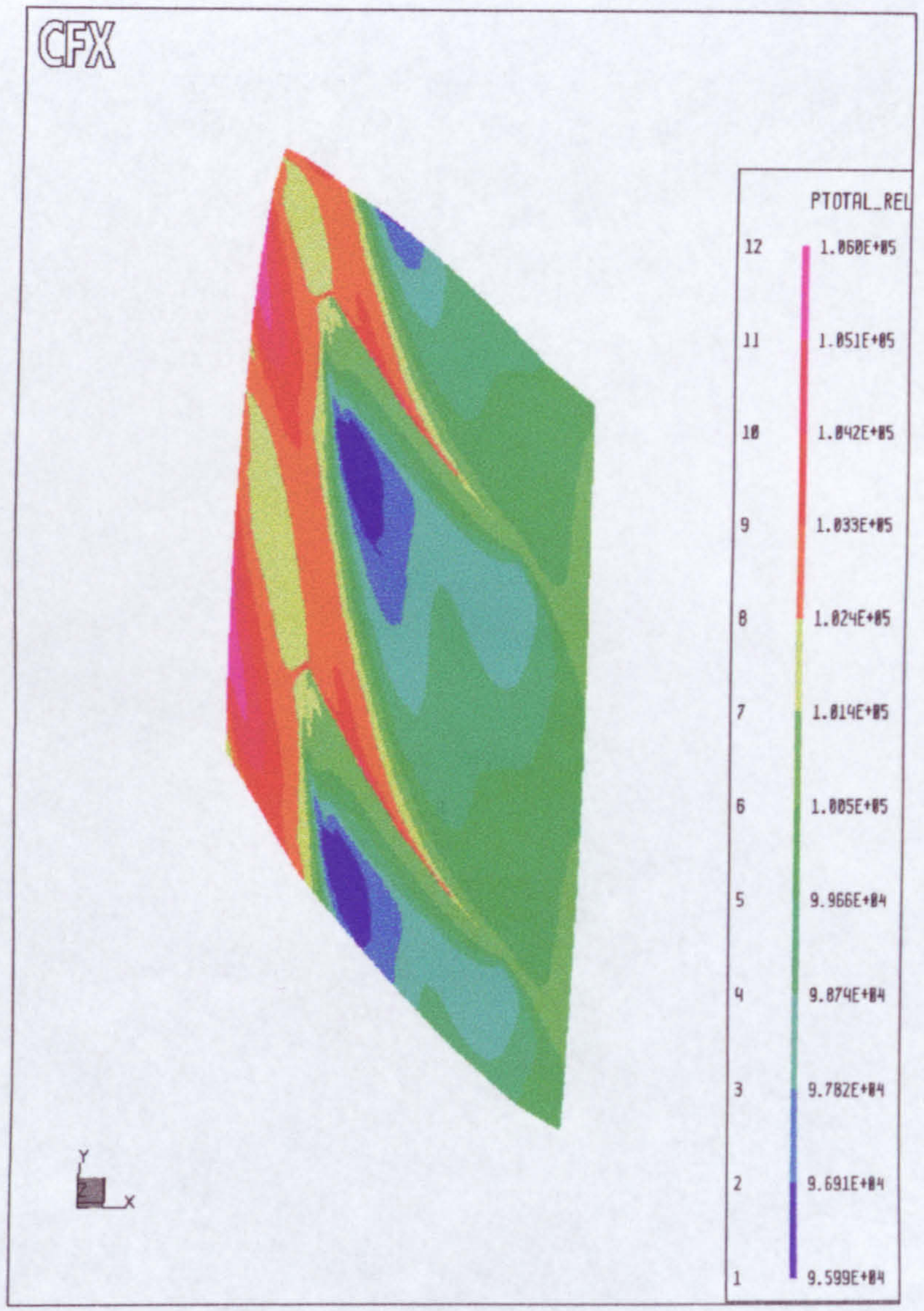


Figure 6-15b Relative total pressure in the tip region of the original blade at design point

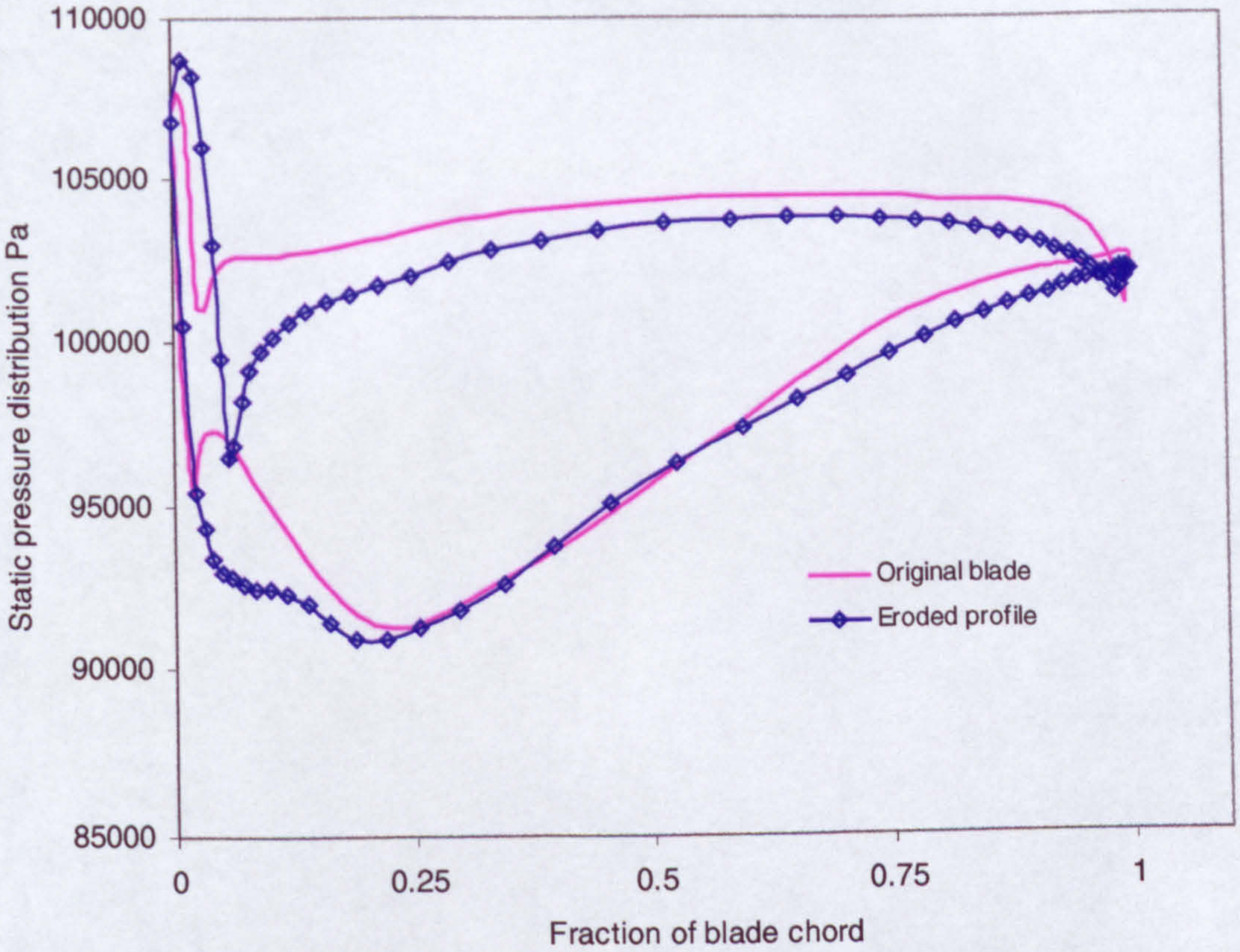


Figure 6-16a Static pressure distribution around mid span section near design point for the original and eroded profile

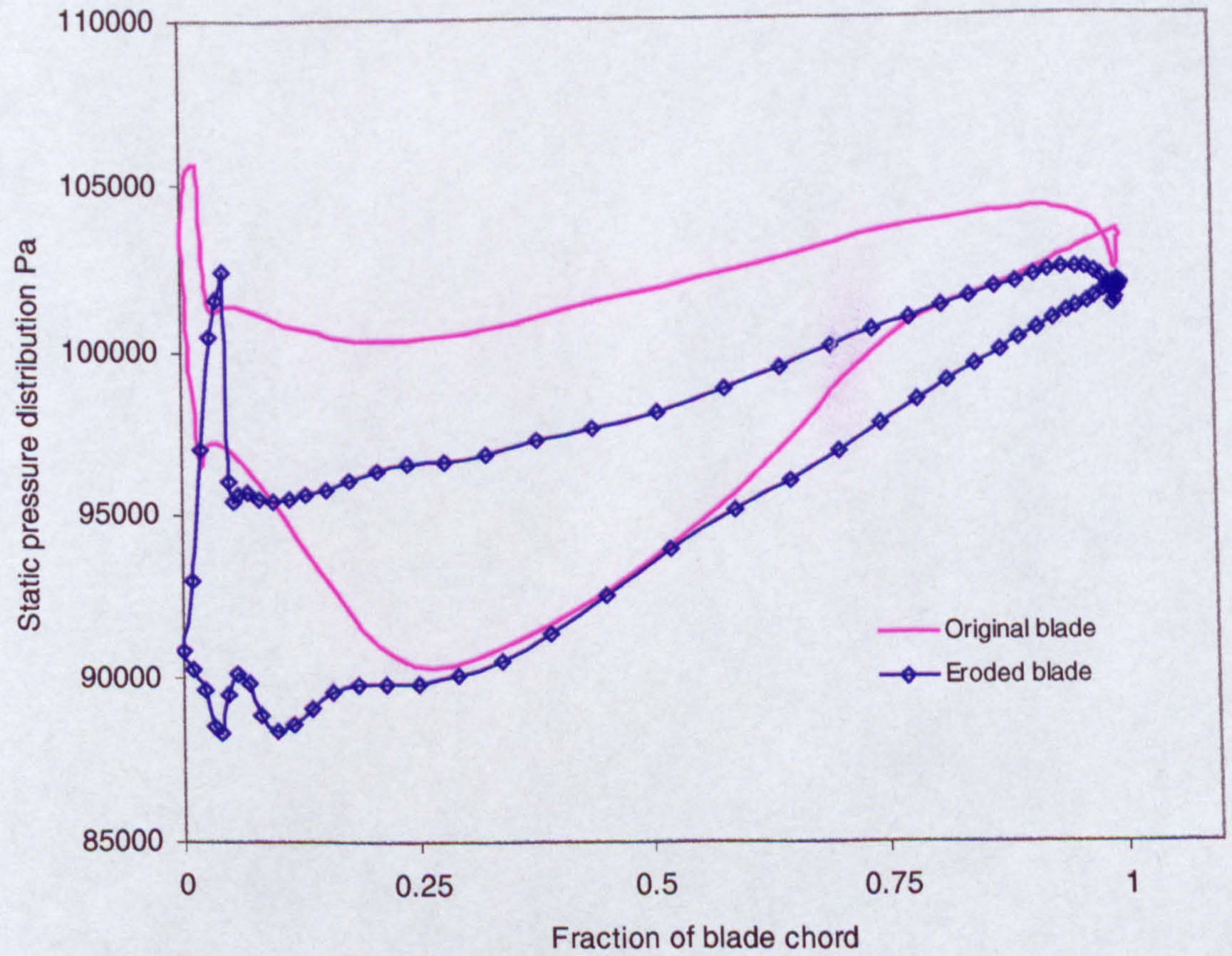


Figure 6-16b Static pressure distribution around tip section near design point for the original and eroded profile

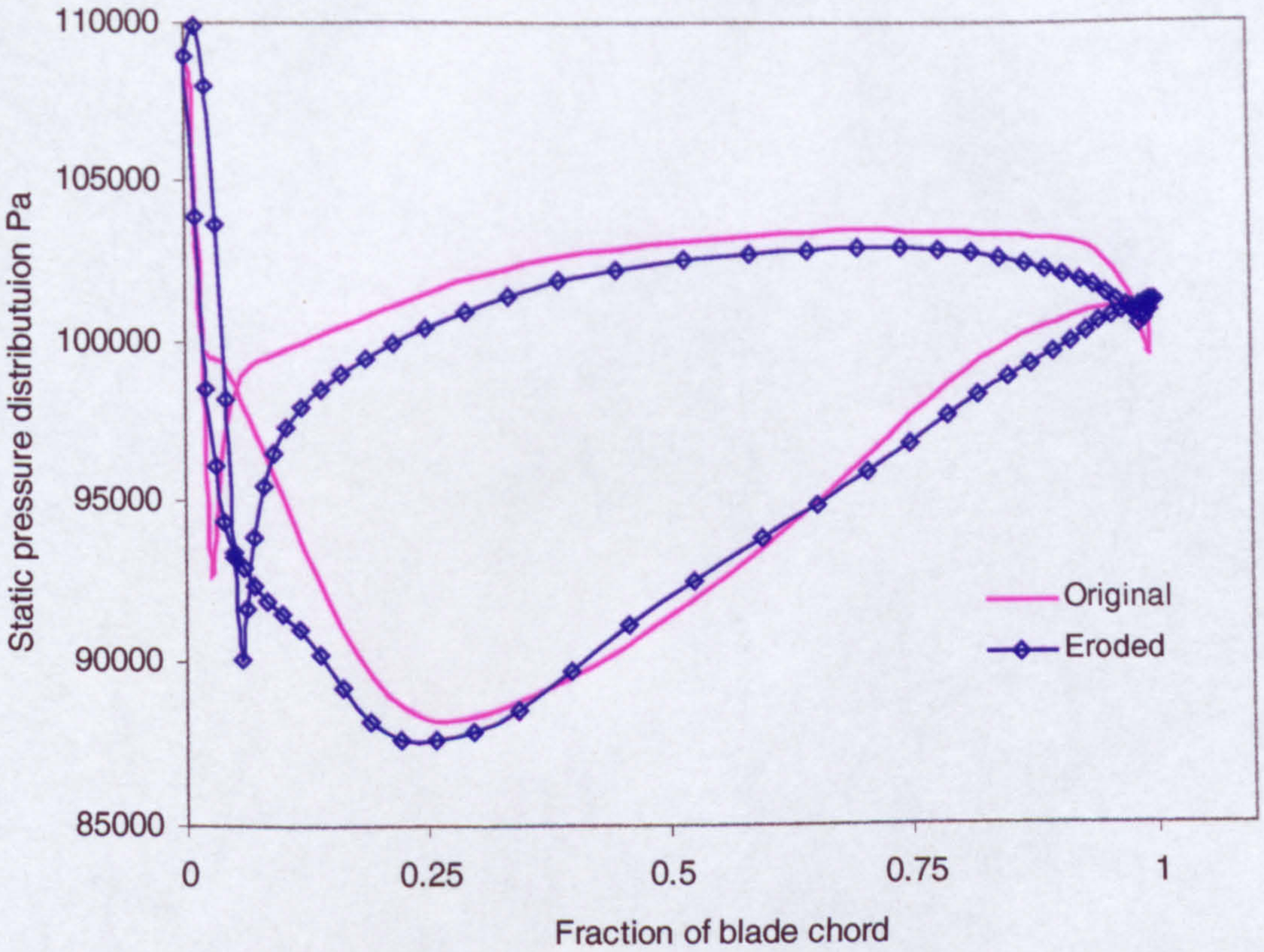


Figure 6-17a Static pressure distribution around mid span section at high mass flow for the original and eroded profile

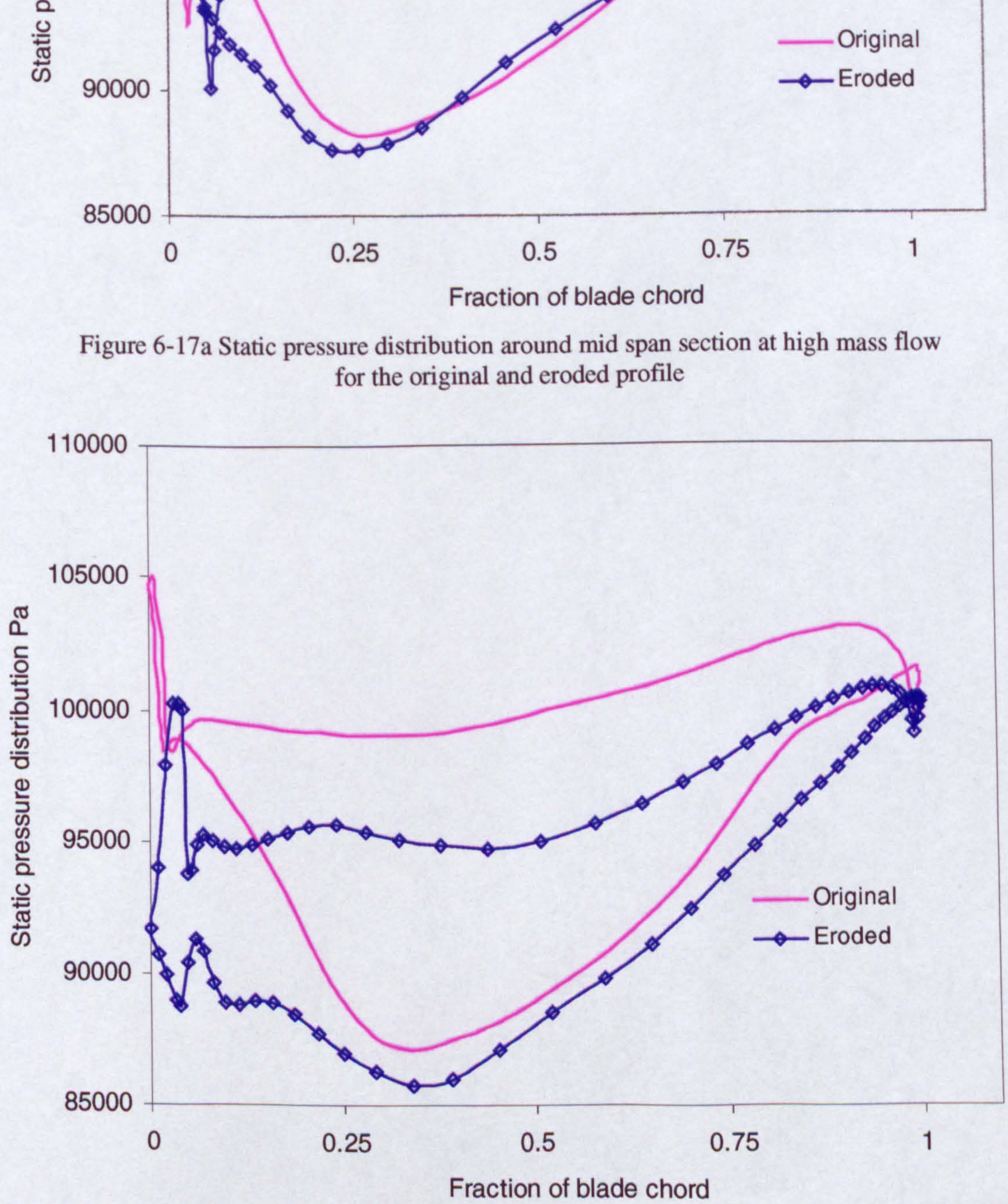


Figure 6-17b Static pressure distribution around tip section at high mass flow for the original and eroded profile

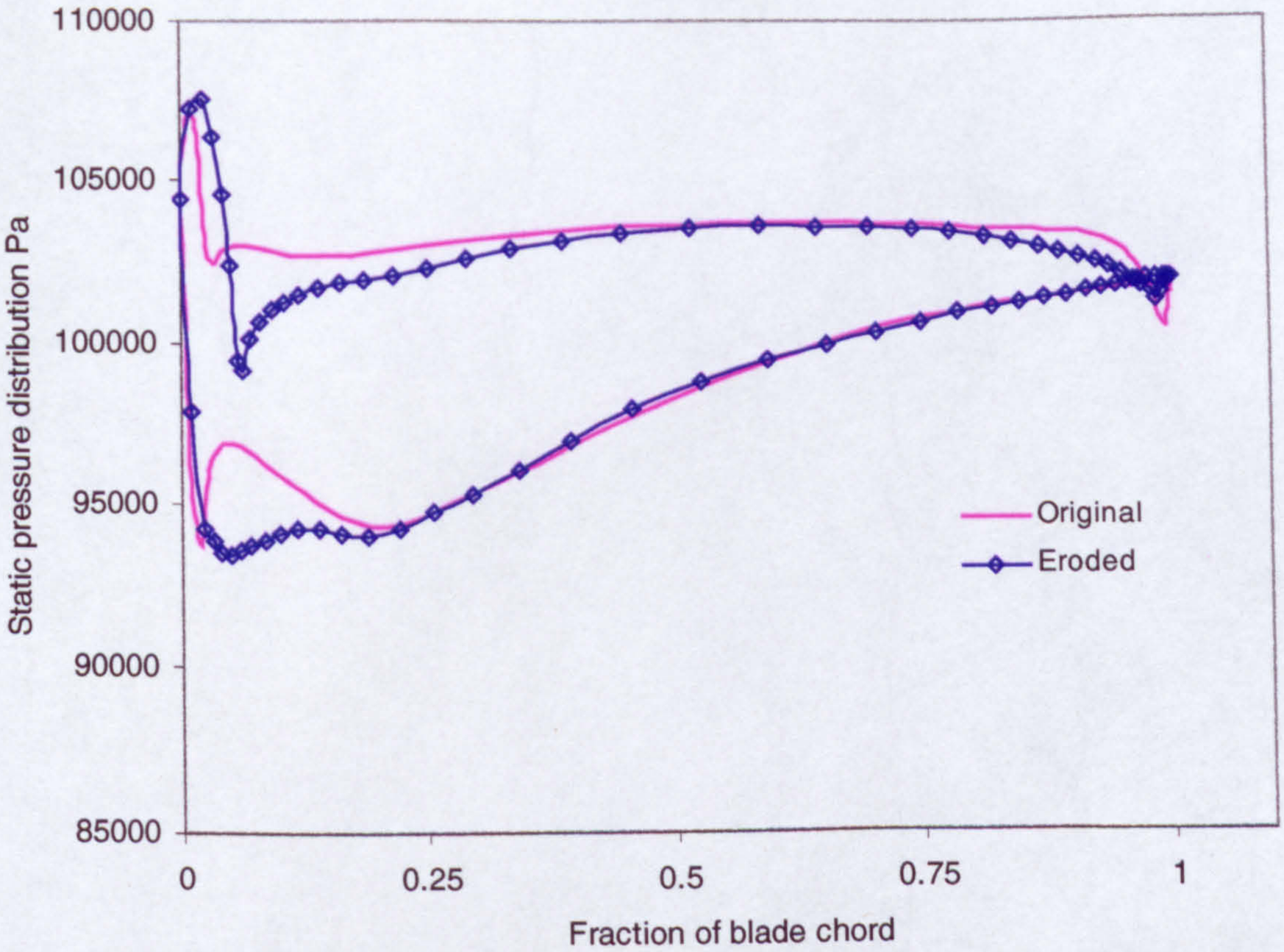


Figure 6-18a Static pressure distribution around mid span section near stalling mass flow for the original and eroded profile

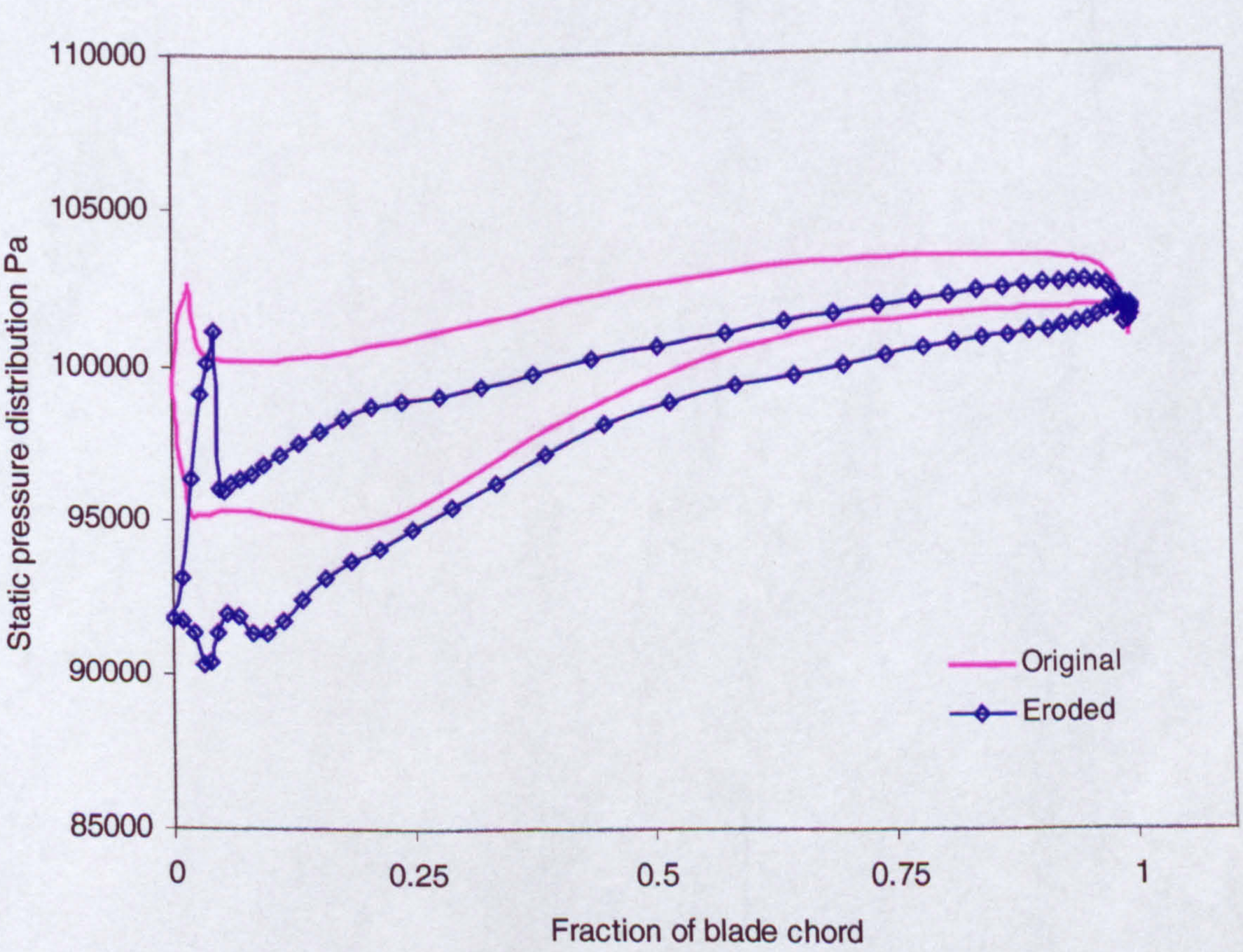


Figure 6-18b Static pressure distribution around mid span section near stalling mass flow for the original and eroded profile

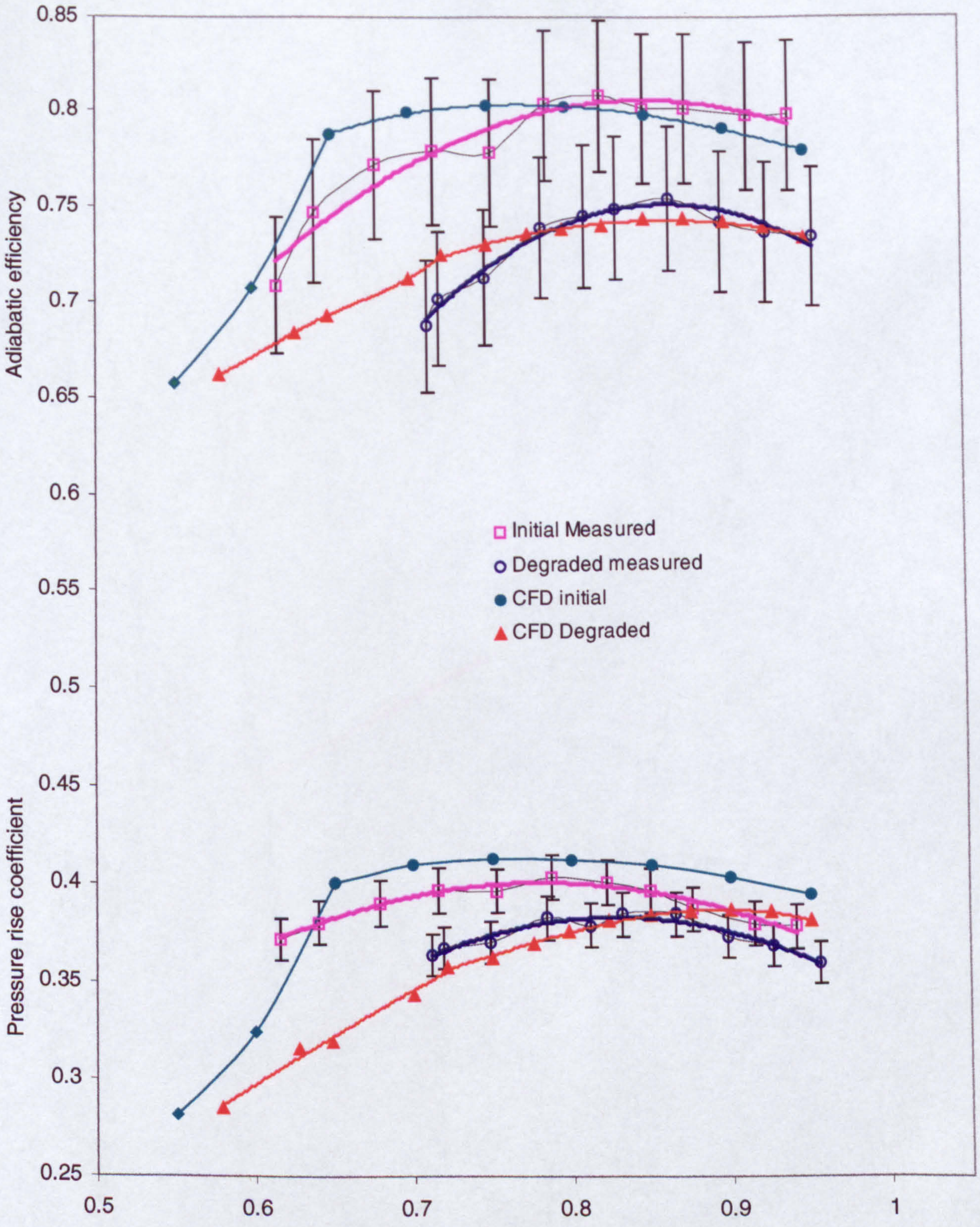


Figure 6-19 Comparison between CFD and measured performance degradation

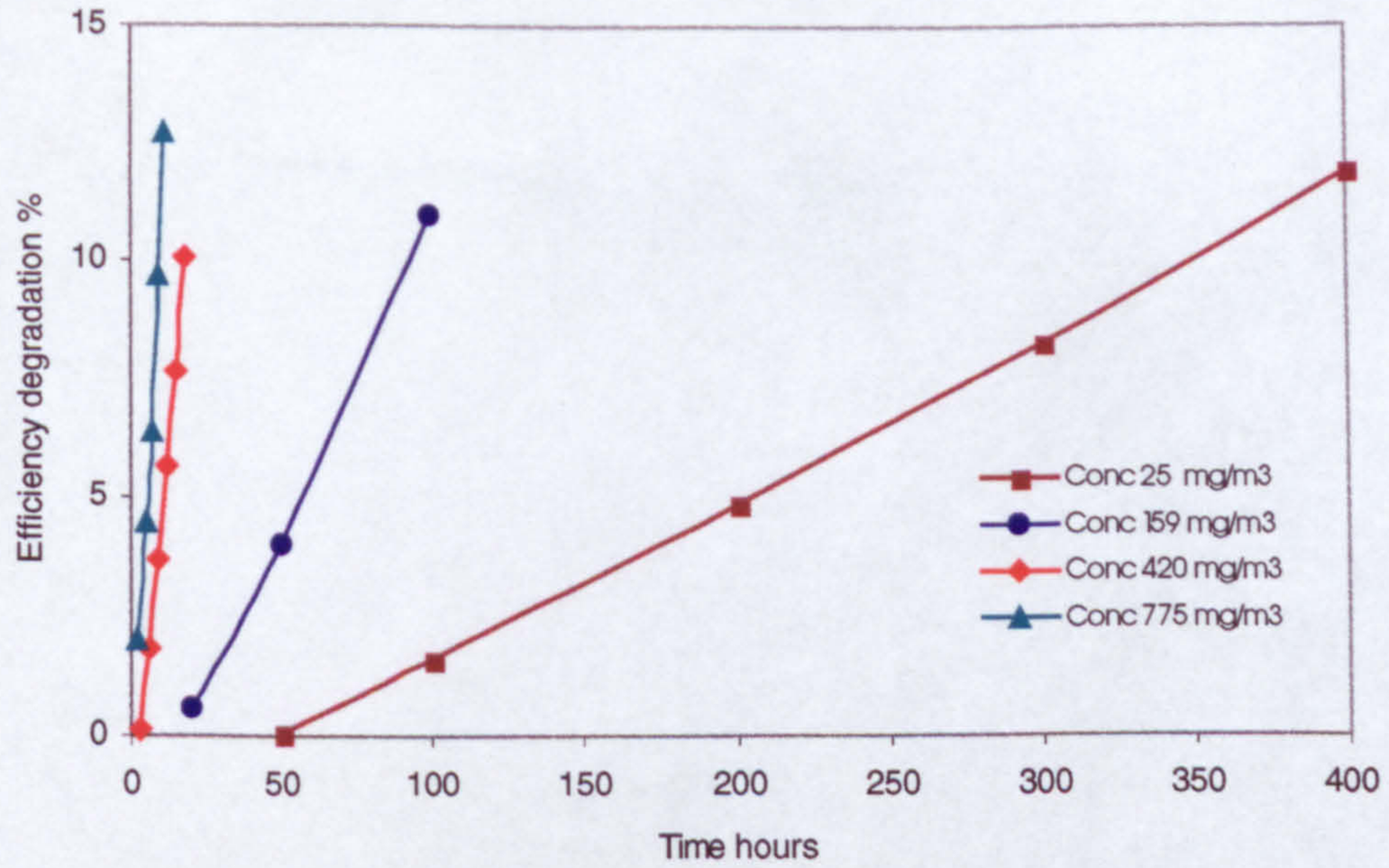


Figure 6-20 Efficiency degradation of the rotor (aluminium) with time at different concentrations

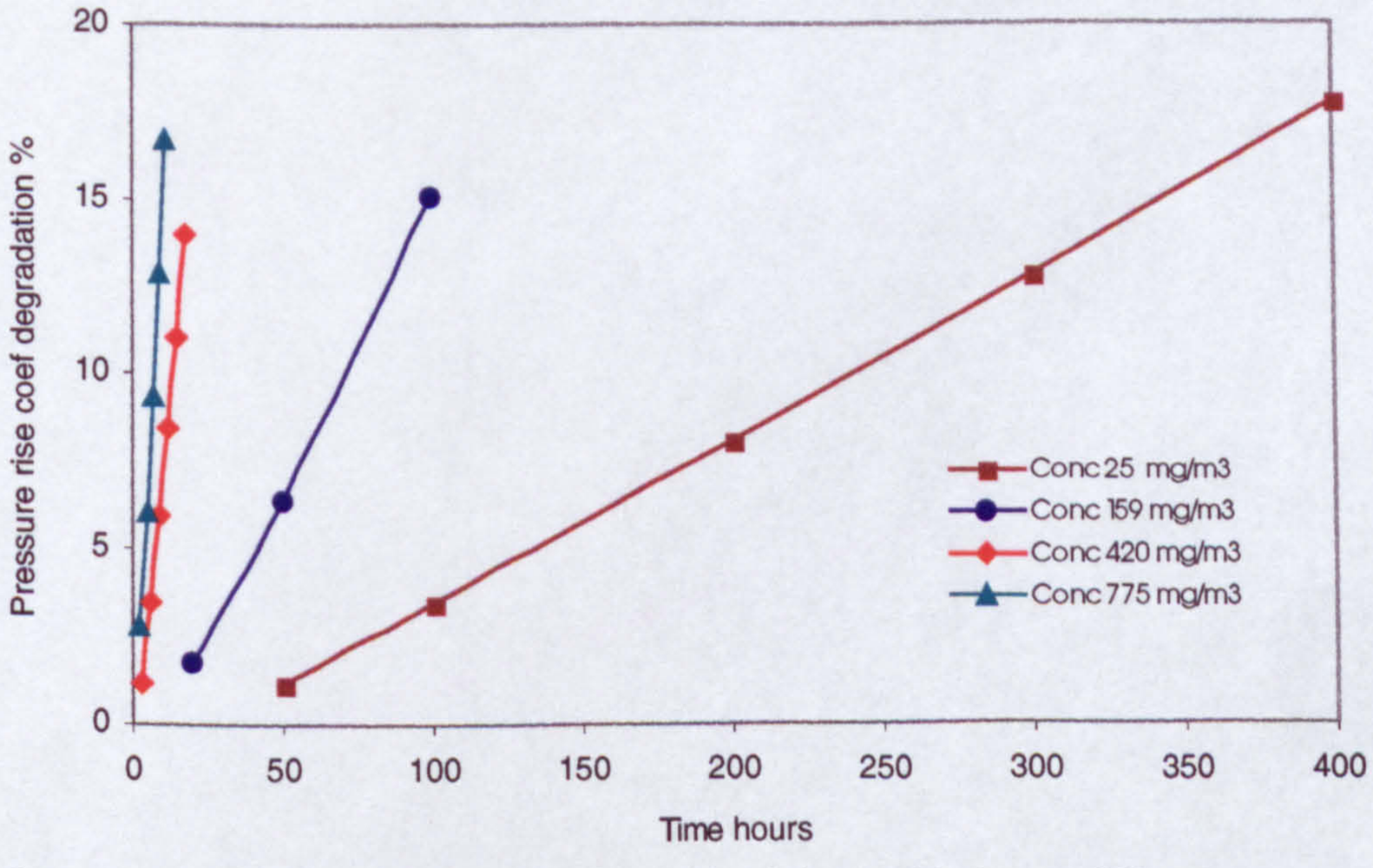


Figure 6-21 Pressure rise degradation of the rotor (aluminium) with time at different concentrations

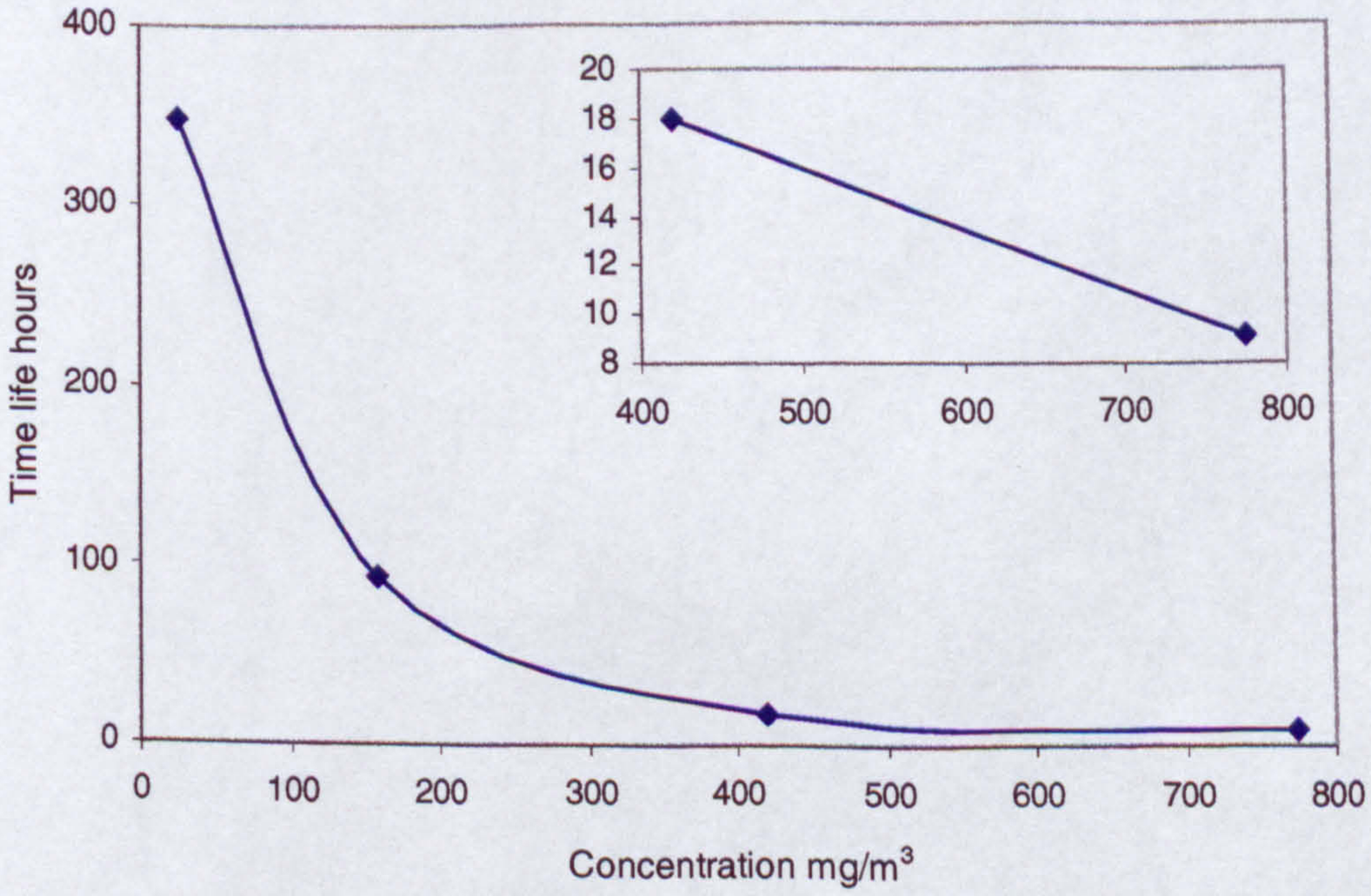


Figure 6-22 Predicted life-time of the rotor (aluminium) with MIL-E 5007E sand concentration

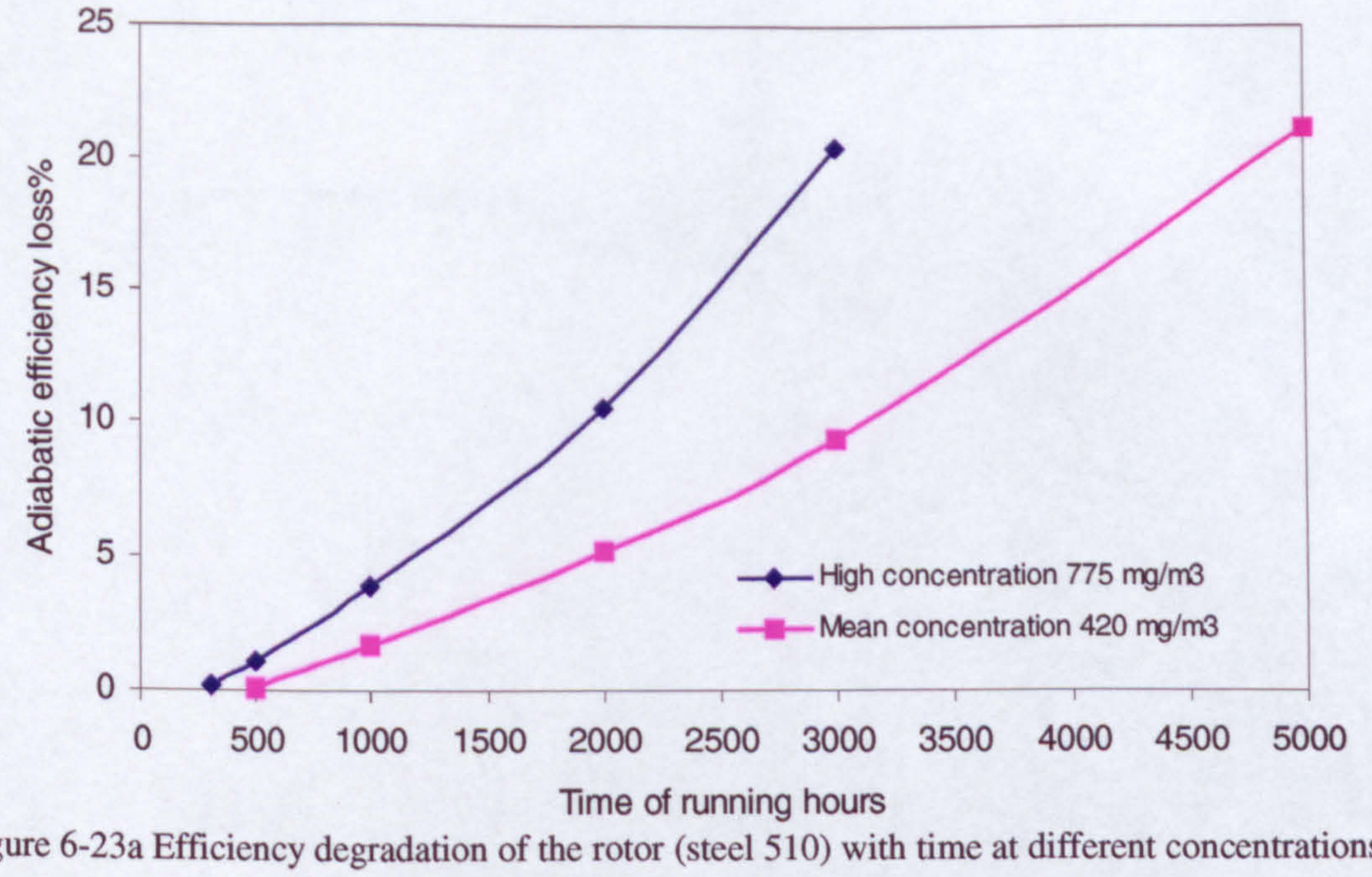


Figure 6-23a Efficiency degradation of the rotor (steel 510) with time at different concentrations

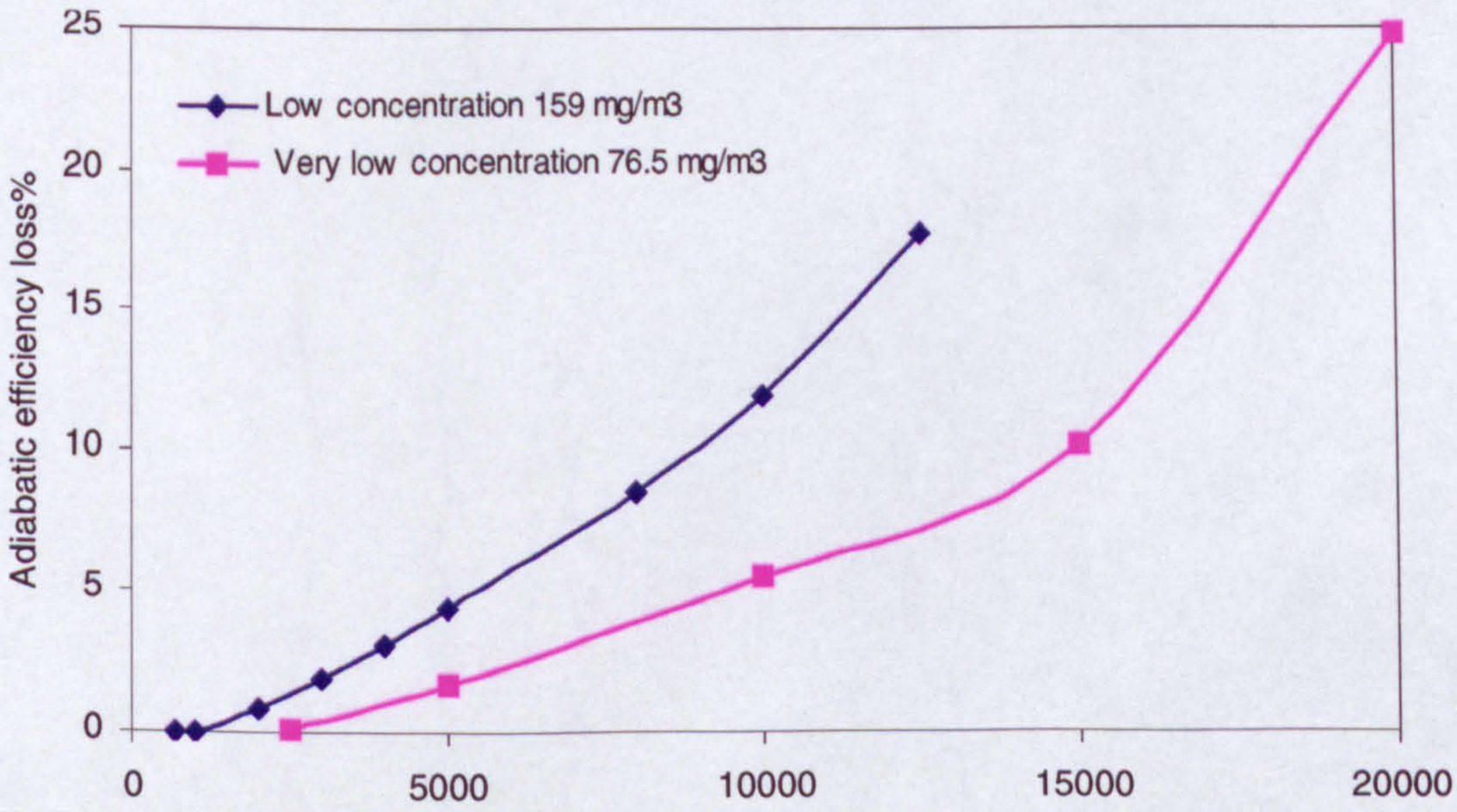


Figure 6-23b Efficiency degradation of the rotor (steel 510) with time at different concentrations

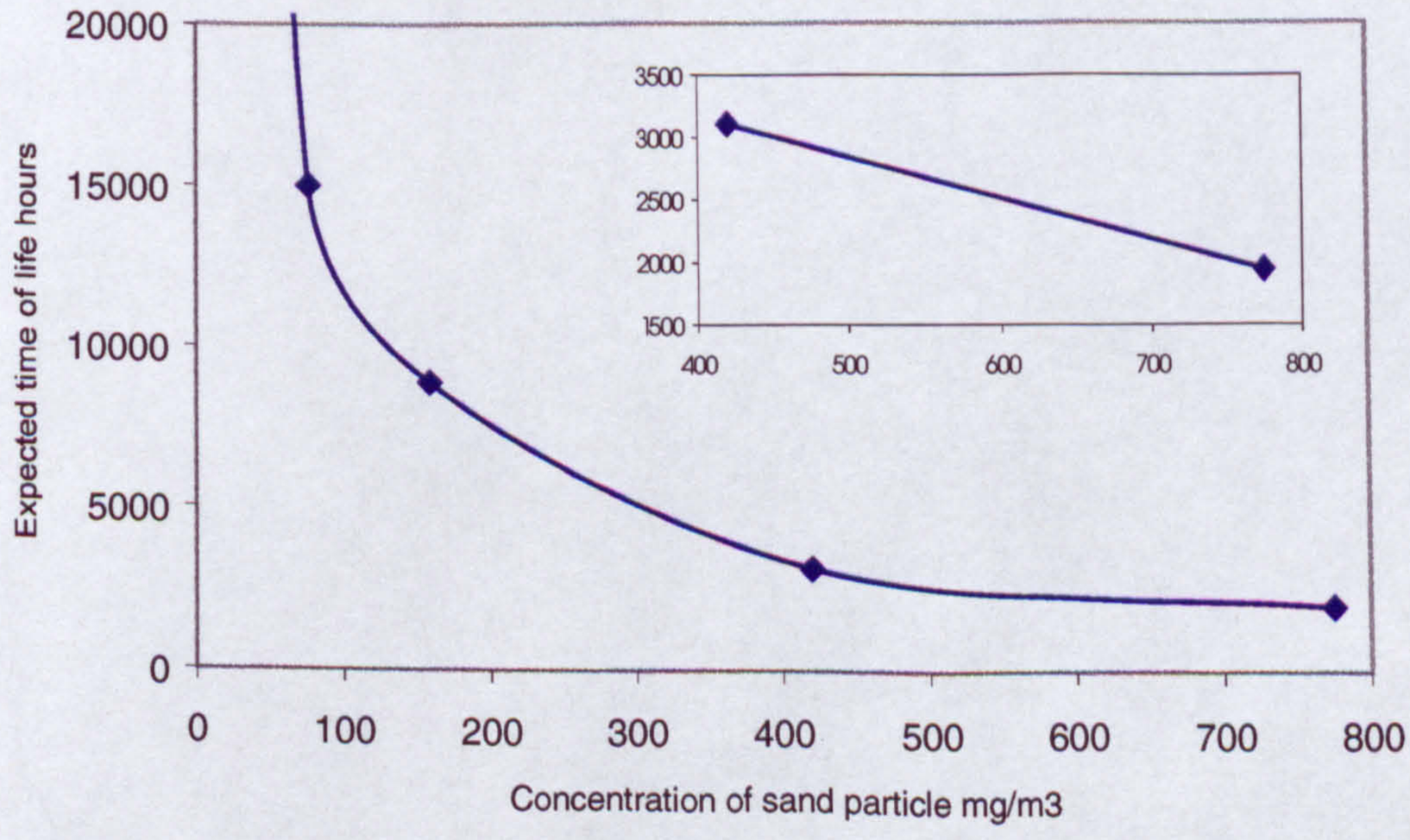


Figure 6-24 Predicted life-time of the rotor (steel 510) with MIL-E 5007E sand concentration

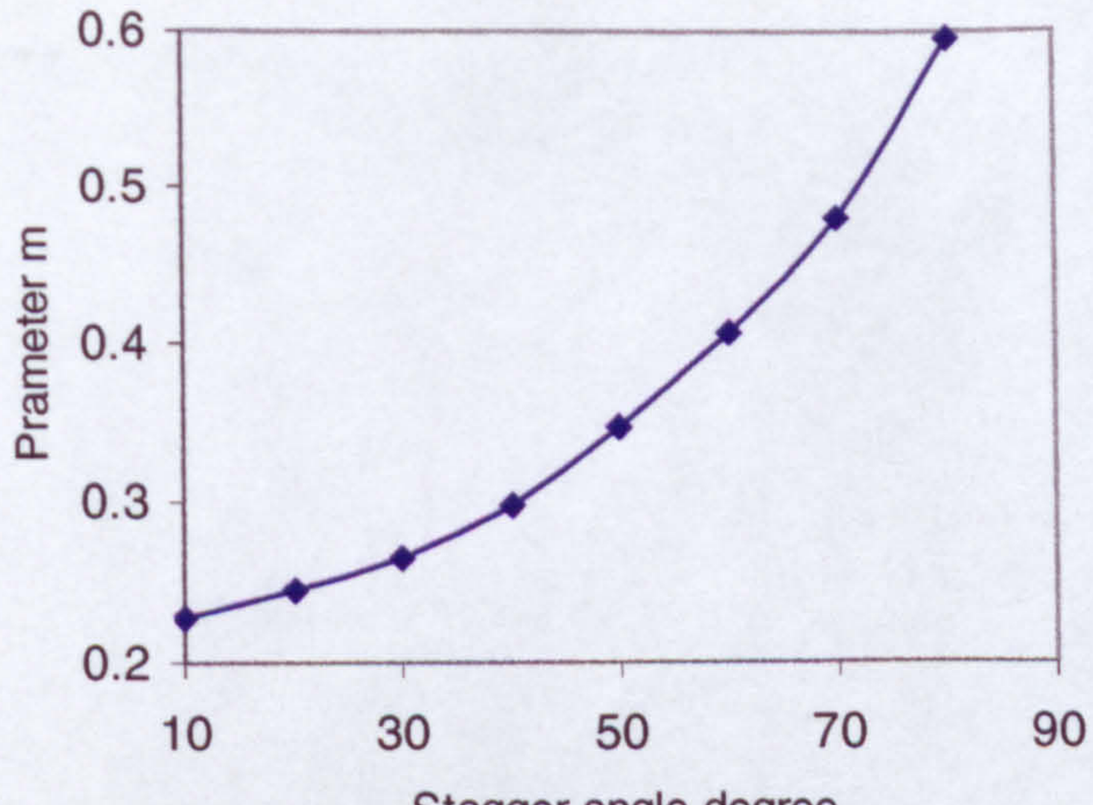


Figure M-1 Wallis extrapolation curve for m parameter

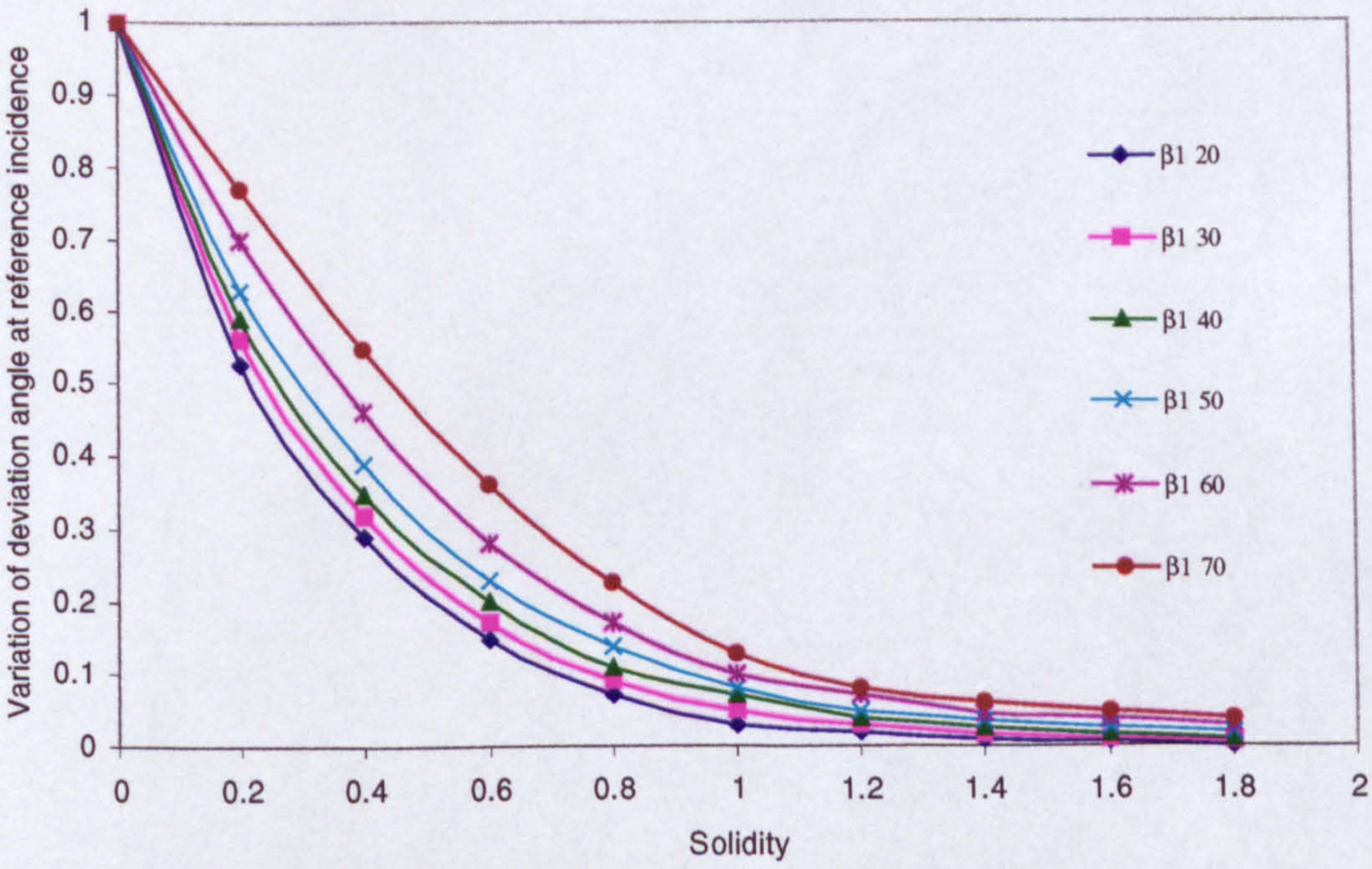


Figure M-2 Slope of deviation angle with inlet flow angle and solidity

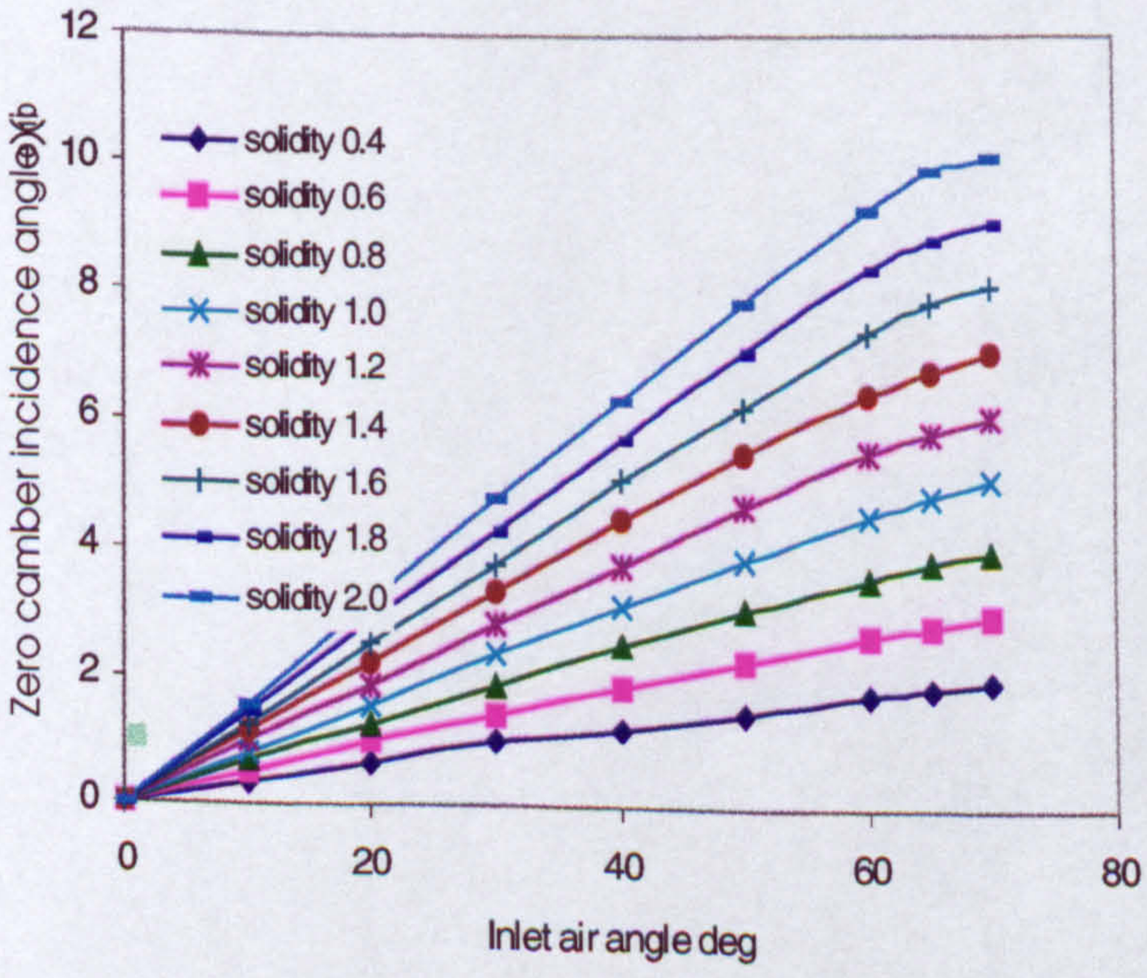


Figure M-3 Zero camber incidence angles

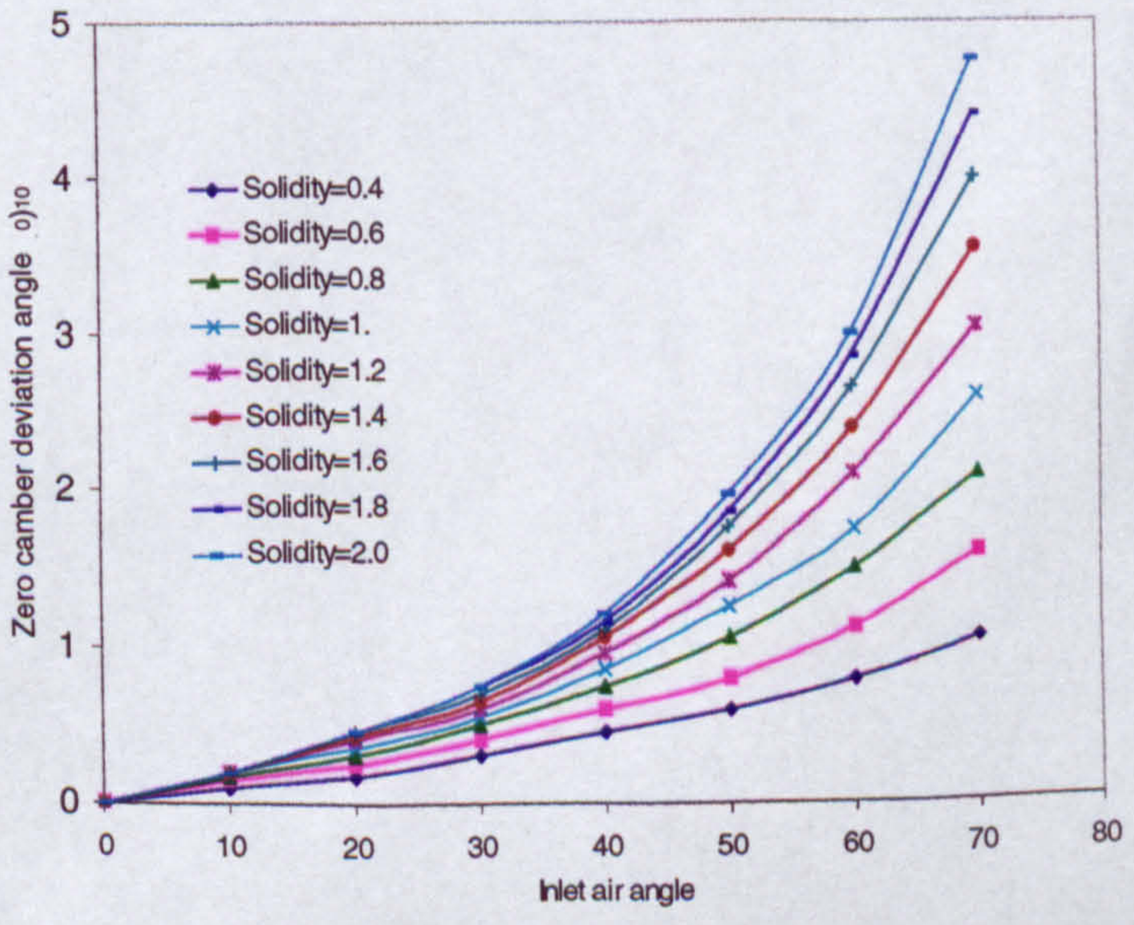


Figure M-4 Zero camber deviation angles

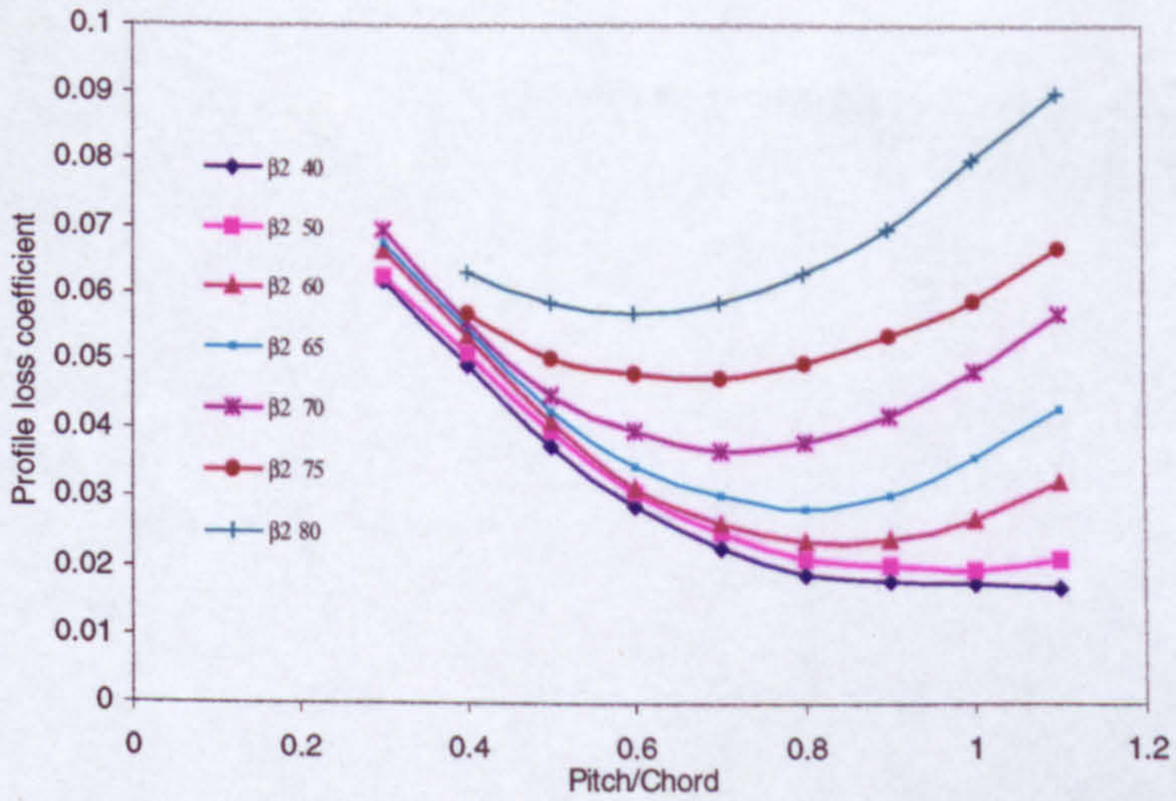


Figure M-5 Ainely Profile loss coefficient

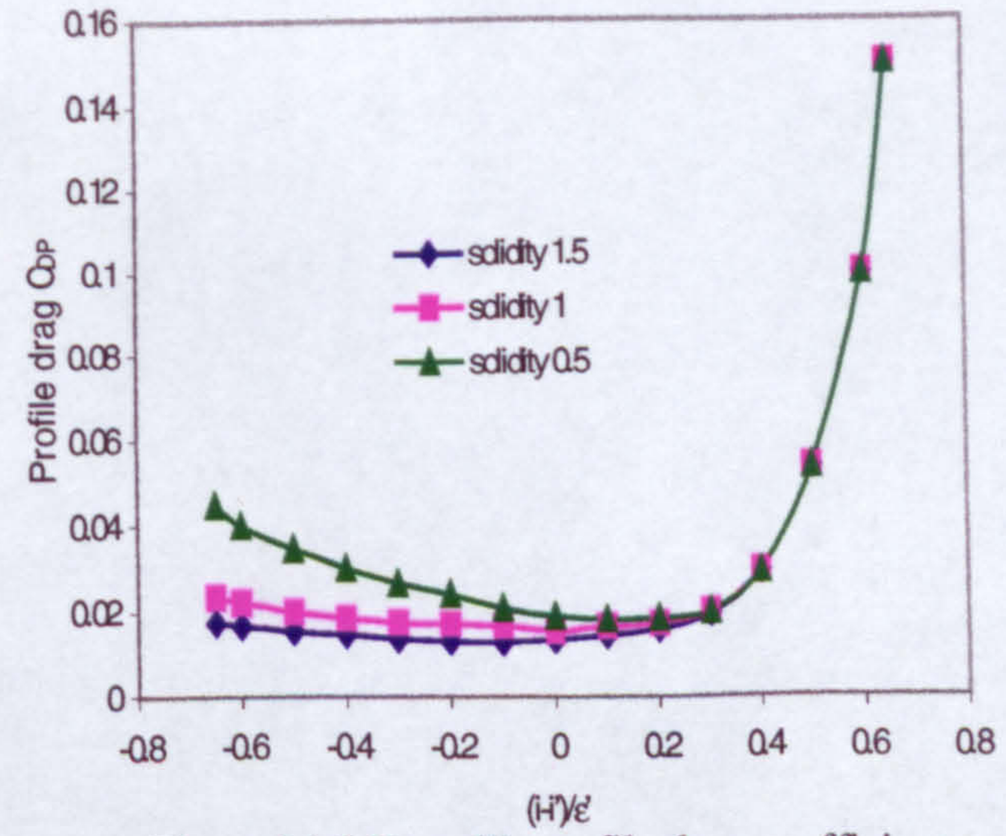


Figure M-6 Howell's profile drag coefficient

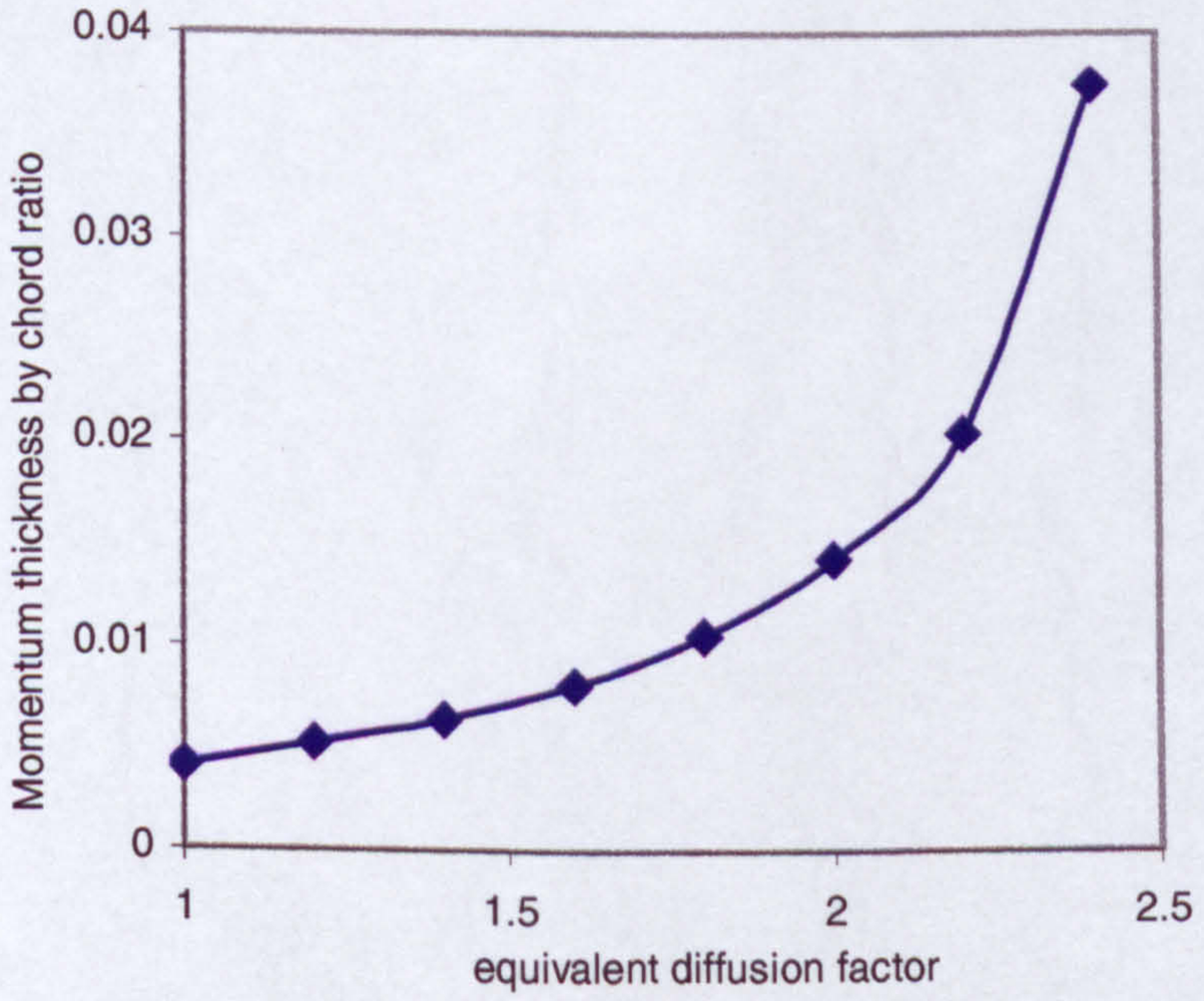


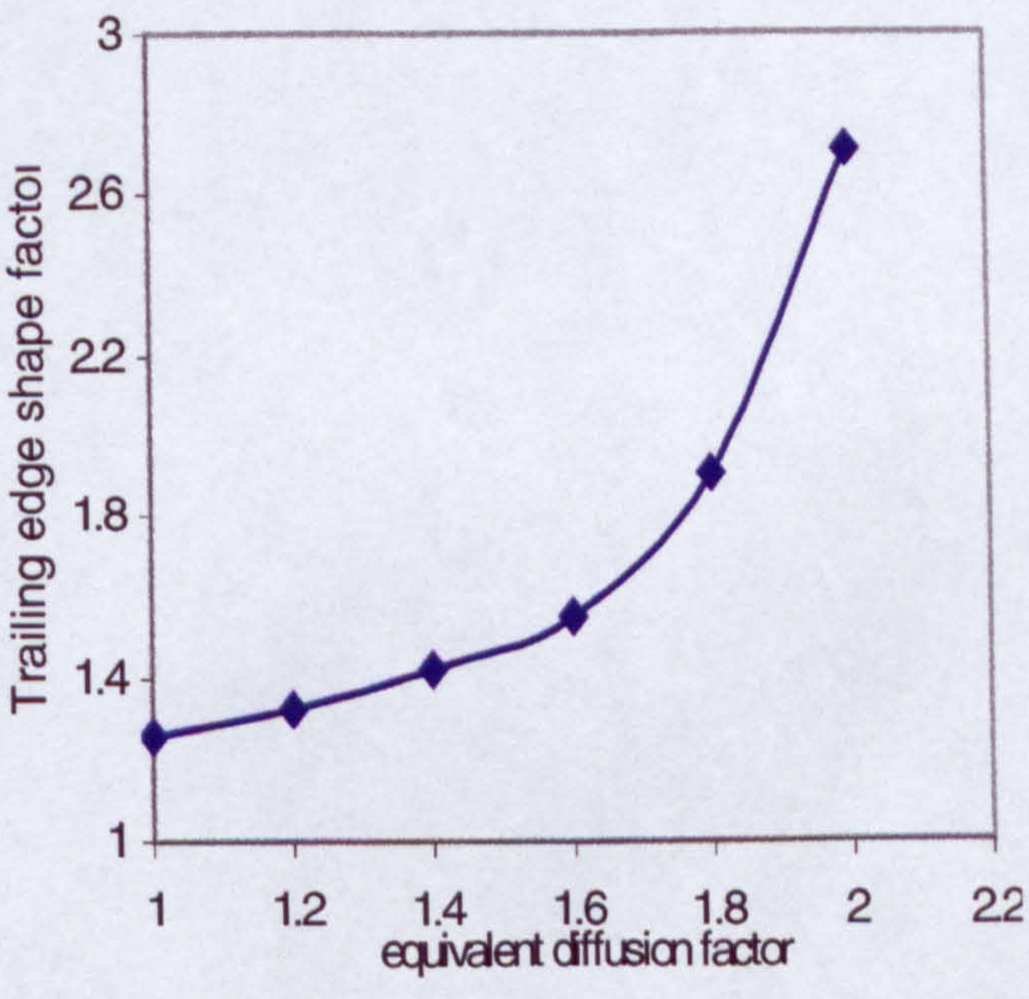


Figure M-7 Profile loss correlation based on momentum thickness

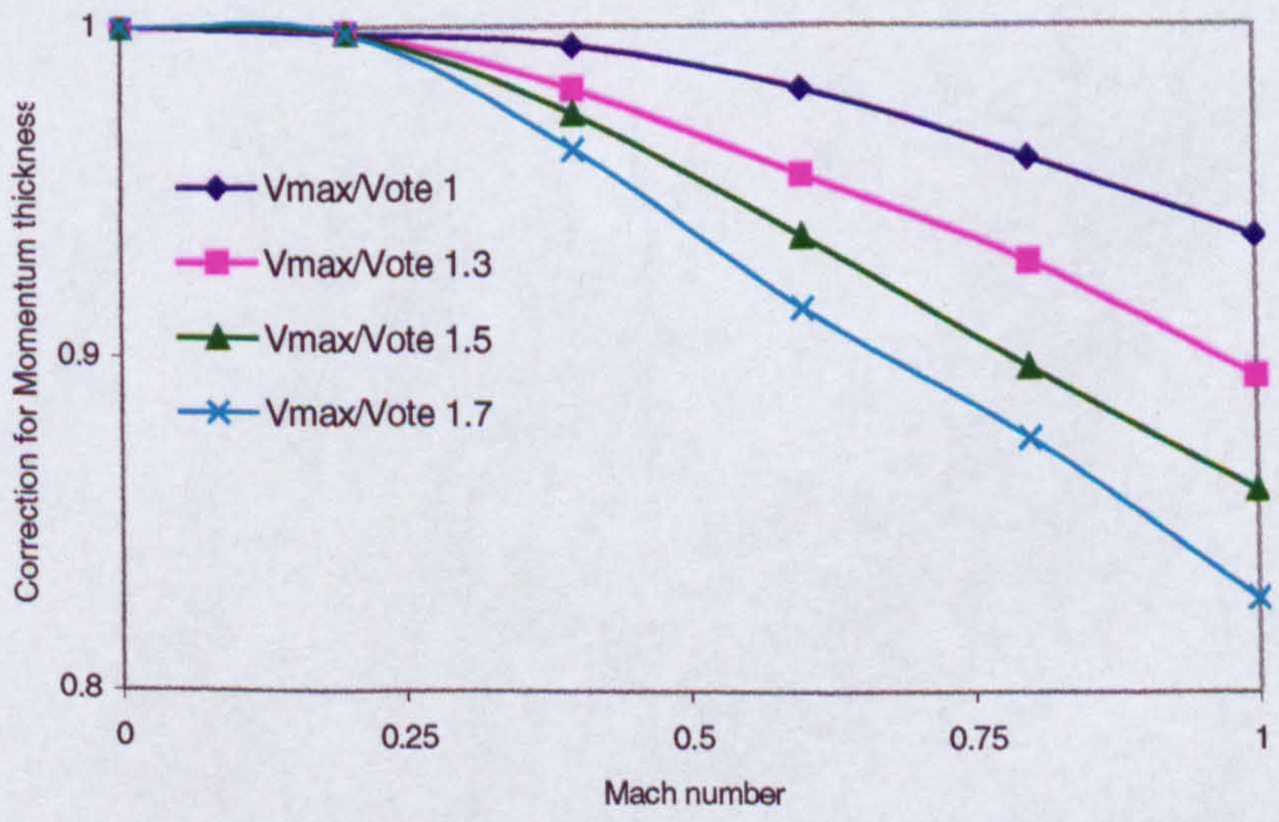


Figure M-8 Correction factor for momentum thickness

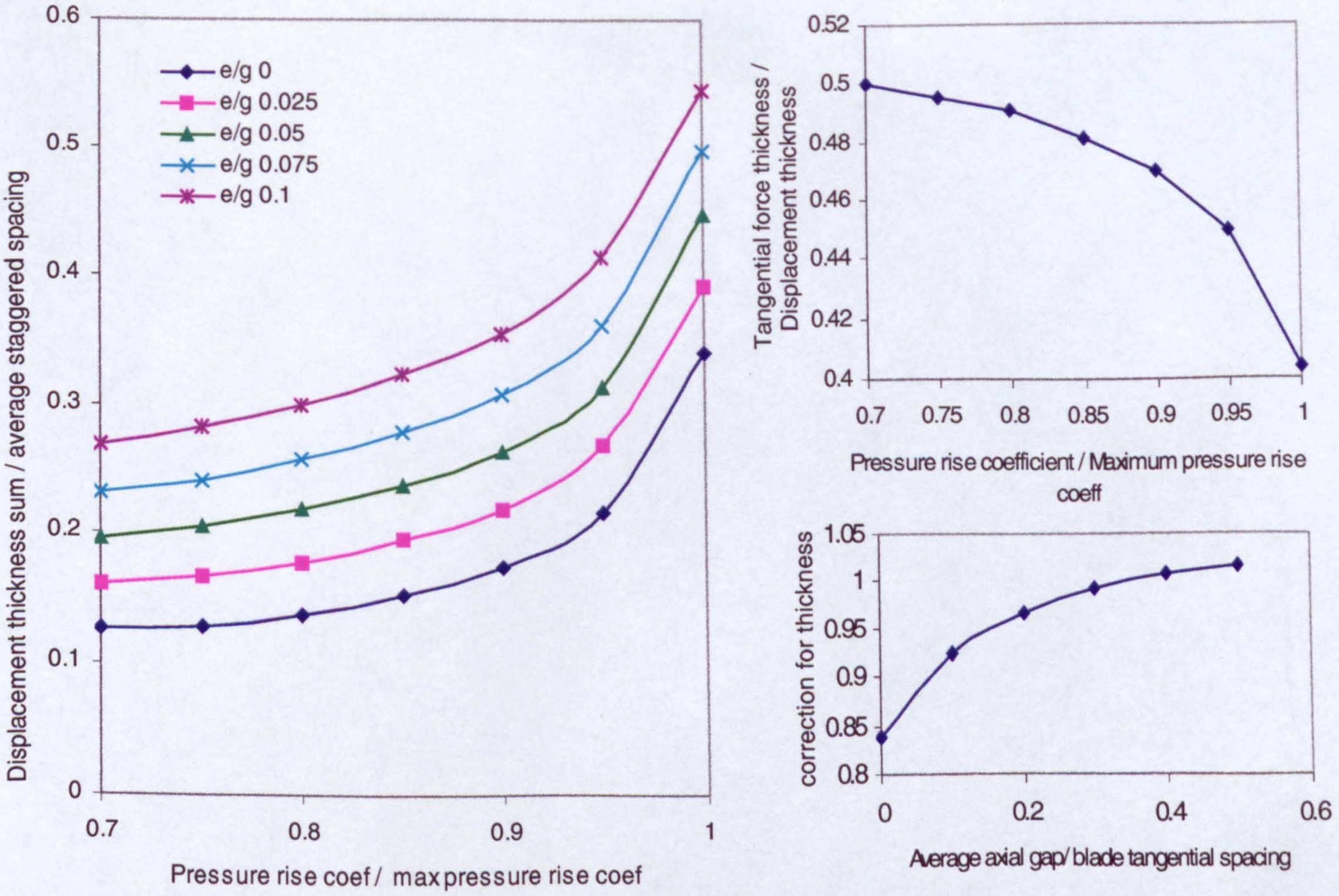


Figures M-9 Koch and Smith graphical correlations for end-wall losses

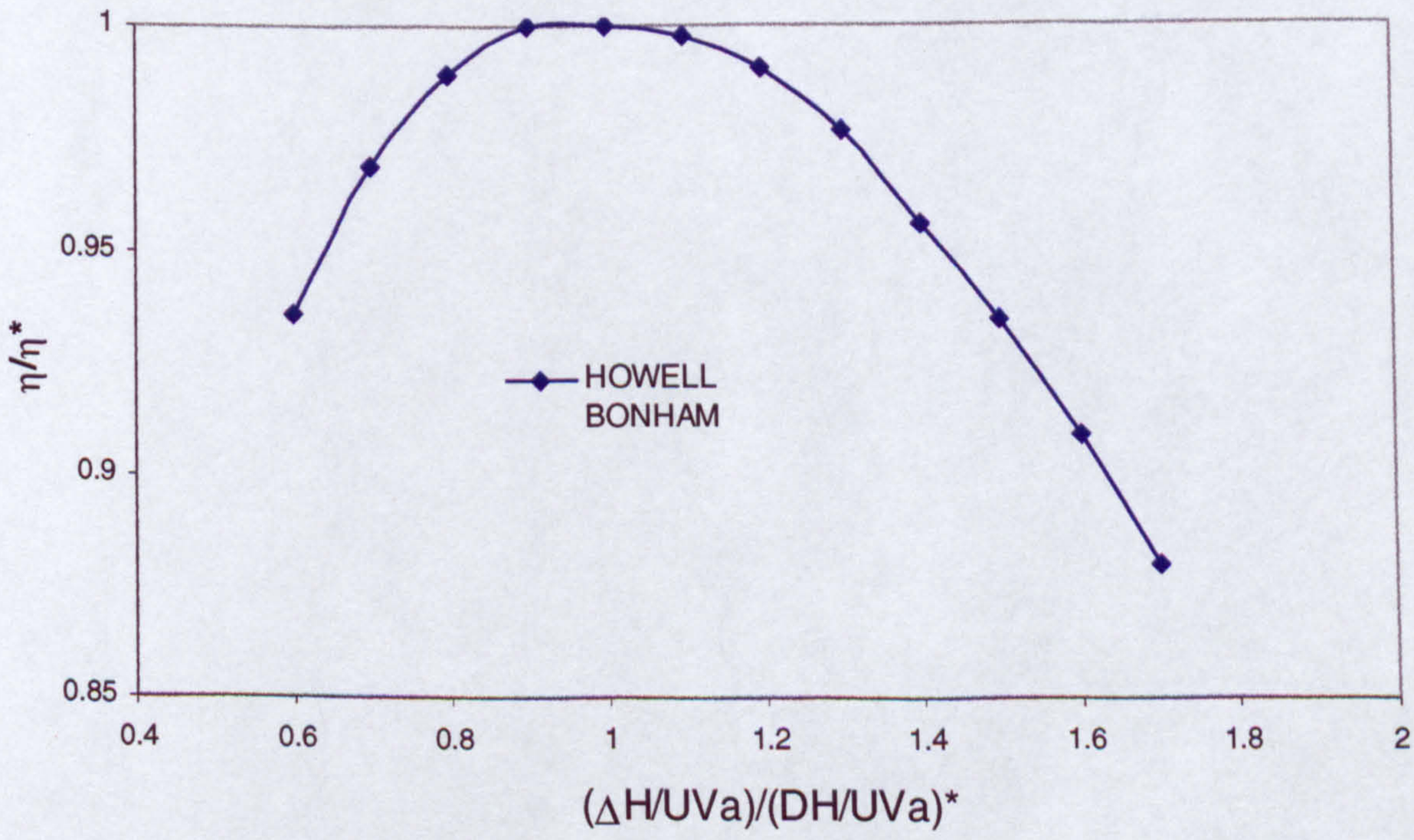


Figure M-10 Howell - Bonham off design characteristic

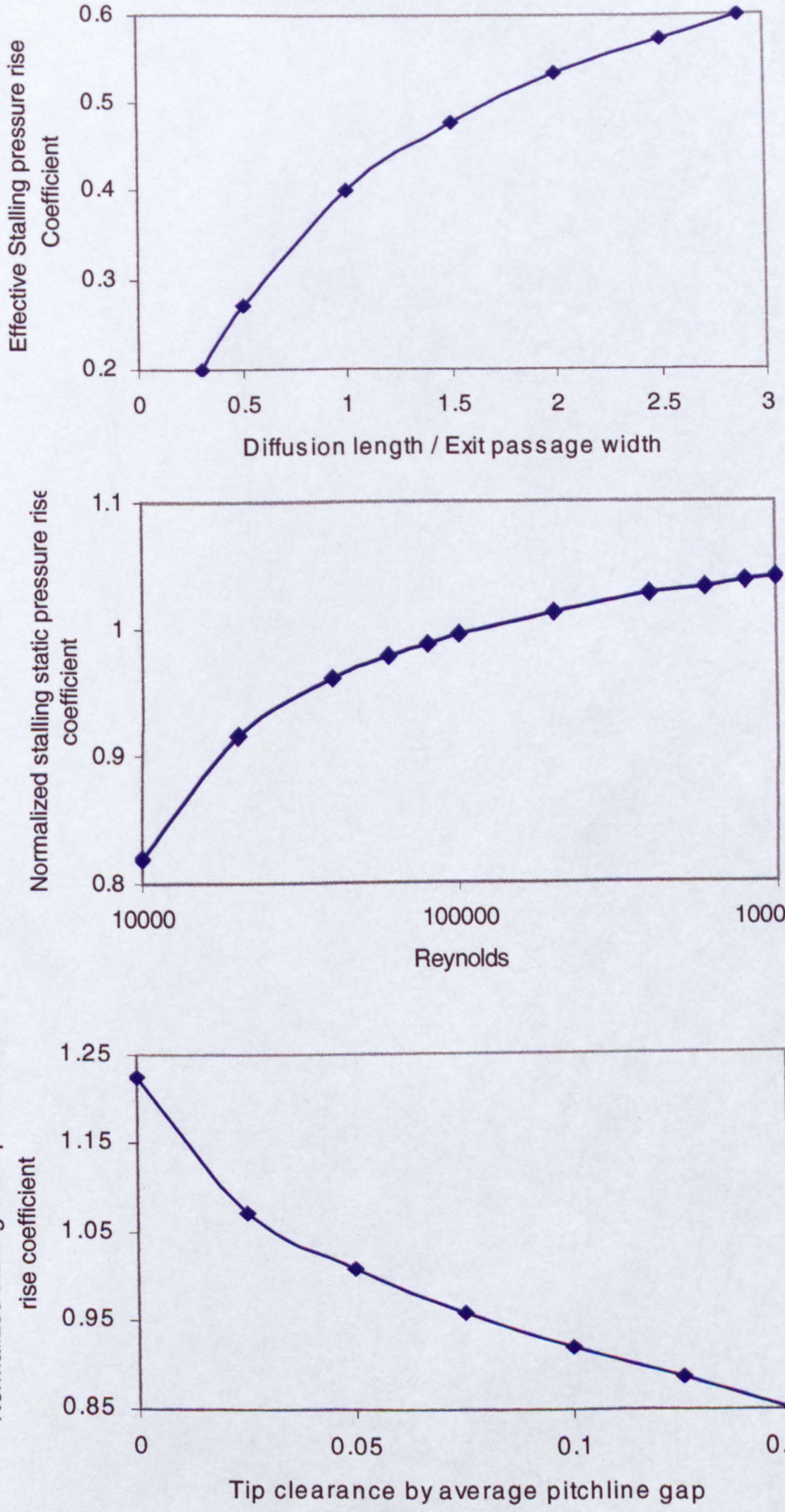


Figures M-11 Koch correlations for stall onset prediction

# TABLES

Table 3-1 *COMMB* file containing different control parameters and memory allocations and the common variables passed through different subroutines

```
      parameter(ipb=35,jpb=29,kpb=24)
      parameter(ips=60,jps=39,kps=24)
      parameter(ipr=60,jpr=39,kpr=30)
      parameter(ipj=40,jpj=29,kpj=50)
      parameter(ielems=191988)
      parameter(inodin=35*29*24)
      parameter(inodstat=60*39*24)
      parameter(inodrot=60*39*30)
      parameter(inodout=40*29*50)
      parameter(ing=195,jng=39,kng=50)
      parameter(iinlet=ielems)
      parameter(inodes=208720)
      parameter(iptles=5000)
      parameter(impact=200,icrash=impact*iptles)
      parameter(iresult=750000)
      parameter(ivortx=30000)
      parameter(iplane=1)
      parameter(ipdia=1)
      parameter(ibins=iptles*ipdia)
      parameter(ifvar=8)
      parameter(iden=1)

       common nop,pi,vratio(3),msect(2),mss1(2),mss2(2),mss3(2),
     +mss4(2),mss5(2),mss6(2),mss7(2),mss8(2),area(inodes),alfdif,
     +ttarea,dratio,theta,r,z,vr,vt,vz,vrf,vtf,vzf,rhof,tke,epsilon,
     +nside,visco,const,dia,dt,ddt,nin2(6),ndpt,irem,istep,rho,cfactr,
     +nduct,rlimit,zlimit,teta,omega,factm,nelmntb,nelmntj,ertime,kdis,
     +nelmnts,nelmntr,dialimit,tiplimit,xmtot,xmasigv,xmasrot,dmean,
     +sigma,avden,cmean,cv1,cv2,betao,volrot,voligv,inject,ifrag,iturb
       common/elems/ilnode(ielems,8),icr(ielems,6),mtype(ielems),
     +cmass(iinlet),nn(ing,jng,kng),xcordnp(inodrot,2),iwstep
       common/nodes/coord(inodes,3),coordp(inodes,3),lt(inodes),
     +isurf(6,4),bvel(ifvar,inodes),fsaf(3)
       common/ptles/brr(iptles),btt(iptles),bzz(iptles),mrel(iptles),
     +diam(iptles),dmter(ipdia),vxpi(iptles),vypi(iptles)
       common/crash/mxxo(icrash),isto(icrash),xdx(icrash,3),emp(icrash)
     +,iristep(icrash),mistep(icrash),unvecs(icrash,3)
       common/result/rs(iresult),tetas(iresult),dias(iresult),sumprot,
     +zs(iresult),ielno(iresult),niter(iptles),sdia(icrash),sumpigv
       common/conds/impdat,iendat,ipvdat,iavdat,ierosion,ipddat,iprof
       common/geomet/isigv,ifigv,jsigv,jfigv,ksigv,kfigv,isrot,ifrot
     +,jsrot,jfrot,ksrot,kfrot,radh,radt,rhot,isector,nbigv,nbrot,iwrot
      +,surf_rot,surf_igv,iigv,jigv,kigv,irot,jrot,krot,iin,jin,kin
```

**ip** number of nodes along z axis of rotation
**jp** number of nodes along x axis
**kp** number of nodes along y axis
**b:** inlet domain / **s:** IGV domain / **r:** Rotor domain / **j:** Outlet domain
**ing:** global nodes along z / **jng:** global nodes along x / **kng:** global nodes along y
**ielems** total number of grid elements
**inodes** total number of grid nodes
**iresult** number of integration steps
**impact** number of impacts per particle
**icrash** total number of impacts
**ifvar** number of flow parameters

Table 3-2 *Dinput.dat* containing initial parameters and control variables read by subroutine *IN_PART*

```
PARAMETER FRAGMENTATION IF YES IFRAG 1 IF NO IFRAG 0
1
PARAMETER TURBULENCE IF YES ITURB 1 IF NO ITURB 0
1
PARAMETER LOCAL INJECTION IF YES INJECT 1 IF NO INJECT 0
0
ISECTOR
1
RADUIS HUB
0.055
RADUIS TIP
0.085
NUMBER OF IGV BLADES
7
NUMBER OF ROTOR BLADES
10
TOTAL AIR MASS FLOW
0.8
PAMB (KPA)
100.5250
TYPE OF PARTICLE MATERIAL
   Solid particle
AERODYNAMIC SHAPE FACTOR (eg. 0.21 FOR QUARTZ,PI/6 FOR SPHERICAL PTLE)
  0.21
PTLE. DENSITY / INITIAL PTLE. VELOCITY RATIOS (r,o,z)
  2650.0                0.85      0.85      0.85
TIME STEP   ERROSION TIME
0.000001      10800
IAVDAT/IPVDAT/IENDAT/IMPDAT/ISELECT/IEROSION/IPROF/IPDDAT/IPWDAT
   0     1      0      0       0       1       1     0      0
TERMINATION LIMIT i.e. ZLIMIT (m)
 1.
TERMINATION LIMIT i.e. RLIMIT (m)
 1.
TERMINATION LIMIT i.e. DIALIMIT (m)
 0.5E-06
TERMINATION LIMIT i.e. TIPLIMIT (m)
0.349E-03
OMEGA (rad/s)
-1183.0
NO. OF GROUP OF WALL MATERIAL
 1
 FIRST ELEMENT / LAST ELEMENT / MATL TYPE (eg. ST.STEEL-1, TITANIUM -2,
                                                    AL -3, RENE -4 )
   1                  191988        3
PARTICLE MASS RATE/ANGLE DISP/PIPE DIAM/RADIAL/ANGULAR LOCATION/AXIAL POSITION
      0.0875           3.75     0.003     0.5       -25.7          -0.10639
FIRST ELEMENT FOR PARTICLES DISTRIBUTION
21253
5
1
```

Table 3-3 *geom_rot.dat* containing geometrical data relative to the rotor domain

```
60    39    30     1
107   141    16    24      1    24
       5    -0.3404E-01       0.4384E-01       0.8812E-01
       5    -0.3296E-01       0.4465E-01       0.8812E-01
       5    -0.3205E-01       0.4531E-01       0.8812E-01
       5    -0.3128E-01       0.4584E-01       0.8812E-01
       5    -0.3064E-01       0.4628E-01       0.8812E-01
       5    -0.3009E-01       0.4663E-01       0.8812E-01
       5    -0.2963E-01       0.4693E-01       0.8812E-01
       5    -0.2925E-01       0.4717E-01       0.8812E-01
       5    -0.2893E-01       0.4736E-01       0.8812E-01
       5    -0.2866E-01       0.4753E-01       0.8812E-01
       5    -0.2844E-01       0.4766E-01       0.8812E-01
       5    -0.2825E-01       0.4777E-01       0.8812E-01
       5    -0.2750E-01       0.4821E-01       0.8812E-01
       5    -0.2674E-01       0.4864E-01       0.8812E-01
       5    -0.2597E-01       0.4905E-01       0.8812E-01
       5    -0.2520E-01       0.4945E-01       0.8812E-01
       5    -0.2442E-01       0.4984E-01       0.8812E-01
       5    -0.2363E-01       0.5022E-01       0.8812E-01
       5    -0.2284E-01       0.5058E-01       0.8812E-01
       5    -0.2204E-01       0.5094E-01       0.8812E-01
       5    -0.2189E-01       0.5100E-01       0.8812E-01
       5    -0.2170E-01       0.5108E-01       0.8812E-01
       5    -0.2147E-01       0.5118E-01       0.8812E-01
       5    -0.2120E-01       0.5129E-01       0.8812E-01
       5    -0.2088E-01       0.5142E-01       0.8812E-01
       5    -0.2049E-01       0.5158E-01       0.8812E-01
       5    -0.2002E-01       0.5176E-01       0.8812E-01
       5    -0.1945E-01       0.5198E-01       0.8812E-01
       5    -0.1877E-01       0.5223E-01       0.8812E-01
       5    -0.1794E-01       0.5252E-01       0.8812E-01
       5    -0.1694E-01       0.5285E-01       0.8812E-01
       5    -0.1574E-01       0.5322E-01       0.8812E-01
       5    -0.1429E-01       0.5363E-01       0.8812E-01
       5    -0.1253E-01       0.5407E-01       0.8812E-01
       5    -0.1040E-01       0.5452E-01       0.8812E-01
       2    -0.4062E-01       0.3815E-01       0.8812E-01
       1    -0.3865E-01       0.4014E-01       0.8812E-01
       1    -0.3693E-01       0.4173E-01       0.8812E-01
       1    -0.3545E-01       0.4300E-01       0.8812E-01
       1    -0.3418E-01       0.4401E-01       0.8812E-01
       1    -0.3310E-01       0.4483E-01       0.8812E-01
```

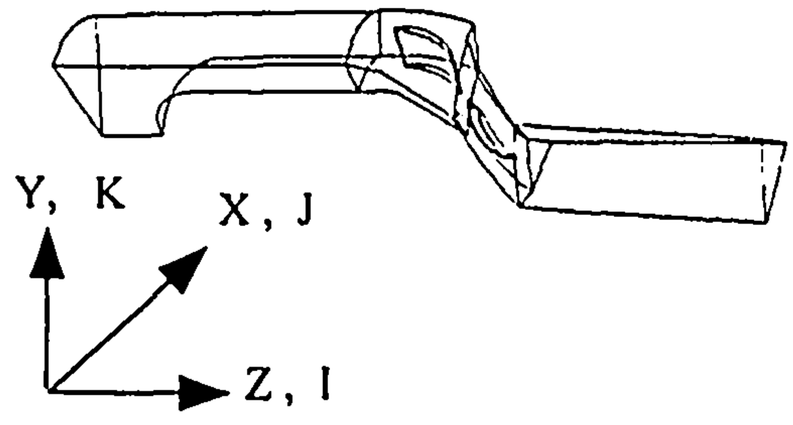


| Number of nodes along z- axis | Number of nodes along x- axis | Number of nodes along y- axis | Co-ordinates type if 1, then Cartesian | | |
|---|---|---|---|---|---|
| 60 | 39 | 30 | 1 | | |
| Start of rotor domain respective to global z- axis nodes | End of rotor domain respective to global z- axis nodes | Start of rotor blade respective to global x- axis nodes | End of rotor blade respective to global x- axis nodes | Start of rotor blade respective to global y- axis nodes | End of rotor blade respective to global y- axis nodes |
| 107 | 141 | 16 | 24 | 1 | 24 |

Table 3-4 *flow_rot.dat* containing flow data relative to the rotor domain

```
IFAR             1
 -9.19580E+01 -9.16519E+01 -9.12780E+01 -9.08206E+01 -9.02579E+01 -8.95636E+01
 -8.87029E+01 -8.76309E+01 -8.62890E+01 -8.45997E+01 -8.24609E+01 -8.12646E+01
.
.
IFAR             2
 -4.07561E+01 -4.14387E+01 -4.22540E+01 -4.32258E+01 -4.43852E+01 -4.57653E+01
 -4.74051E+01 -4.93495E+01 -5.16472E+01 -5.43530E+01 -5.75228E+01 -5.92306E+01
.
.
IFAR             3
 -1.13771E-07 -1.62840E-07 -2.49373E-07 -3.02938E-07 -4.54654E-07 -6.15979E-07
 -8.90527E-07 -1.33776E-06 -1.85353E-06 -2.69619E-06 -3.91286E-06 -4.60322E-06
.
.
IFAR             4
  9.57475E+04  9.69959E+04  9.81315E+04  9.90763E+04  9.97161E+04  1.00066E+05
  1.00247E+05  1.00309E+05  1.00308E+05  1.00282E+05  1.00242E+05  1.00197E+05
.
.
IFAR             5
  2.88982E+02  2.91413E+02  2.91431E+02  2.91413E+02  2.91341E+02  2.91236E+02
  2.91133E+02  2.91055E+02  2.91008E+02  2.90985E+02  2.90977E+02  2.90978E+02
.
.
IFAR             6
  1.12978E+00  1.15082E+00  1.16395E+00  1.17519E+00  1.18268E+00  1.18681E+00
  1.18882E+00  1.18939E+00  1.18928E+00  1.18887E+00  1.18827E+00  1.18761E+00
.
.
IFAR             7
  8.38168E+01  1.23561E+02  1.24919E+02  1.25503E+02  1.25736E+02  1.26001E+02
  1.25579E+02  1.25679E+02  1.25939E+02  1.26116E+02  1.26342E+02  1.26634E+02
.
.
IFAR             8
  6.40888E+06  9.92629E+06  1.00916E+07  1.01686E+07  1.02000E+07  1.02381E+07
  1.01944E+07  1.02149E+07  1.02530E+07  1.02809E+07  1.03212E+07  1.03682E+07
.
.
  2.41830E+06  2.46337E+06  2.18371E+06  1.64172E+06  1.19222E+06  9.65051E+05
  8.88136E+05  8.73500E+05  8.76394E+05  8.80772E+05  8.89024E+05  8.93986E+05
```

IFAR = 1 Flow velocity along y axis
IFAR = 2 Flow velocity along x axis
IFAR = 3 Flow velocity along z axis
IFAR = 4 Static pressure
IFAR = 5 Fluid temperature
IFAR = 6 Fluid density
IFAR = 7 Turbulent kinetic energy
IFAR = 8 Rate of dissipation of kinetic energy

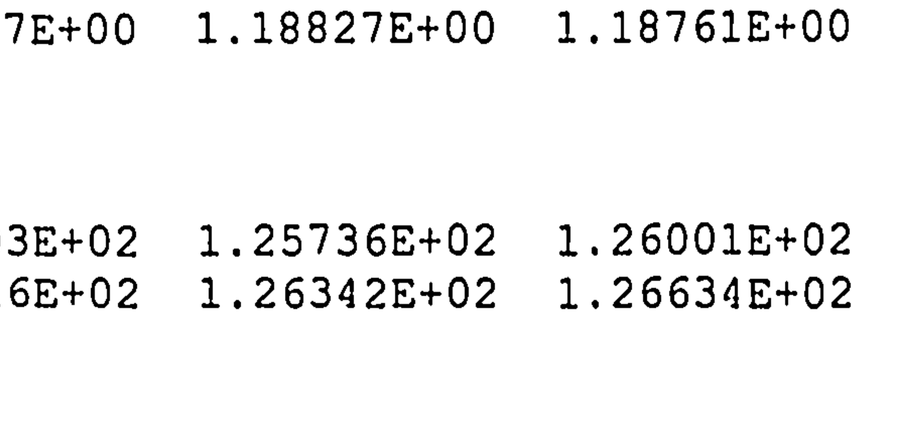

Table 3-5 Concentration profile read by subroutine *DISTRIB*

```
Number of points of particle concentration against fraction of blade height
11
Y-POSITION, CONCENTRATION (g/m^3)
0.0          0.0001
0.0714285    0.019902919
0.1785714    0.123342555
0.285714     0.53261592
0.392857     0.630729311
0.5          0.925069699
0.6071428    1.07224
0.714285     0.637737471
0.8214285    0.145768562
0.9285714    0.024107815
1.           0.0001
```

Table 3-6 Particle diameter distribution dia250.dat as read by subroutine *IN_PART*

```
"Number","of","points","for","diameter",150-300 micron
25
10        0.
20        0.
40        0.
50        0.
60        0.
70        0.
100       0.
112.2     0.
125       0.00578
138.57    0.01156
152.52    0.0289
167.8     0.06358
184.78    0.1156
207.33    0.208
228.2     0.3583
255       0.5375
276.48    0.7
304.32    0.8092
334.96    0.9017
368.69    0.9363
413.68    0.9826
463.4     0.9941
501       1.
600       1.
700       1.
```

Table 3-7 Sample of *ipvdat.dat* containing particle locations, velocities and particle sizes

RESULTS OUTPUT FOR 244.82 MICRON PARTICLE

PARTICLE NO: 15

| Element number. | | | R COORD. | ANGLE(DEG.) | Z COORD | PARTICLE VELOCITIES RADIAL | TANG | AXIAL | DIA |
|---|---|---|---|---|---|---|---|---|---|
| 11591 | | | | | | | | | |
| 21301 | 0 | 0 | 0.056644 | 84.286835 | -0.008731 | -0.019512 | -0.303749 | 37.091492 | 244.818344 |
| 21301 | 0 | 0 | 0.056644 | 84.285912 | -0.008620 | -0.019537 | -0.303756 | 37.091949 | 244.818344 |
| 21301 | 0 | 0 | 0.056644 | 84.285294 | -0.008546 | -0.019553 | -0.303761 | 37.092255 | 244.818344 |
| 21301 | 0 | 0 | 0.056644 | 84.284683 | -0.008471 | -0.019570 | -0.303766 | 37.092560 | 244.818344 |
| 21301 | 0 | 0 | 0.056643 | 84.284065 | -0.008397 | -0.019586 | -0.303771 | 37.092865 | 244.818344 |
| 21301 | 0 | 0 | 0.056643 | 84.283455 | -0.008323 | -0.019602 | -0.303775 | 37.093170 | 244.818344 |
| 21301 | 0 | 0 | 0.056643 | 84.282837 | -0.008249 | -0.019619 | -0.303780 | 37.093475 | 244.818344 |
| 21301 | 0 | 0 | 0.056643 | 84.282227 | -0.008175 | -0.019635 | -0.303785 | 37.093781 | 244.818344 |
| . | | | | | | | | | |
| . | | | | | | | | | |
| . | | | | | | | | | |
| . | | | | | | | | | |
| 72669 | 0 | 0 | 0.056367 | 133.037704 | 0.087932 | 0.043154 | 3.091585 | 39.021790 | 244.818344 |
| 72669 | 0 | 0 | 0.056367 | 133.044006 | 0.088010 | 0.043359 | 3.098219 | 39.022846 | 244.818344 |
| 72669 | 0 | 0 | 0.056367 | 133.050323 | 0.088088 | 0.043566 | 3.104852 | 39.023903 | 244.818344 |
| 72669 | 0 | 2 | 0.056367 | 133.053207 | 0.088124 | 0.043661 | 3.107880 | 39.024387 | 244.818344 |
| 73540 | 1 | 0 | 0.056367 | 133.053207 | 0.088124 | 0.043661 | 69.790192 | 39.024387 | 244.818344 |
| 73540 | 1 | 0 | 0.056367 | 133.124146 | 0.088163 | 0.043828 | 69.793777 | 39.024155 | 244.818344 |
| 73540 | 1 | 0 | 0.056367 | 133.266037 | 0.088241 | 0.044164 | 69.800949 | 39.023689 | 244.818344 |
| 73540 | 1 | 0 | 0.056367 | 133.407928 | 0.088319 | 0.044501 | 69.808121 | 39.023224 | 244.818344 |
| 73540 | 1 | 0 | 0.056367 | 133.549850 | 0.088397 | 0.044839 | 69.815292 | 39.022758 | 244.818344 |
| 73540 | 1 | 0 | 0.056368 | 133.691788 | 0.088475 | 0.045179 | 69.822456 | 39.022293 | 244.818344 |
| 73540 | 1 | 0 | 0.056368 | 133.833740 | 0.088553 | 0.045521 | 69.829620 | 39.021828 | 244.818344 |
| 73540 | 1 | 0 | 0.056368 | 133.975708 | 0.088631 | 0.045864 | 69.836784 | 39.021362 | 244.818344 |
| . | | | | | | | | | |
| . | | | | | | | | | |
| . | | | | | | | | | |
| . | | | | | | | | | |
| 112133 | 1 | 0 | 0.056281 | 156.571655 | 0.119203 | 0.243702 | 69.940239 | 39.154690 | 244.818344 |
| 112133 | 1 | 0 | 0.056282 | 156.714050 | 0.119281 | 0.244245 | 69.933098 | 39.152870 | 244.818344 |
| 112133 | 1 | 0 | 0.056282 | 156.856430 | 0.119359 | 0.244786 | 69.925957 | 39.151051 | 244.818344 |
| 112132 | 1 | 0 | 0.056282 | 156.856430 | 0.119359 | 0.244786 | 69.925957 | 39.151051 | 244.818344 |
| 112132 | 1 | 0 | 0.056282 | 156.927612 | 0.119398 | 0.245134 | 69.921967 | 39.149891 | 244.818344 |
| 112132 | 1 | 0 | 0.056283 | 157.069962 | 0.119477 | 0.245828 | 69.913986 | 39.147568 | 244.818344 |
| 112132 | 1 | 0 | 0.056283 | 157.212311 | 0.119555 | 0.246519 | 69.906013 | 39.145245 | 244.818344 |
| 112132 | 1 | 0 | 0.056284 | 157.283478 | 0.119594 | 0.246762 | 69.899178 | 39.141903 | 244.818344 |
| 112132 | 1 | 0 | 0.056284 | 157.354630 | 0.119633 | 0.246970 | 69.891571 | 39.137939 | 244.818344 |
| 112132 | 1 | 0 | 0.056284 | 157.376495 | 0.119645 | 0.247021 | 69.888977 | 39.136505 | 244.818344 |
| 112132 | 1 | 0 | 0.056284 | 157.376495 | 0.119645 | -2.579909 | 13.794502 | 27.470459 | 243.833740 |
| 112132 | 1 | 0 | 0.056281 | 157.390549 | 0.119673 | -2.530247 | 13.788971 | 27.468929 | 243.833740 |
| 112132 | 1 | 0 | 0.056279 | 157.404572 | 0.119700 | -2.480579 | 13.783524 | 27.467386 | 243.833740 |
| 112132 | 1 | 0 | 0.056276 | 157.418610 | 0.119728 | -2.430906 | 13.778248 | 27.465956 | 243.833740 |
| . | | | | | | | | | |
| . | | | | | | | | | |
| . | | | | | | | | | |
| . | | | | | | | | | |
| 191627 | 1 | 0 | 0.075076 | 178.827591 | 0.302331 | -1.096799 | -3.777641 | 12.067307 | 186.140579 |
| 191627 | 1 | 0 | 0.075074 | 178.821823 | 0.302355 | -1.096245 | -3.780556 | 12.070291 | 186.140579 |
| 191627 | 1 | 0 | 0.075072 | 178.816040 | 0.302379 | -1.095690 | -3.783470 | 12.073274 | 186.140579 |
| 191627 | 1 | 0 | 0.075070 | 178.810257 | 0.302403 | -1.095134 | -3.786383 | 12.076257 | 186.140579 |
| 191627 | 1 | 0 | 0.075067 | 178.804489 | 0.302427 | -1.094578 | -3.789296 | 12.079239 | 186.140579 |
| 191627 | 1 | 0 | 0.075065 | 178.798691 | 0.302452 | -1.094021 | -3.792208 | 12.082220 | 186.140579 |
| 191627 | 1 | 0 | 0.075063 | 178.792908 | 0.302476 | -1.093464 | -3.795120 | 12.085200 | 186.140579 |
| 191627 | 1 | 0 | 0.075061 | 178.787125 | 0.302500 | -1.092906 | -3.798031 | 12.088181 | 186.140579 |
| 191627 | 1 | 0 | 0.075059 | 178.781311 | 0.302524 | -1.092348 | -3.800941 | 12.091160 | 186.140579 |

11591 : number of integration steps
21301 : initial particle element
191627 : final particle element
Second integer : indicator of stage interface, if equal "1" a particle is crossing a stage interface
Third integer : indicator of periodic boundary, if equal "2 "a particle is crossing a periodic surface

Table 3-8 Sample of *impdat.dat* file showing the locations of impacts, particle velocities and rate of erosion

Results output for 242.64 micron particle

info:particle-wall interaction

| ptle. no. | elemnt. no. | (impact location) r coord | ang(deg.) | z coord | impgmnt. ang(deg.) | impgmnt. vel. | rebound vel. | erosion mg/g |
|---|---|---|---|---|---|---|---|---|
| 1 | 101188 | 0.05699 | 140.60651 | 0.10435 | 19.25152 | 78.81715 | 37.87236 | 1.36037E-01 |

Results output for 244.91 micron particle

info:particle-wall interaction

| ptle. no. | elemnt. no. | (impact location) r coord | ang(deg.) | z coord | impgmnt. ang(deg.) | impgmnt. vel. | rebound vel. | erosion mg/g |
|---|---|---|---|---|---|---|---|---|
| 2 | 55997 | 0.05578 | 113.08821 | 0.07555 | 35.80962 | 21.17725 | 7.68839 | 4.39011E-03 |

Results output for 244.91 micron particle

info:particle-wall interaction

| ptle. no. | elemnt. no. | (impact location) r coord | ang(deg.) | z coord | impgmnt. ang(deg.) | impgmnt. vel. | rebound vel. | erosion mg/g |
|---|---|---|---|---|---|---|---|---|
| 2 | 98072 | 0.06288 | 136.03796 | 0.10131 | 24.05821 | 84.74444 | 39.33209 | 2.12826E-01 |

Results output for 238.61 micron particle

info:particle-wall interaction

| ptle. no. | elemnt. no. | (impact location) r coord | ang(deg.) | z coord | impgmnt. ang(deg.) | impgmnt. vel. | rebound vel. | erosion mg/g |
|---|---|---|---|---|---|---|---|---|
| 3 | 49879 | 0.05566 | 103.21839 | 0.06340 | 28.68135 | 19.31173 | 8.03327 | 3.10644E-03 |

Table 4-1 Erosion rate, mass degradation and blade geometry changes due seeding of narrow bandwidth sand particle (150-300micron) at low concentration

```
**************************************************
                    IGV EROSION
**************************************************
                    Time one Second

IGV mass                          =   2.0290660E-02kg
Inlet IGV sector area             =   1.8840001E-03m2
Mass of particles through IGV =   1.2367335E-05kg/s
Surface particles density         =   6.5644025E-07kg/cm2
Mass of particles through IGV =   1.2367335E-05kg
Erosion IGV blade                 =   2.5295813E-04mg
Erosion rate IGV blade            =   2.0453731E-02gm/kg
Reduction in IGV blade            =   1.2466727E-06%

                    Time one Hour

Mass of particles through IGV =   1.2367335E-05kg/s
Surface particles density         =   2.3631847E-03kg/cm2
Mass of particles through IGV =   4.4522408E-02kg
Erosion IGV blade                 =   0.9106494    mg
Erosion rate IGV blade            =   2.0453731E-02mg/g
Reduction in IGV blade            =   4.4880225E-03%

**************************************************
                    ROTOR EROSION
**************************************************
                    Time one second

Rotor mass                        =   1.1197668E-02kg
Inlet Rotor sector area           =   1.3188001E-03m2
Surface particles density         =   6.5644025E-07kg/cm2
Mass particles through Rotor      =   8.6571354E-06kg
Erosion rotor blade               =   2.5604351E-03mg
Erosion rate rotor blade          =   0.2957601    mg/g
Reduction in rotor blade          =   2.2865790E-05%

                    Time one Hour

Surface particles density         =   2.3631849E-03kg/cm2
Mass particles through rotor      =   3.1165686E-02kg
Erosion rotor blade               =   9.217566     mg
Reduction in rotor blade          =   8.2316846E-02%

**************************************************
    Changes in geometry after     10800 seconds
**************************************************
Mean reduction in IGV chord       =   1.0860146E-03%
Tip reduction in IGV chord        =   1.3796901E-03%
Mean reduction in Rotor chord     =   0.1452322    %
Tip reduction in Rotor chord      =   0.3426101    %
Increase in rotor tip clearance   =   2.510715     %
Increase in rotor tip clearance   =   2.538530     %
```

Table 4-2 Erosion rate, mass degradation and blade geometry changes due seeding of narrow bandwidth sand particle (150-300micron) at mean concentration

```
**************************************************
                IGV EROSION
**************************************************
                Time one Second

 IGV mass                        =   2.0290660E-02kg
 Inlet IGV sector area           =   1.8840001E-03m2
 Mass of particles through IGV =   4.3508211E-05kg/s
 Surface particles density       =   2.3093528E-06kg/cm2
 Mass of particles through IGV =   4.3508211E-05kg
 Erosion IGV blade               =   8.4177620E-04mg
 Erosion rate IGV blade          =   1.9347526E-02gm/kg
 Reduction in IGV blade          =   4.1485896E-06%

                Time one Hour

 Mass of particles through IGV =   4.3508211E-05kg/s
 Surface particles density       =   8.3136698E-03kg/cm2
 Mass of particles through IGV =   0.1566296    kg
 Erosion IGV blade               =   3.030395     mg
 Erosion rate IGV blade          =   1.9347526E-02mg/g
 Reduction in IGV blade          =   1.4934923E-02%

**************************************************
                ROTOR EROSION
**************************************************
                Time one second

 Rotor mass                      =   1.1197668E-02kg
 Inlet Rotor sector area         =   1.3188001E-03m2
 Surface particles density       =   2.3093528E-06kg/cm2
 Mass particles through Rotor  =   3.0455749E-05kg
 Erosion rotor blade             =   8.6926119E-03mg
 Erosion rate rotor blade        =   0.2854178    mg/g
 Reduction in rotor blade        =   7.7628771E-05%

                Time one Hour

 Surface particles density       =   8.3136698E-03kg/cm2
 Mass particles through rotor  =   0.1096407    kg
 Erosion rotor blade             =  31.29340      mg
 Reduction in rotor blade        =   0.2794636    %
**************************************************
    Changes in geometry after     9000 seconds
**************************************************

 Mean reduction in IGV chord     =   2.5874383E-03%
 Tip reduction in IGV chord      =   2.7560247E-03%
 Mean reduction in Rotor chord   =   0.3686142    %
 Tip reduction in Rotor chord    =   0.7338540    %
 Increase in rotor tip clearance =   6.767621     %
```

Table 4-3 Erosion rate, mass degradation and blade geometry changes due to seeding of MIL-E5007E sand particle at high concentration

```
**************************************************
                    IGV EROSION
**************************************************
                  Time one Second

 IGV mass                          =   2.0290660E-02kg
 Inlet IGV sector area             =   1.8840001E-03m2
 Mass of particles through IGV =   7.7619508E-05kg/s
 Surface particles density         =   4.1199310E-06kg/cm2
 Mass of particles through IGV =   7.7619508E-05kg
 Erosion IGV blade                 =   2.5369362E-03mg
 Erosion rate IGV blade            =   3.2684263E-02gm/kg
 Reduction in IGV blade            =   1.2502976E-05%

                  Time one Hour

 Mass of particles through IGV =   7.7619508E-05kg/s
 Surface particles density         =   1.4831752E-02kg/cm2
 Mass of particles through IGV =   0.2794302    kg
 Erosion IGV blade                 =   9.132972    mg
 Erosion rate IGV blade            =   3.2684263E-02mg/g
 Reduction in IGV blade            =   4.5010719E-02%
**************************************************
                   ROTOR EROSION
**************************************************
                  Time one second

 Rotor mass                        =   1.1197668E-02kg
 Inlet Rotor sector area           =   1.3188001E-03m2
 Surface particles density         =   4.1199310E-06kg/cm2
 Mass particles through Rotor  =   5.4333657E-05kg
 Erosion rotor blade               =   2.2266423E-02mg
 Erosion rate rotor blade          =   0.4098091    mg/g
 Reduction in rotor blade          =   1.9884876E-04%

                  Time one Hour

 Surface particles density         =   1.4831752E-02kg/cm2
 Mass particles through rotor  =   0.1956012    kg
 Erosion rotor blade               =  80.15913      mg
 Reduction in rotor blade          =   0.7158555    %
**************************************************
    Changes in geometry after      8100 seconds
**************************************************
 Mean reduction in IGV chord       =  3.0789657E-02%
 Tip reduction in IGV chord        =  6.4975090E-02%
 Mean reduction in Rotor chord     =  0.9339241    %
 Tip reduction in Rotor chord      =  1.737934     %
 Increase in rotor tip clearance   = 16.41495      %
```

Table 6-1 Aerodynamic performance program *FANCHAR* input data

Atm pressure (Pa) / Atm temperature (K) / Nr of iterations / Nr of integrations
1.013E5 288. 900 100

RPM / Upper reduced incidence / Lower reduced incidence /
10870. 0.6 -0.6

IGV blades / Rotor blades / Hub radius (m) / Tip radius (m) /
7 10 0.0555 0.084613

Hub IGV chord (m) / Tip IGV chord (m) / Hub IGV thickness / Tip IGV thickness / Trailing IGV radius (m) /
0.0572 0.0572 0.1 0.1 0.00134

Hub IGV camber (deg) / Tip IGV camber (deg) / Hub IGV stagger (deg) / Tip IGV stagger (deg) /
54.76 54.76 27.36 27.36

Hub inlet angle IGV(deg) / Tip inlet angle IGV (deg) / Hub outlet angle IGV (deg) / Tip outlet angle IGV (deg) /
0. 0. 54.76 54.76

Hub rotor chord (m) / Tip rotor chord (m) / Mean rotor chord (m) / Hub blade thick / Tip blade thick /
0.04308 0.04557 0.04424 0.10 0.10

Hub rotor camber (deg) / Tip rotor camber (deg) / Mean rotor camber (deg) / Hub rotor stagger (deg) / Tip rotor stagger (deg) / Mean rotor stagger (deg) /
39.47 34.90 37.12 48.0 55.25
51.71

Hub inlet rotor angle (deg) / Tip rotor inlet angle (deg) / Mean rotor inlet angle (deg) / Hub rotor outlet angle (deg) / Tip rotor outlet angle (deg) / Mean rotor outlet angle (deg) /
67.72 72.69 70.27 28.25
37.79 33.15

Hub blade radius (m) / Tip blade radius (m) / Mean blade radius (m) / Blade trailing edge radius (m) /
0.0638 0.076 0.0695 0.00052

Sand equivalent rough (m) / Stage gap (m) / Tip clearance (m) /
2.96e-6 0.015 0.0004535

IDEGRAD / Percent red chord % / Percent incr clear % / Increase in rough % / CASD /
1 3.8 65.72 0. 0.4

*Note:* If the unit of a parameter is not specified, this parameter is dimensionless

# FLOWCHARTS

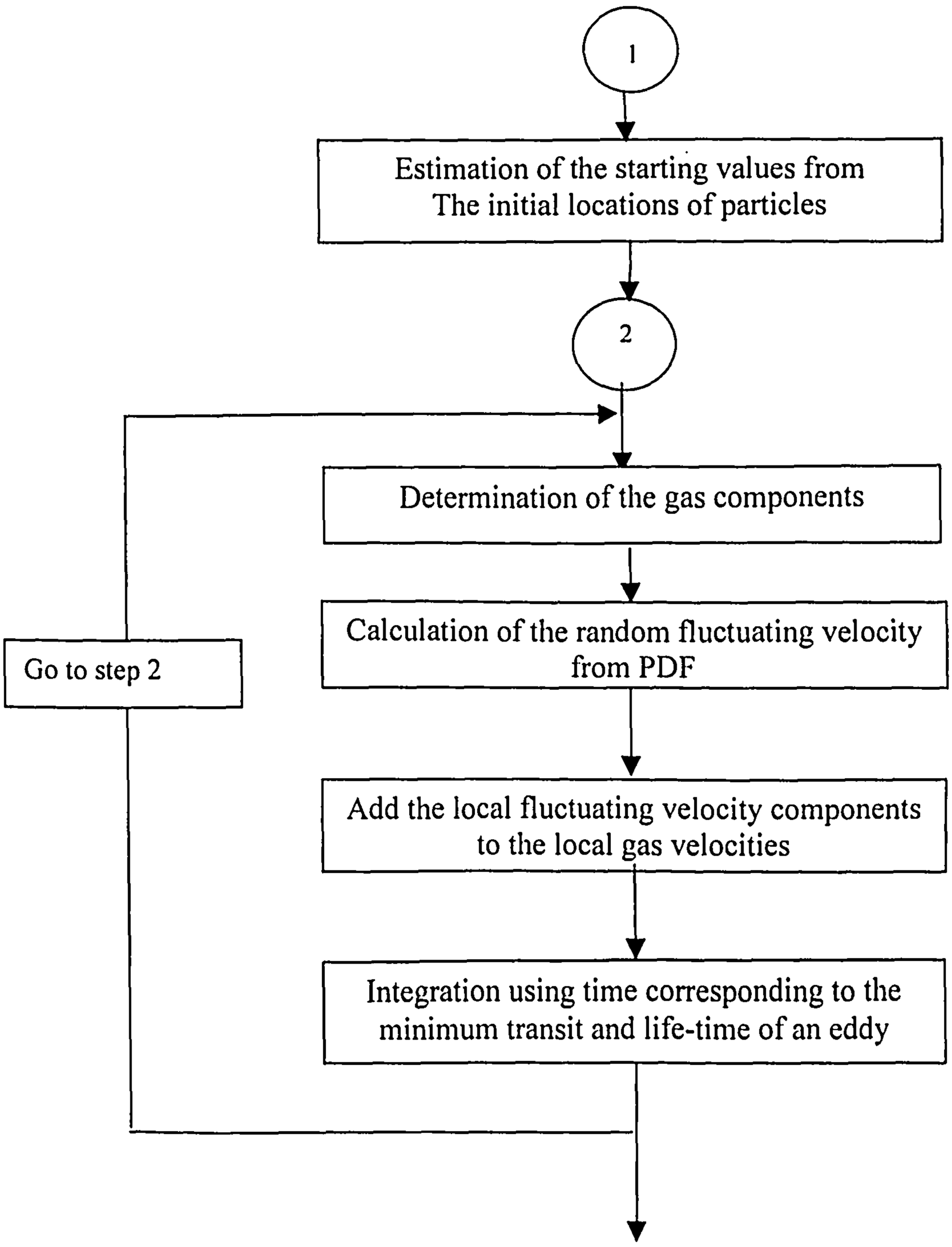


F3-1 Lagrangian method for particle trajectory in a turbulent flow

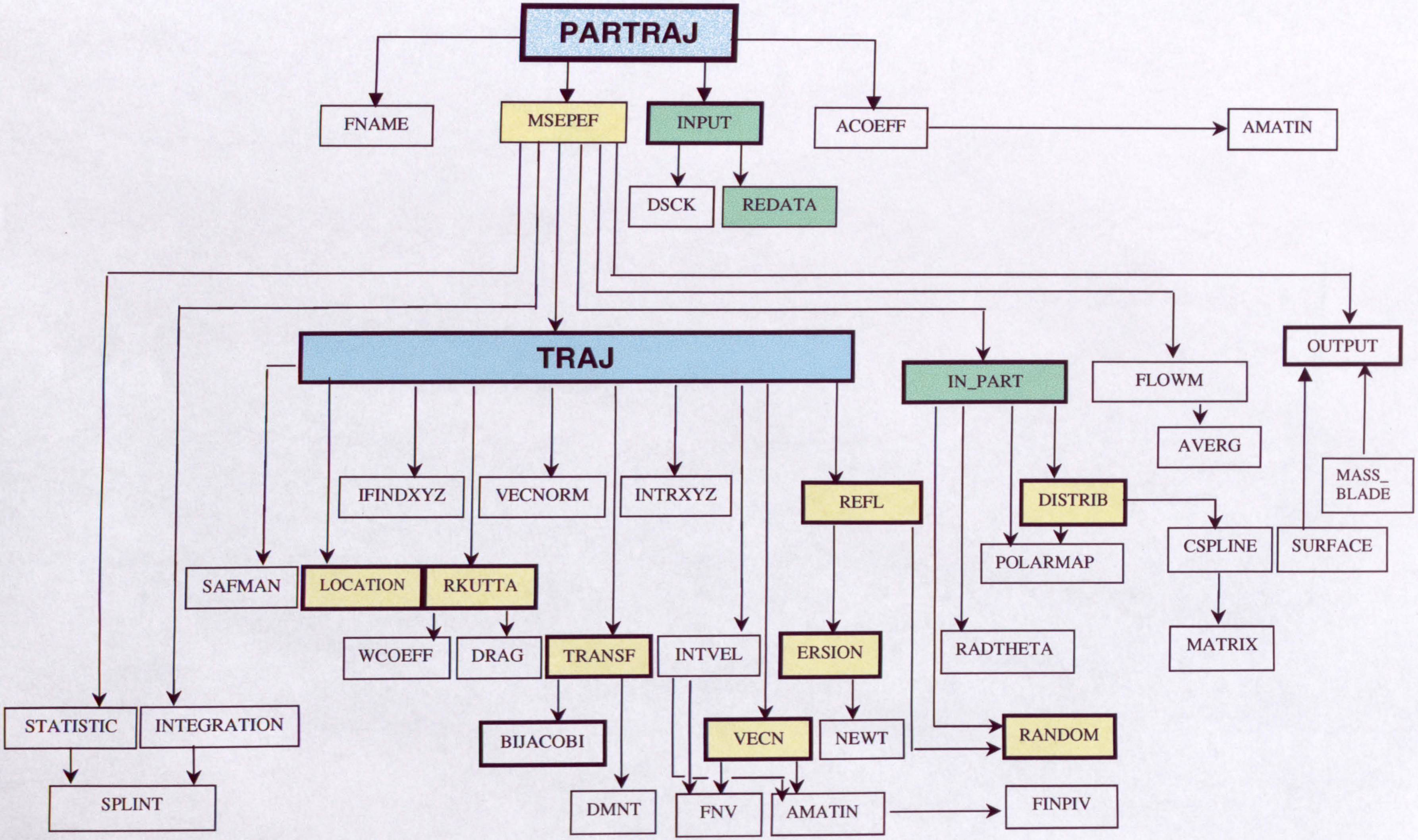


F3-2 Flow-diagram of the trajectory program *PARTRAJ*

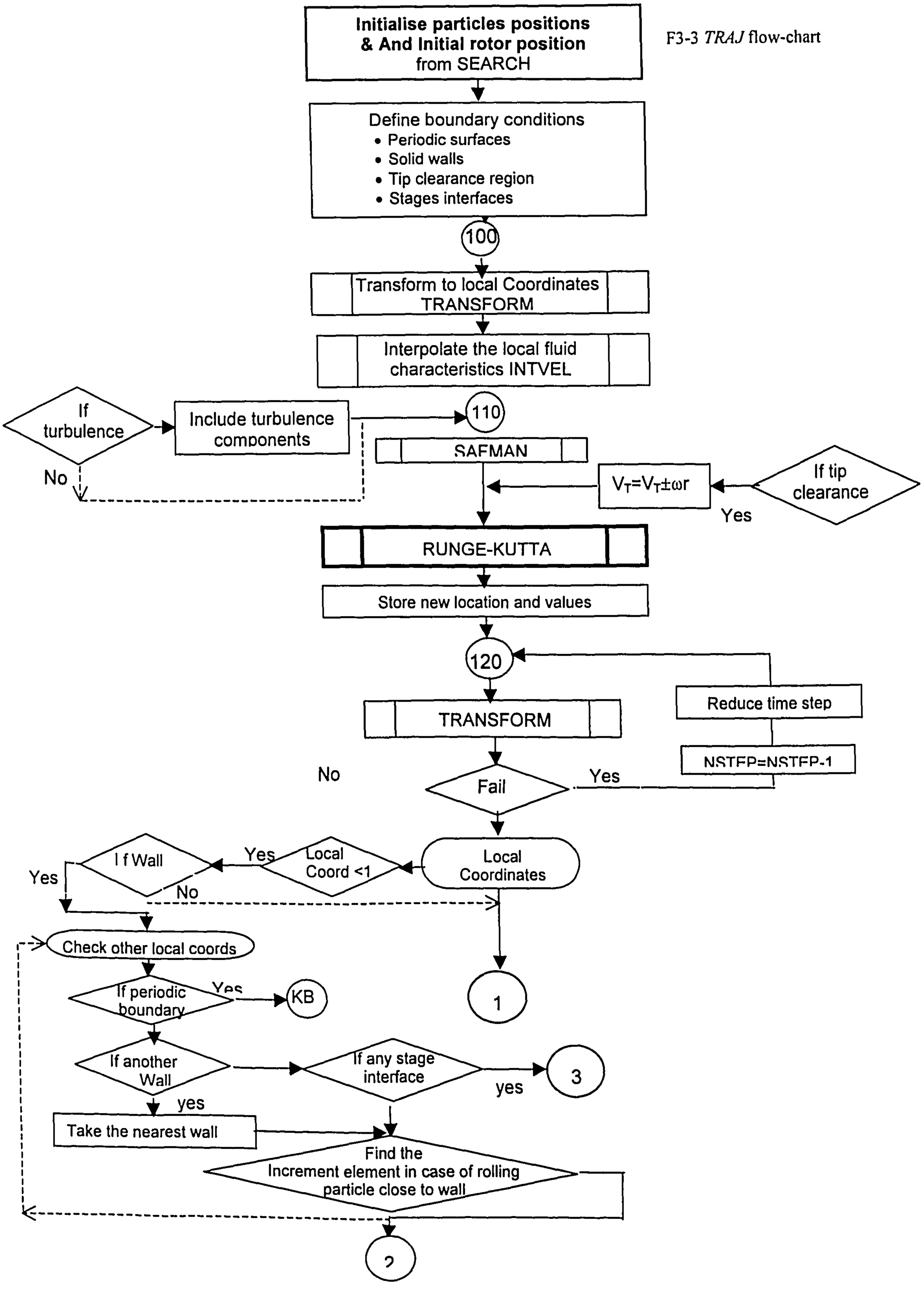


F3-3 *TRAJ* flow-chart

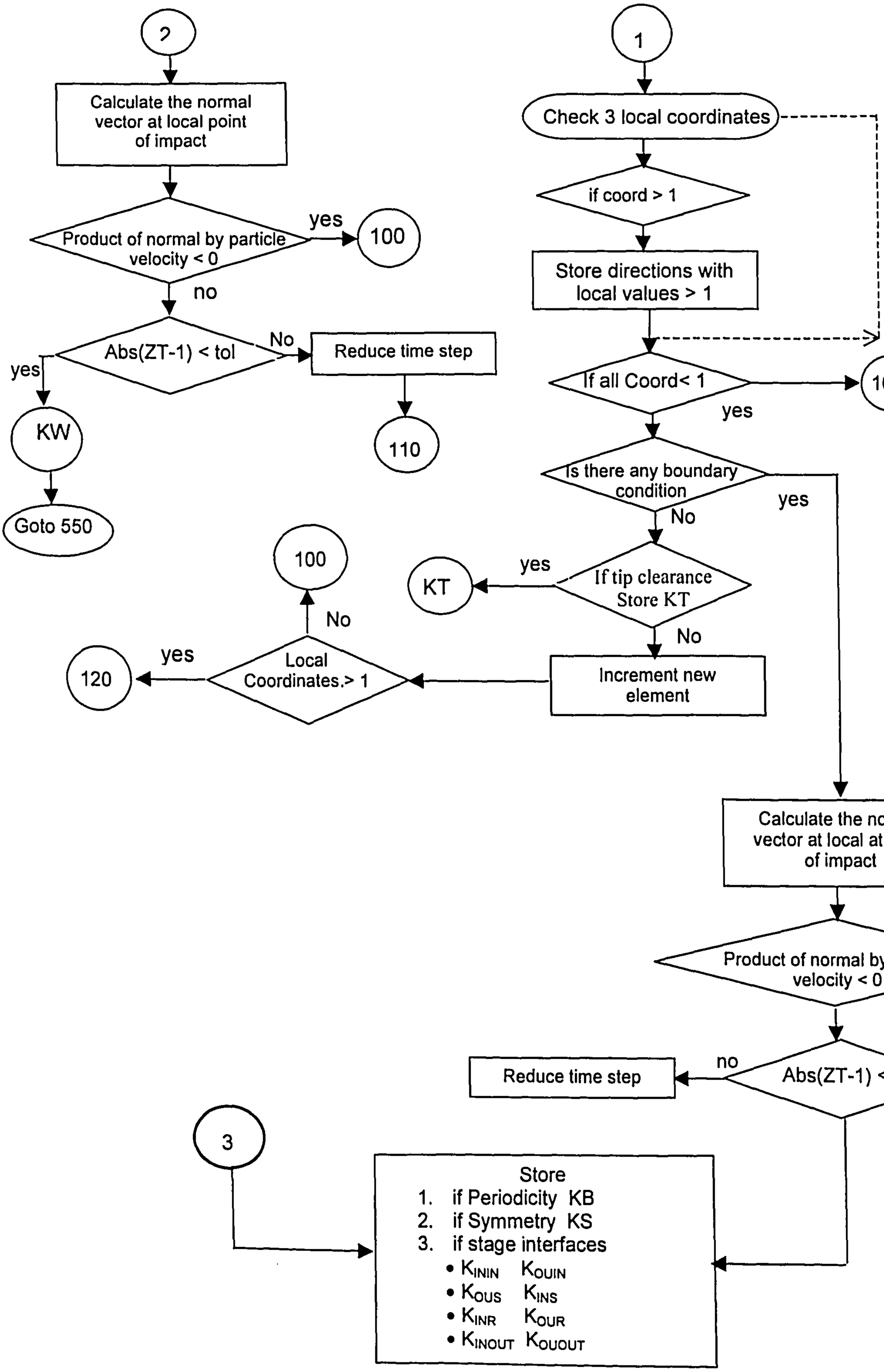
2
Calculate the normal vector at local point of impact
Product of normal by particle velocity < 0
yes
100
no
Abs(ZT-1) < tol
No
Reduce time step
yes
KW
Goto 550
110
1
Check 3 local coordinates
if coord > 1
Store directions with local values > 1
If all Coord< 1
100
yes
Is there any boundary condition
yes
No
If tip clearance Store KT
yes
KT
No
Increment new element
Local Coordinates.> 1
yes
120
No
100
Calculate the normal vector at local at point of impact
Product of normal by particle velocity < 0
Abs(ZT-1) < tol
no
Reduce time step
yes
KW
Goto 550
3
Store
1. if Periodicity KB
2. if Symmetry KS
3. if stage interfaces
• $K_{ININ}$ $K_{OUIN}$
• $K_{OUS}$ $K_{INS}$
• $K_{INR}$ $K_{OUR}$
• $K_{INOUT}$ $K_{OUOUT}$

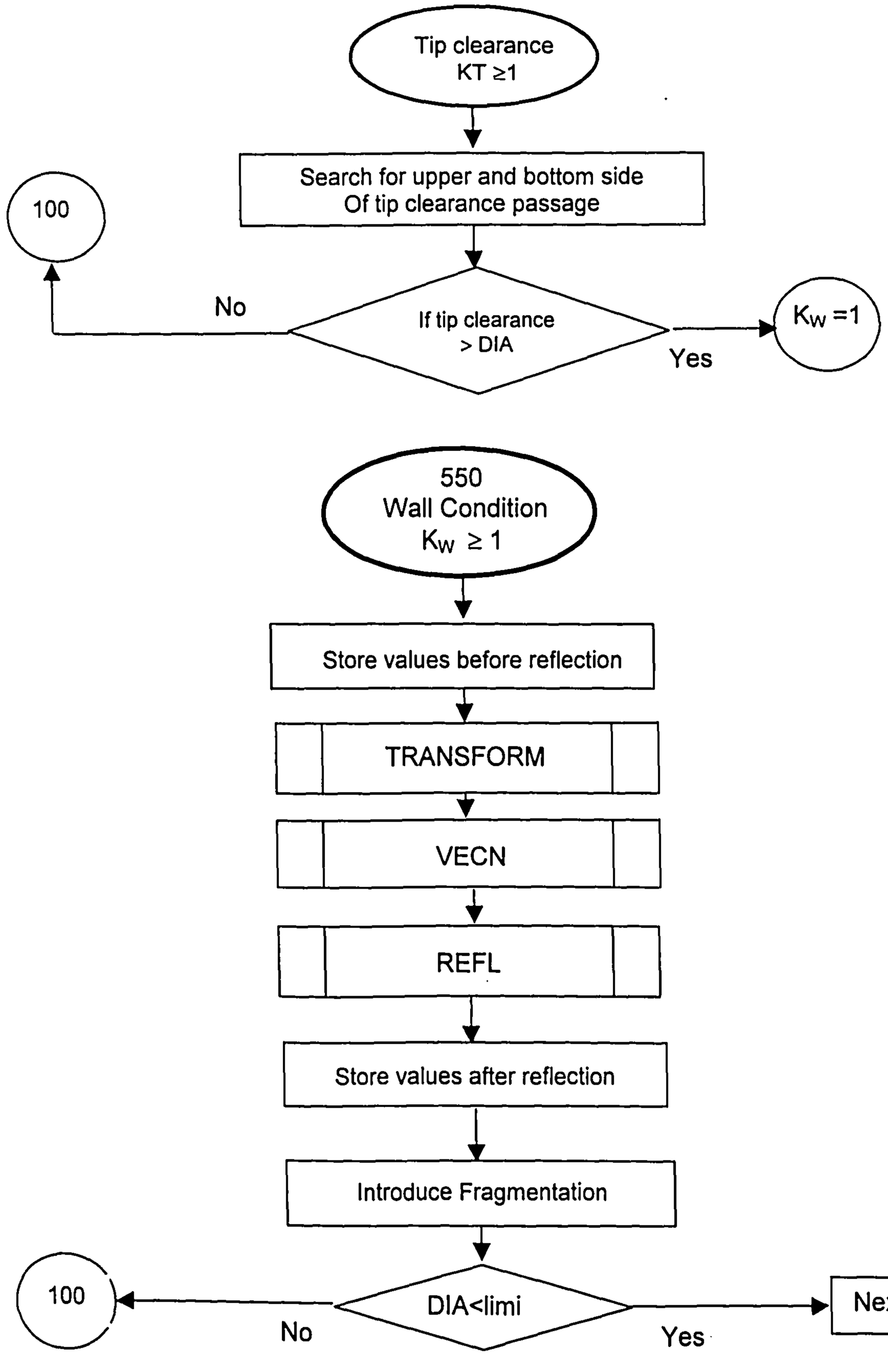
Tip clearance
KT ≥1
Search for upper and bottom side
Of tip clearance passage
If tip clearance
> DIA
No
100
Yes
Kw =1
550
Wall Condition
Kw ≥ 1
Store values before reflection
TRANSFORM
VECN
REFL
Store values after reflection
Introduce Fragmentation
DIA<limi
No
100
Yes
Next particle

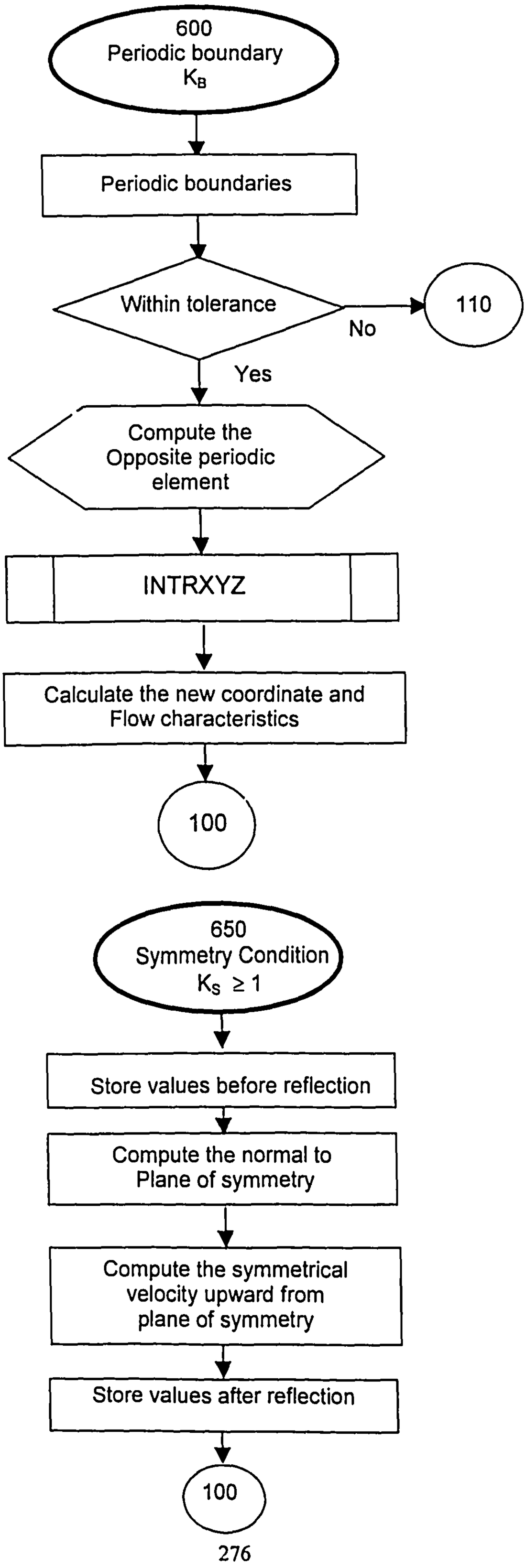
600
Periodic boundary
$K_B$
Periodic boundaries
Within tolerance
No
110
Yes
Compute the
Opposite periodic
element
INTRXYZ
Calculate the new coordinate and
Flow characteristics
100
650
Symmetry Condition
$K_S \geq 1$
Store values before reflection
Compute the normal to
Plane of symmetry
Compute the symmetrical
velocity upward from
plane of symmetry
Store values after reflection
100
276

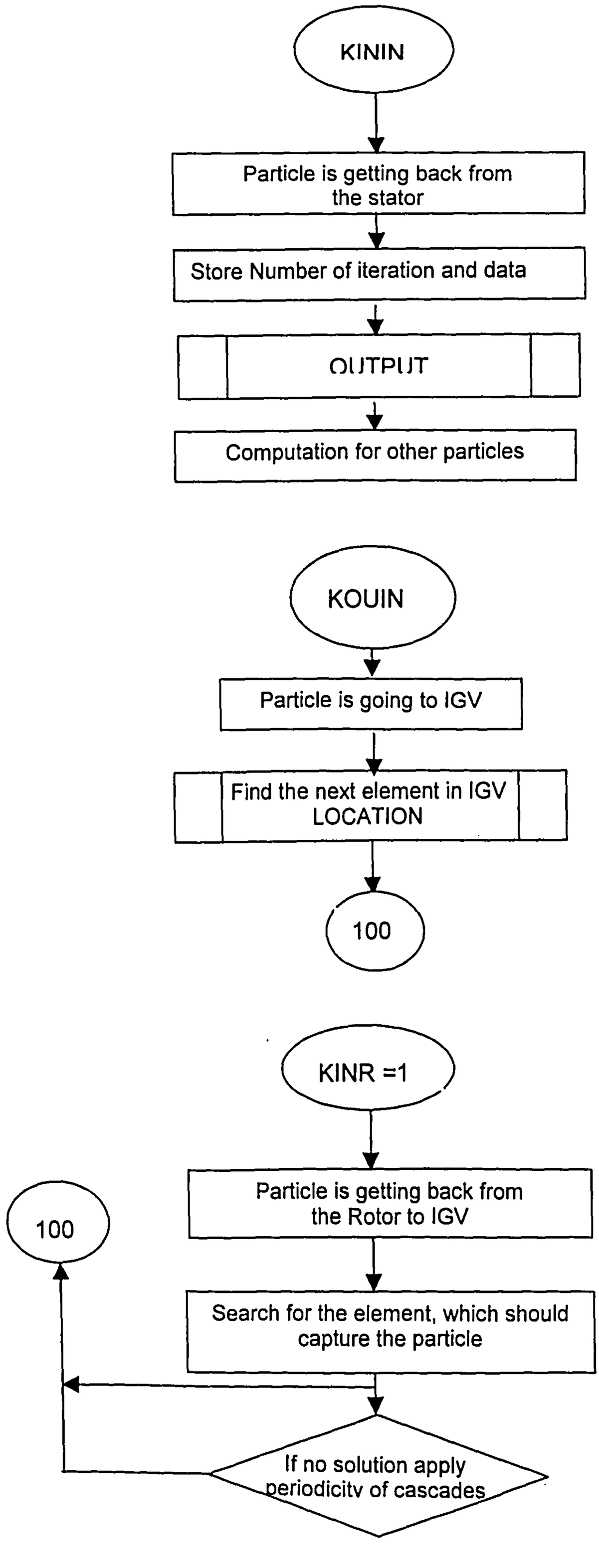
KININ
Particle is getting back from the stator
Store Number of iteration and data
OUTPUT
Computation for other particles
KOUIN
Particle is going to IGV
Find the next element in IGV LOCATION
100
KINR =1
Particle is getting back from the Rotor to IGV
100
Search for the element, which should capture the particle
If no solution apply periodicitv of cascades

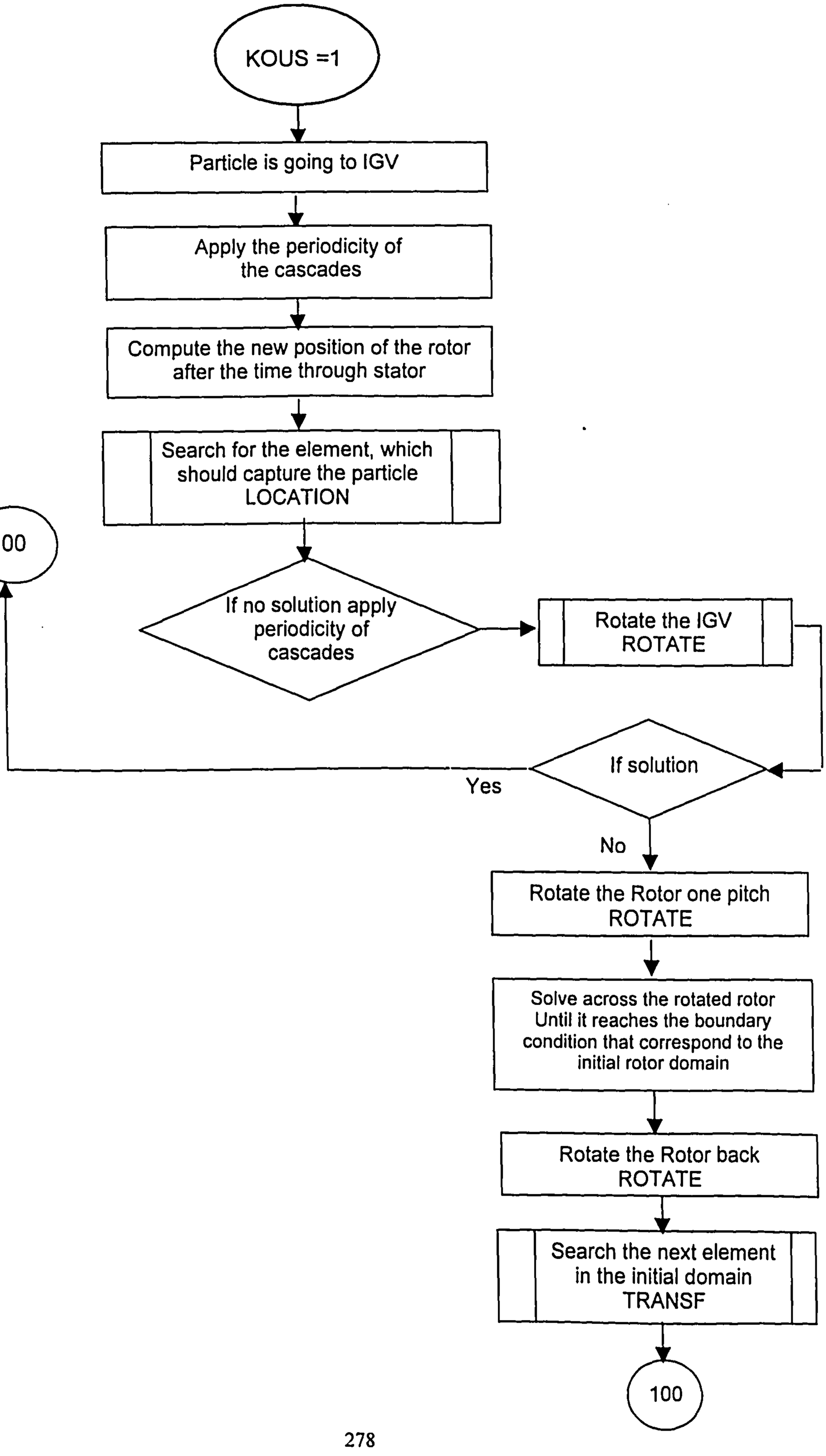
KOUS =1
Particle is going to IGV
Apply the periodicity of the cascades
Compute the new position of the rotor after the time through stator
Search for the element, which should capture the particle LOCATION
100
If no solution apply periodicity of cascades
Rotate the IGV ROTATE
If solution
Yes
No
Rotate the Rotor one pitch ROTATE
Solve across the rotated rotor Until it reaches the boundary condition that correspond to the initial rotor domain
Rotate the Rotor back ROTATE
Search the next element in the initial domain TRANSF
100

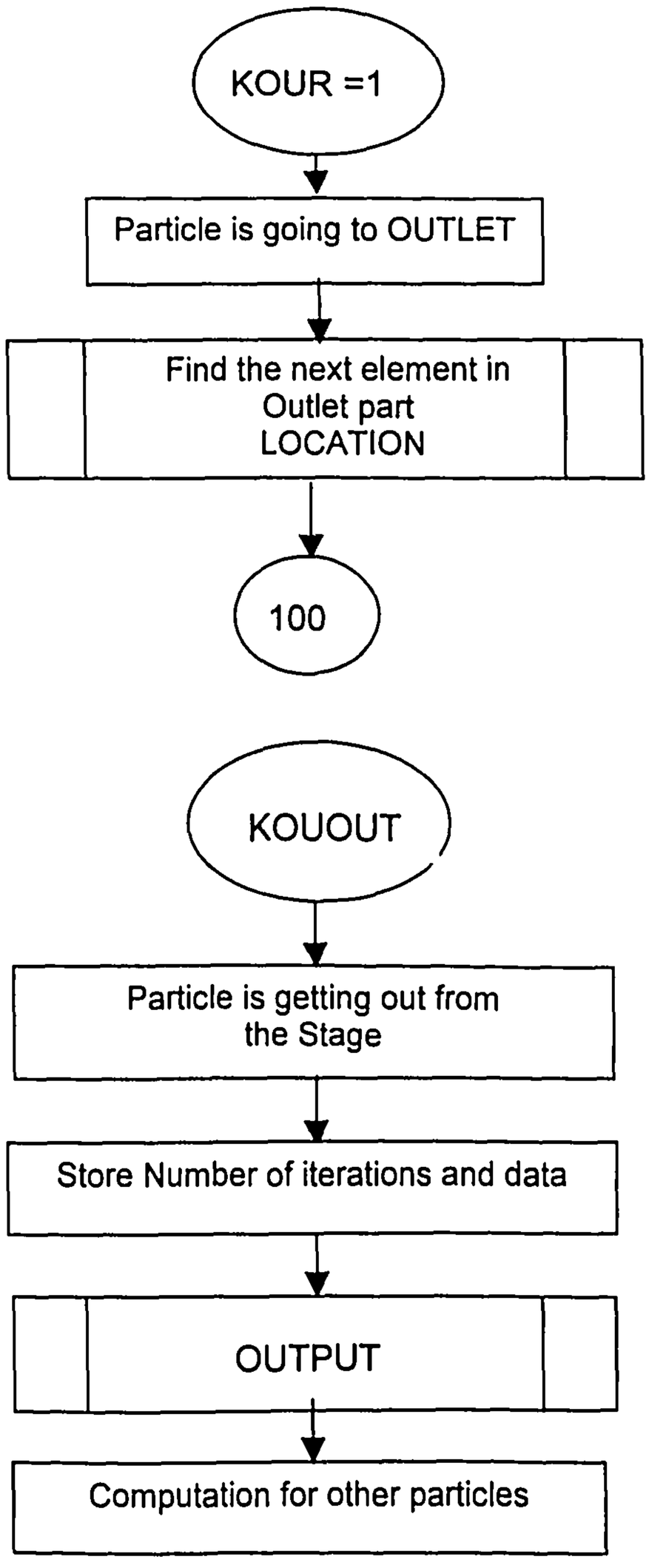
KOUR =1
Particle is going to OUTLET
Find the next element in
Outlet part
LOCATION
100
KOUOUT
Particle is getting out from
the Stage
Store Number of iterations and data
OUTPUT
Computation for other particles

F6-1 Flowchart of the mean line method for predicting axial fan aerodynamic characteristics

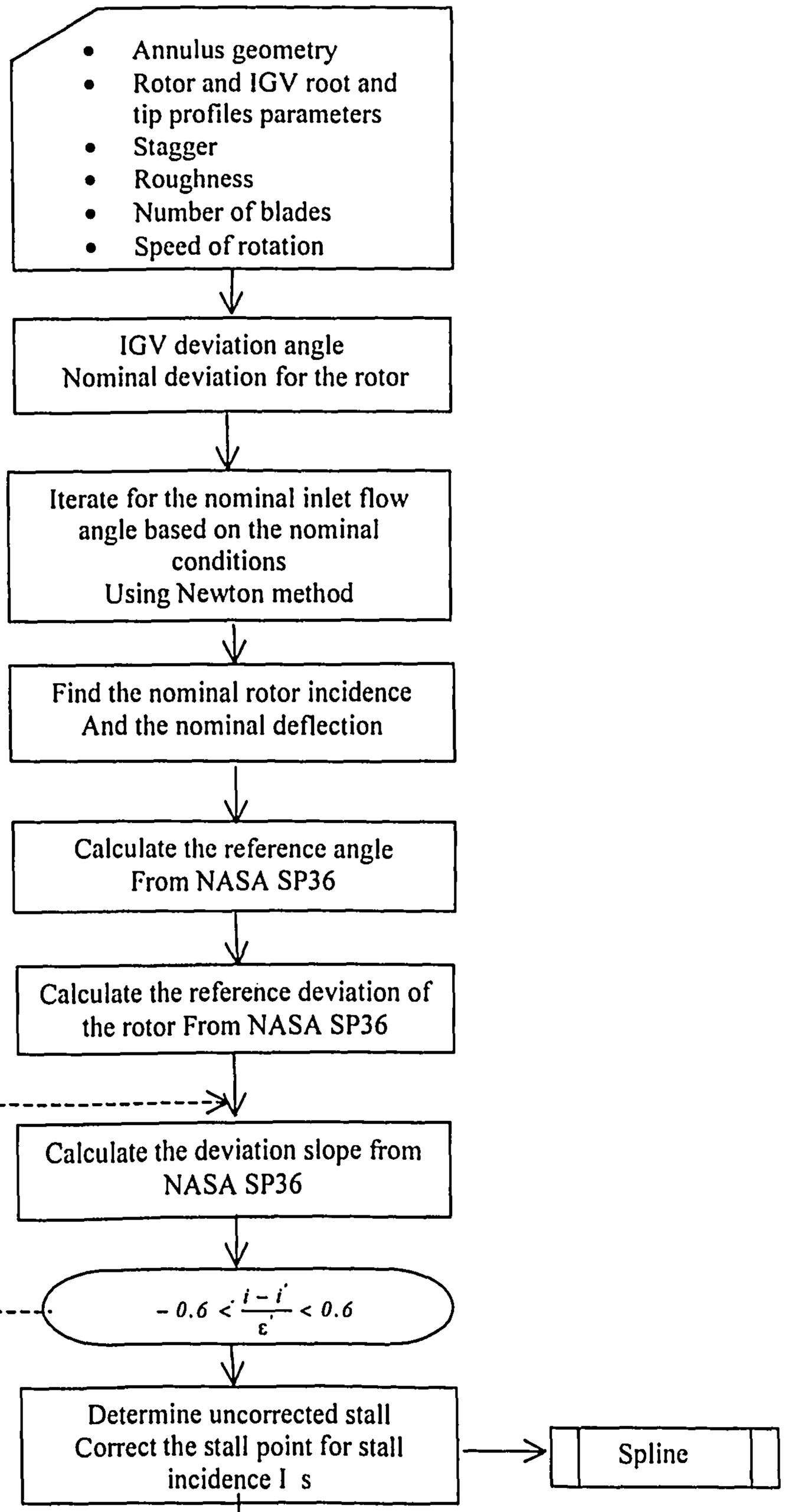

**Method I**
**Howell And Bonham**

$$-0.6 < \frac{i - i'}{\varepsilon'} < 0.6$$

Evaluate off design rotor outlet angle from deviation slope

Ainley

Calculate IGV losses
Calculate Rotor losses
Calculate reference efficiency

Howell-Stewart

Locate the the maximum efficiency
Including Reynolds correction
and tip clearance

Evaluate the stalling mass

$$-0.6 < \frac{i - i'}{\varepsilon'} < 0.6$$

IF mass < mass*

no

Evaluate off design rotor outlet angle from deviation slope

Evaluate off design characteristics from Bonham curves

$$\eta / \eta_{MAX} = \frac{\left(\Delta H_t / V_a\right)}{\left(\Delta H_t / V_a\right)_{MAX}}$$

Integrate axial velocity for the mass flow rate

Calculate the off design efficiency and The pressure rise coefficient

Print mass flow, flow coefficent, efficiency and pressure rise coefficient

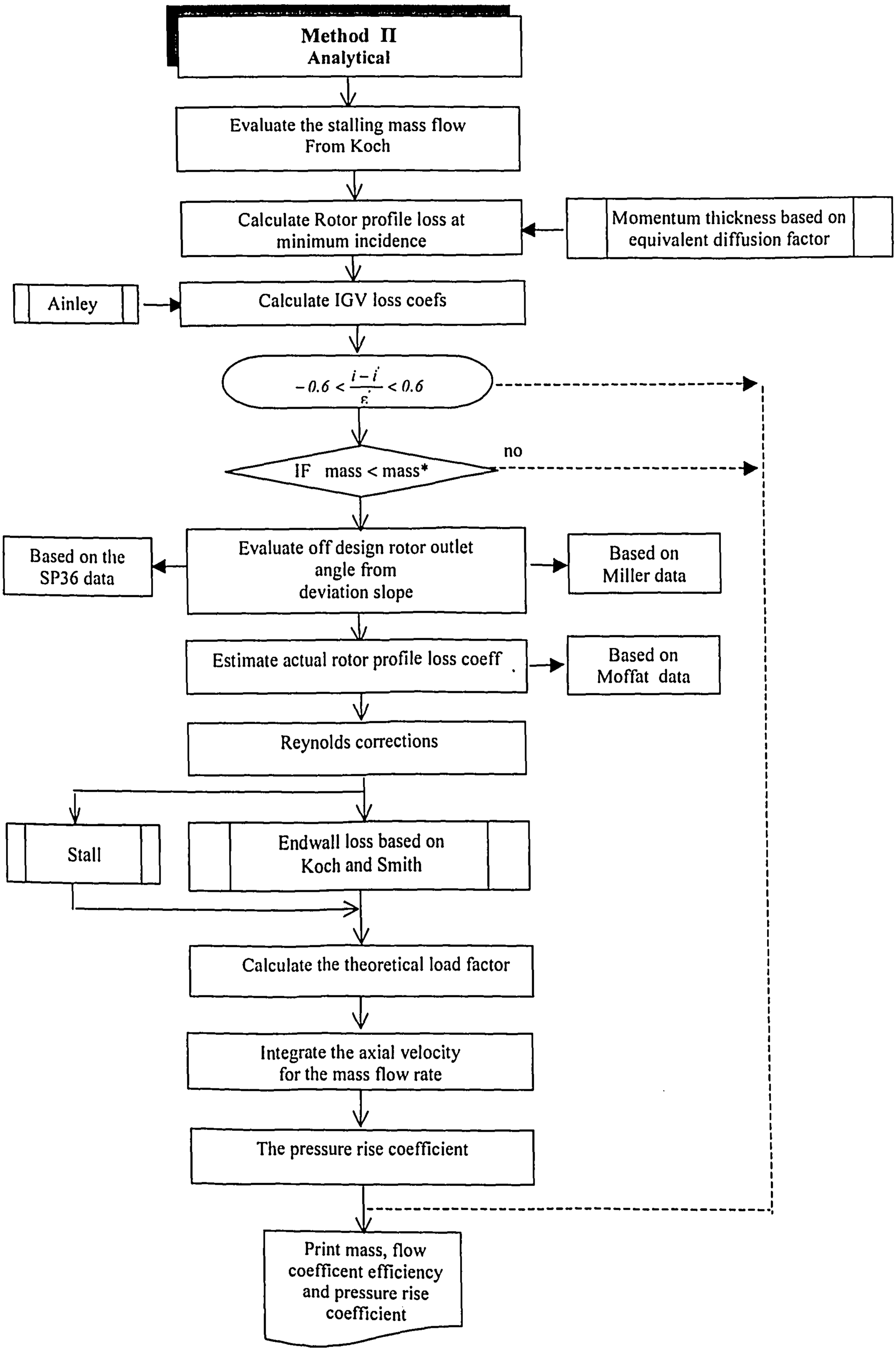
Method II
Analytical
Evaluate the stalling mass flow
From Koch
Calculate Rotor profile loss at
minimum incidence
Momentum thickness based on
equivalent diffusion factor
Ainley
Calculate IGV loss coefs
$-0.6 < \frac{i-i^*}{\varepsilon} < 0.6$
IF mass < mass*
no
Based on the
SP36 data
Evaluate off design rotor outlet
angle from
deviation slope
Based on
Miller data
Estimate actual rotor profile loss coeff
Based on
Moffat data
Reynolds corrections
Stall
Endwall loss based on
Koch and Smith
Calculate the theoretical load factor
Integrate the axial velocity
for the mass flow rate
The pressure rise coefficient
Print mass, flow
coefficent efficiency
and pressure rise
coefficient

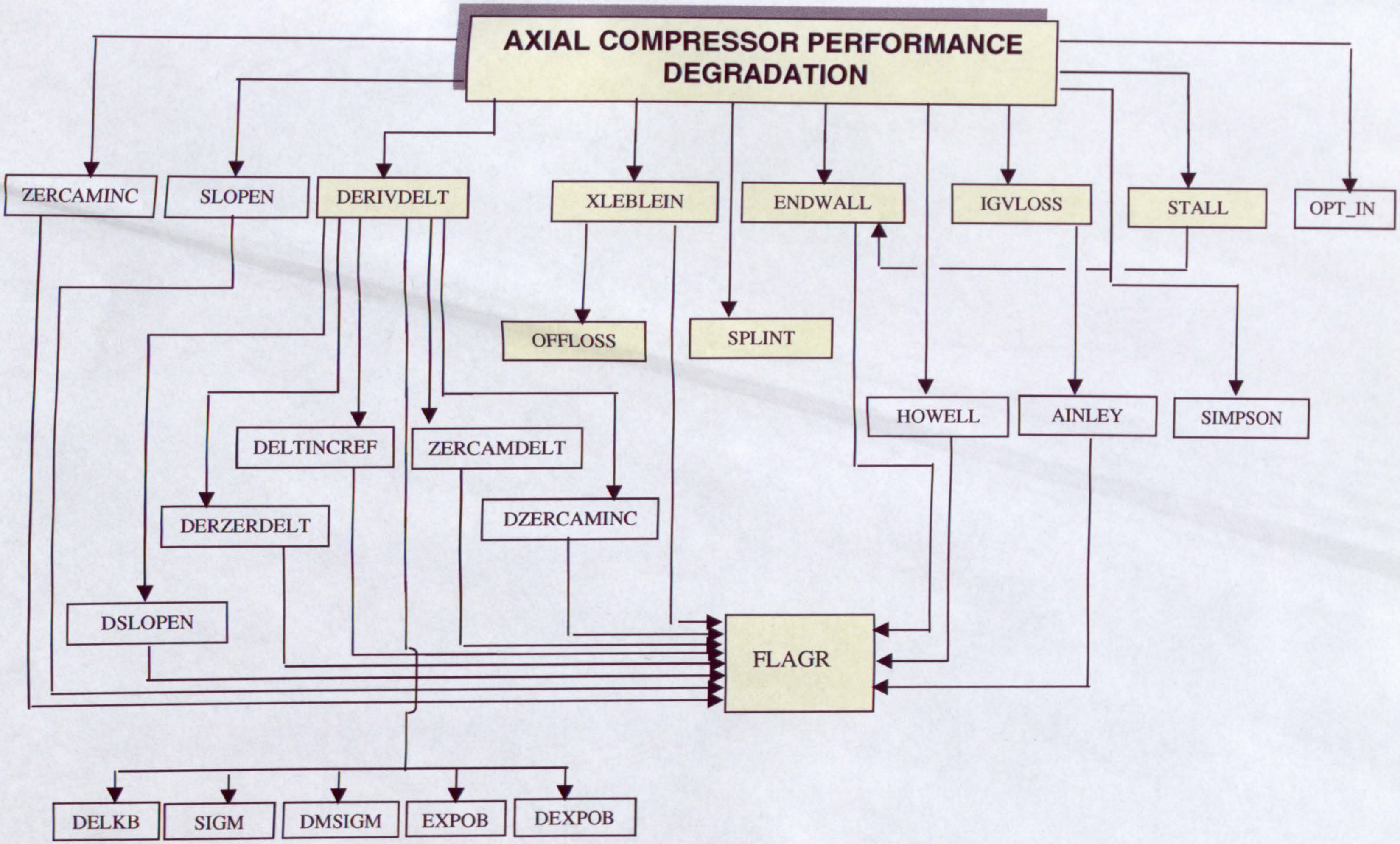


F6-2 Axial fan performance degradation *FANCHAR* Flow-diagram